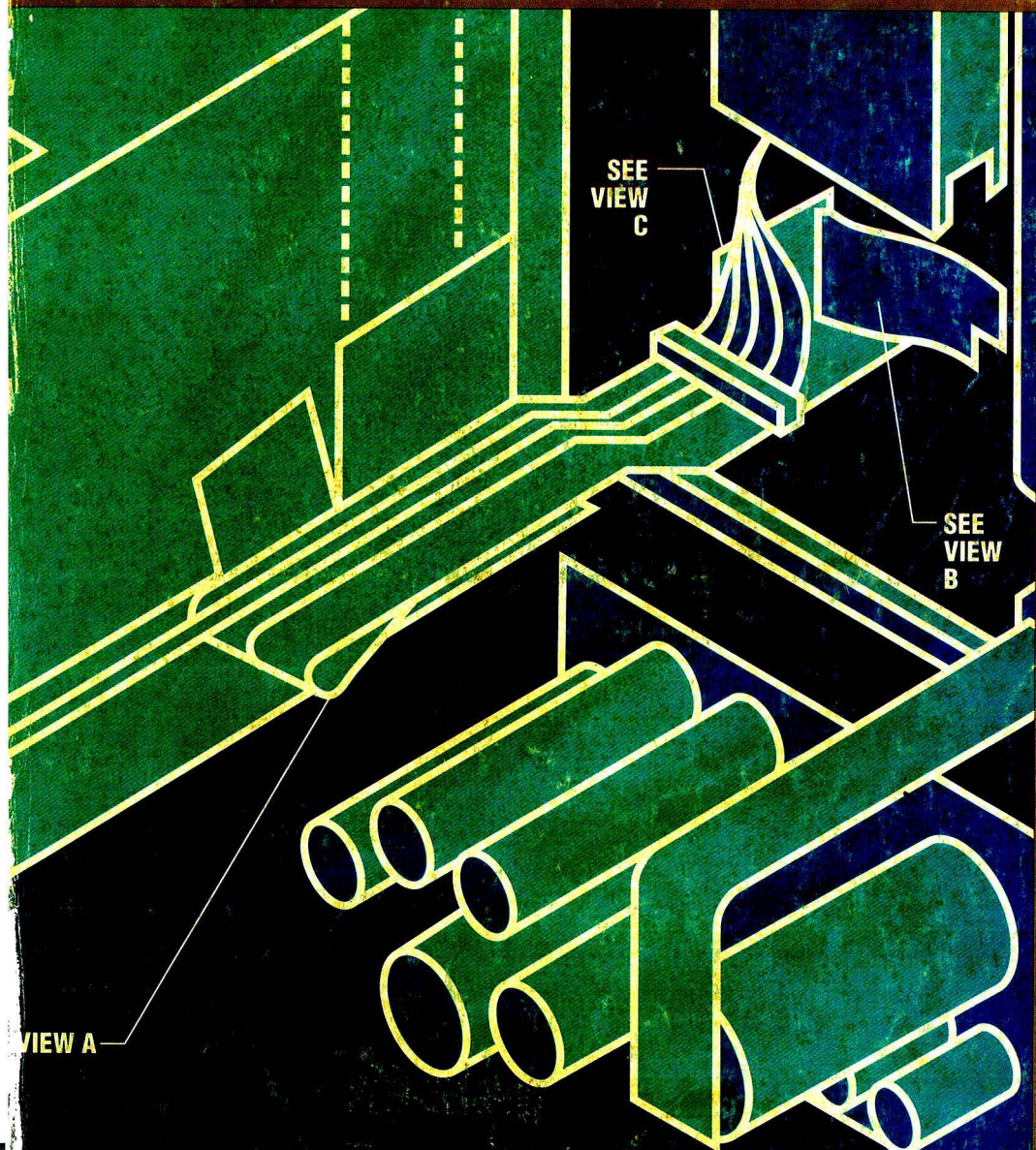


MARCH 1, 1990

# Analytical CHEMISTRY



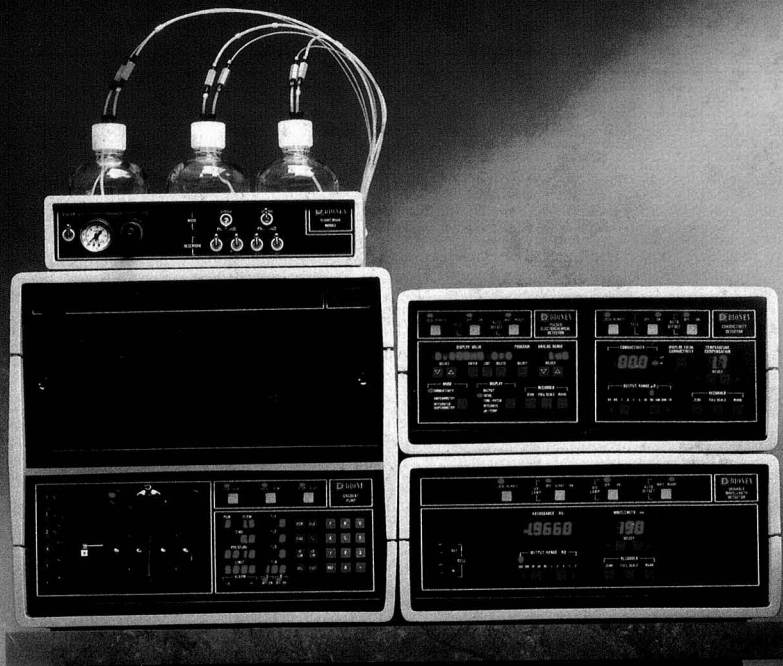
SEE  
VIEW  
C

SEE  
VIEW  
B

VIEW A

**INSTRUMENT DEVELOPMENT AND  
THE ROLE OF ANALYTICAL SCIENTISTS**

67A



## Sorry, but this just doesn't make it.

Without the right chemistry, even the best hardware isn't enough.

And it's precisely the chemistry that sets Dionex apart in ion chromatography.

Patented MicroMembrane™ suppression. IonPac™ columns. Pulsed electrochemical detection. They're just a few of the ways we make your results better. Easier. And in fact, we *guarantee* your success by installing your application.

You wouldn't expect anything less from a company of chemists.

So for the right solutions, right now, call (in U.S.A.) 1-800-227-1817 ext. 42.

It's what you don't see that makes for great IC.

 **DIONEX**  
A BETTER SOLUTION

Dionex Corporation, P.O. Box 3603, Sunnyvale, CA 94088-3603, Canada Dionex Canada Ltd., (416) 855-2551, England Dionex (UK) Ltd., (0276) 691722, West Germany Dionex GmbH, (06126) 6036, France Dionex S.A., (1) 46216666, Italy Dionex S.r.l., (06) 3792979, Netherlands Dionex B.V., (076) 714800. © 1989 Dionex Corporation

CIRCLE 28 ON READER SERVICE CARD



GILSON 232-401

## Transform your HPLC system into a complete auto-analyser.

**I**ncrease laboratory throughput, reduce cost per analysis, improve the consistency of your test results... add Gilson's 232-401 Automatic Sample Processor to your chromatograph.

Gilson has designed the first high capacity sample processor with system control.

It handles more samples, faster. It simplifies your chromatogram. It offers precision and repeatability. Fully programmable, it can be associated with other analytical instruments, computers, and various sample preparation satellites.

The 232-401 is all you need to automate routine handling of large series of LC analytes, from sampling and pretreatment procedures, up to the end report.

The 232-401 is described in our brochure, which explains how to implement such modern techniques as sample clean-up and sample concentration, column backflushing, fraction collection in sealed vials, and reinjection for tests of purity or bioactivity.

 **GILSON**

To receive your copy, please contact your nearest representative, or write to :  
Gilson, BP 45 - 95400 Villiers-le-Bel, France - Tel. : (1) 34 29 50 00 - Tx : 606 682  
Fax : (1) 30 04 51 00

# Because each step is critical for peak performance in chromatography.

## J.T.Baker High Purity Solvents

For HPLC and GC analyses that place you on the leading edge of separations technology, J.T.Baker high purity solvents assure you accurate, reproducible results.

J.T.Baker manufactures high purity solvents by methods that push purification technology to the limits.

When there's no time to retrace your steps, select the high performance solvents that are manufactured and characterized for your specific application: 'BAKER ANALYZED'<sup>®</sup> HPLC grade for HPLC mobile phases; 'BAKER RESI-ANALYZED'<sup>®</sup> and 'BAKER CAPILLARY-ANALYZED'<sup>\*</sup> grades for demanding trace analyte extractions.

Specify J.T.Baker high purity solvents for your next requirement.

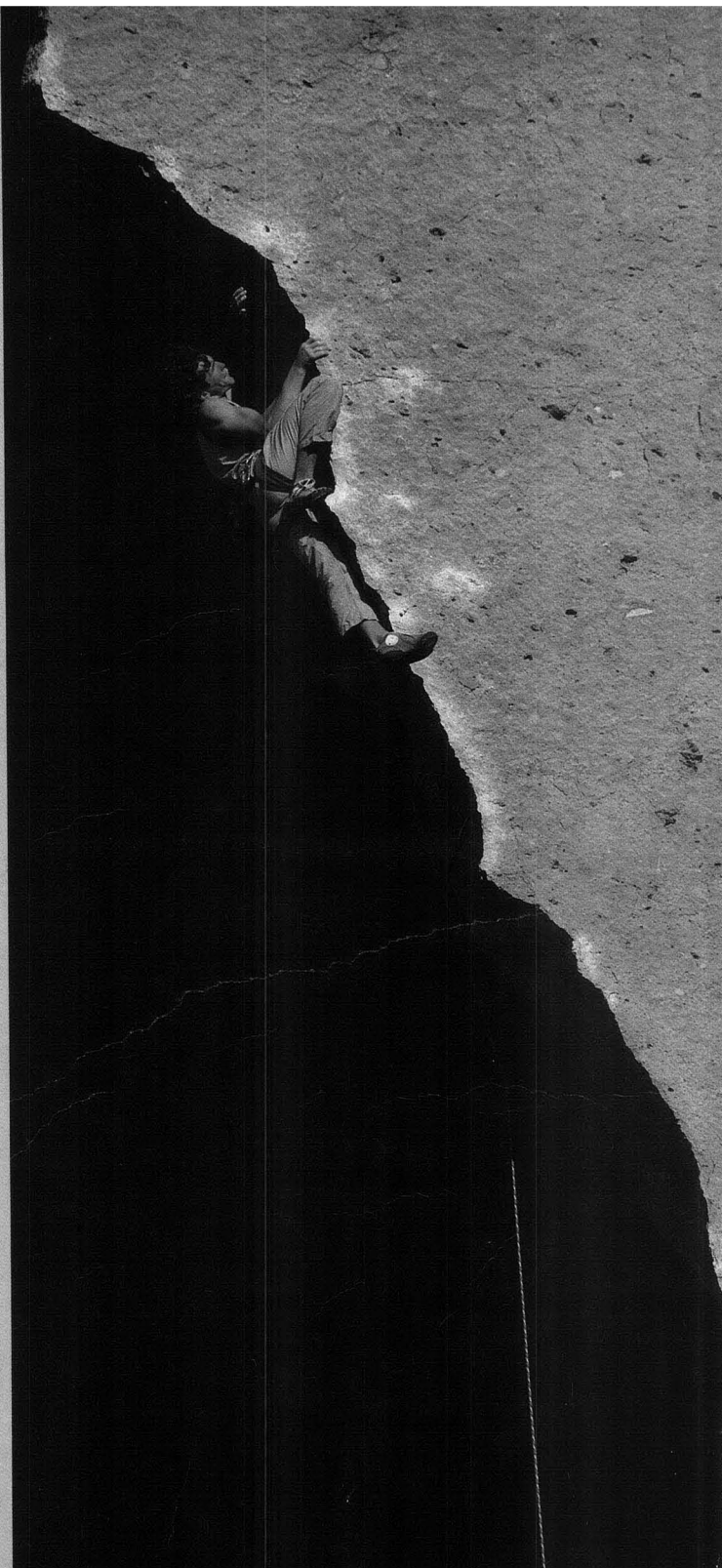
▶ World leading rock climber Stefan Glowacz of West Germany, during his free ascent of the 5.12C rated (Extreme Difficulty) world class 'Chain Reaction' at Smith Rocks, Oregon.



J.T.Baker Inc. • 222 Red School Lane  
Phillipsburg, NJ 08865  
1-800-JTBAKER; in NJ 201-859-2151  
Telex: 299514 BAKR UR • FAX: 201-859-9318

CIRCLE 12 ON READER SERVICE CARD

'BAKER ANALYZED'<sup>®</sup>, 'BAKER RESI-ANALYZED'<sup>®</sup> and 'BAKER CAPILLARY-ANALYZED'<sup>\*</sup> are trademarks of J.T.Baker Inc.



**MARCH 1, 1990**  
**VOLUME 62**  
**NUMBER 5**

# Analytical CHEMISTRY

**The Audit Bureau of Circulations**  
 ANCHAM  
 62(5) 289A-346A/417-544 (1990)  
 ISSN 0003-2700

Registered in U.S. Patent and Trademark Office;  
 Copyright 1990 by the American Chemical Society

ANALYTICAL CHEMISTRY (ISSN 0003-2700) is published semimonthly by the American Chemical Society at 1155 16th St., N.W., Washington, DC 20036. Editorial offices are located at the same ACS address (202-872-4570; FAX 202-872-4574; TDD 202-872-8733). Second-class postage paid at Washington, DC, and additional mailing offices. Postmaster: Send address changes to ANALYTICAL CHEMISTRY Member & Subscriber Services, P.O. Box 3337, Columbus, OH 43210.

Claims for missing numbers will not be allowed if loss was due to failure of notice of change of address to be received in the time specified; if claim is dated (a) North America: more than 90 days beyond issue date, (b) all other foreign: more than one year beyond issue date, or if the reason given is "missing from files."

**Copyright Permission:** An individual may make a single reprographic copy of an article in this publication for personal use. Reprographic copying beyond that permitted by Section 107 or 108 of the U.S. Copyright Law is allowed, provided that the appropriate per-copy fee is paid through the Copyright Clearance Center, Inc., 27 Congress St., Salem, MA 01970. For reprint permission, write Copyright Administrator, Publications Division, ACS, 1155 16th St., N.W., Washington, DC 20036.

**Registered names and trademarks**, etc., used in this publication, even without specific indication thereof, are not to be considered unprotected by law.

**Advertising Management:** Centcom, Ltd., 500 Post Rd. East, Westport, CT 06880 (203-226-7131)

1990 subscription rates include air delivery outside the U.S., Canada, and Mexico

	1 yr	2 yr
<b>Members</b>		
Domestic	\$ 29	\$ 49
Canada and Mexico	64	119
Europe	96	183
All Other Countries	118	227
<b>Nonmembers</b>		
Domestic	59	100
Canada and Mexico	94	170
Europe	186	336
All Other Countries	208	360

Three-year and other rates contact: Member & Subscriber Services, ACS, P.O. Box 3337, Columbus, OH 43210 (614-447-3776 or 800-333-9511).

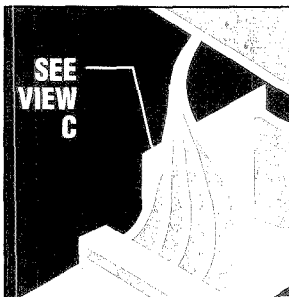
**Subscription orders by phone** may be charged to VISA, MasterCard, Barclay card, Access, or American Express. Call toll free 800-ACS-5558 in the continental United States; in the Washington, DC, metropolitan area and outside the continental United States, call 202-872-8065. Mail orders for new and renewal subscriptions should be sent with payment to the Business Management Division, ACS, P.O. Box 28597, Central Station, Washington, DC 20005.

**Subscription service inquiries and changes of address** (include both old and new addresses with ZIP code and recent mailing label) should be directed to the ACS Columbus address noted above. Please allow six weeks for changes to become effective.

**ACS membership information:** Lorraine Bowlin (202-872-4567)

**Single issues**, current year, \$8.00 except review issue, \$14.00, and LabGuide, \$49.00; **back issues and volumes and microform editions** available by single volume or back issue collection. For information or to order, call the number listed for subscription orders by phone; or write the Microform & Back issues Office at the Washington address.

**Nonmembers rates in Japan:** Rates above do not apply to nonmember subscribers in Japan, who must enter subscription orders with Maruzen Company Ltd., 3-10 Nihonbashi 2-chome, Chuo-ku, Tokyo 103, Japan. Tel: (03) 272-7211.



## REPORT 307 A

**On the cover. Instrument Development and the Role of Analytical Scientists.** Should analytical instruments be designed by analytical chemists? Analytical chemists, in general, do not develop and produce the instruments they use. Andrew T. Zander of the Varian Research Center suggests ways in which analytical scientists can become involved with instrument development



## MEETINGS 319 A

**The 199th ACS spring national meeting** will be held April 22-27 in Boston, MA. The technical program will feature presentation of awards to Henry Freiser, Evan and Marjorie Horning, Barry Karger, John Knox, and Peter Jurs

## BRIEFS 294 A

## EDITORIAL 303 A

**Keeping the Pacific Basin clean.** Approximately 50 scientists met in Honolulu in January to discuss environmental concerns of the Pacific Basin at the Second International Conference on Environmental Analytical Chemistry, sponsored by EPA, NIST, and the Center for Environmental Research at Cornell University

## NEWS 305 A

**AOAC awards announcement.** ▶ Nominations call for Dal Nogare Award. ▶ Polymer batteries. ▶ Real electrochemical surfaces

## FOCUS 337 A

**Seventh International Symposium on Laboratory Robotics.** More than 400 scientists gathered last October in Boston to hear the latest developments in robotics. Talks described automated systems for process analysis, clinical laboratory analysis, pharmaceutical quality control, and biotechnology

## NEW PRODUCTS & MANUFACTURERS' LITERATURE 342 A

## AUTHOR INDEX 417

## Perspective: Analytical Biotechnology

### DNA Sequencing, Automation, and the Human Genome 418

The principles of DNA sequencing and the technologies of both manual radioisotope-based and automated fluorescence-based approaches are described.

George L. Trainor, E. I. du Pont de Nemours and Co., Inc., Central Research and Development Department, Experimental Station, P.O. Box 80328, Wilmington, DE 19880-0328

## Articles

### Indirect Fluorometric Detection of Cations in Capillary Zone Electrophoresis 427

Cations ranging from simple inorganic cations to peptides are separated and detected with CZE using quinine sulfate as the running buffer.

Larry Gross and Edward S. Yeung\*, Ames Laboratory—USDOE and Department of Chemistry, Iowa State University, Ames, IA 50011

### Cluster Analysis Applied to the Selection and Combination of Buffering Electrolyte Systems Used for Capillary Electrophoresis of Anions with Water or Methanol as Solvents 431

Four different methanol electrolyte systems with different pHs are compared with eight aqueous systems. The similarity among the 12 systems is described by Euclidian distances calculated from the electrophoretic mobilities of 55 anions.

Ernst Kenndler\* and Brigitte Gassner, Institute for Analytical Chemistry, University of Vienna, Währingerstrasse 38, A-1090 Vienna, Austria

### Experimental Verification of Parameters Calculated with the Statistical Model of Overlap from Chromatograms of a Synthetic Multicomponent Mixture 436

Gas chromatograms of a synthetic mixture containing more than 50 components are interpreted with the statistical model of overlap. The agreement between the predictions of this model and experiment is excellent at low chromatographic saturations.

Scott L. Delinger and Joe M. Davis\*, Department of Chemistry and Biochemistry, Southern Illinois University, Carbondale, IL 62901

### Use of an On-Column Frit in Capillary Zone Electrophoresis: Sample Collection 443

A frit structure of sintered glass particles is constructed on the side of the capillary wall for electrical contact in CZE. Its use for sample collection is illustrated.

Xiaohua Huang and Richard N. Zare\*, Department of Chemistry, Stanford University, Stanford, CA 94305

### Electrochemical Behavior of Reversible Redox Species at Interdigitated Array Electrodes with Different Geometries: Consideration of Redox Cycling and Collection Efficiency 447

Cyclic voltammetry and chronoamperometry of redox species at interdigitated array electrodes show high sensitivity, high S/N ratios, and a wide dynamic range because of their high redox cycling and collection efficiency.

Osamu Niwa\*, Masao Morita, and Hisao Tabei, NTT Basic Research Laboratories, Nippon Telegraph and Telephone Corporation, Tokai, Ibaraki 319-11, Japan

### Mediated, Anaerobic Voltammetry of Sulfite Oxidase 452

Steady-state, catalytic voltammetry is employed for sulfite oxidase using several different mediators. The rate law is determined, and the second-order rate constant for oxidation of the enzyme by  $[\text{Co}(\text{bpy})_3]^{3+}$  is  $\sim 5 \times 10^4 \text{ L} \cdot \text{mol}^{-1} \cdot \text{s}^{-1}$ .

L. A. Coury, Jr., B. N. Oliver, J. O. Egekeze, C. S. Sosnoff, J. C. Brumfield, R. P. Buck, and R. W. Murray\*, Venable and Kenan Laboratories of Chemistry, University of North Carolina at Chapel Hill, Chapel Hill, NC 27599-3290

### Gold and Platinum Poly(chlorotrifluoroethylene) Composite Electrodes 459

Kel-F/gold and Kel-F/platinum composite electrodes with high electrical conductivities are fabricated. The electrodes have active sites with high perimeter-to-area ratios and therefore exhibit enhanced current densities.

Steven L. Petersen and Dennis E. Tallman\*, Department of Chemistry, North Dakota State University, Fargo, ND 58105

### Combination of the Mahalanobis Distance and Residual Variance Pattern Recognition Techniques for Classification of Near-Infrared Reflectance Spectra 465

The complementary nature of classification using Mahalanobis distance and SIMCA residual variance techniques in principal component subspaces is described. A classification rule that combines the two techniques is reported.

Nilesh K. Shah and Paul J. Gemperline\*, Department of Chemistry, East Carolina University, Greenville, NC 27858

\* Corresponding author

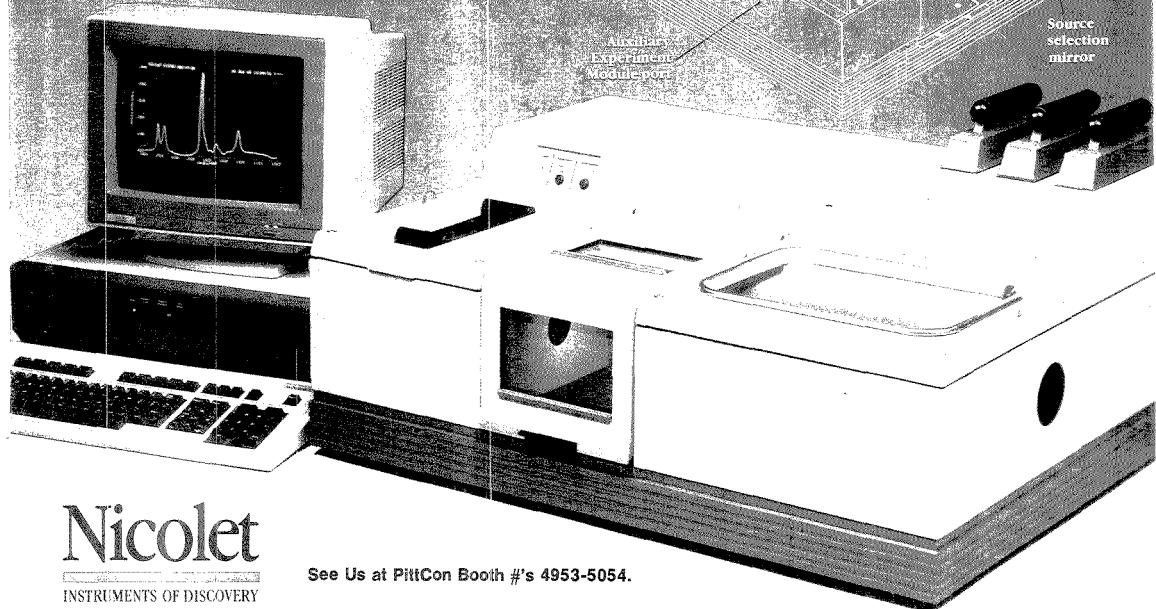
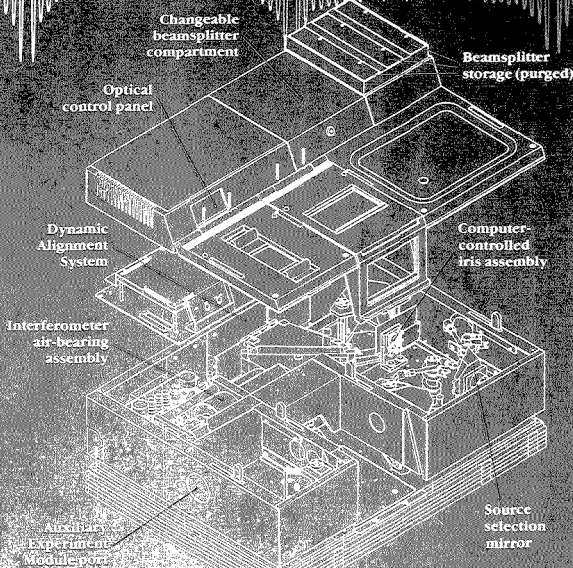
# Discover System 800 FT-IR

*Your best choice in a high-performance research FT-IR system.*

- Superior stability
- Highest sensitivity
- Widest versatility

System 800 gives you superior performance to solve today's research problems with confidence—and unmatched adaptability to respond to tomorrow's challenges. System 800 frees you from the built-in limitations of past instruments.

When you choose the System 800, you're making a cost-effective investment as well as a sound scientific decision. Write us or circle the reader's service number to receive our new brochure, System 800 brochure.



## Nicolet

INSTRUMENTS OF DISCOVERY

See Us at PittCon Booth #'s 4953-5054.

Belgium 02-762-2511  
Canada 416-625-8302

France 1-30-66-3330  
Germany 069-837001

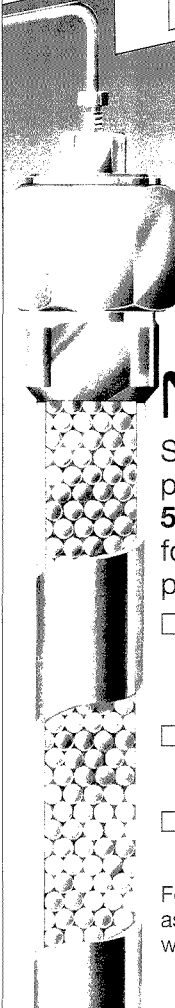
Japan 06-863-1550  
Netherlands 03403-74754

Switzerland 01-251-6133  
United Kingdom 0926-494111

Nicolet Analytical Instruments / 5225-1 Verona Rd. / Madison, WI 53711 / (608) 271-3333 / FAX (608) 273-5046

Circle 88 for information      Circle 89 for demonstration

**SILICA  
PACKINGS  
FOR HPLC**



**NUCLEOSIL®**

Spherical particles with pore diameters from **50 to 4000 Å** for analytical and preparative separations

- outstanding separation performance and high batch-to-batch reproducibility
- high pressure stability even for wide pore packings
- numerous chemically bonded phases available

For further information ask for HPLC catalogue 1987 with more than 500 applications

**MACHERY-NAGEL** 

MACHERY-NAGEL GmbH & Co. KG · P.O. Box 101352 · D-5160 Düren  
West Germany · Tel. (0 24 21) 6 98-0 · Telex 8 33 893 mana d · Fax (0 24 21) 6 20 54  
Switzerland: MACHERY-NAGEL AG · P.O. Box 224 · CH-4702 Densingen  
Tel. (0 62) 76 20 66 · Telex 9 82 908 mnag ch · Fax (0 62) 76 28 64

CIRCLE 90 ON READER SERVICE CARD

**BRIEFS**

**Effects of Inaccurate Reference Lifetimes on Interpreting Frequency-Domain Fluorescence Data** 471

Monoexponential decays can falsely be interpreted as multiexponential or excited-state systems. Unimodal distributions commonly appear as double-exponential decays. A method to remove the errors is presented.

Kevin S. Litwiler, Jingfan Huang, and Frank V. Bright\*, Department of Chemistry, Acheson Hall, State University of New York at Buffalo, Buffalo, NY 14214

**Combined Deconvolution and Curve Fitting for Quantitative Analysis of Unresolved Spectral Bands** 477

The application of least-squares curve-fitting programs is shown to yield improved estimates of the areas of unresolved spectral features after bandwidths are reduced by Fourier self-deconvolution.

John A. Pierce, Richard S. Jackson, Kenneth W. Van Every, and Peter R. Griffiths\*, Department of Chemistry, University of California, Riverside, CA 92521 and Gao Hongjin, Department of Chemistry and Chemical Engineering, Tsinghua University, Beijing, China

**Thermospray Enhanced Inductively Coupled Plasma Atomic Emission Spectroscopy Detection for Liquid Chromatography** 484

Limits of detection for chromatographically separated chromium, arsenic, and iron species are improved by a factor of ~50 using thermospray sample introduction.

S. B. Roychowdhury and J. A. Koropchak\*, Department of Chemistry and Biochemistry, Southern Illinois University, Carbondale, IL 62901

**Application of the Hollow Cathode Discharge Emission Source to the Determination of Nonmetals in Microsamples** 489

Temporal profiles of the emission signal from small samples deposited in the hollow are given for P, Cl, and Se. Detection limits of 9 and 20 pg are reported for P and Cl, respectively.

Fu-yih Chen and J. C. Williams\*, Department of Chemistry, Memphis State University, Memphis, TN 38152

**Interaction of Capillary Zone Electrophoresis with a Sheath Flow Cuvette Detector** 496

Theory predicts and experiments demonstrate that the sheath flow cuvette contributes negligibly to the separation efficiency of CZE. A separation with more than  $2.5 \times 10^6$  theoretical plates is produced for low molecular weight analytes.

Yung Fong Cheng, Shaole Wu, Da Yong Chen, and Norman J. Dovichi\*, Department of Chemistry, University of Alberta, Edmonton, Alberta, Canada T6G 2G2

# Acrodisc: The Difference is Clear.

## **Clearly the Widest Selection.**

Gelman Sciences Acrodiscs® are available in a wide variety of membrane types, with 0.2 $\mu$ m or 0.45 $\mu$ m pore sizes and 13mm or 25mm diameters.

## **Clearly Identified.**

Acrodiscs are printed with identifying information, and are color-coded to the product packaging. Convenient tube containers allow you to see their contents at a glance.

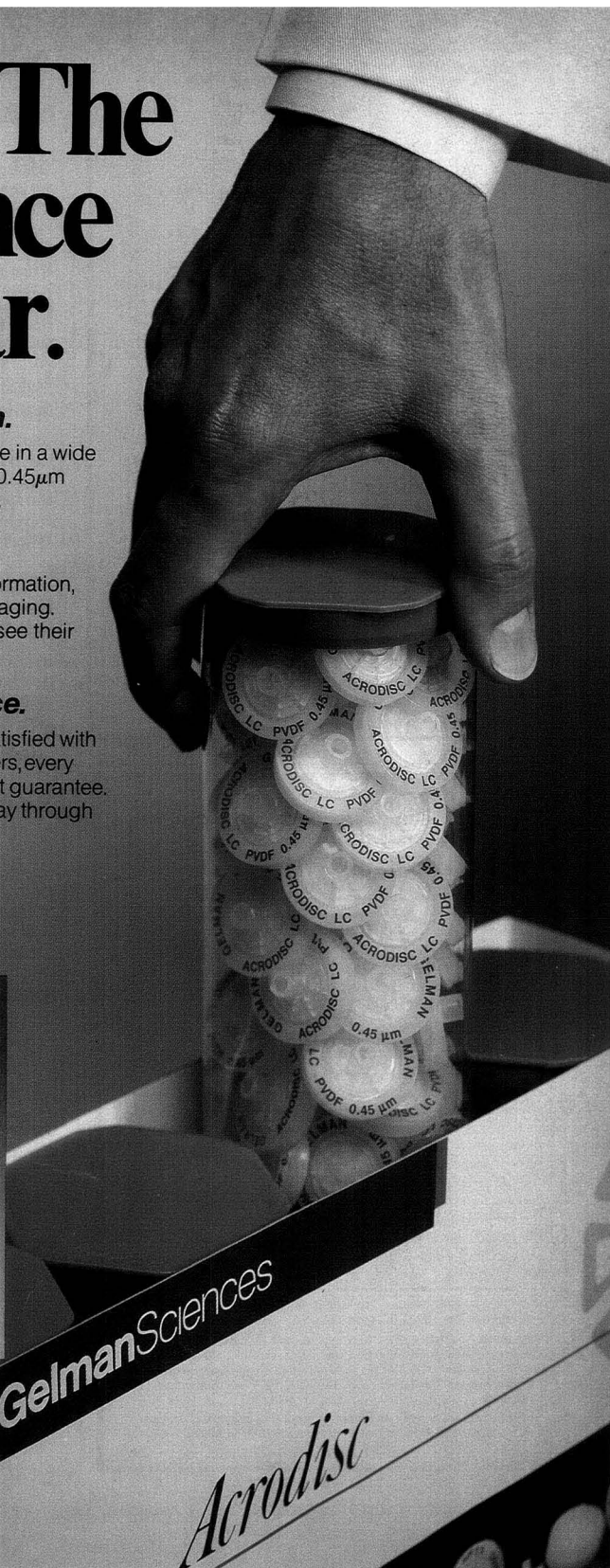
## **Clearly the Best Performance.**

Gelman Sciences is so certain you'll be satisfied with the performance of its Acrodisc syringe filters, every package is covered by a free-replacement guarantee. So order Gelman Sciences Acrodiscs today through your local laboratory products distributor.

CIRCLE 48 ON READER SERVICE CARD

 **Gelman Sciences**

600 S. Wagner Rd. • Ann Arbor, MI 48106-1448 • 313-665-0651



# RENT

Analytical Instruments  
lease or rent-to-own



- ✓ Free Instrument delivery & setup in selected areas.
- ✓ GC•MSD•FTIR•AA•ICP•LC•IR
- ✓ Choose from many major manufacturers
- ✓ Hewlett-Packard GC•MSD Systems in stock
- ✓ New Catalog of Chromatography Supplies.

1-800-7-ON-SITE

On-Site Instruments®  
ENVIRORENTAL®

689 North James Road Columbus, Ohio 43219-1837  
(614) 237-3022  
USA—CANADA

CIRCLE 104 ON READER SERVICE CARD

New from Elsevier and the American Society for Mass Spectrometry!

## JOURNAL OF THE AMERICAN SOCIETY FOR MASS SPECTROMETRY

EDITOR-IN-CHIEF:

Michael L. Gross, University of Nebraska—Lincoln

ASSOCIATE EDITORS:

Kelsey D. Cook, University of Tennessee

Simon Gaskell, Baylor Medical College

Gary L. Glush, Oak Ridge National Laboratory

R.S. Houk, Iowa State University

The *Journal of the American Society for Mass Spectrometry* publishes refereed, original research papers from all fields of scientific inquiry in which mass spectrometry can play a role, including developments in both fundamentals and applications. Contributors investigate new instrumentation and methods, present new discoveries in ion chemistry, and develop problem-solving strategies. The journal also publishes *Short Communications*, which contain ideas for which some experimental or theoretical justification is presented (usually to be followed by a full paper), and *Accounts and Perspectives*, including brief review articles and reflections on the state of research in mass spectrometry.

1990, Volume 1 (six issues) ISSN: 1044-0305  
Subscription rate: \$235.00 (outside USA, add \$24.00 for postage).  
Send North American sample copy requests and all subscription orders to: Elsevier Science Publishing Co., Inc., P.O. Box 832, Madison Square Station, New York, NY 10159. Send all other sample copy requests to: Elsevier Science Publishers, P.O. Box 211, 1000 AE Amsterdam, The Netherlands.

For fastest service when subscribing or requesting a sample issue, call (212) 633-3950, or FAX your request to (212) 633-3990.

135AY

ELSEVIER

1/90

CIRCLE 32 ON READER SERVICE CARD

## BRIEFS

### Coprecipitation of Trace Metals by DNA and RNA Molecules

504

DNA and RNA are used as carriers of trace metals in water for coprecipitation preconcentration. The method allows for the preconcentration of trace metal ions except iron, calcium, and magnesium, which are intrinsically contained in DNA and RNA.

Kitao Fujiwara\*, Ri-e Kojyo, and Kazuma Okada, Faculty of Integrated Arts and Sciences, Hiroshima University, 1-1-89 Higashisenda-machi, Hiroshima 730, Japan and Yukio Kodama, Ocean Research Institute, The University of Tokyo, 1-15-1 Minamidai, Nakano-ku, Tokyo 164, Japan

### Asphaltenes in Crude Oil: Absorbers and/or Scatterers in the Near-Infrared Region?

508

Asphaltenes in crude oils act as absorbers, not scatterers, in the near-IR spectral range. Addition of spectra from the asphaltene and maltene fractions of a crude oil reproduce the spectrum of the crude oil.

Oliver C. Mullins, Schlumberger-Doll Research, Old Quarry Road, Ridgefield, CT 06877

### Elimination of z-Ejection in Fourier Transform Ion Cyclotron Resonance Mass Spectrometry by Radio Frequency Electric Field Shimming

515

Relative abundances of ions with different  $m/z$  values are determined accurately from FT-ICR mass spectral peak magnitudes.

Mingda Wang and Alan G. Marshall\*, Department of Chemistry, The Ohio State University, 120 West 18th Avenue, Columbus, OH 43210

### Field-Corrected Ion Cell for Ion Cyclotron Resonance

520

Modifying the geometry of the FT-ICR cell to produce uniform ion acceleration and homogeneous dc trapping fields results in enhanced sensitivity and resolution.

Curtiss D. Hanson, Department of Chemistry, University of Northern Iowa, Cedar Falls, IA 50614 and Mauro E. Castro, Eric L. Kerley, and David H. Russell\*, Department of Chemistry, Texas A&M University, College Station, TX 77843

### Combustion Tube Method for Measurement of Nitrogen Isotope Ratios Using Calcium Oxide for Total Removal of Carbon Dioxide and Water

526

$\gamma^{15}\text{N}$  values produced by the combustion method differ by 0.11‰ when compared with conventional methods. Because the gas contains less CO, the values are more accurate than those obtained by previously reported methods.

Carol Kendall\* and Elizabeth Grim, U.S. Geological Survey, 431 National Center, Reston, VA 22092

### Suspended Trapping Procedure for Alleviation of Space Charge Effects in Gas Chromatography/Fourier Transform Mass Spectrometry

530

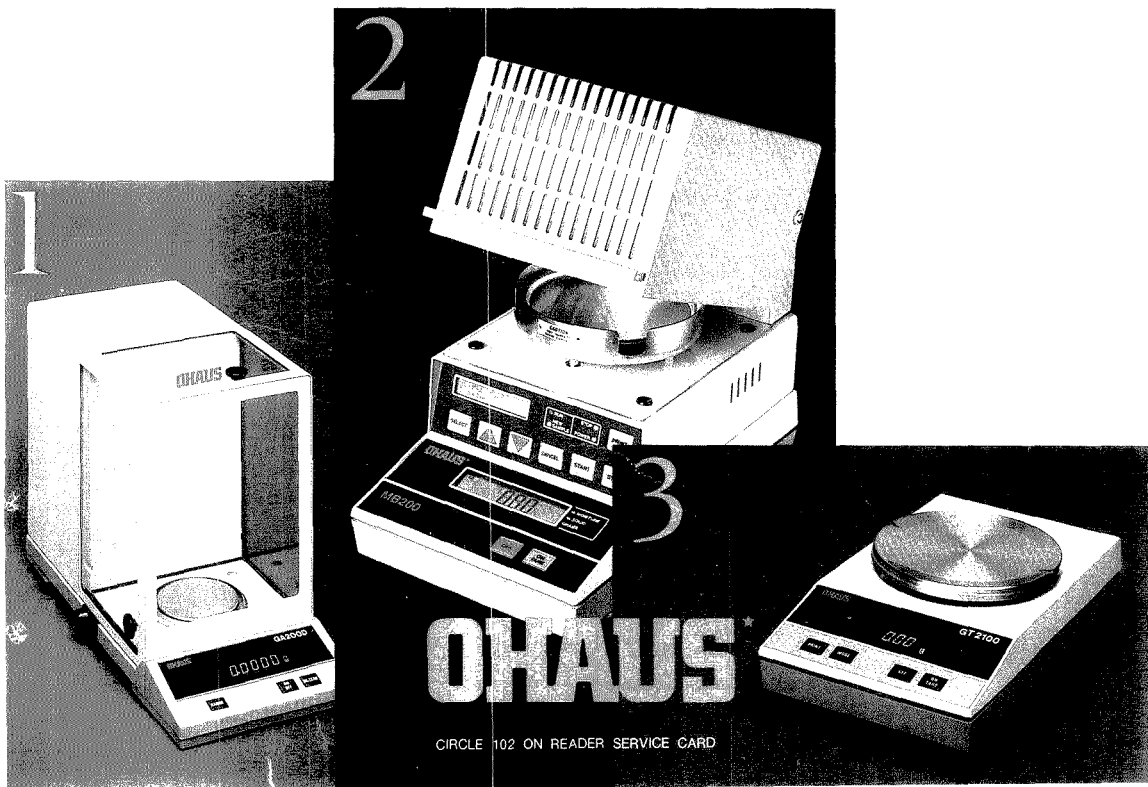
Low-ppm mass measurement accuracy over a 5 order of magnitude neutral concentration range is demonstrated for the FT-MS detection of gas chromatographic effluent.

Jeremiah D. Hogan and David A. Laude, Jr.\*, Department of Chemistry, The University of Texas at Austin, Austin, TX 78712

## SIMPLIFY YOUR LABORATORY WEIGHING WITH THREE SOLID VALUES FROM OHAUS.

These three precise, user-friendly balances from Ohaus can significantly reduce your costs by increasing weighing speed and productivity. 1. The easy-to-use, durable GA Series analytical balances have enhanced stability and rapid response time. Capacities range from 110g to 200g with readabilities from 0.1mg to 0.01mg. Choose this balance when only the highest precision will do. 2. The new MB200 electronic moisture balance is the result of 30 years' experience in this technology. With it you determine solid or moisture content, continuously monitored by a dual display. Multiple temperature settings add to its versatility, and the auto-dry mode gives you a significant time saver. 3. With the versatile GT Series you draw on a broad range of software options. Its capabilities range from batching and mixing to more complex animal weighing and parts counting, and the graphic display lets you access a target filling mode. Let us tell you all about these cost-saving electronic balances. Call or write: Ohaus Corporation, 29 Hanover Rd., Florham Park, NJ 07932. (800) 672-7722.

# Weighing solutions from Ohaus... as easy as 1-2-3:



CIRCLE 102 ON READER SERVICE CARD

## INVITATION TO BID ON PATENT RIGHTS FOR CYANIDE SPECIATION ANALYTICAL APPARATUS

Patent license available for the manufacture and sale of a unique analytical apparatus for cyanide speciation developed by nationally acclaimed water reclamation research organization. Patent No. 4,265,857 "Method and Apparatus for Measuring Cyanide," is for a system which measures the amount of cyanide in a sample more precisely and conveniently than previously possible. The method is used with a system for separating a volatile component from a liquid in which the component is entrained (Patent No. 4,804,631). The inventions are patented in the United States, United Kingdom, Germany and Japan.

Send written proposals to Purchasing Agent, at the address below by March 15, 1990. The successful bidder will be notified shortly thereafter.

Interested parties may arrange to inspect the apparatus and witness its operation at the Water Reclamation District's Egan R&D Laboratory, Des Plaines, Illinois. Telephone Mr. Richard Lanyon, Assistant Director of Research & Development (312/751-3040).

For more information write Mr. George H. Wahl, Purchasing Agent, Metropolitan Water Reclamation District of Greater Chicago, 100 East Erie, Chicago, IL 60611.

## BRIEFS

### Carbon-Isotopic Analysis of Dissolved Acetate 535

Isotopic analysis of acetate in compound mixtures is described. Standard deviations of <0.4% are achieved for acetate samples larger than 5  $\mu\text{mol}$ .

Jeffrey T. Gelwicks and J. M. Hayes\*, Biogeochemical Laboratories, Departments of Chemistry and of Geology, Indiana University, Bloomington, IN 47405

## Correspondence

### Direct Resolution of Enantiomeric Diols by Capillary Gas Chromatography on a Chiral Polysiloxane Derived from (R,R)-Tartramide 539

Kouji Nakamura\*, Takafumi Saeki, and Masaaki Matsuo, Analytical Chemistry Research Laboratory, Tanabe Seiyaku, 3-16-89 Kashima, Yodogawa-ku, Osaka 532, Japan and Shoji Hara and Yasuo Dobashi, Tokyo College of Pharmacy, 1432-1 Horinouchi, Hachioji, Tokyo 192-03, Japan

## Technical Notes

### Palladium Gate Metal-Oxide-Semiconductor Oxygen Sensors 542

Jonas Karlsson, Mårten Armgarth, Svante Ödman, and Ingemar Lundström\*, Laboratory of Applied Physics, Linköping Institute of Technology, S-581 83 Linköping, Sweden

*Choosing a graduate school?  
Need to know who's doing  
research critical to yours?*

**New  
edition!**

## The ACS Directory of Graduate Research 1989

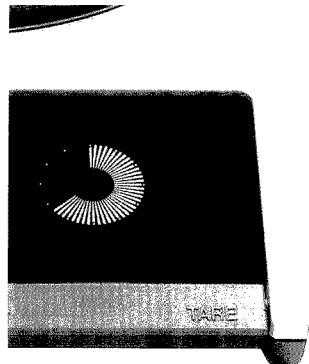
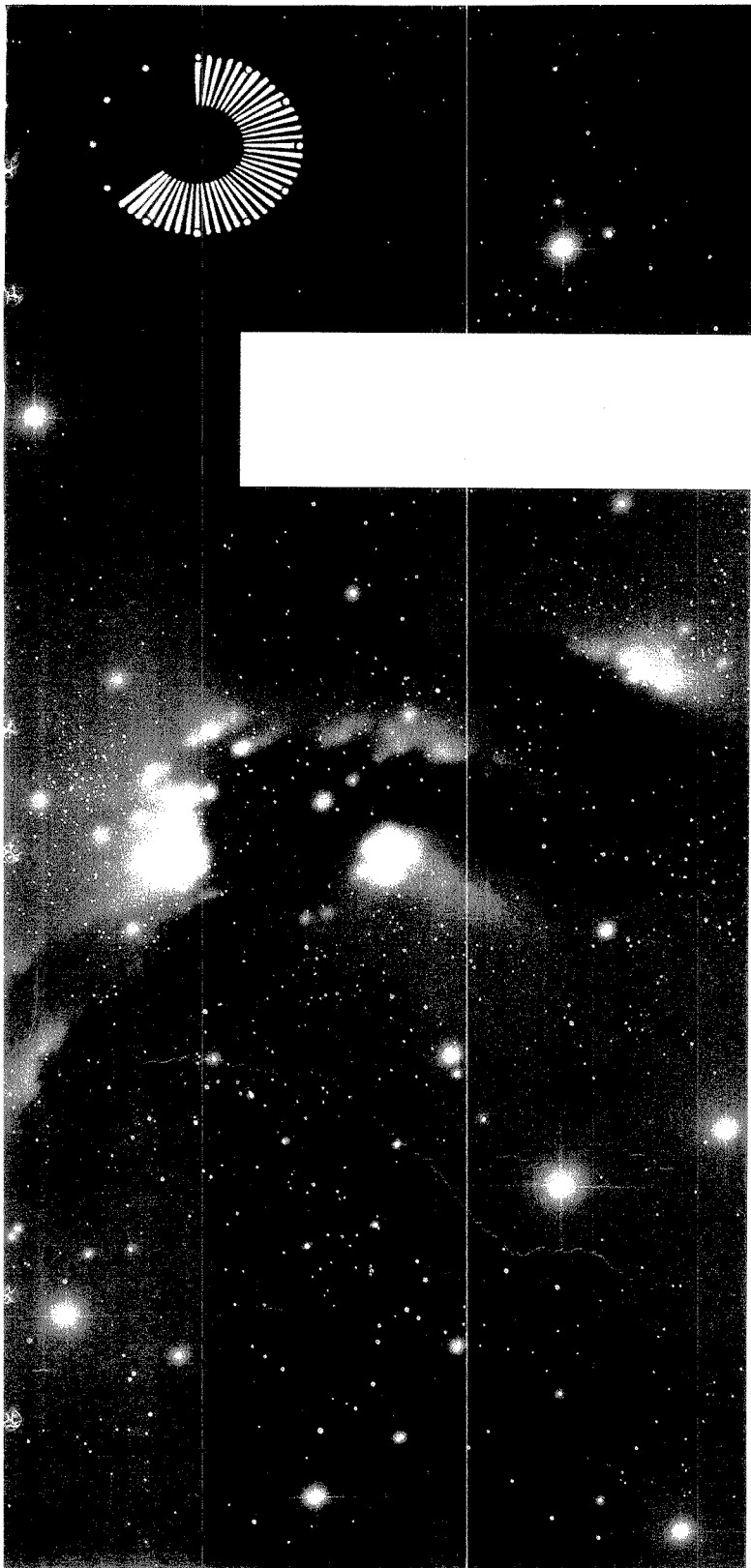
All the information you  
need on chemical research  
and researchers at univer-  
sities in the U.S. and Canada  
... in a single source.

1,36 pages (1989)  
Clothbound  
Price:  
US & Canada \$55.00  
Export \$66.00

- Contains a wealth of facts on 683 academic departments, 11,938 faculty members, and 68,276 publication citations.
- Includes listings for chemistry, chemical engineering, pharmaceutical/medicinal chemistry, clinical chemistry, and polymer science.
- Lists universities with names and biographical information for all faculty members, their areas of specialization, titles of papers published in the last two years, and telephone numbers, FAX numbers, and computer addresses.

Call toll free (800) 227-5558 and charge your credit card. In Washington, DC, call 872-4363. Or order from: American Chemical Society, Distribution Office Dept. 705, P.O. Box 57136, West End Station, Washington, DC 20037.

705



There's nothing like a new dimension to expand your view of the future. METTLER DeltaTrac® shows exactly what we mean.

It adds a unique visual dimension that makes the METTLER PM balance seem light-years ahead of all the rest.

That's because the DeltaTrac display is the fastest way to transmit information from the weighing instrument to the human brain. An automatic tracking device pinpoints precisely where you are in the weighing range — and does it with the speed of sight. No calculations needed.

No other lab balance is so simple to use, yet so advanced it's ready for the labs of tomorrow.

METTLER balances are available only from Fisher Scientific or VWR Scientific.

All products are backed by METTLER Service Plus®. Call 1-800-METTLER for information and put DeltaTrac in your future.

CIRCLE 86 ON READER SERVICE CARD

**Mettler Instrument Corporation**

Box 71

Hightstown, NJ 08520

1-800-METTLER

(NJ 1-609-448-3000)

Come see us at the

Pittsburgh

Conference

Booth

4672

**METTLER**

We understand.  
Precisely.



## In your work, so much depends on so little.

The success of an experiment depends on many factors, the most important being the purity of your filtrate.

Whatman microfiltration devices set a new standard for purity, reliability and excellence. They ensure a purer filtrate because absolutely no sealants, adhesives or releasing agents are ever used.

In addition, a variety of filter media and configurations are available to meet the diverse needs

of your laboratory. And, like all Whatman products, Whatman microfiltration devices are 100% guaranteed.

No wonder more scientists throughout the world trust their experiments to Whatman filters. Whatman microfiltration devices. They may be small, but think how much depends on them.

For more information in the US, call toll-free, 1-800-922-0361, or contact your local Whatman distributor.

**The advantages filter through.**

**Whatman®**  
Whatman is a registered trademark of Whatman International, Inc.

CIRCLE 150 ON READER SERVICE CARD

## **Keeping the Pacific Basin Clean**

There is growing concern for the environment in this country, and communities are working hard to lessen the impact of industry, carefully monitor and manage waste, and encourage or require recycling. The role of analytical chemists will continue to be vital to the assessment and cleanup of our local environments. However, the critical needs of the environment stretch far beyond the confines of our state and national borders, and we must consider the preservation of our environment as a global imperative.

This past January the Second International Conference on Environmental Analytical Chemistry was held in Honolulu to address the global concerns of environmental analysis. Sponsored by the U.S. Environmental Protection Agency, the National Institute of Standards and Technology, and the Center for Environmental Research at Cornell University, the meeting centered on the problems and needs of the nations of the Pacific Rim. More than 50 scientists from Australia, Canada, Hong Kong, Israel, Japan, the People's Republic of China, the Philippines, and the United States attended the meeting. Shigeki Hanamura of the Center for Environmental Research at Cornell organized the event and was greatly responsible for its success.

In addition to general talks covering the broader issues of concern to the conference, a number of technical sessions addressing the analytical needs of global environmental monitoring were held.

Particular emphasis was placed on methods and instrumentation that could be applied in laboratories of both developed and developing nations. The fast pace of industrialization in the Pacific Rim nations is quickly causing environmental damage on a global scale. Migrated pollutants from point sources easily transport the effects of pollution across national borders and oceans. Sessions covering toxicological monitoring, sample preparation, standard materials, and standard methods all sought to help in the assessment and reduction of this pollution. A round-table discussion was also held to identify the problems, methods, and monitoring applications within the Pacific Rim nations.

The conference was a direct outgrowth of the First International Conference reported in this JOURNAL two years ago. The conferences are intended to foster an exchange between environmental scientists and analytical chemists from all nations with environmental concerns in the region. Such exchange is necessary to mitigate and prevent future environmental pollution, especially with regard to drinking water, solid waste, and acid deposition. The meeting also reminds us that while we must continue to do all we can to preserve the environment of our local communities, we must also seek to preserve our global community.



# Reproducibility, time and time again

**Y**ou need reproducible results from your HPLC. That's one reason your HPLC solvent delivery system is so important. That's also why you should be using our Model 9600

The Model 9600 has gradient and flow rate reproducibility that matches even the most expensive HPLC. It includes everything you need for a reproducible HPLC solvent delivery system; it's also easy to get at everything for routine maintenance.

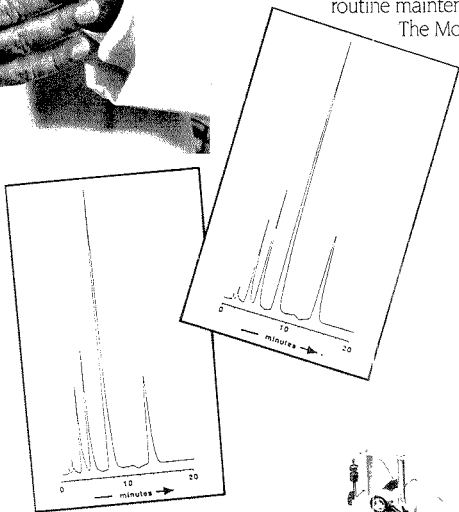
9600 is fully programmable, and works with any other manufacturer's equipment.

Best of all, the Model 9600 sells for thousands of dollars less than what you're used to paying.

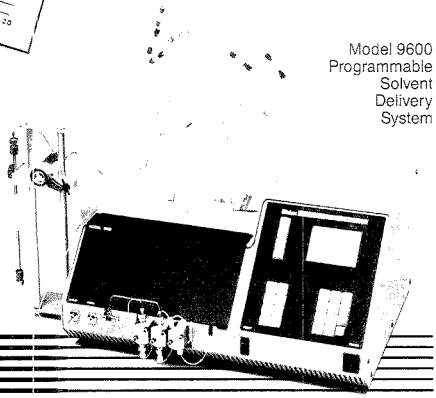
Call or write today for a free brochure or to arrange a demonstration.

**Eldex**  
831 Bransten Road  
San Carlos, CA 94070  
(415) 592-9270

The Model



Model 9600  
Programmable  
Solvent  
Delivery  
System



# Eldex

Precision Equipment for Chromatography

CIRCLE 37 ON READER SERVICE CARD

## Measuring Real Surfaces

The International Union of Pure and Applied Chemistry (IUPAC) Commission on Electrochemistry is seeking comments on a document entitled "Real Surface Area Measurements in Electrochemistry." Knowing real surface areas is important for measuring electrode reaction rates and most double-layer parameters. However, different methods have been proposed, some of questionable value.

The IUPAC document scrutinizes 15 methods, describing the principles and limitations of each approach. A copy of the document is available from the ACS Journals Department, P.O. Box 3330, Columbus, OH 43210. Comments are due by December 31 and should be sent to S. Trasatti, Dipartimento di Chimica Fisica ed Electrochimica, Università di Milano, Via Venezian 21, I-20133 Milano, Italy.

## Nominations for Dal Nogare Award

The Chromatography Forum of the Delaware Valley is requesting nominations for the 1991 Stephen Dal Nogare Award for excellence in and significant contributions to the field of chromatography. All nominations should consist of one or more letters of nomination and a biographical sketch describing the nominee's experience and contributions to the field. Nominations from previous years can be renewed and appended with an updated letter. Nominations should be sent to Mary Ellen McNally, E. I. du Pont de Nemours & Co., Agricultural Products Department, Experimental Station, Wilmington, DE 19880-0402. Deadline is April 1.

## Polymer Battery

Materials scientists at Lawrence Berkeley Laboratory (LBL) have discovered a unique and promising design for lightweight, solid-state batteries based on a polymer reaction. "These batteries," explains Lutgard De Jonghe, "can be made for all types of uses, from the sustained low-power demands of a watch to the high-power demands of electric vehicles." In addition, they should offer better performance in terms of power, lifetime, and shelf life than any commercial battery now available, and pose no danger of leakage.

Essential to these new batteries are thin-film cathodes containing polydisulfide polymers with the general structure  $(-SRS-)_n$ . The "R" group, explains Steven Visco, can be almost anything, ranging from aliphatic groups to thiazoles. To date, about 15 different polymers have been tested and about two-thirds of those look promising.

A polymerization/depolymerization reaction stores and generates electrons. Severing the disulfide bonds provides electrons, whereas polymerization recharges the cathode. LBL scientists have successfully run a polymer cathode through more than 350 polymerization/depolymerization reactions with little energy loss in the first 100 cycles.

Because of the low equivalent weights of the monomers, the batteries can deliver a significant amount of power per unit weight. For example, one polydisulfide battery operat-

ing at 80 °C (a reasonable temperature for an electric car) provided 200 W-h/kg, placing it in the range required to propel an electric car for long distances.

The actual polymer cathodes are a composite thin film cast from a solution of polydisulfide polymer, poly(ethylene oxide) (PEO), possibly an electrolyte, and carbon black. "It looks like black plastic," says Visco. An alkali metal anode, generally Li foil, and a PEO-salt electrolyte film complete the battery. The films are either sandwiched flat for button-shaped batteries or wound like a jellyroll for cylindrical designs.

## AOAC Nominations

The Association of Official Analytical Chemists (AOAC) invites nominations for two annual awards.

The \$2500 Harvey W. Wiley Award is given to an outstanding scientist or research team for contributions to analytical methodology in areas of interest to AOAC. The award was established in 1956 to honor Wiley, a founder of AOAC and the "father" of the Pure Food and Drug Act. Nominations received before December 1 will be considered for the award during the next four years.

The AOAC Scholarship Award provides \$1000 to support an undergraduate student's fourth year of study in a scientific area of interest to AOAC. Additional qualifications are a B average or better and evidence of financial need. Students in medical and premedical programs are not eligible. Nominating forms are available from AOAC, 2200 Wilson Blvd., Suite 400, Arlington, VA 22201-3301 (phone: 703-522-3032; FAX: 703-552-5468). Deadline is May 1.

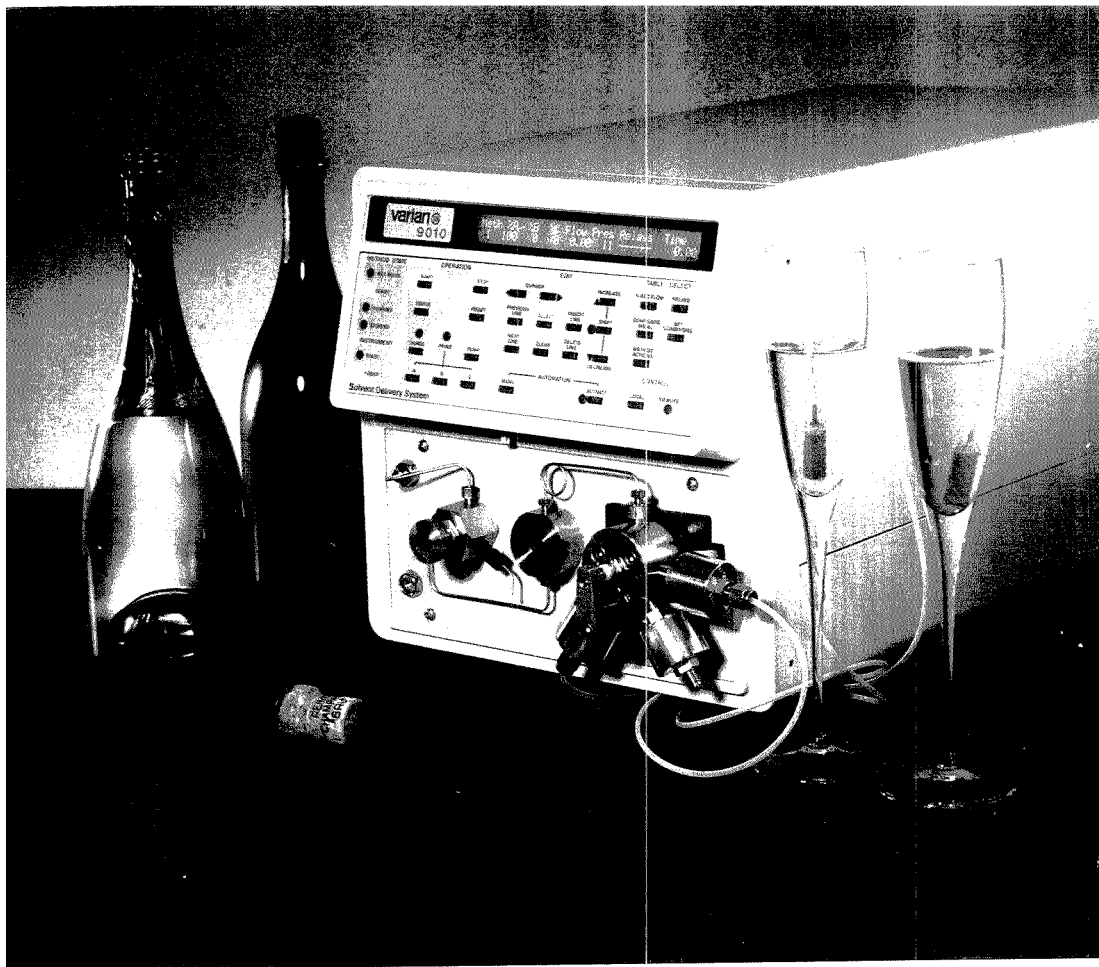
## For Your Information

**Ahmed Zewail** has been named the **first Linus Pauling Professor of Chemical Physics** at the California Institute of Technology. Zewail is a pioneer in femtosecond laser techniques for studying chemical reactions.

The **Association of Official Analytical Chemists (AOAC)** has produced the 15th edition of its **Official Methods of Analysis of the AOAC**. The handbook, which contains 1800 collaboratively tested and approved methods for chemical and microbiological analysis, is available from AOAC (see address above).

The **National Science Foundation (NSF)** has awarded a total of \$22.7 million in **grants targeted at developing or improving undergraduate laboratory and field experiences**. The funds, which are matched by the receiving institution, can only be used to purchase instrumentation.

In collaboration with Grumman Aerospace and General Dynamics, **Brookhaven National Laboratory will build a new, compact synchrotron**. The facility will aid in the development of X-ray lithography, a novel method of producing computer chips.



# ONLY THE BEST FOR THE BEST.

Can your HPLC system pump champagne? Can your HPLC system reliably pump ANY solvent without costly, time consuming degassing procedures?

Only one HPLC pump can — the Varian LC Star 9010. Our 9010 can pump ANY HPLC solvent, without prior preparation, with reliable results, everytime.

Let's face it. If you can't count on your pump, it doesn't matter how well the other parts of your HPLC system work. High performance isn't enough when one tiny bubble can shut down your whole operation.

The unique, patented design of the Star 9010 delivers high performance and dependability with any mobile phase. It eliminates pump cavitation, so your HPLC system can operate for hours on end, even overnight, unattended.

The net result is that, over the long run, you can have more analyses completed in less time, and with greater confidence.

Let us show you how dependable and productive a pump can be. For more information on the Star 9010 Pump and the entire Varian LC Star System, call 800-231-8134. In Canada, call 416-457-4130.

CIRCLE 144 ON READER SERVICE CARD

LC WITH A FUTURE



# INSTRUMENT DEVELOPMENT AND THE ROLE OF ANALYTICAL SCIENTISTS



**Andrew T. Zander**  
Varian Research Center  
Palo Alto, CA 94303

Should analytical instruments be designed by analytical chemists? Analytical chemists, in general, do not develop and produce the instruments that they use. Anyone who regularly relies on analytical instrumentation, however, is concerned about the quality and performance of the equipment, so it seems reasonable to ask, who produces the equipment? Who sees to it that the instrumentation performs in the manner that we think it should? This article will attempt to answer these questions and suggest some ways in which analytical scientists can become involved with these activities.

The instrument business, and the roles it offers analytical chemists, is

## **REPORT**

changing as a result of changes in the nature of instrument development. Today's analytical instruments are complex and sophisticated. Their design requires the input of professional engineers with a variety of different skills. In addition, the potentially lucrative nature of the analytical instrument market and the need to develop instruments with the broadest applicability have increased the competitiveness of the environment in which these systems are produced. There is also a need to reduce the time it takes to develop new instrumentation so that companies can respond more quickly to new needs or new technology.

The change in the nature of instrument development can be seen from a few illustrative trends. The significant growth of the Pittsburgh Conference

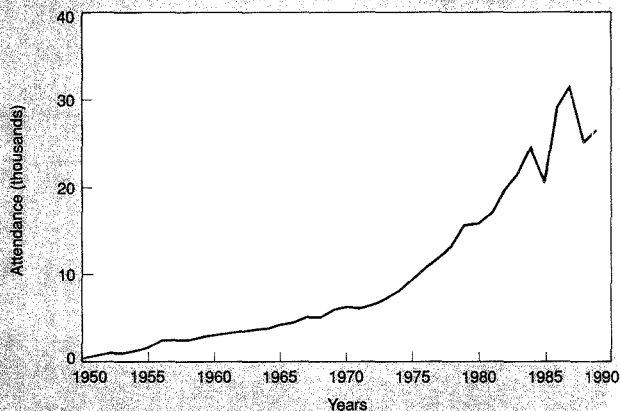


Figure 1. Pittsburgh Conference attendance, 1950–1989.

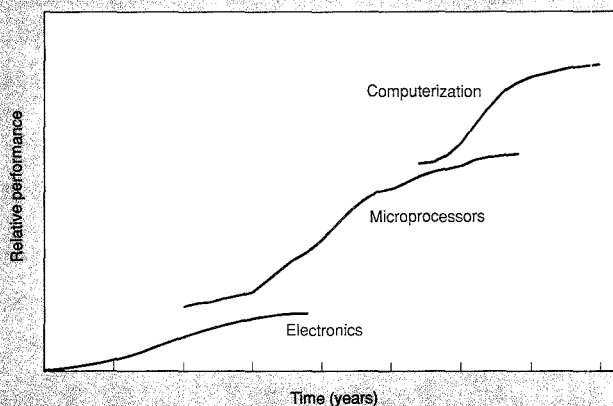


Figure 2. S-curves describing the impact of new technology on performance improvement.

The labels given for the curves suggest one possible sequence of technological advancement that has affected instrument performance.

(Figure 1) is a good indicator that a revolution of some sort is occurring, or has occurred, in the instrumentation market. The increase in attendance figures is matched by increases in the number of companies present, versions of equipment exhibited, booths used, and papers presented. The conversion from manually operated instruments that have been largely unavailable to all but expert users to mostly automat-

ed equipment systems that are broadly accessible to all users seems to have ended, both in terms of adding automation and in numbers of systems. There is still growth in instrument use, but the equipment feeding that growth is more the result of evolutionary instrument alterations—some more influential than others—than the generation of new equipment types.

Figure 2 shows a set of S-curves (also

known as learning curves or use curves) that are popular in many books describing innovation, or the lack thereof, in high-technology businesses. S-curves are intended to show that a technology will eventually reach a plateau of performance and that prominent changes in performance most often come about through a departure from old technology and a jump to a new technology, rather than from a single rising performance curve. In Figure 2, one possible labeling of these S-curves is shown for the changing character of analytical instrumentation. The increase in performance for all types of instruments is a result of a first conversion to internal control by modern analog and hybrid electronics, followed—perhaps less serially than indicated—by a conversion to system control based on digital electronics approaches. The most recent change has been computerized equipment, which provides inherent operating intelligence, a network for data flow, and autonomous analytical systems.

In many cases, analytical scientists were responsible for these transitions; they were needed in the interface region between technologies. Implementation of new technologies depended on the analytical problem at hand. Only after specific systems proved successful were the new technologies transferable to other instrument domains without the need for resident analytical experts.

Technological changes, or the transitions leading to improved performance, will continue to occur. Analytical scientists engaged in research play a major role in identifying the transitions and in generating the environment in which they take effect. They are expected to continue in this role.

Technology transition, though, is not the only thing reshaping the instrument and equipment businesses. What is occurring for the most part is an evolutionary process. It is an unusual evolution, however, in that it is happening at an accelerated rate under the influence of strong market forces. New analytical technology is having very little impact on this process; instead, current technology is being squeezed to provide performance that is less expensive and more reliable.

Producing sophisticated instrumentation that meets these criteria creates many new challenges for instrument R&D groups. They must obtain stabilized or improved performance and reliability in the face of reduced manufacturing costs. For example, how might one duplicate the performance of a mass flow controller using only

# The good news is you can get absolute macromolecular analysis in minutes.

## There is no bad news.

**E**XCEPT, perhaps, that you haven't discovered us sooner. Using one of our DAWN® laser light scattering instruments, you'll learn more about your macromolecules in minutes than you've learned in years. A lot more!

You could, for example, couple our DAWN Model F detector to your existing Size Exclusion Chromatography line to determine *absolute* molecular weights, sizes, distributions and molecular conformations of almost *any* polymer without resorting to column calibrations, reference standards or "fudge factors." And, there's more good news...

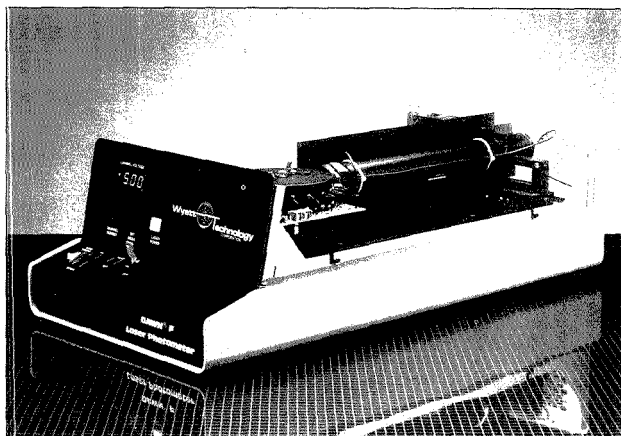
The batch-mode DAWN Model B is the most perfect instrument ever conceived for time-dependence studies. You can study reaction and polymerization phenomena in real time. You can even control the temperature for high, ambient or *below* ambient environments for thermoplastics or biopolymers.

### Ease of Use

Maybe you're familiar with old-fashioned light scattering instruments—how hard they are to use and maintain. Not ours. Wyatt Technology started with the theory of light scattering, threw out the stepper motors, refractive index-matching baths, photomultiplier tubes, swing-arms and all the other features that make light scattering the bane of a chemist's existence. The result is a line of instruments so elegant, so advanced, that they are a pleasure to use.

Imagine an innovative optical instrument with no lenses, mirrors or prisms (which often require realignment and cleaning). Imagine unpacking a laser light scattering photometer, and being up-and-running within 60 minutes! Imagine a multi-angle instrument with no moving parts. Imagine turn-key software solutions, and computer-programmers who implement your suggestions.

Imagine no more. We're here to prove the power of light scattering to solve your toughest problems. The DAWNs make tens-of-thousands of measurements in the time that it used to take to make one. Our multi-angle geometry produces the root-mean-square (rms)

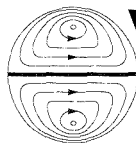


radius of your molecules *instantly*, not after hours of data collection. You won't make any of the arbitrary assumptions about the molecular shape, distribution or homogeneity required by other techniques. This is, after all, a real world—not one populated by perfectly spherical molecules with Gaussian distributions.

### More Good News

At Wyatt Technology we've been producing state-of-the-art instruments for over seven years, and we continue to back our products with training, seminars, consulting and the finest customer service in our industry.

Jump light years ahead of the competition; call us at (805) 963-5904 for a complete information package. With case histories, application notes, a sample-running laboratory, and a long list of delighted customers to confirm our good news, it won't take us long to show you just how much you've been missing!



**Wyatt  
Technology**  
CORPORATION

820 East Haley Street • Santa Barbara, CA 93103  
Tel: (805) 963-5904 • Fax: (805) 965-4898

© 1990 Wyatt Technology Corporation

CIRCLE 148 ON READER SERVICE CARD

## Definitions of analytical chemistry

"Analytical chemistry is a science of chemical characterization and measurement."  
H. A. Laitinen, 1982

"Analytical chemistry is a science of signal production and interpretation."  
E. Pungor, 1987

"In the course of determination, chemical, physicochemical, and physical methods are used. All of them, however, have the same feature: it is the dependence of signal on analyte concentration. The important task of analytical chemistry is therefore the discovery and implantation of these dependencies into analytical procedures."  
A. Lewenstam, J. Zytkow, 1987

passive pneumatic components? How might one eliminate thermal drift of a mechanical linkage without active temperature control? How might one use megabytes of experimental data without incurring time delays in storage and retrieval? How might one obtain very high data resolution with devices allowing only low dispersion of signals? How might one reduce the volume and weight of a machine without altering any other physical characteristic of the system?

In many cases, analytical scientists are not viewed as the best talent available to accomplish these tasks, and other types of professionals are being sought to fill instrument development positions. Yet these other professionals will be on the teams that provide future generations of analytical instrumentation to the analytical community. Shouldn't the analysts be included somewhere? It is going to be their equipment to use, after all.

### Who is an analytical scientist?

It is important to clarify the distinction suggested here between analytical scientists and other physical science or engineering professionals. Lewenstam and Zytkow (1) have explored this topic philosophically, and Kaiser and Ullman (2) have addressed practical aspects of the work of analytical chemists. Why should anyone be concerned about identifying the roles analytical chemists play in general scientific enterprises? Asking this question may not really matter, because it might be considered self-evident. Might this be a nonissue?

It is a substantive issue, because clarification of our roles provides us with a structure or framework within which to perform our productive work. It gives us identity. Even if this identity is not particularly important to us personally, that identity will be useful to others.

Identification as analytical chemists is necessary for us to interact with the outside world in accomplishing our tasks. Furthermore, if we believe analytical chemistry is a specific discipline, how can it be described to those whom we would like to attract to it? Pragmatically, research funds will not flow to analytical chemistry research if the agencies providing the funds are unaware that we have our own departments separate from other science departments.

In addition, identification of what constitutes analytical chemistry is important just because it is so difficult to arrive at a good definition of our specialty. The complexity of the definition is analogous to the complexity of the chemical versus the physical aspects of a sample. Consider the components of even a simple chemical solution: Defining precisely what its constituents are, even if we are the ones who prepared it, is not easy to do. Put in another context, we believe there is merit in the existence of a specialty called analytical chemistry, yet why is there no "analytical physics"?

The purpose of defining analytical chemistry is to draw a distinction between analytical chemists and other professionals within the confines of the specific activities involving instrument development. For example, an rf electronics engineer will view the impact of his design work on a power supply for a quadrupole mass spectrometer much differently than the analytical mass spectroscopist who is supplying the component specifications for the operation of that power supply.

It seems evident that someone with a degree in analytical chemistry is an analytical chemist; the academic curriculum and thesis work establish the definition of analytical chemistry. Reciting the list of courses taken and academic hurdles crossed, however, is not much

of a working definition. In a recent article (3) the comment was made that "analytical chemistry is not the application of various techniques to the measurement of key parameters but, very simply, it is 'problem solving.'" Clearly, any trained investigator or scientist could fit this definition at some time or other.

Several other definitions of analytical chemistry have also been generated (1). These definitions are all similar, but not the same. For the instrument development environment, the description of analytical chemistry as "discovery and implantation of the dependence of signals from physical processes on analyte concentration into analytical procedures" is most appropriate. But what then is "instrument development"?

### Instrument development

Instrument development is the activities that follow original research on new transduction phenomena or processes and that are specifically related to the generation of marketable equipment. When successful, these activities result in the commercialization of a viable approach to perform a specified experimental technique. Implicit in this definition is the capability to manufacture multiple copies of the device. Excluded are one-of-a-kind devices: Anyone can get one of anything to work at least once. Viability pertains to all parties interested in the system—not just the analytical user. If the system takes too long a time or too many people to build and test, fails frequently, or costs orders of magnitude more than a different approach with slightly inferior performance, then it is not viable.

Reasons for developing new instrumentation include analytical inducements, innovative engineering, and market demands. Analytical inducements derive from two principal considerations: the evolution of measurements of chemical parameters and progress in the technology providing the measurements (see p. 311A).

Known methods and techniques can often be made to perform better. Ways to gain additional information, such as extracting useful information from noise sources or retrieving most of the data generated in an atomic spectroscopic experiment that current spectrometer systems discard by design, are types of inducements for new instrument development. In addition, new approaches to obtaining known data can be explored, such as using Hadamard transforms or performing atomic absorption spectrometry with sources other than hollow cathode lamps.

New technology provides us with new types of measurements and information. Superconducting materials may open new vistas on NMR probe designs, for example. Where might progress in nonlinear optical materials lead us in spectral signal processing? Nanoscale techniques are about to alter dramatically our views on micro-miniaturization.

These considerations lead to the next major drive of new instrument development: innovative engineering. Most of the analytical systems available today are the result of the application of innovative engineering to current measurement techniques—not the implementation of new analytical approaches. Aspects of innovative engineering include new components, devices, and systems; materials technology advances; modernized design; enhanced manufacturing processes; and improved fabrication procedures.

Off-the-shelf electronics are often incorporated into such systems, leaving the designers free to concentrate on the cleverness of the system design instead of individual components. Advances in materials and material properties include the use of engineering plastics and ceramics to replace metal parts and devices; integral coatings that provide protection, inertness, RFI shielding, and thermal insulation instead of just paint; and fabrication processes that generate tailored alloys.

Modern engineering design practices allow sophisticated equipment to be developed in the same amount of time previously required for lesser performing systems. The application of computer-aided design (CAD), engineering (CAE), and software engineering (CASE) is providing initial system designs with improved reliability, serviceability, lifetime, and reduced parts count—features that previously emerged only after numerous design iterations.

Enhanced manufacturing processes, improved fabrication techniques, and the attainment of what is being called worldclass manufacturing (4) are leading to substantial improvements in analytical instrumentation. Although materials and labor costs continue to escalate, manufacturing costs are decreasing and system performance and reliability are steadily improving. Opportunities for analytical scientists in innovative engineering roles are not obvious, yet the engineering techniques being applied have a direct impact on analytical performance. The analytical scientist should be involved in the development process—not just a user after the fact.

Modern analytical systems are meant to meet the needs of the current market. Competition among the instrument vendors worldwide does not allow any company to disregard continual product development. These new requirements were stated most dramatically by Tom Peters when he said, "Change everything now" (5).

Higher quality products are needed that possess improved reliability and are easier to maintain while offering more flexible performance. Products must be more cost-effective; they must be less expensive but offer similar or improved performance over previous versions without being unnecessarily complex. Improved measurements will always be demanded until physical limits are reached. New measurement capabilities will be desired as old problems become intractable and as new problems arise.

Regulatory influences also determine market demand. Instrument developments in ICP-AES and GC/MS, for example, have resulted directly from regulatory requirements. Large niche markets are developing as a result of EPA's Contract Laboratory Program, the Department of Defense drug-testing programs, and auto emission regulations, among others.

The impact of analytical scientists on market demands is significant. They are the market. In addition to using the equipment, analytical scientists must go out of their way to properly define and specify the parameters of the analytical problems at hand. Without effective problem identification, we can expect to see general-purpose instrumentation developed with significant engineering overkill, all in the name of operational flexibility. In reality, however, the cleverness and ingenuity of the analytical operator would remain essential to ensure proper operation of these sophisticated arrays of subsystems and components, rather than releasing them for use in solving problems.

#### **Instrument development programs and projects**

Producing new analytical equipment is a time-consuming and expensive proposition. In general, at least two years—and perhaps as many as five years—are needed before a new instrument system can be introduced. This means that today's instrument development teams are working on equipment that will be at the Pittsburgh Conference between 1992 and 1995. Will the technology used in these projects be applicable to the problems at hand two to five years from now? These project

### **Analytical inducements to instrument development**

#### *Addressing chemical parameter measurement needs*

##### **Known measurement modes**

- Perform them better
- Obtain additional information

##### **New modes of making known measurements**

- New information on current problems
- New problems made accessible

#### *Response to progress in science and technology*

##### **New measurements**

##### **New information**

teams need the best possible set of specifications, based on a complete description of the problem to be solved, so that the appropriate technology can be applied. Researchers who develop the specifications should follow the system through to fruition to ensure that the specifications are met.

As an unorthodox alternative, instrument development times could be radically shortened. Immediate problems would be solved by new equipment to be introduced and delivered in six months at most (e.g., the semiconductor industry apparently can respond to market needs with development of new circuits in months, not years.) Exact problem identification would still be mandatory, even in the unlikely situation that instrument development could be made to proceed that quickly. Mechanisms for rapid generation of equipment designs would have to be in place, and the new instruments would have to be manufactured on existing production lines. Currently it is not possible to obtain the requisite exactness of problem descriptions, rapid design, or flexible use of manufacturing facilities for such rapid development to occur.

Analytical chemists can play an important role by working on or collaborating with instrument development project teams. They should be the interpreters of the analytical needs presented by the users. They can partici-

pate in the selection of the technical approach. They can work with the engineers who actually design and develop the systems. It was recently stated (6) that "It is no longer enough to manufacture a good, reliable machine and expect people to buy it. A company must design its machines to do what its customers want." Because the customers in this case are members of the analytical community, the engineering teams need trained analytical scientists to support the design work on those machines. Exactly how an analytical scientist might interact with a design team is not obvious, however. Instrument design projects are complex activities. Demands on the project move rapidly away from technology issues. The classic project management problem is somewhat facetiously described as "on time, on budget, on specification: choose two." How the project manager deals with this dilemma too often becomes a matter of choosing among the least of evils.

"On budget" and "on time" can result in a copycat instrument that has been based on incorrect specifications or simple engineering overkill. "On time" and "on spec" can result in a

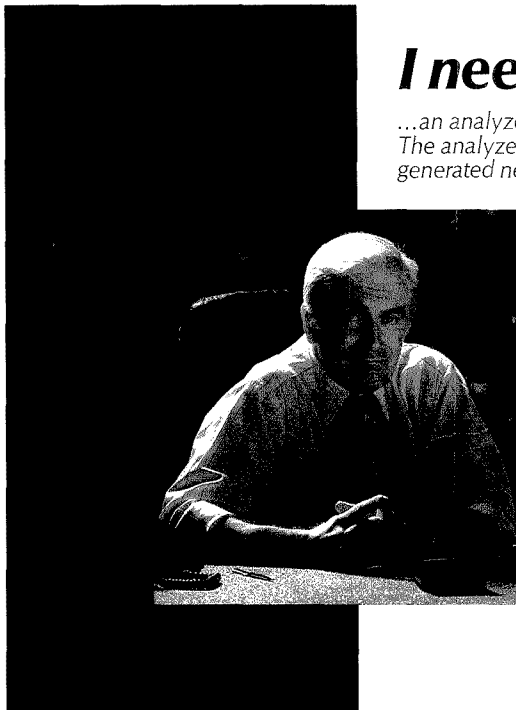
system that is expensive to build and must therefore carry a high price tag. This can be the result of choosing the wrong technical approach, which is inefficient and costly to implement, or of antiquated or inappropriate manufacturing capabilities. "On budget" and "on spec" lead to a late introduction and a potentially missed opportunity. (There is little real advantage in being second on the market and letting the first manufacturer make all the mistakes. That may happen, but the first in line also wins the largest market share.) Late entries can be the result of underestimated development time, insufficient staff, inflexible manufacturing capabilities, or an incorrectly defined market window of opportunity.

Once the analytical problem and exact specifications have been defined, the engineers take over. It is the engineers—not the physical scientists—who have been trained to produce tangible pieces of equipment. The engineering team should include an analytical scientist, however; it is important to verify the instrumental approach chosen and its functional implementation during—not after—the design process so that time and money will not

be wasted unnecessarily.

The product development program team is composed of representatives from the principal support groups within an instrument company. The titles of these groups vary, but the same types of functions are always present. Marketing establishes product need and specifications. Engineering designs the system and produces operational prototypes. Engineering support encompasses many functions, such as drafting, mechanical and electronic shop work, and project administrative and budget control. QA/Test focuses on specification verification and quality issues, although all team members are responsible for ensuring high-quality work. Manufacturing produces the systems, and service oversees installation and maintenance of the instrument.

The leader of the team is generally someone with experience on product development projects. Depending on the scope of the project, the leader can be any of the principal team members. For a brand-new product offering, it might be the marketing representative, for example. For the development of a new version of an older product, the



## *I needed...*

*...an analyzer to monitor additives in polymer melts. The analyzer had to withstand high temperatures generated near the extruder.*

*Bomem's industrial FT-IR analyzer not only proved to be dependable, it was also able to withstand our special conditions.*

*For reliability and dependability, I chose Bomem and I haven't looked back!*

*For information on how Bomem FT-IR can help you, call the measurement experts at 1-800-888-FTIR.*



**Bomem Inc.—Home Office** 450 St. Jean-Baptiste, Québec (Québec) Canada C2E 5S5, Tel.: (418)877-2944, Fax: (418)877-2834

**Bomem Inc.—World Field Operations Center** 1360 Wood Dale Road, Suite B, Wood Dale, IL 60191 USA, Tel.: (708)350-0550, Fax: (708)350-0780, Sales/Service: 1-800-888-FTIR

**Bomem Inc.—European Office** Bizonspoor 6007, 3605 LV Maarssen, The Netherlands, Tel.: 313465.62773, Fax: 313465.63998, Telex: 20000 (mmc 27:nlx712)

See us at **PITTCO**n—Booth #3354

CIRCLE 14 ON READER SERVICE CARD

leader might be the engineering representative.

Analytical scientists can conceivably fill some of these positions. The more probable opportunities are in the marketing group; others exist in either the QA/Test or engineering groups. Any position requires experience in project development. Examination of a generic instrument planned for development should uncover opportunities for analytical chemists to gain experience.

In general, an analytical instrument (Figure 3) is a system in which energy in some form interacts in a controlled fashion with a physical state of the sample for the purpose of characterizing one of the chemical features of the sample or its constituents. The system schematic shows only one of a number of ways that are indicative of the development tasks involved.

The team that actually designs the instrument and proves its functionality in prototypes is usually an engineering department team. The team leader is generally one of the working engineers and also the engineering representative to the product development team. The individuals responsible for design and development of the various subsystems are most frequently professional engineers. On a case-by-case basis, an analytical chemist might fill one of these positions, but that is not generally the situation. The engineers usually are familiar with the analytical techniques for which they are designing gear, but it is not really their responsibility to have a working knowledge of all the subtleties of total system operation. Recall the rf electronics engineer mentioned earlier, working on a new MS power supply. He might know about MS as a technique but would not be conversant in analytical MS. It is helpful if the engineers are teamed with an analytical scientist who can provide guidance and perspective to keep the design team focused.

For this version of the project team, the analytical scientist may fill one of the engineering positions (e.g., dealing with the sample cells or other attendant apparatus). Frequently, analytical chemists are sufficiently experienced and skilled to fill the software engineering positions, particularly for the data output and the user interface.

#### Cycle of instrument generation

Analytical chemists participate in each phase of instrument development (Figure 4), although their impact is much greater in some areas than others. The analytical chemist is predominantly the user and applications specialist operating the instrumentation on a daily

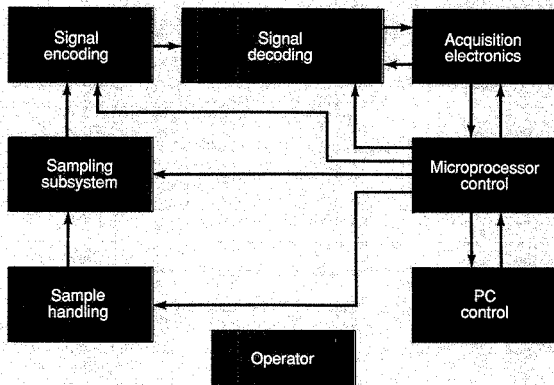


Figure 3. Schematic of a generic analytical instrument system, constructed to suggest development task domains as much as actual device functions.

#### Engineering project team members and responsibilities

1 Electronics engineer	Signal encoding subsystem
1 Mechanical/electrical engineer	Signal decoding subsystem
1 Electronics engineer	Digital electronics; firmware
1 Electronics engineer	Analog electronics
1 Mechanical engineer/physical scientist	Sampling subsystem
1 Mechanical engineer	Structure; manufacturing specifications
3 Software engineers	User interface; communication

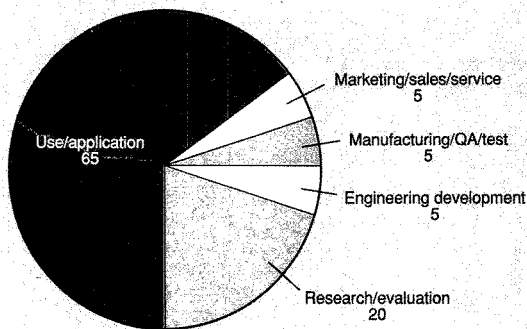


Figure 4. Cycle of instrument development.

Percentages of total analytical science community engaged in portions of the cycle are shown with only analytical science professionals considered.

basis. As problems become intractable with current equipment, the analyst generates new demands for instrumentation. The demands provide direction to analytical research groups who evaluate current instrumentation for potential improvement of performance or apply new technology on the problem. The instrument company enters the cycle to meet the new market needs. The marketing department clarifies the needs and generates system specifications, which the engineering department designs and develops, providing prototypes to QA/Test for verification of functionality and to the manufacturing group as models from which to build production units. The marketing, sales, and service groups then make the new equipment available to the community to restart the cycle.

Although analytical chemists can play a role in every phase of this cycle, they are particularly important in just a few of them. Analytical chemists must be educated and vocal consumers. If instrument companies do not learn of analytical needs, or if the needs come from only a single (or worse, a biased) source, the equipment offered will be less than needed.

Analytical researchers can lead the way to new instrumentation, but they will be most effective in undertaking high-risk/high-payoff research endeavors. They are the most suitable for these activities and need to be members of product development teams. Few of these positions are available, and analytical chemists must compete successfully with the engineering community that traditionally does most instrumentation development. Given an interest in development work, however, an analytical chemist has to learn only a modest amount of engineering to be able to interact credibly on a project team. Then he or she will be able to oversee the needs of the users for whom the instrumentation is being developed and strive to keep the team focused so that the best equipment arrives on time, on spec, and reasonably priced.

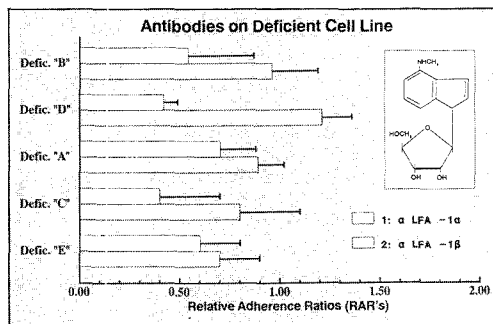
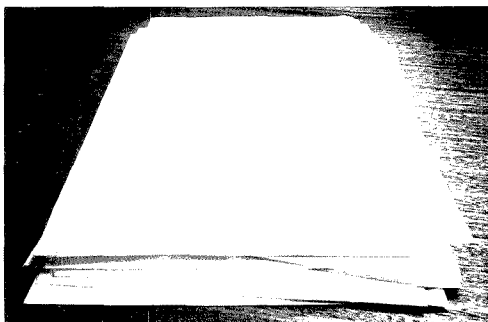
**References**

- (1) Lewenstam, A.; Zytkow, J. M. *Fres. Z. Anal. Chem.* 1987, 326, 30.
- (2) Kaiser, M. A.; Ullman, A. H. *Anal. Chem.* 1988, 60, 323 A.
- (3) Grasselli, J. G. *Spectroscopy* 1989, 4(4), 30.
- (4) Schonberger, R. J. *World Class Manufacturing: The Lessons of Simplicity Applied*; The Free Press; MacMillan: New York, 1986.
- (5) Peters, T. *Peninsula Times Tribune* January 29, 1989, p. F-6.
- (6) Pool, R. *Science* 1989, 243, 1556.



Andrew T. Zander, director of the Systems Laboratory at Varian Research Center, received his Ph.D. in analytical chemistry from the University of Maryland in 1976. He has research management responsibilities for physics, electronics, and instrumentation development projects and has published in the areas of excitation sources, diffraction phenomena, optical detection devices, and signal processing approaches for analytical spectrometry. He has served on the Instrumentation Advisory Panel and Editorial Advisory Board of ANALYTICAL CHEMISTRY and on the Editorial Board of Microchemical Journal.

# Make your data... greater.



No matter how interesting your scientific results are, they're not worth much unless you can communicate them to other people. That's where SlideWrite Plus comes in. You see, our powerful presentation graphics software for the IBM PC and compatibles can turn the data you worked so hard to capture into high impact

charts, graphs, slides and overheads — and do it all *in minutes*. SlideWrite Plus gives you powerful graphing features, full drawing capability, flexible labeling with 16 fonts, and *extremely* high quality output on printers, plotters, and cameras. And that's just for starters. It's no wonder SlideWrite Plus tied for first

place in a recent *PC Week* poll! Call us for a free demo diskette right now. We'll show you how SlideWrite Plus can help your results *get* results.

**Call for your FREE full-featured trial diskette! (408) 749-8620**

Advanced Graphics Software  
333 West Maude Ave., Sunnyvale, CA 94086

**SlideWrite Plus.™ We make your data look terrific.**

CIRCLE 1 ON READER SERVICE CARD

Our easy-to-use catalog features over 20,000 scientific products for research, industry, and education. For your free copy, mail in the attached card or call us toll-free at 1-800-323-4340.

Instruments  
for Research,  
Industry,  
and Education

Call Toll-free:  
1-800-323-4340

COLE-PARMER 1989-1990

Compliments of  
Cole  
Parmer

## This indispensable resource FREE

Our many product lines include:

- Balances • Baths and circulators • Biotechnology instrumentation
  - Fermentation • Electrophoresis • Books • Centrifuges
  - Liquid and gas chromatography products
  - Computer software and data acquisition
- Environmental testing equipment • Filtration products • Flowmeters
  - Mixers and stirrers • Ovens, incubators and furnaces
- pH measurement and control • Plasticware • Pumps • Recorders
  - Spectrophotometers • Thermometry • Tubing...and more

COLE-PARMER INSTRUMENT COMPANY • 7425 NORTH OAK PARK AVENUE • CHICAGO, ILLINOIS 60648

Circle Reader Card No. 22

# NOW!

# FLUORESCENCE

## RESEARCH FLUORESCENCE PERFORMANCE

*At an Affordable Price*

At last, SPEX unmatched performance is available to enhance virtually any analytical application or research investigation. FluoroMax™ is the newest addition to the SPEX lineup of high performance fluorescence instrumentation. Decades of experience with fluorescence instrumentation culminate in a spectrofluorometer with sensitivity demonstrably higher than anything in its price range. Incorporating many of the features that have made our FLUOROLOG-2 spectrofluorometers the standard of fluorescence research, the unique design of the FluoroMax™ includes the following list of features:

- Photon-counting for Maximum Sensitivity
- Full PD control including automated variable slits for simple operation
- Fastest scanning speeds for quick ramping spectra
- Reflective optics for maximum throughput at any wavelength
- 100 nsec data acquisition for rapid kinetic measurements
- Self-calibration for instant start-up
- Rugged unitized construction
- Fully corrected excitation and emission spectra
- Visible-Silver D-DICOM Spectroscopy Option

Now there's no need to wait to get the best data from your fluorescence samples.

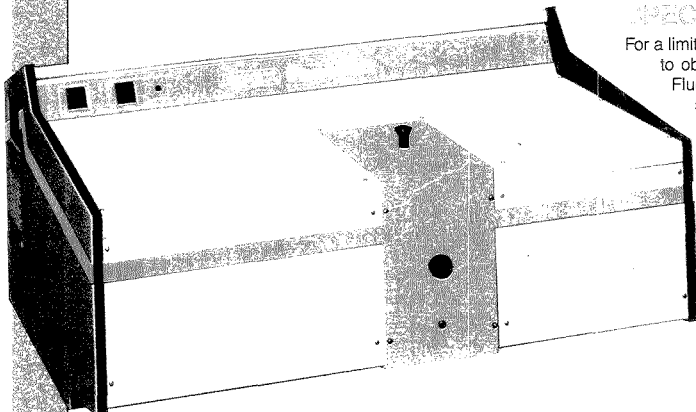
Call SPEX today at 1-800-GET-SPEX, and talk over your application with one of our specialists.

### SPECIAL OFFER

For a limited time, SPEX offers you the opportunity to obtain the outstanding features of the FluoroMax™ spectrofluorometer at a special introductory offer. This includes a PC computer, a full complement of software, plus free installation. Call now to reserve your system and give your application the performance it deserves.

SEE THE FLUOROMAX™ AT THE  
BOTH 5018 AND 5019 STATIONS  
FOR A FLUORESCENCE  
WORKSHOP AND  
SEMINAR FOR

FluoroMax™ at FASEB  
AT FASEB.



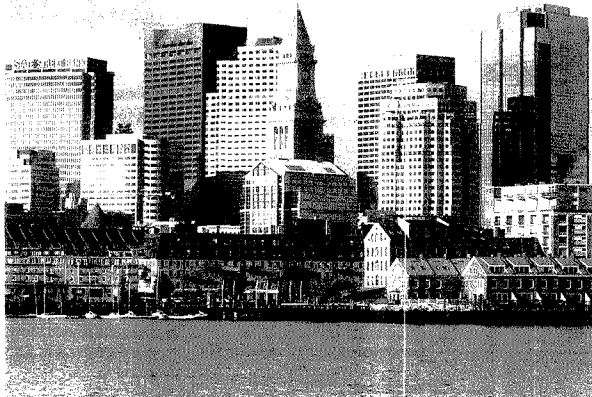
# SPEX

#### HEADQUARTERS

SPEX Industries, Inc.  
3880 Park Avenue  
Edison, NJ 08820 U.S.A.  
Tel: 800-438-7739 or  
[201] 549-7144  
Fax: [201] 549-5125

#### EXPORT HEADQUARTERS

SPEX Export, Ltd.  
2, West Links,  
Tilgate,  
Chandlers Ford,  
Hampshire, SO5 3 TG  
United Kingdom  
Tel: [44] 703-644611  
Fax: [44] 703 613554



PHOTOS COURTESY OF THE GREATER BOSTON CONVENTION & VISITORS BUREAU

## MEETINGS

# 199<sup>TH</sup> ACS National Meeting

The 199th National Meeting of the American Chemical Society will be held in Boston, MA, April 22-27. The Division of Analytical Chemistry will sponsor or cosponsor technical sessions at which more than 180 presentations are scheduled. The meeting will feature a presidential plenary session, "Supply of Scientists in the 21st Century" (Sunday, April 22) and a career development tutorial, "Expanding Your Options" (Sunday, April 22, and Monday, April 23). Other highlights include meetings of the ACS council and board of directors; ACS short courses; a national employment clearinghouse; and a series of social events, including the ACS mixer (Monday, April 23), an alumni hour (Wednesday, April 25), and the Division of Analytical Chemistry dinner (Monday, April 23).

On-site registration facilities will be located in the Hynes Convention Center, Hall B. Hours for registration will be Sunday, April 22, from 2 P.M. to 7 P.M.; Monday, April 23, through Thursday, April 26, from 7:30 A.M. to 3:30 P.M.; and Friday, April 27, from 7:30 A.M. to 10 A.M.

An exposition of instruments, chemicals, technical literature, and other products and services will run for three days in conjunction with the meeting. The exposition, which will be housed in the Hynes Convention Center, will be open Monday, April 23, and Tuesday, April 24, from 9 A.M. to 5 P.M. and Wednesday, April 25, from 9 A.M. to 4 P.M.

The technical program will feature the following award symposia sponsored by the Division of Analytical Chemistry: the ACS Award in Analytical Chemistry; the Frank H. Field and Joe L. Franklin Award for Outstanding Achievement in Mass Spectrometry (cosponsored with the Division of Biological Chemistry); the ACS Award in Chromatography (cosponsored with

the Division of Physical Chemistry); and the ACS Award for Computers in Chemistry (cosponsored with the Division of Computers in Chemistry). The ACS Award in Separations Science, sponsored by the Division of Industrial and Engineering Chemistry, will also be presented.

Other Division sessions will cover measurement problems in atmospheric chemistry, computer simulation and artificial intelligence, gas sensors, immunoassay methods, lasers, colloid science, element-specific chromatographic detection by atomic emission spectroscopy, electrochemistry, spectroscopy, and chromatography.

Also of interest are the following sessions: Recent Developments in the Teaching of Analytical Chromatography and New Experiments for the Instrumental Analysis Course (sponsored by the Division of Chemical Education), Membrane Separations in Biotechnology and Biology and Chromatography and Biological Separations (sponsored by the Division of Industrial and Engineering Chemistry), Instrumental Methods for Polymer Characterization (sponsored by the Division of Polymer Chemistry), Particle-Size Analysis in Polymer Science (sponsored by the Division of Polymeric Materials: Science and Engineering), and Lasers in Nuclear Chemistry and Technology (sponsored by the Division of Nuclear Chemistry).

The program will be highlighted by the presentation of several awards. Barry Karger will receive the ACS Award in Analytical Chemistry and will deliver a talk on Monday, April 23, entitled "Current Trends in the Separation of Biopolymers." The ACS Award in Chromatography will be presented to John H. Knox, who will deliver a talk entitled "Theoretical Plates: Past, Present, and Future" on Tuesday, April 24. The Frank H. Field and

Joe L. Franklin Award for Outstanding Achievement in Mass Spectrometry will be presented to Evan C. Horning and Marjorie G. Horning on Wednesday, April 25. Their talk is entitled "Gas-Phase Analytical Chemistry: The Development and Use of Hyphenated Mass Spectrometry from GC/MS to LC/GC/API-MS/MS." Peter C. Jurs will receive the ACS Award for Computers in Chemistry and will deliver his talk entitled "Computer-Assisted Studies of Structure-Property and Structure-Activity Relationships" on Tuesday, April 24. Also on Tuesday, Henry Freiser, recipient of the ACS Award in Separations Science and Technology, will deliver his talk, "Separation of Metal Ions by Liquid-Liquid Processes—A Forty-Year Perspective."

The Division of Analytical Chemistry dinner is scheduled for Monday, April 23, at the Durgin Park Restaurant, 340 Faneuil Hall Marketplace. The social hour, beginning at 6 P.M., will be followed by dinner at 7 P.M. Cost is \$25. Ticket ordering information is available in the Feb. 26 issue of *Chemical & Engineering News*. Advance purchase of tickets is urged.

The ACS Department of Continuing Education will offer a series of short courses at the meeting. For further information, see p. 320 A or contact the Department of Continuing Education, American Chemical Society, 1155 16th St., N.W., Washington, DC 20036 (1-800-227-5558 or 202-872-4508).

Registration details and additional information about the meeting are available in the Jan. 29 and Feb. 26 issues of *Chemical & Engineering News*. The latter issue contains the final program for the meeting. The program that follows includes all sessions sponsored or cosponsored by the Division of Analytical Chemistry. The Symposium on Liquid-Liquid Separation Processes is also included.

## Short Courses

The following courses are offered in conjunction with the 199th ACS National Meeting in Boston, April 22–27. For information on other ACS courses, contact the Department of Continuing Education, American Chemical Society, 1155 16th St., N.W., Washington, DC 20036 (1-800-227-5558 or 202-872-4508).

■ **Electronics for Laboratory Instrumentation.** April 19–21. Howard Malmstadt, Christie Enke, and Stanley Crouch

■ **Chemical Engineering and Process Fundamentals for Chemists.** April 20–22. Richard Griskey

■ **Molecular Biology and Recombinant DNA Technology.** April 20–22. William Reznikoff and Gary Buell

■ **Experimental Design for Productivity and Quality in R&D.** April 20–22. Stanley Deming and Stephen Morgan

■ **Environmental Analytical Chemistry: Analysis of Water and Waste Samples.** April 21–22. Marcus Cooke, Marvin Miller, Walter M. Shackelford, Thomas A. Bellar, Judith E. Gebhart, and Harold McNair

■ **Fundamentals of High-Performance Liquid Chromatography.** April 21–22. Harold McNair

■ **Effective Management of Chemical Analysis Laboratories.** April 21–22. John H. Taylor, Jr., and Mary Routson

■ **Capillary Gas Chromatography.** April 21–22. Stuart Cram and Milos Novotny

■ **Quality Assurance of Chemical Measurements.** April 21–22. John K. Taylor

■ **Effective Supervision of Scientists and the Technical Staff.** April 21–22. David Gootnick

■ **Spectroscopic Characterization of Polymers.** April 21–22. Jack Koenig and Bruce Chase

■ **Winning at Chemometrics.** April 21–22. Michael Delaney and Barry Lavine

■ **Atomic Absorption, ICP, and ICP/MS.** April 21–22. Marcus Cooke, Marvin Miller, and Gordon Wallace

■ **Spectroscopy for Chemical Analysis: Basics, Advanced Methods, and Rapid Screening.** April 21–22. Tuan Vo-Dinh

## Program

## DIVISION OF ANALYTICAL CHEMISTRY

G. D. Christian, *Chairman*

## MONDAY MORNING SECTION A

## Electrochemistry

G. J. Patriarche, *Presiding*

- 9:20 Amperometric Biosensor for Glucose Based on Nafion Loaded with Redox Couples and Glucose Oxidase. **D. Bélanger**, M. Vaillancourt, G. Fortier
- 9:40 Surface Spectroscopic and Electrochemical Studies of Coal-Derived Model Compounds. **S. L. Michelhaugh**, G. M. Berry, M. P. Sorlage
- 10:00 Electrochemical Behavior of Cellulose at Carbon Paste and Lipid-Modified Carbon Paste Electrodes. **J. Arcos**, J.-M. Kauffmann, **G. J. Patriarche**, P. Sanchez-Batanero
- 10:35 Probing Single-Cell Neurochemistry with Capillary Electrophoresis. **T. M. Oefeltrowicz**, A. G. Ewing
- 10:55 Electrochemical and Spectroscopic Characterization of Noble Metal and Bimetallic Electrocatalysts. **G. M. Berry**, S. L. Michelhaugh, M. P. Sorlage
- 11:15 Preparation of Band Microelectrode Arrays from Tefzel Film and Metal Foil. **W. J. Bowyer**, D. M. Odell

## SECTION B

## ACS Award in Analytical Chemistry Symposium Honoring Barry L. Karger—I

F. E. Regnier, *Presiding*

- 9:00 Introductory Remarks.
- 9:10 High-Performance Size Exclusion Chromatography Using Polyether Bonded Silica Phases. **N. Cooke**
- 9:40 Selectivities of Polymer Encapsulated Stationary Phases. **H. Engelhardt**, H. Low, M. Maub, J. Kohr, W. Eberhardt
- 10:10 Computer-Aided Method Development in HPLC. **R. Gant**
- 10:55 Nonporous Resins for Faster Analysis and Purification of Biopolymers by Reversed-Phase, Ion-Exchange, and Hydrophobic Interaction Chromatography. **R. Eckstein**
- 11:25 Recombinant DNA-Derived Protein Separation by HIC and Spectrum Mapping by On-line Monitoring with UV Photodiode Array and Fluorescence Spectroscopy. **S.-L. Wu**, H.-J. Sievert, W. S. Hancock

## SECTION C

## Symposium on Advances in Computer Simulation and Artificial Intelligence in Analytical Chemistry—I

G. I. Ouchi, *Presiding*

- 8:30 What Lies in the Future for Computer Simulation and Artificial Intelligence in Analytical Chemistry? **G. I. Ouchi**

- 9:00 Expert Systems for Method Development in HPLC. **J. A. van Leeuwen**, L.M.C. Buydens, G. Kateman, M. Mulholland
- 9:30 Spectral Matching in HPLC: A Critical Study of the Requirements for an Expert System. **H.-J.P. Sievert**
- 10:15 Expert System Approach to Optimization Parameter Selection for Reversed-Phase Ion-Pair Chromatographic Separations. **A. Bartha**, G. Vigh
- 10:45 Versatile Strategy for the Optimization of Eluent Conditions for LC. **D. P. Michaud**, F. V. Warren, B. A. Bidlingmeyer
- 11:15 Three-Dimensional Random-Walk Simulation of Chromatographic Separations. **J. H. Wahl**, C. G. Enke, **V. L. McGuffin**
- 11:30 Computer-Aided Optimization of Gas Chromatographic Separation. **J. W. Dolan**, D. E. Bantz

## SECTION D

## Symposium on Modern Gas Sensors—I

E. B. Overton, *Presiding*

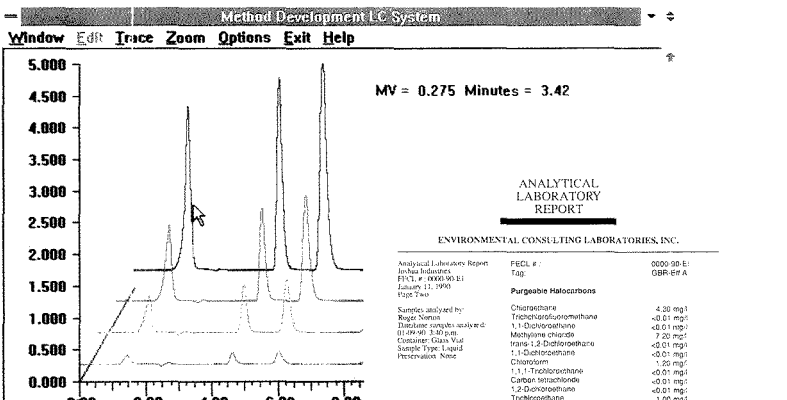
- 9:00 Introductory Remarks.
- 9:05 Solid-State Microelectrochemical Devices. **M. S. Wrighton**, R. Crooks, D. Talham, M. Schloh
- 9:35 Gas Sensors Based on Ion-Selective Polymer Membrane Electrodes. **M. E. Meyerhoff**
- 10:05 Catalytic Gated Semiconductor Devices as Gas Sensors. **R. C. Hughes**, W. K. Schubert, T. E. Zipperian, J. L. Rodriguez
- 10:55 Amperometric Gas Sensors: Use in Air Pollution Measurement. **J. R. Stetter**, W. R. Penrose, G. J. MacLay, M. W. Findlay, C. Yue, L. Pan
- 11:25 NO<sub>2</sub> Gas Sensor Based on a Nitrite-Selective Electrode. **S. A. O'Reilly**, S. Daunert, L. G. Bachas

## MONDAY AFTERNOON SECTION A

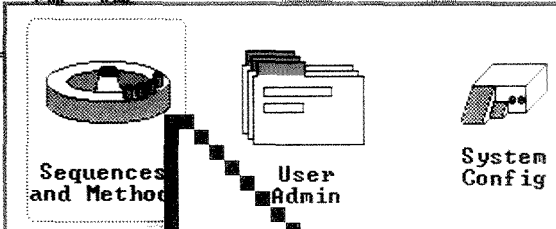
## Symposium on New Methods in Immunoassay—I

M. E. Meyerhoff, *Presiding*

- 1:30 Introductory Remarks.
- 1:35 Immunoassay Methods. **H. H. Weetall**
- 2:00 Practical Considerations for the Use of Immunoassays to Measure Analytes in Biological Fluids. **S. Hochschwender**, M. Chiappetta, G. David, V. Johnson, E. Sevier, J. Strobel, S. Strobel, P. Vasquez
- 2:25 Analytical Characterization and the Long-Term Performance of a Competitive Enzyme-Linked Immunosorbent Assay (ELISA). **M. L. Poor**, D. R. Smith, J. C. Spears, **G. S. Siltampalam**
- 2:50 Use of Enzyme-Linked Immunosorbent Assay in Forensic Serology. **J. L. Mudd**
- 3:30 Fluorescence Immunoassays for Quantifying Low Molecular Weight Therapeutic Compounds in Plasma at Picomolar Levels. **J. R. Sportsman**, L. D. Taber
- 3:55 Improving the Detection Limits of Homogeneous Enzyme-Linked Competitive Binding Assays. **L. G. Bachas**
- 4:20 Interactions of Antibodies and Binding Proteins with Enzyme-Ligand Conjugates: Implications in the Design of Homogeneous and Heterogeneous Binding Assays. **M. E. Meyerhoff**



# Point your way to effortless chromatography!



Finally, chromatography data management is easy with Spectra STATION.™

Fast, flexible and intuitive, Spectra STATION points the way to custom chromatography data management. Now you can develop methods for your LC or GC with just the click of a mouse.

There is no difficult learning curve. Our mouse-driven interface lets you integrate peaks and optimize parameters quickly.

Develop your chromatography method right on screen, knowing that all revisions are saved in the built-in database.

Customizing reports is easy. Select the results you want to report and Spectra STATION prints them automatically, on a form of your choice.

Effortless chromatography data management—Spectra STATION makes it automatic. For more information, call us at 800-424-7666.



SEE YOU AT PITTCON - BOOTH 3317

 **Spectra-Physics**

Discover the Quality

Circle 125 for sales representative. Circle 126 for information.

SECTION B

**ACS Award in Analytical Chemistry  
Symposium Honoring Barry L. Karger—II**

H. Engelhardt, *Presiding*

- 1:30 Introductory Remarks.
- 1:40 Award Address: Current Trends in the Separation of Biopolymers. **B. L. Karger**
- 2:10 Reversed-Phase and Hydrophobic Interaction Chromatography: A Comparison. **C. Horváth**, F. D. Antia, I. Fellegvari, K. Kalghatgi
- 2:40 Progress in the Theory of Nonlinear Chromatography. **M. Czok**, S. Golshan-Shirazi, **G. Guiochon**, A. M. Katti, Z. Ma
- 3:25 Analytical Molecular Biology: An Examination of Deamidation of Recombinant DNA Derived from Human Growth Hormone. **W. S. Hancock**, J. E. Battersby, G. Teshima, S.-L. Wu, E. Canova-Davis, D. W. Aswad
- 3:55 New Type of Restricted-Access Reversed-Phase Packing Material. **F. E. Regnier**, C. Desilets

SECTION C

**Symposium on Advances in Computer  
Simulation and Artificial Intelligence in  
Analytical Chemistry—II**

J. W. Dolan, *Presiding*

- 1:30 Applications of Multivariate Data Processing in Chemical Analysis. **L. S. Ramos**, V. Fishback
- 2:00 Some Applications of Artificial Intelligence in IR Spectroscopy. **S. R. Lowry**, D. T. Sparks
- 2:30 Knowledge-Based Systems for Interpreting IR Spectra. **B. J. Wythoff**, S. P. Levine, **S. A. Tomellini**
- 3:15 Spectral Knowledge Database: Preliminary Studies on CMR and IR Data. **C. F. Hammer**, S. R. Heller, M. Pencia, C.-M. Tseng
- 3:45 Computerized Analysis of Two-Dimensional Double Quantum NMR Spectra. **R. Dunkel**, C. L. Mayne, R. J. Pugmire, D. M. Grant
- 4:15 Development of an Expert System for Structure Elucidation from Ion Trap MS Data. **P. T. Palmer**, C. M. Wong

SECTION D

**Symposium on Modern Gas Sensors—II**

J. Stetter, *Presiding*

- 2:00 Development of a Dual Microchip Gas Chromatographic Instrument for Highly Reliable Vapor Detectors. **E. B. Overton**, K. Carney, R. Wong, J. Stout, C. Steele
- 2:30 From Microsensors to Sensor Systems: A SAW Sensor Array System for Trace Organic Vapor Detection. **J. W. Grate**, M. Klusty, S. Rose-Pehrsson
- 3:00 Feasibility of Man-Portable GC/MS for Air-Monitoring Applications. **H.L.C. Meuzelaar**, N. S. Arnold, W. H. McCleennen, D. T. Urban, D. Hunter
- 3:50 Real-Time Vapor Monitoring with MS/MS. **G. L. Glish**, S. A. McLuckey, K. A. Asano
- 4:20 Sensing of Hazardous Airborne Vapors Using Ion Mobility Spectrometry. **G. A. Eiceman**



TUESDAY MORNING SECTION A

**Symposium on New Methods in  
Immunoassay—II**

G. S. Sittampalam, *Presiding*

- 8:30 Electrochemical Immunoassay: Status and Outlook. **P. I. Hilditch**
- 8:55 Ultrasensitive Electrochemical Immunoassay—Practical Considerations. **H. B. Halsall**, W. R. Heineman
- 9:20 Use of Monoclonal Antienzyme Antibodies for Analytical Purposes. **P. C. Gunaratna**, D. S. Bindra, G. S. Wilson
- 9:45 Immunoassay of Secreted Antibody Molecules at the Individual Cell Level. **K. T. Powell**, **J. C. Weaver**
- 10:25 Fiber-Optic Immunosensor for Rapid Detection of Microorganisms. **F. J. Regina**, S. H. Lin, **J. M. Bolts**
- 10:50 Assay for Host Cell Protein Contar inants in bFGF Using the Threshold System. **C. C. Ting**
- 11:15 Planar Waveguide Optical Immunosensors. **S. J. Choquette**, L. Locascio-Brown, A. L. Plant, R. A. Durst

- 11:40 Chemiluminescent DNA Probe Assay for Campylobacter. **R. A. Martirelli**, E. Carroll, III, J. G. Donahue

**ACS Award for Computers in Chemistry  
Symposium Honoring Peter C. Jurs  
Cosponsored with the Division of  
Computers in Chemistry**

G. W. Small, *Presiding*

- 8:30 Introductory Remarks.
- 8:35 Use of Topological Similarity Measures as Structural Probes in SAR Studies. **E. P. Jaeger**
- 9:15 Quantitative Structure Relationship Studies of Odor-Active Compounds. **P. A. Edwards**, L. S. Anker, P. C. Jurs
- 10:15 Correlation of Segmental Anisotropies of Selected Polymeric Materials with Calculated Polarizability Tensor of Small Molecule Model Compounds. **H. A. Clark**, M. G. Dibbs, S. E. Bales
- 10:35 Pattern Recognition Methods in SAR Studies and in Drug Discovery, Design, and Development. **T. R. Stouch**
- 11:20 Award Address: Computer-Assisted Studies of Structure-Property and Structure-Activity Relationships. **P. C. Jurs**

# DIALOG INTRODUCES ANOTHER TABLE OF BASIC ELEMENTS FOR YOUR LAB.



There's no symbol for *information* in the Periodic Table. Yet nothing could be more crucial to your research than complete, accurate technical and business information.

That's why many chemists consider DIALOG<sup>®</sup> an essential element in the modern lab.

As the world's largest online knowledgebank, DIALOG gives you access to a whole world of critical information. Right in your own lab.

For starters, you can tap into the crucial scientific data. DIALOG has detailed information on everything from

compound identification to chemical safety data, property data, substance and substructure.

Then you can expand your focus by accessing important, related data that will enable you to look at your work in a broader context.

For example, you can investigate patents, competitive projects, new product markets, and worldwide industry trends. In fact, you can investigate any topic, anytime.

And you won't have to sacrifice depth for the sake of breadth. DIALOG is updated continuously, so the data is

always comprehensive and current. And many citations can be conveniently retrieved in full text.

Call today for more information and a free Periodic Table Reference Card. Once you've examined them, you'll see how DIALOG can become a basic element of all your research.

Call us toll free at 800-3-DIALOG, (800-334-2564). Or request information by Fax at 415-858-7069.

**DIALOG** INFORMATION SERVICES, INC.  
A Knight-Ridder Company

*The world's largest online knowledgebank.*



## SECTION B

**ACS Award in Analytical Chemistry  
Symposium Honoring Barry L. Karger—III**

F. E. Regnier, *Presiding*

- 9:00 Introductory Remarks.  
 9:10 New Polymeric Activated Reagents for the Derivatization of Nucleophiles in HPLC Detection. I. S. Krull, A. J. Bourque, D. Schmalzing, C-X. Gao, A. Trogen, M. Szuic  
 9:40 Trace Analysis of DNA Adducts by MS. R. Geise, P. Vouros  
 10:25 Use of Deuterated Cholesterol as an Internal Monitor for the Formation of Cholesterol Oxides. B. A. Wasilchuk, P. Feibush, P. W. Lequesne, P. Vouros  
 10:55 Rapid DNA Sequencing Using Gel-Filled Capillary and Laser-Induced Fluorescence Detection. A. S. Cohen, D. Najarian, B. L. Karger

**Symposium on Liquid-Liquid Separation Processes**

*Sponsored by the Division of Industrial and Engineering Chemistry*

S. Muralidharan, *Presiding*

- 9:00 Introductory Remarks.  
 9:15 Award Address: Separation of Metal Ions by Liquid-Liquid Processes—A Forty-Year Perspective. H. Freiser  
 10:00 Extraction Studies of M(TTA)<sub>2</sub> + Crown Ether Complexes. G. R. Chopplin, J. N. Matruh  
 10:40 "Soft" Donor Ligands for Actinide/Lanthanide Separations. B. F. Smith, G. D. Jarvinen  
 11:10 Interfacial Phenomena in Highly Agitated Solvent Extraction Systems. H. Watarai  
 11:40 Equilibrium and Kinetic Studies on the Complexation of Nickel(II) by 8-Quinoloinis in Micelles and Microemulsions of Neutral and Charged Surfactants. S. Muralidharan, E. Burke, H. Freiser

## SECTION C

**Spectroscopy**

C-N. Ho, *Presiding*

- 9:20 Selective Ion Monitoring for Determining the Position of Isotope Labels. T. A. Lee, J. K. Hardy  
 9:40 Gas-Phase Chemistry of Complexes between Peptides and Group IA and Group IIA Metal Ions. L. M. Teesch, J. Adams  
 10:00 Model Titan Atmospheric Hydrocarbon Analysis by Ion Mobility Spectrometry in Dry Helium. D. R. Kojiro  
 10:35 <sup>27</sup>Al, <sup>29</sup>Si, and <sup>13</sup>C CPMAS/MAS High-Resolution NMR Spectroscopic Studies of Doped Cement Matrices and the Use of a Spectroscopic Data Analysis System to Deconvolute and Integrate the Spectra. H. Akhter, F. K. Cartledge, D. Chalasani, L. G. Butler, M. Jakisch  
 10:55 Aspects of Pharmaceutical Method Development Using GFAAS. S. L. McCall  
 11:15 Determination of Some Important Trace Metals in Chinese Herbs by GFAAS. D-S. Su, C-N. Ho

## SECTION D

**Symposium on Modern Gas Sensors—III**

J. W. Grate, *Presiding*

- 8:45 SAW Gas Sensors Based on Acoustoelectric Effects. A. J. Ricco, S. J. Martin  
 9:15 Progress in the Development of Sensitive, Compound-Specific Piezoelectric Quartz Vapor Detectors. E. B. Overton, X. Yan, X. Zhang, P. Klinkhachorn, G. Newkome  
 9:45 Using Ultrasonic Waves in a Thin Membrane to Sense Chemical and Biochemical Quantities. R. M. W. Frate  
 10:35 SAW Sensor Response and Molecular Modeling. D. G. Stone, M. Thompson, M. D. Frank  
 10:55 Acoustic Wave Chemical Sensors Based on Monitoring Both Velocity and Attenuation. G. C. Frye, S. J. Martin

- 11:25 Use of Temperature-Variied SAW Sensors for Improved Selectivity. D. S. Ballantine, Jr.

**TUESDAY AFTERNOON**
**Symposium on Liquid-Liquid Separation Processes**

*Sponsored by the Division of Industrial and Engineering Chemistry*

R. P. Sperline, *Presiding*

- 1:30 Influence of Diluents on Bifunctional Extractants of the Carbamoyl-Phosphoryl Class. E. P. Horwitz, H. Diamond, R. Chiarizia, K. A. Martin  
 2:00 In Situ FT-IR/IRS for the Study of Flotation Surface Chemistry. J. D. Miller, J. J. Kellar, W. M. Cross  
 2:30 In-situ IR Attenuated Total Reflection Spectroscopic Examination of the Hydrocarbon-Aqueous Interface: Adsorption of Reagents. R. P. Sperline, H. Freiser  
 3:10 Chemically Active Inorganic Membranes for Removal/Concentration of Metal Ions from Dilute Solutions. J. Yi, R. Ferreira, L. L. Tavlarides  
 3:40 Efficient Separation of Trivalent Lanthanides Using Cyanex 272 by Centrifugal Partition Chromatography (CPC). First Demonstration of Gradient pH Elution in CPC. S. Muralidharan, R. Cai, H. Freiser  
 4:10 Enrichment of Trace Metals in Natural Waters on XAD-7 Resin. A. Corsini, M. Thomson

**ACS Award for Computers in Chemistry  
Symposium Honoring Peter C. Jurs  
Cosponsored with the Division of  
Computers in Chemistry**

G. W. Small, *Presiding*

- 1:30 Pattern Recognition Analysis of the Responses from Sensor Arrays for Trace Vapor Detection. S. L. Rose-Pehrsson, J. W. Grate, M. Klusty  
 2:10 Computer Applications for the Study of Chromatographic Data. R. H. Rohrbaugh  
 3:10 Pattern Recognition Studies in Chemical Paleogenetics. B. K. Lavine, J. M. Lavine  
 3:50 Signal-Processing Techniques for Real-Time FT-IR Analysis. G. W. Small

## SECTION A

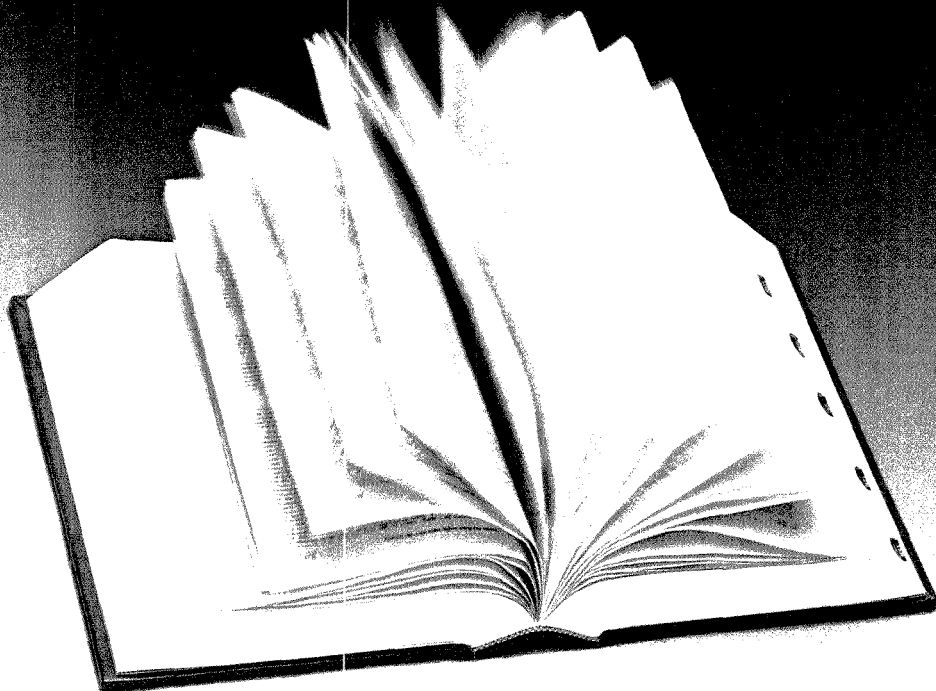
**Lasers**

J. Sneddon, *Presiding*

- 2:00 Laser Ablation for the Study of Solids. J. Sneddon, Z. W. Hwang, Y. Y. Teng  
 2:20 Surface-Enhanced Raman Spectroscopic Measurements in the Liquid Phase. J. W. Haas III, E. Y. Lee  
 2:40 Mechanistic Studies of Surfactant-Enhanced Thermal Lens Measurements. M. Franko, C. D. Tran  
 3:00 Fluorescence Line-Narrowing Spectral Analysis of In Vivo Human Hemoglobin-Benzo[a]pyrene Adducts: Comparison to Synthetic Analogues. R. Jankowiak, B. W. Day, P. Lu, M. M. Doxtader, P. L. Skipper, S. R. Tannenbaum, G. J. Small  
 3:35 Multiphoton Ionization MS of SO<sub>2</sub> at 308 nm and 355 nm. Z. Li, H. Liu, C. Wu  
 3:55 In Situ Fluorescence EEM Studies of Groundwater Contaminants Using a YAG-Laser-Pumped Raman Shifter Source. T. A. Taylor, H. Xu, G. B. Jarvis, J. E. Kenny

NEW

# THE MERCK INDEX Eleventh Edition



## Keeping pace with chemistry and biochemistry... for over 100 years

Since 1889, *The Merck Index* has provided pertinent, authoritative information of interest to scientists the world over. Now we are pleased to present the newly published Eleventh/Centennial Edition. This special leather-bound edition provides expanded coverage of therapeutically important biotechnology products, agriculturals and compounds of environmental impact, and features an entirely new therapeutic category/bioactivity index as well as CAS Registry Number indices. And you'll find information on more than 10,000 significant drugs, chemicals, and natural substances.

To order, call toll-free 1-800-999-3633, extension 750 (VISA or MasterCard only) or complete the coupon.

NEW

THE  
CENTENNIAL  
EDITION



Merck & Co., Inc., a research-intensive company, publishes *The Merck Index* as a non-profit service to the scientific and medical communities.

CIRCLE 88 ON READER SERVICE CARD

Enclosed is my payment for \$35.00 for the Eleventh/Centennial Edition of THE MERCK INDEX. I will not be charged for shipping.

Check enclosed. Make check payable to Merck & Co., Inc.  VISA  MasterCard

Card No.

Exp. Date

Signature

Name

Address

City

State

Zip

Merck & Co., Inc.  
Professional Handbooks  
Department 750  
P.O. Box 2000  
Rahway, NJ 07065-0901

Please allow four to six weeks for delivery.

Maximum performance in a minimum of space

# The new 701 KF Titrino

Even Karl Fischer would have been impressed...

The 701 KF Titrino is barely larger than this page. It is the most compact unit of its kind. This saves you expensive laboratory space. On the other hand no expense has been spared with regard to performance.

New features allow major advances...

Our newly developed control method allows extremely rapid, yet highly precise water determinations. The new drift criterion for improved endpoint recognition is largely responsible for this. The instrument is optimised for operation with any KF reagent.

Overflowing with technical refinements...

An RS 232 interface is standard, as are connections for a balance, printer and pen recorder. As a KF work station under computer control, the KF Titrino is just as flexible as it is in «stand-alone» operation. Talking of improved communication, the KF Titrino speaks English, deutsch, français and español. Olé.

KF water determination — quite simply with Metrohm

 **Metrohm**  
Measurement in Chemistry  
Worldwide with Metrohm

METROHM Ltd.  
CH-9101 Herisau Switzerland  
Phone 071 / 53 11 33  
Telefax 071 / 52 11 14  
Telex 88 27 12 metr ch

CIRCLE 92 ON READER SERVICE CARD

**Brinkmann**

INSTRUMENTS, INC.  
Cantiague Rd., Westbury, New York 11590  
(516) 334-7500 (800) 645-3050



## MEETINGS

- 3:10 Oil-Water Partition Coefficients: Estimation by Reversed-Phase HPLC Capacity Factor. **W. J. Lambert**
- 3:40 Properties of Swollen Polystyloxane Stationary Phases in 10–50- $\mu\text{m}$  I.d. Open-Tubular Columns for Reversed-Phase LC. **S. M. Larsson**
- 4:05 Solvatochromic Studies of Retention Processes in Reversed-Phase LC. **A. J. Dallas, W. J. Cheong, P. W. Carr**
- 4:35 Solvatochromic Studies of Solvated Surface Phases in LC. **J. L. Jones, S. C. Rutan**

### SECTION C

**Frank H. Field and Joe L. Franklin Award for Outstanding Achievement in MS Symposium Honoring Evan C. Horning and Marjorie G. Horning—III**  
*Cosponsored with the Division of Biological Chemistry*

*A. Zlatkis, Presiding*

- 2:00 Introductory Remarks.
- 2:10 Gas Chromatographic Separation of Diastereomeric Silyl Ethers. **C. J. W. Brooks, W. J. Cole, M. Hollywood**
- 2:35 Pharmacokinetics of the Individual Enantiomers of Vigabatrin, A Novel Antiepileptic Agent. **K. D. Haegele**
- 3:00 Dual MS: A Combination of Negative Ion Low-Pressure Chemical Ionization MS with Positive Ion Electron Impact MS. **H. Brandenberger**
- 3:45 Use of GC/MS in Forensic Analysis. **B. Holmstedt**
- 4:10 Continuous Flow FAB in Drug Metabolism Studies. **J. P. Thénot, P. Padovani, S. Vajta**
- 4:35 Steroid Biosynthesis in Normal and Oncogene-Transfected Adrenal Cells: A Study by GC/MS. **B. F. Maume, G. Maume**

### SECTION D

#### Chromatography—I

*J. K. Hardy, Presiding*

- 2:00 Assessment of Centrifugal Partition Chromatography for the Determination of Octanol-Water Partition Coefficients. **S. J. Gluck, E. J. Martin, D. W. Armstrong, R. A. Menges, G. Bertrand**
- 2:20 Automated Quality Control of Whiskies by GC/Principal Component Analysis. **L. M. Headley, J. K. Hardy**
- 2:40 Quantitation of Hydroxy Tetralin Drugs at Low-Nanogram Levels Using Electrochemical Detection/Column Switching HPLC Employing ISRP and  $\text{C}_{18}$  Stationary Phases. **S. C. Ruckmick, B. D. Hench**
- 3:00 Determination of Naproxen and Naproxen Sodium in Human Serum by HPLC. **A. C. Ghosh, S. Agnihotri, C. L. Bhagchandani, A. Dhake, N. Singh, A. Y. Nimbalkar**
- 3:35 Analysis of Semivolatile Chlorinated Acids in Drinking Water. **R. Infante, C. Perez**
- 3:55 Automated Determination of Metallic Impurities Including Crud in High-Purity Water by Ion Chromatography. **Y. Misawa, H. Iwasaki, Y. Okajima**
- 4:15 Determination of Organotins in Process Streams Using GC/ITD and GC/AED. **G. J. Koncar, S. S. Chao**
- 4:35 Determination of Seleno-Methionine by Ion-Exchange HPLC. **W. R. Wolf, M. E. Slagt, D. E. LaCroix**

### THURSDAY MORNING SECTION A

#### Symposium on Measurement Problems in Atmospheric Chemistry—I

*J. Winchester, Presiding*

- 9:00 Introductory Remarks.
- 9:10 Sampling Artifacts Ruin Reputations and Incite Irate Investigators. **B. J. Huebert**
- 9:50 Probing the Chemical Dynamics of Aerosols. **R. C. Flagan**
- 10:45 Problems in Aircraft Measurement of Trace Atmospheric Species. **P. H. Daum**
- 11:25 Problems Encountered in Making Fast-Response Measurements for Atmospheric Chemistry. **R. Pearson, Jr.**

### SECTION B

#### Symposium on Colloid Science and Solution Chemistry in Separation Science—II

*Organized by the Subdivision on Chromatography and Separations*

*J. G. Dorsey, Presiding*

- 8:30 Thermochemical Comparisons of Homogeneous and Heterogeneous Acids and Bases. **E. M. Arnett**
- 9:00 New Insights into Surfactant Self-Assembly. **J. E. Brady, M. P. Turberg**
- 9:30 Design, Synthesis, and Evaluation of Orderly Functional Group Arrays. The Chemistry of Efficacious Organic Molecules. **C. S. Wilcox, J. C. Adrian, Jr., T. E. Webb, C. A. Plummer**
- 10:15 Use of Nonconventional Surfactants in Chromatographic Separations. **W. L. Hinze**
- 10:45 Molecular Recognition: Design of Artificial Receptors for the Selective Complexation of Biologically Important Substrates. **A. D. Hamilton**
- 11:15 Crystalline and Glassy States of Charged Colloidal Particles. **D. Thirumalai**

### SECTION C

#### Symposium on Element-Specific Chromatographic Detection by AES—I

*Organized by the Subdivision on Chromatography and Separations*

*P. C. Uden, Presiding*

- 8:45 Atomic Spectral Chromatographic Detection—An Overview. **P. C. Uden**
- 9:25 SCP Emission Detector for GC. **R. Gross, E. Leitner, M. Michaelis, B. Platzer, G. Knapp, A. Schalk, H. Sinabell**
- 10:00 AES with Helium Plasmas for SFC and LC. **G. K. Webster, J. W. Carnahan**
- 10:50 Quantitative Characteristics of Microwave Plasma Emission Spectrometric Detector for GC. **W. Yu, Y. Huang, Q. Ou**
- 11:25 Characterization of Spectral Interferences Affecting Selectivity in GC-AES. **J. J. Sullivan, B. D. Quimby**

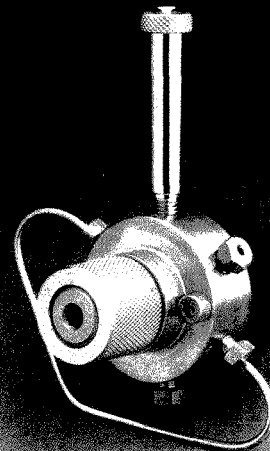
### SECTION D

#### Chromatography—II

*B. K. Lavine, Presiding*

- 8:40 Comparison of Octadecyl-Bonded Alumina and Silica for Reversed-Phase HPLC. **J. E. Haky, S. Vemulapalli**

# VALCO VALVES THE VERY BEST.



## WE PERFORM ALL THE CRITICAL STEPS.

From design, materials selection, machine tooling, inspecting, steam cleaning, polishing, re-inspecting, assembling, leak testing, repairing, actuating, installing, to full one year warranty.

## AND HAVE DONE SO FOR 22 YEARS.

1-800-FOR-VICI

See us at FASEB Booth #954

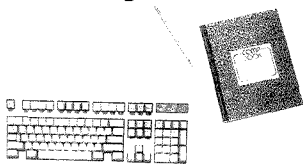
VICI  
VICI  
VICI

Valco Instruments Co. Inc.  
P.O. Box 55603 Houston, Texas 77255  
Tel: (713) 688-9324 Fax: (713) 688-8106

Valco Europe  
Untertannberg 7 CH-6214  
Schönenkon, Switzerland  
Tel: (045) 21 68 68 Fax: (045) 21 30 20

CIRCLE 141 ON READER SERVICE CARD

Still using these tools



to enter your  
analytical/laboratory  
data into a  
spreadsheet?

If so, you need...

## MEASURE



Measure seamlessly integrates engineering and scientific data with either a Lotus 1-2-3 or Symphony spreadsheet where it is ready for immediate analysis, storage, or display. Measure accepts data from IEEE-488 and RS-232 instruments and plug-in data acquisition boards for IBM PC/XT/AT and PS/2 computers.

*Now supports new Lab-PC data acquisition board—high performance at a low cost.*

Call for **Free Catalog**  
and a **Demo Disk**

(800) IEEE-488 • (512) 794-0100

 **NATIONAL  
INSTRUMENTS**<sup>®</sup>  
*The Software Is the Instrument*<sup>™</sup>  
6504 Bridge Point Parkway  
Austin, Texas 78730-5039

JAPAN (3) 788-1922 • FRANCE (1) 48 65 33 70  
UNITED KINGDOM (63) 523 545 • WEST GERMANY (89) 80 7081  
ITALY (2) 4800-1892 • THE NETHERLANDS (7) 099-6360

CIRCLE 96 ON READER SERVICE CARD

## MEETINGS



- 9:00 Neural Network Approach to Deconvolution of Chromatographic Peaks. S. P. Fraleigh, S.M. Cramer
- 9:20 Recent Developments in the Preparative Separation of Enantiomers on Pirkle-Type Columns: The Adsorption Isotherms of Alkanolamine Esters. P. L. Camacho, L. Zimmermann, E. Geiger, J. C. Jaszberenyi, G. Farkas, A. Bartha, G. Vigh
- 9:40 Solute Retention and Chiral Separation Selectivity as a Function of the Mobile-Phase Composition on Cyclodextrin-Silica Columns. A. Bartha, G. Farkas, G. Vigh
- 10:00 Solute Retention in Micellar LC. B. K. Lavine, J. H. Han, A.J.I. Ward
- 10:35 Investigation of the Wave Characteristics of the Microwave-Induced Plasma. G. H. Webster, C. B. Boss
- 10:55 Van Deemter Type Relationship for Temperature-Programmed GC Utilizing Separation Numbers and Pressure Programming. L. A. Jones, W. R. Reiss, T. M. Gerig
- 11:15 Displacement Chromatographic Separation of the Enantiomers of Aryl Alkanoic Acids on Alpha Cyclodextrin-Silica Columns. G. Quintero, M. Vo, G. Farkas, G. Vigh
- 11:35 Recent Progress in the Displacement Chromatography of Anti-Inflammatory Drug Enantiomers on Cyclodextrin-Silica Columns. G. Farkas, G. Quintero, G. Vigh

### THURSDAY AFTERNOON SECTION A

#### Symposium on Measurement Problems in Atmospheric Chemistry—II

B. J. Huebert, *Presiding*

- 2:00 Atmospheric Measurements of Peroxy Radicals. C. A. Cantrell, R. E. Shetter, A. H. McDaniel, H. Reddy, J. G. Calvert

- 2:40 Tropospheric HO Measurement—A High-Risk Occupation. **R. J. O'Brien**, T. M. Hard, C. Y. Chan, A. A. Mehrabzadeh
- 3:35 Analytical Methods Used to Identify Nonmethane Hydrocarbons in Ambient Atmospheres. **H. Westberg**
- 4:15 Application of Inorganic MS to Problems in Atmospheric Chemistry. **W. R. Kelly**

SECTION B

**Symposium on Colloid Science and Solution Chemistry in Separation Science—III**

*Organized by the Subdivision on Chromatography and Separations*

*W. L. Hinze, Presiding*

- 2:00 Electrophoretic Fingerprinting as a Probe of Separable Colloids. **R. L. Rowell**, B. J. Marlow, S.-J. Shiau
- 2:30 Electrostatic Potential at the Reversed-Phase—Mobile-Phase Interface. Influence of Zwitterionic Surfactants. **S. G. Weber**
- 3:00 Use of Surface-Active Agents To Enhance Chromatographic Separations. **B. A. Bidlingmeyer**, F. V. Warren
- 3:45 Extrapolating Retention Indices. **S. J. Hawkes**
- 4:05 Simulating Complex HPLC Experiments. **F. F. Qi**, C. F. Buck, **S. A. Tomellini**
- 4:35 Liquid Chromatographic Determination of Drugs in Physiological Fluids Using a Shielded Hydrophobic Stationary Phase. **C. T. Santasania**

SECTION C

**Symposium on Element-Specific Chromatographic Detection by AES—II**

*Organized by the Subdivision on Chromatography and Separations*

*J. W. Carnahan, Presiding*

- 2:00 Alternating-Current Plasma Emission Detection in HPLC. **L. Colon**, E. F. Barry
- 2:35 ICP-AES Detection in Packed Microcolumn SFC. **K. Jinno**, H. Mae, C. Fujimoto
- 3:10 Trace Selenium Speciation via HPLC with UV and Direct-Current Plasma Emission Spectroscopic Detection (HPLC-UV/DCP). **W. L. Childress**, **I. S. Krull**
- 4:00 Chromatographic Detection by Plasma MS. **J. A. Caruso**, A. Al-Rashdan, J. Creed, C. Story, D. Heitkemper, H. Suyani
- 4:35 Chromatography of Gold-Based Drugs and Metabolites Using an ICP Mass Spectrometer as Detector. **R. C. Elder**, M. L. Tarver, W. B. Jones, K. Tepperman

FRIDAY MORNING

SECTION A

**Symposium on Measurement Problems in Atmospheric Chemistry—III**

*R. J. O'Brien, Presiding*

- 9:00 Collection and Determination of Trace Atmospheric Gases: Why Diffusion-Based Collectors? **P. K. Dasgupta**
- 9:40 Measurement Problems of Atmospheric Nitrogen Species. **D. D. Parrish**
- 10:35 Identifying Aerosol Components of Atmospheric Chemical Importance by Statistical Analysis of Elemental Concentrations Determined by PIXE. **J. W. Winchester**

- 11:15 Progress and Prognosis in Personal Dosimeters. **P. J. Lioy**

SECTION B

General—II

*K. Salomon, Presiding*

- 9:00 Control of the Capillary Electrophoresis Separation of Tricyclic Amines. **K. Salomon**, D. S. Burgi, J. C. Helmer
- 9:20 Application of Quercetin Chemiluminescence System in Analytical Chemistry. **Z. Fan**, C. Yulong, Z. J. Xiong
- 9:40 Chemiluminescent Detection of Biomolecules Using Electrogenerated Tris(2,2'-bipyridine) Ruthenium (III). **S. N. Erune**, D. R. Bobbitt
- 10:15 Industrial Robotics for the Laboratory. **A. L. Bangs**, S. J. Glapa, T. M. Myrick
- 10:35 Simulation of a Precipitation Titration with a pH Electrode for the Detection of the End Point. **T.-K. Hong**, M.-Z. Czae, M.-H. Kim
- 10:55 Chemical and Spectroscopic Analysis of Charcoal Impregnated with Copper, Chromium, and Silver. **A. Birenzvig**, E. Petersen, P. N. Krishnam
- 11:15 Spectrophotometric Determination of Trace Amounts of Molybdenum Using Morin and Cetylpyridinium Chloride. **M.T.M. Zaki**, M. M. Abdalla

SECTION C

**Symposium on Element-Specific Chromatographic Detection by AES—III**

*Organized by the Subdivision on Chromatography and Separations*

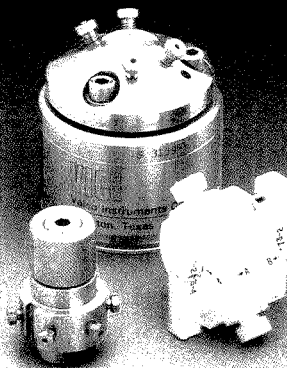
*I. S. Krull, Presiding*

- 8:30 Some Observations on the Analytical Utility of an ICP Chromatographic System for the Speciation and Detection of Transition Metals. **D. J. Gerth**, P. N. Keliher
- 9:00 Approaches to Environmental Analysis Using GC-AED. **L. Ebdon**, R. Evans, **S. J. Hill**, S. J. Rowland
- 9:30 Comparison of a Minitorch and Conventional Torches in GC-MIP for Analysis of Tin, Selenium, and Other Metalloids. **T. M. Dowling**, J. A. Seeley, P. C. Uden
- 10:15 Fiber-Optic Spectrochemical Emission Sensor: A Detector for Chlorinated and Fluorinated Compounds. **K. B. Olsen**, J. W. Griffin, B. S. Matson, T. C. Kiefer
- 10:45 Practical Applications of a Simultaneous AES-MSD GC Detector in Analytical Problem Solving. **D. B. Hooker**, **J. DeZwaan**
- 11:15 Recent Advances in a Helium Discharge Detector for GC. **J. C. Molloy**, **G. W. Rice**
- 11:45 Use of Power Reflected from a Microwave Plasma as a GC Detector. **C. B. Boss**, R. A. Bolainez

# VALCO VALVES

## THE VERY BEST.

# PLUS



## WE PROVIDE ALL THE SUPPORT ESSENTIALS, TOO.

From phone advice, technical assistance, application know-how, training, installation instructions, easy rotor replacement, electric and air valve actuation, valve automation, computer interfacing, custom design, to worldwide distributing.

## AND HAVE DONE SO FOR 22 YEARS.

1-800-FOR-VICI

See us at FASEB Booth #954

VICI

Valco Instruments Co., Inc.  
P.O. Box 55603 Houston, Texas 77255  
Tel: (713) 668-9324 Fax: (713) 668-6106

VICILAG

Valco Europe  
Untertannberg 7 CH-6214  
Schenkon, Switzerland  
Tel: (045) 21 68 68 Fax: (045) 21 30 20

CIRCLE 142 ON READER SERVICE CARD

# THE COMPUTER- INTEGRATED LABORATORY:

*A Hands-On  
Experience in  
Lab Automation*

**Sunday-Friday,  
April 22-27, 1990  
Sunday-Friday,  
December 9-14, 1990**

**at Virginia Tech,  
Blacksburg, Virginia**

*An intensive 5½-day  
laboratory-lecture course that  
will enable you to:*

- find the right laboratory information management system for your needs
- integrate your old analog systems with your new intelligent ones into a network environment
- educate your management and computing center as to why the electronic lab is fiscally and legally essential

For bench and middle-management scientists in QC, pharmaceuticals, petrochemicals, food, paper, clinical chemistry, biology, testing, materials

**FACULTY:** Dr. Raymond E. Dessy, Professor of Chemistry, Virginia Tech., Blacksburg, VA, and members of the Computer-Aided Research Group.

**For more information, call TOLL FREE (800) 227-5558 or (202) 872-4508—and ask for ext. 4220. Or, use the coupon below to request a free descriptive brochure on this dynamic course.**

**American Chemical Society**  
Dept. of Continuing Education  
Meeting Code VP1900481  
1155 Sixteenth Street, N.W.  
Washington, DC 20036

Please send me a free brochure on the ACS Short Course, *The Computer-Integrated Laboratory: A Hands-On Experience in Laboratory Automation*, to be held April 22-27, 1990, and December 9-14, 1990, in Blacksburg, Va.

Name \_\_\_\_\_

Title \_\_\_\_\_

Organization \_\_\_\_\_

Address \_\_\_\_\_

City, State, Zip \_\_\_\_\_

VP1900481

## HERE IT IS! THE BRAND NEW EDITION OF THIS "MUST-HAVE" REFERENCE!

# COLLEGE CHEMISTRY $\Delta$ FACULTIES Eighth Edition

Soft Cover 190 pages  
US & Canada \$74.95  
Export \$89.95

**Just published!** The new edition of CCF, containing the most current information on:

- 2,160 departments of chemistry, chemical engineering, biochemistry, and pharmaceutical/medicinal chemistry in the US and Canada, including:

- complete mailing addresses and phone numbers
- separate listings for each department
- department chair and head listings
- degrees granted by each department
- notation for two- and three-year colleges
- alphabetical listings by state

- 18,357 faculty members in these departments, including:

- major teaching fields
- highest degree earned
- academic rank

Two alphabetical indexes—one by institution and one by faculty member name—make look-up quick and easy.

Academic departments, libraries and personnel offices, recruiters, students, sales and marketing personnel—you'll find yourself turning again and again to this directory.

**Call toll free (800) 227-5558 and charge to your credit card—or mail the coupon below today.**

Please send \_\_\_\_\_ copy(ies) of *College Chemistry Faculties*, 8th Edition, at \$74.95 each (US & Canada), \$89.95 each (export).

Payment enclosed (make checks payable to American Chemical Society).

Purchase order enclosed. P.O.# \_\_\_\_\_

Charge my  MasterCard/VISA  American Express  
 Diners Club/Carte Blanche

Account # \_\_\_\_\_

Expires \_\_\_\_\_ Phone # \_\_\_\_\_

Name of cardholder \_\_\_\_\_

Signature \_\_\_\_\_

Ship books to: Name \_\_\_\_\_

Address \_\_\_\_\_

City, State, ZIP \_\_\_\_\_

ORDERS FROM INDIVIDUALS MUST BE PREPAID. Prepaid and credit card orders receive free postage and handling. Prices are quoted in US dollars and are subject to change without notice. Please allow 4-6 weeks for delivery. Foreign payment must be made in US currency by international money order, UNESCO coupons, or US bank draft. Order through your local bookseller or directly from ACS.

To charge your books by phone, **CALL TOLL FREE (800) 227-5558**. Mail this order form with your payment or purchase order to:

**American Chemical Society, Distribution Office Dept. 209, P.O. Box 57136, West End Station,  
Washington, DC 20037**

209

# BUILDING AN AA SPECTROMETER THIS GOOD REQUIRED SOME BRILLIANT THINKING.

## YOURS.

We listened to your suggestions. Then we made our new Model 3100 AA Spectrometer easier to operate, added new features, and kept it affordable. For superior performance, we developed a new high dispersion optical system and ASIC-based microprocessor electronics. We also added an optional Enhanced Data System with data handling and automation capabilities. Of course, we retained the reliability of its predecessors. For more information on the AA you helped to create, call toll-free 1-800-762-4000.

**PERKIN ELMER**

The Perkin-Elmer Corporation, Norwalk, CT 06859-0012

CIRCLE 110 ON READER SERVICE CARD

# New & Bestselling Books from Wiley...

**New!**

## Destruction of Hazardous Chemicals in the Laboratory

G. Lunn and E.B. Sansone

This book discusses the safe disposal of hazardous compounds now used in research laboratories which pose great health risks to lab personnel. Describes methods used to degrade gram scale quantities, avoiding hazards associated with long term storage, removal from the laboratory to a central facility and shipping to a disposal facility (not to mention the problems of finding a facility to accept these compounds).

approx. 300 pp. 0-471-51063-7 4/90 \$65.00 (tent.)

## Treatise on Analytical Chemistry Part 1: Theory and Practice, 2nd Edition, Volume 11

I.M. Kolthoff and J.O. Winefordner

Coverage includes chapters on mass spectrometry of organic and biological compounds, recent developments in experimental fourier transform-ion cyclotron resonance, spark source mass spectrometry and low energy ion-scattering spectrometry.

311 pp. 0-471-50938-8 1989 \$75.00

## Clinical Chemistry

E. H. Taylor

This book offers reliable, quick, and economical analyses of medical decisions. Topics include the economics of data management sensors, instrument technology, radioimmuno-assays and enzyme immunoassays, light scattering and chemiluminescence, cancer and tumor markers, and biological response modifiers. Excellent for those interested in learning more about the field, its potentials, limitations, and medical relevance to diagnosis.

293 pp. 0-471-85342-9 1989 \$75.00

## Multielement Detection Systems for Spectrochemical Analysis

K.W. Busch and M.A. Busch

This text bridges the gap between the physics and engineering aspects of multichannel detection and analytical chemistry. It presents a unified treatment of multichannel detection systems in the uv/visible range of the spectrum as they relate to multielement spectrochemical analysis. Deals with the foundation optical principles of modern experimental spectroscopy, the operation of detectors for optical spectroscopy and topics related to combining detectors with optical spectrometers to produce detection systems for multielement analysis.

688 pp. 0-471-81974-3 1990 \$89.95

## Determination of Molecular Weight

A.R. Cooper

This volume examines the methods available for determination of molecular weight. Reviews the status of older methods and the theory and applications of newer methods.

526 pp. 0-471-05893-9 1989 \$95.00

## Polymers: Polymer Characterization and Analysis

Editor: J.I. Kroschwitz

Written by leading experts, this condensed volume, derived from the world-renowned Encyclopedia of Polymer Science and Engineering, specializes in polymer characterization and analysis. Contains the most modern methods for structure determination, physical property measurement, stability testing, and prediction of processing and performance behavior. Includes full texts, tables, figures, and reference materials.

957 pp. 0-471-51325-3 1990 \$85.00

## Topological Methods in Chemistry

R.E. Merrifield and H. Simmons

Introducing a new method and language for investigating molecular structure, based on finite topological spaces. Provides qualitative discussion of spaces and their potential uses in chemical theory by developing the topology of finite spaces and applying concepts to molecular structure.

233 pp. 0-471-83817-9 1989 \$35.00

## Chemical Instrumentation: A Systematic Approach, 3rd Ed.

H. A. Strobel and W.R. Heineman

Presents numerous methods of measurement and discussions on chromatography and electrochemistry. New material on microprocessors and microcomputers, statistical control of measurement quality, quantification and extraction of information concerning chromatography and HPLC.

1210 pp. 0-471-61223-5 1989 \$53.00

**Now Available!**

## Heavy Metals in Soils: Their Origins, Chemical Behaviour and Bioavailability

Edited by Brian J. Alloway

A comprehensive review providing an introduction to the processes affecting the chemical behavior of heavy metals in soils, the sources from which the metals originate and the methods used for their analysis. Contains chapters dealing with 17 individual elements. Appendices contain tables of summarized data on metal concentrations found in soils, plants and sewage sludges, and critical concentrations.

339 pp. 0-470-21598-4 1990 \$95.00

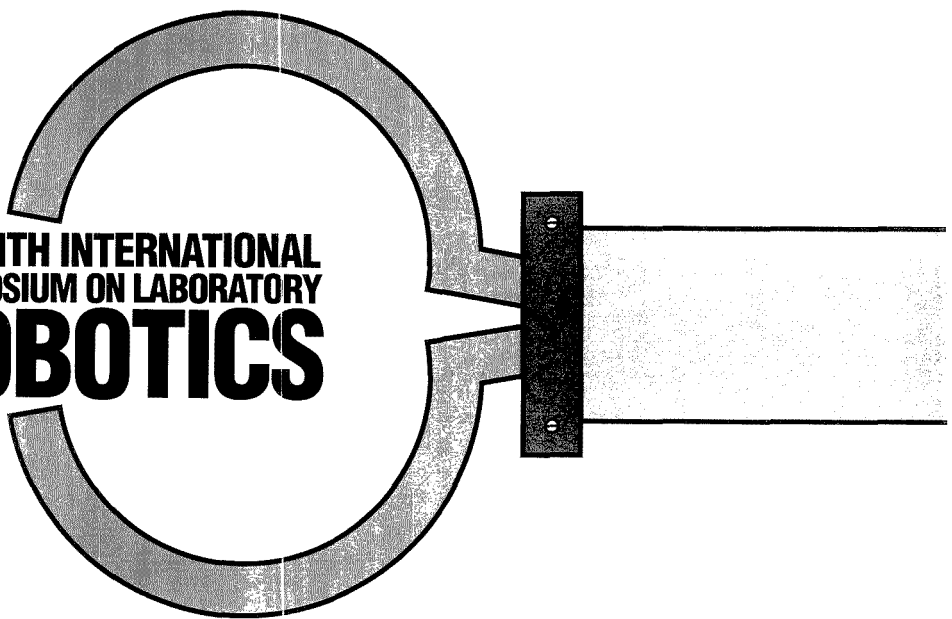
Order through your bookseller or write to: J. Fernandez, Dept. 0-0240 To Order call Toll Free 1-800-526-5368 For other inquiries call (212)850-6418

**WILEY**

John Wiley & Sons, Inc.  
605 Third Avenue  
New York, NY 10158

Prices subject to change & higher outside the U.S.

CIRCLE 152 ON READER SERVICE CARD



# SEVENTH INTERNATIONAL SYMPOSIUM ON LABORATORY ROBOTICS

---

## Vern Berry

Chemistry Department  
Salem State College  
352 Lafayette St.  
Salem, MA 01970  
and  
SepCon Separations Consultants  
326 Reservoir Rd.  
Boston, MA 02167

---

The Seventh International Symposium on Laboratory Robotics, sponsored by Zymark Corp. (Hopkinton, MA) and organized by Janet Strimitus, was held in Boston on October 15-18, 1989. More than 400 scientists attended, representing 13 countries. As at previous meetings (1-4), scientists had ample opportunities to exchange ideas. This recent meeting focused on robotics in process analysis, medicine, pharmaceutical quality control, and biotechnology.

Tom Brotherton from Union Carbide in South Charleston, WV, launched the meeting with an address that described robots as good news/bad news. They provide reliable, high-quality data economically. "The true economic impact of automation is not from analysis, but in the downstream use of that data for decision making," he said. On the other hand, robots suffer from technical deficiencies. They need to work faster (manual methods are often faster than robotics), occupy less space, integrate better into data processing, intercommunicate easier, and be marketed as turnkey systems. Fortunately, Brotherton pointed out,

these problems also offer technical opportunities.

Brotherton envisages that in the future, computer-managed continuous automation will provide on-line analyses that can control process variables virtually instantaneously. "It is not uncommon [now] to make a million pounds of product per hour, and analytical samples are received hours after manufacturing," he said. "A lot can happen between manufacturing and analysis. So we want faster analyses that provide insight into what is happening during manufacturing."

To fill their needs, Union Carbide



workers have been forced to develop their own automation in mechanics, computers, and analytical instruments. However, running a major robotic skill center is costly. "We are in the chemical business, not the robot business," said Brotherton. "We would like to buy off-the-shelf robots, as you would buy a chemical from us."

Zymark's president, Frank Zenie, acknowledged that there is an "urgency" to automate laboratories. This urgency, he said, is driven by a smaller trained work force, a dislike of routine operations, a loss of pride and motivation among workers, and the prospect of more governmental regulation. In particular, Zenie pointed to the need to improve trace analysis, which is grow-

ing in importance as more genetically engineered drugs become available, more potent illegal drugs appear, and better environmental monitoring is demanded.

"Workstations are the critical next step in automation," he said. These stations, created for lab bench chemists, are designed with the robot arm primarily used for material handling rather than complex manipulations.

One such workstation was described by Carnegie Mellon University researchers Jonathan Lindsey and L. Andrew Corkan. They have developed a synthetic chemistry workstation that optimizes a multicomponent synthesis by exploring the effects of different reagents. Reactions are performed with a Techno robot that can transfer by syringe 1-200  $\mu$ L of 18 different reagents into any of 96 5-10-mL vials. The vials can then be individually stirred and thermostated. At appropriate times, a 5-200- $\mu$ L aliquot is automatically withdrawn for analysis by thin-layer chromatography (TLC). A Microto robot automatically spots, develops, and inserts dried 5  $\times$  10 cm TLC plates into a densitometer to quantify results.

Using factorial design experiments, the Carnegie Mellon researchers obtained porphyrin yields versus three variables: time, boron trifluoride (BTF) concentration, and methanol concentration. They located an optimization ridge that gave the best ratio of BTF and methanol to maximize the yield. This finding required 49 reactions (running 6 reactions in parallel),

8 samplings per reaction, and 2400 solvent/reagent syringe manipulations. A total of 40,000 data points were collected on the densitometer in just 130 h of unattended operation.

Gary Kramer from Purdue University described another automated reaction analysis system labeled the Purdue Automated Synthesis System. This system, previously described in *ANALYTICAL CHEMISTRY* (5), analyzes reactions by liquid or gas chromatography. To develop their system, the Purdue scientists examined the model reaction of pH effects on the iodination of phenol at the ortho and para positions.

P. Metivier with the French company Rhône-Poulenc also described a robot system for screening reactions. This system was designed to test the largest possible experimental field and to be flexible, user friendly, and fast. The final design consisted of a robot arm with a fume hood that during set-up pushes up to the ceiling, permitting 360° access to the system. "The hood protects the staff from reactions and protects the robot from the chemists," said Metivier. Thirty 25-mL pyrex test tubes with septum caps can be stirred

and heated to 150 °C for timed periods. A novel device with the system is a -20 °C Peltier cooler that can quickly lower temperatures for thermal quenching. More than 1000 reactions have been run during the one year the system has been in use.

Robots are also finding a place in hospital clinical labs. Robin Felder with the University of Virginia Health Sciences Center in Charlottesville pointed out that as much as \$14 billion is spent annually for hospital laboratory labor. At the same time, the continuous expansion of tests has led to a shortage of laboratory technicians, even as hospitals hope to add more labs to reduce the distance between the testing facility and critically ill patients.

For example, Felder noted that five years ago the University of Virginia designed a hospital with analytical labs on every floor. "Unfortunately, they did not plan for people to staff the labs," said Felder. She solved the problem by placing a robot in each lab that runs analyzers for blood gases and Na<sup>+</sup> and K<sup>+</sup> blood electrolytes, important monitors of traumatic and postsurgery patients.

A nurse activates the robot system by selecting a patient's name. A carousel automatically positions itself, and through an access door the nurse delivers the blood sample syringe. The robot then uses the syringe to feed samples for analysis. Data are sent locally to a central computer where an operator accepts the result or orders the robot to rerun the sample.

Felder predicted that in the future two-arm lab robots might move freely about a clean room, communicating to a central computer by radio. Robots might also be trained with a "data glove" worn by a human operator.

Another clinical test, limulus amoebocyte lysate (LAL), which detects potentially deadly endotoxins, has been automated by G. Seidl at the Sandoz Research Institute in Vienna, Austria. This test is important for analyzing injectable and genetically engineered drugs.

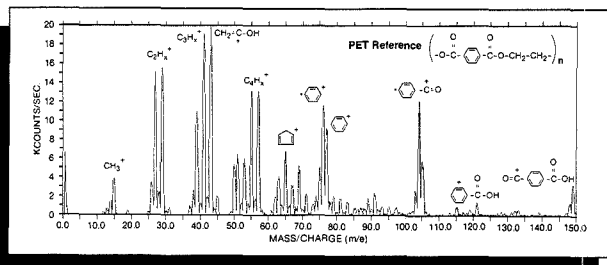
Endotoxins, which are pyrogens, are produced in the cell walls of *E. coli* and other gram-negative bacteria. If injected into humans, endotoxins cause fever; local inflammation; and, in some cases, death. LAL detects these toxins with an enzyme from the horseshoe

# ORGANIC MATERIALS ANALYSIS AT

## EVANS CENTRAL

SPECIALISTS IN ORGANIC MATERIALS CHARACTERIZATION

Introducing the newest international network laboratory!



Positive ion SIMS spectrum for PET.

### Applications in:

- Adhesion/Cohesion Studies
- Plasma Treated Surface Analysis
- Chemical Group Identification
- Co-Polymer Characterization
- Process Control
- Failure Analysis
- Biomedical Materials Characterization
- Aging/Weathering Studies

### CHARLES EVANS & ASSOCIATES™

SPECIALISTS IN MATERIALS CHARACTERIZATION  
301 Chesapeake Drive, Redwood City, CA 94063  
(415) 369-4567 Telex 172747 FAX (415) 369-7921

See us at  
Pittcon in booth 3209

### EVANS CENTRAL

SPECIALISTS IN ORGANIC MATERIALS CHARACTERIZATION  
5909 Baker Road, Ste. 580, Minnetonka, MN 55345  
Phone (612) 933-1215 FAX (612) 933-1940

CIRCLE 34 ON READER SERVICE CARD

crab that produces a gel precipitate with endotoxins. The precipitate is measured by turbidity.

The Sandoz system can evaluate 32 samples in 150 min while protecting analytical samples from human endotoxin contamination. During the analysis the robot dispenses reagent standards, makes serial dilutions, incubates samples, and reads turbidity—all with 1% reproducibility.

Robots can help not only to attain test results but also to avoid false positives from bacterial contamination. According to Nicholas d'Abeloff of Precision Robots, Inc., a laboratory that annually tests 2000 batches of injectable drugs for bacterial contamination will commonly encounter five batches producing a false positive result. These false positives can cost a pharmaceutical company as much as \$100,000 per year from rejected lots, retesting costs, storage, and lost orders.

Typically, 20 samples are tested from each batch of several thousand drug vials. A true positive result would find many of the tubes contaminated. However, if just one vial shows bacterial contamination, the analysis is suspect and can be redone. A false positive

is probable and declared if even one tube is found to be contaminated in the retest. Yet the entire batch must be discarded. The government recently banned second retesting and there is the prospect, according to d'Abeloff, of eliminating the first retest. Thus the need for reliable sterility testing is even more urgent.

Traditionally, manual sterility testing uses what is termed a body glove box. This costly system has been replaced by a small stand-alone robotic system operating in a sterile laminar air-flow hood. The robot can handle 80 containers per hour, and it replaces two technicians. The only access to the robot is through a bottom door below the laminar air-flow region, preventing the introduction of bacteria.

Both robotic and manual sterility testing require cleaning a vial septum and inserting a syringe to draw the sample into a filter/incubation container. Bacterial growth in the container after seven days indicates a positive result. According to d'Abeloff, after four years of using the robotic system no false positives have been declared.

A clever application of robots in the biotechnology industry was described

by Steve Hamilton from Lilly Research Labs in Indianapolis. Hamilton and his co-workers automated a procedure for breaking open bacteria and then isolating intact DNA. These are the first two steps in a restriction enzyme analysis that determines whether fermentation broth bacteria are mutating. (The other steps, cleaving the DNA into small segments and running capillary electrophoresis, are done manually.)

In automating, the Lilly researchers made minimal changes from the manual method. All the steps are performed in 12 × 75 mm test tubes. The procedure requires reagent additions, chilling, vortex mixing, incubations at three different temperatures, centrifugations, and drying. Some steps are combined: Several reagents are premixed, and vortexers heat or cool samples with a liquid heat exchanger.

The Lilly scientists also developed their own 3000-rpm, 1500-g centrifuge. To maximize throughput, they overlapped steps such that samples exit the system every 14 min. However, said Hamilton, "A disadvantage of interleaving steps is that it is virtually impossible to know what is going on in any

## NEW GENERATION TIME-OF-FLIGHT SIMS TFS SURFACE ANALYZER

Now you can simultaneously image with high mass resolution!

### Surface Microanalysis of:

- Polymers
- Pharmaceuticals
- Semiconductors
- Biomolecules
- Ceramics

### Applications In:

- Organic Microanalysis
- Tissue Targeting
- Wafer Contamination
- Particle Analysis

**CHARLES EVANS & ASSOCIATES**  
SPECIALISTS IN MATERIALS CHARACTERIZATION  
301 Chesapeake Dr., Redwood City, CA 94063  
(415) 369-4567 Telex 172747 FAX (415) 369-7921  
See us at PittCon in booth 3209



CIRCLE 35 ON READER SERVICE CARD

particular tube."

Another Eli Lilly scientist, Otis Godfrey, introduced a system aimed at testing soil samples for new actinomycetes molds. Currently 10,000 actinomycetes molds are known, and Godfrey speculated that possibly 100 times this number may exist.

Eli Lilly scientists developed a robotic system that can start with soil samples and inoculate solid nutrient plates. A robotic vision system monitors mold growth and identifies qualities that indicate interesting colonies. The robot then can transfer the interesting colonies into a broth and perform about 30 different assays for possible antimicrobial and insecticide activity.

Godfrey described how, in the later stages of growth, mold colonies stop growing and different metabolic pathways turn on. Frequently this results in the production of spores; pigments; and, most importantly, materials with antibiotic and insecticide activity. Thus the presence of spore-producing "air fibers" hints at possibly useful substances.

To maintain a watch on mold colonies, each plate must be video-scanned

for about 30 min, a task that occurs unattended 24 h every day. Several types of lighting reveal different types of information for each colony. Underlighting gives colony size and shape, overhead lighting distinguishes colony color, and oblique lighting reveals colony height and texture.

As this symposium demonstrated, robotics as one component of laboratory automation is maturing and making important inroads into laboratories because of its economic impact and the strategic competitive advantages it offers companies. As Zenie commented, "Strategy is not predicting the future, it is taking action to determine the future." Some of that future will probably become clearer when Robotics '90 convenes September 16-19 in Boston.

**References**

- (1) Berry, V.; Hahn, J. *Am. Lab* 1989, 21(10), 88.
- (2) Berry, V.; Hahn, J. *Am. Lab* 1988, 20(7), 88.
- (3) Hahn, J.; Berry, V. *Laboratory Robotics and Automation* 1989, 1, 193.
- (4) Berry, V. *Laboratory Robotics and Automation*, in press.
- (5) Newman, A. *Anal. Chem.* 1990, 62, 29 A.



Vern Berry is associate professor of chemistry at Salem State College and president of SepCon Separations Consultants (Boston). He received his Ph.D. (1972) under the direction of Barry Karger at Northeastern University. Following one year of postdoctoral study with Heinz Engelhardt and Istvan Halasz in West Germany, he worked at Gillette and then Polaroid. Berry joined the faculty of Salem State College in 1982. His research interests include electrophoresis, LC optimization, microbore LC, SFC, laboratory automation, and robotics.

*Innovative Catalysis Research Instruments  
for Academia and Industry*

**BTRS-Jr.**

**Bench Top Reactor System**

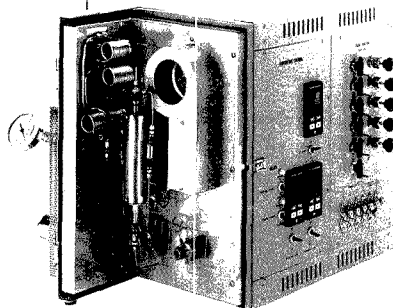
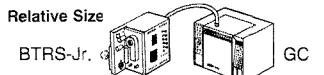
- Catalytic and non-catalytic processes under batch, pulse or continuous flow conditions
- Fixed bed reactor (to 650°C)
- Pressure, temperature and reactant feed controls
- Process contained in heated oven (to 280°C)
- Mixer Vaporizer assembly
- All hardware for GC/HPLC interface

For further information write factory or call toll free:

**1-800-458-0409**

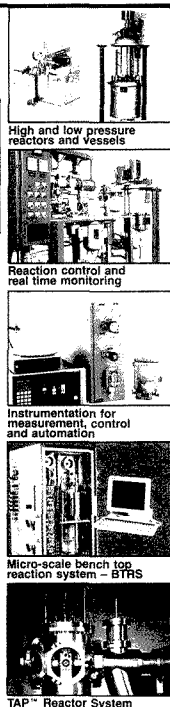
Autoclave Engineers Group  
2930 W. 22nd St.  
Box 4007, Erie, PA 16512 USA

**Complete  
Reaction  
Systems ...**



*BTRS-Jr. — a complete system  
at a component price*

**Autoclave  
Engineers**



CIRCLE 3 ON READER SERVICE CARD

# A BRIEF ANALYSIS OF OUR NEW ICP-MS.

## TERRIFIC.

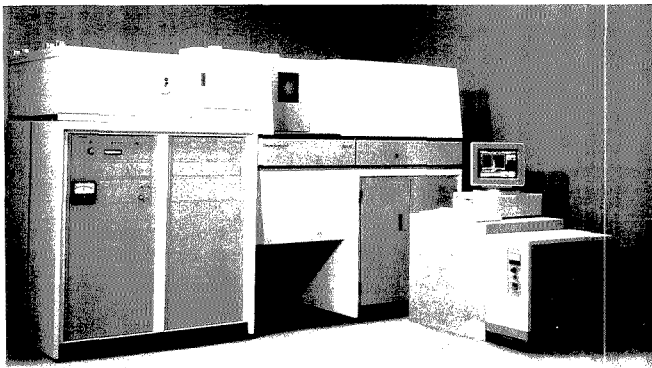
ICP-MS technology took a giant leap forward with the introduction of the ELAN 5000. A product of the joint venture between SCIEX and Perkin-Elmer, the ELAN 5000 combines speed, ease of use and reliability into the next generation ICP-MS. With its small footprint, advanced computer, powerful software and single-button control of the vacuum system and ICP, the ELAN 5000 meets your demanding analytical requirements and productivity needs. For literature or more information, call toll-free 1-800-762-4000. The ELAN 5000. You have to use it to believe it.

**PERKIN ELMER SCIEX**

The Perkin-Elmer Corporation, Norwalk, CT 06859-0012

CIRCLE 111 ON READER SERVICE CARD

# NEW PRODUCTS



**Polyscan 61E simultaneous/sequential ICP spectrometer** includes a  $\frac{3}{4}$ -m polychromator and a  $\frac{3}{4}$ -m scanning monochromator that share the same ICP source and sample introduction system. Thermo Jarrell Ash 401

**Gas analysis.** Model 4000 trace gas analyzer samples, identifies, quantitates, and reports ppb levels of impurities in process gases used in the semiconductor industry. The system is based on GC with helium ionization detection. Valco Instruments 403

**Detector.** Spectral array detector can be used as a stand-alone detector to monitor up to 32 wavelengths over the range 190–800 nm. The control/data reduction software package allows high-speed spectral data acquisition throughout the duration of a chromatogram and full 3D representation of chromatographic and spectral data. Dionex 404

**Luminescence.** Model LS-100 luminescence spectrometer system provides fluorescence and phosphorescence steady-state and lifetime measurements. The system uses a stroboscopic light detection system and a pulsed source to determine lifetimes as short as 200 ps. Photon Technology International 405

**Hydrogen.** Early Warning, a hydrogen detector designed for cryopump monitoring, features a direct readout of  $H_2$  in torr, a helium leak detection mode, and total pressure measurement capability. The system gives an immediate

audible signal indicating increasing hydrogen pressure. Spectramass 406

**Particle counter.** ALPS 120 is a 4000-channel counter for liquid samples designed primarily for pharmaceutical applications. The software allows users to define up to eight size bands or to use the standard intervals selected according to the requirements of U.S. and European pharmacopeias. Malvern Instruments 407

**Oxygen.** Model 315 trace oxygen analyzer features measuring ranges of 0–10 and 0–100 ppm  $O_2$ , a special span range for air calibration, a flowmeter and needle valve to confirm and control sample flow, and a manually operated isolation valve for shut-off of sample flow to the cell compartment. Teledyne Analytical Instruments 408

**FT-IR.** The Selector, designed for collecting diffuse reflectance from solid samples, includes a 4-mm micro cup, a standard 11-mm cup, a tilted cup for collecting total reflectance, and a silicon carbide accessory for problem samples. Aries/QEI 409

**Cooling.** Isotemp chillers provide clean, temperature-controlled fluid for open tanks and instrumentation with closed-loop cooling systems. Pressure

can be regulated up to 60 psi and monitored on a panel-mounted gauge. Fisher Scientific 410

**AA.** FS800 atomic absorption spectrophotometer can be used to determine the concentrations of up to 12 elements in a single liquid sample at a rate of  $\sim 3$  s per element. The system includes a furnace, an autosampler for liquids, and a hydride generator. Analyte 411

**Toxic gases.** MAI computerized toxic gas data management system, designed to monitor eight or more toxic gas sensors, provides a permanent record of the time, date, location, and gas concentration whenever a toxic gas alarm occurs. The system aids in determining the severity of the leak and in identifying its location. ENMET 412

## Software

**Solution chemistry.** EQUIL, designed for the solution of aqueous chemical equilibrium problems, allows the user to select appropriate reactions from a built-in chemical equilibrium database and to choose the desired form of output. MicroMath Scientific Software 414

**Graphics.** Axum is a technical graphics and data analysis package for IBM PCs that features 2D technical plotting, 3D and contour plotting, and data analysis capabilities. Menus are available for importing, entering, editing, transforming, generating, and analyzing data. TriMetrix 415

## Manufacturers' Literature

**LIMS.** Literature describes the ASTRAL laboratory information management system, which features sample management, automated decision making, and report generation capabilities. 8 pp. Applied Research Laboratories/Fisons Instruments 417

For more information on listed items, circle the appropriate numbers on one of our Readers' Service Cards

ACETONITRILE

METHANOL

TETRAHYDROFURAN

WATER

## One filter fits all.

The new Millex®-LCR Filter Unit is compatible with all common aqueous or organic-based HPLC solvents—from water to methanol to tetrahydrofuran.

Its special membrane produces no organic or inorganic contaminants. So risk of introducing unwanted variables and artifacts into your work is eliminated.

Particulates are reduced

below detectable limits, which keeps frits from plugging and extends column life.

Test the HPLC-certified Millex-LCR Filter Unit yourself. Send in the coupon, or call 800-225-1380 (in Mass., call 617-275-9200) for a free sample and technical brief.

### Try the Millex-LCR Unit. Free.

Send to: Joe Peters  
Millipore Corporation  
80 Ashby Road  
Bedford, MA 01730

Name

Title

Co./Inst.

Department

Address

City

State  Zip

Phone (  )  Best time to call

PA 900008 © 1990 Millipore Corporation

CIRCLE 84 ON READER SERVICE CARD

## NEW PRODUCTS

**Newsletter.** *LC Packings Newsletter* includes information on ultrasensitive UV detection in microseparations, fast capillary LC, troubleshooting, and hardware for capillary LC systems. LC Packings 418

**Electrochemistry.** Technical bulletin describes the Model 384B-606 ultra-trace analysis system for the determination of metals. A system description and basic specifications are provided. EG&G Princeton Applied Research 419

**Biotechnology.** Brochure discusses chromatography columns and accessories for biomolecular separations, including affinity, hydroxyapatite, and conventional wide-pore chromatography columns. Alltech Associates 420

**Prep LC.** *Preparative Chromatography Notes*, Vol. 2, No. 1, includes articles on the total synthesis of viscosin, optimization of protein separations, and isolation of kadsurenone from a plant source. 12 pp. Waters Chromatography Division of Millipore 421

**Sample preparation.** Brochure discusses the ASPEC system, which auto-

mates solid-phase extraction for HPLC and GC applications. The system can process up to 108 samples. Gilson Medical Electronics 422

## Catalogs

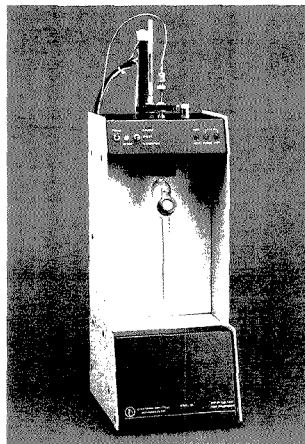
**Laboratory products.** Catalog includes balances, beakers, bottles, calculators, centrifuges, cuvettes, electrodes, filters, funnels, gloves, ovens, pipets, racks, stirrers, tubes, and vials. 64 pp. Fisher Scientific 424

**Isotopes.** Catalog features a variety of stable isotope-labeled compounds, including alcohols, aldehydes, amino acids, carboxylic acids, carbohydrates, drugs, esters, fatty acids, ketones, nucleosides, pesticides, and prostaglandins. Icon Services 425

**Plasticware.** Catalog lists basins, beakers, containers, funnels, pipets, trays, low-temperature equipment, and vials. Also included is a section on the care and use of plasticware. 129 pp. Cole-Parmer 426

**Life sciences.** Catalog features radiochemicals, immunochemicals, bioche-

micals, chromatography adsorbents, animal research diets, and immunodiagnostic instruments and reagents. ICN Biomedicals 428



**Purge-and-trap conditioning unit** collects volatile compounds directly from water samples at ambient temperature. The system also heat-conditions adsorbent tubes. Supelco 402

# LABORATORY SERVICE CENTER

**MRL** (201) 738-1776  
FAX (201) 738-1778

**ANALYSIS SERVICES**  
R & D / QA / FAILURE ANALYSIS  
ESCA•AES•SEM•EDS•WDS•XRD

**MATERIALS RESEARCH LABORATORIES, Inc.**  
SCHOOLHOUSE PLAZA, SUITE 1E  
720 KING GEORGES POST ROAD  
FORDS, NJ 08863

## HELP WANTED ADS

ROP display at ROP rates. Rate based on number of insertions within contract year. Cannot be combined for frequency.

Unit	1-TI	6-TI	12-TI
1" (25 mm)	\$190	\$170	\$160
	24-TI	48-TI	72-TI
	\$150	\$140	\$130

CALL OR WRITE JANE GATENBY

**ANALYTICAL CHEMISTRY**  
500 Post Road East  
P.O. Box 231  
Westport, CT 06880  
203-226-7131  
FAX: 203-454-9939

**Laboratory Service Center** (Equipment, Materials, Services, Instruments for Leasing), Maximum space — 4 inches per advertisement. Column width, 2-3/16"; two column width, 4-9/16". Artwork accepted. No combination of directory rates with ROP advertising. Rates based on number of inches used within 12 months from first date of first insertion. Per inch: 1" — \$165; 12" — \$160; 24" — \$155; 36" — \$150; 48" — \$145.

CALL OR WRITE JANE GATENBY

## ANALYTICAL CHEMISTRY

500 Post Road East  
P.O. Box 231  
Westport, CT 06880  
203-226-7131/FAX: 203-454-9939

## FREE DATA, FAST

To quickly amass data on all of the products you need, consult the Lab Data Service section on our *Analytical Chemistry* reader reply card insert.

USE  
**LABORATORY  
SERVICE  
CENTER**

## INDEX TO ADVERTISERS IN THIS ISSUE

CIRCLE INQUIRY NO.	ADVERTISERS	PAGE NO.	CIRCLE INQUIRY NO.	ADVERTISERS	PAGE NO.
1.....	Advanced Graphics Software, Inc.	314A	144.....	*Varian Lanig Associates	306A
3.....	Autoclave Engineers Group Altman-Hall Associates	340A	150.....	Whatman GrossTownsendFrankHoffman Inc.	302A
12.....	*J. T. Baker, Inc. Stiegler, Wells & Brunswick, Inc.	292A	152.....	John Wiley & Sons, Inc.	336A
16.....	*Bio-Rad Digilab Division Digiart	OBC	148.....	Wyatt Technology Corporation	309A
14.....	Bomem, Inc.	312A	<i>Directory section, see page 344A.</i>		
22.....	*Cole-Parmer Instrument Company C-P Advertising	315A-317A	<i>* See ad in ACS Laboratory Guide.</i>		
30.....	*Dialog Information Services, Inc. HL&S Partners Inc.	323A	<i>** Company so marked has advertisement in Foreign Regional edition only.</i>		
28.....	*Dionex Corporation Rainoldi, Kerzner & Radcliffe	IFC	<i>Advertising Management for the American Chemical Society Publications</i>		
37.....	*Eidex	304A	<b>CENTCOM, LTD</b>		
32.....	Elsevier Science Publishing Company, Inc.	298A	<i>President</i>		
34, 35.....	Charles Evans & Associates	338A-339A	<b>James A. Byrne</b>		
48.....	Gelman Sciences	297A	<i>Executive Vice President</i>		
50.....	*Gilson Medical Electronics, Inc.	291A	<b>Benjamin W. Jones</b>		
51.....	*Gilson Medical Electronics, SA	291A	<b>Clay S. Holden, Vice President</b>		
90.....	Macherey-Nagel GmbH & Co. KG MP Design Werbeagentur	296A	<b>Robert L. Voepel, Vice President</b>		
88.....	Merck & Company, Inc. William Douglas McAdams, Inc.	325A	<b>Joseph P. Stenza, Production Director</b>		
92.....	*Metrohm Ltd. Ecknauer + Schoch Werbeagentur ASW	328A	500 Post Road East		
.....	Metropolitan Water Reclamation District of Greater Chicago	300A	P.O. Box 231		
86.....	*Mettler Instrument Corporation Gilbert, Whitney & Johns, Inc.	301A	Westport, Connecticut 06880		
84.....	*Millipore Corporation Mintz & Hoke	343A	(Area Code 203) 226-7131		
94.....	*National Institute of Standards & Technology	327A	Telex No. 643310		
96.....	*National Instruments	330A	FAX: 203-454-9939		
98, 99.....	*Nicolet Analytical Instruments	295A	<b>ADVERTISING SALES MANAGER</b>		
102.....	*Ohaus Corporation Ballotta Napurano & Company Inc.	299A	<b>Bruce E. Poorman</b>		
104.....	*On-Site Instruments	298A	<b>ADVERTISING PRODUCTION MANAGER</b>		
110-112.....	Perkin-Elmer Corporation Keiler Advertising	335A, 341A, 346A	<b>Jane F. Gatenby</b>		
125, 126.....	*Spectra-Physics	321A	SALES REPRESENTATIVES		
128.....	*Spex Industries, Inc. The Ad Lab, Inc.	318A	Philadelphia, PA . . . CENTCOM, LTD., GSB Building, Suite 405, 1 Belmont		
130.....	*Swagelok Company Falls Advertising Associates	326A	Avenue, Bala Cynwyd, Pa. 19004. Telephone: 215-667-9666, FAX:		
141, 142.....	*Valco Instruments Company, Inc. Technical Advertising Associates	329A, 331A	215-667-9353.		

THE MORE  
FEATURES AN  
ICP SPECTROMETER  
HAS THE MORE  
IT COSTS  
RIGHT?

**WRONG.**

Using your valuable input, we made our Plasma 1000 and Plasma 2000 the fastest, most accurate ICP emission spectrometers in the industry. Better yet, we made them more affordable. Both models offer a high-resolution scanning optical system, powerful computer and high speed monochromators. They also come with a computer-controlled ICP which provides total automation of RF power, gas flows and sample uptake. For literature or more information, call toll-free 1-800-762-4000. We gave you just what you wanted — more features for less money.

**PERKIN ELMER**

The Perkin-Elmer Corporation, Norwalk, CT 06859-0012

CIRCLE 112 ON READER SERVICE CARD

EDITOR: GEORGE H. MORRISON

ASSOCIATE EDITORS: Catherine C. Fenselau,  
Georges Gulochon, Walter C. Herlihy, Robert  
A. Osteryoung, Edward S. Yeung

**Editorial Headquarters**

1155 Sixteenth St., N.W.  
Washington, DC 20036  
Phone: 202-872-4570  
Telefax: 202-872-4574

*Managing Editor:* Sharon G. Boots

*Assistant Managing Editor:* Mary Warner

*Associate Editor:* Louise Voress

*Assistant Editors:* Grace K. Lee,  
Alan R. Newman

*Editorial Assistant:* Felicia Wach

*Contributing Editor:* Marcia Vogel

*Director, Operational Support:* C. Michael  
Phillippe

*Head, Production Department:* Leroy L.  
Corcoran

*Art Director:* Alan Kahan

*Designers:* Amy Meyer Phiifer, Robert Sargent

*Production Editor:* Elizabeth E. Wood

*Circulation:* Claud Robinson

*Editorial Assistant, LabGuide:* Joanne Mullican

**Journals Dept., Columbus, Ohio**

*Associate Head:* Marianne Brogan

*Journals Editing Manager:* Joseph E. Yurvati

*Senior Associate Editor:* Rodney L. Temos

**Advisory Board:** Bernard J. Bulkin, Michael S.  
Epstein, Renaat Gijbels, William S. Hancock,  
Thomas L. Isenhour, James W. Jorgenson,  
Peter C. Jurs, Alan G. Marshall, Lawrence A.  
Pachla, John F. Rabolt, Debra R. Rolison, Ralph  
E. Sturgeon, Shigeru Terabe, George S. Wil-  
son, Mary J. Wirth, Richard N. Zare  
*Ex Officio:* Sam P. Perone

**Instrumentation Advisory Panel:** Daniel W.  
Armstrong, Bruce Chase, Thomas L. Chester,  
R. Graham Cooks, L. J. Cline Love, Sanford P.  
Markey, Brenda R. Shaw, Gary W. Small, R.  
Mark Wightman

*Published by the*  
**AMERICAN CHEMICAL SOCIETY**  
1155 16th Street, N.W.  
Washington, DC 20036

**Publications Division**

*Director:* Robert H. Marks

*Journals:* Charles R. Bertsch

*Special Publications:* Randall E. Wedin

Manuscript requirements are published in the  
January 1, 1990 issue, page 89. Manuscripts  
for publication (4 copies) should be submitted  
to ANALYTICAL CHEMISTRY at the ACS Washing-  
ton address.

The American Chemical Society and its editors  
assume no responsibility for the statements  
and opinions advanced by contributors. Views  
expressed in the editorials are those of the  
editors and do not necessarily represent the  
official position of the American Chemical  
Society.

- Armgarth, M., 542
- Bright, F. V., 471  
Brumfield, J. C., 452  
Buck, R. P., 452
- Castro, M. E., 520  
Chen, D. Y., 496  
Chen, F.-y., 489  
Cheng, Y. F., 496  
Coury, L. A., Jr., 452
- Davis, J. M., 436  
Delinger, S. L., 436  
Dobashi, Y., 539  
Dovich, N. J., 496
- Egekeze, J. O., 452
- Fujiwara, K., 504
- Gassner, B., 431  
Gelwicks, J. T., 535  
Gemperline, P. J., 465  
Griffiths, P. R., 477  
Grim, E., 526  
Gross, L., 427
- Hanson, C. D., 520  
Hara, S., 539  
Hayes, J. M., 535  
Hogan, J. D., 530  
Hongjin, G., 477  
Huang, J., 471  
Huang, X., 443
- Jackson, R. S., 477
- Karlsson, J., 542  
Kendall, C., 526  
Kenndler, E., 431  
Kerley, E. L., 520  
Kodama, Y., 504
- Kojoy, R., 504  
Koropchak, J. A., 484
- Laude, D. A., Jr., 530  
Litwiler, K. S., 471  
Lundström, I., 542
- Marshall, A. G., 515  
Matsuo, M., 539  
Morita, M., 447  
Mullins, O. C., 508  
Murray, R. W., 452
- Nakamura, K., 539  
Niwa, O., 447
- Ödman, S., 542  
Okada, K., 504  
Oliver, B. N., 452
- Petersen, S. L., 459  
Pierce, J. A., 477
- Roychowdhury, S. B., 484  
Russell, D. H., 520
- Saeki, T., 539  
Shah, N. K., 465  
Sosnoff, C. S., 452
- Tabei, H., 447  
Tallman, D. E., 459  
Trainor, G. L., 418
- Van Every, K. W., 477
- Wang, M., 515  
Williams, J. C., 489  
Wu, S., 496
- Yeung, E. S., 427
- Zare, R. N., 443

## PERSPECTIVE: ANALYTICAL BIOTECHNOLOGY

### DNA Sequencing, Automation, and the Human Genome

George L. Trainor

*E. I. du Pont de Nemours and Co., Inc., Central Research and Development Department, Experimental Station, P.O. Box 80328, Wilmington, Delaware 19880-0328*

**DNA sequencing is one of the key analytical operations of modern molecular biology and a crucial element of biotechnology. The principles of DNA sequencing and details of the technologies of both manual, radioisotope-based and automated, fluorescence-based approaches are described. The goals and rationale of the Human Genome Initiative are discussed along with implications for future sequencing technologies. Finally, a glimpse of emerging DNA sequencing technologies is offered.**

#### INTRODUCTION

One of the most exciting technological developments of the last 20 years has been the emergence of the field of biotechnology. Biotechnology can be loosely defined as the art of practical utilization of biological systems, processes, and materials. The impact of biotechnology has been most visible in the medical (therapeutic and diagnostic) arena but it is anticipated that biotechnology will ultimately play a role in such diverse areas as agriculture, material science, and perhaps even information storage and processing.

Much of the current activity in biotechnology focuses on the characterization and modification of biomacromolecules. These materials are particularly challenging targets for analytical methodology (1). In many cases the development of suitable analytical techniques has proven to be the enabling step in the utilization of various classes of biomacromolecules. This is particularly true in the case of nucleic acids. The development of techniques for isolating and analyzing deoxyribonucleic acid (DNA) was clearly catalytic in the emergence of biotechnology in the 1970s.

Of all the analytical techniques comprising biotechnology, perhaps the most important is DNA sequencing. In 1953, Watson and Crick proposed a three-dimensional structure for DNA (2). This now accepted structure features an antiparallel, double-helical pairing of two oligodeoxyribonucleotide chains or strands (Figure 1). The complementary pairing of nucleotide bases (guanine with cytosine and adenine with thymine) in opposite strands via hydrogen bonding suggested an attractive model for replication of the structure. It was clear then that the genetic information contained in DNA was implicit in the linear sequence of nucleotide bases in each strand. In spite of this realization, methods for the rapid determination of DNA sequence did not appear for nearly 25 years!

**Nature of DNA Sequence Analysis.** DNA sequencing, the determination of the linear sequence of nucleotides (A, C, G, or T for deoxyadenosine, deoxycytidine, deoxyguanosine, and thymidine, respectively) in a given stretch of DNA, is a fundamentally nonquantitative process. However, the demands in terms of accuracy are quite stringent—a single error

in a large sequence can be catastrophic. An extra or missing base (an insertion or deletion error) will result in a frame-shift in a coding region of DNA rendering the downstream information gibberish. (This is a consequence of the organization of genetic information into three-nucleotide words or codons in regions that code for protein structure.) A single misassigned base in a coding region can be just as disastrous if it occurs at a position corresponding to an amino acid that is crucial to the protein's stability or catalytic function.

To minimize the number of errors in a finished sequence, a given stretch of DNA is generally sequenced several times. The data from one strand is almost always checked by sequencing the complementary strand. In the final analysis, several individual determinations are compared to generate the finished or consensus sequence.

Virtually all of the DNA sequences reported to date have been determined by using manual techniques. More recently, automated techniques have been introduced that promise to increase the speed of sequence determination and render the process less laborious and costly. In this review, the basic principles of DNA sequencing will be outlined followed by a description of the current generation of automated DNA sequencers. The challenge of the Human Genome Initiative will be discussed, followed by a glimpse of emerging DNA sequencing technologies.

#### MANUAL DNA SEQUENCING

**Preparation of DNA for Sequencing.** One of the factors that delayed the development of techniques for DNA sequencing was the difficulty of obtaining sufficient amounts of DNA in pure form. The discovery of restriction enzymes which cleave DNA at specific sequences allowed discrete samples of DNA to be isolated. The development of cloning techniques provided a method for their purification and in vivo amplification. An example of the use of the bacteriophage M13 as a cloning vehicle (vector) to prepare DNA for sequencing is shown in Figure 2 (3). M13 cloning not only affords pure DNA for analysis but also provides regions of known DNA sequence which may serve as starting points for sequence determination.

An in-depth discussion of cloning techniques as they relate to DNA sequencing is beyond the scope of this review. New, in vitro methods for generating DNA are becoming available (4), but cloning remains the method of choice for preparing DNA for sequence analysis.

**Generation of DNA Sequencing Fragments.** All of the existing methods for DNA sequence analysis are based on a paradigm first applied in the late 1970s. That paradigm is the conversion of sequence information which cannot (as of yet) be measured directly into chain-length information which can be measured directly by physical methods. Specifically, the methods involve the generation of nested sets of DNA

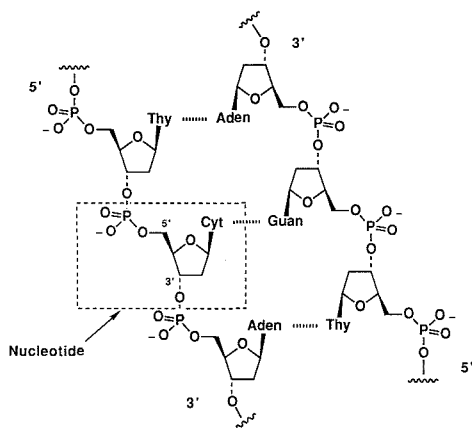


**Figure 1.** Structure of a section of DNA showing the double-stranded, antiparallel arrangement of the strands. The boxed region is a nucleotide, the basic unit of DNA sequence.

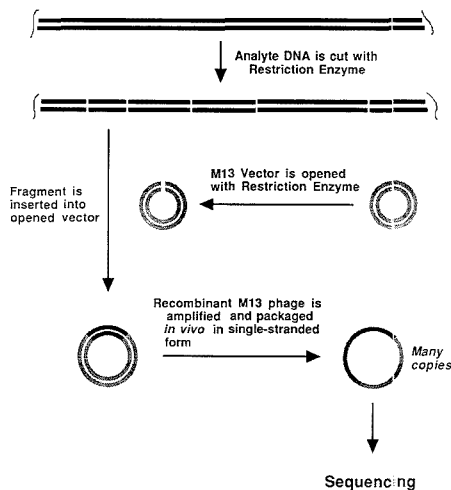


**Figure 2.** Preparation of DNA for sequencing using bacteriophage M13 cloning.

fragments whose lengths relate to sequence. The fragments have one terminus in common and typically have a given nucleotide (A, C, G, or T) at the other terminus. Thus, a measurement of relative chain length in the fragments provides information about the position, relative to the common terminus, of the given nucleotide in the original sequence. See Figure 3.

Most commonly, DNA sequencing fragments are generated by using the Sanger method (also referred to as the primer extension or chain termination method) (5). In this method the nested sets of DNA fragments are created through the use of a DNA polymerase. (The prototypical polymerase for DNA sequencing is the large (or Klenow) fragment of DNA Polymerase I from *E. coli*.) DNA polymerases are enzymes which, when presented with a single strand, catalyze the synthesis of a complementary strand of DNA. They require a stretch of double-stranded DNA as an initiation site. Nucleotides are added in stepwise fashion to the 3'-terminus of the double-stranded region using 2'-deoxyribonucleotide

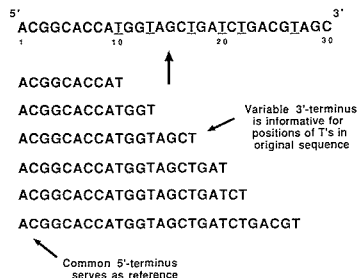


**Figure 3.** Partial reconstruction of a DNA sequence from the lengths of a set of sequencing fragments. By measuring chain-lengths, one can establish that T's occur at positions 10, 13, 17, 20, 22, and 27 in the original sequence.

triphosphates (dNTPs) as monomers. When provided with sufficient quantities of the four requisite dNTPs, a polymerase will catalyze the formation of a complete complementary copy of the original strand.

In the Sanger method, a short complementary oligonucleotide (defined as the *primer*) is allowed to hybridize (form a double-stranded structure through hydrogen bonding) with a known region of the DNA strand to be analyzed (defined as the *template*). The 5'-end of the primer serves as the common reference terminus and the 3'-end serves as the initiation site for the polymerase. To generate a set of sequencing fragments, the polymerization is carried out in the presence of the four natural dNTPs along with a single 2',3'-*dideoxy*ribonucleotide triphosphate (ddNTP). The incorporation of a ddNTP affords a chain which lacks a hydroxy group at the 3'-terminus and thus cannot be further extended. The competition between the ddNTP and its corresponding dNTP for incorporation results in a distribution of fragments which are informative for all positions of the complementary nucleotide in the template. To determine the complete DNA sequence of the template, four parallel reactions are run, each with a different ddNTP, to afford four sets of fragments. See Figure 4.

Other methods for producing sets of sequencing fragments have also been used (6, 7). In the Maxam-Gilbert method, nucleotide-specific chemical reactions are employed to destroy a given nucleotide and thereby create sequencing fragments. The analyte DNA is treated sequentially with reagents which (i) modify specific bases, (ii) remove the modified bases, and (iii) cleave the strand at sites lacking bases. If the analyte DNA is pre-labeled on one end (*vide infra*), then the detected fragments will have one terminus defined by the position of the label and the other defined by the first cleavage site down the chain. (Maxam-Gilbert sequencing fragments differ slightly from Sanger sequencing fragments in that the nucleotide found at the variable terminus will be the nucleotide preceding the nucleotide destroyed by chemical treatment.) Conditions are adjusted for low levels of modification ("single hit conditions") to ensure that all possible fragments are represented in the mixture. Although there are base-specific reactions available for all four bases, more typically single-base-specific reactions are used in conjunction with purine- or pyrimidine-specific reactions.

The actual extraction of sequence information from sets of sequencing fragments requires two additional, and more traditional, analytical methodologies. First, a method of separating the fragments by length is needed. Secondly, a method of detection for the fragments is required. In each case the performance criteria are quite demanding.

**Separation of DNA Sequencing Fragments.** DNA sequencing requires a separation method capable of distin-

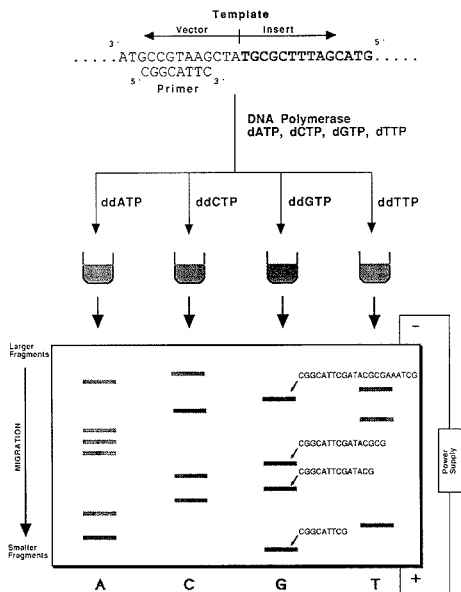


**Figure 4.** Determination of DNA sequence using the Sanger method. The sequencing "ladder" is read from bottom to top to obtain the complement of the template sequence. The full sequence of each fragment produced by termination with ddGTP is shown.

guishing between long oligodeoxyribonucleotides differing by only a single nucleotide in length. To date only a single technique—high resolution gel electrophoresis—has been able to provide the requisite resolving power over a useful range of fragment lengths. Cross-linked polyacrylamide gels are used almost exclusively.

Under denaturing conditions (i.e. in the presence of 8 M urea) in polyacrylamide, a single-stranded oligodeoxyribonucleotide will migrate at a rate determined by its length and, to a lesser extent, by its base-composition and sequence. Since sets of DNA sequencing fragments bear a common terminus and are nested with respect to sequence, base-composition and sequence play a relatively minor role in migration rate. The fragments generally elute in true order of length with the smaller fragments sieving more rapidly through the gel. For the most part, the spacing of nested fragments differing by a single nucleotide in length is quite regular. When viewed from any stationary point along the path of migration, the spacing between fragments is seen to be more or less constant—time of appearance varies linearly with fragment length. Alternatively, if the separation is stopped at any point in time, the *spatial* distribution of fragments along the path of migration is seen to be nonlinear with the slower moving, larger fragments compressed.

Sequencing gels are run in thin slab configuration for a number of reasons. The thin slab provides for more even heat dissipation and hence better resolution. More importantly, a slab gel allows the four sets of sequencing fragments needed to reconstruct the complete sequence to be resolved simultaneously in four parallel lanes. Sequencing fragments are loaded in square wells at the top of the vertical gel and migrate down as thin rectangular bands. In actual practice as many as 20 templates are analyzed in four lanes each on a single gel.

**Detection of DNA Sequencing Fragments.** Once the sequencing fragments have been resolved they must be de-

tected in order to determine the sequence. The overwhelming consideration here is one of sensitivity. In a typical experiment less than 1 pmol of DNA template is available for processing. If the conditions in the Sanger method are adjusted to provide for example 500 fragments, then one can expect the amount of DNA in each band to be approximately 1 fmol. (Variability in chain termination efficiencies and hence in sequencing fragment concentrations in the Sanger method often results in bands having considerably less material.) At these levels direct detection of fragments is impractical so an auxiliary reporter is used. Virtually all of the sequencing that has been carried out to date has been done with a radioisotopic reporter (label) such as  $^{32}\text{P}$ . In the Sanger method, the sequencing fragments are labeled by incorporating  $\alpha$ -[ $^{32}\text{P}$ ]dATP. This approach offers the advantage that the less numerous, longer fragments carry more reporters. The net effect is a more even distribution of signal over the set of fragments. In Maxam-Gilbert sequencing where the dynamic range of fragment concentrations is smaller, a single label is enzymatically appended to one end of the fragment to be sequenced. The labeled end becomes the common terminus of reference; only fragments retaining that terminus are detected.

The radioisotopically labeled sequencing fragments are detected by the process of autoradiography. Electrophoresis is stopped at an appropriate time and the gel is removed from the apparatus, fixed, dried, and sandwiched with a piece of film. After exposure, generally ranging from several hours to several days, the film is developed to reveal the pattern of bands present in the gel. This process of autoradiography is exquisitely sensitive allowing even the faintest of bands to be detected with long exposures.

The final step in the sequencing process is the interpretation of the autoradiogram. The sequence is read by starting with the smallest fragment at the bottom of the gel and moving up, determining the lane (A, C, G, or T) in which the next longest fragment appears at each step. A section of autoradiographic sequence is shown in Figure 5. The sequence is entered into a database either by manual means or with the assistance of a light pen. One moves up the "sequencing ladder" until the bands are so closely spaced that the proper order can no longer be determined with confidence. Typically, between 250 and 350 nucleotides can be read from each set of four lanes.

The radioisotope/autoradiography approach to detection however is not ideal in all respects. Since the detection process involves integration of signal over long periods of time, large gels must be used to spatially resolve as many bands as possible. (Often, the same sets of sequencing fragments are "double loaded" (i.e. a second gel loading in adjacent lanes is carried out after the electrophoresis has progressed) to allow more nucleotides to be read from each template.) Considerable manual manipulation of these large gels (i.e. removal from the electrophoresis apparatus, drying, etc.) is required. Long film exposures place a considerable time-lag between separation and visualization, lengthening the sequence determination process. Finally, the use of short-lived, radioactive isotopes poses both logistical and health and safety problems.

#### IMPROVEMENTS IN MANUAL DNA SEQUENCING

In the years since these techniques were first introduced there have been numerous incremental improvements in the technology. There have been efforts to automate the preparation of DNA and the sequencing chemistries (8, 9). For Sanger sequencing, DNA polymerases with improved properties have been found (10, 11). Desirable properties include a low variability in termination efficiencies with ddNTPs and an ability to operate at high temperatures to minimize the



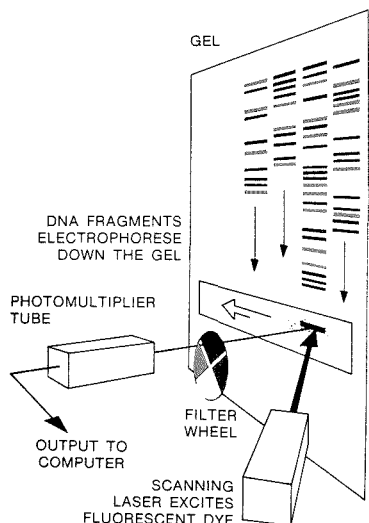


Figure 6. Schematic diagram of the fluorescence-based, automated DNA sequencer from Applied Biosystems Incorporated (ABI).

Excitation of the fluorescence-tagged sequencing fragments at the bottom of the gel was achieved with an argon ion laser operating in multiline mode. (A band-pass filter was used to

select for excitation by the 488- or 514-nm line.) The fluorescent tags were distinguished by sequentially observing the emission with a photomultiplier tube (PMT) through each of four interference filters mounted on a spinning wheel. The raw, digital data output consisted of four elution profiles or traces of fluorescence intensity vs time. Multicomponent analysis afforded four processed traces, one for each dye. The sequence was discernible in the temporal order of peaks in the four aligned, processed traces.

The Caltech system clearly demonstrated the viability of a fluorescence-based approach to DNA sequencing but the system as configured was not practical for high-throughput sequencing. The most significant deficiency was the inability to handle more than a single sample at a time in the tube gel. Further development was undertaken and a commercial system was introduced by Applied Biosystems Incorporated (ABI) (23).

The ABI system, shown schematically in Figure 6, offers a number of improvements over the original Caltech system. The system can handle 16 samples simultaneously on a slab gel. The detection is multiplexed by mounting the excitation and emission optics on a translating stage which scans the bottom of the gel. The chemistry (fluorescent dyes and linker arms) was modified to improve the optical characteristics of the dye-set and to minimize dye-induced differential perturbations in the electrophoretic mobility of sequencing fragments. Finally, algorithms to directly assign DNA sequence were developed. An example of the output from this system is shown in Figure 7.

A DNA sequencing system based on the use of four fluorescent dyes was also developed by a group at Du Pont

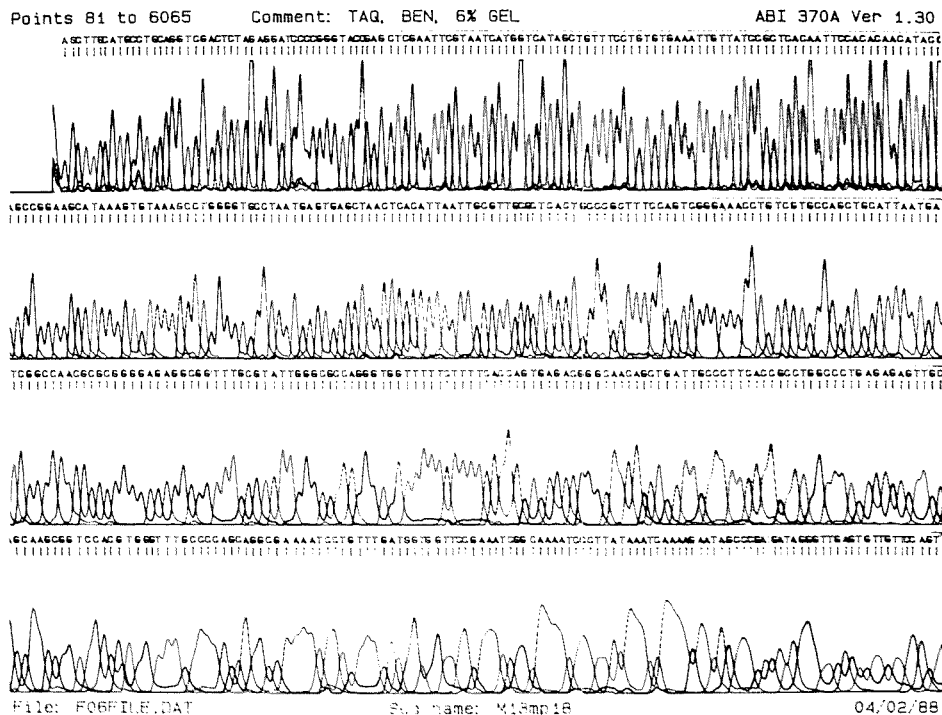
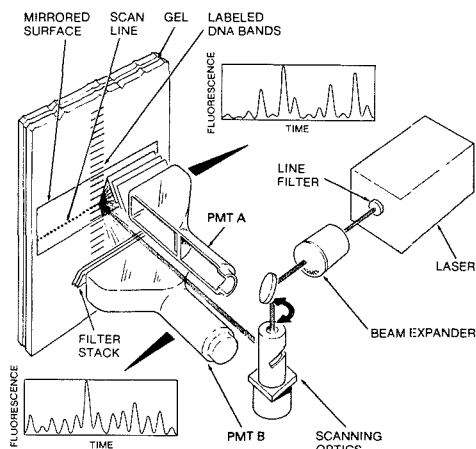


Figure 7. A sample of processed output from the ABI sequencer. The four traces represent the calculated concentration of each dye as a function of time. The color assignments are as follows: A, green; C, blue; G, brown; T, red. The assigned sequence is listed below the traces.



**Figure 8.** Diagram of the excitation/detection module from the Du Pont fluorescence-based DNA sequencer. Reprinted with permission from ref 24. Copyright 1987 by the American Association for the Advancement of Science.

(24). This system differs from the ABI system in several respects. The Du Pont system uses a set of four succinyl-fluorescein dyes with closely spaced emission bands. These

similar dyes were selected to permit efficient excitation with a single argon ion laser line (488 nm) and to minimize differential effects on electrophoretic mobility. Fluorescence-tagged DNA sequencing fragments are generated by using four tagged, chain-terminating ddNTPs. This approach offers a number of advantages. The four sets of sequencing fragments can be generated simultaneously in a single reaction vessel since each terminating nucleotide carries a distinguishable tag. Artifacts arising from the presence of non-dideoxy-terminated fragments are eliminated. Finally, sequencing strategies which involve multiple primers are facilitated by the need for only a single unlabeled primer. The principal disadvantage of the terminator labeling approach is that there is reduced flexibility in the choice of sequencing enzyme. The fluorescence-tagged ddNTPs are poor substrates for some DNA polymerases and generally show increased variability in chain-termination efficiency.

The excitation/detection module of the Du Pont sequencer is shown in Figure 8. Multiple samples (up to 12) are accommodated through the use of a laser scanner consisting of a periscope mounted on a digitally controlled stepper motor. Wide-faced photomultiplier tubes allow for detection across the entire width of the gel. Discrimination between the fluorescent dyes is accomplished by simultaneously viewing the fluorescent emission with two such detectors through filters that are offset in band-pass. As a fragment passes the detectors, signals are observed in the two detectors in a ratio characteristic of the attached dye. An algorithm which locates the peaks and computes the ratio allows the sequence to be

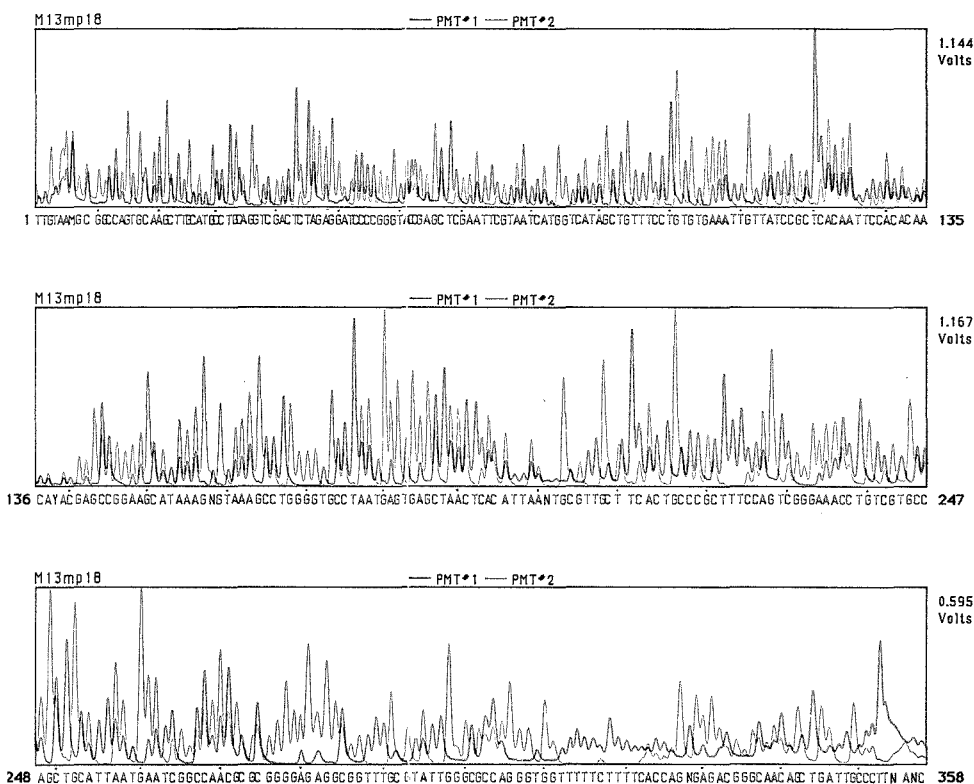


**Figure 9.** A sample of the processed output from the Du Pont DNA sequencer. The two traces correspond to the output of the two photomultiplier tubes. The assigned sequence, derived from the ratio of the two traces at each peak, is shown below.

assessed directly. A sample of the output from this system is shown in Figure 9.

In addition to the two sequencing systems based on the use of four fluorescent dyes, several systems employing a single fluorescent dye have been described. These systems offer the simplicity of requiring only a single fluorescein-labeled primer. However, they have the disadvantage of requiring that the four sets of sequencing fragments from each sample be run in separate lanes. This reduces the capacity of the gel and necessitates compensation for distortions in the alignment of the four lanes.

The single-dye, fluorescence-based sequencing system developed at the European Molecular Biology Laboratory (EMBL) features a detection system with no moving parts (25, 26). Excitation of multiple lanes is achieved by laser irradiation through the edge of the gel. Emission is captured by a bank of photomultiplier tubes, one for each lane. A system developed by Hitachi utilizes the same approach for excitation but images the emission from the multiple lanes onto a linear intensified array detector (27). A University of Nebraska group has reported the development of a third system using more conventional scanning optics (28). This system uses multiply tagged fluorescent primers.

In the few years since the fluorescence-based systems were first described there have been refinements and improvements in the technology. Once the gel has been loaded these systems are capable of delivering reliable sequence with little or no operator intervention. Run lengths out beyond 400 base pairs with accuracies on the order of 98–99% have been achieved (29, 30). (Performance on any given sample is dependent on the nature of the DNA being analyzed: occasionally sequences are refractory to analysis by the Sanger method.) Throughputs approaching 10 000 nucleotides per day are accessible.

It should be noted that the systems which have been described are in fact generic technologies for fluorescence labeling and detection. These technologies may be applied to other analyses which entail the labeling and separation of DNA fragments such as fluorescence-based Maxam–Gilbert sequencing (31). The labeling and analysis of restriction fragments for the purposes of mapping (vide infra) have also been demonstrated (32, 33).

### THE HUMAN GENOME

The existing methods for DNA sequencing have served biology well; the capabilities have been suitable for the tasks at hand. To date, nearly 35 million bases of DNA sequence (34) have been entered into GenBank, a computer database for nucleic acid sequence. Many of the entries are sequences of intact genes gathered from a broad range of organisms. Some of the entries describe the complete genomes of viruses. The determination of the 230 000 nucleotides of DNA sequence of the largest of these viruses, human cytomegalovirus (CMV), required an intense multiyear effort but, still, was within the capabilities of the current technology (35). More recently, a number of groups have set their sights on the genome of the well-studied, prototypic bacterium *Escherichia coli* (*E. coli*). The genome size of *E. coli* is estimated to be 4.7 million base pairs (36). Efforts to obtain the complete sequence of *E. coli* genome will clearly test the limits of the current technology.

The ability to determine DNA sequence is having a revolutionary impact on medicine (37). Through DNA sequencing, some of the molecular events leading to the development of cancer have been elucidated. The genetic defects responsible for many inherited diseases have been determined at the DNA sequence level. This has spurred the development of powerful diagnostic tools and should lead the way to effective therapies. Again, however, the needs are beginning to outstrip the capabilities of the technology. The gene containing the defect

responsible for Duchenne's muscular dystrophy, for example, is thought to be spread over some 2 000 000 bases of DNA sequence (38).

**Human Genome Initiative.** The Human Genome Initiative was conceived in response to the realization that the knowledge of human DNA sequence is both medically and scientifically important. The acquisition of human DNA sequence has been proceeding steadily but without real coordination or planning. Similarly the development of new sequencing technology has been proceeding but at a pace that is not commensurate with the need.

The Human Genome Initiative has as its goal the acquisition of the DNA sequence corresponding to a complete human genome (37, 39). This initiative is expected to coordinate and, indeed, proactively drive the activities needed to accomplish this goal. The development of powerful, new sequencing technologies is clearly one of the key activities of this initiative.

The magnitude of this undertaking is staggering when viewed in the light of current capabilities. The haploid human genome (the genetic material found in a single sperm or egg cell) is estimated to consist of 3 billion base-pairs. A complete determination is a daunting task by even the most optimistic estimates. If one assumes that each strand of human genomic DNA will be sequenced twice (the bare minimum), then it will take 100 automated sequencers of the current vintage 60 years to complete the task once! Even this estimate understates the true problem since the real value of such an undertaking will be in comparisons between individuals and with other species (e.g. mouse). Many "human genome equivalents" of sequence will ultimately need to be acquired.

**What Is the Value of Such an Undertaking?** Put simply this is a mission to acquire the complete text of information, instructions if you will, that each of us carries in most every cell in our body. Our ability to understand that text is still in its infancy but is rapidly advancing. The Human Genome Initiative will provide the starting dataset for fundamental biological studies for far into the future. It will free the researcher from having to track down and independently sequence the gene he is interested in, allowing him to devote his efforts to more scientifically productive tasks from the start. Scientists will be able to tackle such issues as nature of the genetic differences that distinguish individuals, the origins of the more than 4000 known human genetic defects (40), and the factors that lead to susceptibility to such maladies as cancer and heart disease. An understanding of the genetic factors that control development, the progress of a human from a single cell to an organism comprised of many different types of cells, will be within reach.

A concerted effort to acquire the DNA sequence corresponding to a complete human genome should also dramatically increase our understanding of how genetic information is stored and maintained. Most of the sequencing of human DNA today focuses on coding regions. Yet it is estimated that perhaps less than 10% of human DNA codes for proteins. What, if any, information is contained in the remaining 90%? The Human Genome Initiative will allow large tracts of noncoding DNA to be searched for patterns that might answer this question. Under current programs such noncoding sequences would become available only very slowly.

**The Path Forward.** The organizational groundwork for the Human Genome Initiative has been set. An international group of scientists has founded the Human Genome Organization (HUGO) to guide the initiative and facilitate international cooperation (41). In the United States, an Office of Human Genome Research has been established within the National Institutes of Health to fund individual projects and programs (42). The office will also designate and fund centers

for human genome studies. Similar efforts are under way in the Department of Energy (43).

Initial efforts will be focused on mapping activities. There are several different types of mapping (e.g. physical, genetic, and cytological). In a general sense, all mapping involves the ordering and locating of specific sequence landmarks along a stretch of DNA. This allows the DNA to be broken down into manageable chunks in such a way that the overall genomic sequence can be easily reconstructed. The map also allows specific sequence regions of interest to be quickly accessed. A preliminary genetic map of the human genome has recently been constructed (44). Progress is being made on physical maps of several human chromosomes. Techniques for physical and genetic mapping are well established but remain highly labor intensive. Advances in the automation of these existing techniques and fundamentally new approaches will be needed to take on the human genome in its entirety.

Large-scale acquisition of human DNA sequence has not yet begun but it is already clear that the need for new DNA sequencing technologies is acute. The feasibility of sequencing the human genome is most probably staked on such new technologies.

### EMERGING TECHNOLOGIES

A number of programs directed toward the development of rapid sequencing techniques have been initiated in response to this pressing need. Some of the proposed systems entail major improvements in one or more stages of the existing methodology, some represent substantial overhauls, and some involve a major conceptual leap. Regardless of the approach, it is clear that to handle the human genome, the new technology should be capable of processing on the order of 1 megabase of sequence per day. This is roughly a 100-fold increase in throughput over current technology.

**Gel-Based Systems.** The limited throughput of gel electrophoresis remains one of the major barriers to improvements in the current technology. For this reason, recent reports of the successful single-base resolution of oligonucleotides by capillary gel electrophoresis have attracted considerable attention. Separation has been carried out at speeds of up to 20 bases per minute, a 20-fold improvement (on a per lane basis) over current automated sequencers (45).

Plans to couple capillary gel electrophoretic separation with alternative reporter/detection systems have been described (46). Work has begun on an approach where sequencing fragments generated via the Sanger protocol are tagged with a stable isotope. Four isotopes of a given element serve the same purpose as the four dyes in the fluorescence-based systems. As the fragments elute from the capillary, they are pyrolyzed and the resulting gases are analyzed by a mass spectrometer to identify the tagging isotope.

The Church multiplex technique (vide supra) allows many sets of sequencing fragments to be simultaneously resolved in a single gel. However the technology associated with the visualization and interpretation of the patterns limits this technique. A recent paper suggests the use of fluorescence-tagged probes to visualize the sequencing ladders (47).

**Stepwise Methodologies.** To circumvent the inherent limitations of gel electrophoresis, several groups have considered moving away from the sequence/fragment-length paradigm. Two such approaches that have been recently described involve the stepwise addition or removal of nucleotides from an analyte DNA. These approaches are reminiscent of protein sequencing techniques and invoke many of the same technical considerations.

Hyman has devised a system that allows the addition of a nucleotide to a primed template by a DNA polymerase to be detected by monitoring the release of the inorganic pyrophosphate byproduct (48). In this system the primed template

and the DNA polymerase are immobilized and the four possible dNTP substrates are pumped through sequentially. Quantitation of the released inorganic pyrophosphate, via an enzyme cascade leading to a luminescence signal, indicates which nucleotide has been added to the template and how many. The system is currently limited in speed. The ultimate limitation, however, is likely to be in maintaining synchronicity in the growing DNA chains.

A group at Los Alamos proposes to obviate the synchronicity problem by working with a single DNA molecule (49). They plan to enzymatically prepare a long, single-stranded DNA template with every nucleotide fluorescence tagged in a base-specific fashion (four tags). They will select a single molecule and processively remove the nucleotides from one end by using an exonuclease. The released, fluorescence-tagged nucleotides will be swept into a detector capable of registering and identifying single fluorescent molecules. Though technically very challenging, this approach has enormous throughput potential and successful implementation would have a major impact.

**Hybridization-Based Approaches.** Recently, two independent groups have proposed an approach that involves neither synthesis nor degradation of the DNA during the actual sequencing process (50, 51). This approach takes advantage of the strong, selective binding of short, perfectly complementary oligonucleotides to a single-stranded DNA sequence. The specifics of the proposals differ but in each case the DNA to be analyzed is probed with a large panel of short oligonucleotides. In theory, the resulting table of hybridization responses (yes/no) can be computationally processed to deduce the sequence.

This conceptually novel approach poses immense technical problems including the need to synthesize and manipulate perhaps tens of thousands of oligonucleotides and the need to develop algorithms to handle the immense computational requirements. Still, the potential advantages in cost and speed suggest that this novel approach should be explored.

**Direct Observation.** All of the previously described methods rely on some indirect measurement of DNA sequence. There remains the possibility that DNA sequence might be determined by direct observation. Recent advances in the use of the scanning tunneling electron microscope have provided striking images of double-stranded DNA (52, 53). Features such as the helical nature and the major and minor grooves are clearly discernible. There has been speculation that individual base-pairs might be identified by this technique. Although this technology is certain to play an important role in studies on DNA structure, it is not clear if it will ever be possible to accurately and rapidly read continuous stretches of DNA sequence by this method.

The scope of this discussion has been limited to the technologies surrounding the actual acquisition of DNA sequence data. As these technologies improve, other phases of the overall process may become rate limiting. For example, much work is need on the preparation of DNAs for sequencing. Some attention has been given to robotics but entirely new approaches are needed. At the other end of the process, the generation of massive amounts of raw sequence will tax all stages of our existing data processing capabilities. All of the current techniques rely to some extent on manual editing of final sequence; this will be impossible with megabase sequencers. Finally, powerful methods for searching enormous databases and carrying out sequence comparisons will be needed if the tangible product of the Human Genome Initiative is to be used effectively.

### CONCLUSION

The development of DNA sequencing technology is now, by necessity, on interdisciplinary endeavor. The early, manual

methods were developed in individual laboratories. The automated, fluorescence-based systems have been assembled through the collaborative efforts of chemists, biologists, optical specialists, software developers, and systems engineers. This trend will continue as more sophisticated methodologies are brought to bear on the problem.

In its short history, the field of DNA sequencing has benefited from a number of exceptionally creative contributions. The path we are starting down with the Human Genome Initiative will require no less an effort in both creativity and determination. It promises to be an exciting journey. No technical undertaking speaks more directly to the question of what we are.

#### ACKNOWLEDGMENT

The helpful comments of Frank Hobbs, Tony Cocuzza, and Bob Zagursky are greatly appreciated. Simon Edkins, Tim Dambaugh, Betsy Anton, Annie Colberg-Poley, Terry Bonnes, and Marilee Shaffer (ABI) are also thanked for their assistance in producing the paper.

#### LITERATURE CITED

- Smith, L. M. *Anal. Chem.* **1988**, *60*, 381A-390A.
- Watson, J. D.; Crick, F. H. C. *Nature* **1953**, *171*, 737-738.
- Bankier, A. T.; Weston, K. M.; Barrell, B. G. *Methods Enzymol.* **1987**, *155*, Part F, 51-93.
- Gyllenstein, U. B. *BioTechniques* **1989**, *7*, 700-709.
- Sanger, F.; Nicklen, S.; Coulson, A. R. *Proc. Natl. Acad. Sci. U.S.A.* **1977**, *74*, 5463-5467.
- Maxam, A. M.; Gilbert, W. *Proc. Natl. Acad. Sci. U.S.A.* **1977**, *74*, 560-564.
- Gish, G.; Eckstein, F. *Science* **1988**, *240*, 1520-1522.
- Frank, R.; Bosserhoff, A.; Boulin, C.; Epstein, A.; Gausepohl, H.; Ashman, K. *Bio/Technology* **1988**, *6*, 1211-1213.
- Martin, W. J.; Warmington, J. R.; Galinski, B. R.; Gallagher, M.; Davies, R. W.; Beck, M. S.; Oliver, S. G. *Bio/Technology* **1985**, *3*, 911-915.
- Tabor, S.; Richardson, C. C. *Proc. Natl. Acad. Sci. U.S.A.* **1987**, *84*, 4767-4771.
- Innis, M. A.; Myambo, K. B.; Gelfand, D. H.; Brow, M. A. D. *Proc. Natl. Acad. Sci. U.S.A.* **1988**, *85*, 9436-9440.
- Jagadeeswaran, P.; Kaul, R. K. *Gene Anal. Tech.* **1986**, *3*, 79-85.
- Gross, B.; Rosenthal, A. *Gene Anal. Tech.* **1987**, *4*, 57-61.
- Iverson, B. L.; Dervan, P. B. *Nucleic Acids Res.* **1987**, *15*, 7823-7830.
- Biggin, M. D.; Gibson, T. J.; Hong, G. F. *Proc. Natl. Acad. Sci. U.S.A.* **1983**, *80*, 3963-3965.
- Elder, J. K.; Green, D. K.; Southern, E. M. *Nucleic Acids Res.* **1986**, *14*, 417-424.
- Richterich, P.; Heller, C.; Wurst, H.; Pohl, F. M. *BioTechniques* **1989**, *7*, 52-59.
- Church, G. M.; Kieffer-Higgins, S. *Science* **1988**, *240*, 185-188.
- Martin, W. J.; Davies, W. D. *Bio/Technology* **1986**, *4*, 890-895.
- Toneguzzo, F.; Glynn, S.; Levi, E.; Mjolsness, S.; Hayday, A. *BioTechniques* **1988**, *6*, 460-469.
- Smith, L. M.; Sanders, J. Z.; Kaiser, R. J.; Hughes, P.; Dodd, C.; Connell, C. R.; Heiner, C.; Kent, S. B. H.; Hood, L. E. *Nature* **1986**, *321*, 674-679.
- Smith, L. M.; Fung, S.; Hunkapiller, M. W.; Hunkapiller, T. J.; Hood, L. E. *Nucleic Acids Res.* **1985**, *13*, 2399-2412.
- Connell, C.; Fung, S.; Heiner, C.; Brigham, J.; Chakerian, V.; Heron, E.; Jones, B.; Menchen, S.; Mordan, W.; Raff, M.; Recknor, M.; Smith, L.; Springer, J.; Woo, S.; Hunkapiller, M. *BioTechniques* **1987**, *5*, 342-348.
- Prober, J. M.; Trainor, G. L.; Dam, R. J.; Hobbs, F. W.; Robertson, C. W.; Zagursky, R. J.; Cocuzza, A. J.; Jensen, M. A.; Baumeister, K. *Science* **1987**, *239*, 336-341.
- Ansorge, W.; Sproat, B. S.; Stegemann, J.; Schwager, C. J. *Biochem. Biophys. Methods* **1988**, *13*, 315-323.
- Ansorge, W.; Sproat, B.; Stegemann, J.; Schwager, C.; Zenke, M. *Nucleic Acids Res.* **1987**, *15*, 4593-4602.
- Kambara, H.; Nishikawa, T.; Katayama, Y.; Yamaguchi, T. *BioTechnology* **1988**, *6*, 816-821.
- Brumtaugh, J. A.; Middendorf, L. R.; Grone, D. L.; Ruth, J. L. *Proc. Natl. Acad. Sci. U.S.A.* **1988**, *85*, 5610-5614.
- Gocayne, J.; Robinson, D. A.; FitzGerald, M. G.; Gillard, E. F.; Kerlavage, A. R.; Lentes, K.-U.; Lai, J.; Wang, C.-D.; Fraser, C. M.; Venter, J. C. *Proc. Natl. Acad. Sci. U.S.A.* **1987**, *84*, 8296-8300.
- Amorese, D. A.; Hochberg, A. M. *Ann. Biotech. Lab.* **1989**, March, 38-4c.
- Voss, H.; Schwager, C.; Wirkner, U.; Sproat, B.; Zimmermann, J.; Rosenthal, A.; Erfle, H.; Stegemann, J.; Ansorge, W. *Nucleic Acids Res.* **1989**, *17*, 2517-2527.
- Carrano, A. V.; Lamerdin, J.; Ashworth, L. K.; Watkins, B.; Branscomb, E.; Slezak, T.; Raff, M.; de Jong, P. J.; Keith, D.; McBride, L.; Meister, S.; Kronick, M. *Genomics* **1989**, *4*, 129-136.
- Brenner, S.; Llvak, K. J. *Proc. Natl. Acad. Sci. U.S.A.* **1989**, *86*, 8902-8906.
- Genbank, Release 61.
- For a partial sequence see: Weston, K.; Barrell, B. G. *J. Mol. Biol.* **1986**, *192*, 177-208.
- Knott, V.; Blake, D. J.; Brownlee, G. G. *Nucleic Acids Res.* **1989**, *15*, 5901-5912.
- Mapping Our Genes, Genome Projects: How Big, How Fast?*; Congress of the United States, Office of Technology Assessment; U.S. Government Printing Office: Washington, DC, April 1988.
- Burmeister, M.; Monaco, A. P.; Gillard, E. F.; van Ormon, G.-J. B.; Affara, N. A.; Ferguson-Smith, M. A.; Kunkel, L. M.; Lehrach, H. *Genomics* **1988**, *2*, 189-202.
- Mapping and Sequencing the Human Genome*; National Research Council, 1988.
- McKusick, V. A. *Mendelian Inheritance in Man: Catalog of Autosomal Dominant, Autosomal Recessive, and X-Linked Phenotypes, 7th Edition*; Johns-Hopkins University Press: Baltimore, MD, 1986.
- McKusick, V. A. *Genomics* **1989**, *5*, 385-387.
- Watson, J. D.; Jordan, E. *Genomics* **1989**, *5*, 654-656.
- Barnhart, B. J. *Genomics* **1989**, *5*, 657-660.
- Donis-Keller, H.; Green, P.; Helms, C.; Cartinour, S.; Weiffenbach, B.; Stephens, K.; Keith, T. P.; Bowden, D. W.; Smith, D. R.; Lander, E. R.; Botstein, D.; Akots, G.; Rediker, K. S.; Gravius, T.; Brown, V. A.; Rising, M. B.; Parker, C.; Powers, J. A.; Watt, D. E.; Kaufman, E. R.; Bricker, A.; Phipps, P.; Muller-Kahle, H.; Fulton, T. R.; Ng, S.; Schumm, J. W.; Broman, J. C.; Knowlton, R. G.; Barker, D. F.; Crooks, S. M.; Lincoln, S. E.; Daly, M. J.; Abrahamsen, J. *Cell* **1987**, *51*, 319-337.
- Cohen, A. S.; Najjarian, D. R.; Paulus, A.; Guttmann, A.; Smith, J. A.; Karger, B. L. *Proc. Natl. Acad. Sci. U.S.A.* **1988**, *85*, 9660-9663.
- Brennan, T. *Proceedings of the Second International Symposium on Mass Spectrometry in the Health and Life Sciences*, San Francisco, August 27-31, 1989, in press.
- Yang, M. M.; Youvan, D. C. *Bio/Technology* **1989**, *7*, 576-580.
- Hyman, E. D. *Anal. Biochem.* **1988**, *174*, 423-436.
- Jett, J. H.; Keller, R. A.; Martin, J. C.; Marrone, B. L.; Moyzis, R. K.; Ratliff, R. L.; Seitzinger, N. K.; Shera, E. B.; Stewart, C. C. *J. Biomol. Struct. Dynam.* **1989**, *7*, 301-309.
- Bains, W.; Smith, G. C. *J. Theor. Biol.* **1988**, *135*, 303-307.
- Drmenac, R.; Labat, I.; Brunkner, I.; Crkvenjakov, R. *Genomics* **1989**, *4*, 114-128.
- Beebe, T. P.; Wilson, T. E.; Ogletree, D. F.; Katz, J. E.; Balhorn, R.; Salmeron, M. B.; Stekhaus, W. *J. Science* **1989**, *243*, 370-372.
- Lindsay, S. M.; Thundath, T.; Nagahara, L.; Knipping, U.; Rill, R. L. *Science* **1989**, *244*, 1063-1064.

## ARTICLES

# Indirect Fluorometric Detection of Cations in Capillary Zone Electrophoresis

Larry Gross and Edward S. Yeung\*

Ames Laboratory—USDOE and Department of Chemistry, Iowa State University, Ames, Iowa 50011

**A new method for detecting cations separated by capillary zone electrophoresis is described. Quinine sulfate is a useful buffer for indirect fluorescence detection. The positively charged, fluorescent quinine ion is displaced by nonfluorescent solute cations. In contrast to previous work with anions, quinine ion adsorbs to the capillary wall. The effect of adsorption on resolution and reproducibility is discussed. Applications are presented for mono- and divalent cations, amines, and oligopeptides. Because small internal diameter capillaries can be used for this technique, very low quantities of cations injected can be detected.**

Cation-exchange chromatography is widely used to analyze samples from amines to simple inorganic cations (1, 2). Instrumentation for these applications is well-developed and improvements are constantly being made (3). Cations can likewise be separated by isotachopheresis (4). Separation by electromobility and by retention are complementary (5). Capillary zone electrophoresis (CZE) has the capability to separate very small quantities of sample when small inner diameter (i.d.) capillary columns are used. High detection sensitivity and low dead volume are imperative for successful applications (6). CZE is applicable to the separation of cations, but detection of these remains a challenge. Detection by conductivity has been demonstrated (7). There is however still room for improvement when going to lower concentrations or when small capillaries are used.

Capillary zone electrophoresis with indirect fluorescence detection (CZE-IFD) has been demonstrated recently (8). A fluorescing running buffer is used. A reduction in the background fluorescence intensity occurs when a sample zone elutes past the detector, because the solute ions displace the fluorescent buffer ions (to maintain constant conductance along the column). Up to this point CZE-IFD has centered on sodium salicylate as a fluorophore-containing buffer ion (8, 9). This works well with anionic analytes. The separation and detection of cations are best accomplished by using a buffer solution in which the cation contains the fluorophore. Quinine sulfate is shown here to be a useful buffer component for the CZE-IFD analysis of cations in aqueous solution.

The experimental conditions were optimized by applying the principles of electrophoretic separations in capillaries (10).

Because cations and the electroosmotic (EO) flow both migrate in the same direction, toward the cathode, a longer column was used to compensate for the resulting decrease in migration time. To minimize the EO flow velocity, a low pH was chosen for the buffer solution (11). A low pH was also useful for increasing the protonation of weak bases, such as amines, to enhance the displacement-based detection. The concentration of the buffer was chosen comparable to that of the concentration of salicylate buffer which gave the best results previously, which was 0.2–1.0 mM. An important difference between CZE-IFD with anions and cations is the tendency for cations to adsorb to the capillary wall, because of the negative charges existing at that interface (12).

The concentrations of buffer and solutes here are typically below 1.0 mM, so to a good approximation the mobilities of the solutes can be measured independent of activity effects. Therefore, the approximate effective mobilities for the cations studied here can also be determined. In a recent review, mobilities quoted from the literature differed by up to 8% for some of the ions included here (13). The mobilities obtained here were comparable to those results.

### EXPERIMENTAL SECTION

The experimental apparatus was the same, with a few exceptions, as that described previously (8, 9). Since a different fluorophore (quinine sulfate) is used as the indirect fluorescence probe, a different wavelength was used to excite the fluorescence. The argon ion laser (Spectra-Physics Model 2035, Mountain View, CA) lases in the ultraviolet on a pair of lines around 350 and 360 nm. This emission is about 10 times more intense than the line at 330 nm, which was used previously. Together these laser lines were passed directly into the laser stabilizer (LS-100, Cambridge Instruments, Inc., Cambridge, MA). A different pair of UV cutoff filters, both of type GG395 (Melles Griot, Irvine, CA) were purchased to reduce scattered light. A spatial filter was not necessary to mask out scattered light from the capillary when these two filters were used (8, 9).

The capillary columns used were untreated with respect to any covalently bonded stationary phase. Before being used, the following solutions were aspirated in order through the capillary: 0.05 M NaOH, H<sub>2</sub>O, 0.05 N H<sub>2</sub>SO<sub>4</sub>, H<sub>2</sub>O, methanol, H<sub>2</sub>O, and finally the buffer solution. The capillaries were 18  $\mu$ m i.d. and 80–90 cm in length.

The buffer solution was prepared each day from quinine sulfate (Serva, New York, NY) and sulfuric acid stock solution. Two hundred milliliters of a solution containing 0.39 mN quinine and

0.58 mN  $H_2SO_4$  was diluted and then degassed by aspiration for 20 min in an ultrasonic bath. Sample solutions and running buffer were filtered into 20-mL vials with a 25-mL nylon filter cartridge, 0.45- $\mu$ m pore size (Altech Associates, Deerfield, IL).

These vials, along with other glassware involved in preparing samples and buffer, were selected from new supplies and further cleaned as follows: the piece was rinsed with concentrated sulfuric acid, rinsed several times with purified water (Millipore Corp. reverse osmosis system, Bedford, MA), and then filled with 0.05 M NaOH solution and allowed to stand for about 2 h. Upon rinsing several times again with  $H_2O$ , the glassware surface was considered clean. Vials were rinsed with  $H_2O$  after each use and the process was repeated as necessary. This degree of cleanliness helped to prevent unwanted peaks from appearing in the electropherograms.

Samples were diluted in buffer in concentrations ranging from 10 to 100  $\mu$ M. System peaks were minimized by diluting the sample in buffer. The estimated error in sample concentrations given is 10%. Solutions of the alkali and alkaline-earth metal ions were prepared from their sulfate salts. These salts and the substituted amines, including tris(hydroxymethyl)aminomethane (THAM), were obtained from Fisher Scientific (Fair Lawn, NJ). Lithium sulfate (Sigma Chemical, St. Louis, MO) was the exception. Bovine serum albumin and  $\beta$ -casein were also from Sigma.

Samples were injected by electromigration or gravity flow injection. Electromigration was used, for example, when obtaining migration times in order to identify peaks. Gravity flow injection was used when quantitative measurements of peaks were made. Injections were made at the high voltage anode and cations were eluted to, and detected near, the grounded cathode.

## RESULTS AND DISCUSSION

Several buffer solutions were tested in the process of optimizing the operating system. Besides the buffer already described, quinine sulfate dissolved in  $H_2O$  alone (0.96 mM, pH 6.2) or a mixture of quinine ion ( $Q^+$ ) and  $H^+$  ( $[Q^+] = 0.96$  mM; and  $H_2SO_4$ , 10  $\mu$ N, pH 5.7) was used. The most apparent difference between these three was in the migration time ( $t_m$ ) of the system peak. The system peak corresponds to the difference in  $[Q^+]$  between the injected sample and the running buffer. It was always the last peak to elute and thus signified the end of the electropherogram. When the buffer pH was 3.7,  $t_m$  for this peak was typically 15–30 min, depending on the length of the column (60–90 cm). At pH 6.2, 8–10 minutes was typical. Other differences in the results between these buffers included the stability of the background signal (10 times worse at pH 6.2 compared to 3.7), and the occurrence of derivative-shaped peaks for injected solutes at high pH.

The migration time for the system peak depends on the rate of migration for quinine ion. This was shown by injecting solutions of quinine sulfate with concentration greater than, equal to, or less than that of the buffer. The system peak obtained is positive-going (increased fluorescence), null, or negative-going, respectively. The migration time for the system peak also clearly corresponds to the rate of EO flow through the column. This was found by injecting methanol, diluted 10% and 30% (v/v) in buffer, and finding that the peak for the methanol eluted just a few seconds before the system peak. A positive-going peak was obtained for the methanol because quinine is more soluble in the zone containing this solute. The flow rate of EO decreases with lower pH, therefore the  $t_m$  of the system peak is greater at pH 3.7 than at 6.2. It was necessary to allow sufficient time for the system peak to elute from the column before injecting the next sample, otherwise the system peak from the previous injection interfered with the electropherogram being recorded.

Good signal-to-noise ratio (SNR) can be obtained for very low amounts of sample injected, as shown in Figure 1. The speed of analysis (under 6 min) and the resolution of  $Ca^{2+}$ ,  $Na^+$ , and  $Mg^{2+}$  are noteworthy in this electropherogram. Ten

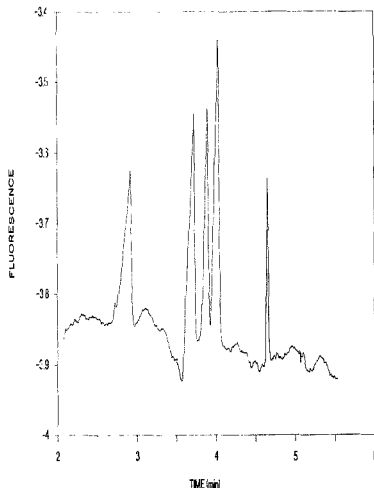


Figure 1. A mixture of alkali and alkaline-earth metal ions separated by CZE-IFD. The sample was injected by electromigration. The conditions and amounts injected are given in Table I. A 21-point Savitsky-Golay smooth was applied to the raw data.

femtomoles or less was injected for each of these ions. It is also worth noting that in ion chromatography, gradient elution is normally required in order to separate these monovalent from divalent ions (14), although isocratic eluant has recently been used (15).

The separation in Figure 1 was also obtained by using the pH 6.2 buffer. A disadvantage of using the higher pH buffer was that positive-going peaks eluted with the analyte peaks. This gave the sample component peaks a derivative shape, which was not reproducible. Large instabilities in the base line also occurred in the region of the electropherogram where the sample peaks were eluting. These made the electropherogram difficult to interpret. These effects were probably due to pH differences between the sample zone and the buffer. pH changes affect the distribution of quinine in the two ionic forms, which have different fluorescence efficiencies.

The sensitivity based on displacement considerations was expected to be greater at pH 6 because then the singly charged quinine cation predominates. At pH 3.7, quinine ion, with  $pK_1 = 5.04$ , is doubly charged (16). Since two sample ions are then needed to displace each quinine ion, the limit of detection (LOD) should be higher. Instead, the sensitivity was roughly equivalent for each of these buffers. The LOD is in the 0.1–0.5 fmol range. This is explained by the fact that the fluorescence of quinine is more intense in a solution with dilute sulfuric acid. A 10-fold increase in the background fluorescence signal was obtained when the capillary was filled with quinine sulfate buffer at pH 3.7 compared to pH 6.2. The increased fluorescence at low pH results in a more stable background signal, even when a lower concentration of quinine is used in the buffer.  $[Q^{2+}]$  and  $[H^+]$  were chosen to be 0.38 and 0.58 mN, respectively, to add to a total of 0.96 mN, the concentration of quinine sulfate used without any added  $H_2SO_4$ .

The operating voltage on the column was 40 kV, the highest that can be used without problems of electrical breakdown. This speeded up the analysis time. Table I lists the migration times for the cations included in Figure 1, along with the effective mobilities ( $\mu_{eff}$ ) calculated from those migration times. It is interesting that the order of elution for  $Na^+$  and  $Mg^{2+}$  is opposite to that which would be predicted from the absolute

**Table I. Migration Times and Effective Mobilities for the Cations Separated in Figure 1<sup>a</sup>**

cation	concn, $\mu\text{N}$	amt injected, fmol	$t_m$ , s	$\mu_{\text{eff}}^a$ , $10^{-5}$ $\text{cm}^2/(\text{V}\cdot\text{s})$	$\mu_{\text{abg}}^b$ , $10^{-5}$ $\text{cm}^2/(\text{V}\cdot\text{s})$
$\text{K}^+$	40	10	173	70.7	76.2
$\text{Ca}^{2+}$	20	4	221	52.1	61.6
$\text{Na}^+$	20	4	233	49.1	51.9
$\text{Mg}^{2+}$	20	4	240	47.0	54.9
$\text{Li}^+$	10	2	279	38.6	40.1

<sup>a</sup> Conditions: The buffer was 0.38 mM quinine sulfate and 0.58 M  $\text{H}_2\text{SO}_4$ , pH 3.7. The column was 18  $\mu\text{m}$  i.d., 82.3 cm overall length, and 70.7 cm from anode to detector. Injection was by electromigration for 1 s at 10 kV. Elution was at 40 kV. The system peak eluted in 18 min, so the flow due to electroosmosis was estimated to be  $13.5 \times 10^{-6}$   $\text{cm}^2/\text{Vs}$ .

**Table II. Migration Times and Effective Mobilities for the Separation Shown in Figure 2<sup>a</sup>**

amine	injected amt, fmol	$t_m$ , s	$\mu_{\text{eff}}^a$ , $10^{-6}$ $\text{cm}^2/(\text{V}\cdot\text{s})$	$\mu_{\text{abg}}^b$ , $10^{-6}$ $\text{cm}^2/(\text{V}\cdot\text{s})$
$\text{NH}_4^+$	7	167	73.5	72.2
dimethyl-	5	227	50.7	53.1
tetramethyl-	5	254	43.9	42.6, 44.9
propyl-	4	273	39.7	37.3, 42.3
diethyl-	4	293	36.1	34.1, 37.9
diethanol-	4	313	33.0	30.6
tetraethyl-	4	320	32.0	30.5, 32.9
THAM	3	341	29.1	26.9, 29.5

<sup>a</sup> The concentration of each amine was 25  $\mu\text{M}$ . The mobilities are compared with values found in the literature (13, 17–20). The conditions for the electropherogram are as given in Table I. <sup>b</sup> In ref 14, more than one value was quoted for several amines.

mobilities ( $\mu_{\text{abg}}$ ) taken from the literature (14). This indicates that some interaction, possibly with the capillary walls, is making the effective mobility of these cations different from their absolute mobility.

The separation of a mixture of several amines is shown in Figure 2. Table II gives the migration times for each of the components and compares their mobilities with the literature. All eight of these amines were also separated when the pH of the buffer was at 5.7. Derivative-shaped peaks, which occurred with the higher pH buffer, were eliminated by using the buffer at pH 3.7. The difference in pH changed the elution order slightly. Tetraethylamine eluted after THAM at pH 5.7. The order of elution of the other amines remained the same.

A pattern of decreasing peak widths with increasing migration time is evident in Figure 2. That is, the peaks eluting around 5–6 min are taller and narrower than those for ammonium or dimethylammonium ion. This pattern also prevails in samples with different component concentrations. This variation in peak widths is observed whether the sample is diluted in water or in buffer or whether gravity flow or electromigration is used to inject the sample.

The asymmetric peak profile is a result of the difference between the electric field in the sample zone and the buffer solution along the rest of the column (21). A theoretical expression to describe the peak profile was derived by Mikkers, Verheggen, and Everaerts (22). They showed that this expression described accurately their trial separations of anions. The parameters which determine the peak profile are the length of the injected zone, the concentration ratio of solute ion to buffer ion, and the mobility of solute ions relative to the buffer ions.

In indirect fluorescence detection, a low buffer ion concentration is used to obtain good sensitivity. As a result, the

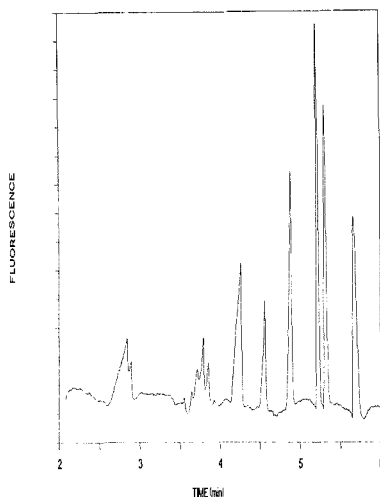


**Figure 2.** An electropherogram of several substituted amines. The conditions are as given in Table I, and the amount injected for each amine is listed in Table II.

ratio of solute ion to buffer ion concentration is greater than the limit necessary for very narrow peaks. Solute ions with effective mobilities close to that of the buffer ions are less affected by this broadening, hence the variation in peak widths in Figures 1 and 2. Despite this limitation, useful analytical results can still be obtained. For example, we have obtained a linear calibration curve (peak area) for phosphate from the detection limit up to a concentration equal to that of the buffer ion, thus spanning a range of 500 (23). The separation efficiency corresponds to 400 000 theoretical plates at the detection limit and 40 000 theoretical plates at the upper concentration.

Apparently, however, the following conclusion of Mikkers et al. is applicable: sample components with mobility greater than the carrier ion migrate with a diffuse leading front, while those solutes having a lower mobility than the carrier ion have sharp leading boundaries and a diffuse trailing boundary. An example of the latter situation is the peak for THAM. A close look at Figure 2 shows that this peak tails to the opposite side than do the earlier eluting peaks. Likewise, in Figure 1, the  $\text{Li}^+$  ion, with lower mobility, also shows a narrower peak. The relationship between the migration time and the peak width is characteristic of the relative mobilities of the sample and the carrier ion, rather than an effect of the solute ion alone. We can conclude that if quinine did not interact with the capillary walls, it would have eluted around 5 min in these electrophoretic runs.

This relationship also has interesting ramifications for the separation of more complicated mixtures, such as those shown in Figures 3 and 4. In Figure 3, the sample is a tryptic digest of  $\beta$ -casein. For comparison purposes, the sample is the same one prepared for another experiment (24). The digest mixture was diluted in the operating buffer one part in ten. A blank digest mixture was also studied. Only two small peaks were obtained for the blank, appearing near 3 and 4 min migration time. In Figure 4, an electropherogram is shown for a similarly prepared digest of bovine serum albumin (BSA). For both electropherograms the injection of the diluted sample was by gravity flow. The height difference between the two ends of the capillary was 13 cm and the duration of the injection was 1 min.

In electromigration injection, there is a well-known bias

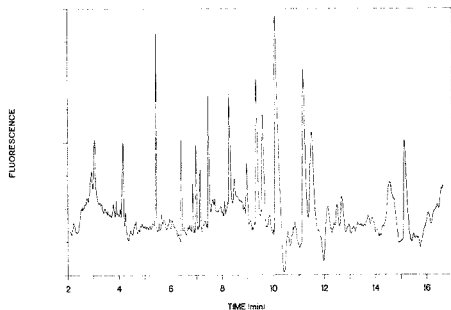


Figure 3. Electropherogram showing the separation of oligopeptides obtained from a tryptic digest of  $\beta$ -casein. The sample was injected by gravity flow for 1 min. Other conditions are as in Table I.

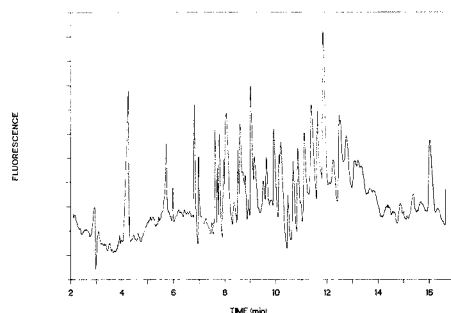


Figure 4. Separation of a tryptic digest of BSA. The conditions and injection are the same as in Figure 3.

favoring ions with high mobility (7). More of the fast-moving ions are injected relative to slow-moving ones during the time while the voltage is applied. The injected amount also depends on sample conductance, which can be a serious problem in dealing with unknown samples. Here, this bias is complicated, however, by the enhancement of the height of peaks with  $t_m$  around 6 min, which was already discussed. The trade-off between these two biases gave an interesting result when the digest samples were injected by gravity flow.

The duration of the gravity injection for the digest samples, 1 min, was much shorter than the 5 min required for gravity injection of alkali-metal cations and amines. For the faster-moving cations, a 5-min gravity injection gave peaks comparable in area to those obtained from 1-s electromigration injection. When electromigration injection was used for the samples of tryptic digest, peaks with  $t_m > 11$  min were not seen. They were attenuated to the base line by the bias against low-mobility ions in the electromigration injection process. Relative to gravity injection, the area of peaks with  $t_m < 11$  min was also inversely proportional to  $t_m$ .

On the other hand, a 5-min gravity injection of the tryptic digest samples gave both peaks that were large compared to 1 s electromigration and peaks that did elute with  $t_m > 11$  min. Decreasing the injection duration to one minute gave a much better separation. The conclusion is that the bias against low mobility ions with electromigration injection becomes significant after  $t_m \approx 6$  min, the migration time where the peak widths are minimized. It also suggests that better resolution could be obtained if shorter injection times by gravity flow were used. Improvements in base-line stability would make shorter injections feasible, because then small peaks would not be lost in the base-line noise.

Digests of proteins are normally separated by high-performance liquid chromatography (HPLC) and the resulting pattern of peaks is used as a "fingerprint" for the identity of the biomolecule. In such an application, replicate separations of a digest must be reproducible. A separate dilution was made of each sample and comparable results were obtained.

A chromatogram (HPLC) of the digest sample was discussed in the previous work (24). It was noted that 16 peptide fragment peaks were obtained for  $\beta$ -casein, and 83 peaks for BSA were obtained by HPLC. The details of the chromatography are given in that report. From Figures 3 and 4 it is apparent that CZE-IFD is approaching the separating power of the HPLC technique, in a time frame considerably shorter than the 2-h run required for that method. Finally, we note that in ref 24, the peptide fragments are separated as anions at pH 10 while here they are separated as cations at pH 3.7. The information is complementary.

## CONCLUSION

Quinine sulfate is a versatile buffer component for separating and detecting cations in CZE-IFD. One set of conditions (ratio of quinine to hydrogen ion in the buffer) was used to separate both small, high-mobility cations and large peptide fragments. With a change in the amount of excess  $H^+$  added, the pH can be adjusted to separate components that coelute at this buffer pH. Since the operating system is in aqueous solution, minimal sample preparation is required and very simple injection techniques can be used. Improved resolution could likely be obtained by using aspiration or positive pressure for injection.

Increasing the proportion of the  $H^+$  in the operating buffer will reduce sensitivity for solutes. A pH less than 3.7 might be desired to separate weaker bases, such as aromatic amines. Weak bases such as aniline did not elute in the operating system used here. Reducing the pH in order to protonate weak bases has the disadvantage of increasing the number of positive charges in the buffer to be displaced by the solute cation. The effect is to increase the LOD for these solutes.

If an application requires the resolution of difficult-to-separate components, then theory indicates that the mobility of the carrier ion and the counterion ( $SO_4^{2-}$  in this case) could be adjusted to enhance resolution. A gain in resolution in one specific part of an electropherogram would necessarily be offset by a reduction elsewhere. For example, if the carrier ion is chosen with lower mobility than quinine sulfate, then the point at which peaks elute symmetrically could be shifted to slower-eluting components. With this method, large peptide fragments such as those that coelute around 12 min, in the electropherogram for BSA in Figure 4, might be better resolved.

## LITERATURE CITED

- (1) Gjerde, D. T.; Fritz, J. S. *Ion Chromatography*; Huthig: New York, 1987.
- (2) Smith, R. E. *Ion Chromatography Applications*; CRC Press, Inc.: Boca Raton, FL, 1988.
- (3) Takeuchi, T.; Murayama, M.; Ishii, D. *Chromatographia* **1988**, *25*, 1072-1074.
- (4) Vack, J.; Muselassova, I. *J. Chromatogr.* **1985**, *320*, 199-203.
- (5) Grossman, P. D.; Colburn, J. C.; Lauer, H. H.; Nielsen, R. G.; Reggin, R. M.; Sittampalam, G. S.; Rickard, E. C. *Anal. Chem.* **1989**, *61*, 1189-1194.
- (6) Jorgenson, J. W.; Lukacs, K. D. *Science* **1983**, *222*, 266-272.
- (7) Huang, X.; Pang, T.; Gordon, M.; Zare, R. *Anal. Chem.* **1987**, *59*, 2747-2749.
- (8) Kuhn, W. G.; Yeung, E. S. *Anal. Chem.* **1988**, *60*, 2642-2646.
- (9) Kuhn, W. G.; Yeung, E. S. *Anal. Chem.* **1988**, *60*, 1832-1834.
- (10) Altria, K. D.; Simpson, C. F. *Chromatographia* **1987**, *24*, 527-532.
- (11) Lukacs, K. D.; Jorgenson, J. W. *HRC CC, J. High Resolut. Chromatogr. Chromatogr. Commun.* **1985**, *8*, 407-411.
- (12) McCormick, R. M. *Anal. Chem.* **1988**, *60*, 2322-2328.
- (13) Pospichal, J.; Gebauer, P.; Bocsek, P. *Chem. Rev.* **1989**, *89*, 419-430.
- (14) Rocklin, R. D.; Rey, M. A.; Stillian, J. R.; Campbell, D. L. *J. Chromatogr. Sci.* **1989**, *27*, 474-479.
- (15) Sato, H. *J. Chromatogr.* **1989**, *469*, 339-349.

- (16) *Handbook of Chemistry and Physics*; Weast, R. C., Ed.; CRC Press, Inc.: Boca Raton, FL, 1985.
- (17) Pospichal, J.; Deml, M.; Zemlova, Z.; Bocek, P. *J. Chromatogr.* **1985**, *320*, 139-146.
- (18) Kenndler, E.; Jenner, P. *J. Chromatogr.* **1987**, *390*, 185-197.
- (19) Kiso, Y.; Hirokawa, T. *Chem. Lett.* **1979**, 891-894.
- (20) Hirokawa, T.; Gojo, T.; Kiso, Y. *J. Chromatogr.* **1986**, *369*, 59-81.
- (21) Mikkers, F. E. P.; Everaerts, F. M.; Verheggen, Th. P. E. M. *J. Chromatogr.* **1979**, *169*, 11-20.
- (22) Mikkers, F. E. P.; Everaerts, F. M.; Verheggen, Th. P. E. M. *J. Chromatogr.* **1979**, *169*, 1-10.
- (23) Gross, L.; Yeung, E. S. *J. Chromatogr.* **1989**, *480*, 169-178.
- (24) Hogan, B.; Yeung, E. S. *J. Chromatogr. Sci.*, in press.

RECEIVED for review September 1, 1989. Accepted December 5, 1989. The Ames Laboratory is operated by Iowa State University for the U.S. Department of Energy under Contract W-7405-Eng-82. This work was supported by the Director of Energy Research, Office of Health and Environmental Research.

# Cluster Analysis Applied to the Selection and Combination of Buffering Electrolyte Systems Used for Capillary Electrophoresis of Anions with Water or Methanol as Solvents<sup>1</sup>

Ernst Kenndler\* and Brigitte Gassner

*Institute for Analytical Chemistry, University of Vienna, Währingerstrasse 38, A-1090 Vienna, Austria*

The use of methanol as a solvent for buffering electrolyte systems used for the electrophoresis in capillaries was examined by cluster analysis. For this general approach, four methanolic electrolyte systems with different pH values were compared with eight aqueous systems. The similarity between these 12 systems was described by the Euclidian distances, calculated from the values of the electrophoretic mobilities of 55 anions. Clusters were constructed by use of a hierarchic algorithm and delineated by dendrograms. On the basis of the structures of the clusters, an appropriate selection is derived for the combination of electrolyte systems. It was found, that at least one methanolic system must be selected for the most favorable combination of three systems. Besides a physicochemical interpretation, the validity of the clusters was empirically proved by comparison with clusters formed by systems characterized by attributes with randomly generated values.

## INTRODUCTION

Organic solvents are used for buffering electrolyte systems in capillary electrophoresis because they often influence the mobilities of the analytes in a direction, which can improve the selectivity in a single system. Furthermore, the combination of aqueous and organic (or mixed) solvents can be used in a multidimensional approach to increase the separability of analytes on the one hand, or to increase the probability of their identification on the other hand. This goal is better reached as the lower electrophoretic properties in the combined systems correlate.

Methanol is an often used organic solvent or solvent constituent in electrophoresis in capillaries, especially in isotachopheresis (1). Besides the effect of the enhanced solubility of organic solutes, the advantage of the application of this solvent as a constituent in mixed aqueous-organic solvents was demonstrated on some examples (2-4). No broader ap-

Table I. Electrolyte Systems for Isotachopheresis of Anions with Water or Methanol as the Solvent<sup>a</sup>

code	solvent	pH of leading electrolyte	counterion
3	H <sub>2</sub> O	3.0	$\beta$ -alanine
4	H <sub>2</sub> O	4.0	$\beta$ -alanine
5	H <sub>2</sub> O	5.0	creatinine
6	H <sub>2</sub> O	6.0	histidine
7	H <sub>2</sub> O	7.0	imidazole
8	H <sub>2</sub> O	8.0	tris(hydroxymethyl)aminomethane
9	H <sub>2</sub> O	9.0	2-amino-2-methyl-1,3-propanediol
10	H <sub>2</sub> O	10.0	ethanolamine
7*	MeOH	7.76	triethanolamine
8*	MeOH	8.06	triethanolamine
9*	MeOH	9.22	tris(hydroxymethyl)aminomethane
10*	MeOH	10.3	cyclohexylamine

<sup>a</sup>Leading ion: in aqueous systems chloride; in methanolic systems perchlorate. The methanol content is above 99.5% (w/w).

proach was given, however, to evaluate the utility of pure methanol in capillary electrophoresis.

Two main methods are proposed in the literature to evaluate the resemblance or the dissimilarity of analytical systems in a general mode: information theory and cluster analysis (5-8). Both methods were applied to isotachopheresis in previous papers (9, 10). In the present paper, cluster analysis is used to characterize and compare electrolyte systems with methanol or water as solvents for the aim of a rational selection of combinations of such systems.

The cluster analysis follows the general scheme (11-13): selection of the taxonomic units (or data units), selection of the variables (or properties, attributes, features), definition of the measure of similarity, construction of the dissimilarity matrix, selection of a clustering procedure for the agglomeration of the units and visualization, e.g. in a dendrogram, and finally the interpretation of the grouping.

According to this scheme eight electrolyte systems with water and four systems with methanol as solvents at different pH values were selected as the taxonomic units. These systems were proposed for the isotachopheresis of anions (14,

<sup>1</sup>This work is dedicated to Professor J. F. K. Huber on the occasion of his 65th birthday.

**Table II. List of Anions Used for the Characterization of the Electrolyte Systems by Cluster Analysis**

acetate	2,3-dibromobutyrate	lactate
acrylate	2,3-dibromopropionate	levulinat
benzoate	dichloroacetate	mandelate
bromate	enanthate	methacrylate
bromide	fluoride	2-naphthalenesul-
bromoacetate	fluoroacetate	fonate
2-bromopropionate	formate	nicotinate
5-bromosalicylate	glucuronate	nitrate
butyrate	glutamate	nitrite
caproate	glycerate	pelargonate
caprylate	glycolate	picrate
chlorate	2-hydroxybutyrate	propionate
chloroacetate	3-hydroxybutyrate	pyrovalate
<i>m</i> -chlorobenzoate	2-hydroxyisobutyrate	salicylate
<i>o</i> -chlorobenzoate	iodate	sorbate
<i>p</i> -chlorobenzoate	iodide	thiocyanate
2-chloropropionate	iodoacetate	trichloroacetate
cinnamate	isovalerate	trifluoroacetate
crotonate		valerate

15). The values of the relative electrophoretic mobilities of 55 anions in each system were chosen as the features for the calculations. Similarity was described by the Euclidian distances between the points, by which the electrolyte systems could be represented in the corresponding (55-dimensional) pattern space. The grouping was finally visualized by a hierarchic clustering method. The interpretation of the grouping found was based on the physicochemical parameters, which influence the effective mobilities of the analytes in the electrolyte systems. The existence of a "real" structure of the data was proved by comparison with systems characterized by features with randomly chosen values.

### EXPERIMENTAL SECTION

The values of the relative mobilities ( $R_E$  values) of 55 anionic compounds, shown in Table I, were used as variables for the cluster analysis of the 12 operational taxonomic units (eight aqueous and four methanolic electrolyte systems, given in Table II). The  $R_E$  values are the ionic mobilities,  $m_i$ , of the analytes,  $i$ , related to the mobility of the leading ion,  $m_L$ :  $R_{E,i} = m_i/m_L$ . They were taken from data published by Hirokawa et al. (14, 15). The data in water were calculated from known absolute mobilities and  $pK_a$  values according to an algorithm described in ref 14. The  $R_E$  values in methanol (purity > 99.5% (w/w)) were measured by isotachopheresis. The  $pK_a$  values were calculated based on these data (15). The leading ions were chloride in aqueous and perchlorate in methanolic buffers.

Only those anions were selected for the present investigation, for which a complete data set, concerning the  $R_E$  and the  $pK_a$  values, was available. For five anions (2,3-dibromobutyrate, 5-bromosalicylate, trifluoroacetate, glutamate, and glucuronate), some of the  $R_E$  values were not given in the literature but could be obtained by extrapolation. In a similar way,  $pK_a$  values not given in refs 14 and 15 could be approximated from data measured in similar solvent systems (2, 16), whereby a data set based on 55 solutes remained.

The clustering procedures were carried out by the statistical package SPSS-X 3.1 (SPSS, Inc., Chicago, IL). The clustering algorithms (average and single linkage) were sequential, agglomerative, hierarchic, and nonoverlapping. The Euclidian distances were calculated from the scaled  $R_E$  values (zero mean, unit variance). The random numbers were generated by using the NAG Fortran Library Mark 12 (Numerical Algorithms Group, Ltd., NAG Central Office, Oxford, U.K.). An IBM 3090/400E-VF was used for the calculations.

### RESULTS AND DISCUSSION

**Comparison of Aqueous Electrolyte Systems Based on Different Numbers of Solutes.** A first step was to clarify whether the actual data units based on the attributes of the 55 anions selected in the pure aqueous solvent can be considered to be representative for the larger data set, consisting

**Table III. Similarity Matrix of the Aqueous Electrolyte Systems Given by the Euclidian Distances<sup>a</sup>**

system	relative Euclidian distance									
	3	4	5	6	7	8	9	10		
3	0.000									
4	0.165	0.000								
5	0.643	0.486	0.000							
6	0.919	0.785	0.321	0.000						
7	0.975	0.846	0.391	0.067	0.000					
8	0.978	0.849	0.396	0.073	0.011	0.000				
9	0.981	0.852	0.400	0.103	0.076	0.069	0.000			
10	1.000	0.872	0.449	0.240	0.231	0.224	0.156	0.000		

<sup>a</sup>The values of the Euclidian distances are related to the largest distance (between the systems 3 and 10). The numbers of the systems correspond with Table I.

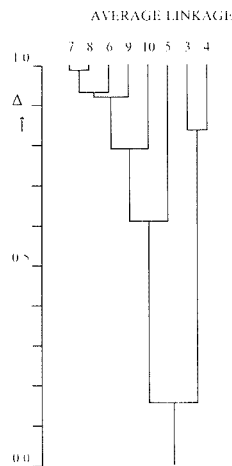


**Figure 1.** Dendrogram as the result of the average linkage algorithm based on the  $R_E$  values of 55 solutes in aqueous electrolyte systems. The symbols of the systems correspond to their pH values, as given in Table I.  $\Delta$  = normalized distance.

of 263 anions, which was investigated in a previous paper (10).

For this comparison the similarity matrix was calculated and is given in Table III. It is based on the Euclidian distances between the points (in a 55-dimensional pattern space), which represent the aqueous buffering systems given in Table II. It can be seen from Table III that systems 3 and 10 show the largest value of 1.000 for the relative distance. This is in agreement with the result previously derived from the larger data set consisting of the values of 263 anions. Accordance is also observed for the sequences of, e.g., the five most similar pairs of systems: the smallest distances are found between (7,8), (6,7), (8,9), (6,8), and (7,9) in the present paper, and between (8,9), (9,10), (7,8), (7,9), and (6,7) in our previous investigation.

The high agreement of the results can also be visualized clearly by comparing the respective dendrograms. The dendrogram based on the data set from 55 anions was calculated with the same average linkage algorithm as the one demonstrated previously and is shown in Figure 1. The  $\Delta$  values in the dendrograms are the Euclidian distances,  $d$ , normalized in the interval [0,1], according to  $\Delta = (d_{\max} - d)/d_{\max}$ ,  $d_{\max}$  being the largest distance.

If this dendrogram is used for the selection of three systems as discussed (10) a grouping into (3,4), (5), and (7,8,6,9,10) is found. This is exactly the same result that was obtained

Table IV. Similarity Matrix of the Aqueous and the Methanolic Electrolyte Systems Given by the Euclidian Distances<sup>a</sup>

system	Euclidian distance											
	3	4	5	6	7	8	9	10	7*	8*	9*	10*
3	0.00											
4	1.06	0.00										
5	4.07	3.12	0.00									
6	5.90	5.04	2.08	0.00								
7	6.26	5.43	2.51	0.43	0.00							
8	6.28	5.45	2.54	0.47	0.07	0.00						
9	6.30	5.47	2.57	0.66	0.49	0.44	0.00					
10	6.42	5.60	2.88	1.54	1.48	1.44	1.00	0.00				
7*	2.19	2.35	4.26	5.82	6.14	6.16	6.18	6.29	0.00			
8*	2.21	2.25	4.07	5.65	5.97	5.99	6.02	6.15	0.54	0.00		
9*	5.06	4.61	3.57	3.79	3.94	3.96	4.12	4.61	4.56	4.34	0.00	
10*	6.09	5.59	4.07	3.70	3.73	3.75	3.91	4.39	5.65	5.43	1.51	0.00

<sup>a</sup>The numbers of the systems correspond with Table I. The methanolic systems are indicated by an asterisk.

when cluster analysis was based on the values from 263 anions.

A small deviation of the results (concerning the sequence within the subcluster containing the systems 6 to 10) is not relevant in practice, because it was found—at least for aqueous systems—that the combination of more than three electrolyte systems out of the properly chosen subclusters does not enhance the identification power of the electrophoretic method significantly (10).

It can be concluded from the results derived that the aqueous electrolyte systems are characterized equivalently by the reduced set of data (obtained from 55 solutes) compared to the larger data set (obtained from 263 solutes).

**Similarity of Electrolyte Systems with Water or Methanol as Solvents.** In order to evaluate the similarities of the electrolyte systems with water or methanol as solvents, again the Euclidian distances (based on the  $R_E$  values) were used as a measure of resemblance. The resulting similarity matrix is given in Table IV. The corresponding dendrograms were calculated with an average linkage and with a single linkage algorithm. They are shown in Figure 2. It can be seen that both dendrograms are well structured; they consist of subclusters with high similarity of the units on the one hand, e.g. with  $\Delta$  values larger than 0.9 for the groups (7,8,6,9) and (7\*,8\*), but also connections of the main subclusters at low  $\Delta$  values (less than 0.2 or 0.5, respectively), on the other hand. Both algorithms connect, however, two different groups on the last level of agglomeration. The average linkage algorithm leads to two main subclusters, both consisting of aqueous as well as methanolic systems: (3,4,7\*,8\*) and (7,8,6,9,10,5,9\*,10\*). From the single linkage algorithm the methanolic systems 9\* and 10\* are found together in one and the other aqueous and methanolic systems in another large subcluster. (It should be mentioned that the single linkage algorithm seems to be the least successful in many cases, compared with other hierarchic clustering algorithms (19).)

If electrolyte systems out of three subclusters were selected in a further step, identical results are obtained with both algorithms: the three subclusters consist of the systems (9\*,10\*), (7\*,8\*,3,4), and (5,6,7,8,9,10). From these results it can be seen that the electrolyte systems with the lowest pH values in both solvents—(3,4) and (7\*,8\*)—behave similar. The aqueous systems with pH values from 5 to 10 are very similar, too, which is in accordance with our previous results. The methanolic systems 9\* and 10\* are forming separate clusters in any case.

If these results are used to select combinations of three electrolyte systems are proposed (10), one system out of each of the three following groups must be chosen: (3,4,7\*,8\*), (9\*,10\*), and (5,6,7,8,9,10). From this result it can be concluded that the application of methanol as solvent of the buffering electrolyte systems leads indeed to an improvement

of the selectivity in the electrophoresis of anions.

It should be mentioned that a variation of the extrapolated  $R_E$  values (see Experimental Section) even by 20% did not influence the structure of the clusters.

**Plausibility of the Results.** The observation of a structure in a set of data by cluster analysis does not imply, per se, that this structure originates by any real relation between the distinct attributes. The resulting structure which is found always has to be critically interpreted based on plausible physicochemical relations.

If this critical sight is applied to the present case, it can be assumed that the most important influence on the changes of the electrophoretic behavior of the analytes is caused by the degree of dissociation. It determines in a very pronounced way the effective mobility,  $m_i^{\text{eff}}$ , which depends on the actual mobility  $m_i$  (the mobility of the fully dissociated species of the analyte,  $i$ , at the given concentration), the pH value of the sample zone, and the  $pK_a$  value of the analyte, given by the relation  $m_i^{\text{eff}} = m_i / (1 + 10^{pK_a - \text{pH}})$ .

It is well-known that organic solvents can influence the dissociation constants of neutral acids of the type HA, often by several orders of magnitude (e.g. ref 2 and the literature cited there). Addition of solvents like methanol, acetonitrile, or dimethyl sulfoxide to water increases the  $pK_a$  values of these acids. In fact, an increase of the  $pK_a$  values of the analytes is found in methanol compared with water, as shown in Figure 3. It can be seen that the  $pK_a$  values in water range from about -3 to +5, whereas the corresponding range in methanol is 3 to 4 pK units higher. The extent of this increase is not identical, considering the particular analytes, but fluctuates within a certain range. This different influence is reflected by the relatively low value of 0.911 for the linear correlation coefficient for the correlation between the  $pK_a$  values in methanol and water, respectively.

The fact that the main part of the analytes have  $pK_a$  values of about 3-5 in water and 6.5-9 in methanol (Figure 3) supports the plausible explanation of the results about the similarities of the electrolyte systems obtained by cluster analysis. The most pronounced variations of the effective mobilities must be expected in buffering systems whose pH values are in the  $pK_a$  region of the main part of the analytes. The systems 3, 4, 7\*, and 8\* are found indeed in the same subcluster. It can be assumed that in pure aqueous electrolyte systems with pH values larger than 5 the variation of the pH value has no relevant influence on the effective mobilities: indeed systems 5 to 10 are found in the same subcluster. In a first view a similar argument should be valid for systems 9\* and 10\*. These systems are not found, however, to be closely related with systems 5 or 6 as expected. A plausible explanation for this deviation can be derived from the different solvation effects of water and methanol on the anions. These

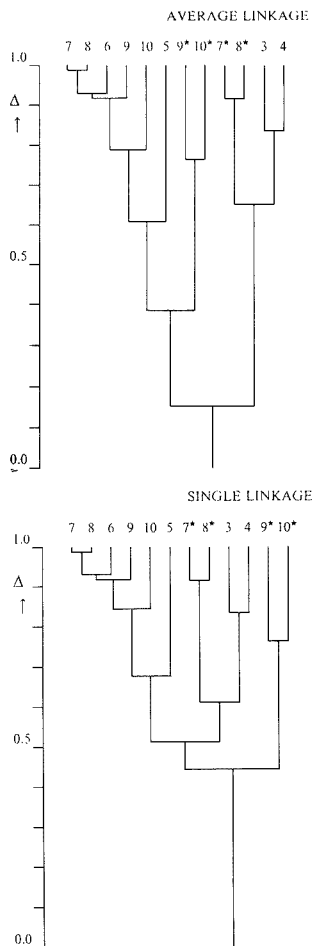


**Figure 2.** Dendrograms as the results of the average linkage and the single linkage algorithm. The calculations were based on the  $R_E$  values of 55 anions in aqueous and methanolic electrolyte systems. The symbols of the systems are according to Table I. The methanolic systems are indicated by asterisks.  $\Delta$  = normalized distance.

different effects can additionally lead to decisive changes of the actual mobilities in both solvents. This assumption is supported by the evaluation of the correlation between the (absolute) mobilities of the (obviously totally dissociated) analytes in water and methanol, respectively (14, 15); a low value of 0.882 is obtained for the linear correlation coefficient. This result reflects that different solvation leads to relevant differences of the electrophoretic properties of the analytes in the buffering systems of higher pH values. Thus, the dissimilarity between the corresponding systems in water and methanol can be plausibly explained.

**Similarity of Systems Characterized by Attributes Based on Random Numbers.** One has to decide from case to case whether the variables of the data units show clustering tendencies that reflect meaningful relations of the systems. The problem of the validity of the structures of clusters is treated in the mathematical literature in several ways (17–22). Nevertheless there is no straightforward algorithm, which delivers a decision criterion on the validation of the resulting

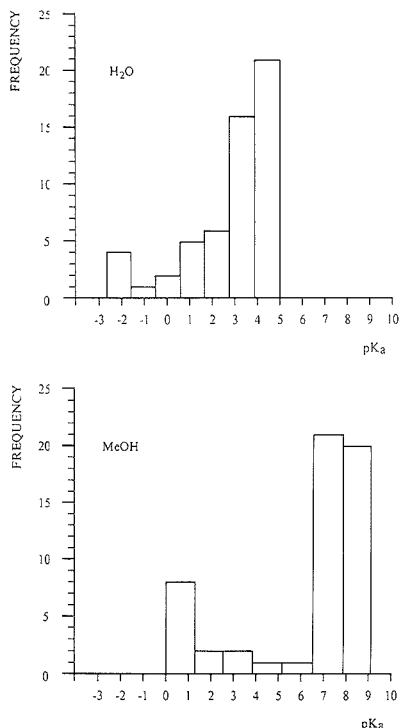


**Figure 3.** Distribution of the  $pK_a$  values of the solutes in water and methanol.

structures of clusters, comparable, e.g., to the criteria for the null hypothesis in statistics. Therefore the problem of the aggregation of entities into clusters was investigated for the case that these entities or units are defined by variables which have randomly chosen values. For this approach the taxonomic units were characterized by a series of random numbers, based on a normal distribution, and a Poisson distribution, respectively. These types of distributions were selected because they often occur in the statistical treatment of analytical chemistry.

Values of 2.58 and 5.0 were taken for the mean and for the standard deviation, respectively, of the normal distribution for the random numbers, since the same values were found taking all relative mobilities into account. For the same reason, the Poisson distribution was characterized by a value of 2.58 for the parameter  $\lambda$ . Both distributions of the random numbers led to nearly identical results. Therefore the discussion is focused to the clusters derived from the Gaussian distribution.

Cluster analysis was applied based on different numbers,  $N$ , of attributes.  $N$  covers the range from  $N = 5$  to  $N = 500$  for each of the 12 units. Small numbers for  $N$  were also considered, because in analytical investigations often only relatively few experimental data are available.

The results of the clustering procedure, based on the average linkage algorithm, are shown in Figure 4, where the units are symbolized in the dendrograms by the letters A to L. One can see very well structured clusters derived from  $N = 5$  variables. Even from  $N = 10$  variables a well-structured cluster is obtained, although random numbers are the source of the interrelation of the data. From 50 variables on, the dendrograms lead to less structured images, where the par-

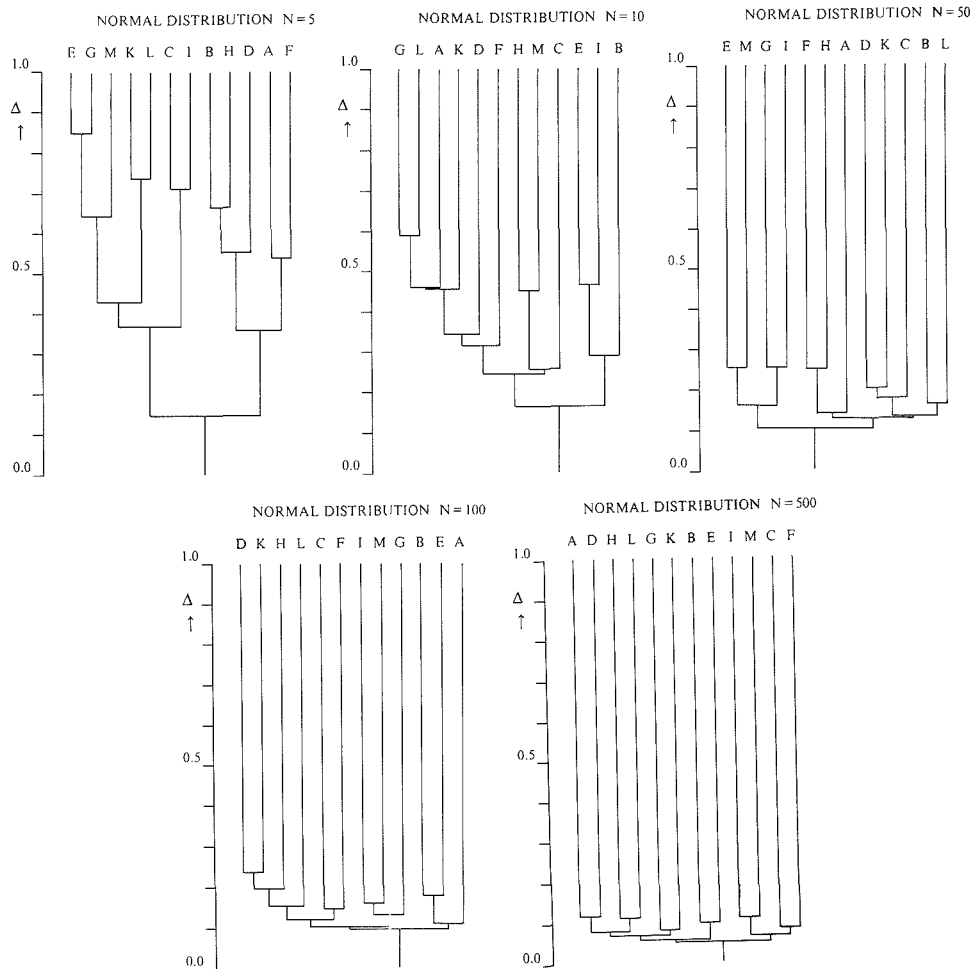


**Figure 4.** Dendrograms illustrating the similarity of taxonomic systems (A to L) characterized by randomly chosen values of the features. The random numbers were generated according to a normal distribution.  $N$  = number of taxonomic attributes per system.  $\Delta$  = normalized distance.

ticular pairs of systems agglomerate at a low level of similarity ( $\Delta$  less than 0.3). This picture is enforced for high numbers of variables where the dendrograms approach the image of the cluster, which is obtained, when the data are in fact totally uncorrelated, and where all systems would be linked together at a  $\Delta$  level of zero.

On comparison of the clusters obtained from  $N = 50$  variables with the randomly chosen values in Figure 4 with that formed by the  $R_B$  values of the electrolyte systems shown in Figure 2, which was derived from a similar number of attributes, two totally different images can be observed. All former units are highly dissimilar (the maximum value for  $\Delta$  is smaller than 0.3). In contrast, the clusters obtained from the electrolyte systems show pairs with high similarities on the one hand—(7,8), (7\*,8\*), etc.—and units aggregating at low values on the other hand. It can therefore be assumed that the similarities between the electrolyte systems, which are elucidated by cluster analysis, are indeed based on their physicochemical properties as discussed above and not by random characters.

Our results show that the structures obtained by clustering

procedures must be interpreted very carefully, because high similarities can originate even from a random character of the attributes, especially when the procedure is based on only few values of the attributes.

#### LITERATURE CITED

- (1) Everaerts, F. M.; Beckers, J. L.; Verheggen, Th. P. E. M. *Isotachopheresis; Theory, Instrumentation and Applications*; Elsevier: Amsterdam, 1976.
- (2) Kenndler, E.; Jenner, P. J. *Chromatogr.* **1987**, *390*, 169.
- (3) Wielders, J. P. M. Thesis, Eindhoven, 1978.
- (4) Koval, M.; Kaniansky, D.; Hutta, M.; Lacko, R. *J. Chromatogr.* **1985**, *325*, 151.
- (5) Massart, D. L.; Dijkstra, A.; Kaufman, L. *Evaluation and Optimization of Laboratory Methods and Analytical Procedures*; Elsevier: Amsterdam, 1978.
- (6) Massart, D. L.; Vandeginste, B. G. M.; Deming, S. N.; Michotte, Y.; Kaufman, L. *Chemometrics: a Textbook*; Elsevier: Amsterdam, 1988.
- (7) Massart, D. L.; De Clercq, H. In *Advances of Chromatography*; Giddings, J. C., Keller, R. A., Eds.; Marcel Dekker: New York, 1978; Vol. 16.
- (8) Kaufman, L.; Massart, D. L. In *Chemometrics, Mathematics and Statistics in Chemistry*; Kowalsky, B. R., Ed.; Reidel: Dordrecht, The Netherlands, 1984.
- (9) Kenndler, E. *Anal. Chim. Acta* **1985**, *173*, 239.
- (10) Kenndler, E.; Reich, G. *Anal. Chem.* **1988**, *60*, 120.

- (11) Sneath, P. H. A.; Sokal, R. R. *Numerical Taxonomy*, Freeman: San Francisco, CA, 1973.
- (12) Anderberg, M. R. *Cluster Analysis for Applications*; Academic Press: New York, 1973.
- (13) Johnson, R. A.; Wichern, D. W. *Applied Multivariate Statistical Analysis*; Prentice-Hall: Englewood Cliffs, NJ, 1982.
- (14) Hirokawa, T.; Nishino, M.; Aoki, N.; Kiso, Y. *J. Chromatogr.* **1983**, *271*, D1.
- (15) Hirokawa, T.; Tsuyoshi, T.; Kiso, Y. *J. Chromatogr.* **1987**, *408*, 27.
- (16) Kenndler, E.; Schwer, Ch.; Jenner, P. *J. Chromatogr.* **1989**, *470*, 57.
- (17) Adamson, G. W.; Bawden, D. *J. Chem. Inf. Comput. Sci.* **1981**, *21*, 204.
- (18) Dubes, R.; Jain, A. K. *Pattern Recognition* **1979**, *11*, 235.
- (19) Panayirci, E.; Dubes, R. *Pattern Recognition* **1983**, *16*, 433.
- (20) Zeng, G.; Dubes, R. C. *Pattern Recognition* **1985**, *18*, 191.
- (21) Willet, P. J. *Chem. Inf. Comput. Sci.* **1985**, *25*, 78.
- (22) Jain, N. C.; Indrayan, A.; Goel, L. R. *Pattern Recognition* **1986**, *19*, 95.

RECEIVED for review August 8, 1989. Accepted November 14, 1989.

## Experimental Verification of Parameters Calculated with the Statistical Model of Overlap from Chromatograms of a Synthetic Multicomponent Mixture

Scott L. Delinger and Joe M. Davis\*

Department of Chemistry and Biochemistry, Southern Illinois University, Carbondale, Illinois 62901

A synthetic mixture of 56 hydrocarbons was prepared and partially resolved by capillary gas chromatography to experimentally test the predictions of the statistical model of overlap. Various statistical parameters characteristic of both the mixture and the chromatographic process, including the expected number of detectable mixture components and the expected numbers of singlet and multiplet chromatographic peaks, were theoretically estimated from several dozen chromatograms of this mixture by using two procedures. These theoretical parameters were then compared to their experimental counterparts, which were known for the synthetic mixture. Excellent agreement between experiment and theory was found at low chromatographic saturations. This agreement affirms earlier predictions based on this model and supports the argument that peak overlap can be addressed in some instances by theoretical means. At higher saturations, systematic departures of experiment from theory were found. In particular, the experimental numbers of singlet and multiplet peaks are smaller and larger, respectively, than those predicted, when the peak capacity is less than roughly twice the number of components.

### INTRODUCTION

A simple statistical theory was developed some years ago (1), in parallel with the work of others (2, 3), to quantify the severity of peak overlap in multicomponent chromatograms. This theory was restricted to the limited but surprisingly common case in which mixture components elute in a random manner from the chromatographic column. The principal conclusion drawn from this theory was that overlap in such chromatograms is surprisingly high and that the number of peaks (especially singlet peaks) is considerably smaller than intuitively expected. A procedure was then suggested by which several statistical parameters characteristic of both the mixture and the chromatographic process could be estimated directly from the chromatogram. These parameters include the expected number of detectable components in the mixture and

the expected numbers of singlet and multiplet peaks in the chromatogram. The validity of this procedure, or slightly modified versions thereof, was verified in several groups by detailed analyses of computer-simulated chromatograms, for which these statistical parameters were known (4-8). These procedures have since been used to estimate these and other statistical parameters from a limited number of experimental gas (6, 9-11) and liquid (8) chromatograms of petroleum, environmental, and natural-product mixtures. Although these parameters were not verified by other types of measurement (and indeed most could not have been), by and large they were consistent with those calculated from computer-simulated chromatograms. The original theory has been reinterpreted (12) and extended by others, particularly by Martin, who has proposed an analogy between the models of peak overlap and polymer degradation (13), developed a theory of peak overlap applicable to chromatograms of both simple and complex mixtures (14), and significantly extended the working range over which statistical parameters can be reliably evaluated from multicomponent chromatograms (15).

Although these studies affirmed that peak overlap is a serious problem in multicomponent chromatograms, our opinion is that the practical implications of this problem are not fully appreciated. One serious implication is that determinations based on the measurement of peak area or height in such chromatograms can often be erroneously high, because one fails to account for the likelihood of overlap. Such errors may have serious consequences in legal issues (11). Similar problems are found in the preparative chromatography of complex mixtures. Unless one deals with simple mixtures, the likelihood of isolating a pure component is vanishingly small, and contamination to some degree is almost inevitable.

One reason that the problem of overlap is not fully appreciated may well be the dearth of experimental evidence directly supporting the predictions of theory. Skeptics can argue that previous studies of overlap in simulated chromatograms are only partially relevant to our understanding of overlap in real-world chromatograms, which behave far less ideally than the simulated ones. They can also point out that the true values of parameters previously estimated by theory from experimental chromatograms were unknown and that theory and experiment could consequently not be compared.

\* Author to whom correspondence should be addressed.

In this paper, we report the first detailed experimental verification of statistical parameters estimated from multicomponent chromatograms by theoretical means. More specifically, we report estimates of several statistical parameters determined from several dozen gas chromatograms of a synthetic mixture of 56 detectable components. These parameters, which include estimates of the expected number of detectable mixture components, the expected numbers of singlet and multiplet chromatographic peaks, and the probability of resolving singlet peaks, were estimated with procedures based on the simplest of theoretical models, the statistical model of overlap (SMO). Because the mixture was prepared and characterized in the laboratory (see below), experimental values of these parameters were known and could be compared directly to theoretical predictions. The excellent agreement confirms the validity of using theoretical models to quantify overlap in multicomponent chromatograms, when well-defined criteria are satisfied. It also affirms the sobering conclusions suggested by previous studies, with respect to the severity of that overlap.

### THEORY

The theory underlying the SMO is well documented (1); only a brief review is given here. In the SMO, the expected number  $p$  of peaks in a multicomponent chromatogram containing  $m$  randomly distributed single-component peaks (SCPs), each of which corresponds to a detectable mixture component, is (1)

$$p = \bar{m}e^{-\bar{m}/n_c} = \bar{m}e^{-\alpha} \quad (1)$$

where  $\bar{m}$ , the expected number of SCPs in the chromatogram, is a statistical approximation to  $m$ ;  $\alpha = \bar{m}/n_c$  is the average component saturation of the chromatogram, and the peak capacity  $n_c$  is

$$n_c = \frac{X}{x_0} = \frac{X}{4\sigma R_s^*} \quad (2)$$

where  $x_0$  is the minimum span required between adjacent SCPs to resolve them by resolution  $R_s^*$ , and  $\sigma$  is the standard deviation of any representative SCP in region  $X$ . Clearly,  $p$  is less than  $\bar{m}$  for all values of  $n_c$ ; some observed peaks are multiplets, because insufficient capacity exists for total resolution.

When specific criteria are satisfied (see below), the number  $\bar{m}$  can be estimated by fitting experimentally determined values of  $p$  and  $n_c$  to eq 1 (16). Alternatively, eq 1 can be linearized, viz.

$$\ln p = \ln \bar{m} - \bar{m}/n_c = \ln \bar{m} - \bar{m}x_0/X \quad (3)$$

and a plot of the experimental data in the form,  $\ln p$  vs  $n_c^{-1}$ , or  $\ln p$  vs  $x_0/X$ , is a line with slope  $-\bar{m}$  and intercept  $\ln \bar{m}$  (1). From such a plot, two independent approximations to  $\bar{m}$  are thus obtained: one from the slope, which is termed  $m_{sl}$ , and the other from the intercept, which is termed  $m_{in}$ . As observed elsewhere (16), these two approximations to  $\bar{m}$  strictly should not be determined independently in this manner. This small procedural error is nevertheless fortuitous, because the two approximations should agree within statistical error, and one can use this agreement (or lack thereof) to evaluate the credibility of the approximations.

Once the approximation to  $\bar{m}$  is so determined, the saturation  $\alpha$  can be calculated from either eq 1 or, if  $n_c$  is known, the definition  $\alpha = \bar{m}/n_c$ . With these approximations to  $\bar{m}$  and  $\alpha$ , the expected numbers of singlet and multiplet peaks in the chromatogram can then be estimated from theory. In particular, the expected numbers  $s$ ,  $d$ , and  $t$  of singlet, doublet, and triplet peaks, respectively, are (1)

$$s = \bar{m}e^{-2\alpha} \quad (4a)$$

$$d = \bar{m}e^{-2\alpha} (1 - e^{-\alpha}) \quad (4b)$$

$$t = \bar{m}e^{-2\alpha} (1 - e^{-\alpha})^2 \quad (4c)$$

With the definition  $\alpha = \bar{m}/n_c$ , one can express eqs 1 and 4 in the alternative dimensionless forms

$$p/n_c = \alpha e^{-\alpha} \quad (5a)$$

$$s/n_c = \alpha e^{-2\alpha} \quad (5b)$$

$$d/n_c = \alpha e^{-2\alpha} (1 - e^{-\alpha}) \quad (5c)$$

$$t/n_c = \alpha e^{-2\alpha} (1 - e^{-\alpha})^2 \quad (5d)$$

These equations express the fractions of the peak capacity utilized in the resolution of peaks, singlet peaks, doublet peaks, and triplet peaks, respectively. These fractions depend on saturation  $\alpha$  only and are surprisingly small; the maximum values of  $p/n_c$  and  $s/n_c$  are about 0.37 and 0.18, respectively (1).

The resolution  $R_s^*$  chosen to resolve adjacent SCPs into separate peaks is somewhat arbitrary and is typically dictated by convenience and experimental limitations. Because the value assigned to  $R_s^*$  determines both  $n_c$  and  $\alpha$ , however, the actual numbers of peaks, singlets, etc., one calculates from the above equations depend on  $R_s^*$ . One useful value of  $R_s^*$ , as determined empirically from analyses of computer-simulated chromatograms, is 0.5. With this assignment, the peak numbers predicted by the above equations can be identified with chromatographic maxima, as long as  $\alpha < 0.5$  or so (4-6, 8). Others have suggested, on both theoretical and empirical grounds, that a more appropriate value of  $R_s^*$  lies between 0.7 and 0.8, when peaks are identified with chromatographic maxima (12, 17). We prefer the assignment,  $R_s^* = 0.5$ , which has proven applicability, because the accuracy of statistical parameters estimated by the SMO with the larger  $R_s^*$  value has not been investigated. All values of  $n_c$  and  $\alpha$  reported in this paper are consequently referenced to  $R_s^* = 0.5$ .

Because the SMO is based on a relatively simple theory of peak overlap, it is not applicable to every multicomponent chromatogram. The basic criteria that must simultaneously be satisfied, if one is to estimate reliable statistical parameters, are discussed in detail elsewhere (6, 7). Here, we simply state them:  $m_{sl}$  must equal  $m_{in}$  within statistical error, the graph of  $\ln p$  vs  $n_c^{-1}$  or  $x_0/X$  must be linear, and  $\alpha$  must be less than 0.5 or so, when  $R_s^* = 0.5$ . Additional criteria may be useful, but these are prerequisite. Unless otherwise noted, the statistical parameters graphed or tabulated in this study were determined from chromatograms that satisfied these criteria.

### EXPERIMENTAL SECTION

**Preparation of Synthetic Mixture.** A synthetic mixture was prepared from 54 C6-C10 alkane and alkene analytical standards (Chem. Service, West Chester, PA), which were dissolved in high-purity tetradecane (Matheson, Coleman, and Bell, Norwood, OH). The identities of these standards are reported in Table I. Tetradecane, which has a much higher boiling point than any standard, was chosen as a solvent to avoid the masking of poorly retained standards by an early eluting solvent peak. (Our initial solvent choice, CS<sub>2</sub>, is supposedly almost transparent to a flame ionization detector (18), but we observed unusually strong responses to our flame, even after purification.) These 54 standards were deliberately selected from a larger set, such that the boiling points of those selected were randomly distributed in temperature ( $r = -0.998$ ; average increment between boiling points, 0.6 °C). This selection was made to increase the likelihood that the standards would elute randomly from the nonpolar capillary chosen for partial resolution of the mixture. In general, nonpolar species elute from nonpolar columns on the basis of boiling point (19).

Prior to the preparation of the mixture, the relative retention times of all standards were measured. Approximately ten small

**Table I. Constituents of 56-Component Test Mixture, Listed in Order of Elution**

component	component
2,2-dimethylbutane	2,3-dimethylhexane
3-methyl-1-pentene	2-methylheptane
2,3-dimethylbutane	3,4-dimethylhexane
1-hexene	4-methylheptane
2-methyl-2-pentene	3-methylheptane
1,1,1-trimethylbutane	2,2,5-trimethylhexane
<i>cis</i> -3-methyl-2-pentene	cyclopentanone
2,2-dimethylpentane	1-octene
2,2,3-trimethylbutane	<i>trans</i> -4-octene
5-methyl-1-hexene	<i>trans</i> -3-octene
cyclohexane	2-octene
<i>trans</i> -2-methyl-3-hexene	ethylbenzene
4-methyl-1-hexene	4-methyloctane
2-methylhexane	3-methyloctane
2,3-dimethylpentane	2-methyl-1-octene
3-methylhexane	1-nonene
2-methyl-1-hexene	<i>trans</i> -4-nonene
1-heptene	<i>trans</i> -3-nonene
2,2,4-trimethylpentane	2-methyl-2-octene
<i>trans</i> -3-heptene	<i>trans</i> -2-nonene
2-methyl-2-hexene	3,6-dimethyloctane
<i>trans</i> -2-heptene	4-methylnonane
<i>cis</i> -2-heptene	2-methylnonane
methylcyclohexane	1-decene
2,5-dimethylhexane	<i>trans</i> -4-decene
2,4-dimethylhexane	<i>trans</i> -5-decene
<i>trans</i> -2-methyl-3-heptene	<i>trans</i> -3-decene
2,3,4-trimethylpentane	<i>trans</i> -2-decene

submixtures were prepared by dissolving six or so different standards in tetradecane (0.1% by volume), and each was chromatographed. Because the resultant chromatograms contained as many maxima as the submixtures contained components, we inferred that these maxima were SCPs, to which relative retention times were assigned. A trial mixture was then prepared by dissolution of the 54 standards in tetradecane (0.1% by volume). This mixture was repetitively chromatographed, until we empirically found separation conditions that appeared to produce a nearly random elution profile. The apparent randomness of this profile was interrupted by two gaps, which were eliminated by the addition of the two compounds, ethylbenzene and cyclopentanone, to the mixture. A chromatogram of this new 56-component mixture was then generated as before. We then compared the retention times of the observed maxima in this chromatogram to the SCP retention times previously determined. (As far as we could tell, the components of the submixtures and trial mixture exhibited the same elution order, although slight changes in absolute retention times were noted.) From this comparison, we determined the experimental numbers of singlet and multiplet peaks in the chromatogram. These numbers were then compared to the values theoretically predicted by eqs 4a-c. The close agreement affirmed that we had, by trial and error, found good conditions for a test of the SMO.

A test mixture was then prepared identically to the trial mixture described above, except that the concentrations assigned to its 56 components were varied exponentially about the mean value, 10  $\mu\text{L}/\text{mL}$  (analyte/solvent), with an exponential random-number generator. This variation was implemented to make the synthetic mixture more closely resemble a "real world" mixture, the chromatograms of which commonly contain peaks that are distributed exponentially or quasi-exponentially in amplitude (3, 6, 8, 20). Each resultant concentration was then increased by the constant amount, 0.1  $\mu\text{L}/\text{mL}$ , to ensure detectability above background noise. Because of this modification, and because the detector response differed for different standards, only an approximate exponential amplitude distribution was obtained in practice.

**Chromatography.** The synthetic mixture was partially resolved on 10- and 30-m segments of a 320- $\mu\text{m}$ -i.d. fused silica capillary, to which was bonded a 1.0- $\mu\text{m}$  film of DB-1 (J and W Scientific, Folsom, CA). The capillary was incorporated into a Shimadzu GC9-AM modular gas chromatograph (Shimadzu Scientific Instruments, Columbia, MD) equipped with a SPL-9

split-splitless injector and a flame ionization detector. Aliquots of 1.0  $\mu\text{L}$  of test mixture were injected with a 10- $\mu\text{L}$  syringe (Hamilton Co., Reno, NV). The chromatographic conditions were as follows: carrier, helium (see below for flow rates); split ratio, 20:1; injector temperature, 275  $^{\circ}\text{C}$ ; detector temperature, 275  $^{\circ}\text{C}$ ; hydrogen flow rate to detector, 35 mL/min; air flow rate to detector, 300 mL/min. Chromatograms and retention times were acquired on a Shimadzu CR-6A Chromatopac data recorder.

The peak capacity, chromatographic saturation, and peak number were changed systematically in different chromatograms by proportionally varying the oven heating rate  $r$  and helium flow rate  $F$ , which maintained throughout the study the random elution profile previously determined (6, 20). The  $r/F$  program for the 30-m capillary was as follows: 25.0 mL at 36  $^{\circ}\text{C}$ ; first ramp, 0.80  $^{\circ}\text{C}/\text{mL}$  to 65  $^{\circ}\text{C}$ ; second ramp, 3.20  $^{\circ}\text{C}/\text{mL}$  to 80  $^{\circ}\text{C}$ ; third ramp, 1.20  $^{\circ}\text{C}/\text{mL}$  to 120  $^{\circ}\text{C}$ ; and fourth ramp, 4.00  $^{\circ}\text{C}/\text{mL}$  to 240  $^{\circ}\text{C}$ . The  $r/F$  program for the 10-m capillary was as follows: 7.89 mL at 30  $^{\circ}\text{C}$ ; first ramp, 1.38  $^{\circ}\text{C}/\text{mL}$  to 45  $^{\circ}\text{C}$ ; second ramp, 2.61  $^{\circ}\text{C}/\text{mL}$  to 100  $^{\circ}\text{C}$ ; third ramp, 5.07  $^{\circ}\text{C}/\text{mL}$  to 150  $^{\circ}\text{C}$ . In both programs, the purpose of the final ramp was to rapidly flush solvent from the capillary. The flow-rate ranges covered by these programs were 1.55-10.00 mL/min for the 30-m capillary and 2.60 to 15.00 mL/min for the 10-m one. (Clearly, the capillaries were operated far from the optimal velocity.) These somewhat complicated  $r/F$  programs were used to overcome slightly systematic elution patterns, which otherwise prevented the attainment of a random elution order.

## PROCEDURES

Several peak numbers must be measured in multicomponent chromatograms, if one is to carry out a regression against eq 3 and calculate statistical parameters. These measurements must be consistent with the somewhat nonintuitive definition of a "peak" (4), as defined by eq 1. Several acceptable methods of peak counting have been reported (4-8); each differs from the others in the value of resolution  $R_s^*$  chosen to resolve adjacent SCPs into separate peaks. Here, we examine two of these methods: one by which several "peak" numbers, and another by which a single peak number, are determined from the same chromatogram. With the former method, sufficient data are acquired from the single chromatogram for purposes of regression. Because the latter method yields only one peak number per chromatogram however, several chromatograms are required for purposes of regression.

**Single-Chromatogram Method.** The details of this method are reported elsewhere (7) and are only briefly reviewed here. In essence, the numbers of spacings between adjacent chromatographic maxima that equal or exceed a set of arbitrarily chosen spacings  $x_0$  are identified with a set of numbers  $p$ . (The arbitrary spacings  $x_0$  effectively define several "peak" capacities in accordance with eq 2; different resolution factors  $R_s^*$  are associated with the different values of  $x_0$ .) These data are then expressed as the ordered pairs  $(x_0/X, \ln p)$ , where  $X$  is the span between the first and last maxima in the chromatogram. For values of  $x_0$  less than  $2\sigma$  or so, the numbers  $p$  are constant; these data are discarded. The remaining ordered pairs are fit to eq 3.

Here, in each chromatogram, the spacings between adjacent maxima were measured as differences between the retention times of adjacent maxima, and span  $X$  was measured as the difference between the retention times of the first and last maxima. The data set  $(x_0/X, \ln p)$  was generated with a computer algorithm written in Applesoft Basic and subsequently fit to eq 3 by procedures previously reported in the Appendix of ref 11. The statistical parameters calculated from these procedures include  $m_{st}$ ,  $m_{tm}$ , a weighted approximation,  $m_{ave}$ , to  $m$  determined from  $m_{el}$  and  $m_{im}$ ,  $s$ ,  $d$ ,  $t$ ,  $\alpha$  (defined by  $R_s^* = 0.5$ ), the expected standard deviations of all these parameters, and a reduced  $\chi^2$ , which is a measure of the goodness of fit of the data set to eq 3.

**Multiple-Chromatogram Method.** The details of this method are also reported elsewhere (4-6, 8). In essence, the

numbers of maxima in a series of chromatograms of different efficiency (i.e., chromatograms with different numbers of theoretical plates) are identified with a set of numbers  $p$ . The peak capacity of each chromatogram in the series is approximated as  $X/2\sigma$  (i.e.,  $R_s^* = 0.5$ ), where  $X$  is the span between the first and last maxima in the chromatogram and  $\sigma$  is the representative standard deviation of SCPs in the chromatogram. The ordered pairs ( $2\sigma/X, \ln p$ ) so determined are then fit to eq 3.

Because multicomponent chromatograms contain peaks that are not necessarily SCPs,  $\sigma$  cannot generally be determined directly from them. Here,  $\sigma$  was estimated by an adaptation of a previously suggested method (1), i.e., by chromatographing one of the simple submixtures described above under conditions identical with that for the test mixture, calculating the standard deviations of the SCPs in the resultant chromatogram, and computing  $\sigma$  from these standard deviations. Because these SCPs are more or less uniformly distributed over span  $X$ , the  $\sigma$  calculated from them is fairly representative of the entire chromatogram. For reasons that will be apparent later, several approaches were used to estimate  $\sigma$  from these standard deviations. In the first approach, we assumed that each of the SCPs in the simple chromatogram was Gaussian and calculated the standard deviation of each from well-known formulas. In the second approach, which precluded any assumptions about peak shape, the SCPs were digitized with a True Grid 1011 Digitizer (Houston Instruments, Austin, TX), second moments were calculated from these digitized representations, and standard deviations were then calculated from these second moments. In both approaches,  $\sigma$  was calculated from these standard deviations both as a simple arithmetic average and as an integrated average. The arithmetic average was straightforwardly calculated as the sum of the standard deviations, divided by the number of standard deviations. In contrast, the integrated average was calculated by plotting the standard deviations as a function of retention time and then determining by numerical integration the average value of the cubic-spline function that fit these data. The arithmetic and integrated averages differed, because the standard deviations of the SCPs varied substantially with retention time (see below). Finally, because visual inspection of the chromatograms suggested that the test mixture and the submixtures produced SCPs with slightly different widths, perhaps due to differences in concentration, we also calculated the standard deviations of known SCPs in chromatograms of the 56-component test mixture. For purposes of this calculation, we assumed that the SCPs were Gaussian. (As observed above, one cannot in general do this, because the SCPs in chromatograms of real-world multicomponent mixtures are typically not known.) Quantity  $\sigma$  was then estimated from these standard deviations as both arithmetic and integrated averages. In all cases, the ordered pairs ( $X/2\sigma, \ln p$ ) were fit to eq 3 by the procedures detailed in the Appendix of ref 11.

**Computer Simulations.** A computer program similar to ones previously described (4-8) was written to compute the amplitude envelope formed from randomly spaced Gaussian SCPs, whose amplitudes were exponentially distributed. With this program, we simulated chromatograms containing 56 SCPs for different values of saturation  $\alpha$ . From these chromatograms, statistical parameters were calculated as detailed above and compared to experiment. The program was written in FORTRAN and executed on the IBM 3081-GX computer at Southern Illinois University.

## RESULTS AND DISCUSSION

Figure 1 is a plot of the dimensionless ratios,  $p/n_c$ ,  $s/n_c$ , and  $d/n_c$ , vs saturation  $\alpha$  (defined by  $R_s^* = 0.5$ ), as determined by the single-chromatogram method. All of these ratios are

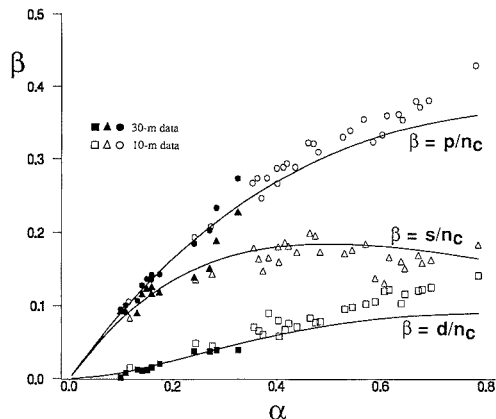


**Figure 1.** Dimensionless plot of the ratios,  $p/n_c$ ,  $s/n_c$ , and  $d/n_c$  vs  $\alpha$  ( $R_s^* = 0.5$ ). All ratios are represented by the generalized ordinate  $\beta$ . Solid curves are graphs of eqs 5a-c; symbols represent experimental results determined by the single-chromatogram method.

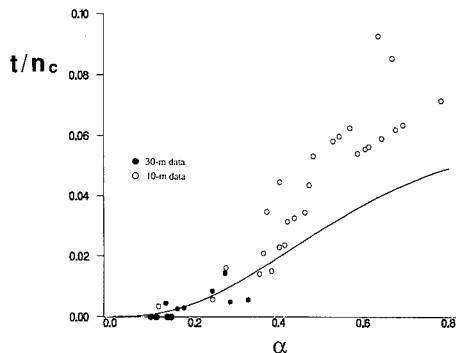


**Figure 2.** Dimensionless plot of  $t/n_c$  vs  $\alpha$  ( $R_s^* = 0.5$ ). Solid curve is a graph of eq 5d; symbols represent experimental results determined by the single-chromatogram method.

represented by the generalized ordinate  $\beta$ , whose appropriate value (e.g.,  $\beta = p/n_c$ ) is assigned to each curve in the figure. Figure 2 is a similar plot of  $t/n_c$  vs  $\alpha$ , as determined by the single-chromatogram method. The solid curves in both figures are graphs of eqs 5a-d, whereas the symbols represent experimental results. (Two symbols in the graphs,  $d/n_c$  vs  $\alpha$  and  $t/n_c$  vs  $\alpha$ , superimpose on one another; hence, these graphs appear to contain one less datum than the others.) The abscissas  $\alpha$  corresponding to the experimental results were calculated from eq 1 as  $-\ln(p_m/m_{ave})$ , where  $p_m$  is the number of maxima in the chromatogram and  $m_{ave}$  is the weighted approximation to  $m$  determined from that chromatogram.

The ordinates of the experimental results depend on both the numbers of peaks, singlets, etc., which were evaluated by direct inspection of chromatograms, and the peak capacities  $n_c$ . Because the original, if shortsighted, objective of this study was to verify statistical parameters as calculated by the single-chromatogram method only, the peak capacities of many of these chromatograms were not measured. (One does not need to know the peak capacity to use the single-chromatogram method.) To express the experimental results in these plots,  $n_c$  was indirectly calculated as  $56/\alpha = -56/[\ln(p_m/m_{ave})]$ . For a value of  $n_c$  so calculated, exact agreement be-

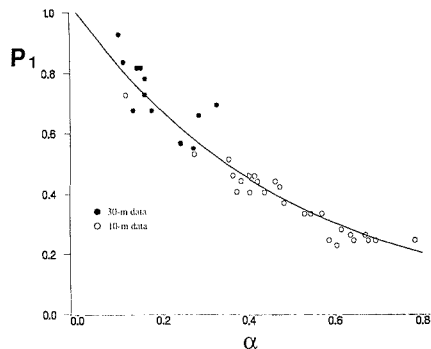


**Figure 3.** Dimensionless plot of the stand-alone probability  $P_1$  vs  $\alpha$  ( $R_s^* = 0.5$ ). Solid curve is defined by eq 4a; symbols represent experimental results determined by the single-chromatogram method.

tween experiment and theory is expected only if  $\bar{m} = m_{ave} = 56$  and the expected number  $p$  of peaks predicted by eq 1 equals  $p_m$ , the number of chromatographic maxima. Inspection of Figure 1 clearly shows that the  $p/n_c$  ratios so calculated agree well with theoretical predictions, when  $\alpha$  is less than or equal to about 0.4, and are greater than predicted by theory, when  $\alpha > 0.4$ . This upper limit to the saturation is perhaps not surprising, because previous analyses of simulated chromatograms suggested that reliable approximations to  $m$  could not be calculated, unless the criterion  $\alpha < 0.5$  was satisfied (6, 7). One conclusion that can consequently be drawn from these experimental results is that this criterion is basically correct. On the other hand, the largest  $p/n_c$  values shown depart from theory, because the number of maxima in multicomponent chromatograms is simply larger than that predicted by eq 1, when  $\alpha > 0.5$  or so (6).

Most previous determinations of statistical parameters by the SMO have been restricted to approximations to  $m$ . Figures 1 and 2 report the first extensive experimental measurements of the ratios  $s/n_c$ ,  $d/n_c$ , and  $t/n_c$  as functions of  $\alpha$ . These ratios, which were determined by the single-chromatogram method, were evaluated analogously to values of  $p/n_c$ , i.e., singlet and multiplet numbers were determined by visual inspection of chromatograms and  $n_c$ 's were calculated as  $-56/[\ln(p_m/m_{ave})]$ . The ratios clearly agree with theoretical predictions at low saturations, but departures are evident with increasing  $\alpha$ . In general, values of  $s/n_c$  are somewhat less than those predicted by theory, and values of  $d/n_c$  and (especially)  $t/n_c$  are greater than those predicted by theory, when  $\alpha > 0.4$ . All three departures are consistent with the merger of singlet peaks into multiplet peaks. These findings suggest a rather sobering conclusion: one's ability to resolve singlet peaks at high saturations is even worse than suggested by theory. This conclusion is elaborated further below.

To affirm that these results were truly representative, and not perhaps some artifact of our treatment of the data, simulated chromatograms containing 56 SCPs were synthesized with the computer program described above. The span  $X$  and standard deviations of SCPs in these simulated chromatograms were equated to values measured from the experimental chromatograms they were supposed to mimic. Values of  $\alpha$  and  $n_c$  were evaluated as described above, and the various ratios (e.g.,  $p/n_c$ ) were then calculated and graphed as shown in Figures 1 and 2. Although these figures did not exactly duplicate Figures 1 and 2 (it would be surprising if they did), the same trends were observed: all ratios agreed well with theory at low saturations, but values of  $p/n_c$ ,  $d/n_c$ , and  $t/n_c$  were greater than, and values of  $s/n_c$  were less than, those expected at higher saturations. The experimental data,

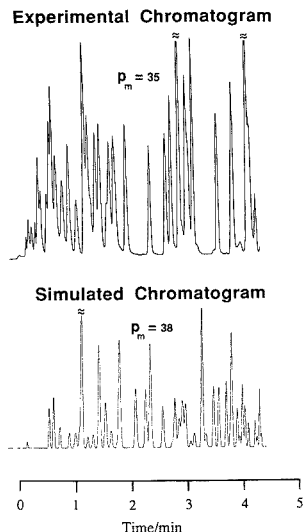


**Figure 4.** Experimental chromatogram (top) of synthetic mixture and simulated chromatogram (bottom) constructed from it. Simulation parameters:  $m = 56$ ,  $\sigma = 1.0$  s,  $X = 4.26$  min, and  $\alpha = 0.439$  ( $R_s^* = 0.5$ ). Parameter  $X$  was measured from the experimental chromatogram; parameters  $\alpha$  and  $\sigma = \alpha X/(2m)$  were estimated by the single-chromatogram method. Numbers  $p_m$  of maxima are indicated.

therefore, are probably representative.

The discouraging finding that singlet peaks are even less abundant than suggested by theory at high saturation is emphasized in Figure 3, which is a plot of the stand-alone probability  $P_1 = s/\bar{m}$  vs  $\alpha$ , as determined by the single-chromatogram method. As defined elsewhere (1),  $P_1$  is the probability that any component appears as a singlet peak. The solid curve is a graph of the theoretical value of  $P_1$ , which is defined by eq 4a. The experimental results in the figure were evaluated as ratios of the numbers of singlet peaks deduced from visual inspection of chromatograms to the number (56) of detectable mixture components. These ratios are more or less randomly scattered about theory at low saturations but are systematically slightly smaller than theory at higher saturations. Consequently, extremely efficient chromatography must be implemented, if one is to resolve components into pure peaks at even modest saturations.

The elusive nature of overlap in multicomponent chromatograms is illustrated in Figure 4, which depicts a typical experimental chromatogram of the test mixture in the upper half of the figure and the computer-simulated chromatogram constructed from it in the lower half. (The statistical parameters prerequisite to this construction were determined by the single-chromatogram method and are reported in the figure caption.) A similar figure has been reported elsewhere (9), for a case in which  $m$  is unknown. Here,  $m$  is known, and a more forceful comparison of the two chromatograms can be made. Both chromatograms contain the same number (56) of SCPs, and each appears, if one allows for slight differences in amplitude, to be a general continuation of the other (9). The numbers of maxima in the simulated (38) and experimental (35) chromatograms closely agree with the theoretically expected number which, to the nearest integer, is 36. Over 32% of the SCPs in both chromatograms are not visually detectable, even though the separation efficiency appears to be quite high and a fair number of base-line-resolved peaks appear to exist. Little, if any, evidence of severe overlap can

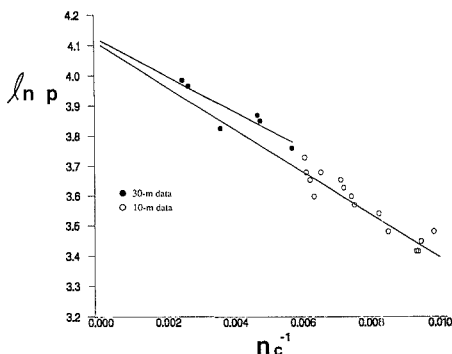


**Figure 5.** Plot of  $\ln p$  vs  $n_c^{-1}$ . Solid lines are least-squares fits of eq 3 to two data sets developed by the multiple-chromatogram method. Each value of  $\sigma$  was calculated as the integrated average of the standard deviations of eight Gaussian SCPs. Approximations to  $m$  are reported in Table II.

be deduced from mere inspection of the chromatograms. The old saw, "One picture is worth a thousand words", is perhaps appropriate here. Few written descriptions could better convey the reality of overlap in multicomponent chromatograms.

Figure 5 is a plot of  $\ln p$  vs  $n_c^{-1}$ , as determined by the multiple-chromatogram method. For reasons discussed below, the data sets developed from the 30-m capillary, and from the 10-m one, were fit separately to eq 3. For each datum in the figure,  $\sigma$  was calculated as an integrated average of the standard deviations of eight (presumably Gaussian) SCPs. As previously observed, these standard deviations were obtained by chromatographing a simple submixture under conditions identical with that for the test mixture. The weighted approximations to  $m$  so calculated are fairly good, if one allows for statistical error. To the nearest whole number,  $m_{ave} = 61 \pm 10$  and  $62 \pm 9$ , as determined from the 30-m and 10-m data sets, respectively. The actual value of  $m$ , 56, lies well within one standard deviation of these predictions, and the absolute errors in the predictions are only about 10% or so.

These approximations to  $m$  are, in fact, among the best of several ones calculated from the peak numbers depicted in Figure 5 and from various approximations to  $\sigma$ , whose values varied somewhat with the means of approximation. Our consideration of these different means was initially motivated by the anomalously high value of  $m_{al}$  ( $91 \pm 14$ ) which was determined by fitting all the peak numbers in Figure 5 to eq 3. In this case,  $\sigma$  was calculated as a simple arithmetic average of the standard deviations of eight (presumably Gaussian) SCPs. Because  $m_{in}$  ( $64 \pm 5$ ) was a much better approximation to  $m$  than  $m_{al}$ , we considered the possible existence of a determinate proportional error in the product,  $4\sigma R_s^*$ , which affects the values of the abscissas,  $n_c^{-1}$ . As shown in basic texts on regression, such an error affects the calculated value of the slope but not the intercept (21). The possibility of this kind of error is not fanciful speculation; it was found in previous studies of the SMO, which demonstrated that the appropriate values of  $R_s^*$  for chromatograms containing either extensive noise or severely tailing SCPs differ considerably from 0.5 (4, 5). Here, because peak shapes are nearly Gaussian and signal to noise is high (see Figure 4), we saw no reason to suspect the assignment,  $R_s^* = 0.5$ . Rather, we suspected that the proportional error, if it indeed existed, originated in the determination of  $\sigma$ .

The most probable origin of this error is the large variation of the standard deviations of the SCPs in chromatograms of the test mixture and submixtures. This variation, which can

**Table II.** Values of  $m_{al}$ ,  $m_{in}$ , and  $m_{ave}$  Calculated from Equation 3 and the Multiple-Chromatogram Method<sup>a</sup>

data set	method of $\sigma$ averaging	$m_{al}$	$m_{in}$	$m_{ave}$
pooled <sup>b</sup>	arithmetic	$91 \pm 14$	$64 \pm 5$	$67 \pm 5$
pooled	integrated	$79 \pm 11$	$65 \pm 5$	$68 \pm 4$
30-m	arithmetic	$66 \pm 45$	$60 \pm 9$	$60 \pm 9$
30-m	integrated	$59 \pm 39$	$61 \pm 10$	$61 \pm 10$
10-m	arithmetic	$80 \pm 31$	$59 \pm 12$	$62 \pm 12$
10-m	integrated	$71 \pm 20$	$60 \pm 10$	$62 \pm 9$

<sup>a</sup> Results are reported to the nearest whole number.  $m = 56$ .  
<sup>b</sup> Combination of 10- and 30-m data sets.

be inferred from close inspection of the experimental chromatogram in Figure 4, is quite substantial and is probably caused by varying the  $r/F$  ratio throughout the chromatogram (19). In particular, peak widths are much smaller in the beginning of the chromatogram than elsewhere. This kind of error is also consistent with our finding that good statistical parameters can be determined from these same chromatograms, when we use the single-chromatogram method. Unlike the single-chromatogram method, the multiple-chromatogram method, at least as initially developed, will not give reliable statistical parameters from chromatograms containing SCPs of nonuniform width (1).

In an attempt to overcome, or at least to alleviate, this restriction, several means were used to estimate  $\sigma$ , from which several approximations to  $m$  were then calculated. Table II reports the approximations  $m_{al}$ ,  $m_{in}$ , and  $m_{ave}$  determined by estimating  $\sigma$  as both arithmetic and integrated averages and by grouping the peak numbers depicted in Figure 5 into three subsets: numbers developed from the 10-m capillary, from the 30-m capillary, and from both. Because the weighting factors in the computation of  $m_{ave}$  from  $m_{al}$  and  $m_{in}$  are the reciprocal variances of  $m_{al}$  and  $m_{in}$  (11),  $m_{ave}$  is closer to  $m_{in}$  than to  $m_{al}$ , which is less precise. Inspection of this table shows several trends, which are enumerated here:

(1) Values of  $m_{al}$  vary more and are generally larger than values of  $m_{in}$ , which are nearly constant and only slightly greater than the true value,  $m = 56$ . The precisions of the  $m_{al}$ 's (as gauged by standard deviations) are considerably poorer than those of the  $m_{in}$ 's.

(2) For both the arithmetic and integrated means of determining  $\sigma$ , the weighted estimate  $m_{ave}$  lies within one standard deviation of the true value, when the 10- and 30-m data sets are fit separately to eq 3. In contrast, the estimate  $m_{ave}$  lies beyond two standard deviations of the true value, when the 10- and 30-m data sets are pooled prior to the regression.

(3) For both the arithmetic and integrated means of determining  $\sigma$ , the estimates' precisions are superior when they are calculated from the pooled sets of data, instead of individual ones.

The poor precision of the  $m_{al}$  values calculated from the 10- and 30-m data sets can simply be attributed to the scatter of the data in Figure 5. In other words, one of the basic prerequisites to the calculation of reliable statistical parameters—the linearity of the plot of  $\ln p$  vs  $n_c^{-1}$ —is clearly not satisfied by these data. Therefore, good calculations cannot be expected. In fact, the precision is so poor that we cannot tell if any statistically significant improvement in  $m_{al}$  is attained by calculating  $\sigma$  as an integrated, instead of an arithmetic, average of SCP widths. On the other hand, the scatter of the data has less effect on the precision of the  $m_{in}$  values, because the abscissas  $n_c^{-1}$  are only slightly greater than zero, and the intercept of eq 3 consequently varies little as the slope is changed. Finally, the  $m_{al}$  values determined by pooling the 10-m and 30-m data sets together are more precise

than those computed from the individual data sets, because the 10-m data set "pushes" the value of  $m_{sl}$  up while the 30-m data set "pulls" it down (see Figure 5). These two effects reduce the range of "good" possible values for  $m_{sl}$  (i.e., narrow the minimum in the  $\chi^2$  space), such that little uncertainty exists in the slope. This relatively high precision of  $m_{sl}$  is responsible for the erroneously large value assigned to the weighted average  $m_{ave}$  when the data sets are pooled.

The possibility exists that the above interpretation of the origin of error in  $m_{sl}$  is incorrect and that, as suggested by others (12, 17), the value assigned to  $R_s^*$  should simply be 0.75 or so, instead of 0.5. As shown in basic texts on regression (21), this assignment would lower  $m_{sl}$  (without affecting  $m_{in}$ ) by the amount,  $0.5/0.75 = 0.67$ , and would considerably improve the  $m_{sl}$ 's determined from the pooled and the 10-m data sets. This assignment would also, however, reduce the  $m_{sl}$ 's determined from the 30-m data set to unacceptably low values. Because reasonable fittings of experimental maxima numbers to eq 3 have been reported, when  $R_s^*$  was assigned the value 0.5 or so and SCP widths were uniform (6, 8), we prefer to attribute the departures outlined above to the variation of SCP widths in the chromatograms, rather than to the value assigned to  $R_s^*$ .

It is tempting to argue that the 10-m and 30-m data sets represent different statistical distributions, because the accuracy of  $m_{sl}$  values determined from the latter appears to be better than from the former. The poor precision of the estimates, however, considerably weakens such an argument. In addition, the  $m_{ave}$ 's computed from both data sets lie within one standard deviation of the true  $m$  value, regardless of the method by which  $\sigma$  was estimated. Furthermore, as observed earlier, the experimental numbers of peaks, singlets, etc., in the chromatograms comprising these sets agree well with theoretical predictions, when the single-chromatogram method is used. It is unlikely that this agreement would be found if the two data sets represented different distributions.

Inspection of the  $m_{in}$  values in Table II, which all nearly equal 60, does suggest that some kind of determinate proportional error exists in the numerical values assigned to  $n_c^{-1}$ . The coefficient of variation for the six  $m_{in}$ 's is only 4.0, which is much lower than that (15.3) for the  $m_{sl}$ 's. It is difficult to rationalize this finding by other explanations. If this interpretation is correct, then this proportional error is indeed the principal origin of the poor accuracy of the  $m_{sl}$ 's. This observation supports an earlier assertion that, in the most general of cases,  $m_{in}$  may be a superior approximation to  $m$  than is  $m_{sl}$  (5), when the multiple-chromatogram method is used.

A detailed discussion of these shortcomings is necessary to point out certain limitations of the multiple-chromatogram method, as determined by this study. One should not, however, lose sight of the fact that the  $m_{ave}$ 's reported in Table II are correct to within 20% or so and are superior to most of the approximations to  $m$  one could make by simply counting maxima in the chromatograms from which they were calculated (7).

Several other means for estimating  $\sigma$  were superficially investigated, in attempts to improve the above estimates. Among these were the calculation of Gaussian SCP standard deviations from a 16-component submixture and from the 56-component test mixture and the rigorous computation of second moments from digitized representations of SCPs. By and large, the  $\sigma$ 's so calculated differed little from those determined by other means. In general, our best results appear to be obtained by calculating  $\sigma$  as an integrated, instead of arithmetic, average of SCP widths. This finding may not be significant, however, in light of the estimates' imprecision.

The standard deviations of  $m_{sl}$  (and, to a less extent,  $m_{in}$ ) reported in Table II differ markedly from those determined by the single-chromatogram method, which typically were only  $\pm 3$ -5 for this test mixture. This method produces superior precisions, simply because it produces highly linear graphs, as shown elsewhere (7, 9-11).

## CONCLUSIONS

This work affirms that accurate statistical parameters can indeed be estimated from experimental chromatograms with the statistical model of overlap and either the single- or multiple-chromatogram method, when basic criteria are satisfied. In terms of simplicity, speed, insensitivity to SCP widths, and graph linearity, our experiences suggest that the former method is preferable to the latter in most cases. This is especially true when complex temperature or solvent gradients must be used to force components into a random elution pattern, because peak widths will vary. The accuracy of these parameters, as determined by either method, should be interpreted as warning signals to the almost ubiquitous problem of overlap in multicomponent chromatograms.

Because predictions of this kind are indeed valid in certain cases, it is perhaps appropriate in closing to consider the place of theoretical overlap models among the many experimental means by which overlap can also be addressed. When it is feasible, the avoidance of overlap is clearly the optimal solution to the problem of overlap. Simple mixtures of fewer than 20 components can commonly be resolved totally through careful optimization. This approach fails with more complex mixtures, however, and one must then resort to ancillary experimental or theoretical means to deal with the problem. One powerful experimental means of detecting overlap is the augmentation of hyphenated analytical methods by chemometrics. These means have deservedly received much attention in recent years and are perhaps the best presently available, especially if one is concerned with detecting overlap in only a few peaks. For cases in which determination and quantitation are more important than actual separation, these means can sometimes entirely circumvent the overlap problem.

The experimental and theoretical means at our disposal for addressing overlap are in fact more complementary than competitive. The experimental means are always applicable (provided that appropriate signals can be generated), can usually provide a definitive answer to the question of overlap, and can target specific analytes. To their detriment, their application requires a substantial initial investment in sophisticated instrumentation. In contrast, theoretical means are applicable only in specific cases, can provide only a probabilistic answer to the question of overlap, and cannot target specific analytes. In their favor, their application costs virtually nothing in money, provided one has a microcomputer to carry out the regression. Some time (e.g., one day) may be required, however, to determine empirically the separation conditions necessary to achieve a random elution order.

In general, experimental means are more robust than the theoretical ones and should be used when possible. The principal niche of theory is 2-fold. The first is the development of a general awareness among us that overlap in multicomponent chromatograms is ubiquitous, serious, and basically unavoidable. The second is the quantitative gauging of overlap in cases where experimental means are not available or are impractical. For example, if one desired to assess the entirety of a multicomponent chromatogram for overlap, a chemometric analysis of each of the 50-100 peaks in it would probably require prohibitively large amounts of computer time. In addition, chemometric methods are not accessible to all, at least for the present, and chromatography in a single dimension remains a method of choice in many laboratories. In such cases, experimental means are simply inapplicable,

and one must rely on the less specific but still powerful predictions of theory.

### LITERATURE CITED

- (1) Davis, J. M.; Giddings, J. C. *Anal. Chem.* **1983**, *55*, 418.
- (2) Rosenthal, D. *Anal. Chem.* **1982**, *54*, 63.
- (3) Nagels, L. J.; Creten, W. L.; Vanpeperstraete, P. M. *Anal. Chem.* **1983**, *55*, 216.
- (4) Giddings, J. C.; Davis, J. M.; Schure, M. R. In *Ultrahigh Resolution Chromatography*; Ahuja, S., Ed.; ACS Symposium Series 250; American Chemical Society: Washington, DC, 1984; p 9.
- (5) Davis, J. M.; Giddings, J. C. *J. Chromatogr.* **1984**, *285*, 277.
- (6) Herman, D. P.; Gonnard, M. F.; Guiochon, G. *Anal. Chem.* **1984**, *56*, 995.
- (7) Davis, J. M.; Giddings, J. C. *Anal. Chem.* **1985**, *57*, 2168.
- (8) Dondi, F.; Kahie, Y. D.; Lodi, G.; Remelli, M.; Reschiglian, P.; and Bighi, C. *Anal. Chim. Acta* **1988**, *191*, 261.
- (9) Davis, J. M.; Giddings, J. C. *Anal. Chem.* **1985**, *57*, 2178.
- (10) Coppi, S.; Betti, A.; Dondi, F. *Anal. Chim. Acta* **1988**, *212*, 165.
- (11) Davis, J. M. *J. Chromatogr.* **1988**, *449*, 41.
- (12) Creten, W. L.; Nagels, L. J. *Anal. Chem.* **1987**, *59*, 822.
- (13) Martin, M.; Guiochon, G. *Anal. Chem.* **1985**, *57*, 289.
- (14) Martin, M.; Herman, D. P.; Guiochon, G. *Anal. Chem.* **1986**, *58*, 2200.
- (15) Martin, M. 17th International Symposium on Chromatography, Vienna (Austria), September 25-30, 1988.
- (16) Davis, J. M., Ph.D. Thesis, University of Utah, Salt Lake City, UT, 1985.
- (17) El Fallah, M. Z.; Martin, M. *Chromatographia* **1987**, *24*, 115.
- (18) Walker, B. L. *J. Gas Chromatogr.* **1966**, *4*, 384.
- (19) Harris, W. E.; Habgood, H. W. *Programmed Temperature Gas Chromatography*; John Wiley & Sons, Inc.: New York, 1966.
- (20) Nagels, L. J.; Creten, W. L. *Anal. Chem.* **1985**, *57*, 2706.
- (21) Bevington, P. R. *Data Reduction and Error Analysis for the Physical Sciences*; McGraw-Hill: New York, 1969.

RECEIVED for review September 12, 1989. Accepted December 1, 1989. The authors thank the Office of Research Development and Administration at Southern Illinois University for support of this research. This work was presented at the 1989 Pittsburgh Conference and Exposition on Analytical Chemistry and Applied Spectroscopy, Atlanta, GA, March 6-10, 1989; No. 1585.

## Use of an On-Column Frit in Capillary Zone Electrophoresis: Sample Collection

Xiaohua Huang and Richard N. Zare\*

Department of Chemistry, Stanford University, Stanford, California 94305

**The design of a simple, on-column frit for capillaries is described. The frit allows electrical connection to be made to the capillary so that the first segment of the capillary (inlet to frit) may be used for electrokinetic separations while the second segment (frit to outlet) is free of applied electric field, facilitating its use either for electrochemical detection or for sample collection. The latter is illustrated, and a quantitative study is made of its performance as a fraction collector.**

Capillary zone electrophoresis (CZE) as it is normally practiced has both the inlet and outlet of the capillary submerged in electrolyte reservoirs to complete a closed circuit (1-3). Consequently, sample zones are directly discharged into the outlet reservoir. This severely hinders sample collection. One way to overcome this problem has been introduced by Rose and Jorgenson (4), who move the capillary outlet from one fraction collector to another in a programmed manner. A similar technique involving interruption of the current flow has been employed by Cohen et al. (5). Both these methods have the drawback that the capillary outlet must contact electrolyte in the fraction collector to complete a circuit. This causes the collected sample to be diluted. There is also a possible problem from electrochemical reactions at the outlet electrode, which is typically submerged in a small amount of electrolyte in the fraction collector.

A superior approach would be to complete the electrical circuit in the capillary prior to its outlet. One method to achieve this has been introduced by Wallingford and Ewing (6), who use a porous glass junction. This junction is prepared by cutting the capillary tubing into two segments and placing both inside a custom-made porous glass sleeve that makes electrical contact to complete the circuit. Dead volume effects are minimized by carefully matching the capillary outside diameter to the inside diameter of the porous glass sleeve. The separation potential may be applied over the first segment

of the capillary without significantly affecting the second segment. The porous glass sleeve permits ion movement but not bulk electrolyte flow, allowing its use for electrochemical detection (6) or sample collection (7).

We describe an alternative method for achieving the same objectives as those of the porous glass junction. We present the use of an on-column frit structure that can fulfill the need to complete the electrical circuit prior to the outlet of the capillary. Such a device offers all the advantages of being able to collect sample with no external dilution caused by the collection procedure. Also, it allows the use of detection schemes in which the detector is at ground potential, such as electrochemical detection (6).

### EXPERIMENTAL SECTION

**Construction of Frit Structure.** We use a focused CO<sub>2</sub> laser to make a hole (about 40  $\mu$ m in diameter) on the side of the capillary wall (8, 9). The capillary is fused silica (Polymicro Technologies, Phoenix, AZ) having an inside diameter of 75  $\mu$ m. We insert a tungsten wire (50- $\mu$ m o.d.) inside the capillary in order to cover the capillary hole. Then a mixture of solder glass (7723, Corning Glassworks, Corning, NY) and powdered fused silica (Thermal American Fused Quartz Co., Montville, NJ, used as received) with particle size between 1 and 10  $\mu$ m is added to amyl acetate to make a slurry, which is used to paste over the hole in the capillary. Once the hole structure has set, which is aided by gentle heating, the tungsten wire is removed. The proportion of Corning solder glass 7723 to fused silica is about 4:1. Next, the hole structure is placed inside a miniature, 1-cm-long heater, made of wound nichrome wire. The sintering temperature of solder glass is about 700 C and that of fused silica is about 2000 C. It has been found that satisfactory frit structures can be made by heating the mixture to about 1000 C for approximately 30 s. This procedure is illustrated in Figure 1.

The capillary is fragile in the region of the frit structure where the polyimide coating has been removed. To reduce its fragility, we have built a protective jacket, shown in Figure 2a. This jacket is made of Delrin with Teflon washers cushioning the capillary. The ends of the jacket are sealed with epoxy (Torrseal, Varian, Lexington, MA). There is a hole in this jacket that allows it to

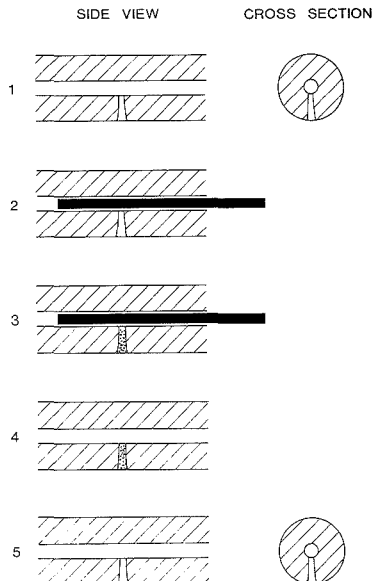


**Figure 1.** Construction steps for fabricating the on-column capillary frit: (1) prepare hole in wall of capillary; (2) insert tungsten wire to cover hole; (3) add slurry of glass solder and fused silica powder, and heat gently until set; (4) remove tungsten wire; and (5) heat locally frit structure to cause particles to sinter.

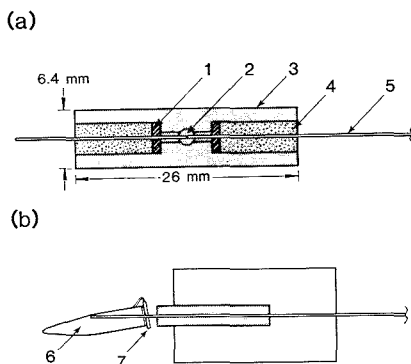


**Figure 2.** (a) Protective jacket for frit structure: 1, Teflon washer; 2, hole in side of jacket lining up with frit so that electrolyte can contact frit structure; 3, jacket body, made from Delrin; 4, epoxy seal; and 5, capillary. (b) Simple device for collecting sample: 6, disposable microcentrifuge tube; and 7, cap with hole allowing insertion of the capillary.

be filled with electrolyte so that the frit structure becomes part of the electrical circuit. This is shown in Figure 3.

We find that we can make this frit structure on a routine basis with a yield of 50%. The major problem is that some frits leak, i.e., do not seal satisfactorily. There seems to be a small variation from one frit to another, discounting those that seal improperly. This variation manifests itself by the observation of different electroosmotic flow rates (see below). Once an acceptable frit structure has been fabricated, no degradation in performance has been observed during several months of operation.

Previous studies by Wallingford and Ewing (6) showed that the separation efficiency decreased as the distance between the grounding structure and the outlet was increased. They found

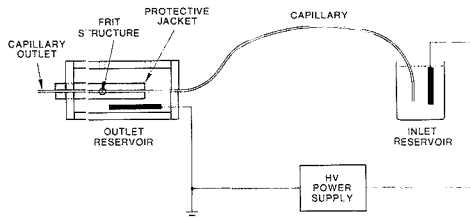


**Figure 3.** CZE setup with on-column frit.

that when this distance is shorter than 2.0 cm the efficiency is virtually no different than that of a standard CZE system employing the same electric field strength and detection conditions. Consequently, we chose to place the frit structure about 1.5 cm from the outlet. If desired, this distance can be easily decreased to as short as 0.5 cm.

When one compares the frit structure with the porous glass junction for on-column electrical contact in CZE, it appears that the frit structure may have a longer lifetime and less dead volume, and its fabrication may be readily automated. However, its construction requires that a small hole be made in the side of the capillary wall, a task that is routine with a focused CO<sub>2</sub> laser but difficult otherwise. On the other hand, the porous glass joint requires "thirsty glass" with dimensions matching the capillary. Unfortunately, this material is not readily available.

**Instrumentation.** The CZE system has been described elsewhere (2). Samples are introduced by gravity at the cathodic or the anodic end of the capillary by raising the inlet a known height (7–12 cm) with respect to the outlet for a fixed period of time. The injection volume is determined in continuous fill mode either by observing the time it takes for the sample to reach the detector or by weighing the amount of eluent collected for a fixed time period. Gravitational injection avoids biases associated with electrokinetic sampling (10). On-column detection is accomplished using UV absorption (Model UVIDECE-100 V, Japan Spectroscopic Co., Tokyo). A reversible high-voltage power supply (Model R50B, Hipotronics, Inc., Brewster, NY) provides a variable separation voltage of 0–30 kV. For sample collection we used disposable microcentrifuge tubes (Applied Scientific, San Francisco, CA).

**Chemicals.** All chemicals are from Sigma Chemical Corp. (St. Louis, MO) and are used without further purification. Different buffers are used, mostly phosphate buffers at pH = 6.8 with a concentration of 10 mM for collection studies and 20 mM for quantitation of collected samples. Water used to prepare solutions is freshly deionized and distilled with a water purifier (Model LD-2A coupled with a Mega-Pure Automatic Distiller, Corning Glassworks).

## RESULTS AND DISCUSSION

### Characterization of Capillaries with On-Column Frits.

It is necessary to ascertain that the frit structure does not adversely affect the operation of the capillary. CZE separations were run for a frit-free capillary and for a frit capillary of the same length. It is found that the value of the current is about the same (<2% deviation in 10 runs) in both capillaries for the same applied electric field strength and buffer. As a further check, the electroosmotic flow rate was measured using the current-monitoring method (11). The grounding was made either through the frit structure or through the capillary outlet, which is about 1.5 cm from the frit structure. It was observed that the electroosmotic flow rate was essentially the same within a single capillary.

We also used the weighing method (12) to calculate the electroosmotic flow for a capillary having a frit. Here the electrolyte leaving the capillary outlet is collected in a 0.5-mL disposable microcentrifuge tube with attached cap that has a 0.8-mm-diameter hole drilled in its center (see Figure 2b). The capillary outlet is inserted inside this hole, making a loose fit. Because there is only a small gap between the capillary (360- $\mu$ m o.d.) and the hole, evaporation of liquid inside the

collector tube is very slow. A control test was done on 10 tubes filled with 3  $\mu$ L of electrolyte and having the capillary inside the hole in the cap for 30 min. The weight loss during this period was less than 0.1 mg in each case. Because collection normally takes less than 30 min, evaporation losses may be considered to be negligible. With this procedure, four capillaries with on-column frits were tested. The results of 10 repeat runs of each capillary show that the CV (coefficient of variation) for each capillary is less than 6%. Between capillaries there is a much larger variation in the electroosmotic flow rate ( $\sim$ 30%). This variation likely represents the differences between the frit structures, which may pass electrolyte to different extents. We have also checked whether the electroosmotic flow rate depends linearly on the applied voltage for a capillary with an on-column frit. We find that a linear relationship holds in the range 100–500 V/cm ( $r = 0.98$ ). In another study we hold the applied electric field strength fixed and vary the collection time from 5 to 30 min. The amount of sample collected shows good linearity with collection time, indicating that the electroosmotic flow rate is stable.

These results encourage us to believe that the on-column frit structure is a useful means for separating the capillary column into two segments, one in which electrokinetic separation takes place, another in which the sample may be detected or collected without an external electric field being applied.

**Sample Collection.** One advantage of the on-column frit structure is that it enables us to collect eluent continuously. It is not necessary to interrupt the electrokinetic separation because the capillary outlet is not part of the electrical circuit. The outlet is at or near ground potential so that it can be manipulated without any safety precautions. Therefore, it is easy to couple it to various collection (or detection) systems.

Two methods are used to collect sample. In the first, we collect the eluent for a fixed period of time in a fraction collector. However, this method may be unsatisfactory when two analytes have nearly identical electrokinetic migration times. In the second method, a detector is placed very close to the capillary outlet and the detector signal is used to trigger the collection procedure. We have implemented the second method with a conductivity detector, fabricated as described previously (8).

To demonstrate that we are able to collect different samples, we carried out the following study. First we prepared a mixture of pyridoxamine dihydrochloride ( $C_8H_{12}N_2O_2 \cdot 2HCl$ ) and adenosine ( $C_{10}H_{13}N_5O_4$ ) in 10 mM phosphate buffer so that the concentration of pyridoxamine was 2 mM and that of adenosine 1 mM. Then 45 nL of this mixture was injected into a capillary with an on-column frit. Eluent was collected during the period 0–6 min. The total volume collected was about 2.8  $\mu$ L, which is greater than the total volume of the capillary used ( $\sim$ 2.4  $\mu$ L). We reinjected 20 nL of the collected sample in a second CZE setup having a UV detector. This setup allowed us to quantitate what had been collected. The resulting electropherogram is shown in Figure 4a. Two peaks are observed, corresponding to pyridoxamine and adenosine, as expected. Under the experimental conditions, pyridoxamine is positively charged and elutes before adenosine, which is almost neutral. The concentration of these species has been reduced by about a factor of 100 by this separation and collection procedure, but is still sufficient for CZE/UV detection.

We have repeated this experiment but collected the eluent into three fractions, one during the period 0–3 min, another during the period 3–6 min, and a third during the period 6–9 min. Each fraction has a total volume of about 1.4  $\mu$ L. We reinjected 20 nL of each fraction, and the resulting elec-

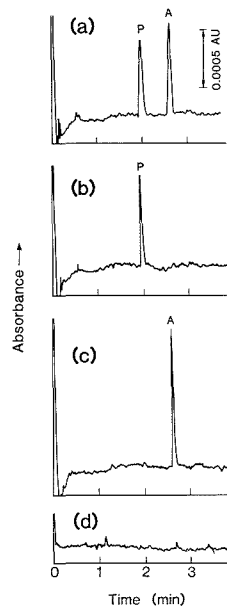


**Figure 4.** Electropherograms of sample fractions containing pyridoxamine (P) and adenosine (A): sample collected (a) 0–6, (b) 0–3, (c) 3–6, and (d) 6–9 min. Operating conditions for collection were 10 mM phosphate buffer at pH = 6.8, capillary length 50 cm from inlet to frit and 1.5 cm from frit to outlet, applied voltage 20 kV, and current 20  $\mu$ A. The electroosmotic flow rate was about 7.5 nL/s. Operating conditions for detection were 20 mM phosphate buffer at pH = 6.8, capillary length 42 cm from inlet to UV detector window and 19 cm from there to outlet, applied voltage 25 kV, and current 32  $\mu$ A. The UV wavelength is 254 nm.

tropherograms are shown in Figure 4b–d. We observe that fraction 1 contained only pyridoxamine, fraction 2 adenosine, and fraction 3 neither pyridoxamine nor adenosine. We conclude that the on-column frit structure allows us to collect different sample species individually.

Next we establish the reproducibility of the collection procedure for small fractions. In these studies we collected only about 0.4  $\mu$ L of eluent. Some additional buffer was added to make the total volume 0.8  $\mu$ L. The collection sample tube was centrifuged 5 s to make the liquid stay at the bottom. Care must be taken in injecting sample from such a small volume. We did an experiment to examine the variance of peak height in 10 runs in 0.8  $\mu$ L of total sample volume. The CV is less than 11% for the species injected.

The frit structure may be operated with the electroosmotic flow either from the anode to the cathode (usual procedure) or from the cathode to the anode (reversed electroosmotic flow). The latter is readily achieved by adding a cationic surfactant to the buffer (13). We find that such surfactants do not interfere with the operation of the frit junction.

We have determined the dilution factor for our sample collector by studying the CZE separation of adenosine diphosphate (ADP) at different concentrations. The results are shown in Figure 5. The initial injection volume is about 40 nL (30-s gravitational injection at a height difference of 10 cm). The collected sample was reinjected on a CZE setup with a UV detector. The concentration of the collected sample was determined from the absorbance signal, which was calibrated against an ADP sample of known concentration. Figure 5 shows that the concentration of sample collected is directly proportional to the concentration of sample injected for the

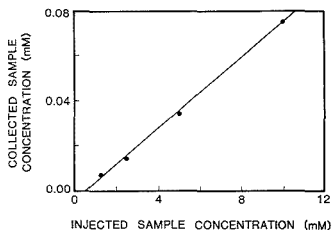


Figure 5. Plot of collected sample concentration versus injected sample concentration for adenosine diphosphate.

concentration range studied ( $r = 0.99$ ). The inverse of the slope gives the dilution factor. For this study we have determined the dilution factor for ADP to be 1:130. Rose and Jorgenson (4) reported that their fraction collector has a dilution factor of about 1:3000 for adenosine, some 25 times larger than that of the present study. It is possible to reduce further our dilution factor by injecting larger amounts of sample, if desired. We have been able to find conditions whereby the dilution factor is only 1:10. However, this decrease in the dilution factor is only obtained by also sacrificing resolution through the use of large sample plug lengths (14).

One possible source of the observed dilution is leakage of injected sample through the frit structure. We have determined the percentage of sample collected by injecting fluorescent sample (dansyl-L-leucine) and determining the ratio of the sample in the reservoir attached to the frit structure to that in the sample collector. We find that the leakage is about 10%, 8%, and 7% for three on-column frit-structure capillaries that we tested. Thus, more than 90% of the injected sample can be collected.

The small dilution factor combined with the high recovery factor for the on-column frit structure represents a particular advantage of this method. In this collection procedure, it is

not necessary to place an electrode with a certain amount of electrolyte in the fraction collector. We therefore avoid external dilution by the electrolyte in the fraction collector (and we also avoid possible interference from electrochemical reactions at the electrode). Thus, the on-column frit structure has many favorable features that recommend its use as a sample collector. Moreover, this frit structure may allow CZE to be readily interfaced to other hyphenated separation schemes.

#### ACKNOWLEDGMENT

We thank R. T. (Skip) Huckaby, Electrical Engineering Department, Stanford University, for assistance in constructing the frit structures.

#### LITERATURE CITED

- (1) Jorgenson, J.; Lukacs, K. D. *Science* **1983**, *222*, 266-272.
- (2) Gordon, M. J.; Huang, X.; Pentoney, S. L., Jr.; Zare, R. N. *Science* **1988**, *242*, 224-228.
- (3) Ewing, A. G.; Wallingford, R. A.; Olefirowicz, T. M. *Anal. Chem.* **1989**, *61*, 292A-303A.
- (4) Rose, D. J.; Jorgenson, J. W. *J. Chromatogr.* **1988**, *438*, 23-34.
- (5) Cohen, A. S.; Najarian, D. R.; Paulus, A.; Guttman, A.; Smith, J. A.; Karger, B. L. *Proc. Natl. Acad. Sci. U.S.A.* **1988**, *85*, 9660-9663.
- (6) Wallingford, R. A.; Ewing, A. G. *Anal. Chem.* **1987**, *59*, 1762-1766.
- (7) Guzman, N. A.; Hernandez, L.; Hoebel, B. G. *BioPharm.* **1989**, *January*, 22-37.
- (8) Huang, X.; Pang, T.-J.; Gordon, M. J.; Zare, R. N. *Anal. Chem.* **1987**, *59*, 2747-2749.
- (9) Pentoney, S. L., Jr.; Huang, X.; Burgi, D. S.; Zare, R. N. *Anal. Chem.* **1988**, *60*, 2625-2629.
- (10) Huang, X.; Gordon, M. J.; Zare, R. N. *Anal. Chem.* **1988**, *60*, 375-377.
- (11) Huang, X.; Gordon, M. J.; Zare, R. N. *Anal. Chem.* **1988**, *60*, 1837-1838.
- (12) Altria, K. D.; Simpson, C. F. *Anal. Proc. (London)* **1986**, *23*, 453-454.
- (13) Huang, X.; Luckey, J. A.; Gordon, M. J.; Zare, R. N. *Anal. Chem.* **1989**, *61*, 766-770.
- (14) Huang, X.; Coleman, W. F.; Zare, R. N. *J. Chromatogr.* **1989**, *480*, 95-110.

RECEIVED for review September 12, 1989. Accepted November 6, 1989. Support for this work by Beckman Instruments, Inc., is gratefully acknowledged.

# Electrochemical Behavior of Reversible Redox Species at Interdigitated Array Electrodes with Different Geometries: Consideration of Redox Cycling and Collection Efficiency

Osamu Niwa,\* Masao Morita, and Hisao Tabei

NTT Basic Research Laboratories, Nippon Telegraph and Telephone Corporation, Tokai, Ibaraki 319-11, Japan

Interdigitated array (IDA) electrodes with different geometric parameters have been fabricated by a lithographic technique and applied to cyclic voltammetric and chronoamperometric measurements of reversible redox species. The collection efficiency is dependent on the average diffusion length of  $W_e/4 + \text{gap}$ , where  $W_e$  is the band electrode width in the IDA. The number of redox cycles rapidly increases by decreasing  $W_e/4 + \text{gap}$  and is closely related to collection efficiency. The difference in species diffusion constant had little effect on the collection efficiency and redox cycling. The high redox cycling and collection efficiency of the IDA's allowed electrochemical measurements to be highly sensitive ( $10 \text{ nmol/dm}^3$ ), with a high signal to noise ratio and a wide dynamic range ( $10 \text{ nmol/dm}^3$  to  $1 \text{ mmol/dm}^3$ ). Chronoamperometric measurement has been performed in a four-electrode configuration where step potential was applied to the generator electrode and constant potential was applied to the collector electrode in the IDA. The generator current reached steady state within a hundred milliseconds and the collector current was not affected by charging. With the IDA, fast sweep cyclic voltammetry with no observable charging current has been also demonstrated.

Microelectrodes are of interest for several reasons such as small  $iR$  drop, fast establishment of steady-state mass transfer, and small capacitive charging currents. A variety of microelectrodes have been constructed and studied both experimentally and theoretically (1-3). Possible applications include fast cyclic voltammetry (4-7), electrochemical measurements in vivo or in low conductive media (8-10), and chemical sensing (11-14). Micro fabrication techniques can be applied to produce a variety of sizes and/or shapes of microelectrodes compared to the conventional fabrication techniques of sealing carbon or metal fibers in a glass capillary tube or sealing metal foil between two glass plates (15). It also allows microelectrodes of the same size and of any shape to be produced without difficulty. Lithographically fabricated microelectrodes have attracted much attention as ion-selective field effect transistors (11, 16) or electrochemical diodes and transistors (17-24).

Interdigitated array (IDA) electrodes are particularly interesting, because their geometric differences from conventional electrodes result in specific electrochemical behavior (25). Nonplanar diffusion to each microband electrode in IDA gives rise to quasi-steady-state currents for moderate sweep rates with a reversible redox couple. The species generated at one band electrode may be collected at adjacent band electrodes when the potential is set to a level at which a reverse reaction can occur. This type of experiment has been carried out with rotating ring-disk electrodes (RRDE) and paired microband electrodes with a small gap (26, 27). Collection efficiency can be defined as the ratio of currents at the generator and collector electrodes. An important feature of IDA compared to RRDE is that the collected species will be electrolyzed at the collector electrodes and then diffuse back

to the generator electrodes (25). This redox cycling or "feedback effect" (26) makes the currents of both the generator and collector electrodes larger.

Another feature is that the collector electrodes are held at a constant potential. This allows us to measure faradaic currents without charging currents caused by potential change. The fast sweep cyclic voltammogram is not distorted by the increased charging current. The collector electrode currents directly reveal the diffusion characteristics between the generator and collector electrodes (28, 29).

Aoki and we discussed reversible diffusion-controlled currents of redox soluble species at IDA electrodes under steady-state conditions (30). In this paper, the relationship between the geometric configuration and the electrochemical characterization of IDA's, particularly collection efficiency and redox cycles are described. High redox cycling and collection efficiency of IDA's allow electrochemical measurements to be highly sensitive, with a high signal to noise ratio and a wide dynamic range. We also demonstrate fast sweep cyclic voltammetry without a charging current by using IDA.

## EXPERIMENTAL SECTION

**Electrodes.** Interdigitated array (IDA) electrodes were fabricated on thermally oxidized silicon wafers. Platinum electrodes were formed by sputter deposition and the lift-off technique as described elsewhere (30, 31). The submicrometer IDA electrodes were fabricated with a combination of electron beam lithography and photolithography. The platinum pad and the lead pattern were formed by photolithography and the lift off technique. Then a PMMA/ $\phi$ -MAC (Daikin Manufacturing Co., Osaka) bilayer electron beam positive resist was spin coated on to the wafers exposed with ELS-5000 (Elionixs, Japan) electron beam exposure, and developed. Both wafers with micrometer and submicrometer patterns were then spin-coated with spin-on-glass (OCD Type-7, Tokyo Ohka Co.), and baked at  $430^\circ\text{C}$  for 30 min. The final thickness of the spin-on-glass was 800 nm. An MP1400-27 (Shipley) positive photoresist pattern was formed on the wafer and used as an etching mask. The silicon dioxide film made from the spin-on-glass was etched by DEM-451 reactive ion etching equipment (ANELVA, Tokyo) with tetrafluoromethane until the surfaces of the IDA electrode and pad were exposed. The photoresist remaining after etching was removed in the methyl ethyl ketone solution.

Each IDA cell was cut to a  $1 \times 2$  cm rectangle and mounted on a custom-made connector to attach it to the electrochemical apparatus. The auxiliary electrode was a platinum wire. The reference electrode was an Ag/AgCl electrode.

The IDA used consists of two series of interdigitated microband electrodes, whose geometric parameters are summarized in Table I. Figure 1 shows an SEM photograph of an IDA with a  $3\text{-}\mu\text{m}$  bandwidth and a  $2\text{-}\mu\text{m}$  gap.

**Apparatus and Reagents.** Electrochemical measurements were performed with a dual potentiostat, DPGS-3 (Nikko Keisoku, Atsugi, Japan) and HECS990 (Fuso, Japan), a digital memory oscilloscope, Model 4094B (Nicolet, Madison, WI), and a universal pulse programmer, Model 175 (Princeton Applied Research, Princeton, NJ).

The reagents were ferrocene, (ferrocenylmethyl)trimethylammonium bromide (aq-ferrocene), potassium ferrocyanide, ruthenium hexamine, tetrabutylammonium tetrafluoroborate, potassium nitrate, and acetonitrile and were used as purchased.

Table I. Geometric Parameters and Collection Efficiencies for Various Redox Species of the IDA Electrodes<sup>a</sup>

$W_0/\mu\text{m}$	IDA size			collection efficiency/%			
	gap/ $\mu\text{m}$	length/mm	no. of bands	aq-ferrocene	ferrocene	ferrocyanide	Ru(NH <sub>3</sub> ) <sub>6</sub>
0.75	0.75	1	135	99.5	99.1	98.5	98.9
1.0	1.0	1	100	100	98.7	98.8	98.1
1.5	1.5	1	100	100	98.5	97.9	97.8
3.0	2.0	2	50	99.3	98.0	98.3	95.9
5.0	2.0	2	50	96.2	96.1	95.7	95.4
10.0	2.0	2	25	93.5	93.7	93.0	95.0
3.0	5.0	2	50	94.6	94.2	94.7	92.2
5.0	5.0	2	50	92.8	93.6	91.5	91.6
10.0	5.0	2	25	90.0	90.1	89.3	91.9

<sup>a</sup>The composition of the solution is in Table II. Key: generator electrode, swept at 10 mV/s; collector electrode, -0.1 V [0 V for Ru(NH<sub>3</sub>)<sub>6</sub>].

Table II. Redox Species

name	concn, mmol/dm <sup>3</sup>	supporting electrolyte	solvent	diffusion constant, cm <sup>2</sup> /s
ferrocene	1.0	Bu <sub>4</sub> NBF <sub>4</sub>	CH <sub>3</sub> CN	2.4 × 10 <sup>-6</sup>
aq-ferrocene <sup>a</sup>	1.0	KNO <sub>3</sub>	H <sub>2</sub> O	6.1 × 10 <sup>-6</sup>
ferrocyanide	1.0	KCl	H <sub>2</sub> O	6.4 × 10 <sup>-6</sup>
Ru hexaamine	1.0	KNO <sub>3</sub>	H <sub>2</sub> O	7.1 × 10 <sup>-6</sup>

<sup>a</sup>(Ferrocenylmethyl)trimethylammonium bromide.

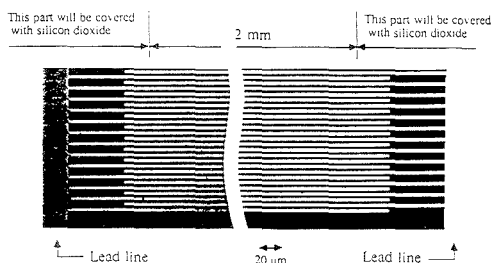


Figure 1. SEM photograph of part of Pt band pattern of IDA. The 3- $\mu\text{m}$  width, 2- $\mu\text{m}$  gap, 2 mm long IDA contains 50 bands on each side. This picture was taken before the spin-on-glass coating. After spin-on-glass coating and etching, the lead lines are covered with silicon dioxide.

The redox species used are summarized in Table II with other parameters.

**Procedure.** Electrochemical measurements were carried out in 1 mmol/dm<sup>3</sup> ferrocene acetonitrile solution or 1 mmol/dm<sup>3</sup> ruthenium hexaamine, aq-ferrocene, or potassium ferrocyanide aqueous solutions purged with nitrogen in the usual three-electrode (open-circuit mode, one of the paired electrodes in the IDA is disconnected) or four-electrode (generation-collection mode) configuration. The resistance between IDA (gap, 2  $\mu\text{m}$ ) is more than 100 M $\Omega$  and about 7 M $\Omega$  at dry and wet (in H<sub>2</sub>O) state, respectively. In measuring the cyclic voltammogram of ferrocene, aq-ferrocene and potassium ferrocyanide, the potential of the collector electrode was held at -0.1 V, and the generator electrode was swept between -0.1 and 0.7 V, at a sweep rate of 10–100 mV/s. In the case of ruthenium hexaamine, the collector was held at 0 V, and the generator was swept between 0 and -0.7 V. In order to obtain steady-state limiting currents in the open-circuit mode, it was necessary to decrease the sweep rate below 5 mV/s or 1 mV/s for ferrocene and other redox species, respectively.

In the generation-collection chronoamperometry of the ferrocene solution, the potential of the generator electrode was stepped up from 0 to 0.5 V, whereas the collector electrode was held at -0.1 V. The potential step current-time transients of both electrodes were stored in a digital memory oscilloscope and then recorded with a two-pen X-Y recorder.

The fast sweep rate cyclic voltammetry of ferrocene was carried out with a 3- $\mu\text{m}$  width, 2  $\mu\text{m}$  gap IDA electrode. The potential of the generator was swept from -0.3 to 0.75 V with rate of 10

V/s and that of the collector held at -0.1 V. The currents were stored in a digital memory oscilloscope and then recorded with a two-pen X-Y recorder.

## RESULTS AND DISCUSSION

**IDA Fabrication.** The lithographic processing of IDA's is almost the same as previously described except for the use of electron beam lithography for fabricating the submicrometer IDA and spin-on-glass as an insulating layer. In the earlier work (30), a hard-baked photoresist was used as an insulator and failed occasionally when nonaqueous solvents were used. It was not sufficiently hard to resist scratching. The use of sputter-deposited silicon dioxide improved the reliability of the insulator (31), although this lengthened the insulator forming process.

The spin-on-glass consists mainly of aqueous silicate solution and can be spin-coated on a wafer like a photoresist coating. High temperature baking (430 °C) makes it cross-link and convert into silicon dioxide. Although the spin-on-glass insulator is inferior to the sputter-deposited one in hardness, it has sufficient quality as an insulator. It also has the advantage of providing smooth and uniform film, which improves the step coverage of the Pt electrodes at their edges.

**Collection Efficiencies of IDA's with Different Geometric Parameters.** The anodic and cathodic currents of ferrocene, aq-ferrocene, and potassium ferrocyanide at IDA electrodes are steady state, in which the potential of the cathode (collector electrode) was held at -0.1 V and the anode (generator electrode) was swept between -0.1 and 0.7 V at 10 mV/s.

Similar steady-state curves were obtained for ruthenium hexaamine, in which the potential of the collector electrode was held at 0 V vs Ag/AgCl and the generator electrode was swept between 0 and -0.7 V. These results are analogous to those obtained by rotating ring-disk measurement, but this steady-state condition was established only by mass transfer. The magnitude of the limiting currents at these IDA electrodes is increased by decreasing the bandwidth and gap in the IDA and corresponds to the theoretical value (30). The collection efficiency in the IDA, which can be calculated from the ratio between the generator and the collector currents, is increased by decreasing the electrode size and approaches unity. Table I also shows the collection efficiency of the IDA with various geometric parameters. Bard et al. (27) reported that the collection efficiency of a generator with two collector band electrodes (three microband electrode configuration) was strongly dependent on the gap, and was expressed as the following equation, when the generator and collector electrodes are the same size:

$$\Phi_{ss} = 0.095 + 0.33 \log \omega_{gap} - 0.035 (\log \omega_{gap})^2 \quad (1)$$

$$\omega_{gap} = 4Dt/gap^2$$

where  $\Phi_{ss}$  is the collection efficiency and  $t$  is the time. The

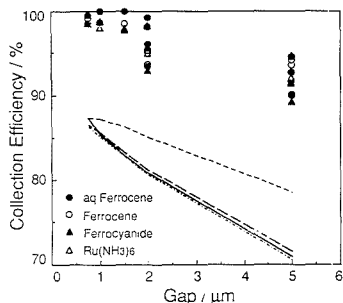


**Figure 2.** Collection efficiencies at the IDA electrodes compared with those resulting from eq 1, which is for one generator with two flanking collector microband electrodes (26). The composition of the solution is in Table II. Key: (---) aq-ferrocene; (---) ferrocene; (—) ferrocyanide; (—) ruthenium hexaamine.

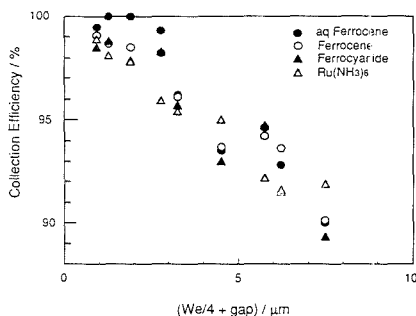


**Figure 3.** Variations of the collection efficiencies at the IDA electrodes as a function of the average diffusion length. The composition of the solution is in Table II.

collection efficiencies in the IDA were compared with theoretical values from eq 1.

Figure 2 shows a comparison of the collection efficiency in the IDA with the theoretical results (from eq 1). There are three main differences in the collection efficiency of IDA and that of the three microband electrode configuration. First, the collection efficiency at the IDA electrodes varies by changing not only the gap but also the bandwidth and does not fit with the results of eq 1. Second, the collection efficiency in the IDA did not change for different redox species despite the large difference in diffusion coefficient between ferrocene ( $D = 2.4 \times 10^{-5} \text{ cm}^2/\text{s}$ ) and other redox species ( $D = (6-7.1) \times 10^{-6} \text{ cm}^2/\text{s}$ ). It suggests that the collection efficiency of the IDA was only influenced by geometric factors like that of RRDE, at least the region we measured. Finally, the collection efficiency in the IDA is much higher than that for three microband electrodes with the same gap, indicating that the alternative array structure could decrease the active species, which diffuse back into the bulk solution.

From the results of the chronoamperometry at the IDA as described in the later section, the good proportionality between the square root of the half-height time when the collector transient current is at 50% of its limiting current and  $W_e/4 + \text{gap}$  was obtained. This shows that the  $W_e/4 + \text{gap}$  could be used to represent the average diffusion length between the generator and collector electrodes.

Figure 3 shows the collection efficiencies of various redox species as a function of average diffusion length ( $W_e/4 + \text{gap}$ ). It is increased by decreasing the average diffusion length, and the average error is small (about +1.5%, see Figure 3). This suggests that  $W_e/4 + \text{gap}$  could be the more suitable param-

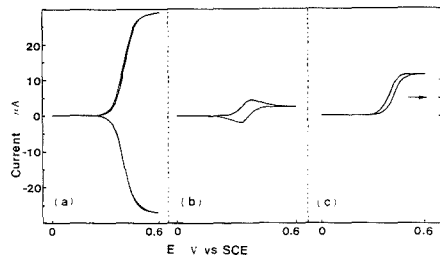


**Figure 4.** Cyclic voltammograms of 1 mmol/dm<sup>3</sup> ferrocene in 0.1 mol/dm<sup>3</sup> tetrabutylammonium tetrafluoroborate acetonitrile solution at a 3- $\mu\text{m}$  width, 2- $\mu\text{m}$  gap IDA with and without potentiostating the collector electrode: (a) generator electrode, swept at 100 mV/s; collector electrode, -0.1 V; (b) generator electrode, sweep at 100 mV/s; collector electrode, open circuit; (c) generator electrode, swept at 5 mV/s; collector electrode, open circuit.

eter from which to evaluate the geometry dependence of the collection efficiency at the IDA electrodes.

**Redox Cycling of IDA.** The remarkable feature of IDA compared to RRDE is its high redox cycling which makes the currents of both the generator and collector electrodes larger. The steady-state waves of ferrocene with redox cycling (Figure 4a) change to a gentle decay of the current plateau as shown in Figure 4b, when the collector electrode is not potentiostated (open-circuit mode). A lower sweep rate of less than 5 mV/s produces a pseudo-steady-state wave, whose magnitude is much lower than those produced when using a collector electrode.

The redox cycles in the IDA can be calculated from the collection efficiency values. When the collection efficiency of the generator to collector electrode is  $\Phi_1$ , and that when the generator and collector electrode are reversed is  $\Phi_2$ , the number of ferrocene molecules which diffuse back to the generator electrode after reducing at the collector electrode can be expressed as  $N\Phi_1\Phi_2$ , where  $N$  is the number of ferrocene molecules oxidized per unit time at the generator electrode. So, the number of ferrocene molecules that diffuse into the bulk solution per cycle is  $N - N\Phi_1\Phi_2$ . Then, the number of redox cycles (Rc) is expressed by

$$\text{Rc} = N / (N(1 - \Phi_1\Phi_2)) = 1 / (1 - \Phi_1\Phi_2) \quad (2)$$

In this experiment,  $\Phi_1$  and  $\Phi_2$  have the same value because the size of the generator and collector electrodes is the same. This method is useful to evaluate the redox cycles of IDA. However, the accuracy of the calculated redox cycles is governed by the experimental errors of the collection efficiency. Particularly, the calculated redox cycles are much scattered because the slight error in the collection efficiency was enhanced by eq 2, when the collection efficiency at the IDA is near unity.

We assumed the average number of redox cycles from the ratio of the limiting current of the generation-collection mode ( $i_g$ ) to that of the open-circuit mode ( $i_o$ ) and compared it with those calculated from eq 2. Figure 5 shows the redox cycles obtained from  $i_g/i_o$ , compared with those obtained from eq 2. Although  $i_g/i_o$  is not the actual number of redox cycles, it is closely related with the number calculated from eq 2, when the  $W_e/4 + \text{gap}$  is more than 3.75  $\mu\text{m}$ . Taking into account the  $i_g/i_o$  shows the good reproducibility, the difference between the calculated redox cycles and  $i_g/i_o$  may be caused by the fluctuation of the calculated results. These results indicate that  $i_g/i_o$  values could be substituted for the values from eq 2 to evaluate the actual number of redox cycles.

Figure 6 shows the average numbers of redox cycles ( $i_g/i_o$ ) for various redox species as a function of the average diffusion length. The number of redox cycles rapidly increases by

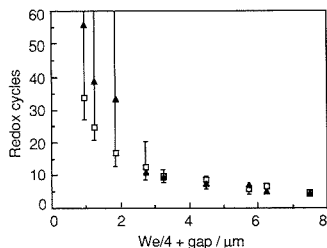


**Figure 5.** Ratio of the generator electrode current of ferrocene in generation-collection mode to that in open circuit mode ( $i_g/i_o$ ) compared with redox cycles calculated with eq 2. The generators monitored in this experiment are 25 (bandwidth, 10  $\mu\text{m}$ ), 50 (bandwidth, 5  $\mu\text{m}$ ), and 100 (bandwidth, less than 1.5  $\mu\text{m}$ ):  $\square$ ,  $i_g/i_o$ ;  $\triangle$ , redox cycles by eq 2.

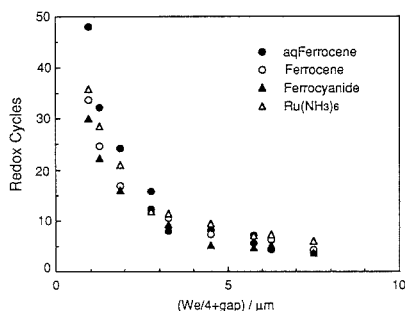


**Figure 6.** Variation of the redox cycles as a function of the average diffusion length. Redox cycles are the ratio of generator current, with the collector electrode open circuited, to generator current with the generator electrode on.

decreasing the average diffusion length and reaches more than 40 in the smaller IDA, which has a 0.75- $\mu\text{m}$  bandwidth and gap. No clear difference in the number of redox cycles can be observed between the redox species.

On the other hand, the number of redox cycles in the three microband electrode configuration with a 1- $\mu\text{m}$  gap is only 2.4 (feedback factor = 0.58 =  $1 - 1/(\text{redox cycling})$ ) (26), which is much smaller than that at an IDA electrode with the same gap. These differences in the number of redox cycles are caused by the following reasons. In the case of the three microband electrode, the generator electrode is located between two adjacent collector electrodes, whereas each collector electrode has only one adjacent generator electrode. Some active species reduced by the collector electrode could diffuse into the bulk solution from the electrode edge, furthest from the generator electrode.

In the case of the IDA electrode, the collection efficiency is almost same, when the generator and the collector electrodes are reversed. The redox species may escape in the bulk solution vertically or escape at the edge of the IDA electrode.

**Concentration Dependence of Steady-State Currents.** Since the voltammograms of the IDA electrode show a relatively high current density due to the high redox cycles, the sensitivity of the IDA was studied by changing the concentration of ferrocene.

Figure 7 shows the concentration dependence of the cathodic and anodic limiting current of ferrocene at an IDA electrode, whose bandwidth and gap are 3 and 2  $\mu\text{m}$ , respectively. The anodic generator and cathodic collector currents were proportional to the concentration of ferrocene from 100  $\text{nmol}/\text{dm}^3$  to 1  $\text{mmol}/\text{dm}^3$  at a sweep rate of 10  $\text{mV}/\text{s}$ . However, the quantitative generator anodic current

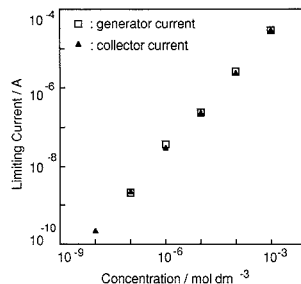


**Figure 7.** Concentration dependence of the cathodic and anodic limiting currents of ferrocene at an IDA with 3- $\mu\text{m}$  width and 2- $\mu\text{m}$  gap. The solvent is acetonitrile containing 10  $\text{nmol}/\text{dm}^3$  to 1  $\text{mmol}/\text{dm}^3$  ferrocene and 0.1  $\text{mol}/\text{dm}^3$  tetraethylammonium tetrafluoroborate.

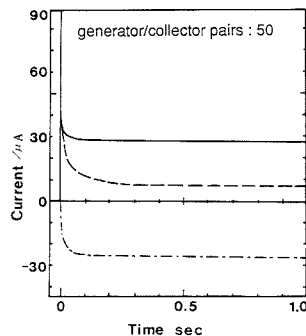


**Figure 8.** Chronoamperometric current-time curve (—) for potential step oxidation of 1  $\text{mmol}/\text{dm}^3$  ferrocene in 0.1  $\text{mol}/\text{dm}^3$  tetraethylammonium tetrafluoroborate acetonitrile solution at a 3- $\mu\text{m}$  width, 2- $\mu\text{m}$  gap IDA electrode with 50 pairs of generator and collector electrodes. (---) represents the current of the collector electrode whose potential is held at  $-0.1$  V. The dashed line shows an open-circuit mode current-time curve of the generator without potentiostating the collector electrode in IDA.

cannot be measured at a higher sweep rate and at a concentration of less than 100  $\text{nmol}/\text{dm}^3$  due to the reduction of the signal to noise (S/N) ratio of the faradaic current to the charging current. On the other hand, the cathodic current was proportional to the concentration of ferrocene from 10  $\text{nmol}/\text{dm}^3$  to 1  $\text{mmol}/\text{dm}^3$  due to the absence of the charging current.

Recently, on conjunction with Aoki we (30) proposed steady-state equations for redox species at an IDA electrode and proved that the limiting current increases by decreasing the gap and bandwidth. Voltammograms of electroactive species with a lower concentration may be realized by using an IDA with a smaller gap and bandwidth. This is now under investigation.

**Chronoamperometry of IDA.** Current-time curves resulting from potential steps for IDA's in ferrocene acetonitrile solution were subjected to a detailed quantitative comparison with microband electrodes (32-34) and three microband electrodes (26). Figure 8 shows typical current-time curves from the generator (—) and the collector (---) of a 3- $\mu\text{m}$  bandwidth, 2- $\mu\text{m}$  gap IDA electrode. The dashed line in Figure 8 shows an open-circuit mode current-time curve of a generator with an unpotentiostated collector electrode in an IDA. The generator current of the generation-collection mode reaches steady-state within a hundred milliseconds. The steady-state response can be improved to 10 ms, when sub-micrometer IDA electrodes are used. The electrochemical response of the previously reported IDA electrode is not so

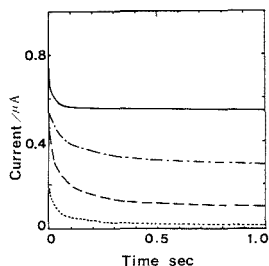


**Figure 9.** Chronoamperometric current-time curve for potential step oxidation of 1 mmol/dm<sup>3</sup> ferrocene in 0.1 mol/dm<sup>3</sup> tetrabutylammonium tetrafluoroborate acetonitrile solution at a 3- $\mu$ m width, 2- $\mu$ m gap IDA electrode: (—) represents the generator current in generator-collector mode, (---) represents the open-circuit mode current. These currents are normalized by dividing the number of bands. (-·-) and (···) represent a theoretical current calculated from the Aoki-Coen equations, and the Cottrell equation, respectively.

rapid, because the bandwidth and gap are 50  $\mu$ m (25). However, like the fast voltammogram of an ultramicroelectrode, our results for a submicrometer size IDA electrode show that a small IDA electrode can be applied to measure the electrochemical property of short lifetime species. Other remarkable characteristics of the IDA are that the current-time curve at the collector electrode consists of only faradaic current and is not affected by large noisy charging current. The transient region until the collection current becomes steady state reflected the redox species diffusion and the concentration gradient establishment.

The square root of the half-height time when the collector transient current is at 50% of its limiting current is proportional to the average diffusion length ( $W_0/4 + \text{gap}$ ), and those plots fit well with the theoretical line of  $d = (\pi Dt)^{1/2}$ .

Aoki et al. (32, 33) derived the theoretical chronoamperometric response at a microband electrode as a function of the dimensionless electrolysis time  $\theta$ , given by

$$\theta = Dt/w^2 \quad (3)$$

where  $t$  is the time in seconds and  $w$  is the electrode width in centimeters. The chronoamperometric curve is expressed as

$$I/(bnFDC^*) = (\pi\theta)^{-1/2} + 0.97 - 1.10 \exp[-9.90/\ln(1.237\theta)] \quad (4)$$

for  $\theta < 10^8$  ( $t < 3.75 \times 10^5$  s for ferrocene, when  $W_0$  is 3  $\mu$ m), where  $b$  is the length of the microband electrode and  $n$ ,  $F$ ,  $D$ , and  $C^*$  have their usual meanings.

Coen et al. (34) derived the following expression for the quasi-steady-state currents at a microband electrode:

$$I/(bnFDC^*) = 5.553/\ln(4\theta) - 6.791/(\ln(4\theta))^2 \quad (5)$$

Equation 3 holds for  $\theta > 7.5$  ( $t > 70$  ms for ferrocene in 10  $\mu$ m bandwidth) and shows approximately the same results in longer time regions as eq 4. Figure 9 shows chronoamperometric current-time curves of both the generator-collector (—) and open-circuit (---) mode for 3- $\mu$ m bandwidth, 2- $\mu$ m gap IDA's, in comparison with the Aoki-Coen equation (-·-) and the Cottrell equation (···). The currents in the IDA's are divided by the number of bands, normalizing in single microband currents. The current in the open-circuit mode shows a higher value than the Cottrellian, indicating that the diffusion profile is not longer planar. It is, however, much lower than the value calculated from the Aoki-Coen equation, because of the shielding effect (26). The current in the generator-collector mode shows a larger value than the Aoki-Coen equation, due to redox cycling. When the gap becomes 2–5  $\mu$ m, the open-circuit mode current becomes larger because of

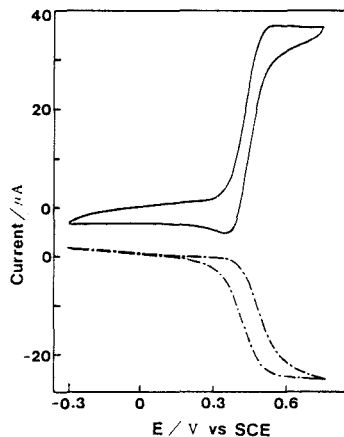


**Figure 10.** Cyclic voltammetry (—) of 1 mmol/dm<sup>3</sup> ferrocene in 0.1 mol/dm<sup>3</sup> tetrabutylammonium tetrafluoroborate acetonitrile solution at a 3- $\mu$ m width, 2- $\mu$ m gap IDA electrode. (---) represents the current of the collector electrode whose potential is held at -0.1 V.

a smaller shielding effect, but the generator-collector mode current becomes smaller because of less redox cycling.

**Fast Sweep Cyclic Voltammetry.** Important features of microelectrodes include their small double layer capacitance, which allows the exploration of extremely short electrolysis times and fast kinetic phenomena. On the other hand, the double layer charging current increases linearly with the sweep rate, whereas the faradaic current increases with the square root of the sweep rate at the high scan rate. Therefore, the signal becomes obscure in large charging current when the sweep rate becomes faster. Although computer digital subtraction between sample and blank solutions improves this problem (5), the essential low signal-to-noise ratio, signal distortion by the ohmic drop, and experiments on both sample and background still remain.

The collector current in the IDA is not affected by the charging current because the potential of the collector is held constant. Therefore, the no-charging current fast sweep rate cyclic voltammogram is expected. Figure 10 shows cyclic voltammetry in the generation-collector mode for ferrocene in a 3- $\mu$ m width, 2- $\mu$ m gap IDA. The sweep rate was 10 V/s, so that the voltammogram of the generator develops current peaks meaning that the radial diffusion profile dimension is approaching that of the electrode. On the other hand, the voltammogram of the collector maintained a steady-state response.

This effect was described 20 years ago in connection with thin-layer electrochemistry, but with no regard to IDA's. Hysteresis is caused by the delay between the generation and collection of redox species. The potential of the generator will be changed when the generated species diffuse and reach to the collector. The difference between cathodic and anodic waves in the collector voltammogram is about 80 mV. The sweep rate is 10 V/s; therefore the difference of 80 mV corresponds to 8 ms, which is close to the theoretical time in which the redox species crosses the gap.

#### ACKNOWLEDGMENT

We thank Professor K. Aoki for his helpful discussions and Dr. T. Tamamura for the fabrication of the IDA's by electron-beam lithography.

#### LITERATURE CITED

- (1) Fleischmann, M.; Pons, S.; Rolison, D.; Schmidt, P. P. *Ultramicroelectrodes*; Datatech Science: Morganton, NC, 1987.

- (2) Pons, S.; Fleischmann, M. *Anal. Chem.* **1987**, *59*, 1391A.  
 (3) Johnson, D. C.; Ryan, M. D.; Wilson, G. S. *Anal. Chem.* **1988**, *60*, 147R.  
 (4) Howell, J. O.; Wightman, R. M. *Anal. Chem.* **1984**, *56*, 524.  
 (5) Howell, J. O.; Wightman, R. M. *J. Phys. Chem.* **1984**, *88*, 3915.  
 (6) Andrieux, C. P.; Garreau, D.; Hapiot, P.; Pinson, J.; Savéant, J. M. *J. Electroanal. Chem.* **1988**, *243*, 321.  
 (7) Andrieux, C. P.; Garreau, D.; Hapiot, P.; Savéant, J. M. *J. Electroanal. Chem.* **1988**, *248*, 447.  
 (8) Amatore, C.; Kelly, R. S.; Dristensen, E. W.; Kuhr, W. G.; Wightman, R. M. *J. Electroanal. Chem.* **1986**, *213*, 31.  
 (9) Ponchon, J.-L.; Cespuoglio, R.; Gonon, F.; Jouvét, M.; Pujol, J.-F. *Anal. Chem.* **1979**, *51*, 1463.  
 (10) Geng, L.; Murray, R. W. *Inorg. Chem.* **1986**, *25*, 3115.  
 (11) Janata, J.; Bezegh, A. *Anal. Chem.* **1988**, *60*, 62R.  
 (12) Ikariyama, Y.; Yamauchi, S.; Yukiashi, T.; Ushioda, H. *Anal. Lett.* **1987**, *20*, 1791.  
 (13) Ikariyama, Y.; Yamauchi, S.; Yukiashi, T.; Ushioda, H. *Anal. Lett.* **1987**, *20*, 1407.  
 (14) Brina, R.; Pons, S.; Fleischmann, M. *J. Electroanal. Chem.* **1988**, *244*, 81.  
 (15) Chidsey, C. E.; Feldman, B. J.; Lundgren, C.; Murray, R. W. *Anal. Chem.* **1986**, *58*, 601.  
 (16) Murakami, T.; Nakamoto, S.; Kimura, J.; Kuriyama, T.; Karube, I. *Anal. Lett.* **1988**, *19*, 1973.  
 (17) White, H. S.; Kittlesen, G. P.; Wrighton, M. S. *J. Am. Chem. Soc.* **1984**, *106*, 5375.  
 (18) Kittlesen, G. P.; White, H. S.; Wrighton, M. S. *J. Am. Chem. Soc.* **1984**, *106*, 7389.  
 (19) Paul, E. W.; Ricco, A. J.; Wrighton, M. S. *J. Phys. Chem.* **1985**, *89*, 1441.  
 (20) Thackeray, J. W.; White, H. S.; Wrighton, M. S. *J. Phys. Chem.* **1985**, *89*, 5133.  
 (21) Bélanger, D.; Wrighton, M. S. *Anal. Chem.* **1987**, *59*, 1426.  
 (22) Natan, M. J.; Mallouk, T. E.; Wrighton, M. S. *J. Phys. Chem.* **1987**, *91*, 648.  
 (23) Natan, M. J.; Bélanger, D.; Carpenter, M. K.; Wrighton, M. S. *J. Phys. Chem.* **1987**, *91*, 1834.  
 (24) Jones, I. T. T.; Chyan, O. M.; Wrighton, M. S. *J. Am. Chem. Soc.* **1987**, *109*, 5526.  
 (25) Sanderson, D. G.; Anderson, L. B. *Anal. Chem.* **1985**, *57*, 2388.  
 (26) Bard, A. J.; Crayston, J. A.; Kittlesen, G. P.; Shea, T. V.; Wrighton, M. S. *Anal. Chem.* **1986**, *58*, 2321.  
 (27) Shea, T. V.; Bard, A. J. *Anal. Chem.* **1987**, *59*, 2101.  
 (28) Licht, S.; Cammarata, V.; Wrighton, M. S. *Science* **1988**, *243*, 1176.  
 (29) Feldman, B. J.; Feldberg, S. W.; Murray, R. W. *J. Phys. Chem.* **1987**, *91*, 6558.  
 (30) Aoki, K.; Morita, M.; Niwa, O.; Tabei, H. *J. Electroanal. Chem.* **1988**, *256*, 269.  
 (31) Morita, M.; Longmire, M. L.; Murray, R. W. *Anal. Chem.* **1988**, *60*, 2770.  
 (32) Aoki, K.; Tokuda, K.; Matsuda, H. *J. Electroanal. Chem.* **1987**, *225*, 19.  
 (33) Aoki, K.; Tokuda, K.; Matsuda, H. *J. Electroanal. Chem.* **1987**, *230*, 61.  
 (34) Coen, S.; Cope, D. K.; Tallman, D. E. *J. Electroanal. Chem.* **1986**, *215*, 29.

RECEIVED for review August 14, 1989. Accepted November 29, 1989.

## Mediated, Anaerobic Voltammetry of Sulfite Oxidase

L. A. Coury, Jr., B. N. Oliver,<sup>1</sup> J. O. Egekeze,<sup>2</sup> C. S. Sosnoff, J. C. Brumfield, R. P. Buck, and R. W. Murray\*

Venable and Kenan Laboratories of Chemistry, University of North Carolina at Chapel Hill, Chapel Hill, North Carolina 27599-3290

The anaerobic voltammetry of the Mo/Fe enzyme, sulfite oxidase (SO), is described for the mediators cytochrome *c*, [Ru(NH<sub>3</sub>)<sub>6</sub>]<sup>3+/2+</sup>, TMPD<sup>+0</sup>, and [Co(bpy)<sub>3</sub>]<sup>3+/2+</sup>. Theory derived for steady-state voltammetric catalysis correctly predicts the observed concentration and scan-rate dependencies of the catalytic waves. The instances for which existing EC<sub>cat</sub> theories may be applied to two catalytic reactions coupled to an interfacial charge transfer are considered. The bimolecular rate constant for the reaction of [Co(bpy)<sub>3</sub>]<sup>3+</sup> with reduced SO is calculated and determined to be approximately 5 × 10<sup>4</sup> L·mol<sup>-1</sup>·s<sup>-1</sup>. The appearance of catalytic prepeaks at low sulfite concentrations is noted and the shape of corresponding *I/I* curves from chronoamperometry is examined. The analytical implications of the novel time dependence of the catalytic current under these conditions are discussed.

### INTRODUCTION

Increasing interest in electrochemical sensors capable of selective response to species of analytical importance has motivated evaluation of various enzyme systems as sensor components (1-3). Perhaps the most widely studied enzymes for this application are the oxidase enzymes (4). Under aerobic conditions, many oxidase enzyme-based sensors seek to amperometrically monitor hydrogen peroxide generated from the

reduction of dioxygen during the enzymatic reaction sequence.

Recently, ferrocene derivatives have been explored as synthetic electron acceptors for some oxidase enzymes under anaerobic conditions (5-7). Electron transfer mediators often offer the advantage of driving enzyme turnover at less extreme potentials than would otherwise be necessary if hydrogen peroxide were the species to be monitored electrometrically. Decreased operating potentials may increase selectivity by eliminating contributions to the measured response from other species undergoing redox reactions at more extreme potentials. In addition, mediators allow experiments under anaerobic conditions, circumventing problems arising from direct (nonenzymatic) oxidation of the enzymatic substrate by dissolved oxygen.

The enzyme sulfite oxidase [EC 1.8.2.1] has previously been incorporated into membranes and used in Clark-type oxygen electrode based sensors (8, 9). There are several disadvantages of the previous approaches. In order to oxidize enzymatically generated peroxide at an appreciable rate, it is necessary to polarize the working electrode at highly positive potentials, where sulfite may itself be oxidized directly. Oxidation of sulfite can lead to passivation of solid electrode surfaces, limiting their useful lifetime (10).

For sulfite sensor work, it is common to stabilize aqueous sulfite solutions from air oxidation by adding formaldehyde or glycerol as stabilizers (8, 11) to the analyte solution. These stabilizers form adducts with sulfite that are not oxygen sensitive (12), thus overcoming the inherent contradiction of employing analyte solutions containing readily oxidizable sulfite but yet saturated with oxygen. Such sensing strategies rely on dissociation of these adducts to supply sulfite for the

<sup>1</sup>Current address: British Gas, London Research Station, Fulham, London, UK SW6 2AD.

<sup>2</sup>Permanent address: Department of Chemistry and Physics, Augusta College, Augusta, GA 30910.

\* Author to whom correspondence should be addressed.

reaction of interest, however. Also, when air-equilibrated, aqueous solutions are used in amperometric sensors, the concentration of the electron acceptor (dioxxygen) cannot be easily systematically varied to alter the sensitivity of the electrode reaction. All of the above complications could be avoided if synthetic electron acceptors were used with sulfite oxidase under anaerobic solution conditions.

We present here the first report of steady-state, catalytic voltammetry of sulfite oxidase (SO) under anaerobic conditions, using several different mediators. From available theoretical treatments for steady-state electrocatalytic processes, we demonstrate the rate law for the mediated, enzymatic oxidation of sulfite to sulfate and determine the bimolecular rate constant for the reaction between the reduced enzyme and the mediator  $[\text{Co}(\text{bpy})_3]^{2+}$ . We also report the observation of voltammetric prepeaks at low sulfite concentrations and discuss the implications of this effect on the time-dependence of catalytic currents monitored in an amperometric mode. The goal of this research is fundamental characterization of the reactions of a particular enzyme to aid in the rational design of new biosensors.

## EXPERIMENTAL SECTION

**Sulfite Oxidase.** Several sources of SO were used. A commercially available preparation from chicken livers (Sigma Chemicals) was diluted 1:5 with 0.02 M Tris buffer, pH 7.5, and stored at 5 °C. The enzyme was also isolated from chicken (13) and rat livers (14) as previously described and stored frozen in small portions until needed. The purity of each batch of enzyme was determined by calculating the ratio of the UV-vis absorbance obtained at 414 nm to that at 280 nm. The absorbance at 414 nm is a Soret band arising from the cytochrome  $b_5$  center in SO (15) while the 280-nm band is a composite absorbance from all aromatic amino acid residues in solution proteins, so this ratio is a measure of the fraction of protein in solution which is SO. For all preparations used this ratio was greater than 0.6.

Molar concentrations of enzyme solutions were calculated as previously described (16). The values of the molecular weights are  $1.08 \times 10^5 \text{ g}\cdot\text{mol}^{-1}$  for the chicken enzyme (13) and  $1.14 \times 10^5 \text{ g}\cdot\text{mol}^{-1}$  for the rat enzyme (16). Enzymatic activity was monitored periodically at pH 8.5 by assaying the ferricyanide reductase activity of SO (15) at saturating concentrations of sulfite (0.4 mM) with respect to the enzyme concentration (0.8 nM). The rate of bleaching of ferricyanide (0.4 mM) was monitored at 420 nm for ca. 300 s. In these experiments, the concentration of enzyme was too low for its Soret band to interfere with the nearly coincident ferricyanide absorbance. Enzymatic activity (reported as the decrease in absorbance at 420 nm) after thawing was found to remain invariant over the course of several days ( $dA/dt = -2.2 \pm 0.2 \times 10^{-4} \text{ AU}\cdot\text{s}^{-1}$ ) when the enzyme solution was stored at 5 °C between experiments.

**Reagents.** Cytochrome  $c$  (type VI, horse heart, prepared without trichloroacetic acid, Sigma Chemicals) was found to be electroactive at edge-plane pyrolytic graphite electrodes without further purification when used shortly after receipt. Tris(2,2'-bipyridine)cobalt(II) complex, or  $[\text{Co}(\text{bpy})_3]^{2+}$ , was prepared by adding an appropriate amount of an aqueous  $\text{CoCl}_2$  solution to a 4-fold molar excess of the ligand (17). The excess ligand in solution, at the concentrations employed for voltammetric experiments (typically  $< 50 \mu\text{M}$ ), had no effect on catalytic currents, as determined by comparisons to solutions prepared from solid  $[\text{Co}(\text{bpy})_3]\text{Cl}_2$ . All other chemicals utilized were high-purity, commercially available materials. Solutions for electrochemical experiments (with the exception of stock sulfite solutions) were prepared daily in 0.02 M Tris/0.1 M KCl buffer, pH 7.5. Sodium sulfite solutions were prepared fresh every few hours in Ar-saturated buffer and kept on ice in a septum-capped vial under a blanket of Ar.

**Apparatus.** Spectrophotometry was conducted with an HP-8452A photodiode-array spectrometer interfaced to a laboratory PC. Locally constructed instruments for cyclic voltammetry (CV) and chronoamperometry (CA) were of conventional design (18). Data from CA experiments were digitized with a Summa Graphics MM1103 Bit Pad Two data tablet interfaced to a PC and ma-

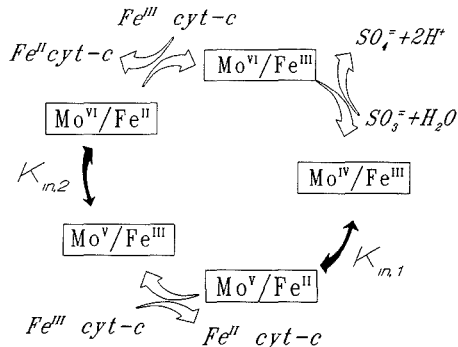


**Figure 1.** Catalytic cycle proposed operative in vivo for the SO catalyzed oxidation of sulfite to sulfate. Mo and Fe represent the enzymic molybdenum and cytochrome  $b_5$  oxidation states.

nipulated with customized software written in Borland Turbo Pascal. The coplanar arrangement of edge-plane pyrolytic graphite (EPG) working, Ag-wire quasi-reference and Pt-ring auxiliary electrodes has been described previously (19). A (0.1 M KCl) Ag/AgCl reference electrode, isolated from the protein-containing solution, replaced the internal Ag-wire reference for later experiments. The area of the EPG working electrode was determined to be  $0.0671 \pm 0.0008 \text{ cm}^2$  (10 replicate measurements; electrode repolished with  $0.05\text{-}\mu\text{m}$  alumina between determinations) by CA measurements on 10.0 mM potassium ferricyanide/1.0 M KCl solutions, assuming  $D_0 = 7.63 \times 10^{-6} \text{ cm}^2\cdot\text{s}^{-1}$  (20).

The electrochemical cell was a single-compartment tube with a threaded top into which the electrode assembly could be sealed with an O-ring bushing and which could accommodate solution volumes as small as 400  $\mu\text{L}$ . One port in the cell was fitted with a septum through which solutions could be introduced via syringe (with Teflon-tipped plunger) under anaerobic conditions, and another was fitted with a degassing tube to maintain a blanket of Ar over the solution during experiments. Care was taken to avoid bubbling Ar through solutions after introduction of enzyme (or cytochrome  $c$ ) aliquots, since this type of agitation produced frothing of the protein and resulted in loss of enzyme activity.

Cell solution volumes of between 500 and 600  $\mu\text{L}$  were most typically employed. The duration of our experiments, for example that in Figure 3 (vide infra), is sufficiently long that  $< 1\%$  depletion of sulfite occurs due to the interfacial electrocatalytic reaction. Further, the diffusion layer depth,  $\Delta$ , may be estimated (generously) as  $\Delta = 6(Dt)^{0.5}$  (21), thus with  $D = 10^{-6} \text{ cm}^2/\text{s}$  and  $t = 150 \text{ s}$  (i.e., the time needed to scan 300 mV beyond  $E^\circ$  at 2 mV/s),  $\Delta = 0.07 \text{ cm}$ . In all cases, the working electrode in our experiments greatly exceeded this distance from the cell bottom and the separation between the working and Pt-ring auxiliary electrodes was at least 3 times this distance.

## RESULTS AND DISCUSSION

**Biological Electron Acceptor of SO.** Sulfite oxidase is a molybdohemoprotein which exists as a dimer of two identical subunits (22). Each subunit contains a molybdenum cofactor comprised of a molybdopterin (23) as well as an iron porphyrin of the cytochrome  $b_5$  type (15). The biological function of the enzyme is to oxidize sulfite in a two-electron step to form sulfate in the terminal step of the oxidative degradation pathway of sulfur-containing amino acids (24).

In the resting (i.e., fully oxidized) form of the enzyme, the formal oxidation states of the Mo and Fe centers are known to be VI and III, respectively. The proposed in vivo catalytic cycle (22) is shown in Figure 1. The two-electron reduction of Mo by sulfite precedes two sequential internal electron transfers to the enzymic Fe center. The reduced iron center transfers an electron to the physiological electron acceptor, cytochrome  $c$ , following each of the two intramolecular

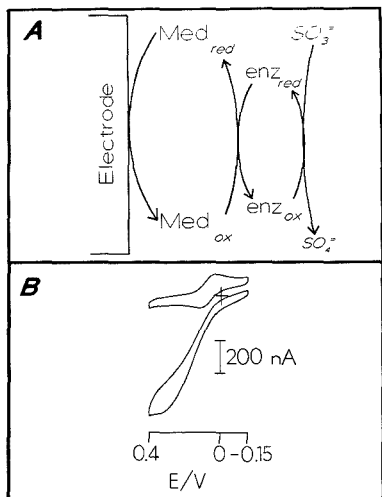


**Figure 2.** (A) Voltammetric mediation scheme for SO. (B) CVs for 94  $\mu\text{M}$  cytochrome *c* (upper curve) and for cyt *c*, 0.55  $\mu\text{M}$  SO, and 180  $\mu\text{M}$  sulfite (lower curve), both at 2  $\text{mV}\cdot\text{s}^{-1}$ . Cross represents 0 V versus Ag/AgCl and no net current.

transfers. The forward and reverse rate constants for the first intramolecular step have recently been reported as  $k_f = 310 \text{ s}^{-1}$  and  $k_r = 155 \text{ s}^{-1}$ , respectively (25), and the reported redox potentials of the enzymic metal centers at pH 7 are  $\text{Fe}^{\text{III/II}} = +0.06 \text{ V}$ ,  $\text{Mo}^{\text{VI/V}} = +0.04 \text{ V}$ , and  $\text{Mo}^{\text{IV/III}} = -0.16 \text{ V}$ , all versus NHE (26).

Initial studies in our laboratories showed no evidence of direct electron transfer between the enzyme and the EPG working electrode for any of the enzyme preparations examined. In order to demonstrate the ability to communicate electrochemically with the enzyme *in vitro*, the biological electron acceptor ferricytochrome *c* was examined as a mediator since its redox interactions with the enzyme have been well characterized. Panel A of Figure 2 depicts the mediation scheme for voltammetric experiments in which the enzyme is reduced by sulfite, the reduced enzyme transfers an electron to the oxidized form of the mediator, and the reduced mediator is reoxidized at the electrode surface.

This is formally an  $\text{EC}_{\text{cat}}\text{C}_{\text{cat}}$  (or  $\text{EC}'\text{C}'$ ) mechanism (21), since two regenerative homogeneous-phase reactions are coupled to the interfacial charge transfer. It should be noted that the scheme shown in Figure 2A is simplified from the catalytic cycle of Figure 1 in that the influence of the internal electron transfers is not shown explicitly. The possibility thus exists for at least two rate-controlling reactions to occur between the catalytic reaction steps shown in the figure.

Panel B of Figure 2 shows an example of the voltammetric response obtained for this system. The upper trace is a cyclic voltammogram of ferricytochrome *c* alone. Like the other voltammograms shown below, this trace is unchanged by adding small concentrations of SO. The lower trace is for 94  $\mu\text{M}$  cytochrome *c* in the presence of 0.55  $\mu\text{M}$  chicken SO and 180  $\mu\text{M}$  sulfite. Upon addition of SO and sulfite to the solution at open circuit, ferricytochrome *c* is reduced *in situ* to the ferro form, consuming  $1/2$  equiv of  $\text{SO}_3^{2-}$ /equiv of the cytochrome, based on the stoichiometry shown in Figure 1. The catalytic electron transfer begins when the potential scan is initiated and ferricytochrome *c* is reoxidized to the ferri- form at the electrode surface. Oxidative generation of the electron acceptor initiates the catalytic reaction sequence and a large, catalytic wave is observed due to the effective oxidation of

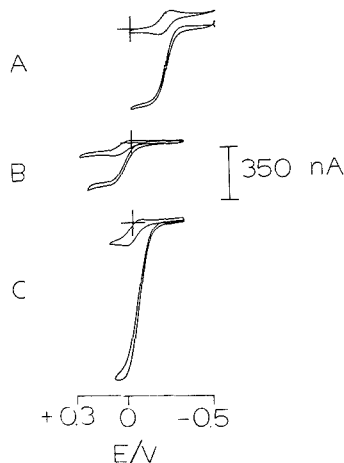


**Figure 3.** Catalytic responses for different mediators: (A)  $[\text{Ru}(\text{NH}_3)_6]^{3+/2+}$ , (B)  $[\text{Co}(\text{bpy})_3]^{3+/2+}$ , and (C)  $\text{TMPD}^{+/0}$ . Upper curve in each case is for mediator alone,  $[\text{med}] = 76 \mu\text{M}$ ; lower curves are steady-state CVs for  $[\text{med}] = 63 \mu\text{M}$ ,  $[\text{SO}] = 1.1 \mu\text{M}$ , and  $[\text{sulfite}] = 1.5 \text{ mM}$ , all at 2  $\text{mV}\cdot\text{s}^{-1}$ .

a given cytochrome molecule several times on the voltammetric time scale.

**Synthetic Electron Acceptors.** It has long been recognized that some redox dyes, ferricyanide, and dioxygen function as electron acceptors for SO (15). This fact has been exploited in several sensitive spectrophotometric assays for the activity of this enzyme as isolated from various sources (13–16). Because of the long-term instability and quasi-reversible nature of the electrooxidation of cytochrome *c*, synthetic electron acceptors should be superior for electrochemical mediation.

Our criteria for selection of redox couples to be evaluated as SO mediators were (i) well-defined, reversible voltammetry, (ii) adequate aqueous solubility, (iii) available or preparable in high purity, (iv) sufficient chemical stability in neutral, aqueous media, (v) lack of cross-reactivity with the enzymatic substrate (*viz.*, sulfite) in the absence of enzyme, and (vi) ability to accept electrons from the reduced enzyme. During the initial screening of compounds for use as mediators for this enzyme system, examples were found of couples which violated one or more of these criteria; these couples will be discussed in a future publication.

Although compounds fulfilling criteria i–iv under certain conditions have been catalogued elsewhere (27–29), candidates satisfying all of the above conditions, particularly criteria v and vi, could only be identified through trial and error. It was empirically observed in the course of experimentation, however, that mediators undergoing one-electron oxidations often displayed vastly diminished (cross-) reactivities toward sulfite, in the absence of enzyme, compared to those undergoing apparent two-electron oxidations. This was usually discerned by observing some sort of change in the voltammetry of the mediator upon addition of sulfite. In the case of  $[\text{Co}(\text{bpy})_3]^{3+/2+}$ , for example, there is no increase in the current for  $[\text{Co}(\text{bpy})_3]^{2+}$  oxidation when sulfite is added to the solution, and current attributable to the oxidation of sulfite, directly or indirectly, does not rise on the EPG electrode at potentials less positive than +0.3 V vs Ag/AgCl. No definitive basis for a priori prediction of reactivity of any given mediator toward the reduced enzyme has yet been discovered.

Figure 3 demonstrates the reactivity of several different ( $n = 1$  equiv/mol) redox couples as electron acceptors for the

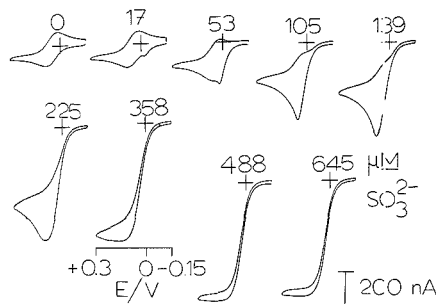


**Figure 4.** Voltammetric behavior in the presence of increasing concentrations of sulfite. Mean concentration  $[\text{Co}(\text{bpy})_3]^{2+} = 123 \mu\text{M}$  (range, 127–119  $\mu\text{M}$ ), mean  $[\text{SO}] = 1 \mu\text{M}$  (range, 1.1–1.0  $\mu\text{M}$ ),  $v = 2 \text{ mV}\cdot\text{s}^{-1}$ . Numbers by each curve refer to concentration of sulfite in  $\mu\text{M}$ ; other components underwent slight dilution during sequential addition of sulfite aliquots as indicated by figure curves.

enzyme, in this case (A)  $[\text{Ru}(\text{NH}_3)_6]^{3+/2+}$ , (B)  $[\text{Co}(\text{tpy})_3]^{3+/2+}$ , and (C)  $\text{TMPD}^{+/0}$  ( $\text{TMPD} = N,N,N',N'$ -tetramethyl-*p*-phenylenediamine). The upper curve of each pair is the CV of the mediator alone. In the lower curves, note that the concentrations of mediator, enzyme, and sulfite are identical in Figure 3. Catalytic wave heights accordingly reflect the various rates at which the mediators oxidize the reduced form of the enzyme and are *not*, as will be explained below, sensitive to the sulfite concentration in solution. The data shown were obtained by using rat liver enzyme, but results were comparable for enzyme isolated from chicken livers. The remainder of the experiments detailed in this paper employed the commercially available chicken enzyme.

Of the mediators shown in Figure 3,  $[\text{Co}(\text{bpy})_3]^{3+/2+}$  was chosen for more detailed study.  $[\text{Ru}(\text{NH}_3)_6]\text{Cl}_3$  (Figure 3A) was also well-behaved, but its most readily available form is the Ru(III) state; thus it is necessary to perform *in situ* reduction of the mediator as described for the case of ferricytochrome *c* (vide supra). This procedure may result in sloping base lines for catalytic waves in cases where the reduction is incomplete, which lowers the precision with which catalytic currents may be determined.

Although the magnitude of the catalytic response obtained with TMPD (Figure 3C) is significantly greater than that for either the ruthenium (Figure 3A) or cobalt (Figure 3B) compound, oxidized TMPD is not very stable in the presence of sulfite. A recent study employing rotated ring-disk voltammetry, spectroelectrochemistry, and digital simulation has demonstrated that the two-electron oxidation products of *N*-alkyl-substituted *p*-phenylenediamines (viz., quinonediimines) undergo rapid sulfonation reactions ( $k_f$  values ca.  $10^5 \text{ L}\cdot\text{mol}^{-1}\cdot\text{s}^{-1}$ ) in aqueous sulfite solutions (30). This may explain the observation of the present work that potential scans more positive than approximately +0.2 V (where the TMPD radical cation may start to undergo further oxidation to the tetraalkylquinonediimine) led to a rapid decrease in the observed catalytic current. Inability to scan to more positive potentials resulted in poorly defined plateaus and thus a degree of uncertainty in measured catalytic wave heights. For all of the above reasons,  $[\text{Co}(\text{bpy})_3]^{3+/2+}$ , which gave the most reproducible results of the three compounds, was utilized for the remainder of the experiments detailed below.

**Mediation of SO by  $[\text{Co}(\text{bpy})_3]^{3+/2+}$ .** Figure 4 presents CV data for mediation by  $[\text{Co}(\text{bpy})_3]^{3+/2+}$  at a series of  $\text{SO}_3^{2-}$  concentrations but nearly constant SO and mediator concentrations. At low concentrations of sulfite, the catalytic process is evidenced by a voltammetric prepeak, which arises from a rapid depletion of sulfite in the catalytic reaction layer

by the enzymatic reaction. A similar effect has recently been observed in the case of an extremely rapid mediation reaction between two proteins, one of which is able to undergo rapid heterogeneous charge transfer and the other of which is not (31). The appearance of such prepeaks in other (nonenzymatic) catalytic systems is similarly known to be indicative of a rapid kinetic step resulting in concentration polarization (i.e., time-dependent depletion) of a reactant in solution, thus we interpret the effect observed in the present case to imply a very rapid rate for the reaction between sulfite and the oxidized form of the enzyme.

The prepeak current begins to rise at the same potential as currents rise from the foot of catalytic waves observed at much higher (saturating) sulfite concentrations, but the peak potential of the prepeak moves to more positive values and merges with the mediator oxidation wave with increasing sulfite concentration. Savéant and co-workers have developed an electrocatalytic theory explaining this phenomenon for  $\text{EC}_{\text{cat}}$  mechanisms (32). The potential difference between the prepeak and the observed redox potential of the mediator ( $E^\circ$ ) is described therein as a function of the voltammetric scan rate ( $v$ ), the homogeneous rate constant for the mediator/substrate reaction ( $k$ ), and the ratio of the concentrations of the substrate to mediator (termed the excess factor) (32).

We have attempted, thus far without success, to extract quantitative kinetic results from the present system by using the Savéant theory (32) under concentration conditions where simplified  $\text{EC}_{\text{cat}}$  behavior would be expected (i.e., very low sulfite concentrations at relatively high enzyme and mediator concentrations, where rate control should be shifted to the sulfite/enzyme reaction). We note, however, that the theory does, qualitatively, predict the features of the observed voltammetry (e.g., decreased splitting between prepeak and mediator oxidation peak with increasing  $v$ ). Trace amounts of oxygen present in solution due to injection of (nondessable) enzyme aliquots would be expected to consume a sizable portion of the sulfite injected into the cell when working at low sulfite concentrations; thus such uncertainties in actual concentrations may contribute to difficulties in quantitation.

As the concentration of sulfite is increased in Figure 4, the prepeak merges with the mediator oxidation wave and the reverse (reduction) peak for the mediator begins to disappear. The concentration of sulfite needed to effect loss of the reduction peak (that is, produce a catalytic reaction which is fast on the potential sweep time scale) depends on the concentration of both enzyme and mediator. For the data shown, concentrations of enzyme and mediator were nearly constant throughout the series since only small aliquots of a concentrated sulfite solution (9.9 mM) were added to avoid dilution effects.

At the highest sulfite concentrations in Figure 4, a steady-state catalytic wave is obtained. Further increases in sulfite concentration do not increase currents but merely serve to dilute the enzyme and mediator (cf. curves for 488 and 645  $\mu\text{M}$   $\text{SO}_3^{2-}$ ). We interpret this as indicating that *rate control in these voltammograms resides entirely with the reduced-enzyme/mediator reaction*. The high concentration of sulfite in this case as well as in the examples shown in Figure 3 serves to ensure that oxidized enzyme generated by the first catalytic step in Figure 2A is reduced virtually instantaneously.

**Elucidation of Rate Law.** Although the formal concentration of enzyme is quite low with respect to that of the mediator in Figure 4 (1  $\mu\text{M}$  versus 120  $\mu\text{M}$ ), we postulate that rapid reduction of enzyme by sulfite results in effective pseudo-first-order reaction conditions: mediator and a kinetically inexhaustible pool of reduced enzyme. Thus, at saturation levels of sulfite, the system behaves as a two-com-

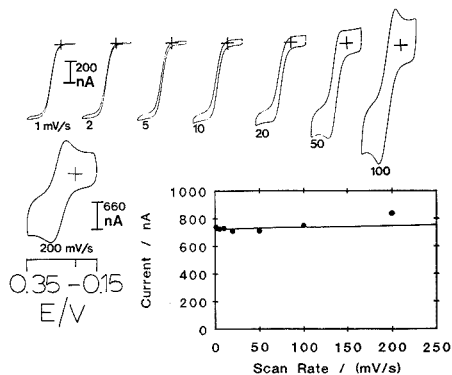


**Figure 5.** Scan rate study for steady-state catalytic wave.  $[\text{Co}(\text{bpy})_3^{2+}] = 118 \mu\text{M}$ ,  $[\text{SO}] = 0.52 \mu\text{M}$ ,  $[\text{sulfite}] = 1.4 \text{ mM}$ . Numbers by curves are scan rates in  $\text{mV}\cdot\text{s}^{-1}$ .

ponent catalytic reaction chain, and existing theory for the steady-state  $\text{EC}_{\text{cat}}$  response (21) may be applied. This is despite the fact that the theory was originally developed for the situation where the formal solution concentrations are pseudo-first-order in mediator (i.e., "flooded" with species being mediated). The presence of a second coupled and rapid catalytic reaction that regenerates reduced enzyme in the present case indicates a different regime of conditions under which this theory may be applied.

The theory of steady-state voltammetric catalysis has been well described (21, 33-35). Derived in terms of a catalytic reaction layer, the steady-state current may be expressed by

$$i_{\text{ss}} = nFA\mu k C_{\text{med}}^* C_{\text{enz}}^* \quad (1)$$

where  $C_{\text{med}}^*$  and  $C_{\text{enz}}^*$  are the solution concentrations of mediator and reduced enzyme in  $\text{mol}\cdot\text{cm}^{-3}$ , respectively,  $k$  is the homogeneous rate constant ( $\text{cm}^3\cdot\text{mol}^{-1}\cdot\text{s}^{-1}$ ),  $\mu$  is the catalytic reaction layer thickness (cm), and the other quantities have their usual significances (21). It may be shown (33) that the reaction layer thickness,  $\mu$ , is expressed by

$$\mu = (D_{\text{med}}/kC_{\text{enz}}^*)^{0.5} \quad (2)$$

where  $D_{\text{med}}$  is the diffusion coefficient of the mediator (assumed to be identical for the oxidized and reduced forms). Substitution of eq 2 into eq 1 yields the well-known relation (21, 34)

$$i_{\text{ss}} = nFAC_{\text{med}}^*(D_{\text{med}}kC_{\text{enz}}^*)^{0.5} \quad (3)$$

This expression predicts a scan-rate-independent, steady-state current which is proportional to the mediator concentration and to the square root of the concentration of the reduced enzyme. It should be noted that the above expression of current is equivalent to a homogeneous solution rate law which is first order in both reactants (36)

$$-d[\text{enz}_{\text{red}}]/dt = -d[\text{med}_{\text{ox}}]/dt = k[\text{enz}][\text{med}] \quad (4)$$

where  $k'$  is expressed in  $\text{L}\cdot\text{mol}^{-1}\cdot\text{s}^{-1}$  and the brackets denote molar concentrations. Determination of the rate constant from the steady-state catalytic current follows in a straightforward manner from eq 3, provided the proper concentration dependencies and lack of scan rate dependence may be verified.

**Scan Rate Independence of  $i_{\text{ss}}$ .** Figure 5 shows catalytic current data that are independent of scan rate acquired over a ca. 2 order of magnitude range of scan rates at saturating concentrations of sulfite. Well-defined, steady-state waves of equal magnitude are obtained at scan rates up to  $20 \text{ mV}\cdot\text{s}^{-1}$  for this set of solution concentrations. At higher scan rates, the interfacial charge transfer is driven too rapidly for the

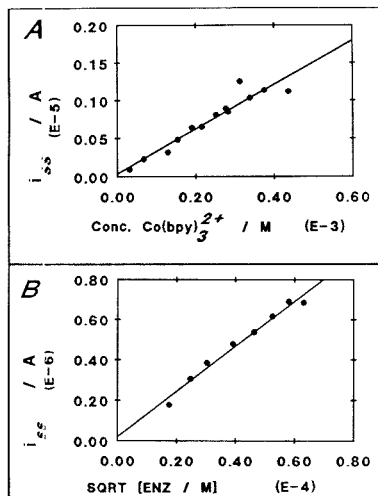


**Figure 6.** Concentration dependencies of steady-state catalytic currents at  $2 \text{ mV}\cdot\text{s}^{-1}$ : (A)  $[\text{SO}] = 1.0 \mu\text{M}$ ,  $[\text{sulfite}] = 2.5 \text{ mM}$ ; (B)  $[\text{Co}(\text{bpy})_3^{2+}] = 110 \mu\text{M}$ ,  $[\text{sulfite}] = 2.1 \text{ mM}$ .

regenerative solution reaction to counterbalance, and non-steady-state currents (i.e., voltammetric peaks) become apparent. A scan rate of  $2 \text{ mV}\cdot\text{s}^{-1}$  was (arbitrarily) chosen for the remainder of the experiments.

**Determination of Concentration Dependencies of  $i_{\text{ss}}$  and  $k$ .** Figure 6A presents steady-state current data obtained with different  $[\text{Co}(\text{bpy})_3^{2+}]$  but constant enzyme ( $1.0 \mu\text{M}$ ) and sulfite ( $2.5 \text{ mM}$ ) concentrations. Each data point represents a separate experiment (i.e., repolished electrode, new solution). As is evident, there is a linear relation between catalytic current and Co complex concentration. The slope of the regression calculated for the data is  $2.9 \times 10^{-3} \text{ A}\cdot\text{L}\cdot\text{mol}^{-1}$ , which corresponds to a rate constant calculated by eq 3 of  $5 \times 10^4 \text{ L}\cdot\text{mol}^{-1}\cdot\text{s}^{-1}$ .

Figure 6B shows data from an analogous set of experiments conducted at constant Co complex ( $110 \mu\text{M}$ ) and sulfite ( $2.1 \text{ mM}$ ) concentrations but with varying enzyme concentrations. The square-root dependence of current on enzyme concentration predicted by eq 3 is confirmed, which supports the rate law proposed for the process by eq 4. Regression of steady-state current onto square root of enzyme concentration yields a slope of  $3.5 \times 10^{-4} \text{ A}\cdot\text{L}^{0.5}\cdot\text{mol}^{-0.5}$ . This result corresponds to a calculated rate constant of  $6 \times 10^4 \text{ L}\cdot\text{mol}^{-1}\cdot\text{s}^{-1}$ , which is in good agreement with the number calculated from Figure 6A. It may also be noted that since sulfite is present in vast excess in these experiments, consumption of small amounts of sulfite through oxidation by trace oxygen in solution should have no effect on calculated rate constants. These data, however, do not permit elucidation of the site of reactivity of the mediator with the enzyme (i.e., the Mo or Fe center), and even the possibility of dual site reactivity cannot be discounted.

In collection of the above data, attempts were also made to conduct similar experiments through sequential additions of small volumes of a (relatively) concentrated solution of either the mediator or the enzyme. This approach was unsuccessful, however, resulting in catalytic current/concentration curves that exhibited negative deviations from linearity at high concentrations of the added reagent. This trend persisted even after correcting the data for the minor dilution effects occurring by using eq 3, above. This difficulty may

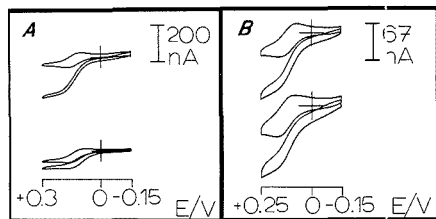


**Figure 7.** Effect of stabilizers on catalytic waves: (A) formaldehyde stabilizer; (B) glycerol stabilizer. Upper pair of curves in each panel is  $[\text{Co}(\text{bpy})_3^{2+}] = 44 \mu\text{M}$ ,  $[\text{SO}] = 0.38 \mu\text{M}$ ,  $v = 2 \text{ mV}\cdot\text{s}^{-1}$  with (larger curve) and without (smaller curve) sulfite  $[\text{sulfite}] = 524 \mu\text{M}$  in panel A,  $358 \mu\text{M}$  in panel B. Lower pair of curves in each panel is the same but with added formaldehyde (2 mM, panel A) and glycerol (0.51 mM, panel B).

be attributable to some combination of accumulation of systematic errors (volume or concentration inaccuracies), loss of mediator (e.g., ligand dissociation and subsequent adsorption on surfaces in the cell), or cumulative fouling of the electrode from sulfite through repetitive potential scanning. Sulfite itself undergoes electrooxidation at fairly positive potentials at EPG electrodes ( $E_{\text{peak,ox}} \approx +0.5 \text{ V}$ ), but at the high concentrations used in the above studies, there may have been significant enough direct oxidation of sulfite at the positive scan limit (+0.3 V) to foul the electrode over an extended period of time.

**Effects of Sulfite Stabilizers in Solution.** As discussed above, species that form adducts with sulfite and prevent its oxidation by  $\text{O}_2$  are often employed in sensor work. The data in Figure 7 demonstrate the effects of two such stabilizers on catalytic voltammetry observed with  $[\text{Co}(\text{bpy})_3]^{2+}$  mediator. The upper pair of curves in each panel shows CVs for the catalytic system in the absence of stabilizers. The lower pair of curves shows the effects of formaldehyde (stock sulfite solution stabilized with 0.1% (v/v) HCHO, panel A) and glycerol (stock sulfite solution 0.1% (v/v) in glycerol, panel B) on the voltammetric responses. In the case of addition of formaldehyde (Figure 7A, bottom curve), the catalytic response is both smaller and non steady state. This is evidently due to slow dissociation of the formaldehyde-sulfite adduct on the voltammetric time scale. By contrast, there is no noticeable effect from the addition of glycerol (Figure 7B, bottom curve), which may be attributable to either a difference in adduct dissociation rate or (less likely) the small 4-fold difference in the formal concentrations used.

For electrochemical kinetic studies of the enzyme, it is hence undesirable to use stabilizers like formaldehyde since sulfite adduct dissociation may assume at least partial rate control in some situations. Conversely, in an analytical setting, addition of such a stabilizing agent may be beneficial for extending the dynamic range of the analysis (vide infra). Since a sensor employing this enzyme would be insensitive to sulfite above that amount resulting in the appearance of a steady-state response, adduct formation and the resulting shift to a non-steady-state response could effectively extend the dynamic range of the sensor to higher formal sulfite solution concentrations. Dilution of the sulfite-containing analyte solution would, however, achieve the same end result.

**Characteristics of Amperometric Responses.** Figure 8 shows results for chronoamperometric experiments in which the potential was stepped from  $-0.15 \text{ V}$  ( $[\text{Co}(\text{bpy})_3]^{2+}$  state) to  $+0.23 \text{ V}$  ( $[\text{Co}(\text{bpy})_3]^{3+}$  state) at time = 0 s. From lowest to uppermost, the individual  $i/t$  curves in the main figure correspond to increasing sulfite concentrations at essentially constant enzyme and  $[\text{Co}(\text{bpy})_3]^{2+}$  concentrations (2  $\mu\text{M}$  and 160  $\mu\text{M}$ , respectively). The lower sulfite concentrations would

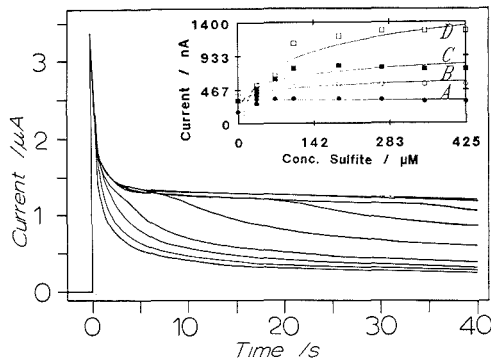


**Figure 8.** Catalytic chronoamperograms:  $E_i = -0.15 \text{ V}$ ,  $E_{\text{step}} = +0.225 \text{ V}$ ;  $[\text{Co}(\text{bpy})_3^{2+}] = 160 \mu\text{M}$ ,  $[\text{SO}] = 2 \mu\text{M}$ . Concentrations of sulfite, from lowest to upper curve: 0, 35.5, 70.4, 105, 189, 270, 349, 425 and 498  $\mu\text{M}$ . Inset: Currents monitored 10 s after potential step plotted as a function of  $\text{SO}_3^{2-}$  concentration. Concentrations  $[\text{Co}(\text{bpy})_3^{2+}]$ ,  $[\text{SO}]$  were as follows: (A) 80  $\mu\text{M}$ , 0.24  $\mu\text{M}$ ; (B) 80  $\mu\text{M}$ , 2.1  $\mu\text{M}$ ; (C) 160  $\mu\text{M}$ , 0.24  $\mu\text{M}$ ; (D) 160  $\mu\text{M}$ , 2.1  $\mu\text{M}$ . Lines plotted through data are logarithmic fits presented only to guide the eye in distinguishing data sets.

result in prepeaks in analogous voltammetric experiments, but in an amperometric mode the result is observation of higher currents at short times before a transition to a lower level at longer times.

High sulfite concentrations yield steady-state currents shortly after the potential step is imposed. The  $i/t$  curves at lower sulfite concentrations deviate from the upper, steady-state traces at high sulfite concentrations because sulfite becomes depleted in the catalytic reaction layer. At the moment monitored currents begin to decrease, the concentration-distance profiles ( $2I$ ) for sulfite begin to move out into bulk solution. In the case of the steady-state currents observed at higher sulfite concentrations, these profiles are stationary throughout the time course of the potential step, since the rate of consumption of sulfite in the reaction layer is offset by diffusion of sulfite from the bulk.

The analytical implications of the  $i/t$  behavior in Figure 8 are manifest both in the time dependence of the dynamic range of the experiment and in the change in sensitivity with respect to sulfite concentration as a function of time. For example, at approximately 5 s after the potential step, the upper five  $i/t$  curves are indistinguishable, whereas at 40 s, all but the uppermost two curves are resolved. This illustrates the point that if the enzyme system under investigation were incorporated into a sensor, the resulting dynamic range would be maximal at long times (>40 s, in this example).

Conversely, the sensitivity to sulfite (i.e., the current monitored at a given concentration of sulfite) is highest at short times for those concentrations of sulfite that do not result in observation of a steady-state current. In experiments such as these, where a synthetic electron acceptor is used, it would be impractical to attempt to measure the height of the prepeak observed in a voltammetric experiment due to the sloping base line and poor resolution of the prepeak from the oxidation peak of the mediator. Potential-step methods such as chronoamperometry are hence more reliable for quantitation of sulfite, but as illustrated above, the time after the potential step (or, for example, introduction of sulfite in a hydrodynamic sensor application) at which the current is monitored is critical to the success of the determination. In principle, calibration curves could be generated for a series of different times, and the optimal time for determining the sulfite concentration from the current could then be chosen.

Alternatively,  $i/t$  curves might be integrated over the duration of a potential step experiment and the total charge determined correlated with sulfite concentration.

The inset of Figure 8 shows current values monitored 10 s after the potential step for a series of sulfite concentrations in experiments conducted as described for the main figure. These curves differ in the concentrations of  $[\text{Co}(\text{bpy})_3]^{2+}$  and enzyme employed in each experiment. Data set D is taken from the experiments shown in Figure 8, while data set B, for example, was extracted from a set of  $i/t$  curves for which the enzyme concentration was identical with that in set D, but for which the  $[\text{Co}(\text{bpy})_3]^{2+}$  concentration was 50% lower. In general, lower enzyme or mediator concentrations result in the appearance of steady-state curves at lower solution sulfite levels, thus both sensitivity and dynamic range are increased at higher enzyme and mediator concentrations.

### CONCLUSIONS

The mediated voltammetry of sulfite oxidase under anaerobic conditions has been characterized for the first time. The compounds cytochrome *c*,  $[\text{Ru}(\text{NH}_3)_6]^{3+/2+}$ ,  $\text{TMPD}^{+/0}$ , and  $[\text{Co}(\text{bpy})_3]^{3+/2+}$  have been demonstrated to function as electron acceptors on the voltammetric time scale. Although Michaelis-Menten kinetic treatments are often used in attempts to describe oxidase enzyme systems, electrocatalytic theory is demonstrated to properly predict the scan rate dependence and the dependencies of steady-state limiting currents on SO and mediator concentrations for the above listed electron acceptors. This allows the calculation of the chemical rate constant for the reaction between the reduced form of the oxidase and the mediator, as demonstrated for the case of  $[\text{Co}(\text{bpy})_3]^{3+}$ . The advantages in the use of mediators in the absence of oxygen are noted. The presence of prepeaks at low sulfite concentrations is shown to be manifest as a novel time dependence of currents monitored in potential step experiments. The implications of this unusual behavior are noted in terms of the dynamic range and sensitivity which would be expected for a sensor incorporating this enzyme system. Future work will be directed toward elucidating the characteristics of different mediators that influence the rate at which they react with the reduced enzyme.

### ACKNOWLEDGMENT

The authors are grateful to K. V. Rajagopalan and J. L. Johnson of the Department of Biochemistry, Duke University Medical Center, Durham, NC, for providing enzyme samples and for valuable technical advice and assistance. Turbo Pascal programs used in driving the digitizer board and in data manipulation were written and generously provided by Timothy T. Wooster of the University of North Carolina at Chapel Hill.

### LITERATURE CITED

- (1) Albery, W. J.; Craston, D. H. In *Biosensors: Fundamentals and Applications*; Turner, A. P. F., Karube, I., Wilson, G. S., Eds.; Oxford

- University Press: Oxford, UK, 1987; pp 180-210.
- (2) Pickup, J. C., In *Applied Biosensors*; Wise, D. L., Ed.; Butterworths: Boston, MA, 1989; pp 227-247.
- (3) Frew, J. E.; Hill, H. A. O. *Philos. Trans. R. Soc. London, B* **1987**, *337*, 95-106.
- (4) Schmidt, H.-J.; Guenther, H. *Philos. Trans. R. Soc. London, B* **1987**, *337*, 73-94.
- (5) Cass, A. E. G.; Davis, G.; Green, M. J.; Hill, H. A. O. *J. Electroanal. Chem.* **1985**, *190*, 117-127.
- (6) McNeil, C. J.; Spoor, J. A.; Cocco, D.; Cooper, J. M.; Bannister, J. V. *Anal. Chem.* **1989**, *61*, 25-29.
- (7) Davis, G. *Biosensors* **1985**, *1*, 161-178.
- (8) Fonong, T. *Anal. Chim. Acta* **1986**, *184*, 287-290.
- (9) Smith, V. J. *Anal. Chem.* **1987**, *59*, 2256-2259.
- (10) Comtat, M.; Mahenc, J. *Bull. Soc. Chim. Fr.* **1969**, *11*, 3862-3869.
- (11) Prants, D. M.; Meyerhoff, M. E. *Anal. Chim. Acta* **1989**, *217*, 123-133.
- (12) Lindgren, M.; Cedergrén, A.; Lindberg, J. *Anal. Chim. Acta* **1982**, *141*, 279-286.
- (13) Kessler, D. L.; Rajagopalan, K. V. *J. Biol. Chem.* **1972**, *247*, 6566-6573.
- (14) Kessler, D. L.; Johnson, J. L.; Cohen, H. J.; Rajagopalan, K. V. *Biochim. Biophys. Acta* **1974**, *334*, 86-96.
- (15) Cohen, H. J.; Fridovich, I. *J. Biol. Chem.* **1971**, *246*, 359-366, 367-373.
- (16) Johnson, J. L.; Rajagopalan, K. V. *J. Clin. Invest.* **1976**, *58*, 543-550.
- (17) Chen Y.-W.; Santhanam, K. S. V.; Bard, A. J. *J. Electrochem. Soc.* **1982**, *129*, 61-66.
- (18) Woodward, W. S.; Rocklin, R. D.; Murray, R. W. *Chem. Biomed. Environ. Instrum.* **1979**, *9*, 95-105.
- (19) Oliver, B. N.; Egekeze, J. O.; Murray, R. W. *J. Am. Chem. Soc.* **1988**, *110*, 2321-2322.
- (20) Von Stackelberg, M.; Pilgram, M.; Toome, V. Z. *Elektrochem.* **1953**, *57*, 342-350.
- (21) Bard, A. J.; Faulkner, L. R. *Electrochemical Methods: Fundamentals and Applications*; Wiley: New York, 1980.
- (22) Rajagopalan, K. V. In *Molybdenum and Molybdenum-Containing Enzymes*; Coughlan, M., Ed.; Pergamon Press: Oxford, UK, 1980; pp 241-272.
- (23) Krarner, S. P.; Johnson, J. L.; Ribeiro, A. A.; Millington, D. S.; Rajagopalan, K. V. *J. Biol. Chem.* **1987**, *262*, 16357-16363.
- (24) Johnson, J. L.; Rajagopalan, K. V. *J. Clin. Invest.* **1976**, *58*, 551-556.
- (25) Kipke, C. A.; Cusanovich, M. A.; Tollin, G.; Sunde, R. A.; Enemark, J. H. *Biochemistry* **1988**, *27*, 2918-2926.
- (26) Crarner, S. P.; Gray, H. B.; Scott, N. S.; Barber, M.; Rajagopalan, K. V. In *Molybdenum Chemistry of Biological Significance*; Newton, W. E., Otsuka, S., Eds.; Plenum Press: New York, 1980; pp 157-168.
- (27) Fultz, M. L.; Durst, R. A. *Anal. Chim. Acta* **1982**, *140*, 1-18.
- (28) Szentirmay, R.; Yeh, F.; Kuwana, T. In *Electrochemical Studies of Biological Systems*; ACS Symposium Series 38; Sawyer, D. T., Ed.; Washington, DC, 1977; pp 143-169.
- (29) Johnson, J. M.; Halsall, H. B.; Heineman, W. R. *Anal. Biochem.* **1983**, *133*, 186-189.
- (30) Kobayashi, H.; Yoshida, K.; Takano, H.; Ohno, T.; Mizusawa, S. *J. Imaging Sci.* **1988**, *32*, 90-94.
- (31) Barker, P. D.; Hill, H. A. O.; Walton, N. J. *J. Electroanal. Chem.* **1989**, *260*, 303-326.
- (32) Andrieux, C. P.; Blocman, C.; Dumas-Bouchiat, J. M.; Halla, F.; Savéant, J. M. *J. Electroanal. Chem.* **1980**, *113*, 19-40.
- (33) Delahay, P. *New Instrumental Methods in Electrochemistry*; Interscience: New York, 1954; R. E. Krieger Publishers: Huntington, NY, 1980; pp 100-113.
- (34) Savéant, J. M.; Vianello, E. *Electrochim. Acta* **1965**, *10*, 905-920.
- (35) Nicholson, R. S.; Shain, I. *Anal. Chem.* **1964**, *36*, 706-723.
- (36) Albery, W. J.; Bartlett, P. N.; Cass, A. E. G. *Philos. Trans. R. Soc. London, B* **1987**, *337*, 107-119.

RECEIVED for review August 11, 1989. Accepted November 27, 1989. This research was sponsored in part by grants from the National Science Foundation and the North Carolina Biotechnology Center.

# Gold and Platinum Poly(chlorotrifluoroethylene) Composite Electrodes

Steven L. Petersen and Dennis E. Tallman\*

Department of Chemistry, North Dakota State University, Fargo, North Dakota 58105

**Two new poly(chlorotrifluoroethylene) (Kel-F)/precious metal composite electrodes are described which contain 14% metal by volume, the Kelgold (Kel-F/gold) and Kelplat (Kel-F/platinum) electrodes. The results of four-probe conductivity measurements on these highly conductive, consolidated composites are reported. The surfaces of these composite electrodes consist of ensembles of active sites (packed metal-particle regions). Scanning electron microscopic observations of the surface morphologies of Kelgold and Kelplat electrodes are discussed, including the influences of certain properties of the conductor powder and the fabrication pressure on active site morphologies. Cyclic voltammetry demonstrates enhanced current densities for these composite electrodes (relative to the corresponding macro disk electrodes). Active areas and large active perimeters for Kelgold and Kelplat electrodes are determined from short-time chronoamperometric data. The chronoamperometric data for Kelgold and Kelplat electrodes over the time range of ca. 10 ms to 100 s is shown to conform to existing microelectrode ensemble theory.**

## INTRODUCTION

Over the past three decades, a variety of composite electrodes have been developed for electroanalytical applications. These electrodes can be categorized into three groups based on their method of fabrication. First, there are electrodes fabricated by impregnating a porous conductor with an insulating material as with the various impregnated carbon-rod electrodes (1) and the epoxy-impregnated reticulated-vitreous-carbon electrode (2). A second group consists of electrodes fabricated by uniformly dispersing a conductor in a viscous liquid as with the various carbon paste electrodes (3) or in a liquid resin (which is subsequently polymerized) as with the epoxy/graphite (4), epoxy/carbon fiber (5), polystyrene/carbon black (6), and polystyrene/carbon fiber (7) electrodes. The composites in this group, which will be referred to as dispersed composites, have a random distribution of conductor particles (or fibers) within the continuous insulator matrix and usually contain a high volume percent of conductor. Belonging to the third group are electrodes fabricated by mixing a powdered conductor with a powdered polymer and compression molding the mixture as with the Teflon/graphite (8), polyethylene/graphite (9), Kel-F/graphite (10), and Kel-F/precious metal (11-13) electrodes (Kel-F is a 3M Company trade name for poly(chlorotrifluoroethylene)). The composites in this group, which will be referred to as consolidated composites (14), have a network of conductor particles pervading the polymer matrix. The continuity of this network can be maximized by minimizing the time that the polymer is molten during molding and by using conductor particles that are small relative to the polymer particles. How this particle size discrepancy promotes the continuity of the conductor particle network has been discussed previously in relation to our Kel-F/silver composite (11, 12).

Nearly all of the composite electrodes classified above contain some form of carbon as the conducting phase. We have recently described three new precious metal composite electrodes: the Kel-F/silver, Kel-F/gold, and Kel-F/platinum electrodes, hereafter referred to as Kelsil, Kelgold, and Kelplat electrodes, respectively (11, 13). To our knowledge, these are the first silver, gold, and platinum composite electrodes developed for electroanalytical application. Kel-F/precious metal composites are consolidated composites and, as a result, have certain advantages over dispersed composites. For instance, a consolidated composite has a highly connected network of conductor particles, leading to higher electrical conductivity than obtained with dispersed composites having the same volume percent conductor (vide infra). Consequently, conducting consolidated composites with low volume percent conductor can be fabricated, an advantage when working with precious metal composites. For example, we have fabricated conducting Kel-F/silver composite electrodes with as little as 10% silver by volume (11). Furthermore, the necessity of maintaining dispersion of the conductor particles during the curing of a dispersed composite is avoided with consolidated composites.

In this paper, we present the results of optical and scanning electron microscopic observations of and electrochemical measurements at Kelgold and Kelplat electrodes. In addition, we report the results of four-probe conductivity measurements for all three precious metal composites. As with Kelsil electrodes (11), Kelplat and Kelgold electrodes exhibit behavior typical of microelectrode ensembles, including enhanced current densities and high perimeter-to-area ratios. In addition, they possess high electrical conductivities and are mechanically robust and machinable.

## EXPERIMENTAL SECTION

**Reagents and Materials.** All chemicals were of reagent grade. Hexammineruthenium(III) chloride (AESAR) and potassium ferricyanide (Mallinckrodt) were used as received. All solutions were prepared from Milli-Q water (Millipore Corp.). A diffusion coefficient of  $6.5 \times 10^{-6} \text{ cm}^2/\text{s}$  was determined for  $\text{Ru}(\text{NH}_3)_6^{3+}$  in 1.00 M  $\text{KNO}_3$  at 25 °C at a Au macro disk electrode. An average diffusion coefficient of  $7.3 \times 10^{-6} \text{ cm}^2/\text{s}$  was determined for  $\text{Fe}(\text{CN})_6^{3-}$  in 1.00 M  $\text{KCl}$  at 20-23 °C at a Pt macro disk electrode. The gold disk electrode was made by sealing a 2.0 mm diameter gold wire (99.9985%, AESAR) in epoxy (Dow Epoxy Resin 332 with tetraethylenepentamine as the curing agent). The platinum disk electrode was a 6.5 mm diameter Pt inlay electrode (Corning).

Kelgold and Kelplat electrodes were prepared from 1.8-2.3  $\mu\text{m}$  gold (99.95%, AESAR) and 0.5-2.5  $\mu\text{m}$  platinum (99.9%, AESAR), respectively, by the method previously described for Kelsil (11). In short, this method consists of an ambient temperature vacuum prepress followed by a hot compression molding step. Some electrodes were fabricated in the usual manner with a 500-800 lb (2200-3600 N) prepress, while others were given a 10 000 lb (44 000 N) prepress (all other steps were as described previously (11)). These different electrodes will be referred to as LP (low pressure) and HP (high pressure) composites, respectively, (i.e., LP-Kelgold and HP-Kelgold). All Kelgold and Kelplat electrodes used in this work contained 14.0% metal by volume (corresponding to 59.9% gold or 62.4% platinum by weight); subsequent references to electrode composition refer to volume percent conductor. The composite electrodes employed in this work had

\* To whom correspondence should be addressed.

diameters of 0.250 in. (6.35 mm) and thus had (total) geometric areas of 0.317 cm<sup>2</sup>. Active areas were estimated by multiplying the geometric area by the metal volume fraction.

**Instrumentation.** Optical and scanning electron microscopies were performed on an Olympus Model SZH microscope and a Jeol Model JSM-35 scanning electron microscope, respectively, at the North Dakota State University Electron Microscopy Laboratory.

Four-probe conductivity measurements were made with a homemade Plexiglas jig which allowed voltage probe spacings of 2.0, 3.0, and 4.0 mm. Current was supplied by a low-voltage power supply in series with a 5- $\Omega$ , 3-W resistor to facilitate control of the applied current, which was monitored with a 3<sup>1</sup>/<sub>2</sub> digit digital multimeter. The voltage drop across a portion of a composite pellet was monitored with copper wire voltage probes, the tips of which had been sanded to points. The voltage probes were in turn connected to the inputs of an instrumentation amplifier (15) whose output was monitored with a 4<sup>1</sup>/<sub>2</sub> digit digital multimeter.

Cyclic voltammetry and potential-step chronoamperometry were performed with a recently constructed computer-based wide-bandwidth potentiostat (16). This system employs bidirectional direct memory access such that control of the applied potential and sampling of the current are performed totally under hardware control. The counter electrodes were glass-sealed platinum coil electrodes. The reference electrodes (against which all potentials are reported) were Ag/AgCl/3.5 M KCl and were isolated from the cells by salt bridges containing the supporting electrolyte.

**Procedure.** Four-probe conductivity measurements were performed in the following fashion. Once a composite pellet had been positioned in the four-probe conductivity jig and all four probes connected, a single run consisted of (1) ensuring electrical continuity between the voltage probes using an ohmmeter, (2) setting the current to a desired value and measuring the resulting voltage drop between the voltage probes, and (3) repeating step 2 for typically eight additional current settings. The resulting data was used in an Ohm's law plot to calculate a resistance which (along with the cross-sectional area of the pellet and the voltage probe spacing) was used to calculate the conductivity of the composite. For a given pellet, ca. 10 such runs were typically performed at each of two different voltage probe spacings, with each run being performed on a different region of the pellet.

For cyclic voltammetry and potential-step chronoamperometry, solutions were deoxygenated with purified, solvent-presaturated nitrogen prior to each experiment and the solution was blanketed with nitrogen during measurement. Experiments were performed with a dual cell arrangement. Usually, the sample cell was thermostated at 20 or 25 °C, while the background cell was left at room temperature (typically within 1 °C of the sample cell). To avoid vibrations, water circulation was interrupted for runs lasting longer than 80 s. For chronoamperometry at platinum electrodes, both cells were left at room temperature (20–23 °C). Prior to each cyclic voltammetry or chronoamperometry experiment, electrodes were polished with 0.3- $\mu$ m alumina on Mastertex polishing cloth (Buehler), polished on bare cloth to remove residual alumina (11), rinsed thoroughly with water, transferred to the background cell, and the potential cycled 10 times at 100 mV/s between the potential limits of the upcoming experiment. The experiment then consisted of recording and averaging several background runs, transferring the electrode to the sample cell, and recording and averaging several sample runs.

## RESULTS AND DISCUSSION

**Microscopy.** The relative particle sizes of the conductor and Kel-F powders strongly influence the continuity of the conductor network in these consolidated composites (11). Other properties of the conductor powder that may affect the continuity of this network are the shape of the particles and the particle size distribution. Figure 1 shows scanning electron micrographs (SEMs) of typical samples of the Au and Pt powders used to fabricate Kelgold and Kelplat composites. As shown in Figure 1A, the Au particles are spherical and quite monodisperse. Analysis of a number of samples gave a Au particle size range of 0.5–2.5  $\mu$ m, with most particles being in the range of 1.6–2.0  $\mu$ m. On the other hand, the Pt particles

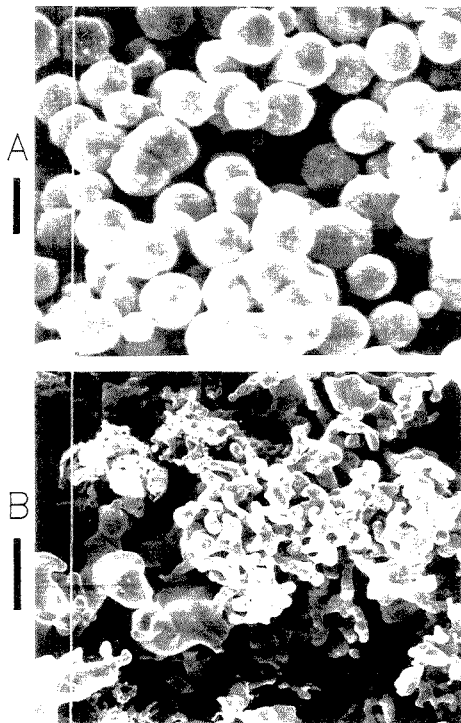


**Figure 1.** Scanning electron micrographs of the (A) gold (bar = 2  $\mu$ m) and (B) platinum (bar = 10  $\mu$ m) powders used to fabricate Kelgold and Kelplat composite materials.

(Figure 1B) are very irregular in shape and range from 1 to 20  $\mu$ m in size, with ca. 25% of the particles being larger than 10  $\mu$ m. Optical microscopy has shown that the Kel-F particles used to fabricate these composites range in size from 20 to 100  $\mu$ m with ca. 50% of the particles being 20–30  $\mu$ m in size. During mixing of the composite powders, the smaller Au particles should more readily fit within the interstitial space between Kel-F particles than do the larger Pt particles. Additionally, the much more spherical and monodisperse Au particles should pack more tightly within these interstitial spaces than do the Pt particles. Therefore, Kelgold might be expected to have a more highly connected conductor network than Kelplat, an expectation borne out by microscopy and conductivity measurements.

Scanning electron micrographs of typical surface regions of LP-Kelgold and LP-Kelplat electrodes are shown in Figures 2A and 2B, respectively. The gray regions are metal and the black and white regions are Kel-F, consistent with our earlier SEM data for Kelsil (11, 12). The assignment of these regions has been confirmed by energy-dispersive X-ray analysis (EDXA) (not shown). The complex shapes of the packed metal-particle regions (active sites) on LP-Kelgold and LP-Kelplat electrodes are similar to those observed on LP-Kelsil (11, 12). Many sites have main bodies ca. 30–50  $\mu$ m in diameter, with appendages of various lengths and ca. 10–20  $\mu$ m in width. Other sites are bandlike, with widths of ca. 10–30  $\mu$ m and lengths of ca. 100–200  $\mu$ m. The active sites are separated from each other by ca. 1–3 site diameters. Figures 2B and 3B show enlarged views of individual active sites on LP-Kelgold and LP-Kelplat, respectively. The active sites

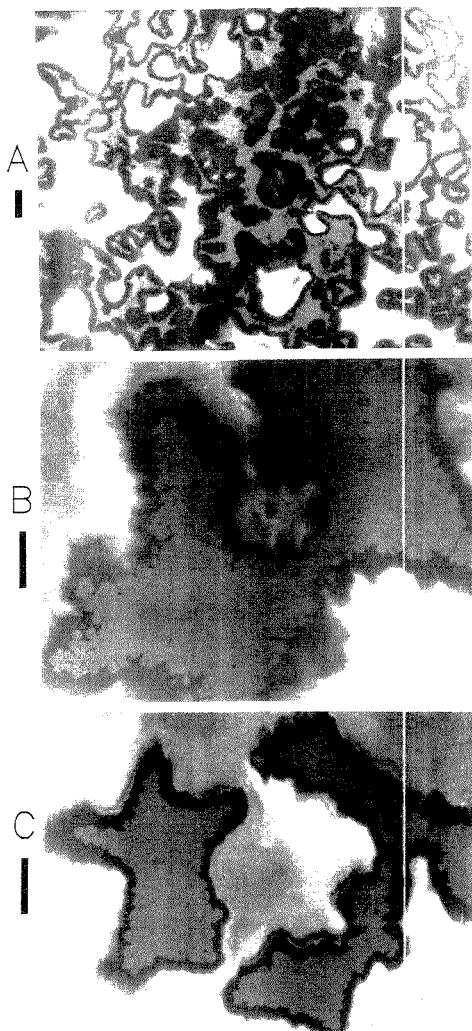


**Figure 2.** Scanning electron micrographs of (A) a surface region on LP-Kelgold, (B) an active site on LP-Kelgold, and (C) an active site on HP-Kelgold. Bars equal (A) 50  $\mu\text{m}$  and (B and C) 10  $\mu\text{m}$ .

on LP-Kelgold (Figure 2B) consist of tightly packed Au particles, and individual particles can be discerned primarily near the perimeters. Conversely, the active sites on LP-Kelplat (Figure 3B) are fragmented, being made up of loosely packed Pt particles, some of which are separated from adjacent particles by insulating Kel-F (confirmed by EDXA). These results support our predictions concerning the influence of conductor particle size, size distribution, and sphericity on the continuity of the conductor network.

In an effort to force the conductor particles to pack more tightly within active sites (13), a number of electrodes were fabricated at higher pressures. Figures 2C and 3C show SEMs of typical active sites on HP-Kelgold and HP-Kelplat, respectively. Comparison of parts B and C of Figure 2 reveals that the major difference between the active sites of LP- and HP-Kelgold is that individual Au particles are more difficult to discern around the perimeters of sites on HP-Kelgold. High

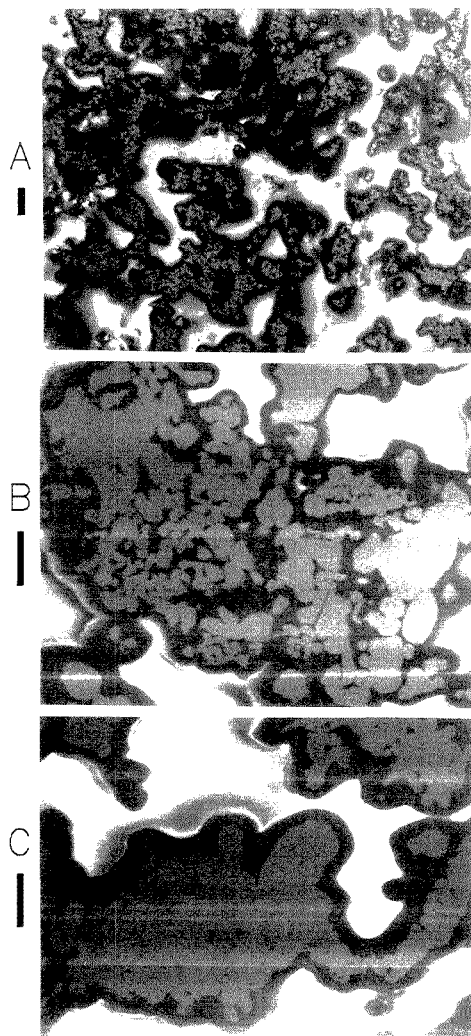


**Figure 3.** Scanning electron micrographs of (A) a surface region on LP-Kelplat, (B) an active site on LP-Kelplat, and (C) an active site on HP-Kelplat. Bars equal (A) 50  $\mu\text{m}$  and (B and C) 10  $\mu\text{m}$ .

contrast SEMs show that there is also a slight decrease in the already small number of inter-metal-particle voids within active sites on going from LP- to HP-Kelgold. More conspicuous is the considerably lower fragmentation of active sites on HP-Kelplat (Figure 3C) relative to those on LP-Kelplat (Figure 3B). The active sites of HP-Kelplat are more like the tightly packed sites of Kelgold than the fragmented sites of LP-Kelplat. However, the active sites of HP-Kelplat (Figure 3C) are still not as continuous as those of even LP-Kelgold (Figure 2B). The smaller voids (areas unoccupied by metal) within the active sites of all four composite materials are probably devoid of Kel-F, consistent with capacitance measurements that suggest the presence of excess area in the form of microporosity within active sites (13). Some of the larger voids within the active sites of LP-Kelplat (Figure 3B) may also be devoid of Kel-F. Consequently, SEM observations would suggest that active site microporosities should decrease

**Table I. Four-Probe Conductivity Data for Low-Pressure Kel-F/Precious Metal Composites**

composite material	metal vol %	measured conductivity, S/cm	RSD <sup>a</sup> (no. of trials)	pellet resistance, <sup>b</sup> Ω
Kelplat	14.0	95	43% (19)	$1.6 \times 10^{-2}$
Kelgold	14.0	7600	70% (20)	$2.0 \times 10^{-4}$
Kelsil	14.0	5900	61% (21)	$2.6 \times 10^{-4}$
Kelsil	12.0	990	29% (30)	$1.6 \times 10^{-3}$
Kelsil	10.0	280	23% (20)	$5.6 \times 10^{-3}$
Kelsil	8.0	0	— (3)	$>2.0 \times 10^{+7}$

<sup>a</sup>Relative standard deviation. <sup>b</sup>Values calculated from the measured conductivities, except for the 8.0% Kelsil for which the resistance was measured with a digital multimeter. Calculated values are for 5 mm long, 6.4 mm diameter pellets (the size used to make electrodes).

in the order LP-Kelplat > HP-Kelplat > LP-Kelgold  $\approx$  HP-Kelgold, which is consistent with capacitance data (not given). Comparisons of Figures 2A and 3A with the corresponding SEMs of the HP composites (not shown) show no apparent differences in active site sizes or geometries for the LP and HP composites.

**Conductivity Measurements.** The results of the four-probe conductivity measurements at LP Kelplat, Kelgold, and Kelsil composite pellets are summarized in Table I (no measurements were made on the HP composites). Although the variance of the data is quite high (as would be expected for such heterogeneous materials), some observations can be made. The conductivities of 14% LP-Kelsil and 14% LP-Kelgold are essentially equivalent and are approximately 100 times lower than the conductivities of the corresponding pure metals. The active sites on LP-Kelsil, as determined by SEM (11), appear to be as closely packed as those on LP-Kelgold. The conductivity of 14% LP-Kelplat, on the other hand, is about 1000 times lower than that of pure platinum, likely reflecting the lower continuity of the Pt particle network relative to those of Au and Ag (vide supra). The resistances listed in the last column of Table I (for pellets of the size normally used for electrodes) demonstrate that resistive electrode effects are negligible with Kel-F/precious metal composite electrodes having at least 10% metal by volume. The sharp decrease in the conductivity of LP-Kelsil with decreasing percent silver is typical for composite materials (17). The 9 orders of magnitude change in the conductivity of LP-Kelsil between 8% and 10% indicates a percolation threshold (17) between these compositions. The position of this threshold will likely be dependent on conductor and Kel-F particle sizes but has not been determined for the other Kel-F composites.

Since conduction in consolidated composites occurs along tortuous interconnected paths that cannot be geometrically described, it is impossible to make an a priori calculation of the conductivities of these composites (14). However, it is informative to compare the measured conductivities for Kel-F composites with those predicted by theory for dispersed composites. Maxwell derived an equation that can be used to calculate the conductivity of a two-phase dispersed composite, consisting of monodisperse spherical conductor particles (with negligible surface resistance) embedded in an insulating medium (14). Although this equation is most accurate for volume percents under 10, results at 14% are within a factor of 2 of those obtained from equations more appropriate to higher volume percents (14). From SEM data, it is known that the gold particles used to fabricate Kelgold are spherical and monodisperse. Therefore, Maxwell's equation can be employed to predict what the conductivity of 14% Kelgold would be if the gold particles were completely dis-

persed in the Kel-F matrix. Using  $8.3 \times 10^{-19}$  S/cm as the conductivity of Kel-F (18), one obtains a conductivity for "dispersed Kelgold" of  $1.2 \times 10^{-18}$  S/cm. This conductivity is more than 21 orders of magnitude lower than our experimental value, demonstrating that consolidated composites can possess much higher electrical conductivities than the corresponding dispersed composites. The small increase in the conductivity of "dispersed Kelgold" from that of pure Kel-F indicates a percolation threshold (17) for "dispersed Kelgold" that is considerably higher than that for consolidated Kelgold.

**Cyclic Voltammetry.** Optical microscopy and SEM have shown the surface morphologies of Kel-F/precious metal composite electrodes to be extremely complex (11, 12). The surface of a typical 6.4 mm diameter pellet may contain several thousand active sites, each with its own shape, size, and nearest neighbor distance. Consequently, it is impossible to rigorously predict the time dependence of the diffusion-limited current at these electrodes for all times. However, it is possible to predict the current for at least two limiting cases (19). One limiting case is at very short times, when the diffusion layer thickness is small compared to the dimensions of the individual active sites. Under these conditions, linear diffusion to each active site dominates such that the current is proportional to the active area of the composite. The second limiting case occurs at very long times, when all the diffusion layers of the individual sites completely overlap (forming a new single diffusion layer). Under these conditions, linear diffusion to the entire geometric area of the composite dominates. Between these limiting cases, both convergent diffusion to the individual sites and overlap of individual diffusion layers will likely be important (19). For a composite electrode having active sites the size of microelectrodes but well separated from one another, there should be a time interval (prior to diffusion layer overlap) during which there is a quasi-steady-state flux to each active site, resulting in a near-steady-state current. In order to probe the nature of the diffusion limited current observed at Kelgold and Kelplat electrodes, we performed cyclic voltammetry over 4 orders of magnitude in scan rate and chronoamperometry over both short and long time ranges.

The results of the cyclic voltammetry experiments are presented in parts A and B of Figure 4 for LP-Kelgold and LP-Kelplat, respectively. For linear diffusion, the peak current in cyclic voltammetry varies as the square root of the scan rate, and thus a plot of the log of peak current vs the log of scan rate is linear with a slope of one-half (20). The upper line in each figure corresponds to the theoretical response for linear diffusion to the entire geometric area of the composite electrode. The lower line in each corresponds to the theoretical response for linear diffusion to the projected active area (geometric area multiplied by metal volume fraction) of the composites. Both LP-Kelplat and LP-Kelgold approach the short time limit of linear diffusion to the individual active sites at high scan rates and the long time limit of linear diffusion to the geometric area of the electrode at slow scan rates. There does not appear to be a time interval over which either of the composites approaches a steady-state response, not surprising in view of the active site sizes and the intersite spacings noted above. The same experiment performed at HP-Kelgold (not shown) gave similar results.

Figure 4 also demonstrates the magnitude of the current density enhancement that is obtained with these composites relative to a disk electrode with the same active area. For a given scan rate, this enhancement is simply the peak current for the composite divided by the current represented by the lower theoretical line. Data obtained at a 2-mm Au disk electrode (and scaled to the estimated active area of the composite electrodes) are also shown in Figure 4A to verify that theoretical response was achieved over this large range

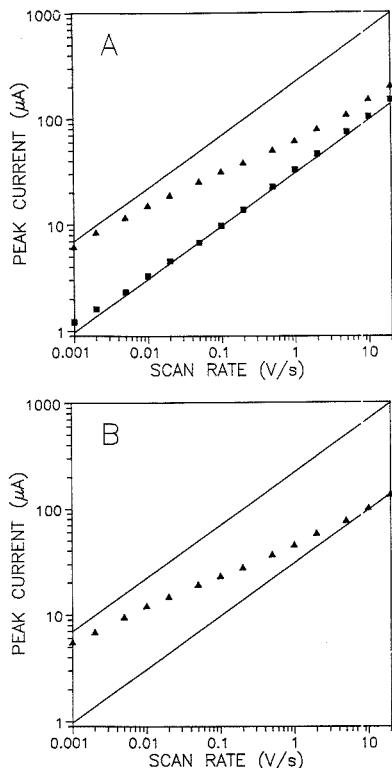


**Figure 4.** log peak current vs log scan rate plots for cyclic voltammograms of 1.01 mM  $\text{Ru}(\text{NH}_3)_6^{3+}$  in (A) 1.0 M  $\text{KNO}_3$  (buffered with 0.02 M phosphate, pH 6.9) at LP-Kelgold (▲) and 2-mm Au disk (■) electrodes (disk data scaled to the projected active area of the composite) and in (B) 1.0 M  $\text{KNO}_3$  (unbuffered) at a LP-Kelplat electrode (▲). See text for a description of the upper and lower solid lines.

of scan rates. The positive deviation of the disk response at the slowest scan rates is likely due to a combination of convective effects and edge diffusion but is minor compared to the current density enhancement observed with the composites at those scan rates.

The enhancement in current density is more clearly shown in Figure 5, which compares cyclic voltammograms (normalized to active area) obtained at LP-Kelgold and Au macro disk electrodes at 100 mV/s. At this scan rate, the peak current density for LP-Kelgold is 3.3 times larger than that for the Au disk. It is also obvious from Figure 5 that the LP-Kelgold electrode displays a larger peak potential difference than the Au disk electrode, indicative of a voltammogram having some steady-state character (21). Finally, the average polish-to-polish reproducibility of the peak currents at these composites was characterized by a relative standard deviation (RSD) of 1.0%.

**Chronoamperometry.** The chronoamperometric current to an inlaid electrode at short times is described by (22)

$$i = nFDC \left[ \frac{A}{(\pi Dt)^{1/2}} + \frac{P}{2} + \dots \right] \quad (1)$$

where  $A$  and  $P$  are the active area and perimeter of the electrode, respectively, and the other symbols have their usual electrochemical meanings. The first term of eq. 1 is the familiar Cottrell term, while the second term describes a per-

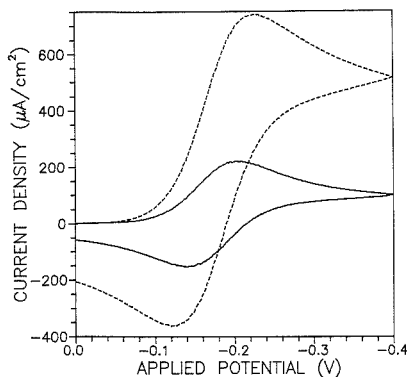


**Figure 5.** Cyclic voltammograms (normalized to active area; see text) of 1.01 mM  $\text{Ru}(\text{NH}_3)_6^{3+}$  in 1.0 M  $\text{KNO}_3$  (buffered with 0.02 M phosphate, pH 6.9) at Kelgold (dashed line) and 2-mm Au disk (solid line) electrodes. Scan rate = 100 mV/s.

imeter-dependent, steady-state contribution to the observed current (22). For typical millimeter sized disk electrodes, the perimeter term is usually insignificant. However, for microelectrodes and for small electrodes with high perimeter-to-area ( $P/A$ ) ratios, the perimeter term can often be measured (23). Equation 1 was derived for a single isolated electrode, but it can be applied to an electrode ensemble as long as there is negligible overlap of the diffusion layers of adjacent sites. Under such conditions, the total current at an electrode ensemble is simply the sum of the currents at the individual sites of the ensemble, and  $A$  becomes the sum of the areas of the active sites and  $P$  the sum of the active perimeters.

Chronoamperometry at short times (1–100 ms) was performed at LP- and HP-Kelgold and LP- and HP-Kelplat electrodes to assess the applicability of eq 1 (which applies to electrodes of arbitrary geometry (22)) for extracting average geometric parameters for these highly complex composite surfaces. The Cottrell plots for all Kelgold and Kelplat electrodes tested possessed surprisingly large linear regions (typically extending from ca. 10 ms to ca. 100 ms) and large positive intercepts at infinite time. Experiments performed at the corresponding macro disk electrodes (to determine diffusion coefficients) revealed that the electrochemical systems were well behaved and gave intercepts of zero.

Table II contains the results of analysis of the short time chronoamperometric data by eq 1. The last two entries in Table II are results from individual electrodes to be discussed below. The electrochemically determined areas for the HP composites are in good agreement with those projected from electrode composition, while the electrochemical areas for the LP composites are consistently larger than the projected areas. For both Kelgold and Kelplat, the SEM results discussed above have shown the active sites of the HP composites to have fewer inter-metal-particle voids than the active sites of the corresponding LP composites. During the time interval used to determine electrochemical areas (ca. 10–100 ms), diffusion layers would have been ca. 5–15 μm thick, which should have been sufficiently large so as to envelop any voids within these active sites, yet small enough to avoid diffusion layer overlap between adjacent active sites. Thus, electrochemical areas of the LP composites would be expected to be larger than those of the corresponding HP composites, consistent with the data in Table II. The large active perimeters determined for these composites (Table II) are consistent with the complex active site geometries observed by SEM, and the  $P/A$  ratios (Table II) are equivalent to those of disk microelectrodes with radii of 12–18 μm. A square array of disk

Table II. Geometric Parameters Determined from Short-Time Chronoamperometric Data and Equation 1<sup>a</sup>

composite (no. of electrodes, no. of trials)	projected area, <sup>b</sup> cm <sup>2</sup>	area A, cm <sup>2</sup>	perimeter P, cm	P/A, <sup>c</sup> cm <sup>-1</sup>
LP-Kelgold (4, 11)	0.0443	0.0544 (0.0076)	75.9 (3.0)	1430 (220)
HP-Kelgold (2, 2)	0.0443	0.0476 (0.0004)	80.4 (0.6)	1680 (20)
LP-Kelplat (3, 7)	0.0443	0.0569 (0.0030)	61.9 (1.5)	1100 (90)
HP-Kelplat (2, 3)	0.0443	0.0422 (0.0028)	50.2 (1.4)	1190 (50)
LP-Kelgold (1, 8)	0.0443	0.0592 (0.0011)	72.7 (3.9)	1230 (70)
LP-Kelplat (1, 3)	0.0443	0.0569 (0.0003)	61.5 (2.9)	1080 (60)

<sup>a</sup> Mean values with relative average deviations in parentheses. <sup>b</sup> Estimated active area based on geometric area and volume percent conductor. <sup>c</sup> Perimeter-to-area ratio.

Table III. Geometric Parameters Determined from Least-Squares fit of Chronoamperometric Data to equation 2

geometric parameter <sup>a</sup>	LP-Kelgold	LP-Kelplat
$N2\pi r_0^2$ , cm <sup>-1</sup>	310	260
$N\pi r_0^2$	0.202	0.198
$r_0$ , $\mu$ m	13.0	15.2
$N$ , cm <sup>-2</sup>	37800	27200
$A$ , cm <sup>2</sup>	0.0580	0.0569
$P/A$ , cm <sup>-1</sup>	1530	1310
$P$ , cm	89.0	74.8

<sup>a</sup> The first two entries are the adjustable parameters of the least-squares fit and were used to calculate  $r_0$  and  $N$ . The area,  $A$ , was calculated from  $N\pi r_0^2$  and the geometric area and was corrected for overlap of active sites (see text). The perimeter-to-area ratio,  $P/A$ , was taken as  $(N2\pi r_0/N\pi r_0^2)$ . The Perimeter,  $P$ , was calculated from  $P/A$  and  $A$ .

electrodes (with the same fractional active area as the composites, 0.14) would have an active site separation (edge-to-edge) of 33 and 49  $\mu$ m, respectively, for disk radii of 12 and 18  $\mu$ m. For a given composite electrode, the active area and perimeter could be reproduced from polish to polish with RSDs of 1-2% and ca. 7%, respectively.

Scharifker developed an approximate theory for the diffusion-limited current to an array of inlaid disk microelectrodes (19). For a random array (ensemble) of disk microelectrodes, the chronoamperometric current is given by

$$i = \frac{nFA_g DC}{(\pi Dt)^{1/2}} \left[ 1 - \exp \left[ \frac{-(\pi Dt)^{1/2}}{2} (N2\pi r_0) - (N\pi r_0^2) \right] \right] \quad (2)$$

where  $A_g$  is the (total) geometric area of the microelectrode ensemble,  $r_0$  is the radius of an individual microelectrode,  $N$  is the number density of microelectrodes in the array, and the other symbols have their usual electrochemical meanings (19). Unlike eq 1, which (though exact) is only applicable at short times, eq 2 (though approximate) is applicable at all times because it accounts for diffusion layer overlap between active sites. The short time expansion of eq 2 yields eq 1, whereas the long time expansion gives the Cottrell equation (19). The terms  $N2\pi r_0$  and  $N\pi r_0^2$  are the total perimeter and the total area, respectively, of the microelectrodes in an ensemble with a geometric area of unity. Since eq 2 was derived by using the Avrami theorem, which permits overlap of microelectrodes, the actual active fraction of the ensemble's area is not  $N\pi r_0^2$  but rather  $(1 - \exp(-N\pi r_0^2))$  (19).

In order to evaluate the utility of eq 2 for describing the transient current at consolidated composite electrodes over a large time range, chronoamperometry was performed at a LP-Kelgold electrode and a LP-Kelplat electrode at both short and long times. Least-squares fits of eq 2 to the experimental data (ca. 100 current values selected at evenly spaced intervals of  $t^{-1/2}$ ) were performed by using  $N2\pi r_0$  and  $N\pi r_0^2$  as the adjustable parameters of eq 2. Cottrell plots comparing the

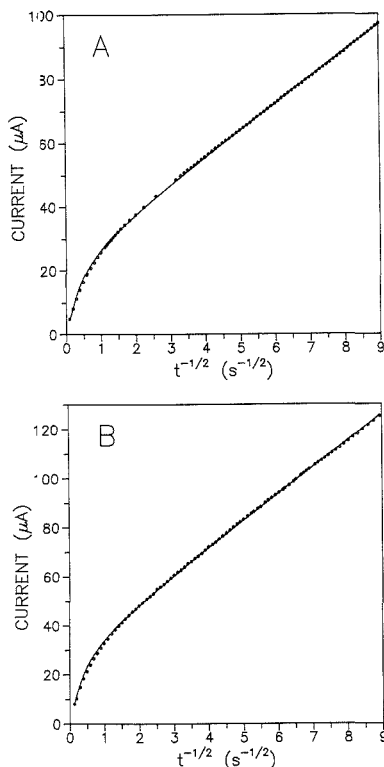


Figure 6. Cottrell plots of the chronoamperometric response of (A) a LP-Kelgold electrode for 1.00 mM  $\text{Ru}(\text{NH}_3)_6^{3+}$  in 1.0 M  $\text{KNO}_3$  (buffered with 0.02 M phosphate, pH 6.9) and (B) a LP-Kelplat electrode for 1.23 mM  $\text{Fe}(\text{CN})_6^{4-}$  in 1.0 M  $\text{KCl}$  (unbuffered). The points are experimental data; the solid lines are theory (least-squares fits; see text).

experimental data with the best fit theoretical curves, over the time range of ca. 10 ms to 100 s, are shown in parts A and B of Figure 6 for the LP-Kelgold and LP-Kelplat electrodes, respectively.

The qualitative agreement between the experimental data and eq 2 is rather exceptional, in view of the approximate nature of the theory and the fact that the microelectrode geometry assumed by the theory (disk) is quite different from the active site geometries observed for these composites. The best-fit parameters and geometric quantities calculated from them are summarized in Table III. Geometric parameters for these same two electrodes obtained from short time chronoamperometric data using eq 1 are given in the last two rows of Table II. The active areas obtained by the two ap-

proaches agree well, a consequence of the area parameter of eq 2 ( $N\pi r_0^2$ ) dominating at short times (i.e., in the time range where eq 1 was applied). The values of  $r_0$  and  $N$  in Table III characterize the random (site overlap allowed) disk electrode ensemble that would display transient diffusion current equivalent to the corresponding composite. It is both surprising and encouraging that the transient diffusion current at these composite electrodes, whose surface morphologies are essentially impossible to define geometrically, can be predicted from model ensembles consisting of well-defined (disk) active site geometry.

### CONCLUSION

Kel-F/precious metal composite electrodes with low volume percent conductor have been shown to possess high electrical conductivities and to exhibit behavior typical of microelectrode ensembles. The enhanced current densities displayed by these composites should result in higher signal-to-noise ratios than obtained at the corresponding macro disk electrodes, making them attractive alternative electrode materials for electroanalytical measurements, including amperometric detection in flowing streams (24). Furthermore, the enhanced current density coupled with the high conductivity and low precious metal content of these composites may make them attractive for energy generation and storage applications, particularly where weight and cost are considerations. Further optimization of the fabrication and composition of Kel-F/precious metal composites should lead to improvements in the advantageous properties reported here for these first generation Kelgold and Kelplat electrodes. Work in these areas is in progress.

### ACKNOWLEDGMENT

We are grateful to 3M Company for donating the Kel-F-81 used in this work.

### LITERATURE CITED

- (1) Adams, R. N. *Electrochemistry at Solid Electrodes*; Marcel Dekker: New York, 1969; pp 278-280.

- (2) Sleszynski, N.; Osteryoung, J.; Carter, M. *Anal. Chem.* **1984**, *56*, 130.  
 (3) Lindquist, J. J. *Electroanal. Chem. Interfacial Electrochem.* **1974**, *52*, 37.  
 (4) Anderson, J. E.; Tallman, D. E. *Anal. Chem.* **1976**, *48*, 209.  
 (5) Lipka, S. M.; Cahen, G. L., Jr.; Stoner, G. E.; Scribner, L. L., Jr.; Gileadi, E. *J. Electrochem. Soc.* **1988**, *135*, 368.  
 (6) Park, J.; Shaw, B. R. *Anal. Chem.* **1989**, *61*, 848.  
 (7) Creasy, K. E.; Shaw, B. R. *Anal. Chem.* **1989**, *61*, 1460.  
 (8) Klatt, L. N.; Connell, D. R.; Adams, R. E.; Honigberg, I. L.; Price, J. C. *Anal. Chem.* **1975**, *47*, 2470.  
 (9) Mascini, M.; Pallozzi, F.; Liberti, A. *Anal. Chim. Acta* **1973**, *64*, 126.  
 (10) Anderson, J. E.; Tallman, D. E.; Chesney, D. J.; Anderson, J. L. *Anal. Chem.* **1978**, *50*, 1051.  
 (11) Petersen, S. L.; Tallman, D. E. *Anal. Chem.* **1988**, *60*, 82.  
 (12) Petersen, S. L.; Weisshaar, D. E.; Tallman, D. E.; Schulze, R. K.; Evans, J. F.; DesJarlais, S. E.; Engstrom, R. C. *Anal. Chem.* **1988**, *60*, 2385.  
 (13) Petersen, S. L.; Tallman, D. E.; Shepherd, G.; MacKellar, W. J. *J. Electroanal. Chem. Interfacial Electrochem.* **1989**, *261*, 249.  
 (14) Meredith, R. E.; Tobias, C. W. In *Advances in Electrochemistry and Electrochemical Engineering*; Delahay, P., Tobias, C. W., Eds.; Interscience: New York, 1962; Vol. 2, Chapter 2.  
 (15) *Linear Data Book*; National Semiconductor Corporation, 1976; pp 3-12.  
 (16) Tallman, D. E.; Shepherd, G.; MacKellar, W. J. *J. Electroanal. Chem. Interfacial Electrochem.*, in press.  
 (17) Chen, I.-G.; Johnson, W. B. *J. Mater. Sci.* **1986**, *21*, 3162.  
 (18) *Kel-F 81 Plastic*; Technical Data Brochure, 3M Co.: St. Paul, MN, 1979.  
 (19) Scharifker, B. R. *J. Electroanal. Chem. Interfacial Electrochem.* **1988**, *240*, 61.  
 (20) Bard, A. J.; Faulkner, L. R. *Electrochemical Methods*; John Wiley and Sons: New York, 1980; p 218.  
 (21) Reller, H.; Kirova-Eisner, E.; Gileadi, E. *J. Electroanal. Chem. Interfacial Electrochem.* **1984**, *161*, 247.  
 (22) Oldham, K. B. *J. Electroanal. Chem. Interfacial Electrochem.* **1981**, *122*, 1.  
 (23) Myland, J. C.; Oldham, K. B. *J. Electroanal. Chem. Interfacial Electrochem.* **1983**, *147*, 295.  
 (24) Tallman, D. E.; Weisshaar, D. E. *J. Liq. Chromatogr.* **1983**, *6*, 2157.

RECEIVED for review September 26, 1989. Accepted November 27, 1989. This work was supported by the U.S. Department of the Interior/Geological Survey through Grant No. 14-08-0001-G1581 administered through the North Dakota Water Resources Research Institute as Project No. 6575 and by the National Science Foundation through Grant No. CHE-8711595.

## Combination of the Mahalanobis Distance and Residual Variance Pattern Recognition Techniques for Classification of Near-Infrared Reflectance Spectra

Nilesh K. Shah and Paul J. Gemperline\*

Department of Chemistry, East Carolina University, Greenville, North Carolina 27858

Principal component analysis of near-infrared reflectance (NIR) spectra is used for the calculation of Mahalanobis distances and for the construction of soft independent modeling of class analogy (SIMCA) classification models. The space spanned by the primary eigenvectors is used in the Mahalanobis distance classification and the space spanned by the secondary vectors is used in SIMCA residual variance classification. The complementary behavior of these two classification methods is discussed and a new classification rule based on a combination of the two methods is described. The application of NIR spectroscopy and the pattern recognition technique for identifying and classifying raw materials used in pharmaceutical industry is also discussed.

### INTRODUCTION

Multivariate data analysis based on pattern recognition is a collection of classification techniques that can be used to analyze the near-infrared reflectance (NIR) spectra of raw materials. The aim of pattern recognition techniques is to classify new samples by comparing them to a set of measurements of predetermined classes. Derde and Massart have reviewed a number of pattern recognition techniques in order to select an optimal technique for a given application (1). These techniques were distinguished into two categories; parametric techniques that account for population distributions and nonparametric techniques that do not require any assumptions regarding the shape of the underlying population

distributions. These authors concluded that parametric techniques have better class models because the shape of the population distribution is taken into account (2).

Near-infrared reflectance spectroscopy is a rapid measurement technique that has found numerous applications in analyzing agricultural products and pharmaceutical materials (3). The development of this technique for quantitation is primarily due to the availability and use of multiple regression analysis (4, 5); however, quantitation is limited to samples of controlled composition. The qualitative information available in the NIR spectral region can be used by pattern recognition techniques for the identification and classification of samples of unknown origin.

Mark and Tunnell have reported the qualitative identification of raw materials by NIR spectroscopy using a Mahalanobis distance classification technique (6, 7). In their procedure, two or more wavelengths from NIR spectra were used for classification of samples. The classification of spectra was based on the generalized square distance of an observation from the centroid of a cluster. In addition, one mathematical model was constructed for all materials. A classification technique named UNEQ has been developed that uses a Mahalanobis distance classification function, except the class models in UNEQ were constructed separately for each of the training classes (8). The UNEQ classification technique has been used to classify olive oils according to their geographic origin using GC data. The classical linear discriminant analysis (LDA) has also been used to find linear functions at optimal wavelengths that divide pattern spaces into as many regions as there are classes in the training set. The disadvantages of this technique are the inability to recognize samples that are outliers and the inability to estimate the probability of misclassification for samples in overlapping regions.

Recently, Gemperline et al. reported the qualitative identification of raw materials using soft independent modeling of class analogy (SIMCA) by NIR spectroscopy (9). The SIMCA classification technique uses principal component analysis (PCA) of full NIR spectra for the construction of mathematical models for each training set. The classification of samples was achieved by calculating the sum of squares of the difference between the original spectrum and the reproduced spectrum. In addition, the probability level for each sample was estimated by using an *F* test.

This paper reports a combination of the two pattern recognition techniques for the classification of NIR spectra. The Mahalanobis distance classification technique is modified by first calculating the principal components of full NIR spectra, instead of selecting a few wavelengths for classification. The use of full NIR spectra of samples ensures that all of the information available in a spectrum is retained for classification. The Mahalanobis distance model is then calculated in the subspace defined by the significant principal components. A separate class model is used for each different class of raw materials. SIMCA also uses principal component analysis for the construction of class models. The SIMCA residual variance is calculated in the subspace defined by the nonsignificant principal components.

### THEORY

Principal component analysis (PCA) is used for constructing the mathematical models for both pattern recognition techniques. Principal components are orthogonal to each other and define a pattern space which explains all of the variation in the data. Additionally, if the original variables are strongly correlated, then almost all of the variability in the original data can be modeled by the first few principal components.

One interesting observation that was not previously recognized in the pattern recognition literature is the complementary nature of classification using the Mahalanobis dis-

tance and SIMCA residual variance in the principal component pattern space. In order to explain the complementary behavior of these two classification methods, the "inside model space" (IMS) and "outside model space" (OMS) defined by Van Der Voet et al. is used (10). During principal component analysis of a training set, a set of eigenvectors is produced that can be divided into two sets: a primary set of eigenvectors that span the "inside model space" of the training set and a secondary set of eigenvectors that span the "outside model space" of the training set. The IMS is the subspace that spans all of the significant correlated behavior in the original data variables. The OMS is the subspace that spans the residual variation (e.g. measurement noise) left in the original data variables. The primary eigenvectors and the secondary eigenvectors are mutually orthogonal to each other. The Mahalanobis distance is calculated in the IMS by using the primary eigenvectors while the SIMCA residual variance is calculated in the OMS by using the secondary eigenvectors.

The primary set of eigenvectors can be identified by using any of the well-known tests for determining the significance of eigenvalues (11). In this paper, the number of primary eigenvectors was adjusted until optimal classification of independently measured test samples was obtained. The figures of merit used in this selection process included proper classification of acceptable samples (e.g. percent correct) and rejection of unacceptable samples (e.g. percent rejected).

**Mahalanobis Distance.** The Mahalanobis distance calculation assumes a multivariate normal distribution  $N(\mu, \Sigma)$  for the class population. The class model consists of a single point in multidimensional space, the class centroid  $\mu$ . The distance between an *i*th sample,  $x_i$ , to the centroid is given by the generalized squared distance

$$D_i^2 = (x_i - \mu)' \Sigma^{-1} (x_i - \mu) \quad (1)$$

where  $\Sigma$  is the training set's variance-covariance matrix, which explains the dispersion of data around the centroid. In practice, the true centroid and the variance-covariance matrix of the class population are unknown and, therefore, must be estimated by the mean vector  $\bar{x}$  and the variance-covariance matrix  $S$  from a sample of size *n*. The sample Mahalanobis distance can then be calculated from eq 2

$$D_i^2 = (x_i - \bar{x})' S^{-1} (x_i - \bar{x}) \quad (2)$$

where

$$S = 1/(n-1) \sum_{i=1}^n (x_i - \bar{x})'(x_i - \bar{x}) \quad (3)$$

In principal component analysis, the absorbance data matrix **A** (where rows of **A** are spectra of samples) is decomposed into an abstract solution expressed by eq 4, where  $\bar{A}$  is the mean

$$A = \bar{A} + TL \quad (4)$$

absorbance spectrum, **T** is the score matrix, and **L** is the loading matrix that consists of eigenvectors. The purpose of principal component analysis is to project a sample observation from the raw data space into the principal component subspace. A vector of *k* scores,  $t_i$ , gives the location of an *i*th sample in the principal component subspace where *k* is the number of significant principal components. Replacing the sample observation  $x_i$  with the vector of principal component scores,  $t_i$ , the variance-covariance matrix in eq 3 can be written as

$$S = 1/(n-1) \sum_{i=1}^n (t_i - \bar{t})(t_i - \bar{t}) \quad (5)$$

Since the principal components are orthogonal, the variance-covariance matrix constructed from the principal component scores is a diagonal matrix. In addition, the mean of

the principal component scores for each principal component is equal to zero due to mean correction of the raw data so that eq 5 simplifies to

$$s_{ij} = 1/(n-1) \sum_{i=1}^n (t_{ij})^2 \quad (6)$$

The modified Mahalanobis distance for the  $i$ th sample can be calculated from eq 7

$$D_i^2 = \mathbf{t}_i \mathbf{S}^{-1} \mathbf{t}_i' \quad (7)$$

which simplifies to

$$D_i^2 = (n-1) \sum_{j=1}^k t_{ij}^2 / s_{jj} \quad (8)$$

Geometrically, the Mahalanobis distance class model is an ellipsoid-shaped cluster with the population mean at its centroid and its size defined by the value of chi-squared at a user-specified confidence level with  $k$  degrees of freedom. A spectrum is classified as a member if its Mahalanobis distance falls inside the 95% probability level. Alternatively, the chi-squared distribution function can be evaluated at a sample's Mahalanobis distance to estimate the probability level (12). The spectra are then classified according to the probability levels obtained from the chi-squared distribution function. Samples having a probability level in the range from 1.0 to 0.05 are classified as members. Samples having a probability level in the range from 0.05 to 0.01 are classified as outliers. Samples having a probability level in the range from 0.01 to 0.0 are classified as nonmembers.

**SIMCA Residual Variance.** In SIMCA, the classification of a sample is achieved by calculating the sum of squares of the difference between the original spectrum and the reproduced spectrum (residual spectrum). Although the theory for SIMCA classification technique has been thoroughly reviewed in the literature (13), the description of a sample in the "outside model space" requires explanation. The residual variance,  $s_i^2$ , of spectrum  $i$  fitted to class  $g$ , indicates how similar the spectrum is to the class model and can be calculated according to eq 9, where  $t_{ij}$  is the principal component

$$s_i^2 = \sum_{j=k+1}^p t_{ij}^2 / (p-k) \quad (9)$$

score of  $i$ th sample for  $j$ th component,  $p$  is the number of wavelengths, and  $k$  is the number of significant principal components. The so-called "normal range" defined by Wold is omitted here (13). To avoid the accumulation of rounding errors due to inaccuracies in the scores associated with very small eigenvalues, the alternate formula in eq 10 is actually used, where  $a_{ij}$  is the raw absorbance spectrum and  $a_{ij}^*$  is the

$$s_i^2 = \sum_{j=1}^p (a_{ij} - a_{ij}^*)^2 / (p-k) \quad (10)$$

reproduced absorbance spectrum from the abstract solution. The total variance between the samples belonging to a class and the class model can be calculated by using the standard equations described by Wold (13).

Since the secondary eigenvectors are used to calculate the residual variance, the space spanned by these eigenvectors are known as "outside model space". SIMCA is a parametric technique and, therefore, the residuals are assumed to be normally distributed. The variance ratio

$$F = (s_i^2 / s_0^2) (1 / (n-k-1)) \quad (11)$$

can be calculated to estimate the probability level for samples.  $1/(n-k-1)$  degrees of freedom are used for comparing the calculated  $F$  value of a single unknown spectrum with the tabulated  $F$  value (9). The spectra are then classified according to the probability levels obtained from the  $F$  test. The

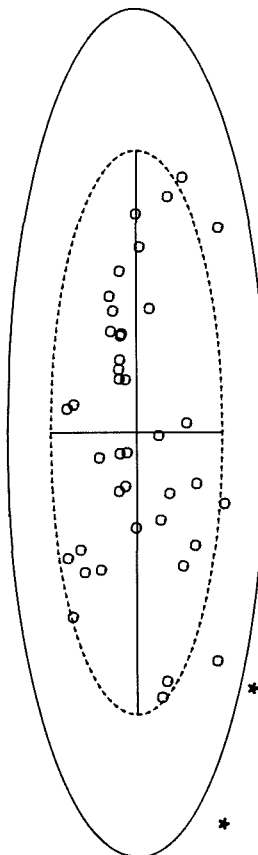


**Figure 1.** Scatter plot of 40 samples of microcrystalline cellulose using scores for principal components two and three as  $x, y$  plotting coordinates: (O) acceptable samples; (\*) reject samples. Ellipses are drawn at two standard deviations (---) and at three standard deviations (—).

same probability levels used for the previously described Mahalanobis distance test are used here.

The class models in SIMCA consist of linearly defined hyperplanes which are constructed from the significant principal components. In previous applications, a hyperbox structure was defined by the range of scores of the training set along each of the significant principal components. For normally distributed data, the principal component scores are linear combinations of the original variables and are also normally distributed giving ellipsoid-shaped clusters, not hyperbox-shaped clusters. Figure 1 shows a two-dimensional scatter plot of 40 samples of microcrystalline cellulose using the scores from principal components two and three as  $x, y$  plotting coordinates. Ellipses were drawn at  $\pm 2.0$  and  $\pm 3.0$  standard deviations. Several unacceptable samples are plotted in the figure (stars) that clearly lie outside the ellipse drawn at  $\pm 3.0$  standard deviations. If a box was drawn at  $\pm 3.0$  standard deviations in Figure 1, regions that do not fall in the ellipsoid-shaped cluster would be naively included, causing some of the unacceptable samples to be incorrectly classified as members. To avoid this problem associated with SIMCA's normal range, a combination of the Mahalanobis distance and the SIMCA residual variance is used.

**Combined Classification.** Since the Mahalanobis distance and SIMCA residual variance classification techniques provide truly complementary information, the results obtained by these techniques can be combined. In the Mahalanobis and SIMCA techniques large values of the test statistic are significant. When the tests are used independently, the null hypothesis is rejected for small probability levels of the corresponding test statistic. In the combined rule, the overall null hypothesis to be tested is the logical conjunction of  $H_{o1}$  and  $H_{o2}$ , the null hypotheses for the Mahalanobis and SIMCA techniques, respectively

$$H_o = H_{o1} \cap H_{o2} \quad (12)$$

Genest and Zidek have reported a comprehensive review of techniques for combining probability distributions (14). Some of the most common techniques include computing the sum of the probabilities with nonnegative weights, computing the mean, or computing the product of the probabilities. Although each method has advantages and limitations, a major difficulty with all of them is accounting for different degrees of freedom used in estimating the probability levels to be combined. Mudholkar and George (15) describe a simple combination statistic,  $\min(P_i)$ , which they attribute to Tippett (16) that avoids the problems mentioned above.  $P_i$  is the probability level of the  $i$ th test statistic in the above combination rule.

The combined classification rule used in this study is based on using the minimum probability level obtained for the two pattern recognition methods (15). In the combined classification rule, samples classified as members by both the methods are classified as members and samples classified as outliers by both methods are flagged as outliers. Samples classified as members by one technique and outliers or nonmembers by the other are classified as outliers or nonmembers, respectively. Similarly, samples that are rejected by either method are classified as nonmembers in the combined classification.

## EXPERIMENTAL SECTION

**Instrument.** Spectral data of all the raw materials used in the present study were collected with a Technicon InfraAlyzer 500S NIR spectrophotometer (Bran+Leubbe Analyzing Technologies) connected to an IBM PS/2 computer. The spectral data were recorded from 1100 to 2500 nm at 4-nm intervals using IDAS software provided by Bran+Leubbe Analyzing Technologies. The samples were packed into a standard sample cup and measured against a highly reflective ceramic disk as a reference.

**Materials.** The raw materials analyzed were three different types of microcrystalline cellulose, capsulating grade lactose, sulfamethoxazole, and a proprietary ingredient. The raw materials were obtained from the same suppliers cited in an earlier study (9). The first four materials are used as binders in tableting processes and the latter two are active ingredients. The three types of microcrystalline cellulose were Avicel PH101, Avicel PH102, and Avicel RC581. The only difference between the first two Avicels was the particle size, whereas the third Avicel contained sodium carboxymethylcellulose. Different lots of Avicel PH101 and Avicel PH102 which were rejected by FMC during the manufacturing process were obtained to study the ability of the pattern recognition method to reject "unacceptable" samples. Four different grades of microcrystalline cellulose were also tested. These were Avicel PH103, PH105, RC591, and CL611. All of the above raw materials were obtained commercially from various suppliers and the details can be found elsewhere (9). To study the ability of the pattern recognition techniques to discriminate against samples containing minor impurities, two different lots of sulfamethoxazole were spiked with 0.1–2.0% by weight of sulfanilic acid. The adulterant was mixed with sulfamethoxazole using the low-shear mixing technique described in a previous study (9).

**Procedure.** The binary raw data files from IDAS were imported to the pattern recognition software (PRS) implemented in Turbo Pascal (Borland International). In PRS, data pre-treatment options can be selected including the wavelength range

**Table I. Summary of Mahalanobis Distance Analysis**

raw material	no. of factors	recognition rate	prediction rate	rejection rate
Avicel PH101	5	100.0 (40)	100.0 (10)	86.0 (50)
Avicel PH102	6	100.0 (26)	100.0 (6)	62.5 (16)
Avicel RC581	4	97.5 (40)	100.0 (10)	100.0 (4)
lactose	5	100.0 (20)	100.0 (7)	100.0 (2)
proprietary ing	5	100.0 (22)	100.0 (6)	100.0 (3)
Sulfamethoxazole <sup>a</sup>	7	97.6 (42)	100.0 (13)	71.4 (28)
Sulfamethoxazole <sup>b</sup>	7	100.0 (42)	100.0 (13)	92.8 (28)

<sup>a</sup> Full spectra used for classification (e.g. 1100–2500 nm).

<sup>b</sup> Partial spectra used for classification (e.g. 1548–1712 nm, 1876–2004 nm).

and the step size to be used by principal component analysis, the raw data type such as absorbance, first derivative or second derivative, and the number of principal components to be calculated by principal component analysis. In addition, options for mean centering and autoscaling the data prior to analysis are available. The standard deviations for samples in the training set and test set are estimated by using Mahalanobis and SIMCA techniques described in the theory section. Probability levels for each sample are estimated by integrating the appropriate portion of the chi-squared distribution function and the  $F$  distribution function for Mahalanobis distance and SIMCA residual variance, respectively.

Approximately 400 NIR spectra of raw materials were acquired and analyzed using the two pattern recognition techniques. Eighty percent of the available NIR spectra were used in the training set and the remaining 20% were used in the test set. The variation between lots of different raw materials was included in the training set by repeatedly measuring samples from various lots on different days. The test set contained samples from lots not included in the training set. At least two lots of each type of raw materials were reserved for exclusive use in the test set. The sample cup was cleaned with USP grade alcohol and dried with air prior to filling. Dust from previous samples was removed from the sample cup with pressurized air before filling with a sample of a different lot of the same raw material to reduce the carry-over.

## RESULTS AND DISCUSSION

Several figures of merit were used to evaluate the validity of the classification functions including the recognition rate, the prediction rate, and the rejection rate. The recognition rate and the prediction rate correspond to the percentage of acceptable training samples or test samples correctly classified as members of the training set. The rejection rate is the percentage of unacceptable samples correctly classified as nonmembers. The number of principal components giving the optimum prediction rate and rejection rate is selected for classification. The classification of samples is based on the previously described probability levels. Spectra were sampled at every 12 nm prior to principal component analysis. The number of spectra actually used are given in parentheses in Tables I and II.

**Mahalanobis Distance Analysis.** Table I summarizes the classification results obtained for six raw materials using the Mahalanobis distance analysis. The class models were constructed by using the number of principal components given in Table I. All samples of these raw materials were correctly classified as members of their respective classes except one sample from each of the following materials: Avicel RC581 and sulfamethoxazole. The misclassified samples were classified as outliers. The overall recognition rate and the prediction rate were 98.9% and 100.0%, respectively, which helped to establish the robust character of the classification model. Overall, the rejection rate was 79.6% for the Mahalanobis distance technique.

One lot of Avicel PH101 and two lots of Avicel PH102 rejected materials were consistently misclassified as members resulting in a relatively low rejection rate. These lots were

Table II. Summary of SIMCA Residual Distance Analysis

raw material	no. of factors	recognition rate	prediction rate	rejection rate
Avicel PH101	5	100.0 (40)	100.0 (10)	84.0 (50)
Avicel PH102	6	100.0 (26)	100.0 (6)	56.2 (16)
Avicel RC581	4	100.0 (40)	100.0 (10)	100.0 (4)
lactose	5	100.0 (20)	100.0 (7)	100.0 (2)
proprietary ing	5	100.0 (22)	100.0 (6)	100.0 (3)
sulfamethoxazole <sup>a</sup>	7	100.0 (42)	100.0 (13)	89.3 (28)
sulfamethoxazole <sup>b</sup>	7	100.0 (42)	100.0 (13)	96.4 (28)

<sup>a</sup> Full spectra used for classification (e.g. 1100–2500 nm).

<sup>b</sup> Partial spectra used for classification (e.g. 1548–1712 nm, 1876–2004 nm).

rejected and never shipped by the manufacturer because they failed to meet the internal quality assurance specifications for conductivity and density measurements. The classification model constructed for Avicel RC581 was used to discriminate against different types of Avicel, those being PH103, PH105, RC591, and CL611. The results indicate that all four of the Avicel grades were correctly classified as rejects, thereby demonstrating the pattern recognition method's ability to discriminate against similar grades of materials. Since Avicel PH101 and Avicel PH102 only differed in particle size, the distance between the two clusters is small in the principal component pattern space and the clusters may partially overlap. To demonstrate the separation between the PH101 and PH102 clusters, samples of PH102 were fitted to the class model developed for PH101 and vice versa. None of the samples were misclassified.

Different grades of lactose, 60S and 80S, were also analyzed to verify the discriminating power of Mahalanobis distances for similar materials. According to Table I, both "foreign" grades of lactose were classified as nonmembers as expected. In addition, one capsulating grade of lactose was obtained from a different supplier. This sample was not included in the training set and was correctly identified as a member of the training set. The result illustrates the ability of the method to identify identical materials from different suppliers. In the case of sulfamethoxazole, eight samples spiked with sulfanilic acid were misclassified as members by this technique. These samples were the two lots of sulfamethoxazole spike with 0.1–0.5% of sulfanilic acid. Sulfamethoxazole containing less than 1.0% sulfanilic acid as impurity cannot be detected reliably by using the Mahalanobis distance classification technique.

**SIMCA Residual Variance Analysis.** The classification results obtained for the six raw materials by SIMCA residual variance analysis are also given in Table II. The SIMCA model was constructed by using the same number of principal components as used in the Mahalanobis distance model. The overall recognition rate as well as the prediction rate was 100.0%. No samples in the training set and the test set were flagged as outliers or nonmembers. The overall rejection rate obtained by using the SIMCA technique was 82.5%. No significant improvement in the rejection rate was obtained by using the first derivative spectra.

The two lots of Avicel PH102 and one lot of Avicel PH101 rejected materials that were identified by Mahalanobis distance as members were also misclassified as members by the SIMCA technique. Different grades of Avicels, PH103, PH105, RC591, and CL611, which were not included in the training set of Avicel RC581, were tested. All of the foreign grades of Avicel were readily detected as nonmembers by this technique. The ability of SIMCA to discriminate between Avicel PH101 and Avicel PH102 was also studied. There were no cases in which a PH101 sample was classified as a member or an outlier of PH102 or vice versa. In addition, the SIMCA

Table III. Summary of Combined Classification Analysis

raw material	no. of factors	recognition rate	prediction rate	rejection rate
Avicel PH101	5	100.0 (40)	100.0 (10)	88.0 (50)
Avicel PH102	6	100.0 (26)	100.0 (6)	68.8 (16)
Avicel RC581	4	97.5 (40)	100.0 (10)	100.0 (4)
lactose	5	100.0 (20)	100.0 (7)	100.0 (2)
proprietary ing	5	100.0 (22)	100.0 (6)	100.0 (3)
sulfamethoxazole <sup>a</sup>	7	97.6 (42)	100.0 (13)	92.9 (28)
sulfamethoxazole <sup>b</sup>	7	100.0 (42)	100.0 (13)	96.4 (28)

<sup>a</sup> Full spectra used for classification (e.g. 1100–2500 nm).

<sup>b</sup> Partial spectra used for classification (e.g. 1548–1712 nm, 1876–2004 nm).

residual variance pattern recognition method was also used to discriminate between different grades of lactose, 60S and 80S. Both grades of lactose were correctly classified as rejects by this technique. The capsulating grade of lactose that was obtained from a different supplier was classified as a member by SIMCA. The above results reflect the ability of SIMCA to discriminate between similar materials. Three samples of sulfamethoxazole spiked with sulfanilic acid were found as members by SIMCA technique. These samples were sulfamethoxazole spiked with 0.1% to 0.5% sulfanilic acid. The limit of detection for sulfanilic acid by this method is therefore estimated to be about 1.0%.

**Combined Classification Analysis.** The combined classification results are given in Table III. The overall recognition rate and the prediction rate obtained by using the combined classification rule were 98.9% and 100.0%, respectively. One sample from each Avicel RC581 and sulfamethoxazole was identified as outlier. These samples were also misclassified as outliers by Mahalanobis distance technique but were classified as members by SIMCA residual variance. According to the combined classification rule, the samples that are classified as members by one technique but outliers by the other are still considered outliers.

The most interesting observation is the classification of Avicel PH101 and PH102 rejected materials and the spiked sulfamethoxazole samples using the combined classification rule. The combined classification of PH102 rejected materials showed that only five samples were misclassified as members of the training set by both techniques, instead of six by Mahalanobis distances and seven by SIMCA residual variance. In the combined classification of Avicel PH101 rejected materials, five samples were consistently misclassified as members. These five samples were obtained from one lot and were also repeatedly measured with the training set for long-term variation. In addition, the six out of the eight spiked samples that were identified as members by Mahalanobis distance were actually detected as outliers or nonmembers by SIMCA residual variance analysis. Therefore, these samples are classified as "reject" samples based on the combined classification rule. The overall rejection rate for the combined classification rule was 87.4% compared to the overall rejection rates of 79.6% and 82.5% for the Mahalanobis distance and SIMCA techniques, respectively.

**Detecting Minor Components.** Lower limits of detection for sulfanilic acid in sulfamethoxazole were obtained by selecting regions of the NIR spectrum where strong absorption bands for sulfanilic acid and weak absorption bands for sulfamethoxazole were observed. The wavelength ranges from 1548 to 1712 nm and 1876 to 2004 nm (8-nm increments) were chosen for the classification of sulfamethoxazole. These spectral regions were selected from observed dissimilarities in the first derivative spectra of sulfamethoxazole and sulfamethoxazole spiked with sulfanilic acid reported in a previous study (9). Principal component analysis was performed on

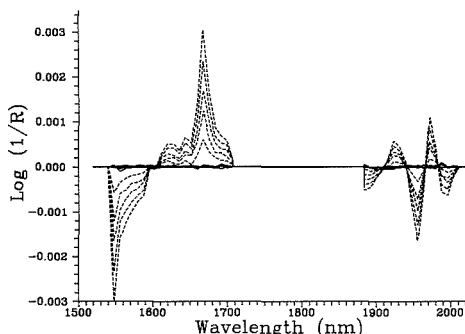


**Figure 2.** Residual spectra of sulfamethoxazole and sulfamethoxazole spiked with sulfanilic acid using seven principal components in the mathematical model: five different lots of sulfamethoxazole (—); sulfamethoxazole spiked with 1%, 2%, 3%, 4%, and 5% sulfanilic acid (---).

the reduced spectra prior to Mahalanobis and SIMCA analysis. Figure 2 shows the residual spectra of sulfamethoxazole and sulfamethoxazole spiked sulfanilic acid obtained by using seven principal components in the mathematical model.

The results obtained with the reduced wavelength range for the spiked samples of sulfamethoxazole are given at the bottom of Tables I, II, and III. By use of seven principal components in the model, the recognition and prediction rates were 100.0% using both the Mahalanobis distance and the SIMCA classification techniques. The recognition rate was improved from 97.6% to 100.0% for the Mahalanobis distance technique. The rejection rate was improved significantly for both classification techniques. SIMCA misclassified only one sample spiked with 0.1% sulfanilic acid as a member compared to three samples for the results obtained by using the entire spectral region. In the case of the Mahalanobis distance technique, one sample spiked with 0.1% sulfanilic acid and one sample spiked with 0.2% sulfanilic acid were misclassified as a member, as compared to eight samples for the results using the entire NIR spectra. The combined classification rule misclassified only one spiked sample. These results indicate that a detection limit of about 0.5% can be reliably achieved by narrowing the wavelength region of interest.

**Long-Term Instrumental Variation.** The instrument long-term reproducibility seems to be the limiting factor in obtaining low limits of detection for impurities. Spectra of a polystyrene disk have been acquired over a period of 3 months to evaluate the long-term reproducibility of the Technicon NIR instrument. By use of five principal components, residual spectra have been examined and indicated that small wavelength shifts (ca. 1 nm or less) are responsible for a significant portion of the observed deviations. The magnitude of the deviations are small, approximately  $2 \times 10^{-4}$

AU (absorbance units). A portion of the polystyrene spectra was also acquired immediately after performing the wavelength calibration procedure in the PRISM software package. The PRISM software package is available commercially from Bran+Lubbe Analyzing Technologies. The wavelength calibration procedure did not yield any significant improvement in the residuals for the polystyrene spectra. The long-term wavelength reproducibility problem of scanning NIR instruments, however slight, seems to be an important source of variation for data analysis techniques that employ full spectra. It is essential to adequately represent the long-term instrumental variation in training sets.

## CONCLUSIONS

The spectroscopic classification of raw materials by a single pattern recognition technique may not be specific enough for proper classification of unacceptable materials. A combination of several independent techniques may provide a more reliable classification. Pattern recognition analysis of NIR spectra can detect many foreign grades of raw materials, materials with low levels of contamination, and materials with physical or chemical properties that lie outside of product specifications. The ability to detect samples having one or more of the above conditions must be verified on a case-by-case basis. The long-term instrumental variation seems to be one of the important limiting factors in obtaining low limits of detection for impurities.

## ACKNOWLEDGMENT

The authors are grateful to Dale A. Von Behren of the FMC Corp. for supplying rejected samples of Avicel PH101 and Avicel PH102.

## LITERATURE CITED

- (1) Derde, M. P.; Massart, D. L. *Anal. Chim. Acta* **1986**, *191*, 1-16.
- (2) Derde, M. P.; Massart, D. L. *Chemom. Intell. Lab Syst.* **1988**, *4*, 65-91.
- (3) Wetzul, D. L. *Anal. Chem.* **1983**, *55*, 1165A-1176A.
- (4) Watson, C. A. *Anal. Chem.* **1977**, *49*, 835A-840A.
- (5) Mark, H.; Workman, *Spectroscopy* **1986**, *1*, 39-46.
- (6) Mark, H. L.; Tunnell, D. *Anal. Chem.* **1985**, *57*, 1449-1456.
- (7) Mark, H. L. *Anal. Chem.* **1987**, *59*, 790-795.
- (8) Derde, M. P.; Massart, D. L. *Anal. Chim. Acta* **1986**, *184*, 33-51.
- (9) Gemperline, P. J.; Webber, L. D.; Cox, F. A. *Anal. Chem.* **1989**, *61*, 138-144.
- (10) Van Der Voet, H.; Coenegracht, M. J.; Hemel, J. B. *Anal. Chim. Acta* **1987**, *192*, 63-75.
- (11) Malinowski, E. R. *J. Chemom.* **1987**, *1*, 33-40.
- (12) Johnson, R. A.; Wichern, D. W. *Applied Multivariate Statistical Analysis*; Prentice Hall: NJ, 1988; pp 134-135.
- (13) Wold, S.; Sjorstrom, M. In *Chemometrics: Theory and Application*; Kowalski, B. R., Ed.; American Chemical Society: Washington, DC, 1977; pp 242-282.
- (14) Genest, C.; Zidek, J. V. *Stat. Sci.* **1986**, *1*, 114-148.
- (15) Mudholkar, G. S.; George, E. O. In *Optimizing Methods in Statistics*; Rustagi, J. S., Ed.; Academic Press: New York, 1979; pp 345-365.
- (16) Tippett, L. H. C. *The Method of Statistics*, 1st ed.; Williams and Norgate: London, 1931.

RECEIVED for review July 11, 1989. Accepted November 28, 1989. Financial support for this research was provided by Burroughs Wellcome Co.

# Effects of Inaccurate Reference Lifetimes on Interpreting Frequency-Domain Fluorescence Data

Kevin S. Litwiler, Jingfan Huang, and Frank V. Bright\*

Department of Chemistry, Acheson Hall, State University of New York at Buffalo, Buffalo, New York 14214

The effects of assigning inaccurate reference lifetimes in lifetime determinations are predicted theoretically by using standard equations. This theory leads to a method to remove reference error effects using common least-squares software. This method cannot, however, be used to deconvolute data collected with isochronal references. Uncorrected data can always be exactly solved with models containing one more degree of freedom than the true model. Monoexponential decays are fit by double-exponential decays or excited-state processes. Unimodal distributed decays often appear as discrete, double-exponential decays.

## INTRODUCTION

The emissive characteristics (spectral, temporal, and polarization) of fluorophores are widely used to probe the local environments of fluorescent centers (1-10). Over the years, the utility of such fluorescence measurements has made a tremendous impact in numerous subdisciplines of chemistry (11-17). Fluorescence lifetime measurements are particularly important when one is examining systems involving distributed environments, energy transfers, and excimer and exciplex formations. The kinetics of these systems are often complex; therefore low-noise, unbiased data are necessary to extract accurate and precise information. Although new instrumental designs will continue to increase the signal-to-noise ratio of fluorometric measurements, experimentalists may still unknowingly introduce errors in their data.

An inaccurately assumed reference fluorophore lifetime value in phase modulation fluorometry is an important example of this type of error (18). Frequency-domain fluorometry, like time-domain fluorometry, requires the use of a reference in the measurement of fluorescence lifetimes (12). The phase shift and demodulation factor for the reference are used as a calibration point to determine the lifetime of the sample, if the reference lifetime is known. Obviously, if it is not accurately known, the sample lifetime will be shifted in the same direction as the reference inaccuracy. But the effects are more deeply rooted than a simple shift in the recovered lifetime. Reference lifetime errors can drastically affect the interpretation of fluorescence decay data in additional, non-trivial ways.

In this paper the theory predicting this behavior is given. Simulations that illustrate these effects and their interpretation are generated, first for discrete exponential decays followed by distributed decays. A method to extract accurate sample kinetics that are acquired by using incorrect reference lifetime values is given.

## THEORY

The theory of phase modulation fluorometry is well documented (12). It is important however to recall some basic equations describing the photoemission process of a fluorophore excited by sinusoidal, amplitude-modulated radiation.

Because all fluorophores have a finite, average lifetime in the excited state following excitation, the emission is delayed in time and dampened in modulation amplitude compared to the excitation. The phase shift ( $\theta$ ) and demodulation factor ( $M$ ) of a fluorophore can be used independently to calculate its lifetime:

$$\tau_p = 1/\omega \tan \theta \quad (1)$$

$$\tau_m = 1/\omega(1/M^2 - 1)^{1/2} \quad (2)$$

where  $\omega$  is the angular frequency of the excitation ( $\omega = 2\pi f$ ;  $f$  is the linear modulation frequency in hertz).  $\tau_p$  and  $\tau_m$  are the lifetimes calculated from the phase shift and the demodulation factor, respectively.

If the reference is scattered excitation, the reference lifetime is assumed to be zero. The reference triggers the detectors in order to correct for optical and electronic delays within the instrumentation. Although scattered excitation has been used, color effects limit the accuracy of lifetime measurements (19, 20), and no simple solutions to solve the color effects have appeared (19, 21, 22). Reference fluorophores therefore have become more popular since they have the same spatial and energetic emissive qualities as those of the sample (19, 21-23). However, the lifetime of the reference fluorophore ( $\tau_r$ ) must be known to calculate the absolute sample phase shifts and demodulation factors (18).

$$\theta = \theta_s - \theta_r + \arctan(\omega\tau_r) \quad (3)$$

and

$$M = M_s/M_r[(\omega\tau_r)^2 + 1]^{1/2} \quad (4)$$

In these equations  $\theta$  and  $M$  are the actual phase angle and modulation amplitude of the sample used to calculate the sample kinetics.  $\theta_s$  and  $M_s$  are the measured sample phase shift and modulation, and  $\theta_r$  and  $M_r$  are the measured reference phase shift and modulation.  $\theta$  and  $M$  are calculated at several frequencies and are then fit by using theoretical lifetime models (22):

$$\theta = \tan^{-1}(S/G) \quad (5)$$

$$M^2 = S^2 + G^2 \quad (6)$$

where

$$S = \sum_{i=1}^n F_i \omega \tau_i (1 + \omega^2 \tau_i^2)^{-1} \quad (7)$$

$$G = \sum_{i=1}^n F_i (1 + \omega^2 \tau_i^2)^{-1} \quad (8)$$

Here,  $\tau_i$  and  $F_i$  are the lifetime and fractional contribution of the  $i$ th component in the fitting model, respectively. If the experimentally determined phase and modulation (eqs 3 and 4) are set to equal the theoretical phase and modulations, then for a monoexponential decay with a reference lifetime error

$$\tan^{-1}(\omega\tau_s) - \tan^{-1}(\omega\tau_r) + \tan^{-1}(\omega\tau_r) = \tan^{-1}(S/G) \quad (9)$$

\* Author to whom correspondence should be addressed.

and

$$M_s(M_r'/M_r) = (S^2 + G^2)^{-1/2} \quad (10)$$

If there is no reference error, the equations collapse, leaving  $\tau_s = \tau_1$  for both phase and modulation. In order for the equations to be solved for a monoexponential decay with an error, the index ( $i$ ) must be 2. On the left (experimental) side of the equations, there is one independent variable ( $\tau_s$ ) when there is no error. With error, there are three ( $\tau_s$ ,  $\tau_r$ , and  $\tau_r'$ ). Therefore, there must be three variables on the theoretical sides of the equations so they are balanced. Only if  $i = 2$  are there three independent variables ( $\tau_1$ ,  $\tau_2$ , and  $F_1$ ). Solving these equations gives  $\tau_s = \tau_1$ ,  $\tau_r' = \tau_2$ , and

$$\tau_r = \tau_1 + F_1(\tau_2 - \tau_1) \quad (11)$$

or

$$F_1 = (\tau_r - \tau_s) / (\tau_r' - \tau_s) \quad (12)$$

These equations could be extended to include more complicated multiexponential decays, but in all cases, one extra component must be added to the model ( $i$  is incremented by 1) to account for the added degree of freedom from the reference lifetime error.

It is clear that even if the sample and reference fluorophores are confirmed monoexponentials, phase modulation data for the sample could appear to be multiexponential because there is a reference assignment error and an extra component is needed in the fit. The model yielding the best fit to the data would indicate kinetic models that are not expected or even impossible.

Barrow and Lentz (18) have briefly described this effect for single- and double-exponential decays using phase fluorometry at three frequencies. Their work was directed toward minimizing the effect by using isochronal references, references whose lifetimes are equal to the sample lifetimes. Considering the results above, their reasoning is understood. As the sample and reference lifetimes become more similar,  $F_1$  approaches unity (a single exponential), and any apparent heterogeneity would vanish.

## EXPERIMENTAL SECTION

Discrete exponential simulated data were generated with SLM 48000 software by using frequencies of 1, 2, 3, 4, 5, 7, 10, 12, 15, 20, 25, 30, 35, 40, 45, 50, 60, 70, 80, 90, 100, 120, and 150 MHz. Distributed decay simulated data were generated by using a global analysis software package (24) graciously donated by J. M. Beechem at Vanderbilt University. All data were analyzed with the global analysis package. The error induced from inaccurate reference lifetimes was propagated into simulated phase shift and demodulation data by using software written in-house (IBM BASIC) based on the equations described above. All lifetimes are reported in nanoseconds. Fractional intensity contributions ( $F_i$ ) are reported as percentages.

## RESULTS AND DISCUSSION

Even though the effects of inaccurately assumed reference lifetimes can be exactly modeled as in the theoretical section, it is useful to study the interpretation of these data by using (1) models that exactly describe the system with the added component and (2) models that are as complicated as the simulation model and do not perfectly describe the system. There is no noise (random error) introduced into any of these simulations; however, the simulations are analyzed assuming a constant phase and modulation error (noise) of 0.2° and 0.002, respectively. In this way conclusions can be drawn based on the relative and absolute reduced chi-squared ( $\chi^2$ ) values. If the  $\chi^2$  approaches zero, the model fits perfectly. These are models predicted by theory. If the  $\chi^2$  is less than unity but not near zero, the model is not exact and would not be predicted theoretically. However, since the fit is so close,

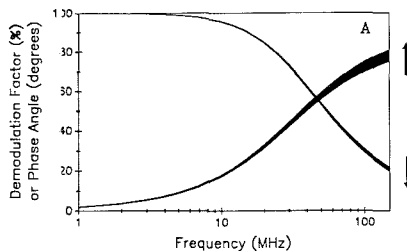


**Figure 1.** Multifrequency phase and demodulation traces for simulated monoexponential decay with a lifetime of 5 ns. The reference lifetime is varied from  $-10\%$  to  $+10\%$  of the actual value (1 ns). The direction of the arrows indicates the increase in reference error ( $-10\% \rightarrow +10\%$ ).

**Table I.** Effects of Inaccurate Reference Standard Lifetimes on the Recovered Lifetimes of Single-exponential Samples

no.	conditions			recovered values			$\chi^2$ <sup>g</sup>
	$\tau_r^a$	$\tau_r'^b$	$\tau_s^c$	$\tau_1^d$	$\tau_2^e$	$F_1^f$	
1	1.00	0.90	5.00	4.84		100	19.0
				5.00	0.90	98	0.00
2	1.00	1.10	5.00	5.16		100	16.9
				5.00	1.10	103	0.00
3	5.00 <sup>h</sup>	4.50	5.00	4.50		100	0.00
4	5.00 <sup>h</sup>	5.50	5.00	5.50		100	0.00
5	5.00	4.50	1.00	0.80		100	201
				1.00	4.50	114	0.00
6	5.00	5.50	1.00	1.21		100	13.8
				1.00	5.50	89	0.00
7	1.00 <sup>h</sup>	0.90	1.00	0.90		100	0.00
8	1.00 <sup>h</sup>	1.10	1.00	1.10		100	0.00
9	1.0	9.00	5.00	4.41		100	33.8
				5.00	9.00	125	0.00
10	1.0	11.0	5.00	5.60		100	23.2
				5.00	11.0	83	0.00

<sup>a</sup> Actual reference lifetime (ns). <sup>b</sup> Assumed reference lifetime (ns). <sup>c</sup> Actual lifetime for the sample (ns). <sup>d</sup> Recovered lifetime for component 1 (ns). <sup>e</sup> Recovered lifetime for component 2 (ns). <sup>f</sup> Recovered fractional percentage of component 1 ( $F_1 + F_2 = 100\%$ ). <sup>g</sup> Chi-squared value. <sup>h</sup> Denotes the use of an isochronal reference.

deviation in the fit to experimental data with noise would not be detected. On the basis of  $\chi^2$  values, an experimentalist could not choose a "perfect" model over a "close" model since both  $\chi^2$  values are less than 1.

Throughout the following discussions the term "error" will refer to the difference between  $\tau_r$  and  $\tau_r'$ . In most of the simulations, relative reference lifetime errors of  $\pm 10\%$  are assumed, 10% error not being an unreasonable assumption considering the range of some reference lifetimes reported in the literature (21, 22). Simulations are examined in order of increasing complexity. Monoexponential decays are first investigated, followed by multiexponential, discrete decays. Finally, three types of distributed models are examined.

**Monoexponential Decays.** Figure 1 shows changes in the phase modulation trace of a 5-ns monoexponential decay observed by varying the 1-ns reference lifetime from  $-10\%$  (0.9 ns) to  $+10\%$  (1.1 ns). The arrows indicate the direction of increasing  $\tau_r'$ . Note that the deviations are not constant with frequency. In this case, at higher frequencies there is a larger relative error. The recovered values for theoretical fits to this data and four other typical monoexponential decay simulations with reference lifetime errors are compiled in Table I. Data were simulated by using the sample lifetime listed in the table. The phase and demodulation were then

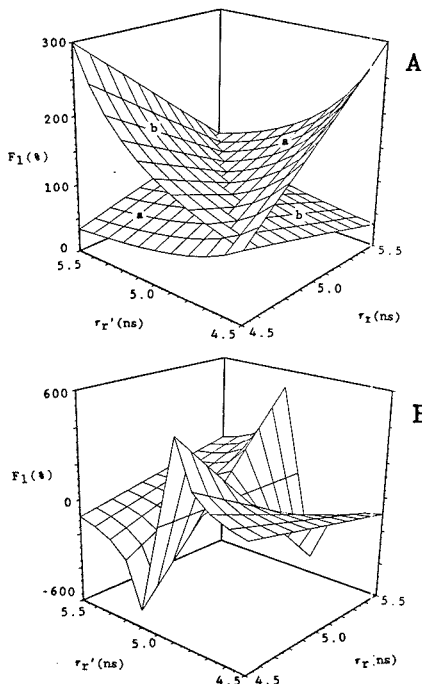


**Figure 2.** (Panel A) Recovered fractional contribution of component 1 ( $F_1$ ) as a function of true reference lifetime ( $\tau_r$ ) and assumed reference lifetime ( $\tau_r'$ ) for sample lifetimes of 1 ns (surface a), and 6 ns (surface b). (Panel B) Recovered  $F_1$  as a function of  $\tau_r$  and  $\tau_r'$  for sample lifetimes of 5 ns.

shifted according to the difference between the actual reference lifetime and the assumed reference lifetime ( $\pm 10\%$ ). The modified data sets were fit by using single- and double-exponential decay models.

With no  $\tau_r$  error, the monoexponential model exactly fits the simulated data; the  $\chi^2$  value is zero. When a reference lifetime error is induced, however, some general trends can immediately be seen (Table I). When an isochronal reference is assumed, a monoexponential decay perfectly fits the data. This agrees with the theory presented above and the conclusions of Lentz and Borrowers (18). Isochronal references remove heterogeneity regardless of how large the absolute reference error is. This would, of course, argue for the use of isochronal references. However, it is important to point out that even though there is no heterogeneity, the recovered sample lifetimes are still inaccurate (Table I, simulations number 3, 4, 7, 8). They logically always equal  $\tau_r'$  instead of  $\tau_r$ .

To perfectly fit nonisochronal data sets, a second component is required in the fitting model. The recovered lifetimes and fractional contributions are equivalent to those predicted by theory (eqs 11 and 12) for a monoexponential decay with a reference lifetime error. Trends in fractional contribution can be modeled by using the theory above (eq 12). The fractional contribution of the first component, which typically is used as an indicator of the degree of heterogeneity, is plotted in Figure 2 as a function of  $\tau_r$  and  $\tau_r'$ . When the sample lifetime is shorter or longer than the reference lifetime regime (Figure 2A), smooth surfaces result. When  $\tau_r$  equals  $\tau_r'$  (no error),  $F_1$  equals unity. This corresponds to the intersection of the two surfaces in Figure 2A. As their difference increases,  $F_1$  in-

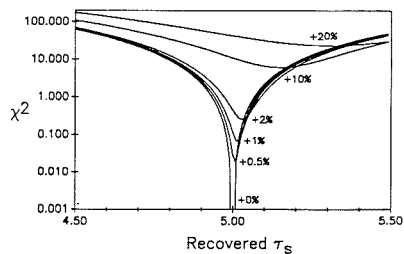


**Figure 3.**  $\chi^2$  versus recovered sample lifetime ( $\tau_s$ ) for monoexponential fits to a monoexponential decay of 5 ns. The reference lifetime is shifted from 0% to 20% greater than the actual value reference lifetime (1 ns).

creases or decreases from unity, indicating excited-state processes (25) or ground-state heterogeneity (20, 22), respectively.

Figure 2B shows the surface of fractional contribution versus  $\tau_r$  and  $\tau_r'$  which are near an isochronal reference. As  $\tau_r'$  approaches  $\tau_r$ ,  $F_1$  approaches plus or minus infinity. Thus, theoretically, the smaller the error in the reference lifetime for isochronal references, the more  $F_1$  and  $F_2$  diverge from unity. To perfectly fit data, ridiculous fractional contributions would be required. Of course, in reality, this is not the case. As the error becomes smaller, a single-exponential decay appears to fit just as well as a double-exponential decay (vide infra) and the double-exponential model is discarded on the basis of the complexity of the model and  $\chi^2$ .

When one considers that 10% heterogeneity (Table I, simulations 5, 6, 9, 10) can reproducibly be measured with current phase fluorimeters, erroneous fractional contributions would easily be recorded and reported even if the sample and reference both emit monoexponentially. A method to simultaneously determine the lifetimes for monoexponential samples and references, removing error effects, would be a useful tool. A method is proposed here. It is based on the equations described above. After data is experimentally acquired, an extra component ( $\tau_r'$ ) is added to the fitting model. This model (a double-exponential decay) is used to fit the experimental data, fixing the lifetime of the second component to  $\tau_r'$ , but floating its fractional contribution. The second component factors out any deviations in the data due to inaccurate reference lifetimes. The recovered lifetime of the first component equals the true sample lifetime. The fractional contribution can then be used as a check. If the fractional contribution calculated from eq 12 does not equal the recovered fractional contribution, the second component could be real. The true reference lifetime can be calculated from eq 11. The advantages of this method are (1) its speed in recovering the true sample lifetime, (2) an internal check, and (3) the lack of extra software required.

Finally, the interpretation of data using a fitting model equivalent to the model used for its simulation is considered. Figure 3 shows the changes in the confidence intervals as the reference lifetime error increases from 0% to 20% for a monoexponential decay of 5 ns. As the error increases, the recovered sample lifetime shifts to longer lifetimes (for this system). This increase in  $\tau_s$  is proportional, but not equal, to the absolute shift in  $\tau_r$ . The proportionality constant depends on  $\tau_s$ . It is also important to notice from Figure 3 that the  $\chi^2$  versus lifetime curves become more shallow with increasing reference error. This indicates that  $\tau_s$  is not fit as well with a monoexponential model with increasing error; the model is less appropriate.

A series of multiexponential simulations are also presented below. The results are similar to those found for the mo-

**Table II. Effects of Inaccurate Reference Standard Lifetimes on the Recovered Lifetimes of Double-Exponential Samples**

no.	conditions		recovered values					$\chi^2$ <sup>h</sup>
	$\tau_r^a$	$\tau_r'^b$	$\tau_1^c$	$\tau_2^d$	$\tau_3^e$	$F_1^f$	$F_2^g$	
For 50% 5 ns and 50% 10 ns								
1	1.00	0.90	6.72			100		135
			3.12	8.37		21	79	2.94
			5.00	10.0	0.90	50	48	0.00
2	1.00	1.10	7.12			100		28.2
			6.43	15.1		86	14	6.36
			5.00	10.0	1.10	51	51	0.00
3	5.00	4.50	6.29			100		97.6
			4.50	10.0		55	45	0.00
4	5.00	5.50	7.55			100		33.4
			5.50	10.0		44	56	0.00
5	7.00	6.30	6.21			100		60.0
			4.88	10.3		64	36	0.01
			5.00	10.0	6.30	77	40	0.00
6	7.00	7.70	7.64			100		58.3
			4.98	10.0		36	64	0.01
			5.00	10.0	7.70	37	65	0.00
7	7.50	8.25	6.19			100		52.6
			4.93	10.2		66	34	0.05
			5.00	10.0	8.25	71	40	0.00
8	7.50	6.75	7.65			100		64.9
			4.95	10.2		37	63	0.02
			5.00	10.0	6.75	39	71	0.00
9	10.0	9.00	6.14			100		25.7
			5.00	9.00		63	37	0.00
10	10.0	11.0	7.71			100		97.9
			5.00	11.0		42		0.00
11	13.0	11.7	6.11			100		10.1
			4.09	6.68		21	79	0.17
			5.00	10.0	11.7	60	100	0.00
12	13.0	14.3	7.75			100		134
			5.17	12.2		49	51	0.02
			5.00	10.0	14.3	43	35	0.00
For 20% 5 ns and 80% 10 ns								
13	1.00	0.90	8.38			100		96.2
			2.24	9.32		7	97	1.60
			5.00	10.0	0.90	20	79	0.00
14	1.00	1.10	8.82			100		11.8
			8.29	16.4		90	10	6.57
			5.00	10.0	1.10	21	80	0.00
For 80% 5 ns and 20% 10 ns								
15	1.00	0.90	5.48			100		68.0
			2.68	6.45		18	82	2.55
			5.00	10.0	0.90	78	20	0.00
16	1.00	1.10	5.84			100		11.4
			5.71	25.7		98	2	8.06
			5.00	10.0	1.10	82	20	0.00

<sup>a</sup> Actual reference lifetime (ns). <sup>b</sup> Assumed reference lifetime (ns). <sup>c</sup> Recovered lifetime for component 1 (ns). <sup>d</sup> Recovered lifetime for component 2 (ns). <sup>e</sup> Recovered lifetime for component 3 (ns). <sup>f</sup> Recovered fractional percentage of component 1 ( $F_1 + F_2 + F_3 = 100\%$ ). <sup>g</sup> Recovered fractional percentage of component 2 ( $F_1 + F_2 + F_3 = 100\%$ ). <sup>h</sup> Chi-squared value.

noexponential models. Single-, double-, and triple-exponential fits to true double-exponential simulations are summarized in Table II. In cases where  $\tau_r$  equals one of the sample lifetimes, the system can be modeled accurately with a double-exponential decay model. This is similar to the isochronal fits to the monoexponential decays. In each of these cases one recovered component of the fit equals the assumed reference lifetime. The second recovered component equals the lifetime of the other component in the simulation. When reference lifetimes lower and higher than both sample lifetimes are used, only triple exponentials can exactly describe the decays. In all cases the added component equals  $\tau_r'$  and the other components equal the simulated sample lifetimes.

Double-exponential fits to some data sets (e.g.,  $\tau_r$  equals

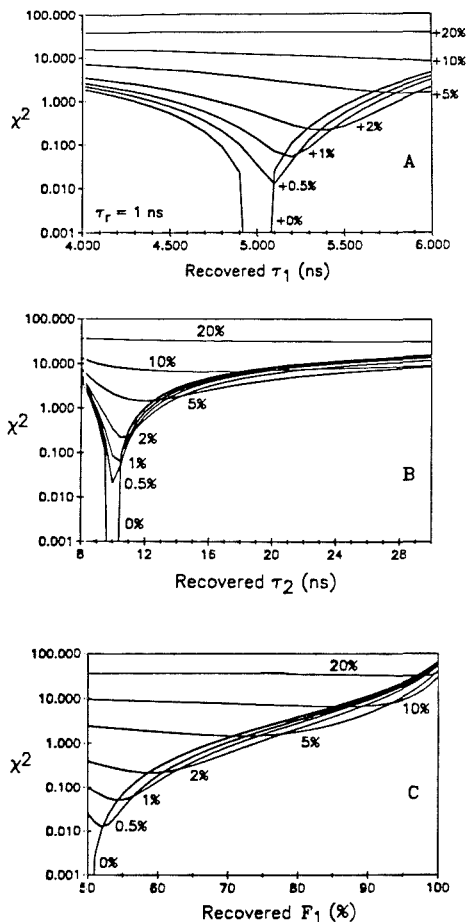


**Figure 4.** (Panel A) Confidence intervals for the recovered lifetime component 1 ( $\tau_1$ ) of a double-exponential decay (50% 5 ns, 50% 10 ns) as a function of reference lifetime error. The assumed reference lifetime is varied from 1 to 1.2 ns (0% to 20% error). (Panel B) Confidence intervals for the recovered lifetime component 2 ( $\tau_2$ ) as a function of increasing reference lifetime error. (Panel C) Confidence intervals for the recovered fractional contribution of component 1 ( $F_1$ ) as a function of reference lifetime error.

the weighted average of the sample lifetimes, Table II, simulations 5-8), however, have  $\chi^2$  values less than 1. The fits are close enough that differences between experimentally obtained data and the fit could not be detected above instrumental noise, yet the recovered fractional contributions would be incorrect by more than 10%. Adding the third component to fits of this type does not change the  $\chi^2$  value substantially.

As the error in  $\tau_r$  is increased, the  $\chi^2$  surfaces of all components in multiexponential decays become more shallow. The  $\chi^2$  surfaces for the two components and the fractional contribution to the first component of a double-exponential decay are shown in Figure 4. In each case, the recovered values systematically deviate from the actual values. At +20% error the  $\chi^2$  curves are nearly flat.

It is also important to note the potential for the accidental removal of true heterogeneity by choosing an inappropriate

$\tau_r$ . As an example, if a double-exponential decay is simulated consisting of 95% of a 3-ns component and 5% of a 5-ns component, the system appears to be homogeneous if the 5-ns reference lifetime is only 2% low (4.9 ns). The system appears to be undergoing an excited-state process if  $\tau_r'$  is less than 4.9 ns.

Fits to simulated triple- and quadruple-exponential decays are included in this discussion for completeness. Predictably, each set requires one more component than the original decay to reach a perfect fit. The added component equals  $\tau_r'$ , and its fractional contribution can be positive or negative. The method of adding an extra component to a fit to remove a reference lifetime error is theoretically valid for any multiexponential decay. In each case only one degree of freedom has been added (the added fractional contribution) since the lifetime of the added component is fixed to  $\tau_r'$ . However, it is questionable whether these models are appropriate given the current limits in signal to noise ratio and resolution (26).

**Distributed Lifetimes.** Because of the increasing interest in distributed kinetics to describe dynamic fluorescence (27–32), the effects of inaccurate reference lifetimes on distributed models are included in this section. All distributed lifetime simulations were generated and fit by using the three most common models (31): Gaussian, Lorentzian, and uniform. In the following sections the term “width” will correspond to one standard deviation for Gaussian distributions and one half-width at half maximum for all other distributions. A syntax of “5 w 1 (G)” will be used to describe a Gaussian distribution centered at 5 ns with a width of 1 ns. The recovered values from several theoretical fits to distributed simulations with reference lifetime errors are listed in Table III. Simulations of other distributions (5 w 2 (G), 1 w 0.1 (G), for example) have also been analyzed but are not tabulated here. The results are similar to those discussed below.

The data were best fit ( $\chi^2 < 10^{-3}$ ) with models equivalent to the simulation model plus an added discrete component. For example, a unimodal distribution (5 w 0.5 (G)) with a reference lifetime error is best fit by a model having one distributed lifetime component (5 w 0.5 (G)) and one discrete lifetime component equal to  $\tau_r'$ . Less complicated models (listed in Table III) do not fit as well and have  $\chi^2$  values at least 100 times greater than those of the unimodal-discrete fits.

The double-exponential decay fits to all of the data sets in Table III would be no worse than the “exact” fit from a model with one unimodal and one discrete lifetime. Therefore, based on  $\chi^2$  values, it would be difficult to justify applying the method described above to remove any reference lifetime error. Furthermore, the  $\chi^2$  values for discrete double-exponential models are usually measurably lower than for any unimodal distributed model. Nearly all of these data sets, therefore, would be judged to be double-exponential decays rather than any type of distributed process. Any theory predicting distributed environments, although possibly correct, would be contradicted by the assignment of a nondistributed decay. Finally, if only unimodal models are considered, any unimodal data set with a reference lifetime error can appear to be any other type of unimodal distribution on the basis of their  $\chi^2$  values (depending on  $\tau_s$ ,  $\tau_r$ , and  $\tau_r'$ ).

Specific examples of effects of this nature can be seen in Table III. Fits to 5 w 0.5 (G) with  $\tau_r = 1$  ns – 10% are better for a double-exponential (discrete) decay ( $\chi^2 = 0.05$ ) than for any single distribution ( $\chi^2 = 1.26$ ). The monoexponential, however, is 17 times worse than the best distributed monoexponential (a Lorentzian). Therefore, this data set would most likely be judged to be a discrete double-exponential decay on the basis of the  $\chi^2$  values even though there is only a 3.4% contribution to the second component. In cases where the

**Table III. Effects of Inaccurate Reference Lifetimes on Unimodal, Distributed Samples with Centers at 5 ns and Widths of 0.5 ns<sup>a</sup>**

conditions		recovered parameters					$\chi^2$
SM <sup>b</sup>	FM <sup>c</sup>	$\tau_r'$ <sup>d</sup>	$\tau_1$ <sup>e</sup>	w <sup>f</sup>	$\tau_2$ <sup>g</sup>	$F_1$ <sup>h</sup>	
G	G	0.9	4.98	1.25			4.51
	L		4.94	0.94			1.26
	U		4.98	2.13			5.76
	S		4.81				21.8
G	D		5.02		1.11	97	0.05
	G	1.1	NSF <sup>i</sup>	NSF			NSF
	L		5.07	-0.06			13.9
	U		5.13	0.02			11.9
	S		5.13				11.6
L	D		NSF		NSF	NSF	NSF
	G	0.9	4.98	1.29			4.33
	L		4.95	0.96			0.90
	U		4.98	2.22			5.84
	S		4.79				25.1
L	D		5.04		1.20	96	0.08
	G	1.1	NSF	NSF			NSF
	L		5.10	-0.01			10.3
	U		5.18	0.00			9.84
	S		5.12				9.59
U	D		5.02		0.68	101	0.12
	G	0.9	4.98	1.19			4.96
	L		4.97	0.92			1.88
	U		4.98	2.02			5.97
	S		4.83				18.7
U	D		5.01		0.97	97	$6.1 \times 10^{-8}$
	G	1.1	NSF	NSF			NSF
	L		5.18	-0.02			14.6
	U		5.15	0.00			15.1
	S		5.15				13.9
D			5.01		1.01	102	$5.8 \times 10^{-8}$

<sup>a</sup>The best fit (a unimodal plus a discrete) for each simulation is not included in the table (see text). <sup>b</sup>Simulation model (SM) represents the model used to simulate the data sets. Symbolism is as follows: G, Gaussian; L, Lorentzian; U, uniform. <sup>c</sup>Fitting model (FM) represents the model used to analyze the simulated data after a reference lifetime error was induced. Symbolism is as follows: G, unimodal Gaussian distribution; L, unimodal Lorentzian distribution; U, unimodal uniform distribution; S, single discrete exponential; D, double discrete exponential. <sup>d</sup>Assumed reference lifetime (actual reference lifetime equals 1 ns) (ns). <sup>e</sup>Center of distribution for distributed models, lifetime of component 1 for discrete models (ns). <sup>f</sup>Width of distribution (detailed in text) (ns). <sup>g</sup>Lifetime of component 2 (ns). <sup>h</sup>Fractional percentages of component 1 ( $F_1 + F_2 = 100\%$ ). <sup>i</sup>Chi-squared value. <sup>j</sup>NSF means no solution was found because there was no convergence when this model was used.

$\tau_r'$  is 10% high, the  $\chi^2$  value for the monoexponential is nearly equal to that of the best unimodal distribution model. For the uniform distributions, the discrete double-exponential model is much better than any other model.

The confidence intervals for the recovered lifetime (Figure 5A) and width (Figure 5B,C) of a 5 w 0.5 (G) distribution ( $\tau_r = 1$  ns) are shown as a function of reference lifetime error. For these plots the model used to fit the data is the same as the model used to simulate the data before the reference lifetime error was induced. As noted previously, the surfaces of both sets of curves become shallower as the error increases, indicating that the model becomes less appropriate. Although the center of the distribution remains essentially unchanged with increasing reference error (Figure 5A), the width narrows considerably (Figure 5B). In Figure 5C the center of the distribution is plotted versus positive reference lifetime error, the height of the shaded region being two standard deviations wide. The distribution width quickly narrows and reaches a minimum width by a reference lifetime error of +5% error. When the error is greater than +5%, the best model for this

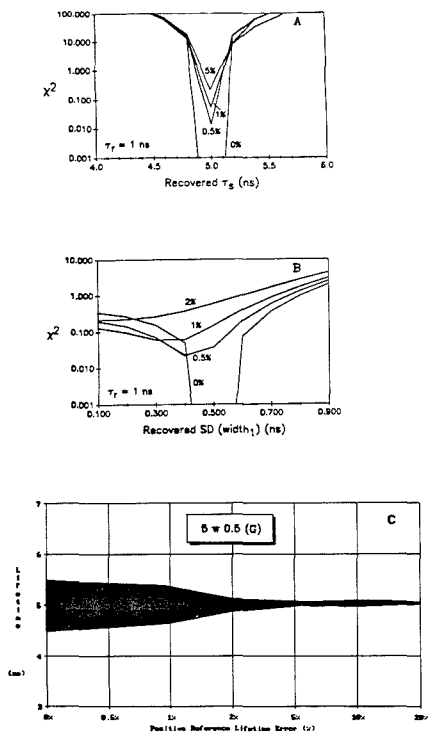


**Figure 5.** (Panel A) Confidence intervals for the center ( $\tau_s$ ) of a Gaussian distribution (5 w 0.5) with increasing error in reference lifetime (1 ns). (Panel B) Confidence intervals for the width of a Gaussian distribution (5 w 0.5) with increasing error in the reference lifetime. (Panel C) Lifetime center and width (standard deviation) of a Gaussian distribution (5 w 0.5) versus increasing (positive) reference lifetime error. The assumed reference lifetimes are in the range of 1–1.2 ns. The vertical height of the shaded region is two standard deviations wide.

system would appear to be a discrete decay law.

### CONCLUSIONS

Frequency-domain fluorometry is still a relatively new tool; however, as it matures more complicated decays will undoubtedly be investigated. To be confident in the validity of the experimental data, one must not introduce extra variables, such as reference lifetime errors (biases). Considering the range of reported lifetimes for common fluorophores, it is best to verify experimental assumptions and results. For the simpler decays, removing reference induced errors can be accomplished by using the method described above. Unfortunately, it is not useful for data sets obtained by using isochronal references.

Measuring lifetimes versus more than one reference fluorophore is a second procedure commonly used in this labo-

ratory. In this manner, results can be checked for internal consistency. Finally, although  $\chi^2$  values give insight into the goodness of fit, residuals to fits provide useful information about the randomness of deviations. Data sets with  $\chi^2$  values less than unity may have systematic deviations in the residuals, implying that the model is not an accurate representation of the true decay kinetics.

### LITERATURE CITED

- (1) Brand, L.; Gohlke, J. R. *Annu. Rev. Biochem.* **1972**, *41*, 843.
- (2) Warner, I. M.; Patony, G.; Thomas, M. P. *Anal. Chem.* **1988**, *57*, 463A.
- (3) Bright, F. V. *Anal. Chem.* **1988**, *60*, 1031A.
- (4) *Modern Fluorescence Spectroscopy*; Wehry, E. L., Ed.; Plenum Press: New York, 1976; Vol. 1–4.
- (5) Bright, F. V. *Appl. Spectrosc.* **1988**, *42*, 1245.
- (6) Cline Love, L. J.; Habarta, J. G.; Dorsey, J. G. *Anal. Chem.* **1984**, *56*, 1133A.
- (7) Demas, J. N. *Excited State Lifetime Measurements*; Academic Press: New York, 1983.
- (8) Lakowicz, J. R.; Laczko, G.; Gryczynski, I. *Rev. Sci. Instrum.* **1986**, *57*, 2499.
- (9) Tao, T. *Biopolymers* **1969**, *8*, 609.
- (10) Beechem, J. M.; Knutson, J. R.; Brand, L. *Biochem. Soc. Trans.* **1986**, *14*, 632.
- (11) Weber, G.; Farris, F. J. *Biochemistry* **1979**, *18*, 3075.
- (12) Lakowicz, J. R. *Principles of Fluorescence Spectroscopy*; Plenum Press: New York, 1983.
- (13) Barbara, P. F.; Jarzaba, W. *Acc. Chem. Res.* **1988**, *21*, 95.
- (14) Barbara, P. F.; Walker, G. C. *Rev. Chem. Intermed.* **1988**, *10*, 1.
- (15) Kosower, E. M.; Huppert, D. *Annu. Rev. Phys. Chem.* **1986**, *37*, 127.
- (16) Maroncelli, M.; Fleming, G. R. *J. Chem. Phys.* **1987**, *86*, 6221.
- (17) Lee, M.; Hochstrasser, R. M. *Chem. Phys. Lett.* **1988**, *153*, 1.
- (18) Barrow, D. A.; Lentz, B. R. *J. Biochem. Biophys. Methods* **1983**, *7*, 217.
- (19) Bauer, R. K.; Balter, A. *Opt. Commun.* **1979**, *28*, 91.
- (20) Gratton, E.; Jameson, D. M.; Hall, R. D. *Annu. Rev. Biophys. Bioeng.* **1984**, *13*, 105.
- (21) Lakowicz, J. R.; Cherek, H.; Balter, A. *J. Biochem. Biophys. Methods* **1981**, *5*, 131.
- (22) Jameson, D. M.; Gratton, E.; Hall, R. D. *Appl. Spectrosc. Rev.* **1984**, *20*(1), 35.
- (23) Lakowicz, J.; Cherek, H.; Bevan, D. R. *J. Biol. Chem.* **1980**, *255*(10), 4403.
- (24) Beechem, J. M.; Gratton, E. *SPIE Conf. Proc.* **1988**, *909*, 70.
- (25) Lakowicz, J. R.; Balter, A. *Biophys. Chem.* **1982**, *16*, 99.
- (26) Gratton, E.; Limkeman, M.; Lakowicz, J. R.; Maliwal, B. P.; Cherek, H.; Laczko, G. *Biophys. J.* **1984**, *46*, 479.
- (27) Lakowicz, J.; Cherek, H.; Gryczynski, I.; Joshi, N.; Johnson, M. *Biophys. Methods* **1987**, *28*, 31.
- (28) Fiorini, R.; Valentino, M.; Wang, S.; Glaser, M.; Gratton, E. *Biochemistry* **1987**, *26*, 3864.
- (29) Alcalá, J. R.; Gratton, E.; Prendergast, F. G. *Biophys. J.* **1987**, *51*, 597.
- (30) Alcalá, J. R.; Gratton, E.; Prendergast, F. G. *Biophys. J.* **1987**, *5*, 925.
- (31) Alcalá, J. R.; Gratton, E.; Prendergast, F. G. *Biophys. J.* **1987**, *51*, 57.
- (32) Bright, F. B.; Catena, G. C.; Huang, J. Evidence for Lifetime Distribution in Cyclohexatin Inclusion Complexes. *J. Am. Chem. Soc.* **1990**, *112*, 1343–1346.

RECEIVED for review September 5, 1989. Accepted November 28, 1989. This work was supported by BRSG S07 RR 07066 awarded by the Biomedical Research Support Grant Program, Division of Resources, National Institutes of Health, by the donors of the Petroleum Research Fund, administered by the American Chemical Society, the Health Care Instruments and Devices Institute at SUNY—Buffalo, by a NonTenured Faculty Grant from 3M, Inc., by a New Faculty Development Award from the New York State/United University Professions, by the Center for Advanced Technology (SUNY—Buffalo), and by the National Institute of Mental Health. Finally, K.S.L. wishes to acknowledge support in the form of a 1989 ACS Analytical Division Summer Fellowship sponsored by the Pittsburgh Conference.

# Combined Deconvolution and Curve Fitting for Quantitative Analysis of Unresolved Spectral Bands

John A. Pierce, Richard S. Jackson,<sup>1</sup> Kenneth W. Van Every, and Peter R. Griffiths\*<sup>1</sup>

Department of Chemistry, University of California, Riverside, California 92521

Gao Hongjin

Department of Chemistry and Chemical Engineering, Tsinghua University, Beijing, China

Curve-fitting programs usually only yield accurate parameters for unresolved spectral bands when the separation of neighboring bands exceeds their average half-width. By reduction of the width of each spectral feature in a heavily overlapped band multiplet by Fourier self-deconvolution (FSD), the conditioning of curve-fitting algorithms is improved to the point that the area of each band in the multiplet can be estimated with much improved accuracy. The practical limitations of this approach are discussed in this paper. Most FSD programs are strictly applicable to Lorentzian bands; the effect of increasing the Gaussian fraction of isolated bands on the accuracy of band area estimation has also been investigated. Finally, the application of combined deconvolution and curve fitting to synthetic band multiplets in which the relative peak absorbances and bandwidths are varied is shown to yield accurate estimates of band areas until the band separation approaches the width of the instrument line-shape function, which is determined by the truncation, exponentiation, and apodization of the Fourier domain array.

## INTRODUCTION

Many techniques have been developed for the quantitative analysis of complex mixtures by infrared spectrometry. The majority of these, including classical least squares (K-matrix) (1), inverse least squares (P-matrix) (2), partial least squares (3), and principal components regression (3, 4), depend on the availability of calibration spectra of mixtures of known composition. For certain samples, such as fossil fuels, the composition of the mixture may be so complex that calibration spectra are unavailable and all of the above approaches break down.

An alternative approach that can provide useful chemical information involves the use of least-squares curve-fitting techniques to fit the individual bands in an envelope (see for example refs 5-9). The achievement of a good representative fit requires the knowledge of the number of distinguishable bands into which the spectrum can be decomposed and an assumption about the shape of these bands. By use of an iterative procedure that minimizes the sum of the squares of the differences between the curve-fitted spectrum and the data, appropriate initial estimates of the individual positions, heights, and widths of the bands are varied to arrive at a best fit, i.e. to calculate an optimized model for the spectrum. The most important values for input to the curve-fitting routine are the number of bands and their positions (10).

One of the main drawbacks of curve fitting is that as the bands become more overlapped, or the number of overlapped bands increases, the problem becomes progressively more

ill-conditioned. Consequently, small errors in the data (e.g. noise or base-line distortions) or the assumptions (e.g. that the bands are Lorentzian in shape) can be magnified to give very large errors in the parameters of the final model. Vandeginste and de Galan (11) have discussed the effect of several sources of error that can arise in curve-fitting procedures. Audo et al. have addressed the specific problems of an incorrect base line (12) and the presence of small, undetected peaks (13), while Anderson et al. have investigated the effects of peak shape in the curve fitting of chromatographic data (14, 15). In all cases the conclusions were the same, namely that for well resolved bands curve fitting is a useful quantitative data analysis technique. If it is applied to complex systems of heavily overlapped bands, however, any errors in the original data are often magnified in the final band parameters to the point that the attachment of any physical meaning to these bands is impossible. Clearly, if curve fitting is to be a useful technique for the analysis of overlapped bands, then the conditioning of the problem must be improved in some way and a method is required that allows an estimate of the number of component bands to be obtained.

Calculation of the second or fourth derivative has been used to obtain an estimate of the number of component bands present and the position of these bands (16). A degree of quantitative analysis based on derivative spectra is also possible, since the height of each feature is directly proportional to its intensity in the original spectrum (17). Bands that are separated by less than their full width at half-height (FWHH), however, are still not resolved in the second derivative spectrum (18); in this case, even semiquantitative conclusions can be seriously in error because secondary lobes can suppress, enhance, or otherwise be confused with neighboring weaker spectral features (11). Furthermore, a very good signal-to-noise ratio (SNR) is required in the original spectrum if high-order derivative spectra are to be obtained, since differentiation greatly enhances the high-frequency components such as noise.

Fourier self-deconvolution (FSD) is an alternative technique for the determination of band number and position in unresolved multiplets (19, 20). This technique does not suffer as badly as derivative techniques from the problems imposed by secondary lobes, although a high SNR is still needed. A spectral envelope subjected to FSD results in all the bands being reduced in width by approximately equal values (but not necessarily by equal factors) and increased in height by the ratio of the original FWHH of the band to its FWHH after deconvolution. This procedure allows previously unresolved bands to become apparent, provided that their separation is greater than the instrument resolution. Although secondary lobes of the type observed in derivative spectra should not normally be observed after FSD, the formation of side lobes will occur if the bandwidth is reduced to the point that it becomes comparable to the instrument resolution (19, 21). In this case, it becomes difficult to distinguish between weak real

<sup>1</sup>Current address: Department of Chemistry, University of Idaho, Moscow, ID 83843.

features and artifacts that result from the finite extent of the interferogram. It is therefore important that an apodization function be applied to reduce these artifacts. Kauppinen et al. showed that the Bessel function is a good choice for apodizing deconvolved spectra (22).

After resolution enhancement by FSD using a fairly large resolution enhancement factor (vide infra), it becomes possible to estimate the number of bands whose separation exceeds the resolution at which the spectrum was measured. The position, in wavenumbers, of each feature that is just resolved can then be estimated by using the center-of-gravity technique (23). Kauppinen et al. (19) have previously suggested this use of FSD for determining the input parameters for a curve-fitting algorithm, and this application has been applied experimentally by Jasse to the spectra of polymers (24) and by Davis and White to vapor-phase spectra (25).

The most commonly applied technique for FSD was originally developed (19) for spectra in which each band has a Lorentzian shape; i.e. the absorbance,  $A_i(\bar{\nu})$ , of each band, at wavenumber  $\bar{\nu}$ , is given by

$$A_i(\bar{\nu}) = A_i^\circ \frac{\gamma_i^2}{\gamma_i^2 + 4(\bar{\nu} - \bar{\nu}_i^\circ)^2} \quad (1)$$

where  $A_i^\circ$  is the peak absorbance of the  $i$ th band, which is centered at  $\bar{\nu}_i^\circ$ , and  $\gamma_i$  is its full width at half-height. The spectrum is given by

$$A(\bar{\nu}) = \sum_{i=1}^N A_i(\bar{\nu}) \quad (2)$$

where  $N$  is the number of bands.

The inverse Fourier transform (FT) of  $A(\bar{\nu})$  is

$$Y(x) = 0.25 \sum_{i=1}^N \gamma_i A_i^\circ \exp(-2\pi j \bar{\nu}_i^\circ x) \exp(-\pi \gamma_i x) \quad (3)$$

where  $j = -1^{1/2}$ . Deconvolution involves multiplying the Fourier domain array by  $\exp(\pi \gamma' x)$  so that the rate of decay is decreased:

$$Y'(x) = Y(x) \exp(\pi \gamma' x) \quad (4)$$

$$= 0.25 \sum_{i=1}^N \gamma_i A_i^\circ \exp(-2\pi j \bar{\nu}_i^\circ x) \exp[-\pi(\gamma_i - \gamma')x] \quad (5)$$

Provided that  $\gamma' < \gamma_i$ , on computing the forward FT of  $Y'(x)$  in the absence of noise, we have

$$A'(\bar{\nu}) = \int_{-\infty}^{\infty} Y'(x) \exp(2\pi j \bar{\nu} x) dx \quad (6)$$

$$= \sum_{i=1}^N \frac{A_i^\circ \gamma_i}{(\gamma_i - \gamma')} \frac{(\gamma_i - \gamma')^2}{(\gamma_i - \gamma')^2 + 4(\bar{\nu} - \bar{\nu}_i^\circ)^2} \quad (7)$$

The band shapes are still Lorentzian, but the width of each band is decreased by  $\gamma'$  and the peak absorbance has been increased by the factor  $\kappa = \gamma_i/(\gamma_i - \gamma')$ . This factor is approximately equal to the resolution enhancement factor,  $K$ , defined by Kauppinen et al. (19, 22).

In practice the limits of the integration in eq 6 are not infinite. For spectra measured at a nominal resolution of  $R$   $\text{cm}^{-1}$ , the Fourier domain array is multiplied by a boxcar truncation function,  $D(x)$ , which is unity when  $|x| \leq R^{-1}$ , and zero when  $|x| > R^{-1}$ . Thus the spectrum,  $A'(\bar{\nu})$ , is convolved with a sinc function,  $(\sin x)/x$ , which is the FT of  $D(x)$ . Yang and Griffiths (26) showed that if the amplitude of the sinusoidal modulations in  $Y'(x)$  at  $x = R^{-1}$  has not decayed to approximately 10% or less of its value at  $x = 0$ , then side lobes become apparent in the spectrum. This corresponds to the condition for which  $(\gamma_i - \gamma') \leq 2R$ . If  $(\gamma_i - \gamma') < R$ , intolerably large side lobes are observed unless they are suppressed by apodization. Conversely, if  $(\gamma_i - \gamma') > R$  then the amplitude

of the sinusoidal modulations in  $Y'(x)$  decays to a very small level for values of  $x$  that are greater than  $R^{-1}$ . In this case inclusion of  $Y'(x)$  values at higher spatial frequencies only serves to increase the noise level in the spectrum without significant increase in the available information, and  $Y'(x)$  may be further truncated without introducing side lobes into  $A'(\bar{\nu})$ . In practice, therefore,  $Y'(x)$  is multiplied by a truncation function which is unity for  $|x| \leq F/R$ , where  $F$  is the fraction of the Fourier transform of the original spectrum used in these calculations and takes a value between 0 and 1. For  $|x| > F/R$ ,  $Y'(x) = 0$ .

The main disadvantage of FSD is that the choice of the parameters,  $\gamma'$  and  $F$  is often very subjective and, if incorrect, can lead to erroneous results. To obtain objective, quantitative information, these parameters need to be optimized to give the maximum achievable resolution enhancement without the introduction of side lobes or excessive noise, both of which will mask real weak spectral features.

One method for doing this was previously suggested by Yang and Griffiths (26, 27). They define a quantity  $\text{SNR}_d$  (the signal-to-noise ratio after deconvolution) as  $\text{SNR}_d = A'_{\text{peak}}/R_{3-8}$ , where  $A'_{\text{peak}}$  is the peak absorbance after deconvolution and  $R_{3-8}$  is the root mean square of the difference between each datum and the mean in a region estimated to be between  $3\gamma_i$  and  $8\gamma_i$  from the center of the closest strong band. They showed that this quantity exhibits a maximum if plotted as a function of  $\gamma'$  and  $F$ . This maximum exists because the magnitude of  $R_{3-8}$  is governed by three competing effects, the relative magnitudes of which depend on  $\gamma'$  and  $F$ ; these are side-lobe formation, noise, and the average gradient in the region  $3\gamma_i$ - $8\gamma_i$ . The average gradient, however, also changes if the region is chosen between different bounds, say  $4\gamma_i$  and  $10\gamma_i$ , and consequently the position of the maximum changes. This is an undesirable feature, since the bounds of the region can only be estimated. The position of the maximum in  $\text{SNR}_d$  is also dominated by changes in only one band in the multiplet.

An alternative approach is to curve-fit the deconvolved spectrum. The deviations between the curve-fitted spectrum and the data can then be used to monitor the average noise and the side-lobe formation in all the bands in the spectrum, without interference from gradient effects. Curve fitting the deconvolved spectrum also has a second advantage; since the resolution of the bands is greater than in the original spectrum, the conditioning of the curve-fitting problem is significantly improved and the errors in the calculated band parameters should therefore be reduced in comparison to the case where the original spectrum is curve-fitted.

To summarize, a combination of FSD and curve fitting is potentially a very powerful technique for the analysis of complex spectra. It should allow objective optimization of the parameters in FSD and determination of the number of component bands present. Curve fitting the optimally deconvolved spectrum should also produce more accurate band parameters than curve fitting the original spectrum in which the bands are heavily overlapped. Susi and Byler have applied FSD with subsequent curve fitting to the FT-IR (28, 29) and Raman (30) spectra of proteins, but did not undertake any systematic study of the advantages or disadvantages of this method.

To investigate the advantages of combining the two techniques, two sets of spectra were synthesized from a number of Lorentzian bands. Since the main advantage was expected to be an improvement in the conditioning of the curve fitting, small errors were introduced into these spectra. In all cases these included base-line errors. Some of the spectra also included peak shape errors. The first set was composed of a series of single bands. These had a small, variable Gaussian

fraction included. Each spectrum also had a linear base line removed, such that the ordinate value of the points at each end of the spectral range selected was zero. The curve-fitting program was not allowed to compensate for this by including a base line in the fit. Clearly, in the fitting of a real spectrum at least a linear base line should be included, and some problems would be likely to occur due to base-line curvature if the spectral range is large. The method given above for introducing base-line errors was chosen because it is common practice to base-line-correct real spectra in this manner, and such corrections are unlikely to be exact. It has the added advantage that during FSD it precludes the generation of oscillations at the extremes of the spectrum.

The second set was composed of several spectra that were synthesized by adding five broad Lorentzian bands. Again, a linear base line was removed from each spectrum, and the possibility of a base-line error was not allowed for in the curve-fit. The separation of the bands was  $5.5 \text{ cm}^{-1}$ , which is approximately equal to the effective resolution after truncation of a 0.25-cm retardation interferogram with  $F = 0.75$ .

### ISOLATED SPECTRAL BANDS

It has been shown that many fundamental absorption bands in infrared spectra are well described by a linear combination of Lorentzian and Gaussian bands where the Gaussian fraction is quite small (31). To investigate the effect of deconvolution on band shape, six synthetic Lorentzian/Gaussian bands described by the expression

$$A(\bar{\nu}) = (1 - \beta)A_0 \frac{\gamma^2}{\gamma^2 + 4(\bar{\nu} - \bar{\nu}_0)^2} + \beta A_0 \exp \frac{-4 \ln 2 (\bar{\nu} - \bar{\nu}_0)^2}{\gamma^2} \quad (8)$$

were generated, where  $A_0$  is the maximum peak absorbance,  $\bar{\nu}_0$  is the position, in wavenumbers, of the maximum peak absorbance, and  $\gamma$  is the FWHH of the Lorentzian and Gaussian components. The six spectra differed only in the amount of their Gaussian character,  $\beta$ . For each of them,  $A_0 = 0.200$ ,  $\gamma = 30 \text{ cm}^{-1}$ , and  $\bar{\nu}_0 = 2960 \text{ cm}^{-1}$ . The  $\beta$  values for the six trials were as follows: I, 0.000; II, 0.025; III, 0.050; IV, 0.100; V, 0.150; VI, 0.200. Bands with  $\beta > 0.200$  were not synthesized because they would not be relevant to the infrared spectra of molecules in the condensed phase (31). After removal of the base line from each spectrum the inverse FT was computed to a spatial frequency of 0.25 cm. The Fourier domain array was then multiplied by an exponential function,  $\exp(\pi\gamma'x)$ , truncated by using a value of  $F = 0.75$ , and apodized with a Bessel function to give an effective resolution of about  $5.1 \text{ cm}^{-1}$ . Finally, the FT of this array was computed, giving the deconvolved spectrum. A constant value of  $F = 0.75$  was used because changing its value was found to have little effect on the deconvolution of noise-free, synthetic spectra.

The resulting band was then fitted by using a curve-fitting program obtained from the National Research Council of Canada. This program uses a least-squares criterion for optimization based on the method of Levenberg (32). The peak shape used in the curve fitting was also a linear combination of Lorentzian and Gaussian bands, with a Gaussian fraction  $\alpha$ . The initial estimates for height and FWHH were 1.0 absorbance unit (AU) and  $10 \text{ cm}^{-1}$ , respectively; the actual input values of these parameters were found to have negligible effect on the accuracy of the fit. The value  $\bar{\nu}_0$  was determined from a highly deconvolved spectrum by using the center-of-gravity technique and was always within  $0.1 \text{ cm}^{-1}$  of the true value. The curve-fitting program allowed the height, width, and position, but not the number of bands (specified in this case as 1) or the Gaussian fraction,  $\alpha$ , to vary. A "damping factor" controlled the amount by which each parameter could be changed during each iteration. For most cases, a damping

factor of 0.01 was employed. In the case of  $\gamma' = 29 \text{ cm}^{-1}$ , where side lobes were apparent in the deconvolved spectrum, it was necessary to use a damping factor of 0.09 in order for the fitting program to converge. To reduce computation time, a maximum of five iterations was allowed. It was found that, in the work presented here, allowing a greater number of iterations or changing the damping factor did not significantly affect the final parameters in the fit.

The output of the curve-fitting routine provided a value for the deviations, which is the square root of the sum of the squares of the differences between the data and the best fit curve. The area of the fitted band was also used as a quantitative measure of the goodness-of-fit by comparison with the area of the original band (i.e. the area before deconvolution). As part of the investigation of the capability of the curve-fitting program to simulate spectra after deconvolution, the effect of the Gaussian fraction,  $\alpha$ , used in the curve fitting was investigated. This was done by incrementing  $\alpha$  from 0 to 1 in steps of 0.025 in the curve-fitting analysis of each deconvolved spectrum.

Figure 1 shows the variation of the computed deviation obtained on fitting the bands generated by using eq 8, after deconvolution with several values of  $\gamma'$ , plotted against the value of  $\alpha$  used in the curve-fitting program. Each part of the figure contains six lines corresponding to the Gaussian character of each band,  $\beta$ , with curve I indicating the behavior for  $\beta = 0.000$  and curve VI the behavior for  $\beta = 0.200$ . The changes in ordinate scale in this figure should be noted, since the deviations show very large increases with the value of  $\gamma'$ . The minimum ordinate of the plot for  $\gamma' = 29 \text{ cm}^{-1}$  is 0.018, while the minimum ordinate value for each of the other plots is zero.

The behavior for  $\gamma' = 0, 15$ , and  $20 \text{ cm}^{-1}$  is shown in parts a, b, and c of Figure 1. In each of these cases,  $\kappa \leq 3$ . When  $\gamma' = 0$ , a minimum in the deviations of nearly zero and a linear relationship between the deviations and the value of  $\alpha$  used in the curve fitting are observed for all values of  $\beta$ . This behavior is expected because the spectrum was only minimally perturbed, the original band being broad and subjected only to removal of the base line and the inverse and forward FT. The Fourier domain array was not multiplied by an exponential weighting function (i.e.  $\gamma' = 0$ ) but was apodized. When  $\gamma'$  is varied from 0 to  $20 \text{ cm}^{-1}$ , a marked change is seen in the shape and minimum value in the lines corresponding to each value of  $\beta$ . Most notably, when bands that contain a relatively high original Gaussian character ( $0.10 \leq \beta \leq 0.20$ ) are deconvolved and curve-fitted, their deviations vary less sharply around the minimum value than those observed for  $\beta < 0.10$ . The most important trend, which is consistent for each of the cases studied, is that as higher values of  $\gamma'$  are employed, the value of  $\alpha$  required to obtain the "best fit" (i.e. the lowest deviations) increases and the optimum value of  $\alpha$  is often twice the value of  $\beta$  in the original spectrum.

The corresponding data for deconvolution with  $23 \leq \gamma' \leq 29 \text{ cm}^{-1}$  are shown in parts d, e, and f of Figure 1. These data represent the case for  $\kappa$  values greater than 3. For  $\gamma' = 23 \text{ cm}^{-1}$  ( $\kappa \approx 4.3$ ), the behavior is quite different from the behavior illustrated in Figure 1a-c. At this level of deconvolution, the minimum values of the deviations in all six plots ( $0.00 \leq \beta \leq 0.20$ ) occur at  $\alpha \approx 0.25$ . It becomes difficult to explain the trends in the results for spectra computed with  $\gamma' > 23 \text{ cm}^{-1}$ , when  $(\gamma - \gamma')$  becomes less than the resolution. At this level of deconvolution the Lorentzian and Gaussian components are narrowed (although after deconvolution the "Gaussian component" is no longer Gaussian) to the extent that the line shape approaches that of the FT of the apodization function (FWHH =  $5.1 \text{ cm}^{-1}$ ). In practice, however, it is rare to use a value of  $\kappa$  greater than 3 because the SNR

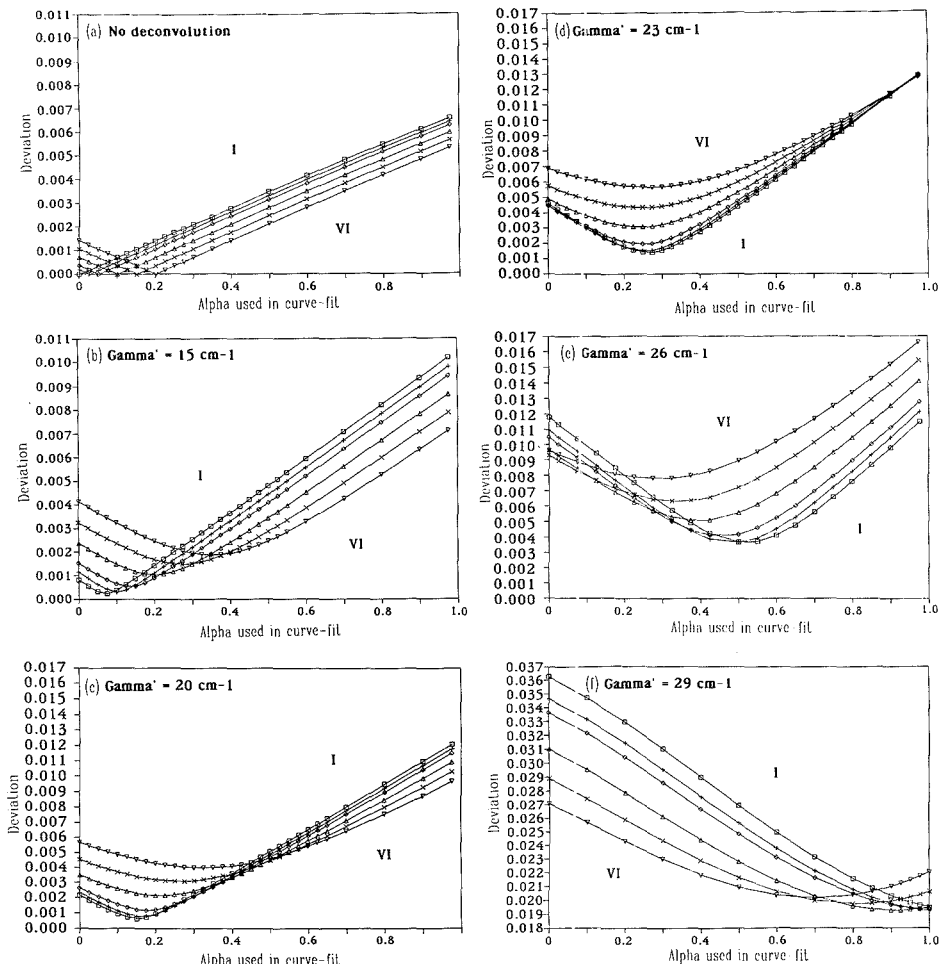


**Figure 1.** Variation of the deviation of the least-squares best fit to a series of bands with varying Gaussian fraction,  $\beta$ , as a function of the Gaussian fraction,  $\alpha$ , of the fitted band for several levels of deconvolution: (a)  $\gamma' = 0 \text{ cm}^{-1}$ ; (b)  $\gamma' = 15 \text{ cm}^{-1}$ ; (c)  $\gamma' = 20 \text{ cm}^{-1}$ ; (d)  $\gamma' = 23 \text{ cm}^{-1}$ ; (e)  $\gamma' = 26 \text{ cm}^{-1}$ ; (f)  $\gamma' = 29 \text{ cm}^{-1}$ . The values of  $\beta$  are  $\square$ , 0.000;  $+$ , 0.025;  $\diamond$ , 0.050;  $\Delta$ , 0.100;  $\times$ , 0.150;  $\nabla$ , 0.200.

of the deconvolved spectrum becomes unacceptably low (22). Thus the plots in Figure 1 for  $\gamma' > 20 \text{ cm}^{-1}$  are of largely academic interest. Nonetheless, it may be noted that even for noise-free synthetic spectra, side-lobe formation results in unacceptably high deviations in the curve fit when  $(\gamma_i - \gamma') \lesssim R$  ( $R = 5.1 \text{ cm}^{-1}$ ), particularly for high values of the original Gaussian fraction,  $\beta$ .

The value of the Gaussian fraction,  $\alpha$ , required to give the best fit increases with  $\gamma'$  for all the bands studied ( $0 \leq \beta \leq 0.20$ ) up to the point that side lobes become discernible in the deconvolved spectrum. At this point, the deviations become very large, as noted above. Furthermore, from the high value of  $\alpha$  required to fit a spectrum computed under very high levels of deconvolution ( $\gamma' = 29 \text{ cm}^{-1}$ ), it may be deduced that the FT of the Bessel apodization function is fitted better by a Lorentzian-Gaussian sum than by a pure Lorentzian.

The area of the band described by eq 8 is proportional to  $\gamma A_0$  and is not changed during FSD. As the value of  $\gamma'$  increases, however, the capability of a Lorentzian-Gaussian sum to fit the resulting band shape becomes progressively worse.

Nevertheless, it was found that the maximum error in the area of any of the bands generated by the curve-fitting program relative to the area of the original (undeconvolved) band was less than 1%, even for strongly deconvolved spectra with a high original Gaussian fraction. Even when side lobes were apparent after deconvolution, a very good estimate of the band area was still obtained. The band with a Gaussian fraction of 20%, after deconvolution with  $\gamma' = 29 \text{ cm}^{-1}$ , is shown in Figure 2 along with the best fit generated by curve fitting and the difference spectrum. Even though the difference spectrum shows many excursions corresponding to the side lobes, the relative error between the area of the original band and the area determined by curve fitting the deconvolved band was less than 1%. In practice, if a deconvolved spectrum is to be curve-fitted, the appearance of side lobes should be stringently avoided.

#### BAND MULTIPLETS

Several composite spectra, each containing five bands, were synthesized for FSD and curve-fitting analysis. The results

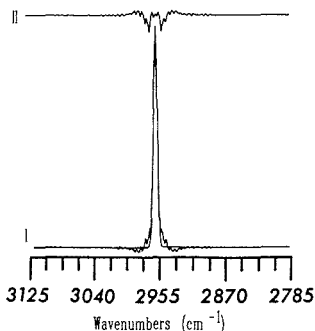


**Figure 2.** Result of curve fitting a band with a FWHH of  $30\text{ cm}^{-1}$  and  $\beta = 0.200$  after deconvolution with  $\gamma' = 29\text{ cm}^{-1}$ . The deconvolved spectrum, which shows the presence of side lobes, and its best fit are shown together as curve I; their difference is shown as curve II.

**Table I. Parameters of Synthetic Band Multiplets Discussed in This Paper**

	band				
	I	II	III	IV	V
	Spectrum A				
position, $\text{cm}^{-1}$	2966.00	2960.50	2955.00	2949.50	2944.00
height, AU	0.050	0.125	0.200	0.163	0.088
FWHH, $\text{cm}^{-1}$	15.0	15.0	15.0	15.0	15.0
area	1.18	2.95	4.71	3.84	2.07
	Spectrum B				
position $\text{cm}^{-1}$	2966.00	2960.50	2955.00	2949.50	2944.00
height, AU	0.200	0.200	0.200	0.200	0.200
FWHH, $\text{cm}^{-1}$	30.0	30.0	30.0	30.0	30.0
area	9.42	9.42	9.42	9.42	9.42

for one of these (spectrum A) will be discussed in detail in this section, and one other will also be mentioned specifically; further details can be found in ref 33. Information on the individual band parameters for each of these two multiplets is contained in Table I. For these spectra, the bands were 100% Lorentzian and neighboring bands were separated by  $5.5\text{ cm}^{-1}$ . Each spectrum was generated at  $2\text{ cm}^{-1}$  per data point, which is equivalent to a resolution of  $4\text{ cm}^{-1}$  after an inverse and forward FT. In each case the separation was much less than the FWHH of any of the component bands, which were therefore completely unresolved prior to deconvolution. For spectrum A,  $\gamma_i$  for each band was equal while the heights (and hence the areas) varied by a factor of 4. The results for spectrum A were typical of each case in which all the component bands were of approximately the same width, which in practice is usually the case when each component is due to a particular vibrational mode of a functional group in several different environments. As mentioned earlier, the only error introduced into these spectra was removal of the base line, which was subsequently not allowed for in the curve fitting.

The input positions for the curve-fitting analysis were again determined from the center-of-gravity of each band measured from a heavily deconvolved spectrum of the type shown, for example, in Figure 3. The advantages of FSD over the use of the fourth derivative are also evident from this figure. The method of deconvolution and curve fitting was identical with that in the single-band case. The peak shape described by the Lorentzian-Gaussian sum (eq 8) was used in the curve-fitting program because it was shown to provide a better fit after deconvolution, even for bands in which the initial Gaussian fraction was zero. For multiplets, two parameters were used to assess the efficiency of the technique. One of

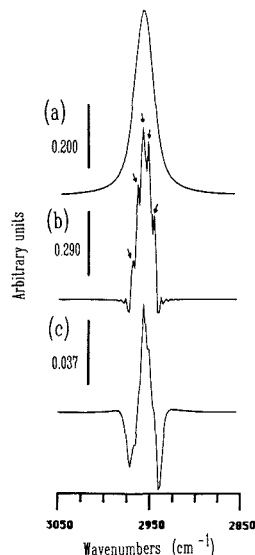


**Figure 3.** Spectrum A: (a) original envelope; (b) strongly deconvolved spectrum ( $\gamma' = 17\text{ cm}^{-1}$ ,  $F = 0.75$ ) with arrows indicating the five bands, the center of gravity of which was input to the curve-fitting program; (c) fourth derivative of the original spectrum.

these was the deviation, i.e. the square root of the sum of the squares of the difference between the deconvolved spectrum and the sum of the five bands calculated by using the curve-fitting program. In addition, the sum of the individual band area relative errors,  $E$ , was calculated as

$$E = \sum_{i=1}^5 \left| \frac{(\text{calculated area} - \text{true area}) \text{ of } i\text{th band}}{\text{true area of } i\text{th band}} \right| \times 100 \quad (9)$$

The deviation indicates the capability of simulating the overall spectrum accurately, but does not indicate the accuracy to which the areas of the individual bands are calculated. In the case of samples of unknown composition the latter information can never be determined without analysis by an alternative technique. In many cases such an alternative technique may not be available, in which case the deviation is the only measure of the goodness-of-fit. We were interested in investigating the relationship between the deviation and  $E$  for synthesized band multiplets subjected to deconvolution with different values of  $\gamma'$ .

The variation of the positions,  $\bar{\nu}_i^0$ , of two bands obtained by curve fitting spectrum A after deconvolution with various values of  $\gamma'$  is shown in Figure 4, where each line corresponds to a different value of the Gaussian fraction,  $\alpha$ , used in the curve-fitting procedure. The results shown are representative of the results of most of the bands in the synthetic multiplets studied. As  $\gamma'$  is increased, the bands approach their true positions, with the lowest errors at the lower levels of deconvolution being found when  $\alpha = 0$ . After  $\gamma'$  exceeds a certain value, the error starts to increase again, presumably because of the effects of the side lobes.

In general it was found that the outer components of the multiplets were calculated to be closer to the band center when undeconvolved or mildly deconvolved spectra were curve-fitted than when an optimally deconvolved or heavily deconvolved spectrum was curve-fitted. An incorrect value for the Gaussian fraction,  $\alpha$ , was found to lead to very large errors when the original spectrum or a mildly deconvolved spectrum was

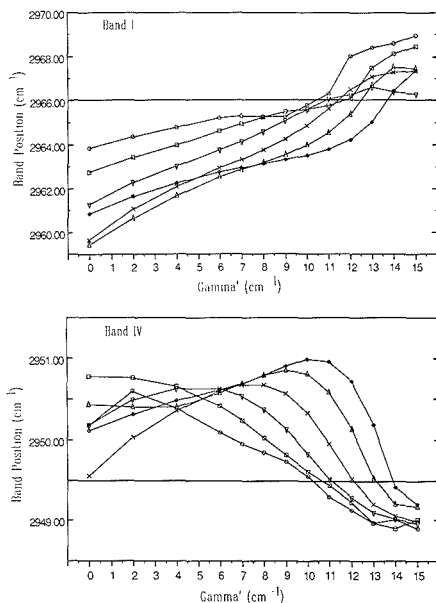


**Figure 4.** Variation of the computed centers of bands I and IV of spectrum A obtained after deconvolution with various values of  $\gamma'$ , plotted for six values of  $\alpha$ : O,  $\alpha = 0.00$ ; □,  $\alpha = 0.20$ ; ▽,  $\alpha = 0.40$ ; X,  $\alpha = 0.60$ ; Δ,  $\alpha = 0.80$ ; ◇,  $\alpha = 1.00$ . For  $\alpha = 0.00$ , the best positions are found when  $\gamma' = 10 \text{ cm}^{-1}$  ( $\kappa = 3.0$ ). The correct positions are indicated by the horizontal lines.

curve-fitted, but its exact value was less critical if the bands had been significantly narrowed. It is worth noting that the band positions calculated when the original (undeconvolved) spectra were curve-fitted were sometimes computed to fall well outside the spectral range, presumably because one of the wings of the band can then act as a variable base line so that the resulting deviations in the fit are lower than if all five bands are in approximately the correct positions.

For the spectra in which the FWHH had been reduced so that  $(\gamma - \gamma')$  was about 1.5 times the resolution, the band positions obtained by curve fitting were usually accurate to  $\pm 0.5 \text{ cm}^{-1}$ . Only in the case of spectra in which the group of bands possessed varying widths was a deviation greater than  $1.5 \text{ cm}^{-1}$  from the true position evident for any band. Typically the band for which the largest wavenumber error is observed has the largest width of any of the bands in the multiplet and hence the smallest value of  $\kappa$  for any given value of  $\gamma'$ . In any event, the positions found after deconvolution for all the synthetic multiplets studied were still much more accurate than when the original spectrum was curve-fitted. For spectrum A the positions found by curve fitting were within  $\pm 1 \text{ cm}^{-1}$  of their true values for  $\gamma' > 8 \text{ cm}^{-1}$ , which represents only a modest amount of deconvolution ( $\kappa \approx 2$ ).

The effect of  $\gamma'$  on the individual band areas in spectrum A is shown in Figure 5. Again this result is quite typical of the results obtained for most synthetic multiplets where the FWHH of each band was much greater than the resolution. After only a mild amount of deconvolution, the calculated band areas are significantly different from their true values, but the true areas are approached as higher values of  $\gamma'$  are employed. For a spectrum computed with a high enough value of  $\gamma'$  that  $(\gamma - \gamma')$  approaches the band separation, the band areas are quite close to their true values. Finally, for  $\gamma'$  values producing very heavily deconvolved spectra ( $(\gamma - \gamma') < R$ ),

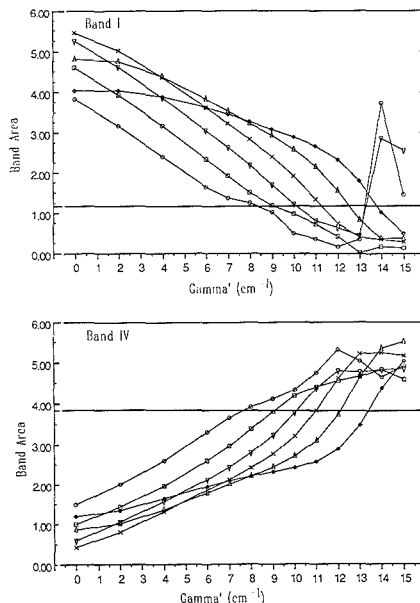


**Figure 5.** Variation of the computed areas of bands I and IV of spectrum A after deconvolution with various values of  $\gamma'$  plotted for the same six values of  $\alpha$  shown in Figure 4. The correct areas are indicated by the horizontal lines.

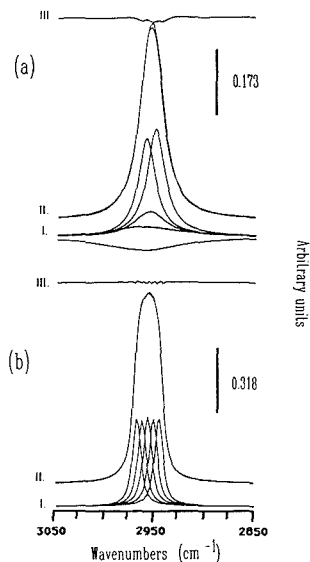


**Figure 6.** Result of fitting spectrum B, (a) before deconvolution and (b) after deconvolution with  $\gamma' = 22 \text{ cm}^{-1}$  ( $\kappa = 3.75$ ): I, five bands computed to give the best fit; II, original and best fit spectrum plotted superimposed; III, difference spectrum.

the areas; again diverge from their true values as side-lobe formation becomes evident.

When each component band of a multiplet is completely unresolved, the curve-fitting program is frequently capable of generating negative values for height and width, for example

**Table II. Band Parameters Calculated for Spectrum A before and after Deconvolution with  $\gamma' = 9.0 \text{ cm}^{-1}$  ( $\kappa = 2.5$ )<sup>a</sup>**

	band				
	I	II	III	IV	V
Before Deconvolution					
position ( $\bar{\nu}_i^\circ$ ), $\text{cm}^{-1}$	2963.8	2959.74	2955.20	2950.71	2946.09
error ( $\Delta\bar{\nu}_i^\circ$ ), $\text{cm}^{-1}$	-2.15	-0.76	+0.20	+1.21	+2.09
width, $\text{cm}^{-1}$	17.30	9.17	9.71	9.10	16.90
height, AU	0.141	0.086	0.168	0.104	0.208
area ( $a$ )	3.83	1.24	2.56	1.46	5.52
% error ( $\Delta a$ )	224.6	-58.0	-45.6	-61.5	+166.7
After Deconvolution					
position ( $\bar{\nu}_i^\circ$ ), $\text{cm}^{-1}$	2965.49	2960.22	2955.00	2949.81	2944.50
error ( $\Delta\bar{\nu}_i^\circ$ ), $\text{cm}^{-1}$	-0.55	-0.28	0.00	+0.31	+0.50
width, $\text{cm}^{-1}$	7.85	8.49	8.66	8.34	8.19
height, AU	0.102	0.242	0.384	0.310	0.188
area ( $a$ )	1.18	3.01	4.83	3.79	2.26
% error ( $\Delta a$ )	0.0	2.0	2.5	-1.3	9.2

<sup>a</sup> For the original spectrum  $\alpha = 0.00$ , and after deconvolution,  $\alpha = 0.25$ .

as shown in Figure 6 for spectrum B in which all peak heights and widths are identical. As before, this is probably because lower deviations can be obtained in the curve fit if one or more of the bands act as a base line. In fact, curve fitting was rarely found to produce useful results if the component bands of a multiplet were separated by much less than their FWHH. Even though the total area of the multiplets determined by curve fitting any spectrum was very close to its true value, the individual band area relative errors calculated when the original undeconvolved spectra were fitted ranged from 20% to 424%, i.e. from about 5 times too small to almost 5 times too large. From Table II it can be seen that dramatically better results were obtained after deconvolution. It can also be seen from the data in Table II that even though the calculated band areas are accurate after deconvolution, the heights of the five bands in the best fit to the optimally deconvolved spectrum are slightly less than the value calculated by using eq 7 while the widths of these bands are slightly greater than  $(\gamma - \gamma')$ , i.e.  $6 \text{ cm}^{-1}$ . This is a result of these fairly narrow bands being convolved with the FT of the Bessel apodization function, which has a FWHH of  $5.1 \text{ cm}^{-1}$  for these spectra, in which  $R^{-1} = 0.25 \text{ cm}$  and  $F = 0.75$ .

It may be recalled that the input positions for the curve-fitting program are determined from a strongly deconvolved spectrum. The values of  $\bar{\nu}_i^\circ$  obtained in this way are expected to be a fairly good approximation to the true values of  $\bar{\nu}_i^\circ$ . It was believed that a better value for the individual band areas might be obtained if the value of  $\bar{\nu}_i^\circ$  for each band was held constant during the curve fitting. This procedure, however, gave values for the areas of each individual band in mildly deconvolved spectra that were just as inaccurate as when the  $\bar{\nu}_i^\circ$  values were allowed to vary, and this approach was subsequently discarded.

Plots of the deviation and  $E$  against  $\gamma'$  allow a comparison of these two measures of the goodness-of-fit. The plots for spectrum A are shown in Figure 7. The six different lines correspond to the values of  $\alpha$  used in the curve fit. In practice, when the true band parameters are not known, the deviation must be used to give an indication of the goodness-of-fit to the multiplet. A low deviation is seen up to  $\gamma' = 10 \text{ cm}^{-1}$  ( $\kappa = 3$  for spectrum A) when  $\alpha = 0.00$ . At higher values of  $\gamma'$ , larger values of  $\alpha$  are required to obtain a low deviation.

The value of  $E$  shows such a large dependence on  $\gamma'$  that it was necessary to plot its logarithm against  $\gamma'$  for the range of  $\gamma'$  values used in this study. It can be seen from Table II that when spectrum A was originally curve-fitted,  $E$  was equal to 556%, i.e. an average error of over 100% for each band.

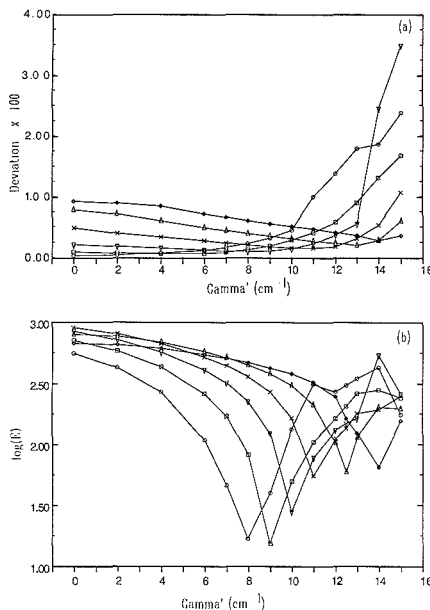


**Figure 7.** Result of curve fitting spectrum A shown as plots of (a) deviation and (b)  $\log E$  vs  $\gamma'$  for the same six values of  $\alpha$  used in Figures 4 and 5. Note that the deviation starts to increase at the value of  $\gamma'$  for which  $E$  is a minimum.

When the spectrum was fitted after deconvolution with  $\gamma' = 9 \text{ cm}^{-1}$ ,  $E$  was reduced to 15%, corresponding to an average error of 3% for each band. The value of  $E$  is also strongly dependent on  $\alpha$ , but for any given value of  $\alpha$  the best results were always obtained after the width had been reduced to a value approximately equal to the FWHH of the FT of the Bessel apodization function. Results similar to this were obtained whenever the synthesized spectrum contained bands with approximately the same FWHH. It may be noted that the best fit to an original, undeconvolved spectrum is not necessarily obtained when  $\alpha$  is zero in the curve-fitting program, despite the fact that the multiplet was composed of five purely Lorentzian bands ( $\beta = 0.00$ ). This result is in part due to the effect of the limited resolution and apodization and in part due to the base-line removal. Although the optimum value of  $\alpha$  to be used in the curve fitting depends on the value of  $\gamma'$  that was used in deconvolution, a good compromise seems to be  $\alpha = 0.25$ .

For each value of  $\alpha$  used,  $\log E$  decreases to a minimum for the  $\gamma'$  values that are required to just resolve the component bands without generating side lobes. The minimum value of  $E$  is found at the value of  $\gamma'$  at which the plots of the deviation as a function of  $\gamma'$  just begin to show a significant increase in their slope. The value of  $\gamma'$  at which the minimum occurs in the plot of  $\log E$  against  $\gamma'$  can vary with  $\alpha$ , as shown in Figure 7b. Nevertheless, the point at which the deviation starts to show a rapid increase always corresponds to the value of  $\gamma'$  at which  $E$  is a minimum, regardless of the value of  $\alpha$  that is used in the curve-fitting program.

## CONCLUSIONS

It has been shown that for synthetic multiplets the combination of FSD and curve fitting overcomes many of the inherent limitations of the individual methods. The approach allows the objective optimization of the value of  $\gamma'$  used in FSD, significantly improves the conditioning of curve fitting

for heavily overlapped bands, and leads directly to quantitative information.

We believe that these results can form the basis of a method for obtaining accurate quantitative information on the areas of unresolved components in real, complex spectra. In this procedure, spectra would be divided into regions in which all bands would be expected to have approximately the same width. A series of deconvolved spectra would then be computed with values of  $\gamma'$  equally spaced between 0 and the value causing the onset of side lobes. If each spectrum is then used as the input for a curve-fitting program, the best quantitative information (i.e. those values at which  $E$  is a minimum) would be found from the results of fitting the spectrum that was deconvolved by using the value of  $\gamma'$  just lower than that at which the deviation starts to increase rapidly.

This method has been applied to coal spectra (33-35) but has not yet been tested rigorously.

#### LITERATURE CITED

- Haaland, D. M.; Easterling, R. G. *Appl. Spectrosc.* **1982**, *36*, 665.
- Brown, C. W.; Lynch, P. F.; Obremski, R. J.; Lavery, D. S. *Anal. Chem.* **1982**, *54*, 1472.
- Beebe, K. R.; Kowalski, B. R. *Anal. Chem.* **1987**, *59*, 1007A.
- Cowe, I. A.; McNicol, J. W. *Appl. Spectrosc.* **1985**, *39*, 257.
- Painter, P. C.; Snyder, R. W.; Starsinic, M.; Coleman, M. M.; Kuehn, D. W.; Davis, A. *Coal and Coal Products: Analytical Characterization Techniques*; Fuller, E. L., Jr., Ed.; ACS Symposium Series 205; American Chemical Society: Washington, DC, 1982.
- Antoon, M. K.; Koening, J. H.; Koening, J. L. *Appl. Spectrosc.* **1977**, *31*, 518.
- Painter, P. C.; Rimmer, S. M.; Synder, R. W.; Davis, A. *Appl. Spectrosc.* **1981**, *35*, 102.
- Starsinic, M.; Otake, Y.; Walker, P. L., Jr.; Painter, P. C. *Fuel* **1984**, *63*, 1002.
- Gold, H. S.; Rechsteiner, C. E.; Buck, R. P. *Anal. Chem.* **1976**, *48*, 1540.
- Maddams, W. F. *Appl. Spectrosc.* **1980**, *34*, 245.
- Vandeginste, B. G. M.; De Galan, L. *Anal. Chem.* **1975**, *47*, 2124.
- Audo, D.; Armand, Y.; Arnaud, P. *J. Mol. Struct.* **1968**, *2*, 287.
- Audo, D.; Armand, Y.; Arnaud, P. *J. Mol. Struct.* **1968**, *2*, 409.
- Anderson, A. H.; Gibb, T. C.; Littlewood, A. B. *J. Anal. Chem.* **1970**, *42*, 434.
- Anderson, A. H.; Gibb, T. C.; Littlewood, A. B. *J. Chromogr. Sci.* **1970**, *8*, 640.
- Maddams, W. F.; Mead, W. L. *Spectrochim. Acta* **1982**, *38A*, 437.
- Susi, H.; Byler, D. M. *Biochem. Biophys. Res. Commun.* **1983**, *115*, 391.
- Griffiths, T. R.; King, K.; Hubbard, H. V. St. A.; Schwing-Weill, M.-J.; Meullerrestre, J. *Anal. Chim. Acta* **1982**, *193*, 163.
- Kauppinen, J. K.; Moffatt, D. J.; Mantsch, H. H.; Cameron, D. G. *Appl. Spectrosc.* **1981**, *35*, 271.
- Yang, W.-J.; Griffiths, P. R.; Byler, D. Michael; Susi, H. *Appl. Spectrosc.* **1985**, *39*, 282.
- Parientz, G. A.; Griffiths, P. R. *TRAC, Trends Anal. Chem. (Pers. Ed.)* **1986**, *5*, 209.
- Kauppinen, J. K.; Moffatt, D. J.; Cameron, D. G.; Mantsch, H. H. *Appl. Optics* **1981**, *20*, 1866.
- Cameron, D. G.; Kauppinen, J. K.; Moffatt, D. J.; Mantsch, H. H. *Appl. Spectrosc.* **1982**, *36*, 245.
- Jasse, B. In *Fourier Transform Infrared Characterization of Polymers*; Ishida, H., Ed.; Plenum Publishing Corporation: New York, 1987; pp 245-259.
- Divis, F. A.; White, R. L. *Anal. Chem.* **1989**, *61*, 33.
- Yang, W.-J.; Griffiths, P. R. *Comput. Enhanced Spectrosc.* **1983**, *1*, 157.
- Yang, W.-J.; Griffiths, P. R. *Comput. Enhanced Spectrosc.* **1984**, *2*, 69.
- Susi, H.; Byler, D. M. *Arch. Biochem. Biophys.* **1987**, *258*, 465.
- Byler, D. M.; Susi, H. *Biopolymers* **1986**, *25*, 469.
- Byler, D. M.; Farrell, H. M., Jr.; Susi, H. *J. Dairy Sci.* **1988**, *71*, 2622.
- Jones, R. N. *Pure Appl. Chem.* **1969**, *18*, 303.
- Leventerg, K. *Quart. Appl. Math.* **1944**, *2*, 164.
- Pierce, J. A. Ph.D. Dissertation, University of California, Riverside, 1986.
- Griffiths, P. R.; Wang, S. H. In *Fourier Transform Infrared Characterization of Polymers*; Ishida, H., Ed.; Plenum Publishing Corporation: New York, 1987; pp 231-244.
- Griffiths, P. R.; Pierce, J. A.; Hongjin, Gao. In *Computer-Enhanced Analytical Spectroscopy*; Meuzelaar, H. L. C.; Isenhour, T. L., Eds.; Plenum Publishing Corporation: New York, 1987; Chapter 2.

RECEIVED for review June 15, 1989. Accepted November 6, 1989. This work was supported in part by Grant No. DE-FG22-87PC79907 from the U.S. Department of Energy and by Cooperative Agreement No. CR814909-01 from the U.S. Environmental Protection Agency.

## Thermospray Enhanced Inductively Coupled Plasma Atomic Emission Spectroscopy Detection for Liquid Chromatography

S. B. Roychowdhury and J. A. Koropchak\*

Department of Chemistry and Biochemistry, Southern Illinois University, Carbondale, Illinois 62901

Thermospray sample introduction is studied as an interface between liquid chromatography and inductively coupled plasma atomic emission spectrometry for metal speciation studies. Detection limits for chromium species separated by ion chromatography or mobile phase ion-pairing chromatography are improved by factors of 24 and 36, respectively, for 50 and 25  $\mu\text{m}$  aperture based thermospray systems, as compared to pneumatic sample introduction. For arsenic species separated by ion chromatography, relative response factors between the two sample introduction systems were species dependent. Lower enhancements for certain species with thermospray were thought to result from thermal decomposition to form volatile species which were lost during desolvation. For nonaqueous size exclusion studies of organoiron species, detection limits were improved by a factor of about 50 with thermospray compared to a pneumatic sample introduction system.

\* Author to whom correspondence should be sent.

The determination of the chemical forms (i.e. speciation) of trace metals is well-known to be important to a wide range of chemical systems (i.e. environmental, biochemical, etc.). One approach to such measurements is to separate the various metal species using liquid chromatography and employ a detector, such as inductively coupled plasma atomic emission (ICP-AES) or mass spectrometry (ICP-MS), for selective detection of the metal(s) of interest ( $I$ ). These types of atomic spectrometers are particularly advantageous as high-performance liquid chromatography (HPLC) detectors since simultaneous multielement analysis is possible, and the speciation of more than one metal may be evaluated during a single chromatogram.

In many speciation applications, detection is required at extremely low levels (sub-nanogram-per-milliliter to nanogram-per-milliliter). The nature of the sample and the lability of the various species may preclude the reliable use of preconcentration techniques. Although ICP-AES and ICP-MS have low limits-of-detection (LOD's) for direct sample introduction (1  $\sim$  ng/mL to sub-ng/mL, respectively), LOD's for

chromatographically injected discrete samples are generally substantially higher based on the dilution and dispersion which unavoidably occurs during the chromatographic process and sometimes on matrix interferences resulting from the mobile phase. As an example of these effects, the commonly reported LOD for chromium by ICP-MS with direct aspiration is 0.02 ng/mL, while HPLC-ICP-MS LOD's were 50 ng/mL or greater, depending on chromatographic conditions (2). Consequently, improvements in the detection capabilities of ICP-AES or ICP-MS should be of advantage to the practical application of metal speciation studies employing HPLC-ICP detection.

One aspect of ICP methods that has long been considered to be a hindrance to detection is the sample introduction process (3, 4). Conventional sample introduction systems involve the pneumatic generation of aerosols which are processed in a spray chamber prior to injection into the ICP. During the course of this processing, typically 98–99% of the analyte goes to waste and never reaches the ICP. In principle, this analyte loss corresponds to 99% of the potential signal, as well. Further, these pneumatic sample introduction systems are thought to introduce a substantial amount of noise to the measurement process, further degrading potential LOD's.

Recently, the alternative use of thermospray for aerosol generation (5) and sample introduction to ICP-AES (6) has been described. With thermospray, aerosols are generated by pumping liquids through an electrothermally heated capillary where partial vaporization occurs at appropriate temperatures, resulting in a jet of vapor and aerosol. Thermospray aerosol particles have been shown to be smaller on average than those for pneumatic aerosols, leading to higher analyte transport efficiencies (7). With a decrease in the capillary exit diameter, such as through the use of a limiting aperture (8), transport efficiency increases; with a 25  $\mu\text{m}$  aperture based thermospray vaporizer, >60% of the input analyte may be transported to the plasma, resulting in a 20–25-fold signal enhancement (9). Further, background noise levels typically 2–3 times lower have been reported for our thermospray system (6, 7) resulting in up to 50-fold signal-to-noise ratio (SNR) and LOD improvements for thermospray sample introduction compared to pneumatic sample introduction (9). Thermospray systems operated under optimum conditions for ICP-AES have also been shown to be surprisingly resistant to clogging even with high dissolved solids levels (10). Thermospray systems also have inherently low liquid dead volumes, minimizing dispersion effects in the liquid phase. An earlier study described the use of a thermospray interface for HPLC-ICP-AES of tin species (11).

In this report, we will describe the application of thermospray sample introduction as an interface between HPLC and ICP-AES for metals study with aqueous, mixed-phase, and nonaqueous chromatographies. The system will be described for ion exchange, reverse-phase (mobile phase ion pairing), and gel-permeation separations. The advantages of this system will be specifically discussed with regard to studies of chromium speciation in environmental aerosols.

## EXPERIMENTAL SECTION

A detailed list of the various instrumental facilities is provided in Table I. For chromium speciation, a Leeman Labs (Lowell, MA) Model 2.5 ICP was used with a McPherson (Acton, MA) Model 270 monochromator. A Perkin-Elmer ICP/5500 was employed for arsenic speciation with the monochromator being purged with nitrogen during study. Wavelength modulation using a quartz refractor plate was used for dynamic background correction in both instrumental setups.

**Pneumatic Nebulizer Interface.** A Hildebrand grid (Leeman Labs, Lowell, MA) pneumatic nebulizer with a polyethylene spray chamber (Leeman Labs) was used for conventional sample introduction to the plasma. A jacketed, double-pass spray chamber

Table I. Instrumentation

<b>A. HPLC system</b>	
pump	Autochrom M500 dual piston
pump controller	Autochrom OPG/S
injector	Rheodyne Model 7125
pulse dampner	SSI Model LP-21
<b>B. Leeman Labs ICP system</b>	
torch box	Leeman Model 2.5
monochromator	McPherson Model 270
	0.35 m focal length
	2400 grooves/mm grating
	30 $\mu\text{m}$ slit width
preamplifier	Keithly Model 485 picoammeter
<b>C. Perkin-Elmer ICP system</b>	
torch box/monochromator	Model 5500
	0.408 m focal length
	2880 grooves/mm grating
	30 $\mu\text{m}$ slit width
preamplifier	Keithly Model 610B
<b>D. wavelength modulation frequency generator</b>	
	Wavetek Model 114
	185 Hz
lock-in amplifier	Stanford Research Systems Model SR510
<b>E. data acquisition/manipulation</b>	
computer	Multitech 700 PC Compatible
interface	Metabyte Dash-16
software	Assystant +

that was cooled to  $-4^\circ\text{C}$  followed by a cold-finger condenser cooled to  $-50^\circ\text{C}$  in a dry ice acetone slush bath was used for solvent vapor removal for chromatographic experiments employing tetrahydrofuran (THF) as the solvent.

**Thermospray Nebulizer Interface.** The aperture-based thermospray vaporizer begins with a capillary of 0.127 mm i.d. by 1.6 mm o.d. stainless steel obtained from Alltech (Deerfield, IL). J-type thermocouples were spot-welded 1.5 cm and 30 cm from the vaporizer tip. The assembly of the exit aperture was identical with that described elsewhere (8), except that the apertures were of slightly smaller diameter (3.125 mm) and were placed into a cup-shaped back ferrule which was used instead of the supporting washer described previously. This back ferrule was of appropriate size to slide over the ferrule, sandwiching the aperture in place. This arrangement was found to reduce mechanical wear to the aperture during tightening and simplified the process of centering the exit hole of the aperture upon the exit hole of the 1.6-mm nut. The apertures (0.13 mm thick) were laser drilled (25 or 50  $\mu\text{m}$ ) and were obtained from National Aperture, Inc. (Windham, NH). A heated spray chamber (145  $^\circ\text{C}$ ) and Friedrich's condenser (0  $^\circ\text{C}$ ) were employed with thermospray for desolvation and were identical with those described previously (6). For experiments with THF, the condenser was followed by the cold-finger condenser described above for the pneumatic nebulizer.

Both nebulizers were connected to the sample source (i.e. injector for flow injection analysis or column exit for chromatographic analysis) using a 10 cm length of 0.13 mm i.d. tubing.

With the pneumatic nebulizer, the exit of this tube was butted against the inlet tube of the nebulizer and joined by means of a Tygon sleeve to minimize dead volume. Flow systems were connected with the thermospray probe by means of a 1.6-mm Kel-F union (Upchurch Scientific Model U-402K, Oak Harbor, WA) which also provided electrical isolation. The assembled probe was used with a Vestec (Houston, TX) triac-controlled thermospray power supply (5).

**HPLC-ICP-AES.** The mobile phase was metered with a high-pressure liquid chromatography pump (Auto Chrom OPG/S system with an M 500 dual-piston pump). A Rheodyne Model 7125 injector with a 200  $\mu\text{L}$  injection loop was used for analyte injection. Dionex HPIC AS4 and HPIC AS4A columns were used for ion chromatography separations of chromium and arsenic species, respectively. An Adsorbosphere (Alltech, Deerfield, IL) C-18 column was used for mobile-phase ion pair (MP/IP) separations. A Phenogel 100 A (Phenomenex, Palos Verdes, CA) column was used for gel permeation chromatography (GPC).

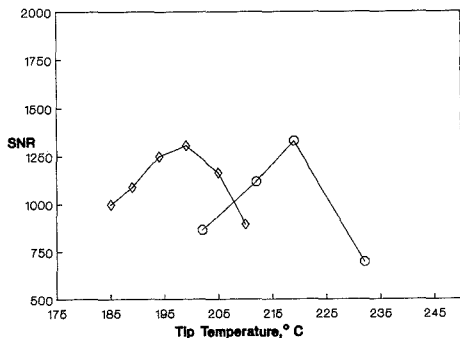


Figure 1. Effect of thermospray tip temperature on SNR for 2 µg/mL Cr(VI) after ion chromatography (◇) and mobile phase ion-pairing chromatography (○), 50-µm thermospray.

The plasma operating parameters were optimized following standard procedures. The nebulizer flow was controlled by a Tylan (Carson, CA) Model FC280 mass flow controller. The rest of the plasma operating gases were controlled by the standard rotameters. For experiments with THF, 0.15 L/min of O<sub>2</sub> was metered into the aerosol carrier/nebulizer flow with a Tylan FC 260 mass flow controller. The pneumatic and also the thermospray nebulizers were operated at the liquid flow rate employed for the HPLC separation, i.e. at a carrier flow rate of 1.0 mL/min. Further, with THF mobile phases a low-flow ICP torch operating at 12 L/min and 1.2 kW was employed.

**Reagents.** All the chemicals used were reagent grade. Standard solutions were prepared freshly from chromium nitrate and potassium dichromate for chromium speciation studies. The solutions for arsenic speciation were prepared from sodium arsenite, sodium arsenate, dimethylarsinic acid (DMA), and phenylarsonic acid (PhAs). The Constan S-21 nonaqueous multielement standard was obtained from Conoco (Ponca City, OK) and diluted with THF as required.

The eluent used for ion chromatography of Cr species was potassium hydrogen phthalate (KHP) at a concentration of  $5 \times 10^{-4}$  M. The pH was adjusted to the desired value with either hydrochloric acid or potassium hydroxide solutions.

The eluent in mobile phase ion-pairing chromatography (MPIP) was prepared from the sodium salt of pentanesulfonic acid (Aldrich). The sodium salt of pentanesulfonic acid was ion exchanged with Amberlite CG-120 (200-800 mesh) (Mallinckrodt) to replace sodium with magnesium. This procedure was conducted to reduce the suppression effect of sodium on the Cr II 283.563 nm emission line. Magnesium acetate was added to this solution at a concentration of 0.01 M. Acetic acid (1% by volume) and methanol (10% by volume) were also added. The pH of the eluent was adjusted to the value of 3.5 with dilute acetic acid.

The anion chromatography of arsenic species was carried out using a linear gradient from 100% distilled deionized water to 100% 0.05 M ammonium carbonate containing 0.2% methanol. Ammonium salts were chosen to minimize easily ionizable element effects within the plasma once again.

## RESULTS AND DISCUSSION

**Flow Injection Analysis (FIA) and HPLC-ICP-AES for Cr.** The optimization of the thermospray nebulizer was carried out in a flow injection mode by using the intended chromatographic solvent as the carrier stream, prior to the study of separation of the species. Figure 1 shows the effect of probe tip temperature on signal to noise ratio (SNR) obtained for 2 ppm Cr(VI) with a 50 µm aperture-based thermospray vaporizer using two different solvent systems. The probe tip temperature influences the degree of vaporization of the carrier fluid through the thermospray capillary and is dependent on the composition and flow rate of the carrier fluid (7). Optimum temperatures may vary somewhat from vaporizer to vaporizer. Operating tip temperatures were chosen

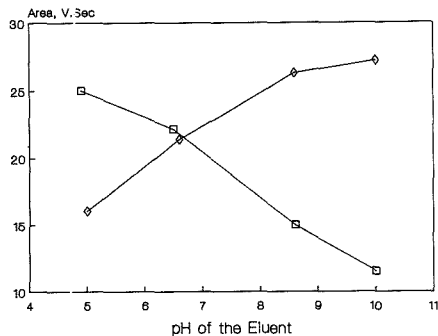


Figure 2. Peak area versus pH for Cr(III) (□) and Cr(VI) (◇) after ion chromatography.

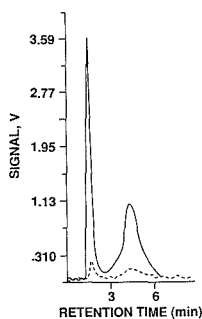


Figure 3. Separation of chromium species by ion chromatography with 50-µm thermospray (—) and pneumatic (---) sample introduction.

to optimize SNR. At excessively higher temperatures, non-volatile species may deposit inside the probe and may eventually clog the probe. The optimum tip temperatures chosen for chromium were 200 °C for anion chromatography and 220 °C for MPIP. At these temperatures, capillary clogging was extremely rare and could be alleviated via short-term ultrasonication of the aperture.

For anion exchange chromatography, Cr(III) was complexed with ethylenediaminetetraacetic acid (EDTA) to form the anionic complex of Cr(III) with EDTA. The pH values of the sample and the eluent were important to the separation and response observed. Figure 2 shows the effect of eluent pH on peak area for Cr(III) and Cr(VI) species with the Dionex HPIC AS4 column. A pH of 6.5 was chosen for subsequent studies. The retention time and the peak profile for Cr(III)-EDTA were not affected by the pH of the eluent, but the retention time and the peak profile of Cr(VI) were strongly influenced by the pH of the eluent. Figure 3 is a chromatogram for the separation of Cr(III) and Cr(VI) which also compares the response obtained with a pneumatic sample introduction system to that with a 50-µm thermospray system. In this chromatographic mode, Cr(III) eluted early (1.4 min) while Cr(VI) eluted at 4.2 min. Clearly indicated is the much higher response for chromium species obtained with the thermospray system. The broad peak for Cr(VI) was likely due to an oxidative interaction of this species with the column. Peak areas per unit mass were identical for the two species, however.

Figure 4 indicates the separation of Cr(III) and Cr(VI) by MPIP and also compares the response obtained for the two sample introduction systems. Once again, the response obtained with the 50-µm thermospray system was substantially higher than that obtained with the pneumatic system. With

Table II. Limits of Detection (ng/mL)<sup>a</sup>

species	nebulizer	FIA <sup>c</sup>	IC <sup>c</sup>	FIA <sup>d</sup>	MPIP	FIA <sup>d</sup>	GPC
Cr(III)	25- $\mu$ m thermospray	2 (0.4)	10 (2)		7 (1.4)		
	50 $\mu$ m thermospray pneumatic	48 (9.6)	244 (48.8)		10 (2) 252 (50.4)		
Cr(VI)	25- $\mu$ m thermospray	2 (0.4)	30 (6)	2 (0.4)	7 (0.4)		
	50- $\mu$ m thermospray pneumatic	48 (9.6)	526 (105)	3 (0.6) 71 (14.2)	10 (2) 254 (50.8)		
As(III)	25- $\mu$ m thermospray pneumatic	63 (12.6)	1170 (234)				
As(V)	25- $\mu$ m thermospray	3 (0.6)	17 (3.4)				
	pneumatic	63 (12.6)	306 (61.2)				
DMA	25- $\mu$ m thermospray	47 (9.4)	155 (31)				
	pneumatic	63 (12.6)	253 (50.6)				
PhAs	25- $\mu$ m thermospray	4 (0.8)	12 (2.4)				
	pneumatic	63 (12.6)	254 (50.8)				
ferrocene	50- $\mu$ m thermospray					39 (7.8)	120 (24)
	pneumatic					2000 (400)	5600 (1120)
Conostan S-21	50- $\mu$ m thermospray					13.5 (2.7)	39 (7.8)
	pneumatic					630 (126)	1791 (358)

<sup>a</sup> Absolute LOD's in nanogram are listed in parentheses. <sup>b</sup> Flow injection analysis using ion chromatographic mobile phase as carrier stream. <sup>c</sup> Flow injection analysis using ion-pairing mobile phase as carrier stream. <sup>d</sup> Flow injection analysis using THF as carrier stream.

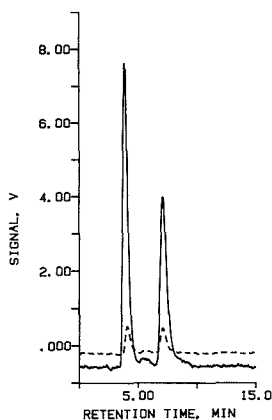


Figure 4. Separation of chromium species by MPIP with 50- $\mu$ m thermospray (—) and pneumatic (---) sample introduction.

this separation, Cr(VI) was now the early eluting species. The retention of Cr(III) was substantially affected by the age and matrix of the solution. The chromatogram in Figure 4 was obtained for a mixture of freshly prepared solutions. Figure 5 shows a chromatogram obtained for a Cr(III) standard solution which had been aged for 12 h. In this case, a second peak has appeared at a shorter retention time. This peak was still well-resolved from the Cr(VI) peak, however. With samples derived from extracts of environmental aerosol samples, as many as five different peaks for Cr(III) have been observed, with three additional minor species having retention times from 7 to 10 min (12). These multiple peaks for Cr(III) likely result from the fact that coordination complexes for Cr(III) are highly kinetically stable (13). In aqueous solutions where they are not chelated, a variety of hydrolysis species are possible (14), to include:  $\text{Cr}(\text{H}_2\text{O})_6^{3+}$ ,  $\text{Cr}(\text{H}_2\text{O})_5\text{OH}^{2+}$ ,  $\text{Cr}(\text{H}_2\text{O})_4(\text{OH})_2^+$ , and  $\text{Cr}(\text{H}_2\text{O})_4(\text{OH})_4^-$ . These species are stable enough to survive the MPIP chromatographic process with different retention times. This feature of MPIP-ICP-AES with Cr(III) may be used to advantage for providing detailed information concerning the distribution of Cr(III) among these various complexes.

The peak widths at half height obtained with both the nebulizers were equivalent for each chromatographic system.

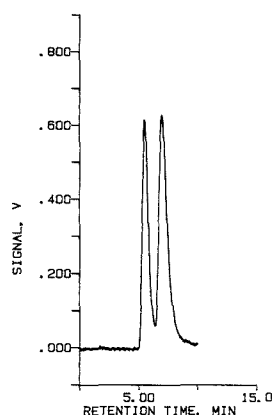


Figure 5. Ion-pairing chromatogram for 1  $\mu$ g/mL Cr(III) after 12 h of aging, 50- $\mu$ m thermospray interface.

The large difference in nebulizer spray chamber dead volumes (118 mL for the pneumatic nebulizer and 570 mL for the thermospray system) did not appear to contribute to peak broadening.

The slopes of the calibration curves were equivalent for the two different Cr species studied in a flow injection mode and with MPIP chromatography with either nebulizer; a difference in slope for Cr(III) and Cr(VI) with ion chromatography was attributed to the broadened peak shape for Cr(VI). The equivalent slopes indicated the independence of the sensitivity of the measurement process for the two different Cr species with either mode of aerosol generation. The process of heating within the thermospray did not have an effect on the Cr analyte. With the thermospray nebulizer, the slopes of the calibration curves were over an order of magnitude superior to those with the pneumatic nebulizers. The reduced noise level with the thermospray nebulizer also enhanced the detection capability for the analyte (6).

Detection limits, based on  $3\sigma$  values, were estimated by using the slope method (15). The detection limits obtained for Cr in FIA-ICP-AES and HPLC-ICP-AES are listed in Table II. In FIA, the detection limit was determined with a carrier stream consisting of the chromatographic mobile phase. The 50- and 25- $\mu$ m thermospray nebulizers offered

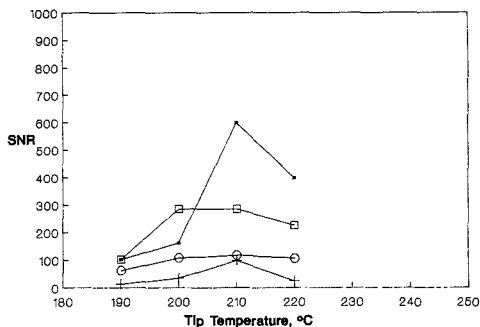


Figure 6. The effects of thermospray tip temperature on SNR for 5  $\mu\text{g/mL}$  of PhAs (■), arsenate (□), DMA (○), and arsenite (+), 25- $\mu\text{m}$  thermospray.

improvements in detection limit of factors of 24 and 36, respectively, compared to the conventional pneumatic nebulizer. The detection limits obtained with the 25- $\mu\text{m}$  thermospray (7 ng/mL or 1.4 ng) for Cr(III) and Cr(VI) in the HPLC studies are comparable to the best reported detection between 5 and 15 ng/mL (0.5–1.5 ng) for HPLC–DCP–AES (16), 20 ng/mL (4 ng) for HPLC–ICP–AES (17), and 50 ng/mL (1 ng) for HPLC–ICP–MS (2). The moderate resolution spectrometer employed in these studies was likely a substantial hindrance to the generation of lower absolute limit of detection values (18); the relative LOD's for the conventional and thermospray nebulizers are considered to be of greater relevance. The poorer detection limit for Cr(VI) with ion chromatography was also attributed to the broad peak observed for this species. The superior LOD for Cr(VI) obtained with MPIP chromatography made this separation the method of choice for studies with chromium aerosols which are described elsewhere (12).

**FIA and HPLC–ICP–AES for As.** The thermospray nebulizer was optimized for arsenic compounds at an analytical wavelength of 193.7 nm in an analogous fashion to that employed for chromium (i.e. flow injection). The plot of SNR vs probe tip temperature is shown in Figure 6. The optimum temperature was found to be 215 °C. The responses for various arsenic compounds with the thermospray probe were not identical. As in the case of chromium, the slopes of calibration data obtained with the thermospray nebulizer generally were much higher than those for the pneumatic nebulizer. The detection limits obtained in flow injection analysis for the arsenic species are listed in Table II. Negative intercepts of the calibration curves for DMA and arsenite in the case of the thermospray nebulizer suggested a possible sample loss within the sample introduction system. This resulted in an apparently lower sensitivity of the thermospray nebulizer ICP–AES system for these two compounds. This lower sensitivity was also observed for the chromatographic analysis. The loss of arsenite was thought to arise from a thermal disproportionation within the thermospray vaporizer or heated spray chamber, forming arsenite and free arsenic (19). Although the fraction of arsenite converted to arsenate would be likely to be transported to the plasma, arsenic sublimates at 100 °C and the resultant vapors would likely be trapped by the condenser employed with the desolvation system. The comparable calibration data for DMA suggest that a thermal decomposition process may also account for the lower response for DMA, although no similar mechanism can be rationalized. The responses for DMA and arsenite however, were still comparable to or better than those provided by the pneumatic sample introduction system. The precision of analysis for the individual arsenic compounds with both

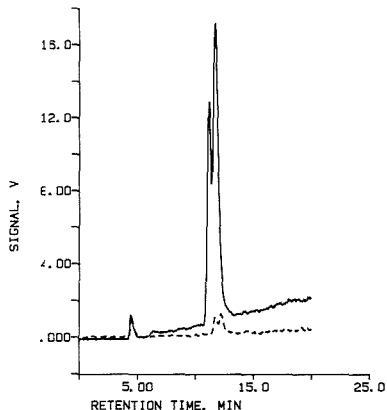


Figure 7. Separation of arsenic species by ion chromatography with 25- $\mu\text{m}$  thermospray (—) and pneumatic (---) sample introduction.

the nebulizers was within 2%, except for DMA which was 6% with the thermospray.

The separation of the arsenic species on the Dionex HPIC AS4A column using a linear gradient from distilled deionized water to 0.05 M  $(\text{NH}_4)_2\text{CO}_3$  containing 0.2% methanol in 20 min was established by using the pneumatic nebulizer. The order of elution of the different arsenic compounds was as expected with the singly charged arsenic and DMA eluting before the doubly charged arsenate and PhAs.

A chromatogram of DMA, arsenate, and PhAs comparing the response for the thermospray and the pneumatic nebulizers is shown in Figure 7. The detection limits obtained on a  $3\sigma$  basis are shown in Table II. The thermospray nebulizer offered superior detection for DMA, arsenate, and the PhAs species. The improvement factors in detection with the thermospray nebulizer were 1.6, 18.5, and 20.7 for DMA, arsenate, and PhAs, respectively. The detection limit for arsenite was higher with the thermospray nebulizer. The response for arsenate and PhAs compounds with the thermospray nebulizer was also hindered by the sloping base line which arose from the spectral broadening of the carbon emission line at 193.09 nm due to the increasing concentration of the carbonate in the mobile phase. The effect was greater with the thermospray nebulizer and attributed to the higher transport efficiency of this sample introduction system for not only the analyte but also the nonvolatile matrix components. The detection limits obtained for arsenite (234 ng or 1171 ng/mL), DMA (31 ng or 155 ng/mL), and arsenate (3.4 ng or 17 ng/mL) with the thermospray were superior to the  $2\sigma$  LOD values of 390 ng (arsenite), 60 ng (DMA), and 126 ng (arsenate) as reported for anion exchange chromatography ICP–AES by Spall et al. (20).

**Nonaqueous FIA and HPLC–ICP–AES.** Evaluation of the thermospray interface for nonaqueous applications was conducted with THF as the mobile phase for gel permeation chromatography. As before, response for iron at 259.9 nm was optimized in a flow injection mode. For a 50- $\mu\text{m}$  thermospray, a tip temperature of 200 °C was found to be optimum for both ferrocene and the Conostat S-21 standard. Figure 8 depicts the relative response obtained for a 5  $\mu\text{g/mL}$  solution of the Conostat standard injected on to the GPC column. As before, the response obtained with thermospray sample introduction was substantially higher than that obtained with pneumatic sample introduction. LOD's for ferrocene and the Conostat standard in FIA and GPC modes are listed in Table II. The relative improvements in LOD with thermospray ranged from 46 to 51. Of particular note was the high response for ferrocene

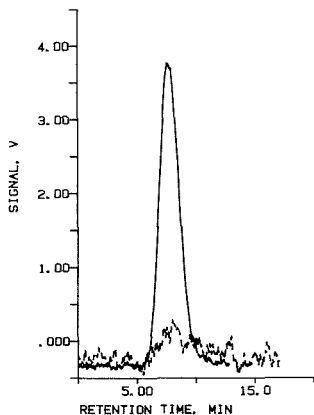


Figure 8. Gel permeation chromatography of 5  $\mu\text{g/mL}$  Fe via Conostan S-21 organometallic standard with 50  $\mu\text{m}$  thermospray (—) and pneumatic (---) sample introduction.

despite its substantial volatility (sublimes above 100  $^{\circ}\text{C}$ ).

### CONCLUSION

The use of thermospray sample introduction as a means for interfacing HPLC with ICP-AES offers substantial improvement in detection for most of the elemental species described herein. Limits of detection for chromium species are better than HPLC-ICP-AES values reported elsewhere and generally as good as or better than those reported for other plasma methods (DCP-AES or ICP-MS). These improvements in detection can be used to advantage for aqueous samples containing low concentrations of chromium or to reduce the collection time for samples such as atmospheric aerosols. In the latter case, for example, the collection time for aerosols required for reasonable measurements can be reduced by a factor equivalent to the LOD improvement. In our case, sampling times could be reduced from up to 24 h to 1 h, or less (12). For chromium, similar improvements were

observed for aqueous (IC) and mixed phase (MPIP) separations. For arsenic species separated by ion chromatography, LOD's were improved by a factor of about 20 for some compounds but were only comparable to those obtained with pneumatic sample introduction for species which are apparently thermally labile. The thermospray sample introduction system also provided substantial LOD improvements ( $\sim 50$  times) for organometallic species in nonaqueous systems.

### LITERATURE CITED

- (1) Uden, P. C. *TrAC, Trends Anal. Chem.* **1987**, *6*, 238.
- (2) Thompson, J. F.; Houk, R. S. *Anal. Chem.* **1986**, *58*, 2541.
- (3) Browner, R. F.; Boorn, A. W. *Anal. Chem.* **1984**, *56*, 787A.
- (4) Browner, R. F.; Boorn, A. W. *Anal. Chem.* **1984**, *56*, 875A.
- (5) Vestal, M. L.; Ferguson, G. J. *Anal. Chem.* **1985**, *57*, 2373.
- (6) Koropchak, J. A.; Winn, D. H. *Anal. Chem.* **1986**, *58*, 2558.
- (7) Koropchak, J. A.; Winn, D. H. *Appl. Spectrosc.* **1987**, *41*, 1311.
- (8) Koropchak, J. A.; Aryamanya-Mugisha, H. *Anal. Chem.* **1988**, *60*, 1838.
- (9) Koropchak, J. A.; Aryamanya-Mugisha, H.; Winn, D. H. *J. Anal. At. Spectrosc.* **1988**, *3*, 799.
- (10) Koropchak, J. A.; Aryamanya-Mugisha, H. Pittsburgh Conference on Analytical Chemistry and Applied Spectroscopy, New Orleans, LA, 1988; Abstract 724.
- (11) Koropchak, J. A.; Winn, D. H. *TrAC Trends Anal. Chem.* **1987**, *6*, 171.
- (12) Koropchak, J. A.; Roychowdhury, S. B., unpublished results.
- (13) Cotton, F. A.; Wilkinson, G. *Advanced Inorganic Chemistry*, 3rd ed.; Wiley-Interscience: New York, 1972; p 836.
- (14) Hem, J. D. *Study and Interpretation of the Chemical Characteristics of Natural Water*, 3rd ed.; U.S. Geological Survey-Water Supply Paper 2254; US Government Printing Office: Washington, DC, 1985; p 138.
- (15) Boumans, P. W. J. M. *Line Coincidence Tables for Inductively Coupled Plasma Atomic Emission Spectrometry*, 2nd Ed.; Pergamon Press: New York, 1984.
- (16) Krull, I. S.; Panaro, K. W.; Gershman, L. L. *J. Chromatogr. Sci.* **1983**, *21*, 460.
- (17) LaFreniere, K. E.; Fassel, V. A.; Eckles, D. E. *Anal. Chem.* **1987**, *59*, 879.
- (18) Boumans, P. W. J. M.; Vrakking, J. J. A. M. *Spectrochim. Acta* **1984**, *39B*, 1261.
- (19) Parker, G. D., Ed. *Mellors Modern Inorganic Chemistry*; John Wiley: New York, 1967; p 840.
- (20) Spall, W. D.; Lynn, J. G.; Andersen, J. L.; Valdez, J. G.; Gurley, L. R. *Anal. Chem.* **1986**, *58*, 1340.

RECEIVED for review September 18, 1989. Accepted November 22, 1989. Partial support of this work was provided by Vestec Corp. and the U.S. Department of Energy through Grant DE-FC22-87PC 79863.

## Application of the Hollow Cathode Discharge Emission Source to the Determination of Nonmetals in Microsamples

Fu-yih Chen and J. C. Williams\*

Department of Chemistry, Memphis State University, Memphis, Tennessee 38152

The use of the hollow cathode discharge source for the excitation of nonmetals in volume-limited samples is discussed. The effects of breakdown voltage, fill-gas composition, electrode composition, hollow size, sample deposition mode, current, and fill-gas pressure on the emission signal from phosphorus and chlorine are reported. Instrumentation, operation, and sample preparation procedures are described. Temporal profiles of the emission signal from very small samples deposited in the hollow are given for P, Cl, and Se. Detection limits of 9 and 20 pg are reported for P and Cl, respectively.

### INTRODUCTION

The hollow cathode discharge (HCD) has been successful

as a source of radiation for atomic spectroscopy for a very long time. It provides a spectrum with very narrow emission lines, which contributes significantly to its sensitivity and selectivity as an atomic emission source (1, 2). As compared to metals, there are many fewer reports of determination of nonmetallic elements using the hollow cathode emission source. The nonmetals, P, Se, and Cl, have many known functions in life processes; thus, analytical methods, including trace analysis of small samples and analysis of nanoliter-size samples of physiological fluids, are needed. The HCD source fills the need for nonmetal determination in volume-limited samples. The analysis is very important because renal physiologists typically employ either micropuncture or microperfusion obtaining tubule fluid samples ranging from picoliters to nanoliters. Common physiological fluids contain Na, K, Ca, Mg, Cl, and P, which frequently must be determined in very

small samples. The HCD has been shown to offer an extremely high analytical sensitivity (3-7) and has been recently demonstrated as having useful precision and sufficient powers of detection needed for determination of Na, K, and Ca in renal fluid (8). Extension of the use of the HCD to the determination of Cl and P in renal fluid was the main objective of this research. Although investigated to a lesser extent than was Cl and P, selenium, which is present in most tissue, is very difficult to determine by present methods and was thus included in this survey.

In the hollow cathode discharge source, excitation of the fill-gas is carried out primarily by high-energy electron impact (1). Metastable species are formed in the discharge by first-kind collisions. Metastable atoms of argon have lifetimes several orders of magnitude longer than common excited states and play an important role in the continuity of the discharge. The role of metastable argon atoms is significant because they have high energy which can be transmitted to other species during the second-kind collisions causing excitation or even ionization. Because argon is present in great excess, the probability of collision with an analyte atom is large. In addition, the high-energy spectral lines of nonmetals may be excited in this process. The two more frequently used rare gases have the metastable energy levels of 11.55 eV ( $4S_{3/2}$ ) and 11.72 eV ( $4S_{1/2}$ ) for argon and 19.82 eV ( $^3S_1$ ) and 20.62 eV ( $^1S_0$ ) for helium (9). Another criterion, sputtering efficiency, is maximized when the inert gas has about the same mass as the material to be sputtered (10); thus, Ar is most commonly used. If necessary, a mixture of He and Ar is used He for high-level excitation and Ar for sputtering efficiency. Ne has metastable levels and a sputtering efficiency intermediate to He and Ar; however, it is very expensive and is used only if both He and Ar are unacceptable.

When the diameter of the cathode is 2 mm or less (11), the radiation output has been found to increase significantly following the empirical formula  $I \times d = K$ , where  $I$  is the intensity of the spectral line,  $d$  the cathode inner diameter, and  $K$  a constant. A length to diameter ratio of hollow cathode at least 3:1 is recommended (12). Depending on experimental conditions and design, the optimal distance between cathode and anode is 20-25 mm (13, 14). Ionization becomes more difficult at much shorter distances. On the other hand, a much larger distance causes prolonged scintillations before a steady, stable discharge is attained. The HCD source offers a greater signal to noise (S/N) intensity ratio of HCD than that of most conventional sources. There are some reports that the water-cooled HCD tends to be independent of matrix effects (15-17). In the cold HCD, sample is injected into the plasma by sputtering, thus avoiding distillation effects observed with a hot cathode. An additional benefit of the mini-HCD is the ability to analyze minute sample volumes whereas most common techniques, such as inductively coupled plasma or flame atomic emission sources, require much large sample volumes.

## EXPERIMENTAL SECTION

Several spectrometer configurations from this laboratory have been described recently (8, 18-20). Briefly, a water-cooled hollow cathode discharge source is mounted on an optical rail and the light divided among a series of narrow-band interference filters or monochromators, which are mounted along the rail. Samples are delivered to the hollow cathode, which is mounted on the stage of a low-power stereomicroscope (Bausch & Lomb, Stereo Zoom 4), using a micromanipulator upon which either a micropipet (Drummond Scientific Co., Broomall, PA) or a syringe with a plastic capillary is mounted. The pipet tip is bent at nearly 90° so that the sample can be easily deposited on the bottom of the hollow cathode. The sample is drawn up by syringe suction until its meniscus reaches the center of the constriction and immediately deposited into the hollow. The pipet tip was positioned on the

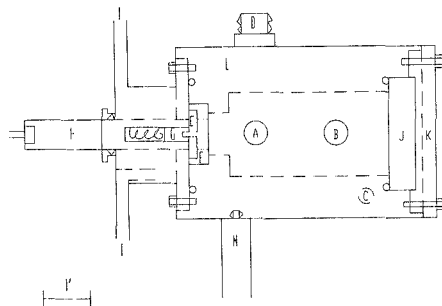


**Figure 1.** Schematic diagram of the hollow cathode emission source housing: A, anode; B, water-cooled secondary electrode; C, gas inlet; D, gas outlet; E, quartz insulator with a hole; F, PTFE insulator; G, hollow cathode; H, hollow cathode holder; I, water in and out; J, quartz window; K, house cap; L, hollow cathode house made out of molybdenated nylon; M, hollow cathode house holder.

center of the cathode bottom, then the sample was deposited on the cathode surface. The syringe was moved very slowly to expel the pipet contents evenly on a portion of the bottom surface of the cathode hollow. As soon as the total sample solution was out of the pipet, one hand continued to press the syringe and the other hand moved the pipet tip up from the cathode surface simultaneously; this procedure prevented the sample solution from being sucked back to the pipet. The sample solution was dried by an infrared lamp and the residue subjected to the hollow cathode discharge.

Subnanogram quantities of analytes are quickly depleted in the discharge producing a temporal emission signal that lasts for only a few tenths of a second. Light from the hollow cathode is focused on an aperture, collimated by a lens, and then directed along the optical rail to a neutral beam splitter which divides the light between two channels. Each channel has an independent monochromator, one at the end of the main rail and the other mounted at a right angle to the main rail. Appropriate wavelength settings were selected and data were collected in two channels simultaneously. The output of each of the PM tubes was fed into a multichannel integrator box before being sent to an analog-to-digital converter for processing by a computer. The integrator box was made in this laboratory and includes six commercially available integrator cards (Evans integrator board 4130A) and three dual amplifier cards (Evans dual amplifier board 4163A) under computer control through Metabyte's PIO-12 and Dash-16 boards, thus providing up to six independent channels.

Although the basic HCD source design is described elsewhere (8, 20), the most recent design has some improvements and a scale drawing is shown in Figure 1. The  $1/2$ -in. vacuum port is much larger than that of the original house, decreasing pump-down time thus reducing the time required for an analysis. The higher gas flow also serves to minimize the effects of vacuum leaks by sweeping molecular gases from the house very rapidly. All ports to the house were made with Cajon ultra-torr fittings (B-8-UT-1-8) and are clearly superior to those used in previous designs. Scale drawings and a detail parts list may be obtained by writing the corresponding author.

Contamination from the air during sampling and drying is a serious problem when such small samples are to be analyzed. A "clean bench" by NUAIRE, Model NU-201-S24, was used as a work space for sample preparation to reduce contamination. The sample solutions were prepared from doubly deionized water (Millipore deionized  $H_2O$ , 18-M $\Omega$  resistance) using anhydrous disodium phosphate ( $Na_2HPO_4$ ), selenious acid ( $H_2SeO_3$ ), and sodium chloride (NaCl) for phosphorus, selenium, and chlorine analysis respectively.

The presence of water vapor in the HCD house may lower the sputtering rate (21) by dissociating in the discharge to produce significant quantities of  $H^+$ , a mobile ion that can then carry a disproportionate share of the discharge current yet contribute little to the overall sputtering rate because of its low mass. In addition, water vapor may act as a quencher of metastables in

the discharge, as has been documented (22, 23). We have effectively used a second vacuum chamber to remove water from the deposited sample prior to mounting the cathode in the HCD (20).

Current, voltage, and timing of the discharge were controlled by a Metrabyte Dash-16 board through Pascal programs written here. In the present operation procedure, a low current discharge is established at the beginning to preheat the cathode and avoid erratic discharges, which we call spikes, frequently caused by sudden current changes. After 100–200 ms, the entire preselected current (high current) is turned on. Temporal emission profiles for each sample are stored for subsequent data reduction.

## RESULTS AND DISCUSSION

In the application of glow discharges to solid samples, the discharge is begun and allowed to stabilize during a preburn period, which may last more than 30 s before data are taken. The very small samples in this report are consumed rapidly, thus producing a transient signal. The largest part of this transient signal occurs first obviating a preburn period. It is thus imperative that the initial discharge be stable and reproducible in order that all the emission signal may be collected without a preburn.

For a given cathode metal, the breakdown voltage is a function only of the product of gas pressure and electrode distance (17). In lower pressure ranges, <1 Torr, we found that the breakdown was erratic and the discharge unstable. Between 1 and 10 Torr, the breakdown voltage increases with pressure, using a fixed electrode distance of 1.25 in. Breakdown with copper cathodes in 10 Torr argon is near the 1000-V limit of the power supply; however, under the same conditions breakdown occurs at  $\approx 900$  V with an aluminum cathode.

As discussed by Cobine, the time delay, or lag, between the application of voltage and breakdown varies at random and is markedly affected by the character of the surface of the electrodes for a given electrode material (24). At times, we have observed time lags several seconds long for both copper and aluminum; however, the problem is significantly less with aluminum. Cobine classified the time lag into three groups. In the first group, the lag is large and caused by weak irradiation and low overvoltage as a result of the random time required for the appearance of suitably placed initial electrons. In the second group, gaps are adequately irradiated but are only slightly overvolted, producing lags of roughly the same order of time as that required for positive ions to cross the gap. In the third group, where the irradiation is adequate and the overvoltage is high, the time lag is probably approximately the same as the time required for the first exponentially increasing electron avalanche to cross the gap.

The use of a radioactive source in the hollow cathode house to render the atmosphere conducting from ionization produced by the nuclear decay was investigated. The breakdown voltage of the HCD under the same conditions using  $<0.01 \mu\text{Ci}$  sealed sources of the radioactive elements,  $^{60}\text{Co}$ ,  $^{22}\text{Na}$ ,  $^{137}\text{Cs}$ , and  $^{138}\text{Ba}$ , in the cathode house was determined. Apparently, the radioactive elements have little effect on the magnitude of the breakdown voltage; however, the occurrence of "delayed discharge" is greatly reduced.

There is little doubt that the radioactive elements can reduce the possibility of a time lag occurring, and this should be used to enhance stability, reproducibility, and precision when the full discharge is begun at the hollow cathode containing the sample. We have obtained our best results, however, when the full discharge is not begun at the hollow cathode; two methods have been developed:

- (1) The discharge can be initiated at a secondary cathode, allowed to stabilize, and then switched in stages to the hollow cathode (8).
- (2) Only one cathode was used in the procedure developed and applied in this report. A low-current discharge of  $\approx 1.5$

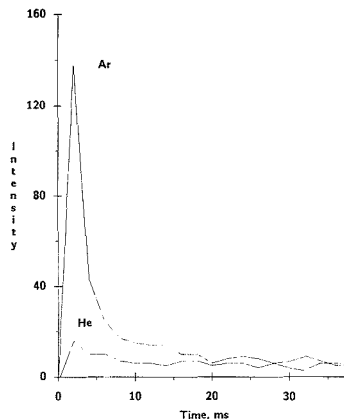


**Figure 2.** Temporal emission profile of phosphorus taken at 213.6 nm in He and Ar. The signal was produced from 1 ng of phosphorus, which was deposited in the hollow from a 50- $\mu\text{L}$  pipet.

mA was established initially in order to pre-heat the cathode and minimize chances of erratic discharge frequently seen if the current is immediately set to its full operating value. After a  $\approx 200$  ms delay, the entire discharge current desired was switched on.

In both cases, breakdown occurs well in advance of the analytical signal. Thus, effects of a variable time lag in breakdown are avoided and a temporally consistent signal is generated from the small amount of analyte.

In this report we used aluminum electrodes. In addition to contributing to discharge stability, the sputtering rate of cathode material from an aluminum cathode is approximately one-fourth that of copper (11) and the emission spectrum of aluminum is somewhat simpler than that of copper. Three sizes of the hollows were compared:  $d = 1.5$  mm,  $D = 5$  mm;  $d = 2.0$  mm,  $D = 5$  mm;  $d = 4$  mm,  $D = 12$  mm (where  $d$  is diameter and  $D$  is depth). We found that a cathode with a 1.5 mm diameter and a depth of 5 mm gave the highest signal intensity for both Cu and Al cathodes. We also found that sputtering for 30 s after the end of a run was sufficient to clean the cathode and to recondition the cathode surface for subsequent runs. These relatively long cleaning times are not as damaging to an Al cathode as with Cu.

**Phosphorus.** We collected the temporal signals for P(I) at 253.6 and 213.6 nm simultaneously using two channels in one of the integrator/amplifiers described earlier. Examples of the emission signal from 1 ng of P in a discharge of 80 mA using both He and Ar as fill gas are shown in Figure 2. The temporal phosphorus signal decays very rapidly giving a very sharp profile. Most of the transient signal occurs in two 2-ms integration period and the signal appears to be almost completely gone by  $\approx 20$  ms. The emission intensity is poor with He.

The optimum pressure for maximum spectral line intensity is shown in Figure 3. Each combination of hollow cathode variables—size, fill gas, fill-gas pressure, hollow size, and cathode metal—has an optimum current. Figure 4 illustrates this by showing the emission intensity as a function of discharge current for P and Cl. The intensity reaches a maximum near 80–120 mA and then decreases with increasing current.

The 213.6-nm emission line is preferred to that at 253.6 nm because its background is much lower and spectral interferences are less. The background signal at 253.6 nm always showed a significant temporal component even for a clean electrode which had been exposed to air; thus, spectral interference from some species on the cathode is indicated.

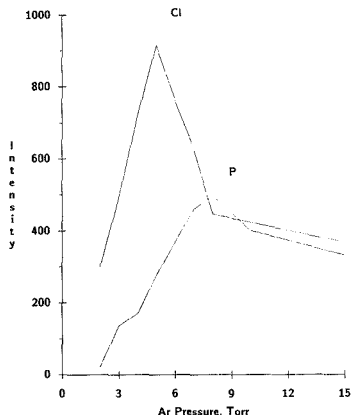


Figure 3. Optimum argon pressure in the hollow cathode source using a constant current of 112 mA for chlorine and 80 mA for phosphorus.

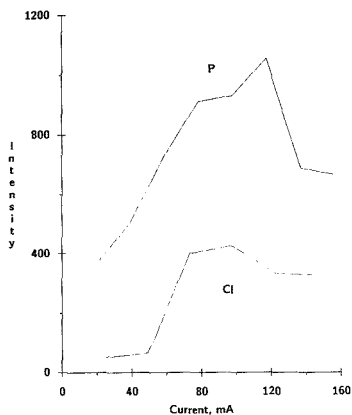


Figure 4. Optimum current for the hollow cathode source using a constant argon pressure of 5 Torr for chlorine and 8 Torr for phosphorus.

Working curves obtained at 213.6 nm for 0 to 1 ng of P deposited from 50 nL solution aliquots using 80 mA in 8 Torr Ar are shown in Figure 5. The data were obtained from temporal profiles of standards and solution blanks by subtracting the solution blank from each sample giving the net peak area for each temporal profile. The curves are virtually linear and show very good precision with correlation coefficient  $>0.99$ . Each line represents a different integration time, 2 ms, 4 ms, and 0.5 s, respectively. An integration time of 0.5 s is some 25 times longer than the initial 20-ms period where most of the analyte signal appears. Because the background is almost negligible, this excessive integration period was used to ensure that all the useful emission signal was collected. One 0.5-s period was used to collect the signal and one later on was used to establish the base line. The average signal from several integration periods taken 0.5 s after discharge initiation was used as background for runs using 2- and 4-ms integration periods. The detection limit for P was calculated from the 0.5-s integration data as  $DL = 2\sigma_{bg}/\text{slope} = 60 \text{ pg}$ .

Two experiments were conducted to investigate the effect of the mode of sample deposition on the emission intensity. In the first experiment, 1 ng of P was deposited in the hollow using different volumes (0.85, 24.1, and 50 nL) of solution

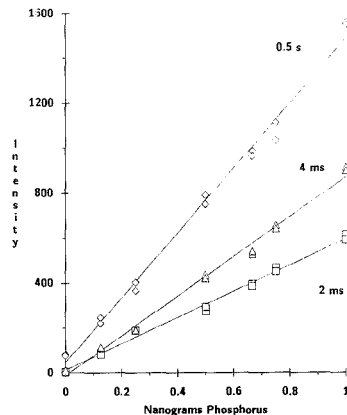


Figure 5. Calibration curves for P made with the hollow cathode source by depositing 50-nL volumes of solutions containing from 0 to 1 ng of P.

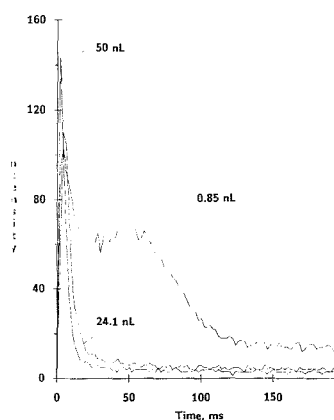
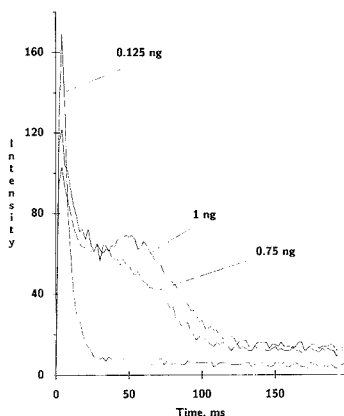


Figure 6. Temporal profiles produced from the discharge of 1 ng of phosphorus deposited from sample solution volumes of 0.85, 24.1, and 50 nL. These curves are representative of five replicas of each volume.

producing net peak areas of  $4965 \pm 22$ ,  $973 \pm 13$ , and  $800 \pm 14$ , respectively. The effects of analyte concentration and solution volume on the temporal profiles are shown in Figure 6. Obviously, a more persistent temporal signal was obtained with the smaller volume even though the total amount of the sample and the operating conditions were the same. This experiment proves that the total emission signal from a given amount of analyte depends sharply on how the analyte was deposited in the hollow. It does not seem reasonable that the physical form of solid deposit should affect the actual residence time of an analyte atom in the hollow; however, it is reasonable that the rate of analyte entry into the hollow is affected by the particle size of solid analyte deposits.

The rapid evaporation of water from the small sample volumes is readily observed under the microscope. A 0.85-nL volume evaporates almost immediately after deposition with little spreading. On the other hand, 50 nL (which is still only one-thousandth of a drop) spreads over a larger area and evaporates much more slowly. Although we have not verified particle size of the solid deposits by microscopy, it seems reasonable that the sample layer from the small-volume high-concentration solution covers a smaller area and would therefore be thicker than the deposit made by the same mass



**Figure 7.** Temporal emission profiles made from different masses of phosphorus deposited in the hollow in a constant solution volume of 0.85 nL.

of solute deposited from a more dilute solution on a relatively larger area.

In sputtering, the charged particle must interact with the sample and impart its kinetic energy to the sample particles to cause ejection into the plasma. Subsequently, collision with metastable Ar causes excitation and perhaps ionization. The sputtering process is expected to remove analyte from a thick deposit more slowly as compared to the same mass of analyte deposited over a much larger area.

It is clear from the temporal shape of the curves in Figure 2 and Figure 6 that most of the 1-ng of P deposit is removed from the hollow surface in 4 ms when the analyte is deposited from a 50-nL volume. On the other hand, the same mass of P deposited from 0.85 nL is released into the hollow over a period of approximately 100 ms. Moreover, the integrated signal of the small-volume high-concentration deposit is over 6 times larger. Two explanations for this phenomenon come to mind.

If atomization were not complete, analyte could escape the hollow without the opportunity to be excited. It is easy to accept that surface area affects the rate at which analyte is removed; however, it seems unlikely that surface area would affect the atomization efficiency.

If a sample atom released from the cathode surface cannot be immediately excited by collisions, then this atom will be pumped out of the hollow without contributing to the emission signal. This might occur if the composition of the gas in the hollow were significantly changed during the rapid entry of the analyte. There are  $1.8 \times 10^{15}$  Ar atoms in the hollow (1.5 mm radius by 5 mm deep, 5 Torr, ambient temperature). There are  $1.5 \times 10^{14}$  atoms from 1 ng of P as  $\text{Na}_2\text{HPO}_4$ . Thus, assuming that all atoms from the  $\text{Na}_2\text{HPO}_4$  are gaseous, the pressure in the hollow would increase by  $\approx 10\%$  as the analyte was rapidly injected into the hollow from a relatively large surface area by sputtering.

In the second experiment, 0.85 nL of sample solution containing 1, 0.75, or 0.125 ng of P was deposited in the hollow. The results are shown in Figure 7. The area under the peaks is proportional to the mass of P. Figure 8 shows a phosphorus calibration curve for 0–1 ng of phosphorus deposited from 0.85 nL solution aliquots. The sensitivity and precision are very much improved as compared to the result in Figure 5, giving a detection limit for P of  $\approx 9$  pg and a correlation coefficient of  $>0.999$  for the linear regression fit.

**Chlorine.** Chlorine was evaluated in the same source and using the same parameters as with P above except that 112-

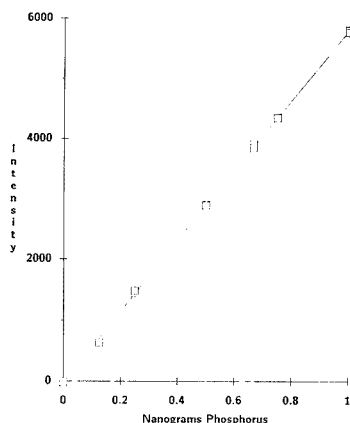


**Figure 8.** A calibration curve for phosphorus, which was prepared by using a constant volume of 0.85 nL and solutions varying in concentration from 0 to 1 ng per 0.85 nL, shows better precision and sensitivity as compared to those in Figure 5. The integration time used was 2 ms.

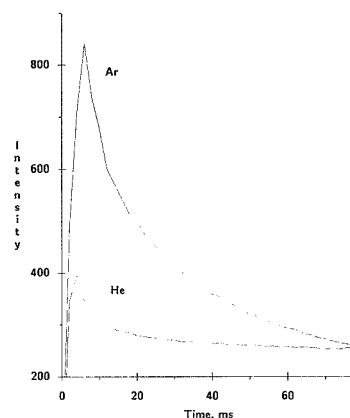


**Figure 9.** Temporal emission profiles of chlorine taken at 725.6 nm in both He and Ar fill gas (5 Torr) from 1 ng of Cl deposited in a solution volume of 0.85 nL.

mA current and 5-Torr pressure were used. The temporal profile of chlorine, from NaCl, at 725.6 nm (Interference filter, Spectro-Film, Inc., Winchester, MA) is shown in Figure 9 with both Ar and He fill gas. The emission intensity in He is low as it was with P; however, Cl has a higher emission signal and a longer residence time in the hollow than P.

In contrast to the temporal profile of chlorine shown in Figure 9, the temporal emission profile observed for sodium from NaCl consists of two distinct peaks (8, 20). In order to compare the profiles directly, we collected Cl (725.6 nm) and Na (588.9 nm) emission signals simultaneously using two monochromators. As shown in Figure 10, the emission signal of both Na and Cl show only a single peak. The early portion of the discharge is expanded in Figure 10A to show the shape of the temporal emission at that time. The shape of the temporal profile of Na emission using Al cathodes as shown in Figure 10 is quite different from the dual peaks observed for alkali metals using Cu cathodes (8, 20). Notably, there is no secondary peak in the Na temporal profile obtained using Al cathodes. Previous work in this laboratory (8, 20) was done by using copper electrodes in an argon pressure of 5 Torr with

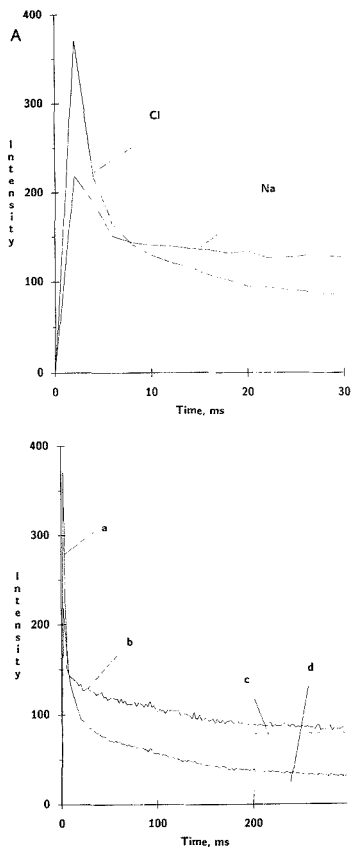


**Figure 10.** Temporal emission profiles of chlorine and sodium: (a) 100 pg of Cl at 725.6 nm, (b) 65 pg of Na at 588.9 nm, (c) base line set by the sodium background limit, and (d) base line set by the chlorine background limit. (A) The first part of Figure 10 is expanded to allow better comparison of the peaks.

a discharge current of 80 mA; all of the parameters used in this investigation are the same as those in the previous work except that the discharge current was 112 mA and the cathode material was Al. These moderate changes in the discharge current are not expected to significantly affect the shape temporal emission profile. Thus, the cathode metal itself may affect the analyte's temporal behavior, thus producing the secondary peaks which have consistently been observed with alkali metals excited from copper cathodes (8, 20).

A working curve obtained for 0–100 pg of Cl as NaCl deposited from 0.85 nL solution aliquots is shown in Figure 11. Considerable scatter is observed in the working curve raising questions as to its linearity; however, a correlation coefficient  $>0.99$  was obtained for a linear regression fit giving a detection limit of less than 20 pg.

**Selenium.** In a manner similar to that used for P and Cl, the emission intensity of Se(I) at 196 and 204 nm was investigated by using a current of 60 mA and a fill-gas pressure of 6 Torr. The emission intensity was approximately the same at both wavelengths; 196 nm was arbitrarily chosen for this report. The temporal profile of 1.25 ng/50 nL and 0.85 ng/0.85 nL Se as selenite is shown in Figure 12 with Ar as fill gas. Although not as dramatic, a more persistent signal was observed for the small-volume deposit similar to that seen with

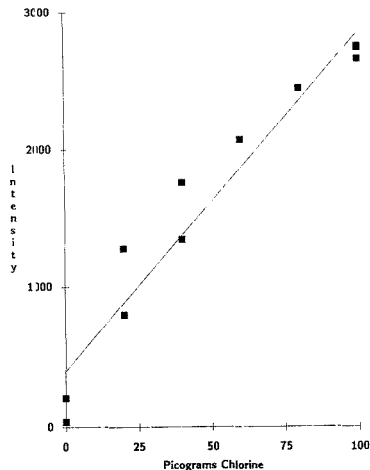


**Figure 11.** A calibration curve for chlorine taken at 725.6 nm for 0 to 100 pg of chlorine deposited in 0.85-nL volumes of solution as NaCl.

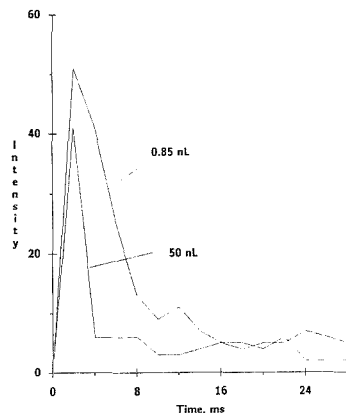


**Figure 12.** Temporal emission profiles for 1.25 ng of Se deposited from 50-nL solution and 0.85 ng of Se deposited from 0.85-nL solution. These curves are representative of five replicates each.

P. The net peak area was 128 for 0.85 ng/0.85 nL compared to 62 for 1.25 ng/50 nL. The S/N for the data 0.85 ng/0.85 nL in Figure 12 is 115 and is representative of that obtained frequently, which is between 80 to 120. Se gives a temporal signal that persists for less than 20 ms and the spectral line intensity is less than that observed for either Cl or P. It is well-known that Se and many of its compounds are volatile even at relatively low temperatures. Thus, depending on the solution composition which existed at the time of deposition, Se may be lost from the deposits on the cathode wall during pump-down to an operation pressure of  $<10$  Torr. Solution conditions must be selected so that nonvolatile Se compounds are formed during deposition. Thus, evaporation would be avoided and Se would be injected into the plasma by sputtering as is desirable.

Matrix modifiers are commonly used in GFAAS to stabilize volatile elements so that they remain in the atomizer until after the matrix has been removed. This technique has performed well for Se analysis by graphite furnace atomic absorption spectroscopy (25). The temporal emission signals of 0.85 ng of Se with different amounts of Cu added as a

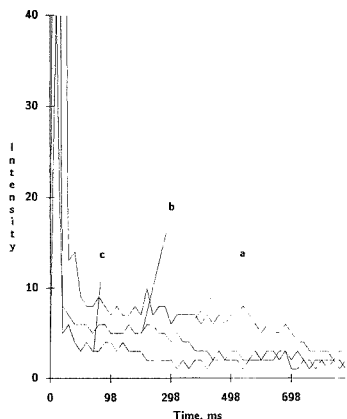


**Figure 13.** Temporal profiles of selenium with various volumes of 1000 ppm copper added to the selenium in the hollow as matrix modifier to form copper selenide: (a) 100 nL, (b) 50 nL, (c) 0.85 nL.

chemical modifier are shown in Figure 13. Three different amounts of modifier (100, 50, and 0.85 nL of 1000 ppm Cu) shows three different temporal emission profiles. It is possible that the addition of modifier produced a compound which is sputtered off the surface much more slowly than the sodium selenite; however, no net selenium signal was obtained when compared to blanks using similar amounts of modifier. A large initial signal at the first point occurs when the high current is turned on. The intensity of this initial spike decreased as the mass of copper modifier was decreased from 100 to 0.85 ng. These modifier atoms will be released from the cathode surface by collisions just as sample atoms and may thus significantly change the atmosphere in the hollow cathode, thus complicating the ionization and excitation processes.

Efforts to make a subnanogram calibration curve for Se using the present apparatus were unsuccessful. A means of observing the emission spectrum of the transient signal in the vicinity of the emission line and the ability to pulse the HCD are needed before further work with Se is attempted.

### CONCLUSION

Although the electron probe liquid microdroplet method (26) shows significantly better detection limits than HCD, the detection limits reported here and elsewhere (8) for the HCD indicate that all six common physiological elements (Na, Cl, K, Mg, Ca, and P) may be determined in a single nanoliter sample of renal fluid. The electron probe instrument is very expensive and requires at least one full-time technician for operation. Because of these limitations, electron probe liquid droplet microanalysis is not widely available. The HCD is the only other analytical method with suitable detection limits to compete with the electron probe microdroplet method and, in addition, it can be made much more readily available to renal physiological studies.

The many advantages of the HCD method—stability, reproducibility, precision, time saving, and cost—make it nearly the ideal source as defined by Ingle and Crouch (27). The detection limits of phosphorus and chlorine of <9 and <20

pg, respectively, represent significant progress toward the development of the HCD source. The reproducibility of the temporal signal from selenium suggests that useful working curves can eventually be demonstrated for Se. These results clearly show that the HCD has much potential for the analysis of nonmetallic elements. The HCD may thus find use in the trace analyses of both metals and nonmetals, complementing graphite furnace AA. The results reported here were obtained with a straightforward HCD source. Other techniques, such as supplemental excitation by microwave and operating the HCD in the pulsed mode, may further improve the performance of the HCD for useful analysis.

### ACKNOWLEDGMENT

We wish to thank John Craig, Robert McCoy, and John Coltart for electronic and mechanical assistance. The very helpful comments from Steven T. Griffin are gratefully acknowledged.

Registry No. P, 7723-14-0; Se, 7782-49-2; Cl, 7782-50-5.

### LITERATURE CITED

- Caroli, S. *Prog. Anal. At. Spectrosc.* **1983**, *6*, 253-292.
- Slevin, P. J.; Harrison, W. W. *Appl. Spectrosc. Rev.* **1975**, *10*(2), 201-255.
- Harrison, W. W.; Prakash, N. J. *Anal. Chim. Acta* **1970**, *49*, 151-159.
- Caroli, S.; Delle Femmine, P. *Spectrosc. Lett.* **1978**, *11*, 299-321.
- Caroli, S.; Senofonte, O. *Can. J. Spectrosc.* **1980**, *25*, 73-80.
- Buzasi-Gyorti, A.; Caroli, S.; Alimonti, A.; Senofonte, O. *Acta Chim. Hung.* **1983**, *113*, 295-302.
- Broekaert, J. A. C. *Spectrochim. Acta* **1980**, *35B*, 225-232.
- Ryu, Jong-Yul; Davis, R. L.; Williams, J. C., Jr. *Appl. Spectrosc.* **1988**, *42*, 1379-1387.
- Wagatsuma, K.; Hirokawa, K. *Spectrochim. Acta* **1987**, *42B*(No. 4), 523-531.
- Rosenberg, D.; Wehner, G. K. *J. Appl. Phys.* **1962**, *33*, 1842-1845.
- Czakow, J. In *Improved Hollow Cathode Lamps for Atomic Spectroscopy*; Caroli, S., Ed.; Ellis Horwood, Ltd.: Chichester, 1985; Chapter 2.
- Papp, L.; Racz, L. *J. Anal. At. Spectrosc.* **1987**, *2*, 405-406.
- Caroli, S.; Senofonte, O.; Alimonti, A.; Zimmer, K. *Spectrosc. Lett.* **1981**, *14*(8&9), 575-587.
- Von Engel, A. *Ionized Gases*, 2nd ed.; Oxford at the Clarendon Press: Oxford at the Clarendon, 1965; Chapter 8.
- Caroli, S.; Senofonte, O.; Delle Femmine, P. *Analyst* **1983**, *108*, 196-203.
- Caroli, S.; Alimonti, A.; Petrucci, F. *Anal. Chim. Acta* **1982**, *136*, 269-276.
- Caroli, S.; Alimonti, A.; Delle Femmine, P.; Shukla, S. K. *Anal. Chim. Acta* **1982**, *136*, 225-231.
- Williams, J. C.; McDonald, J. T.; Davis, R. L. *Anal. Instrum.* **1987**, *16*, 241-261.
- McDonald, J. T.; Williams, J. C., Jr. *Appl. Spectrosc.* **1989**, *43*, 697-702.
- Kuan, Yu-ji. *Microanalysis and Matrix Effects in the Hollow Cathode Emission Source*; Master Thesis, Memphis State University, Memphis, TN, 1989.
- Smith, R. L.; Serxner, D.; Hess, K. R. *Anal. Chem.* **1989**, *61*, 1103-1108.
- Velazco, J. C.; Kolts, J. H.; Setser, J. W. *J. Chem. Phys.* **1978**, *69*, 4357-4373.
- Loving, T. J.; Harrison, W. W. *Anal. Chem.* **1983**, *55*, 1526-1530.
- Cobine, J. D. *Gaseous Conductors*; Dover Publication, Inc.: New York, 1958; Chapter 7-8.
- Martin, C. K.; Williams, J. C. *J. Anal. At. Spectrom.*, in press.
- Roinel, N. *J. Microsc. Biol. Cell.* **1975**, *22*, 261-268.
- Ingle, J. D., Jr.; Crouch, S. R. *Spectrochemical Analysis*; Prentice-Hall, Inc.: Englewood Cliffs, NJ, 1988; Chapter 8.

RECEIVED for review July 31, 1989. Revised manuscript received November 22, 1989. Accepted November 29, 1989. This research was supported by the Memphis State Department of Chemistry and the Memphis State University Foundation.

# Interaction of Capillary Zone Electrophoresis with a Sheath Flow Cuvette Detector

Yung Fong Cheng,<sup>1</sup> Shaole Wu, Da Yong Chen, and Norman J. Dovichi\*

Department of Chemistry, University of Alberta, Edmonton, Alberta, Canada T6G 2G2

In a capillary zone electrophoresis system with a sheath flow detector, the pressurized detector induces a component of flow opposite to that of electrophoresis. This pressure-induced flow, because of its nonuniform velocity profile, can degrade the separation. However, theory predicts and experiment verifies that, under normal operating conditions, the detector does not degrade the separation. The major source of band broadening at pH 9 and 10 is due to longitudinal diffusion, although injection volume can limit the performance of the system. When injection volume is minimized, over 2.5 million theoretical plates are obtained for the analysis of fluorescein thiocarbonyl derivatives of amino acids in a 10-min separation. Also, diffusion coefficients and electrophoretic mobilities may be measured with good accuracy. The low flow rate of capillary zone electrophoresis affects the performance of the sheath flow cuvette. Theory predicts and experiment verifies that the peak height in capillary zone electrophoresis with the sheath flow detector increases linearly with separation voltage. A model is also presented for the sample stream radius expected in the sheath flow cuvette for analytes that undergo radial diffusion.

Capillary zone electrophoresis is a particularly powerful technique for the analysis of ions (1-10). In the technique, separation is based on differential migration of analyte in a buffer-filled capillary under the influence of an electric field. Because the number of theoretical plates produced during the separation is proportional to the applied voltage, very efficient separations may be produced by very high potentials. In this laboratory, theoretical plate counts greater than  $10^6$  are routinely produced with separation potentials of 30 kV.

Successful application of capillary zone electrophoresis requires careful attention to minimize sources of band broadening. To achieve the highest possible separation efficiency, it is necessary to minimize the injection volume, analyte concentration, and detection volume. Very small amounts of analyte, often less than a femtomole, must be injected to obtain optimum separation performance (1).

The sheath flow cuvette is well suited for laser-induced fluorescence detection of small-volume, low-concentration samples (11-17). Although the cuvette is most commonly found in instrumentation designed for the biomedical technique of flow cytometry (18), analytical applications of the device have included laser-induced fluorescence detection in liquid chromatography (11), in flow injection analysis (12), in the study of neat solutions (13-15), and in capillary zone electrophoresis (16, 17) and refractive index detection of neat solutions (19, 20), refractive index gradient detection in capillary zone electrophoresis (21), and thermo-optical absorbance detection of neat solutions (22). A similar device has been used for postcolumn labeling in capillary zone electrophoresis (23, 24).

<sup>1</sup> Present address: 4500 S. Mail Stop 6101, Oak Ridge National Laboratory, PO Box 2008, Oak Ridge, TN 37831-6101.

The sheath flow cuvette is valuable in capillary electrophoresis because detection occurs in a flow chamber with excellent optical quality. Concentration detection limits for capillary zone electrophoresis produced with the sheath flow cuvette are roughly 4 orders of magnitude superior to those produced by on-column fluorescence detectors (9, 17). However, before the sheath flow cuvette can be routinely applied to capillary electrophoresis detection, it is necessary to understand the interaction of the two techniques. The back-pressure induced by the sheath flow cuvette in the electrophoresis capillary must be studied to minimize band broadening. Also, the low volumetric flow rates produced in electrophoresis must be considered in designing the sheath flow cuvette.

In the sheath flow cuvette, a sample stream is injected into the center of a flowing sheath stream under laminar flow conditions. The sample flows as a narrow stream through the center of the flow chamber. If the sheath stream has a composition similar to that of the sample, there is no refractive index boundary between the two streams and no light is scattered from their interface. By restriction of the field of view of the detector to the illuminated sample stream and by use of a flow chamber with flat windows, a very low background fluorescence measurement may be produced. In favorable cases, the fluorescence detection limit approaches the single molecule level (14, 15).

The sheath flow cuvette operates at a pressure greater than ambient. The pressure difference between the detection and injection ends of the capillary leads to Poiseuille flow, which might act to degrade the separation efficiency of capillary zone electrophoresis. Other examples that might induce significant nonuniform flow in capillary zone electrophoresis include hydrostatic pressure due to unequal height of the injection and detection reservoirs, a nonuniform temperature profile that leads to lower viscosity solution in the center of the capillary, introduction of derivatization reagent before the column outlet (25), and analyte flow in a capillary located after the terminal electrode (26). To optimize the performance of capillary zone electrophoresis, it is necessary to understand the behavior of this source of band broadening.

Also, the behavior of the sample stream in the sheath flow cuvette depends upon the relative flow rates of the sample and sheath streams. In applications to capillary zone electrophoresis, very low sample stream volumetric flow rates are encountered. Under these conditions, radial diffusion of the analyte becomes important. To optimize detection using the sheath flow cuvette, it is necessary to understand the performance of the cuvette under this low flow rate regime.

## THEORY

A number of symbols are used in this paper. For convenience, they are collected, along with their definitions, in Table I. In general, SI units are used for each symbol. However, in the body of the paper, more conventional units are occasionally employed.

In capillary zone electrophoresis, solvent flow is driven by electroosmosis and is uniform across the capillary radius. Under this condition, longitudinal diffusion is the only source

Table I. Glossary

*a* slope of the plate count vs applied potential curve, V<sup>-1</sup>  
*b* path length of a fluorescence measurement, m  
*C* analyte concentration, mol m<sup>-3</sup>  
*C*<sub>max</sub> analyte concentration at the peak maximum, mol m<sup>-3</sup>  
*D* analyte mass diffusion coefficient, m<sup>2</sup> s<sup>-1</sup>  
*e* charge on an electron (1.6 × 10<sup>-19</sup> C)  
*g*(*κT*) shape factor ranging from 1.0 to 1.5  
*k* Boltzmann constant (1.38 × 10<sup>-23</sup> J K<sup>-1</sup> molecule<sup>-1</sup>)  
*L* length of the capillary, m  
*n*<sub>m</sub> concentration of ion *m* in the separation buffer, ions m<sup>-3</sup>  
*N*<sub>diffusion</sub> plate count due to diffusion (dimensionless)  
*N*<sub>limit</sub> plate count due to sources of band broadening other than diffusion (dimensionless)  
*P* pressure rise due to electroosmosis, Pa  
*P*<sub>fluorescence</sub> fluorescence power, W  
*P*<sub>laser</sub> laser power, W  
*Q*<sub>sample</sub> volumetric flow rate of the sample, m<sup>3</sup> s<sup>-1</sup>  
*Q*<sub>sheath</sub> volumetric flow rate of the sheath stream, m<sup>3</sup> s<sup>-1</sup>  
*Q*<sub>total</sub> total volumetric flow rate in the sheath flow cuvette, m<sup>3</sup> s<sup>-1</sup>  
*r* radius of the capillary, m  
*r*<sub>diffusion</sub> radius of the sample stream due to diffusion, m  
*r*<sub>hydrodynamic</sub> radius of the sample stream predicted by a hydrodynamic model, m  
*r*<sub>molecular</sub> radius of the molecule, m  
*r*<sub>sample stream</sub> radius of the sample stream in the sheath flow cuvette, m  
*R*<sub>s</sub> resolution of two peaks in electrophoresis (dimensionless)  
*t* transit time from the exit of the capillary to a distance *x* downstream, s  
*T* absolute temperature, K  
*V* electrical potential applied across the capillary, V  
*v*<sub>cuvette center</sub> linear velocity of analyte in the center of the sheath flow cuvette flow chamber, m s<sup>-1</sup>  
*v*<sub>electroosmosis</sub> linear velocity of analyte that is due to electroosmosis, m s<sup>-1</sup>  
*v*<sub>electrophoresis</sub> linear velocity of analyte that is due to electrophoresis, m s<sup>-1</sup>  
*v*<sub>pressure</sub> linear velocity of analyte that is due to the pressure difference across the capillary, m s<sup>-1</sup>  
*v*<sub>total</sub> linear velocity of analyte in the capillary, m s<sup>-1</sup>  
*x* distance downstream from the exit of the capillary in the sheath flow cuvette, m  
*z*<sub>m</sub> charge per ion  
*α* a proportionality constant relating the pressure-induced flow in the capillary to the volumetric flow rate in the sheath flow cuvette, m<sup>-2</sup>  
*χ* cross sectional area of the flow chamber, m<sup>2</sup>  
*ε* dielectric constant for the solvent (dimensionless)  
*ε*<sub>0</sub> permittivity of free space (8.8 × 10<sup>-12</sup> C<sup>2</sup> J<sup>-1</sup> M<sup>-1</sup>)  
*ε* analyte molar absorptivity, m<sup>2</sup> mol<sup>-1</sup>  
*κ* Debye parameter, m<sup>-1</sup>  
*ζ* zeta potential, V  
*μ*<sub>electroosmosis</sub> electroosmotic mobility of the column, m<sup>2</sup> V<sup>-1</sup> s<sup>-1</sup>  
*μ*<sub>electrophoresis</sub> electrophoretic mobility of the analyte, m<sup>2</sup> V<sup>-1</sup> s<sup>-1</sup>  
*μ*<sub>1</sub> electrophoretic mobility of peak 1 in a mixture, m<sup>2</sup> V<sup>-1</sup> s<sup>-1</sup>  
*μ*<sub>2</sub> electrophoretic mobility of peak 2 in a mixture, m<sup>2</sup> V<sup>-1</sup> s<sup>-1</sup>  
*μ* average electrophoretic mobility of a mixture, m<sup>2</sup> V<sup>-1</sup> s<sup>-1</sup>  
*σ*<sup>2</sup> total variance of a peak, m<sup>2</sup>  
*σ*<sup>2</sup><sub>diffusion</sub> peak variance due to longitudinal diffusion, m<sup>2</sup>  
*σ*<sup>2</sup><sub>pressure</sub> peak variance due to the nonuniform flow velocity, m<sup>2</sup>  
*σ*<sup>2</sup><sub>other</sub> contribution to peak variance from sources other than longitudinal diffusion and pressure-induced flow, m<sup>2</sup>  
*η* viscosity of the solvent, kg m<sup>-1</sup> s<sup>-1</sup>

of band broadening, and very high theoretical plate counts may be obtained. However, this assumption of uniform velocity profile fails when the detector is pressurized. This pressure difference induces flow from the detector to the injector and is expected to take the familiar radial parabolic distribution of Poiseuille flow. Parabolic flow profiles give rise to additional band broadening because analyte in the center of the capillary travels at a different velocity than analyte at the walls.

Appendix 1 considers the behavior of capillary zone electrophoresis in the presence of pressure-driven flow. The average linear velocity of analyte through the column is given

by the sum of the velocity due to electroosmosis, electroosmosis, and pressure-driven flow:

$$v_{\text{total}} = v_{\text{electroosmosis}} + v_{\text{electrophoresis}} + v_{\text{pressure}} = [\mu_{\text{electroosmosis}} + \mu_{\text{electrophoresis}}] \frac{V}{L} + v_{\text{pressure}} \quad (1)$$

For a pressurized detector, the pressure-driven flow opposes the electrophoretic driven velocity and takes a negative sign. A plot of the analyte velocity vs the applied potential should be linear, but with a nonzero intercept. Under conditions where electroosmosis and electrophoresis driven flow are opposed by the pressure-driven flow, the radial flow profile is parabolic but with the highest velocity near the capillary walls and lowest velocity in the center of the tube.

The pressure-driven flow not only acts to slow the separation but also can lead to a decrease in the number of theoretical plates. This decrease in plate count arises both from enhanced longitudinal diffusion, because of the increased length of time that the analyte spends in the column, and from the parabolic flow profile induced by the pressure-driven velocity. The number of theoretical plates may be written as

$$N = \frac{L^2}{\sigma_{\text{diffusion}}^2 + \sigma_{\text{pressure}}^2 + \sigma_{\text{other}}^2} = \frac{L^2}{\frac{2DL}{v_{\text{total}}} + \frac{r^2 v_{\text{pressure}}^2 L}{24Dv_{\text{total}}} + \sigma_{\text{other}}^2} \quad (2)$$

Strictly speaking, this equation is only valid for a detector placed at the capillary outlet, such as the sheath flow cuvette.

Under conditions of negligible pressure-driven flow, the plate count reduces to

$$N = \frac{1}{\frac{1}{N_{\text{diffusion}}} + \frac{1}{N_{\text{limit}}}} = \frac{1}{\frac{2D}{[\mu_{\text{electroosmosis}} + \mu_{\text{electrophoresis}}]V} + \frac{\sigma_{\text{other}}^2}{L^2}} \quad (3)$$

A plot of the number of theoretical plates versus applied potential will be linear for low potential but level off to a constant value at higher potential.

Appendix 2 considers the effect of applied potential upon the peak maximum fluorescence intensity observed with the sheath flow cuvette. A rather complicated result is obtained. However, if the pressure-induced flow is small compared with the electroosmotic and electrophoretic induced flow velocity of the analyte, the fluorescence signal expected at the peak maximum is given by

$$P_{\text{fluorescence}} = P_{\text{laser}} \epsilon \frac{\text{moles injected}}{2\pi r} v_{\text{total}} \left( \frac{\chi}{2\pi Q_{\text{sheath}} DL} \right)^{1/2} \quad (4)$$

Note that the fluorescence signal in the sheath flow cuvette increases linearly with the sample velocity and, hence, with the applied potential. The linear relationship between peak height and applied potential arises because of two phenomena. First, the concentration of analyte at the peak maximum scales as the square root of the number of theoretical plates and with the square root of applied potential. Any on-column detector for capillary zone electrophoresis should produce a square root increase in peak height with applied potential. Second, the sample radius in the cuvette increases, for small ratio of sample to sheath flow rate, with the square root of sample volumetric flow rate, which also scales linearly with applied potential in capillary zone electrophoresis. Because the fluorescence

sensitivity is proportional to the path length, i.e. diameter measured across the sample stream, the fluorescence sensitivity for neat samples scales with the square root of applied potential. The combination of increased maximum analyte concentration with increased sensitivity leads to a linear dependence of peak height on potential.

Larger signals are expected for early eluting analyte (where  $v_{\text{total}}$  is large). It is interesting to note that under electroosmosis injections, the amount of analyte is also proportional to this sum (27). As a result, fast moving, early eluting analyte will generate much larger signals than a similar concentration of slow moving analyte.

### EXPERIMENTAL SECTION

The capillary zone electrophoresis system and laser-induced fluorescence detector have been described before (16, 17). A 1 m long piece of 50  $\mu\text{m}$  inner diameter fused silica capillary (Polymicro Technology) was used for the separation. A 30-kV power supply (Spellman) was used to drive the electrophoresis. A platinum electrode provided electrical contact with the separation buffer at the high-voltage, injection end of the capillary. This end of the capillary was enclosed within a safety-interlock-equipped Plexiglas box. The detector end of the capillary was inserted into a sheath flow cuvette (Ortho) that was held at ground potential. The sheath fluid was pumped by a high-pressure syringe pump (Isco) at flow rates ranging from 0.1 to 12  $\text{mL h}^{-1}$ ; typical values were 0.5  $\text{mL h}^{-1}$ . Fluorescence was excited by a 50-mW argon ion laser (Coherent) operating at 488 nm. The beam was focused with an 18 mm focal length (7 $\times$ ) microscope objective (Melles Griot) into the cuvette. Fluorescence was imaged with either an 18 $\times$ , 0.45 numerical aperture (NA) microscope objective (Melles Griot) onto a 200  $\mu\text{m}$  radius pinhole or a 32 $\times$ , 0.65 NA objective (Wild/Leitz) onto a 300  $\mu\text{m}$  radius pinhole. The collected light was filtered with a 495-nm long-wavelength pass glass filter (Shott) and a 560-nm short-wavelength pass interference filter (Ealing) and was detected with a photomultiplier tube (Hamamatsu). For most experiments, the output of the photomultiplier tube was conditioned with a 0.4-s RC filter and then sent to a strip chart recorder; for the data of Figure 3, a 20-ms time constant was used and a digital oscilloscope was used to record the data.

Fluorescein and fluorescein isothiocyanate derivatized amino acids were used to characterize the system. The fluorescein thiocarbonyl derivatives of leucine, proline, and threonine were prepared as before (16, 17). A 5 mM, pH 10 carbonate buffer or a 5 mM, pH 9 borate buffer was used for all of the experiments. Typical injection conditions are 1 kV for 10 s. The sheath stream composition was identical with that of the separation buffer.

### RESULTS AND DISCUSSION

**Effect of Sheath Flow on Electrophoretic Velocity.** To demonstrate the effect of the pressurized flow chamber, the velocity of fluorescein was measured as a function of applied potential at a relatively high sheath volumetric flow rate of 20  $\text{mL h}^{-1}$  (Figure 1). As predicted by eq 1, the velocity is linear with potential,  $R = 0.99$ , over a range of 6–29 kV, but with a nonzero intercept. The pressure-induced flow velocity is given by this intercept,  $v_{\text{pressure}} = -1 \times 10^{-4} \text{ m s}^{-1}$ . The negative sign arises because the flow is directed from the detection to the injection end of the capillary.

At sheath volumetric flow rates typically employed, the pressure rise induced by the cuvette is quite small. To estimate the pressure rise, the flow rate produced by changing the relative height of the injection and receiving buffer reservoirs, at zero sheath flow rate, was compared with the flow rate induced by the pressurized flow chamber. A 1  $\text{mL h}^{-1}$  sheath flow rate corresponds to a pressure difference of 6 mm of water, equal to 65 Pa or 0.5 Torr. Most analytical data is taken at a sheath volumetric flow rate less than 1.0  $\text{mL h}^{-1}$ , producing a negligible pressure rise in the system.

The analyte linear velocity was measured at different sheath flow rates and at a separation potential of 22 kV. As predicted by eq 1, the velocity is linearly related to the sheath volumetric flow rate,  $R = 0.99$  and  $n = 5$ . The slope of the line,  $-2 \times 10^4$

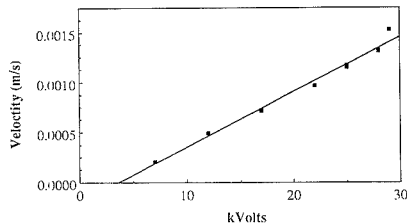


Figure 1. Analyte velocity vs applied potential in capillary zone electrophoresis with a sheath flow detector. A 50  $\mu\text{m}$  inner diameter, 1 m long capillary was employed. A very high sheath volumetric flow rate, 20  $\text{mL h}^{-1}$ , was used to generate a significant component of pressure-induced flow. The line is the least-squares fit of the data to a straight line.

$\text{m}^{-2}$ , is a conversion factor between the sheath volumetric flow rate (in  $\text{m}^3 \text{s}^{-1}$ ) and the induced linear flow velocity (in  $\text{m s}^{-1}$ ) in the capillary.

**Electrophoretic and Electroosmotic Behavior.** The analyte velocity vs applied potential data may be used to characterize the electrophoretic and electroosmotic behavior of the system. The slope of the velocity vs applied potential line,  $6.4 \times 10^{-8} \text{ m s}^{-1} \text{ V}^{-1}$ , may be used to estimate the sum of the electroosmotic and electrophoretic mobilities. For a column length of 1 m, the total mobility of the ion is

$$\mu_{\text{electroosmosis}} + \mu_{\text{electrophoresis}} = 6.4 \times 10^{-8} \text{ m}^2 \text{ V}^{-1} \text{ s}^{-1} \quad (5)$$

As suggested by Huang et al., the electroosmotic mobility could be determined by monitoring the current flowing through the capillary during an analysis that used a 5.0 mM, pH 10 leading electrolyte and a 5.1 mM, pH 10 trailing electrolyte (28). The current increased linearly during the procedure until the capillary was filled with the new buffer. On the basis of the time necessary for the current to reach a constant value, an electroosmotic mobility of  $1.01 \times 10^{-7} \text{ m}^2 \text{ V}^{-1} \text{ s}^{-1}$  was determined for this system. This experimental value may be compared with the Helmholtz-Smoluchovsky equation (29)

$$\mu_{\text{electroosmosis}} = \epsilon \epsilon_0 \zeta / \eta \quad (6)$$

where, for water at 25  $^{\circ}\text{C}$ ,  $\epsilon = 80$  and  $\eta = 8.9 \times 10^{-4} \text{ kg m}^{-1} \text{ s}^{-1}$ . The zeta potential responsible for the electroosmotic mobility is estimated to be  $\zeta = 0.13 \text{ V}$ , a value consistent with that reported for silica-water at lower pH (29). Due to the negative charge of the capillary wall, an excess of positive charge, found in the outer portion of the double layer, acts to propel the solvent from the positive (injection) end of the capillary to the negative (detection) end of the capillary. Both the electroosmotic mobility and the zeta potential have a positive sign.

An independent estimate of the zeta potential comes from the pressure-induced flow data. As noted by Moore (30), the pressure rise induced by electroosmotic flow is given by

$$P = 8\epsilon\epsilon_0\zeta L/r^2 \quad (7)$$

In our system, a pressure difference of 0.7 Pa would balance the electroosmotic plus electrophoretic flow at 1 V for fluorescein. Because the electroosmotic mobility in the system is 1.6 times the total mobility, a pressure of 1.1 Pa would balance the electroosmotic flow rate induced by a 1-V potential in a 1 m long, 50  $\mu\text{m}$  diameter capillary. The zeta potential predicted by this data is then 0.13 V, identical to the value predicted by the Helmholtz-Smoluchovsky equation.

If the overall mobility of the ion is  $6.4 \times 10^{-8} \text{ m}^2 \text{ V}^{-1} \text{ s}^{-1}$  and the electroosmotic mobility is  $1.01 \times 10^{-7} \text{ m}^2 \text{ V}^{-1} \text{ s}^{-1}$ , then the electrophoretic mobility of fluorescein is  $-3.7 \times 10^{-8} \text{ m}^2 \text{ V}^{-1} \text{ s}^{-1}$ . The negative sign for the electrophoretic mobility comes

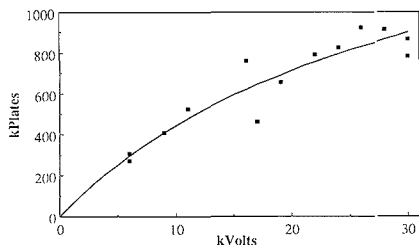


**Figure 2.** Plate count vs applied potential. A 50  $\mu\text{m}$  inner diameter, 1 m long capillary was used to analyze fluorescein. Injection proceeds at 1 kV for 10 s. The sheath stream volumetric flow rate was 0.5 mL  $\text{h}^{-1}$ . The data are shown as the closed squares. The least-squares fit of the data with eq 7 is shown as the smooth curve

from the negative charge on fluorescein at pH 10; in the absence of electroosmosis, the analyte would travel from the detector toward the more positive injection end of the capillary. The Debye-Hückel-Henry theory may be used to model the electrophoretic mobility of the analyte (31-33):

$$\mu_{\text{electrophoresis}} = \frac{ze\eta(\kappa r_{\text{molecular}})}{6\pi\eta r_{\text{molecular}}(1 + \kappa r_{\text{molecular}})} = -3.7 \times 10^{-8} \text{ m}^2 \text{ V}^{-1} \text{ s}^{-1} \quad (8)$$

where the Debye parameter is given by

$$\kappa = \left( \frac{2e^2 \sum_{m=1}^{\infty} z_m^2 n_m}{\epsilon_0 \kappa T} \right)^{1/2} \quad (9)$$

where the summation is over each ion in solution. At pH 10, fluorescein is a dianion so  $z = -2$  (34). For a 5 mM carbonate buffer at pH 10,  $\kappa = 1.4 \times 10^8 \text{ m}^{-1}$ . The radius of the analyte necessary to produce the observed mobility is 0.48 nm, in excellent agreement with the value calculated from van der Waals radii (32). This value will be compared below with the molecular radius predicted from the analyte diffusion coefficient.

**Plate Count.** As an example of the behavior of capillary zone electrophoresis where the plate count is limited by both diffusion and injection volume but not sheath flow, Figure 2 presents the number of theoretical plates for fluorescein measured as a function of the applied potential. For this data, the sheath flow cuvette was operated at a typical flow rate, 0.5 mL  $\text{h}^{-1}$ . The plate count was estimated from the full width at half-height based on a strip chart recording and suffers rather poor precision as a result. To minimize the effect of drift, the applied voltages were chosen with the aid of a random number generator. Voltages below 5 kV were not employed because of the long time required for analysis. At low applied potential, the plate count increases linearly with potential. However, the data obtained at higher potential approach a constant value of about a million plates, albeit with a significant amount of scatter. The scatter is due, in part, to uncertainty in the measurement of peak width.

Simple theory predicts a linear relationship between plate count and applied potential. Although a straight line can be fit to the data, the line has a significant nonzero intercept and is not consistent with the simple theory. Instead, to understand the plate count produced in capillary electrophoresis, it is necessary to account for extracolumn peak broadening. The plate count observed for a system with constant extracolumn band broadening is given by

$$N_{\text{obsd}} = \frac{1}{\frac{1}{N_{\text{diffusion}}} + \frac{1}{N_{\text{limit}}}} = \frac{1}{\frac{1}{aV} + \frac{1}{N_{\text{limit}}}} \quad (10)$$

where  $a$  is given by (2)

$$a = [\mu_{\text{electroosmosis}} + \mu_{\text{electrophoresis}}]/2D \quad (11)$$

A plot of  $1/N_{\text{obsd}}$  vs  $1/V$  has a slope of  $1/a$  and an intercept of  $1/N_{\text{limit}}$  and, for the data presented in Figure 2, yields  $a = 58 \text{ plates V}^{-1}$  and  $N_{\text{limit}} = 1.8 \times 10^6$  plates. These parameters were substituted into eq 7, and the result is plotted as the smooth curve in Figure 2. At low applied potential, diffusion dominates the plate count whereas a nondiffusional source of band broadening limits the number of theoretical plates.

To understand the plate count observed at low applied potential, it is necessary to know the diffusion coefficient. The slope of the plate count vs applied potential curve in the absence of extracolumn band broadening is 58 plates  $\text{V}^{-1}$  and may be used to estimate the diffusion coefficient of fluorescein. For a peak broadened only by diffusion, the slope is given by the ratio of the total mobility to diffusion coefficient

$$\frac{N}{V} = \frac{\mu_{\text{electroosmosis}} + \mu_{\text{electrophoresis}}}{2D} = 58 \text{ plates V}^{-1} \quad (12)$$

From the value of  $\mu_{\text{electroosmosis}} + \mu_{\text{electrophoresis}} = 6.4 \times 10^{-8} \text{ m}^2 \text{ V}^{-1} \text{ s}^{-1}$ , the diffusion coefficient of fluorescein is estimated to be  $5.5 \times 10^{-10} \text{ m}^2 \text{ s}^{-1}$  ( $5 \times 10^{-6} \text{ cm}^2 \text{ s}^{-1}$ ), which may be used to estimate the radius of a fluorescein molecule in solution. From the Stokes-Einstein formula, the diffusion coefficient of a molecule is given by (31)

$$D = \frac{kT}{6\pi\eta r_{\text{molecular}}} \quad (13)$$

A diffusion coefficient of  $5.5 \times 10^{-10} \text{ m}^2 \text{ s}^{-1}$  in water at 25  $^{\circ}\text{C}$  corresponds to a molecular radius of 0.44 nm, within experimental error identical with the value predicted from the electrophoretic mobility.

Diffusion dominates the peak width at low applied potential. However, some extracolumn band broadening becomes noticeable at higher potentials. Several workers have studied the effect of injection volume on separation efficiency (35, 36). A limiting plate count of  $1.8 \times 10^6$  would be produced by an injection volume of  $1.5 \times 10^{-9} \text{ L}$  in this 50  $\mu\text{m}$  diameter, 1 m long column. The nominal  $1.2 \times 10^{-9} \text{ L}$  injection volume employed in this experiment is consistent with the observed band broadening.

Although the injection volume appears to dominate the extracolumn band broadening, two other contributions to band broadening can be considered: detector time constant and pressure-induced flow. The detector time constant, 0.4 s, would lead to a plate count of over  $3 \times 10^6$  for fluorescein eluting at 12 min. Detector time constant is insignificant compared with injection volume as the limiting contribution to plate count. The effect of pressure-induced flow on plate count is calculated from eq 26 of Appendix 1. First, the pressure-induced linear velocity is estimated from the slope of the linear velocity versus sheath volumetric flow rate data. The sheath volumetric flow rate of 0.5 mL  $\text{h}^{-1}$  is expected to produce a pressure rise of 0.2 Torr and a pressure-induced linear flow velocity of  $3 \times 10^{-4} \text{ m s}^{-1}$ , about 0.2% of the total analyte velocity. Equation 26 predicts that, at the very low pressure-induced flow in the sheath flow cuvette, pressure-induced flow will increase the plate count by less than 0.5%, assuming a linear flow velocity of  $3 \times 10^{-6} \text{ m s}^{-1}$  due to pressure-driven flow, a diffusion coefficient of  $5 \times 10^{-10} \text{ m}^2 \text{ s}^{-1}$ , and a 50  $\mu\text{m}$  diameter capillary.

To demonstrate that sheath flow does not degrade the performance of capillary zone electrophoresis, a mixture of the fluorescein thiocarbonyl (FTC) derivative of leucine, proline, and threonine was analyzed (Figure 3). Efforts were made to minimize nondiffusional sources of band broadening: The injection volume was reduced to less than 0.5 nL (500

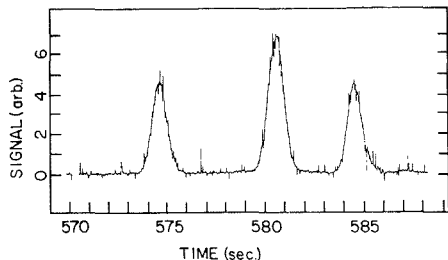


**Figure 3.** Separation demonstrating over 2.5 million theoretical plates. A mixture of fluorescein thiocarbonyl derivatives of leucine, proline, and threonine was studied. The analyte concentration was  $10^{-9}$  M, the sample was injected at 500 V for 10 (injection volume = 0.5 nL), the separation buffer was 5 mM pH 9 borate, the capillary was 97 cm long, and the separation was run at 29 kV. Leucine and threonine demonstrate plate counts greater than 2.5 million, estimated by regression analysis, whereas proline generated 2.3 million plates.

V and 10-s injection,  $N_{\text{limit}} > 2 \times 10^7$ , the analyte concentration was  $10^{-9}$  M, the detector time constant was reduced to 20 ms ( $N_{\text{limit}} > 10^9$ ), and a digital storage oscilloscope was used to record the peaks at a sampling rate of one point every 20 ms—the stored data were then plotted with an x-y plotter. As a result of the very short time constant, the peaks are rather noisy. A Gaussian function was fit to each peak with excellent results. The theoretical plate count was  $2.5 \times 10^6$  for FTC-leucine,  $2.3 \times 10^6$  for FTC-proline, and  $2.6 \times 10^6$  for FTC-threonine, corresponding to a peak standard deviation less than 0.4 s for the 570-s elution time. The height equivalent to a theoretical plate for this data was 390 nm, less than 1% of the capillary diameter. The plate counts correspond to a diffusion coefficient and molecular radius respectively of  $3.5 \times 10^{-6}$  cm<sup>2</sup> s<sup>-1</sup> and 0.70 nm for FTC-threonine and FTC-leucine and  $3.8 \times 10^{-6}$  cm<sup>2</sup> s<sup>-1</sup> and 0.64 nm for FTC-proline. A 5 mM, pH 9 borate buffer and a different column were used for the data of Figures 1 and 2; analyte elutes more quickly in this column compared with the pH 10 data.

The theoretical plate count appeared to depend on the condition of the tip of the capillary used for injection. If the tip was not cut smoothly, the peaks would demonstrate tailing; a capillary tip that was in poor condition could produce a factor of 2 or more degradation in plate count. However, if the tip was formed from a sharp and uniform break, then very high plate counts could be obtained.

**Detection.** Appendix 2 models the perturbation induced on the fluorescence detector by capillary zone electrophoresis. Under conditions of low pressure-induced flow, the fluorescence power is given by

$$P_{\text{fluorescence}} = P_{\text{laser}} \epsilon \frac{\text{moles injected}}{2\pi r} \left\{ \mu_{\text{electroosmosis}} + \mu_{\text{electrophoresis}} \left[ \frac{V}{L} \right] \left( \frac{\chi}{2\pi Q_{\text{sheath}} DL} \right)^{1/2} \right\} \quad (14)$$

The fluorescence signal was measured as a function of the applied potential for injection of fluorescein into the capillary. The peak height for fluorescein increased linearly,  $R > 0.99$  and  $n = 10$ , with applied potential ranging from 6 to 30 kV and a constant sheath volumetric flow rate of 20 mL/h.

The model also predicts an inverse square root relationship between fluorescence signal and sheath volumetric flow rate (Figure 4). At high sheath volumetric flow rates, the model is qualitatively correct; the signal does decrease with the inverse square root of the sheath volumetric flow rate, smooth curve in Figure 4, for the data obtained at the higher sheath volumetric flow rate. However, the peak height decreases at

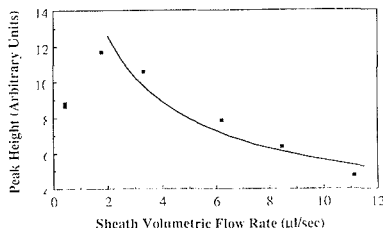


**Figure 4.** Peak height vs sheath flow rate. The sample of fluorescein was analyzed at a potential of 28 kV. The smooth curve is the peak height radius predicted assuming an inverse square root dependence of peak height upon sheath flow rate.

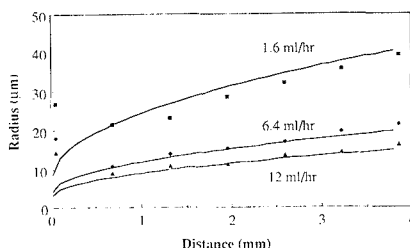


**Figure 5.** Sample stream radius as a function of distance downstream from the capillary exit. The sample is continuously injected at 25 kV. The radius is estimated by inspection with a calibrated microscope. The smooth curve is the sample stream radius predicted from eq 14.

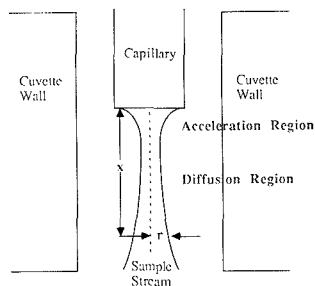


**Figure 6.** Behavior of the sample stream in the sheath flow cuvette. An initial acceleration region, where the sample stream radius contracts, is followed by a region where the sample radius increases due to diffusion.

very low sheath volumetric flow rate. This decrease in peak height arises as the sample stream broadens so that its image overfills the limiting aperture in the collection optical train. Much of the fluorescence intensity is blocked by the aperture and fails to reach the photomultiplier tube. In an optimized system, the aperture would be matched in size to the image of the illuminated sample stream, maximizing the fluorescence signal while minimizing the background signal due to Raman and Rayleigh scatter.

To investigate further the variation of sample stream radius with sheath volumetric flow rate, a reticle was placed in the microscope eyepiece and focused upon the sample stream. The radius of a fluorescein sample stream continuously supplied at a potential of 25 kV was estimated at several positions downstream from the exit of the capillary, Figure 5. The sample stream appears first to be focused to a small radius about 50 μm downstream from the exit of the capillary and then increases with further distance. Also, the sample stream radius decreases as the sheath volumetric flow rate increases.

Figure 6 presents a schematic of the sheath flow cuvette to describe the behavior of the sample stream as it passes through the flow chamber. Qualitatively, the initial decrease in sample radius is associated with the rapid acceleration of the analyte from a low linear velocity in the capillary to a much higher linear velocity in the center of the flow chamber (37). For incompressible fluids, this acceleration produces a concomitant decrease in the area of the sample stream. After the sample travels a distance given by 1 or 2 times the cuvette width, the sample presumably reaches a steady linear velocity and, neglecting diffusion, a constant radius. A hydrodynamic model, which predicts that the sample stream radius as a function of the ratio of the sheath and sample stream volumetric flow rates, was verified for micrometer size polystyrene particles that do not suffer appreciable diffusion during transit through the cuvette (38). However, diffusion will be significant for low volumetric flow rates and small molecular weight analyte.

A model may be developed for the sample stream radius that takes into account analyte diffusion. The radius of the sample stream is assumed to be equal to the sum of a hydrodynamic component, predicted by the earlier model, and a diffusion component

$$r_{\text{sample stream}} = r_{\text{hydrodynamic}} + r_{\text{diffusion}} \quad (15)$$

where the hydrodynamic sample radius is predicted by eq 30 and the diffusion-induced radius, measured after some transit time from the capillary exit, is given by

$$r_{\text{diffusion}} = (2Dt)^{1/2} \quad (16)$$

The linear velocity in the center of a square duct is given by (39)

$$v_{\text{cuvette center}} = \frac{9}{16} \frac{Q_{\text{total}}}{x} \quad (17)$$

The total volumetric flow rate is dominated by the sheath volumetric flow rate in this experiment. The diffusion induced flow rate is then given by

$$r_{\text{diffusion}} = \left( \frac{2Dx}{v_{\text{cuvette center}}} \right)^{1/2} \quad (18)$$

The sum of the diffusion and hydrodynamic radii are included as the smooth curve in Figure 5 and are in good agreement with the data for distances beyond the initial acceleration region. There is only one disturbing note in these data; to make the data and theory agree for fluorescein, it was necessary to multiply the diffusion induced radius by 2. This factor may have several origins. Most likely, the visual estimation of the sample radius is biased; diffusion will induce an error-function distribution of fluorescence intensity. Presumably, the eye estimates the radius of the sample stream as the distance corresponding to an intensity that is two standard deviations decreased from the maximum. Alternatively, the flow velocity in the center of the cuvette has not relaxed to a steady state and analyte are traveling at a lower than predicted velocity leading to more diffusion than calculated. Also, some turbulence at the exit of the capillary would cause broadening.

The radius of the sample stream is both predicted and observed to be proportional to the inverse square root of the sheath volumetric flow rate. A low sheath volumetric flow rate is desirable because it results in a large hydrodynamic radius and large fluorescence intensity. However, a large diffusion radius is undesirable because it leads to dilution of the analyte. Under conditions of constant laser irradiance, the fluorescence sensitivity will decrease when diffusion in the cuvette is significant because diffusion leads to a dilution that is proportional to the square of the sample radius whereas

the path length increases linearly with sample radius. To optimize the fluorescence sensitivity, the laser beam should be located as near as possible to the exit of the capillary to minimize diffusion. Furthermore, a larger sample radius is obtained by detecting in the acceleration region of the flow profile. Last, a very low sheath volumetric flow rate is desirable to maximize the sample radius. These conclusions hold for direct measurement of the fluorescence intensity. A different set of conclusions will hold for single molecule detection where minimization of the probe volume is of paramount importance—in single molecule detection, the optimum fluorescence detection region will be near the minimum in the sample stream radius.

One might worry about diffusion in the sheath flow cuvette leading to enhanced band broadening in capillary zone electrophoresis. At a typical sheath volumetric flow rate of 0.5 mL h<sup>-1</sup>, the analyte will diffuse about 5 μm during the 50-μm transit distance from the exit of the capillary to the laser beam, ultimately limiting the separation efficiency of the capillary to about 10<sup>11</sup> plates. Clearly, in any practical system, diffusion of the analyte in the sheath flow cuvette produces a negligible contribution to band broadening.

## CONCLUSION

Under practical conditions of low sheath volumetric flow rate, the sheath flow cuvette does not degrade the performance of capillary zone electrophoresis. However, the maximum pressure difference studied was quite small, about 12 Torr. Larger pressure-driven flow could arise from a large difference in height between the injection and detection ends of the capillary or direct addition of derivatization reagent to the separation capillary. In fact, the rather modest plate count observed in systems that add postcolumn derivatizing reagents may be due to a large component of pressure-driven flow (23–25). Other, more subtle examples of nonuniform flow can be produced by a nonuniform radial temperature distribution in the capillary and a pressurized injector that has not fully relaxed to ambient pressure.

Although Poiseuille flow has been described in terms of degradation of the separation efficiency, it paradoxically might prove useful in improving the resolution of two closely eluting analytes, Appendix 1. If pressure-induced flow balances the average velocity of two closely spaced analytes, then the resolution of the analyte becomes infinite as the faster component eventually escapes to the detector and the slower moving analyte is driven back to the injector. This approach of a balancing pressure gradient to improve the resolution of a separation is similar to the effect of electroosmosis that opposes electrophoresis, as pointed out by Jorgenson and Lukacs (2). These approaches share a common disadvantage of long analysis time. However, the pressure-driven resolution enhancement offers the potential advantage of programing where the retarding pressure is decreased in steps to allow the elution of successive sets of closely eluting analyte. Pawliszyn has described a clever way of generating the sheath fluid based on electroosmotic flow; his method could easily be controlled by a computer to automate flow programing (40). Further work will be required to discover if pressure-programmed capillary zone electrophoresis is a useful tool in the analysis of complex mixtures.

## ACKNOWLEDGMENT

Jed Harrison of the Chemistry Department of the University of Alberta kindly provided the x-y chart recorder used to generate Figure 4.

## APPENDIX 1

For an electrophoretic system without a pressurized flow chamber, the analyte travels through the column at a velocity proportional to the potential gradient (2)

$$v = [\mu_{\text{electroosmosis}} + \mu_{\text{electrophoresis}}] \frac{V}{L} \quad (19)$$

The pressurized flow chamber of the detector will generate a component of flow that opposes the electroosmotic and electrophoretic flow; that is, at zero applied potential, the analyte will travel from the detector to the injection end of the capillary. In our sheath flow cuvette, solvent is introduced into the flow chamber at some volumetric flow rate. For incompressible fluids, the pressure-induced flow velocity will be linearly related to the sheath volumetric flow rate

$$v_{\text{pressure}} = \alpha Q_{\text{sheath}} \quad (20)$$

The overall linear velocity of analyte in the cuvette is then given by the sum of the electroosmotic, electrophoretic, and pressure-induced flow velocity

$$v = [\mu_{\text{electroosmosis}} + \mu_{\text{electrophoresis}}] \frac{V}{L} + \alpha Q_{\text{sheath}} \quad (21)$$

The observed analyte velocity is expected to increase linearly with the electric field strength and to decrease linearly with the sheath volumetric flow rate. The time for separation will increase as the sheath flow rate increases

$$r = \frac{L}{v_{\text{total}}} = \frac{L}{[\mu_{\text{electroosmosis}} + \mu_{\text{electrophoresis}}] \frac{V}{L} + v_{\text{pressure}}} \quad (22)$$

Electroosmotic flow in capillaries produces a flow velocity profile that is uniform across the tube diameter. Under conditions of pluglike flow, longitudinal diffusion is the major contribution to dispersion of a peak. The peak variance due to electroosmosis is simply

$$\sigma_{\text{diffusion}}^2 = 2Dt \quad (23)$$

where  $D$  is the diffusion coefficient and  $t$  is the time for separation.

In the absence of any other effect, the increased time required for analysis using a pressurized detector chamber will result in an increase in peak variance. The pressure-driven flow component induces an additional source of band broadening. Because this flow component is driven by a pressure difference and not by electroosmosis, the flow component due to the pressure difference between the injector and detector is expected to have the classic parabolic shape. Note that the expected flow profile in capillary zone electrophoresis with a pressurized detector is the difference of the flow profile produced by electroosmosis and pressure-driven flow: the flow profile is predicted to be faster near the walls of the capillary and slowest near the center. The parabolic flow profile due to the pressurized sheath flow cuvette produces a contribution to the peak variance given by (41)

$$\sigma_{\text{pressure}}^2 = 2 \frac{r^2 v_{\text{pressure}}^2}{48D} t \quad (24)$$

where  $r$  is the radius of the capillary.

The overall variance is given by the sum of the variance due to diffusion and sheath flow

$$\sigma^2 = \sigma_{\text{diffusion}}^2 + \sigma_{\text{pressure}}^2 = 2 \left[ D + \frac{r^2 v_{\text{pressure}}^2}{48D} \right] t \quad (25)$$

The overall variance due to both diffusion and a parabolic flow profile is given by substituting eq 21 into eq 24

$$\sigma^2 = 2 \left[ D + \frac{r^2 v_{\text{pressure}}^2}{48D} \right] \times \frac{L}{[\mu_{\text{electroosmosis}} + \mu_{\text{electrophoresis}}] \frac{V}{L} + v_{\text{pressure}}} \quad (26)$$

Finally, the number of theoretical plates expected for capillary zone electrophoresis with a sheath flow detector, neglecting contributions due to extracolumn band broadening, is given by

$$N = \frac{L^2}{\sigma^2} = \frac{L \left\{ [\mu_{\text{electroosmosis}} + \mu_{\text{electrophoresis}}] \frac{V}{L} + v_{\text{pressure}} \right\}}{2 \left[ D + \frac{r^2 v_{\text{pressure}}^2}{48D} \right]} \quad (27)$$

The number of theoretical plates will increase linearly with the applied potential; however, the plate count will not extrapolate to zero at zero potential. Also, the number of theoretical plates will decrease with an increase in the flow component associated with the sheath flow cuvette. It is interesting to note that the plate count would increase if the flow component induced by the sheath flow cuvette were in the same direction as the flow induced by electroosmosis.

The resolution of two peaks that elute close together is given by (2)

$$R_s = \frac{N^{1/2}}{4} \frac{\mu_1 - \mu_2}{\bar{\mu} + \mu_{\text{electroosmosis}} + v_{\text{pressure}} \frac{L}{V}} \quad (28)$$

Substituting eq 26 into eq 27 yields

$$R_s = 0.177(\mu_1 - \mu_2) \times \left( \frac{V}{\left[ D + \frac{r^2 v_{\text{sheath}}^2}{48D} \right] \left[ \bar{\mu} + \mu_{\text{electroosmosis}} + v_{\text{pressure}} \frac{L}{V} \right]} \right)^{1/2} \quad (29)$$

To improve the resolution of a separation, the applied potential should be increased, the capillary diameter decreased, or the sheath volumetric flow rate should balance the flow velocity associated with electrophoresis and electroosmosis. In the latter case, the first peak would elute after a very long time and the second peak would be driven to the injector.

## APPENDIX 2

For very low concentration samples, the fluorescence power is proportional to laser power, path length, analyte molar absorptivity, and analyte concentration

$$P_{\text{fluorescence}} \propto P_{\text{laser}} b \epsilon C \quad (30)$$

The path length of the measurement is equal to the diameter of the sample stream in the sheath flow cuvette. The sample stream diameter may be adjusted over a wide range by varying the sample and sheath stream volumetric flow rates. Neglecting diffusion for the moment, the radius of the sample stream predicted by a hydrodynamic theory is given by (38)

$$r_{\text{hydrodynamic}} = \left( \frac{X}{\pi} \right)^{1/2} \left( 1 - \frac{1}{\left( \frac{Q_{\text{sample}}}{Q_{\text{sheath}}} + 1 \right)^{1/2}} \right)^{1/2} \quad (31)$$

This model has been verified for a sample of micrometer diameter particles that would not suffer appreciable diffusion in the cuvette. For a small sheath volumetric flow rate, the binomial expansion may be used to approximate the hydrodynamic radius as

$$r_{\text{hydrodynamic}} = \left(\frac{\chi}{\pi}\right)^{1/2} \left(\frac{Q_{\text{sample}}}{2Q_{\text{sheath}}}\right)^{1/2} \quad (32)$$

The volumetric flow rate of the sample stream is given by the product of the average linear velocity of the sample times the area of the capillary

$$Q_{\text{sample}} = \pi r^2 \left\{ [\mu_{\text{electroosmosis}} + \mu_{\text{electrophoresis}}] \frac{V}{L} - v_{\text{pressure}} \right\} \quad (33)$$

The radius of the sample stream is then related to the electrical field strength, the electrophoretic and electroosmotic mobilities, and the sheath volumetric flow rate

$$r_{\text{hydrodynamic}} \approx \left( \frac{\chi r^2 \left\{ [\mu_{\text{electroosmosis}} + \mu_{\text{electrophoresis}}] \frac{V}{L} + v_{\text{pressure}} \right\}}{2Q_{\text{sheath}}} \right)^{1/2} \quad (34)$$

Under conditions where the pressure-induced component of flow is small compared to the electroosmotic flow, the sample stream radius, and hence fluorescence intensity for neat solution, is expected to increase with the square root of applied potential.

The sheath volumetric flow rate and the applied potential will influence the sample stream radius and the fluorescence intensity. These parameters also influence the fluorescence intensity through a second parameter, the analyte concentration at the peak maximum. Assuming a Gaussian peak shape, the concentration distribution eluting from the capillary is given by

$$C(t) = \text{moles injected} \times \frac{1}{\pi r^2 \sigma (2\pi)^{1/2}} \exp \left[ -\frac{1}{2} \left( \frac{t - t_0}{\sigma} \right)^2 \right] \quad (35)$$

The concentration at the peak maximum is given by

$$C_{\text{max}} = \frac{\text{moles injected}}{\pi r^2 \sigma (2\pi)^{1/2}} \quad (36)$$

Substituting eq 25, the peak variance, into eq 36 yields

$$C_{\text{max}} = \frac{\text{moles injected}}{2\pi r^2} \times \left( \frac{[\mu_{\text{electroosmosis}} + \mu_{\text{electrophoresis}}] \frac{V}{L} + \alpha Q_{\text{sheath}}}{\pi \left[ D + \frac{r^2 v_{\text{sheath}}^2}{48D} \right] L} \right)^{1/2} \quad (37)$$

The maximum fluorescence signal should be proportional to the voltage gradient, laser power, and molar absorptivity; should be inversely proportional to the radius of the capillary; and should have a complicated dependence upon the sheath volumetric flow rate

$$P_{\text{fluorescence}} = P_{\text{laser}} \epsilon \frac{\text{moles injected}}{2\pi r} \times \left\{ [\mu_{\text{electroosmosis}} + \mu_{\text{electrophoresis}}] \frac{V}{L} + \alpha Q_{\text{sheath}} \right\} \times \left( \frac{\chi}{2\pi Q_{\text{sheath}} \left[ D + \frac{r^2 v_{\text{pressure}}^2}{48D} \right] L} \right)^{1/2} \quad (38)$$

Under conditions where the pressure-induced flow velocity is negligible, the fluorescence signal is given by

$$P_{\text{fluorescence}} = P_{\text{laser}} \epsilon \frac{\text{moles injected}}{2\pi r} \left\{ [\mu_{\text{electroosmosis}} + \mu_{\text{electrophoresis}}] \frac{V}{L} \right\} \left( \frac{\chi}{2\pi Q_{\text{sheath}} DL} \right)^{1/2} \quad (39)$$

The signal is proportional to the potential gradient and inversely proportional to the square root of the sheath flow volumetric flow rate.

## LITERATURE CITED

- (1) Mikkers, F. E. P.; Everaerts, F. M.; Verheggen, T. P. E. M. *J. Chromatogr.* **1979**, *169*, 11–20.
- (2) Jorgenson, J. W.; Lukacs, K. D. *Anal. Chem.* **1981**, *53*, 1298–1302.
- (3) Jorgenson, J. W.; Lukacs, K. D. *Science* **1983**, *222*, 266–272.
- (4) Gordon, M. J.; Huang, X.; Pentoney, S. L.; Zare, R. N. *Science* **1988**, *242*, 224–228.
- (5) Ewing, A. G.; Wallinford, R. A.; Olefirowicz, T. M. *Anal. Chem.* **1989**, *61*, 292A–303A.
- (6) Grossman, P. D.; Colburn, J. C.; Nielson, R. G.; Riggan, R. M.; Sittampalam, G. S.; Rickard, E. C. *Anal. Chem.* **1989**, *61*, 1186–1194.
- (7) Gassmann, G.; Huo, J. E.; Zare, R. N. *Science* **1985**, *230*, 813–814.
- (8) Gozel, P.; Gassmann, E.; Michelsen, H.; Zare, R. N. *Anal. Chem.* **1987**, *59*, 44–49.
- (9) Kuhr, W. G.; Yeung, E. S. *Anal. Chem.* **1988**, *60*, 1832–1834.
- (10) Kuhr, W. G.; Yeung, E. S. *Anal. Chem.* **1988**, *60*, 2642–2646.
- (11) Hershberger, L. W.; Callis, J. B.; Christian, G. D. *Anal. Chem.* **1979**, *51*, 1444–1446.
- (12) Kelly, T. A.; Christian, G. D. *Anal. Chem.* **1981**, *53*, 2110–2114.
- (13) Dovichi, N. J.; Martin, J. C.; Jett, J. H.; Keller, R. A. *Science* **1983**, *219*, 845–847.
- (14) Dovichi, N. J.; Martin, J. C.; Jett, J. H.; Trkula, M.; Keller, R. A. *Anal. Chem.* **1984**, *56*, 348–354.
- (15) Nguyen, D. C.; Keller, R. A.; Jett, J. H.; Martin, J. C. *Anal. Chem.* **1987**, *59*, 2158–2160.
- (16) Cheng, Y. F.; Dovichi, N. J. *Science* **1988**, *242*, 562–564.
- (17) Wu, S.; Dovichi, N. J. *J. Chromatogr.* **1989**, *480*, 141–155.
- (18) Pintel, D. *Anal. Chem.* **1982**, *54*, 503A–508A.
- (19) Cheng, Y. F.; Dovichi, N. J. *Mikrochim. Acta* **1986**, *III*, 351–357.
- (20) Cheng, Y. F.; Dovichi, N. J. *Can. J. Spectrosc.* **1989**, *34*, 90–93.
- (21) Pawliszyn, J. *Liquid Chromatogr.* **1987**, *10*, 3377–3392.
- (22) Cheng, Y. F.; Dovichi, N. J. *Can. J. Spectrosc.* **1989**, *34*, 70–75.
- (23) Rose, D. J.; Jorgenson, J. W. *J. Chromatogr.* **1988**, *447*, 117–131.
- (24) Tsuda, T.; Kobayashi, Y.; Hori, A.; Matsumoto, T.; Suzuki, O. *J. Chromatogr.* **1988**, *456*, 375–381.
- (25) Pentoney, S. L.; Huang, X.; Burgi, D. S.; Zare, R. N. *Anal. Chem.* **1988**, *60*, 2625–2629.
- (26) Wallinford, R. A.; Ewing, A. G. *Anal. Chem.* **1987**, *59*, 1762–1766.
- (27) Huang, X.; Gordon, M. J.; Zare, R. N. *Anal. Chem.* **1988**, *60*, 375–377.
- (28) Huang, X.; Gordon, M. J.; Zare, R. N. *Anal. Chem.* **1988**, *60*, 1837–1838.
- (29) Reijenga, J. C.; Aben, G. V. A.; Verheggen, Th. P. E. M.; Everaerts, F. M. *J. Chromatogr.* **1983**, *260*, 241–254.
- (30) Moore, W. A. *Physical Chemistry*, 4th ed.; Prentice Hall: New York, 1972; p 516.
- (31) Mosher, R. A.; Dewey, D.; Thormann, W.; Saville, D. A.; Bier, M. *Anal. Chem.* **1989**, *61*, 362–366.
- (32) Edwards, J. T. *Adv. Chromatogr.* **1966**, *2*, 63–98.
- (33) Henry, D. C. *Proc. R. Soc. London, A* **1931**, *133*, 106–129.
- (34) Diehl, H.; Markuszewski, R. *Talanta* **1987**, *34*, 739–741.
- (35) Zare, R. N. Paper presented at the First International Symposium on High Performance Capillary Electrophoresis, Boston, April 1989.
- (36) Grushika, E.; McCormick, R. M. *J. Chromatogr.* **1989**, *471*, 421–428.
- (37) Lucas, J. N.; Pintel, D. *Cytometry* **1986**, *7*, 575–581.
- (38) Zarrin, F.; Dovichi, N. J. *Anal. Chem.* **1985**, *57*, 2690–2692.
- (39) Bird, R. B.; Steward, W. E.; Lightfoot, E. N.; Chapman, T. W. *Lectures in Transport Phenomena*; American Institute of Chemical Engineers: New York, 1969.
- (40) Pawliszyn, J. *Anal. Chem.* **1988**, *60*, 2796–2801.
- (41) Sternberg, J. C. *Adv. Chromatogr.* **1966**, *2*, 205–270.

RECEIVED for review August 11, 1989. Accepted November 29, 1989. This work was funded by the Natural Sciences and Engineering Research Council of Canada through both the operating and equipment grant programs.

# Coprecipitation of Trace Metals by DNA and RNA Molecules

Kitao Fujiwara,\* Ri-e Kojoyo, and Kazuma Okada

Faculty of Integrated Arts and Sciences, Hiroshima University, 1-1-89 Higashisenda-machi, Hiroshima 730, Japan

Yukio Kodama

Ocean Research Institute, The University of Tokyo, 1-15-1 Minamidai, Nakano-ku, Tokyo 164, Japan

**Coprecipitation of trace metal ions in the aqueous sample was investigated by using several nucleic acids (DNA and RNA) as the carrier. After the pH of the solution containing metal ion was adjusted, DNA or RNA dissolved in NaOH solution was added. Precipitation of DNA (or RNA) was done by the salting-out method, adding sodium chloride and acetone to the DNA-metal solution. Coprecipitation efficiencies for most positive metal ions were found to be maximum at pH 2-3 when sodium hydroxide-acetate buffer was used. Negative ions such as  $\text{Cr}_2\text{O}_7^{2-}$ ,  $\text{Mo}_7\text{O}_{24}^{6-}$ , and  $\text{PtCl}_6^{2-}$  were not precipitated with DNA in the pH range from 1 to 12. It is also found that coprecipitations of cobalt(III) complexes were dominated by their charge, i.e., the complexes having plus three charge are coprecipitated with DNA at the high rate but the complexes of zero or minus charge are not. The anticancer drug *cis*-platin is negligibly coprecipitated with DNA. The present coprecipitation method also allows the preconcentration of trace metal ions except iron, calcium, and magnesium, which were intrinsically contained in DNA and RNA at the appreciable concentration.**

When trace metal distribution was measured in natural waters, preconcentration and isolation of analyte from the sample matrices are required; their concentration is lower than the detection limit and appreciable interferences of coexistent species sometimes appear in the measurement methods. Solvent extraction and coprecipitation methods were, therefore, reported as the sample pretreatment for analyzing the trace metals in natural waters. Hydroxides of metal ions such as  $\text{Al}(\text{OH})_3$  and  $\text{Fe}(\text{OH})_3$  are the common coprecipitator (1-3). Also, gallium (4), indium (5, 6), magnesium (7), hafnium (8), and zirconium (9) hydroxides are utilized as the coprecipitator for multielements detection in aqueous samples by inductively coupled plasma (ICP) atomic emission spectrometry. Other than the hydroxide formation of metal ions, neodymium fluoride (10) was used for collection of actinide ions. Also, the complex formation between cobalt and 1-pyrrolidine-carbodiimide (Co-APDC) is investigated as coprecipitation techniques for seawater analysis for Ni, Cu, Cd (11), Cr (12), V, and Mo (13, 14).

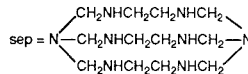
In the present paper, a new coprecipitation method using biological materials such as nucleic acids is investigated for collection of trace metal ions in the aqueous samples. It is known that several transition metals combine with DNA and RNA and increase their stabilities. Also, zinc and magnesium participate with the transformation of nucleic acids (15, 16). Recently, some DNA and RNA molecules are commercially available at a rather inexpensive price, and here, we would like to evaluate these species as coprecipitating agents for trace metal ions in aqueous samples in terms of elucidation of interaction between trace metal ions and nucleic acids in natural waters.

## EXPERIMENTAL SECTION

**Reagents.** Deoxyribonucleic acids extracted from salmon sperm purchased from Wako Pure Chem. Ind., Ltd. (047-17322), herring sperm purchased from Sigma Chemical Co. (D-3159), and deoxyribonucleic acid sodium salt from salmon testes (Type III)

purchased from Sigma (D-1626) were used as the coprecipitation agents of DNA. ribonucleic acid from Tolula yeast purchased from Sigma (R-6625) and ribonucleic acid sodium salt from yeast purchased from Kojin Co., Ltd. (1600), were used as RNA.

The standard solutions of metal ions measured were as follows: (Co)  $\text{CoCl}_2$  (1000  $\mu\text{g}$  of Co/mL) in 1 mol/L HCl; (Cu)  $\text{CuCl}_2$  (1000  $\mu\text{g}$  of Cu/mL) in 0.1 mol/L HCl; (Cd)  $\text{CdCl}_2$  (100  $\mu\text{g}$  of Cd/mL) in 1 mol/L HCl; (Mn)  $\text{MnCl}_2$  (1000  $\mu\text{g}$  of Mn/mL) in 0.02 N HCl; (Ni)  $\text{NiCl}_2$  (1000  $\mu\text{g}$  of Ni/mL) in 0.1 N HCl; (Pt)  $\text{H}_2\text{PtCl}_6$  (1000  $\mu\text{g}$  of Pt/mL) in 1 mol/L HCl, which were purchased from Wako. Chromium(III) nitrate ( $\text{Cr}(\text{NO}_3)_3 \cdot 6\text{H}_2\text{O}$ ) at analytical grade purchased from Kanto Chemical Co. and spectroscopy grade potassium dichromate purchased from Katayama Chemical Co. were dissolved in the aqueous solution and used as the chromium standard solution. Ammonium molybdate ( $(\text{NH}_4)_6\text{Mo}_7\text{O}_{24} \cdot 4\text{H}_2\text{O}$ ) purchased from Katayama was dissolved in aqueous solution and was used as the molybdenum standard. The following cobalt(III) complexes synthesized by Dr. Katsuhiko Miyoshi, Hiroshima University, were also investigated in their ability to absorb to nucleic acids:  $[\text{Co}(\text{NH}_3)_6]\text{Cl}_3$ ,  $[\text{Co}(\text{NH}_3)_5\text{Cl}]\text{Cl}_2$ ,  $[\text{Co}(\text{sep})]\text{Cl}_3$ ,  $[\text{Co}(\text{dien})\text{Cl}_2]\text{ClO}_4$ ,  $[\text{Co}(\text{en})_3]\text{Cl}_3$ ,  $\text{K}[\text{Co}(\text{C}_2\text{O}_4)_2(\text{gly})_2]$ ,  $\text{Na}[\text{Co}(\text{edta})]$ , *cis*-Platin [*cis*- $[\text{Pt}(\text{NH}_3)_2\text{Cl}_2]$ ], anticancer drug, was a gift from Nippon Keyaku Co. Ltd. Abbreviations of ligands are as follows: en = ethylenediamine, dien = diethylenetriamine, and



**Apparatus.** Atomic absorption spectrometry was done with a Perkin-Elmer Model 603 atomic absorption spectrophotometer for flame atomic absorption spectroscopy (AAS) and a Shimadzu Model AA 640-13 atomic absorption spectrophotometer with a graphite furnace controller, Model GF-A-4, and an autosample injector, Models ASG-1 and AU-1, for graphite furnace AAS. pH dependence of coprecipitation efficiencies of the metal ions was determined by the air-acetylene flame AAS. Metal amounts (28 elements) intrinsically contained in DNA and RNA used in the present study were surveyed by a Seiko Model JY-48 ICP atomic emission spectrometer. A centrifuge made by Kubota, Model KN-70, was used in the separation of precipitates.

**Procedure.** To calculate the collection efficiency of metal ions in the coprecipitation with DNA and RNA, the following procedure was performed: Metal ions were diluted into a buffer solution of 1 mol/L sodium acetate and 1 mol/L acetic acid. After the pH was adjusted, volume of solution was made to 3 mL. A 0.5-mL portion of DNA or RNA solution (2% (w/v)) was then added, where DNA or RNA was made by dissolving them into 10 mmol/L NaOH solution. The mixed solution was left for at least 30 min at 1-5 °C, and 0.5 mL of 2 mol/L NaCl and 6 mL of acetone were added to the solution in this order. The white precipitate appears when acetone is added. After this solution was allowed to stand for 30 min, the precipitate was collected by centrifugation (2000 rpm, 15 min). The centrifugal rotor was a swing type and tubes made of glass were used for this centrifugation. After the supernatant was discarded, the centrifugal tube with the precipitate was rinsed with ethanol once. The precipitate was dissolved into a mixture of 0.5 mol/L ammonia water and 0.2 mol/L ethylenediaminetetraacetic acid diammonium salt ( $(\text{NH}_4)_2\text{-EDTA}$ ).

## RESULTS AND DISCUSSION

**Optimization of Coprecipitation Procedure.** Several ways are known for the precipitation of DNA or RNA from their solutions. Denaturation by the strong acids such as

Table I. Contents of Metals in Nucleic Acids Used in this Study,  $\mu\text{g/g}^a$ 

	AHW(1)	AHW(2)	AHW(3)	AHW(4)	AHW(5)	D-3159	D-1625	R-6625	K-1600
As	11	13	12	14	12	<5*	22	<5*	<5
Ag	<0.7*	<0.7*	<0.7*	<0.7*	<0.7*	<0.7*	<0.7*	<0.7*	<0.7*
Al	<3*	<3*	<3*	<3*	<3*	<3*	72	<3*	<3*
Au	0.6	1.0	0.8	0.8	1.3	<0.2*	13	<0.2*	<0.2*
B	<5*	-5	<5*	<5*	<5*	<5*	<5*	<5*	<5*
Ba	<0.4*	1.2	0.5	0.5	0.6	<0.4*	2.9	<0.4*	<0.4*
Ca	101	139	136	130	121	748	45	1420	22800
Cd	<0.3*	<0.3*	<0.3*	<0.3*	<0.3*	<0.3*	3	<0.3*	<0.3*
Cr	5.1	5.2	5.2	5.2	5.4	<0.7*	6.8	2	<0.7*
Cu	8.0	9.6	8.4	11	9.3	<0.5*	8.8	<0.5*	<0.5*
Fe	23.0	22.7	23.4	20.0	23.1	7.8	6.7	31.3	18.1
Ga	<8*	<8*	<8*	<8*	<8*	<8*	85	<8*	<8*
Ge	5	7	6	7	7	44*	36	<4*	<4*
Mg	70	77	79	79	73	190	19	7430	112
Mn	0.3	0.3	0.3	0.3	0.3	<0.1*	1	80	0.4
Mo	3.2	3.4	3.4	3.4	3.5	<0.8*	4.1	<0.8*	<0.8*
Ni	<2*	<2*	<2*	<2*	<2*	<2*	9.5	<2*	<2*
Pb	<4*	<4*	<4*	<4*	<4*	<4*	32	<4*	<4*
Sb	<5*	<5*	<5*	<5*	<5*	<5*	39	<5*	<5*
Si	<1*	<1*	<1*	<1*	<1*	<1*	3	<1*	200
Sn	2	2	2	2	2	<2*	7	<2	<2
Sr	<0.4*	<0.4*	<0.4*	<0.4*	<0.4*	15	2	15	7
Ti	<4*	<4*	<4*	<4*	<4*	4*	4	<4*	<4*
V	35	35	35	35	36	13	8	<0.8*	<0.8*
Y	<0.4*	<0.4*	<0.4*	<0.4*	<0.4*	<0.4*	-	<0.4*	<0.4*
Zr	<0.7*	<0.7*	<0.7*	<0.7*	<0.7*	<0.7*	-	<0.7*	<0.7*
Zn	4.0	4.3	4.1	4.2	4.2	2.0	2.9	1.7	38

<sup>a</sup> Nucleic acids (sample) of the various commercial DNA and RNA were dissolved into 8% ammonium water at 1% concentration, and the elements listed in the table were simultaneously measured by the ICP atomic emission spectrometry by directly nebulizing the above solutions. AHW(1-5) show the different bottles of the same reagent number (DNA, Wako, 047-17322). D-3159, DNA (Sigma); D-1625, DNA sodium salt (Sigma); R-6625, RNA (Sigma); K-1600, RNA sodium salt (Kohjin). Asterisk indicates an amount less than the detection limit.

trichloroacetic acid (TCA) or perchloric acid with decreasing pH causes precipitation of DNA and RNA. However, the precipitate made by this method can not adsorb metal ion; i.e., DNA was added to the solution including cobalt(II) ion at a few micrograms per milliliter, and TCA or perchloric acid was added at the concentration of 1% for making the precipitate. However, this precipitate included cobalt less than 5% in collection recovery. Salting-out by adding an organic solvent is better than denaturation by acid for precipitation of DNA or RNA. The collection efficiencies of cobalt(II) ion at pH 4 after addition of NaCl and 1% DNA (Wako, 047-17322) were 65 + 5%, 43 + 8%, and <3% for using acetone, ethanol, and perchloric acid, respectively.

When the filtration was adopted instead of the centrifuge for collecting DNA precipitate, some portion of precipitate was passed through the filter even using a membrane filter with a pore size of 0.2  $\mu\text{m}$ . It is also confirmed that the coprecipitation rate is almost constant against the time for producing the precipitate after adding DNA solution from 2 to 40 min. The solution temperature during the formation of the precipitate did not affect the metal collection in the range from 5 to 25  $^{\circ}\text{C}$ .

#### Metal Contents Intrinsicly Found in DNA and RNA.

For the purpose of using DNA and RNA molecules for collecting the trace metals in the aquatic samples, the original metal contents of these species must be measured. Table I shows the metal concentrations in the nucleic acids used in the present study. These values are calculated based on the analytical results obtained by nebulizing the solutions of DNA and RNA without digestion or pretreatment. Since the solubilities of these nucleic acids are rather low, 1% solutions were analyzed. Contents of Ca, Mg, and Fe are high, and appreciable amounts of Cu, Cr, Mo, V, and Zn can be found in some DNAs and RNAs used in the present experiment according to Table I. When these DNA and RNA molecules are used as the coprecipitation carrier for the trace metal analysis, it is probable that the large interference of Ca and

Mg might occur in the case of ICP atomic emission analysis.

**Dependence of Coprecipitation Efficiency on pH of Solution.** Figure 1 shows the coprecipitation rates of various metal ions where sodium acetate-acetic acid buffer (3 mL) is used and 1% DNA (Wako, 047-17332) solution (0.5 mL) was added as the coprecipitation carrier. It can be seen that maximum efficiency of coprecipitation is found in the range of pH 2-3 for most metal ions which have a positive charge.  $\text{Cd}^{2+}$  is the exception and a few percent is collected with the DNA molecule. It is confirmed that the collection recovery of  $\text{Cd}^{2+}$  is also very low up to pH 6 where potassium phosphate-sodium borate buffer is used.  $\text{Cr}^{3+}$  shows the optimum pH of coprecipitation below pH = 2, reaching almost 100% recovery.  $\text{Ni}^{2+}$  possesses the widest optimal pH range extending up to pH 3.5. Most of positive metal ions show recovery rates (coprecipitation rate) greater than 80% for DNA at a DNA concentration of 0.14% in the final solution.

Metal ions in negative species such as  $\text{Cr}_2\text{O}_7^{2-}$  and  $\text{PtCl}_6^{2-}$  show extremely low coprecipitation efficiencies in most pH ranges from 1 to 13.5, where the pH was adjusted by 0.1 mol/L phosphate + 0.05 mol/L borate buffer and a concentration of 20  $\mu\text{g}$  of Cr or Pt/mL solution was inspected. An exception was a slight increase (about 25%) in the recovery found in the case of molybdate ( $\text{Mo}_7\text{O}_{24}^{6-}$ ) at very low pH (Figure 2). It is evident that DNA molecules do not adsorb metal-containing species of negative charge.

Figure 3 shows the pH dependence of coprecipitation efficiency of  $\text{Co}^{2+}$  using different DNA and RNA molecules other than the previous DNA (Wako, 047-17322). Significant differences among the use of different coprecipitation carriers could not be found in these figures. RNA has a single strand structure and DNA takes a double strand. Therefore, in DNA, bases such as adenine, guanine, cytosine, and thymine (or uracyl), which show the potential to coordinate to metal ions, pair with each other. Therefore, it can be assumed that phosphates oriented outside the DNA attract metal ions. In contrast, RNA can contact metal ions with both bases and

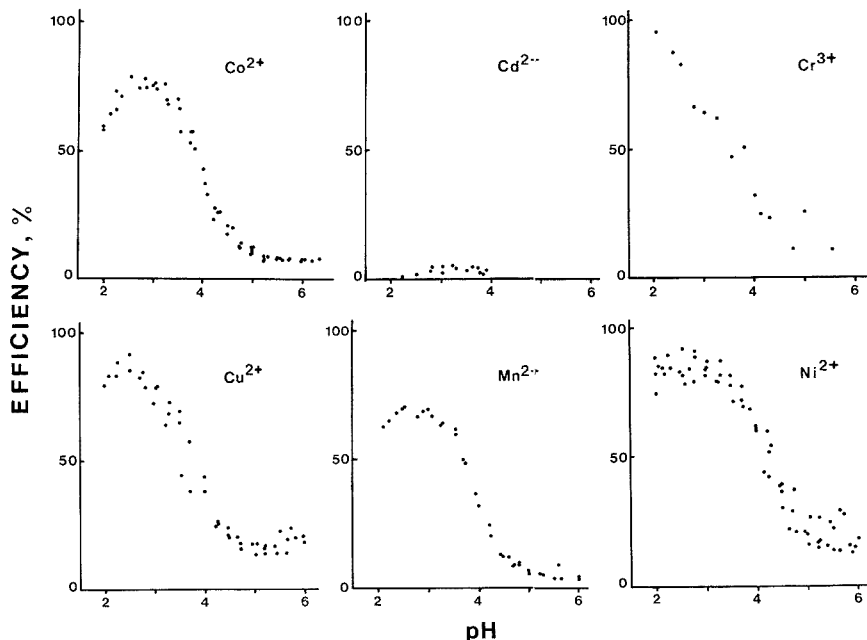


**Figure 1.** pH dependences of coprecipitation efficiencies of metal ions having positive charge. The concentrations of metal ions were as follows:  $\text{Co}^{2+}$ , 10  $\mu\text{g/mL}$ ;  $\text{Cu}^{2+}$ , 3  $\mu\text{g/mL}$ ;  $\text{Ni}^{2+}$ , 5  $\mu\text{g/mL}$ ;  $\text{Cd}^{2+}$ , 3  $\mu\text{g/mL}$ ;  $\text{Mn}^{2+}$ , 10  $\mu\text{g/mL}$ ; and  $\text{Cr}^{3+}$ , 20  $\mu\text{g/mL}$ . A 0.5-mL portion of DNA solution at 1% concentration was added to 3 mL of metal solution.

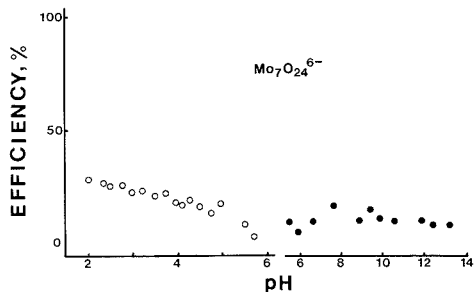


**Figure 2.** pH dependence of coprecipitation efficiencies of molybdate ion. The concentration of solution is 20  $\mu\text{g}$  of  $\text{Mo}$ /mL. The volumes of the solutions added were the same as those given Figure 1. The values shown by the solid circle were obtained with 0.1 mol/L phosphate + 0.05 mol/L borate buffer. The values shown by the open circle were obtained with 1 mol/L sodium acetate buffer.

phosphate groups. However, this structural difference between DNA and RNA was not revealed in this coprecipitation study. It is probable that RNA molecules wind and their bases do not interact with metal ions.

Apart from the above discussion, metal species possessing a negative charge did not coprecipitate with DNA. This suggests that the adsorption site of DNA is phosphate and electrical repulsion affects binding of negative metal species.

**Dependence of Coprecipitation Efficiency on the Amount of Carriers.** Figure 4 shows the dependence of coprecipitation efficiency on the amount of carrier added. A decrease in the amount of nucleic acid below 10 mg/mL (1%) causes a linear decrease in coprecipitation efficiency of  $\text{Co}^{2+}$ . In this figure, a large difference could not be found in the different coprecipitation carriers. Addition of nucleic acids

**Table II.** Coprecipitation Efficiencies of Metal Complexes with Adding 0.15% DNA (Wako, 047-17332) Solution<sup>a</sup>

complex	pH <sup>b</sup>	% efficiency
$[\text{Co}(\text{NH}_3)_6]^{3+}$	11.8	89.1
$[\text{Co}(\text{en})_3]^{3+}$	11.8	72.5
$[\text{Co}(\text{dien})_2]^{3+}$	11.8	70.9
$[\text{Co}(\text{sep})]^{3+}$	11.8	67.4
$[\text{Co}(\text{NH}_3)_5\text{Cl}]^{2+}$	11.9	33.3
$[\text{Co}(\text{C}_2\text{O}_4)(\text{gly})_2]^-$	12.1	12.1
$[\text{Co}(\text{edta})]^-$	12.0	2.4
<i>cis</i> -platin ( $\text{Pt}(\text{NH}_3)_2\text{Cl}_2$ )	11.5	<d.l. <sup>c</sup>

<sup>a</sup> Aqueous solutions containing 10–20  $\mu\text{g}$  of metal were measured. <sup>b</sup> pH measured after dissolving the complex. <sup>c</sup> <d.l., less than the detection limit.

at >20  $\mu\text{g/mL}$  (2%) provides recovery close to 100%, except RNA-sodium salt, which shows rather low coprecipitation efficiency compared to other nucleic acids.

It is confirmed that the coprecipitation efficiency is constant from 10 ng to 10  $\mu\text{g}$  of  $\text{Co}$ /mL within the precision of measurement. Therefore, the present method can be used for preconcentration of trace metal ions in the aqueous samples. In the case where centrifugation is employed as the collecting method of precipitates, the maximum concentrating rate is ~100 times, which means a few tens parts per thousand is the detection limit of cadmium, cobalt, nickel, and so on which possess the detection limit of a few parts per billion in carbon furnace atomic absorption spectrometry and of which intrinsic contents in the DNA and RNA used are negligible.

**Coprecipitation of Complexes.** The present method was also applied to the coprecipitations of cobalt(III) complexes and *cis*-platin. The complexes were dissolved in distilled water (no pH adjustment), and then coprecipitation using 1% DNA (Wako, 047-17332) solution was performed. The results are

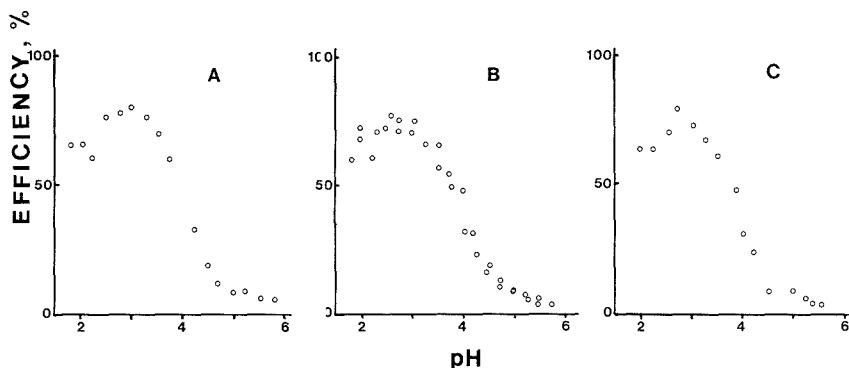


**Figure 3.** Coprecipitation of cobalt(II) ion against various nucleic acids. 0.5 mL of nucleic acid at 1% concentration was added to 3 mL of cobalt(II) solution of 10  $\mu\text{g}$  of Co/mL. Key: (A) DNA from herring sperm (Sigma, D-3159); (B) RNA from Tolula yeast (Sigma, R-6625); (C) RNA sodium salt from yeast (Kohjin, R-1600).

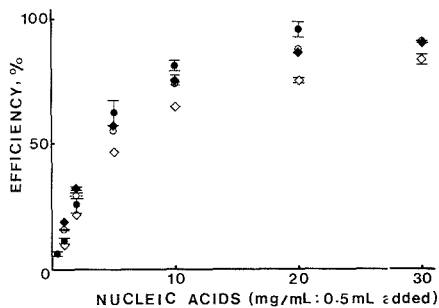


**Figure 4.** Dependence of coprecipitation amount on the amount of nucleic acids: (●) DNA from salmon sperm (Wako, 047-17322); (○) DNA from herring sperm (Sigma, D-3159); (◆) RNA from Tolula yeast (Sigma, R-6625); (◇) RNA sodium salt from yeast (Kohjin, R-1600).

shown in Table II. It is evident that the coprecipitation of complexes with DNA is dominated by the charge of complexes: The complexes having charge of +3 coprecipitate at about 70% efficiency, and 0 or minus charges do not. Among the complexes of +3 charge, hexaamminecobalt shows an exceptionally high coprecipitation rate. A high affinity of hexaamminecobalt complex was also found in the case of cobalt uptake into *E. coli* cells (17, 18).

It is found that when tris(hydroxymethyl)aminomethane (Tris) was used as the buffer instead of acetate, cobalt(II) ion coprecipitates at a high rate with DNA at high pH value (pH > 8) (see Figure 5). This result might be interpreted according to the complex formation between cobalt(II) ion and Tris, which can be easily adsorbed to DNA.

In conclusion, DNA or RNA molecules may be used as the collector (carrier) of trace metal ions. The amount of carrier to be added is similar to other coprecipitation methods. Essential differences were not observed in the DNA and RNA from the different source in terms of pH response and amount of addition. Compared with other coprecipitation techniques, such as cobalt-APDC complex formation or hydroxide formation of aluminum and iron, the present method does not use toxic heavy metal ions as the carrier. This is one advantage of the present method for eliminating or collecting trace metal ions in aqueous samples. Furthermore, when trace elements are measured in natural water, it has been pointed out that coprecipitation by inorganic substances such as metal hydroxide cannot capture some ions in the dissolved forms as organic complexes (19, 20). The present method has a possibility of collecting these species. Also, when the total dis-

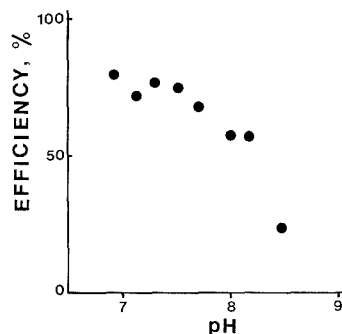


**Figure 5.** Coprecipitation efficiency of cobalt(II) ion in Tris buffer. The experimental conditions are the same as those given in Figure 1 except that 0.1 mol/L Tris was used as the buffer instead of acetate-sodium acetate.

solved metals have to be measured, some digestion procedures of sample are recommended prior to the measurement.

In natural waters such as river water and seawater, the distributions of trace metals are mainly dominated by the biological activities, in which adsorption and desorption of trace metals through the ecological systems are essential: ingestion, excretion, and decomposition of organic habitant determine the trace metal distributions (21-23). According to the present results, nucleic acids themselves are not strong adsorbers in the pH region found in natural waters. However, when some ligands such as amines exist and when complex formation of metal ions occur, these nucleic acids can become good metal adsorbers. In the open ocean, molybdenum (molybdate) is classified as a conservative element that homogeneously distributes in seawater, where the eliminating mechanisms by marine organisms do not work. In contrast, the distributions of metal ions having positive charge such as  $\text{Co}^{2+}$ ,  $\text{Cu}^{2+}$ , and  $\text{Ni}^{2+}$  are influenced and show a good correlation to nutrient ions (phosphate, nitrate + nitrite, and silicate). These facts correspond to the present result. Therefore, the coprecipitation of trace metal ions by the salting out technique may be an informative method to evaluate the interaction between trace metals and organic matter (or organisms themselves) in natural water.

#### ACKNOWLEDGMENT

The authors thank Katsuhiko Miyoshi, Department of Chemistry, Hiroshima University, for giving us his products

of cobalt complexes. The authors thank Hiroyuki Tsubota, Faculty of Integrated Arts and Sciences, Hiroshima University, for his helpful suggestions.

**Registry No.** Cu, 7440-50-8; Mn, 7439-96-5; Ni, 7440-02-0; Co, 7440-48-4; Cd, 7440-43-9; Cr, 7440-47-3; Mo, 7439-98-7; Pt, 7440-06-4; [Co(NH<sub>3</sub>)<sub>6</sub>]<sup>3+</sup>, 14695-95-5; [Co(en)<sub>3</sub>]<sup>3+</sup>, 14878-41-2; [Co(dien)<sub>2</sub>]<sup>3+</sup>, 18703-28-1; [Co(sep)]<sup>3+</sup>, 72496-77-6; [Co(NH<sub>3</sub>)<sub>5</sub>Cl]<sup>2+</sup>, 14970-14-0; [Co(C<sub>2</sub>O<sub>4</sub>)(gly)<sub>2</sub>], 33846-70-7; [Co(edta)]<sup>-</sup>, 15136-66-0; water, 7732-18-5.

### LITERATURE CITED

- Nakayama, E.; Tokoro, H.; Kuwamoto, T.; Fujinaga, T. *Nature* **1981**, *290*, 766.
- Hiraide, M.; Yoshida, Y.; Mizuike, A. *Anal. Chim. Acta* **1976**, *81*, 185.
- Nakayama, E.; Kuwamoto, T.; Tokoro, T.; Fujinaga, T. *Anal. Chim. Acta* **1981**, *131*, 247.
- Akagi, T.; Fuwa, K.; Haraguchi, H. *Anal. Chim. Acta* **1985**, *177*, 139.
- Hiraide, M.; Ito, T.; Baba, M.; Kawaguchi, H.; Mizuike, A. *Anal. Chem.* **1980**, *52*, 804.
- Hiraide, M.; Sakurai, K.; Mizuike, A. *Anal. Chem.* **1984**, *56*, 2851.
- Buchanan, A. S.; Hannaker, P. *Anal. Chem.* **1984**, *56*, 1379.
- Hirano, K.; Yanagisawa, Yuki, T.; Nakamura, Y. *Bunseki Kagaku* **1984**, *32*, 743.
- Akagi, T.; Nojiri, Y.; Matsui, M.; Haraguchi, H. *Appl. Spectrosc.* **1985**, *39*, 662.
- Hindman, F. D. *Anal. Chem.* **1986**, *58*, 1238.
- Boyle, E. A.; Edmond, J. M. *Anal. Chim. Acta* **1977**, *91*, 189.
- Fujiwara, K.; Toda, S.; Fuwa, K. *Bull. Chem. Soc. Jpn.* **1981**, *54*, 3209.
- Cole, F. C.; Eckert, J. M.; Williams, K. L. *Anal. Chim. Acta* **1983**, *153*, 61.
- Fujiwara, K.; Morikawa, T.; Fuwa, K. *Bunseki Kagaku* **1986**, *35*, 361.
- Eichhorn, G. L. *Inorganic Biochemistry*; Eichhorn, G. L., Ed.; Elsevier: Amsterdam, 1973; Vol. 2, pp 1191.
- Eichhorn, G. L.; Berger, N. A.; Butzow, J. J.; Clark, P.; Rifkind, J. M.; Shin, Y. A.; Tarnen, E. *Inorganic Chemistry: Advances in Chemistry Series 100*; American Chemical Society: Washington, DC, 1971; pp 135.
- Fujiwara, K.; Toda, S.; Fuwa, K. *Agric. Biol. Chem.* **1979**, *43*, 1255.
- Tanabashi, K.; Fujiwara, K.; Fuwa, K. *Bull. Chem. Soc. Jpn.* **1978**, *51*, 945.
- Sugimura, Y.; Suzuki, Y.; Miyake, Y. *Deep-Sea Res.* **1978**, *25*, 306.
- Nakayama, E.; Suzuki, Y.; Fujiwara, K.; Kitano, Y. *Anal. Sci.* **1989**, *5*, 129.
- Bruiland, K. W.; Franks, R. P.; Knauer, G. A.; Martin, J. H. *Anal. Chim. Acta* **1979**, *105*, 42.
- Broecker, W. S.; Peng, T.-H. *Tracers in the Sea*; a publication of the Lamont-Doherty Geological Observatory, Columbia University: New York, 1982.
- Nakayama, E. *Mar. Sci. Monthly, Jpn.* **1986**, *18*, 749.

RECEIVED for review July 27, 1989. Accepted November 22, 1989. This work was supported by Grants in Aid 62610508, 63610009, and 01610006 from the Ministry of Education, Science, and Culture, Japan.

## Asphaltenes in Crude Oil: Absorbers and/or Scatterers in the Near-Infrared Region?

Oliver C. Mullins

Schlumberger-Doll Research, Old Quarry Road, Ridgefield, Connecticut 06877

The question of the relative magnitudes of light absorption and scattering by asphaltene particles in crude oils is addressed for the near-infrared spectral range. The effect of dilution with carbon tetrachloride on crude oil spectra is determined for asphaltic crude oils and these results are contrasted with similar measurements on crude oils with an immiscible wax phase. This comparison implies the dominance of absorption over scattering for asphaltic crude oils while scattering and absorption are found to be significant for waxy crude oils. Separation of crude oils into asphaltenes and maltenes allows for measurement of the absorption of individual crude oil components. The comparison of the original and composite spectra clearly shows that absorption dominates over scattering in the near-IR region. The functional forms expected for absorption and scattering are examined and found to be consistent with the experimental data.

### INTRODUCTION

Asphaltenes are one of the primary components of crude oil and have been the subject of a variety of studies ranging from efforts to unravel their enigmatic structure, to clarify their association with resins in crude oil, and to understand their impact on crude oil distillation and cracking (1-3). The classification asphaltene is defined largely by solubility characteristics; asphaltenes, which are quite polar and polarizable, are solids that are insoluble in small alkanes such as heptane and are soluble in benzene and carbon tetrachloride. They are suspended in crude oils within structures similar to micelles with the resins acting as the surfactants.

The asphaltenes interact favorably with the polar functions of the resins while the alkyl groups of the resins interact favorably with the predominantly saturated alkanes of the continuous phase of the crude oil. Resins are also defined operationally in terms of their separation characteristics; they are soluble in *n*-heptane but insoluble in liquid propane (1).

Asphaltenes are a dark brown to black, friable, infusible solid component of crude oil. They are characterized by a CH ratio close to one and specific gravities close to one and are highly aromatic. Heteroatom content varies but is greater than the corresponding oil. The heavy metal content of oils is frequently contained in the asphaltenes, often in porphyrin structures. The molecular structure of the asphaltenes have long been of interest and a wide variety of experimental methods have been used to explore this issue. Infrared spectroscopy and NMR performed on asphaltenes indicate the presence of saturated substituents (primarily methylene groups) while the CH ratio, UV-visible spectra, and X-ray scattering indicate the presence of large fused aromatic ring systems (1-3).

Various methods have been used to determine the structure and size of the asphaltene particles; typically these studies rely on separating the asphaltenes from the crude oils. The aromatic sheets within (and between) asphaltene molecules have been shown to stack in complexes roughly 12 Å wide and 20 Å high (4). The asphaltenes appear to be polydispersed and there may be some variation in asphaltene particle sizes among different crude oils. Small-angle X-ray scattering yields sizes (radii) of the asphaltene particles of approximately 30-50 Å (5, 6). Similar results are obtained from electron microscopy (7). Gel permeation chromatography results generally agree with this range indicating a mean size of approximately 30

Å and with a considerable range in sizes (8). Furthermore, large scale aggregation is important for asphaltenes. The differing aggregations of asphaltenes are considered the primary cause of the wide range (a factor of ~100) in the experimental determinations of molecular weights of asphaltenes (9).

The determination of the sizes of the micelles is much more relevant to the present study and much less certain due to limitations imposed by the study of unaltered crude oils. Some evidence indicates that the micelles are not much larger than the asphaltene particles themselves (10). This would imply that perhaps only a few asphaltene molecules are contained in a micelle and would also imply that the association of resins with asphaltenes does not increase the size of the complex much beyond the size of the asphaltene particles. The size of the asphaltene particles should establish a lower limit for the micelles which are composed of the asphaltenes plus resins. The extent of asphaltene aggregation is difficult to determine and may vary depending on the particular crude oil. Conclusive evidence particularly concerning the shape and nature of the micelles and even of the chemical identity of the constituent components remains elusive.

Our interest has been to explore the broad light extinction profile of crude oils in the near-infrared (near-IR) spectral range; here, crude oils exhibit a wide range of extinction coefficients. Two possible mechanisms can account for the extinction of transmitted light in this spectral range: electronic absorption and scattering from the asphaltene complexes. It is the purpose of this report to discern the relative importance of absorption and of scattering in producing attenuation of transmitted light in the near-IR region. The coloration of crude oils in the visible region indicates that absorption contributes to the extinction coefficient. By inference, absorption is also expected to contribute to the extinction coefficient in the near-IR region, but scattering can also significantly contribute to extinction as it does in coal for the visible region (11-14). The spectroscopy of crude oils in the near-IR range can facilitate chemical analysis, but the relative contributions of absorption and scattering must be known to make use of the spectroscopic data.

Various mechanisms of electronic absorption are possibly operative for asphaltenes. Large aromatic ring systems can undergo  $\pi\pi^*$  and  $n\pi^*$  transitions thereby producing visible and near-IR absorption. As the size of the aromatic ring system increases, the absorption band edge shifts to lower energy. Only large aromatic fused-ring systems possess electronic transitions in the near-IR range. Ring systems with heteroatoms possess  $n\pi^*$  transitions that are appreciably red-shifted compared to  $\pi\pi^*$  transitions but are also much weaker in intensity (15). In addition, charge-transfer complexes can produce absorption at long wavelengths; this mechanism may contribute to the spectrum of coal (11, 16). Electron paramagnetic resonance (EPR) measurements suggest that free radicals may contribute to the spectrum of coal (11) and similarly may contribute to the spectrum of asphaltenes (17). In this report, we do not attempt to discern the relative contributions of the different electronic excitation processes. The structure of the absorption edge is dependent on both the spectra and concentration of the individual chromophores in the crude oil. Vibrational overtone transitions can also be observed in the near-IR region but are not of interest here.

Extensive work has been performed on the light scattering and absorption properties, as well as other physical properties, on coal (11-14) and carbon (18). Recent work has also focused on the relative significance of scattering vs absorption in coal (14). Coal possesses light-absorbing species such as large aromatic molecules, free radicals, and possibly charge-transfer

complexes (11, 12, 16). Coal has scattering centers composed of mineral inclusions and voids dispersed in the carbon matrix (11-13). Thus, the issue of the relative strengths of scattering and of electronic absorption applies to coal as well as to crude oil. For coal, scattering of visible light was found to be quite strong, even for path lengths of a few micrometers (11-14). Even though coal appears black in the backscatter direction, scattering is a significant source of attenuation for transmission. The scattering could be greatly reduced (but not eliminated) by filling the voids in coal with organic solvents (14). However, it is difficult to compare coal and crude oil quantitatively. The mismatch of the index of refraction between the continuous and discrete phases is significantly larger in coal than in crude oil where both phases are predominantly hydrocarbons. Additionally, the size of the scatters in coal is frequently much larger than in crude oil. Furthermore, because coal is much more aromatic than crude oil, the electronic absorption per unit length is expected to be much greater. Furthermore, (petroleum) asphaltenes may be qualitatively or quantitatively different from coal with regard to the absorption by charge-transfer complexes or free radicals (11, 17). Thus, it is difficult to directly compare conclusions regarding coal to crude oil, but the question comparing the relative strengths of absorption to scattering applies in both cases.

## THEORY

Here, we establish some of the considerations of light scattering and absorption in the case of crude oils. We are concerned with the possible scattering of light of wavelength  $\lambda \sim 1 \mu\text{m}$  by particles which are approximately  $0.01 \mu\text{m}$ ; thus, the scattering regime is in the Rayleigh limit. With regard to absorption, even though the transitions of interest are electronic, which are normally quite strong, the radiation of interest is of sufficiently low energy that the absorption cross sections per unit mass for the crude oils and even for the asphaltenes are not large; these materials can be considered slightly lossy. For slightly lossy dielectric spheres in the Rayleigh limit, the scattering and absorption processes contribute separately to the extinction coefficient (19). That is

$$\sigma_{\text{tot}} = \sigma_{\text{sc}} + \sigma_{\text{abs}} \quad (1)$$

where  $\sigma_{\text{tot}}$ ,  $\sigma_{\text{sc}}$ , and  $\sigma_{\text{abs}}$  are the total, scattering, and absorption cross sections, respectively. The differential Rayleigh scattering cross section  $d\sigma_{\text{sc}}/d\Omega$  is obtained from the ratio of square of the electric field in incident  $\mathbf{E}_{\text{inc}}$  and scattered  $\mathbf{E}_{\text{sc}}$  beams (19)

$$d\sigma_{\text{sc}}/d\Omega = R^2 |(\mathbf{e} \cdot \mathbf{E}_{\text{sc}})|^2 / |(\mathbf{e}' \cdot \mathbf{E}_{\text{inc}})|^2 \quad (2)$$

where  $\mathbf{e}'$  and  $\mathbf{e}$  are polarization vectors for the incident and scattered radiation and  $R$  is the distance away from the scatterer. In the radiation zone the electric and magnetic fields take the form of spherical waves

$$\mathbf{B}_{\text{sc}} = k^2 \exp(ikR)/R \exp(-i\omega t) (\mathbf{n} \times \mathbf{p}) \quad (3)$$

and

$$\mathbf{E}_{\text{sc}} = \mathbf{B}_{\text{sc}} \times \mathbf{n} \quad (4)$$

where  $\mathbf{n}$  is the unit vector in the direction of the scattered radiation,  $k = 2\pi/\lambda$ ,  $\omega = kc$ , and  $\mathbf{p}$  is the dipole moment. The magnetic susceptibility is assumed to be zero. For small dielectric spheres the dipole moment is given by

$$\mathbf{p} = (\epsilon - 1)/(\epsilon + 2)r^3\mathbf{E}_{\text{inc}} \quad (5)$$

where  $\epsilon$  is the dielectric constant; for slightly lossy dielectrics  $\epsilon = \epsilon' + i\epsilon''$  and  $\epsilon' \gg \epsilon''$ .  $\sigma_{\text{sc}}$  is obtained by integration of the differential cross section over all directions and summed over both polarizations of light (19)

$$\sigma_{\text{sc}} = (8\pi/3)k^4 r^6 (\epsilon - 1)/(\epsilon + 2)^2 \quad (6)$$

For the scattering cross section,  $\epsilon$  represents a ratio of the dielectric constants of the discrete and continuous phases. The relative scattering cross section, which is given by the ratio  $\sigma_{sc}/\pi r^2$ , scales with  $(r/\lambda)^4$  which is the well-known result for Rayleigh scattering. In the absence of multiple scattering and in the Rayleigh limit, a greater number of smaller spheres is a much less efficient scatterer than a smaller number of larger spheres, for a given mass of scattering material. If the size of the scatterer becomes comparable to the wavelength of light, the Rayleigh scattering description no longer applies and, furthermore, the wavelength dependence of the scattering is reduced.

The rate of energy loss  $Q$  due to absorption is given by (19)

$$Q = 1/2 \operatorname{Re}(\mathbf{p} \cdot d(\mathbf{E}_{inc}^*)/dt) \quad (7)$$

again assuming the magnetic susceptibility is zero. Dividing  $Q$  by the energy flux density in the incident wave  $c|\mathbf{E}_{inc}|^2/8\pi$  results in eq 8. Thus, for  $\epsilon' \gg \epsilon''$ , the absorption is linear in

$$\sigma_{abs} = 12\pi k r^2 \epsilon'' / [(\epsilon' + 2)^2 + \epsilon''^2] \quad (8)$$

$\epsilon''$ , the imaginary part of the permittivity and the absorption also scales with the volume of the sphere. The ratio of the scattering to absorption cross sections scales with  $r^2$ ; so for a given value of  $\epsilon''$ , the particle size is critically important in determining the relative significance of scattering.

It is important to remember that the two assumptions, the dielectric spheres being slightly lossy and in the Rayleigh limit, both strongly depend on wavelength, so caution must be used when extrapolating the above arguments.

The scattering and absorption cross sections result in an exponential attenuation of transmitted light as shown in eq 9 where  $I_0$  and  $I$  are the intensities of incident and transmitted

$$I = I_0 \exp(-N\sigma_{tot}) \quad (9)$$

light and  $N$  is the number of particles of cross section  $\sigma_{tot}$ . Thus, the cross section is linearly related to optical density (OD)

$$\text{OD} = \log(I_0/I) = 0.434N\sigma_{tot} \quad (10)$$

Up to this point we have considered the light attenuation characteristics of a single particle. For cases where the scattering centers are far apart and where the mean free path of light is greater than the sample cell, one can neglect multiple scattering. However, with crude oils the concentration of asphaltenes can be sufficiently large that the correct description would include multiple scattering with either coherence or incoherence in the scattered wave. Multiple scattering complicates the description considerably and the specific form of the total cross section depends on the particular multiple scattering regime. Different crude oils contain widely different quantities of asphaltene and thus would cover a variety of multiple scattering regimes. We do not list results regarding multiple scattering but point out that the results from eqs 6 and 8 must be modified and that scattering and absorption can no longer be treated separately. Nevertheless, for multiple scattering with absorption, the total cross section is in general still strongly wavelength dependent and eqs 6 and 8 can be used as a guide to understanding this wavelength dependence.

## EXPERIMENTAL SECTION

Fourteen crude oils were obtained from North America, the Middle East, the Far East, and Africa. The oils differed considerably in chemical and physical properties such as asphaltene fraction, aromatic content, viscosity, color, and density. The asphaltene fraction was prepared as follows: Crude oils were diluted with *n*-heptane in a ratio of 1 g of crude oil/40 cm<sup>3</sup> *n*-heptane and the resulting solution was allowed to stand for approximately 24 h. The solution was then filtered (pore size of 200  $\mu\text{m}$ ) and the resulting asphaltene was washed with hot *n*-

heptane until this heptane was colorless. The asphaltene was then air-dried and weighed. It is important to note that the details of the separation procedure can strongly influence the properties of the resulting asphaltenes (20). The asphaltene content of the 14 crude oils varies from 0% to 15% by weight; this sample set is suitable to reveal light attenuation characteristics of crude oils and asphaltenes. We note that certain crude oils possess two immiscible hydrocarbon phases and the precipitation procedure is complicated by the presence of waxlike materials which are insoluble in light hydrocarbons but which do not possess typical chemical properties of asphaltene.

All near-IR spectra were obtained with a Mattson Cygnus 100 FTIR spectrometer equipped with a W-I<sub>2</sub> lamp and a liquid-nitrogen-cooled InSb detector. Various path-length spacers were used in a cell with sapphire windows to obtain the spectra of the crude oils and a 20-mm quartz cell was used for the diluted crude oil samples. The CCl<sub>4</sub> solutions of asphaltenes were heated to ensure total dissolution of the asphaltene and then cooled to room temperature in order to run spectra. However, some small dilution errors (perhaps 1%) were introduced due to the residual temperature differences of the cooled solution with ambient temperature. Weighing errors also contribute approximately 1% errors.

The electronic absorption spectra of the maltenes were needed to create the composite absorption spectra for the crude oils. The maltenes were obtained as a product of the asphaltene separation procedure; consequently, the maltenes were diluted with large volumes of *n*-heptane. The spectra of the diluted maltenes contained large overtone peaks associated with the *n*-heptane; these peaks could not be accurately subtracted from the maltene spectra. In light of these difficulties the following procedure was used to obtain the electronic absorption spectra of the maltenes: the spectrum of *n*-heptane was subtracted from the spectrum of the maltene diluted in large volumes of *n*-heptane. A 2 cm path length cell was used to obtain appreciable attenuation due to the maltene. However this long path length resulted in the CH stretch-plus-bend and the CH two-stretch peaks being beyond the linear range of the spectrometer. Consequently, only the spectral ranges of 4800–5200 and 6200–10000 cm<sup>-1</sup> were used to determine the broad attenuation due to the maltene. These two spectral ranges were least-squares fit to a single exponential function of the form  $\text{OD} = a \exp(bx(\text{cm}^{-1}))$ , where  $a$  and  $b$  are constants whose values are to be determined and  $x$  is the wavenumber of the photon. The factor  $a$  was scaled by the concentration ratio of the maltene in the crude oil and in the dilute solution. This method allowed for the determination of the broad attenuation of the maltene but not for the overtone and combination band structure of the maltene.

The detection of fluorescence emission can interfere with the measurement of accurate absorption data (21). Our FTIR data would only be sensitive to infrared-excited fluorescence; nevertheless, fluorescence emission can even occur with infrared excitation (1). Because fluorescence emission from solutions is isotropic, the small solid angle (0.02) of the light collection optics results in the collection of only ~0.17% of any fluorescence. The optical densities employed in our studies are almost always less than 1.0; thus, even quantum yields of unity for infrared-excited fluorescence would produce very small errors. Furthermore, quantum yields of infrared-excited fluorescence in crude oils and asphaltenes are expected to be less than unity.

## RESULTS AND DISCUSSION

Figure 1 shows typical near-IR spectra of three crude oils where two distinct mechanisms for the extinction of light are apparent. Each spectrum consist of a series of peaks with decreasing intensity at higher energy superimposed on a broad continuum characterized by an increasing extinction at higher energy. The progression of peaks corresponds to vibrational overtones, and combination bands of predominantly saturated hydrocarbons and their general assignments are given in Table I.

The origin of these absorption peaks is generally well understood and these peaks are relatively invariant in the different spectra (of course, their intensity scales with path length). At least in the near-IR range, all peaks in the spectra

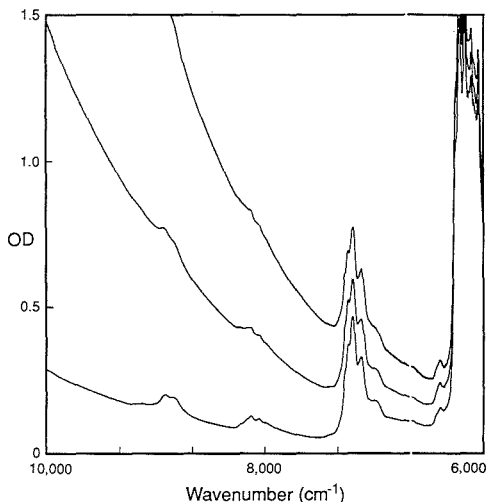


Figure 1. Near-IR spectra of three crude oils for a 1 mm path length. Two distinct attenuation processes are evident: one resulting in similar peaks in all spectra, the other resulting in a variable broad attenuation.

Table I. Assignments and Positions (in  $\text{cm}^{-1}$ ) for Some Overtone and Combination Bands in Crude Oil Spectra

	$\text{CH}_2$	$\text{CH}_3$
CH stretch plus bend	4334	4398
	4262	4375
CH two-stretch	5813 <sup>a</sup>	5810
	5778	5872
	5677	
CH two-stretch plus bend	7188	
	7085	
	6990	
	8262	8387

<sup>a</sup> Composite peak with significant  $\text{CH}_3$  character.

of crude oils correspond to vibrational transitions. These peaks provide little information about the significance of scattering by asphaltene particles and are not of further interest in this report.

(A) **Dilution Effects on Crude Oil Spectra.** In order to determine whether scattering or absorption dominates the extinction characteristics in the near-IR region for crude oils, four crude oils were subjected to dilution with  $\text{CCl}_4$  in an attempt to dissolve the asphaltenes.  $\text{CCl}_4$  is known to be an excellent solvent for asphaltene as well as for malenes. It is expected that this dilution of crude oils causes dissociation of micelle components such as dilution of pure asphaltenes results in the dissociation of asphaltene aggregates (8). Dilution factors for the crude oils varied from 20:1 to 80:1, giving asphaltene concentrations in the  $\text{CCl}_4$  solutions between  $10^{-8}$  and  $10^{-6}$  g/cm<sup>3</sup>. With these low concentrations, we have found that Beer's law applies. Gel permeation chromatography (GPC) results indicate that concentrations of asphaltenes of approximately  $10^{-8}$  g/cm<sup>3</sup> are dilute; asphaltene aggregation should be significantly reduced at these concentrations (8). With such extensive dilution, some effect is expected on the asphaltene dispersion and thus the scattering strength of the crude oil. Because dilutions of crude oils in the ratio of 40:1 result in asphaltene precipitation when poor solvents for asphaltenes are used, it is reasonable to expect significant solvating effects from the same ratio of dilution of crude oil

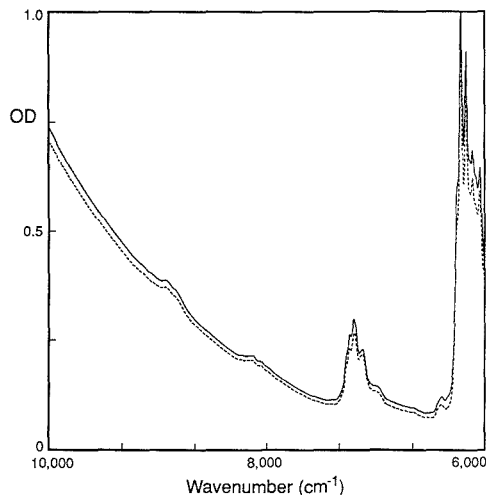


Figure 2. Effect of  $\text{CCl}_4$  dilution on the spectrum of an asphaltic crude oil. The solid curve is the near-IR spectrum for a crude oil which is 5.6% by weight asphaltene and the dashed curve is the spectrum of the same crude oil diluted 40:1 with  $\text{CCl}_4$  (with a factor of 40 increase in path length). Extensive dilution is accompanied by only subtle spectral changes.

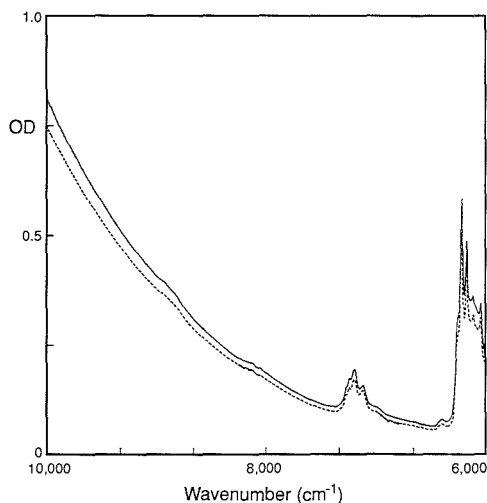


Figure 3. Effect of  $\text{CCl}_4$  dilution on a spectrum of an asphaltic crude oil. The solid curve is the near-IR spectrum for a crude oil which is 9.0% by weight asphaltene and the dashed curve is the spectrum of the same crude oil diluted 80:1 with  $\text{CCl}_4$  (with a factor of 80 increase in path length).

using a "good" solvent for asphaltenes.

Figures 2 and 3 show overlays of spectra of diluted and undiluted samples of the crude oils; similar data were obtained with other crude oils. The path length of the diluted samples was increased in the ratio of the dilution factor. Although some small differences exist between the spectra of diluted and undiluted crude oils, the dominant finding is that dilution has very little impact on the spectra of crude oils. Scattering by the asphaltene particles varies as the sixth power of the radius (eq 6) and should be strongly influenced by this substantial dilution. For instance, a decrease in the radius of only

12% from dilution would change the scattering optical density by a factor of 2. Additionally, the extensive dilution increases the index of refraction of the continuous phase from  $\sim 1.4$  to 1.46; the scattering cross section depends on the dielectric mismatch between the continuous and discrete phases (eq 6). Consequently, the scattering cross section and the scattering component of the optical density should decrease by a factor of  $\sim 2$  with dilution due to the refractive index change. The lack of a significant influence of dilution on the spectra of crude oils implies that the broad attenuation in the near-IR region is due to absorption.

The wavelength dependence of the broad attenuation observed in crude oil spectra is similar to  $1/\lambda^4$  dependence produced by Rayleigh scattering. Reduced chi-square values of  $\sim 2 \times 10^{-4}$  were obtained in fitting the data to the functional form  $OD = a/\lambda^4$ , where  $a$  is the variable to be determined and  $\lambda$  is the wavelength. Scattering certainly can be neither ruled out nor proven based on the shape of the spectrum. Other factors complicate the description of the wavelength dependence of the broad attenuation. The combination of scattering and absorption would cause the wavelength dependence to deviate from the standard Rayleigh description. The breakdown of the single scattering approximation, such as at higher optical densities, would also produce deviations from the  $1/\lambda^4$  dependence. Therefore, the wavelength dependence of the attenuation profile is not used here to discern the relative significance of scattering.

Small variations in optical density occur with dilution and may be caused in part from experimental error such as dilution errors (see Experimental Section). Some of the variation of the vibrational overtones and possibly in any electronic absorption is due to solvent effects. Variation in the electronic absorption could also result from the change in aggregation of the asphaltenes; the concentration-dependent complex formation of asphaltenes involves the  $\pi$  electron orbitals and thus could influence the low-energy electronic transitions. These intramolecular transitions are only subtly influenced by environmental effects.

**(B) Scattering from Suspended Particles.** It is instructive to compare the spectral effects of dilution of asphaltic crude oils and of crude oils with suspended waxy particles. These suspended particles are composed of hydrocarbons as shown by their solubility in carbon tetrachloride, and for want of a more accurate description, we refer to these particles as wax. Wax dispersions in crude oils have been studied by using small-angle X-ray scattering. These studies show that colloidal particle sizes for many waxes are considerably larger than those of asphaltenes (6). The presence of the suspended particles was determined by visual inspection of the crude oil under a microscope; clearly some of the particles were large compared to the wavelength but this does not preclude the presence of small particles and wavelength-dependent scattering. Figure 4 shows the spectral change that results from diluting a waxy crude oil in a ratio of 40:1 with carbon tetrachloride; the path length of the diluted sample was accordingly increased by a factor of 40. The undiluted crude oil (dashed curve) shows appreciable attenuation of light at all wavelengths. Upon dilution the crude oil becomes much more optically transmissive (solid curve). Similar data have been obtained with another crude oil with suspended wax particles. The large spectral effect of dilution for these waxy crude oils is to be contrasted with the minor spectral influence of diluting asphaltic crude oils.

The scattering from the wax particles appears to be somewhat wavelength dependent; that is, the spectrum for the undiluted sample is not simply vertically offset from the diluted sample. The broken-line curve of Figure 4 equals the dashed curve with a constant base line removed. Clearly, the

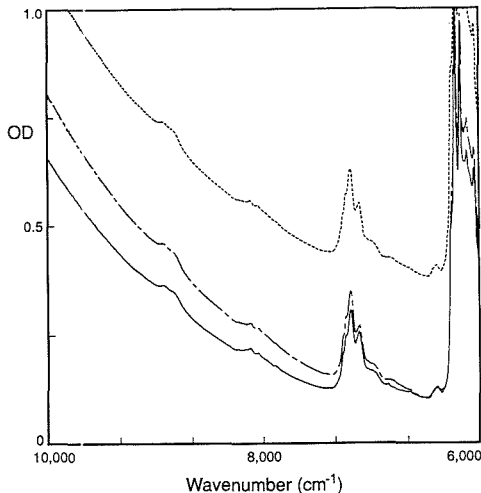


**Figure 4.** Near-IR spectra for a crude oil with an immiscible wax phase. The dashed curve is the spectrum of the crude oil and the solid curve is the spectrum of the crude oil diluted with  $\text{CCl}_4$  in a ratio of 40:1 thereby dissolving the wax. Comparison of the spectrum of the crude oil offset by 0.28 OD (broken-line curve) and the spectrum of the diluted crude oil (solid curve) illustrates a wavelength dependence in the scattering.

spectra for the diluted sample and undiluted sample differ by more than only a vertical offset. The strong implication is that the size of some of the particles is comparable to or smaller than the wavelength of light. Visual inspection shows some large particles as well; thus the scattering is not only in the Rayleigh limit. Fitting the spectrum to the absorption profile obtained from the diluted crude oil plus a Rayleigh scattering term is totally inadequate, suggesting that the scattering particles are comparable to the wavelength.

**(C) Spectra of Components of Crude Oils.** Another stringent test to determine the relative contributions of absorption and scattering is to separate the crude oil into the individual constituents, obtain the near-IR spectra for these components, add the spectra of the constituents, and finally compare with the spectrum of the original crude oil. Scattering produced by the asphaltene particles is of interest, so it is the asphaltenes which must be separated from the crude oil. The asphaltenes were separated and their mass fraction in the different crude oils was determined; the near-IR spectra of the asphaltenes in  $\text{CCl}_4$  solutions were obtained. Scattering produced by micelles in crude oil should be considerably different than by asphaltene particles in  $\text{CCl}_4$ . Here, the asphaltenes are no longer associated with the maltenes and the degree of asphaltene association is most likely different in the  $\text{CCl}_4$  solution than in the crude oil. Changes in the radius of the asphaltene particles in  $\text{CCl}_4$  compared to the micelles in the crude oils should strongly affect the scattering cross section due to its  $r^6$  dependence. Also, the change with dilution in the refractive index of the continuous phase, saturated alkanes vs  $\text{CCl}_4$ , should produce a factor of 2 reduction in the scattering cross section of the suspended asphaltenes.

The spectra of the corresponding maltenes (crude oils minus asphaltenes) were also obtained. The maltenes were diluted in large volumes of *n*-heptane in the asphaltene separation procedure and thereby showed large overtone peaks due to *n*-heptane. As described in the Experimental Section, only the electronic absorption was taken into account for the

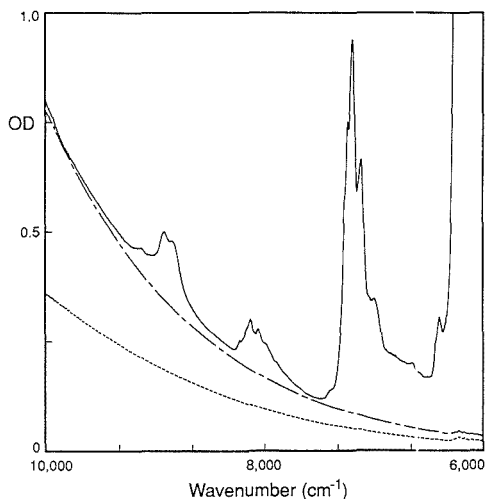


**Figure 5.** Comparison of a crude oil spectrum and the added spectra of the crude oil components. The solid line is the spectrum of the crude oil which is 0.5% asphaltene by weight. The dashed line is the spectrum of the asphaltene, scaled by its fraction in the crude oil, and the broken line is the sum of the asphaltene spectrum and broad attenuation portion of the maltene spectrum. The composite spectrum accounts for the broad attenuation in the crude oil.

maltenes, not the overtone absorption. Figures 5 and 6 individually show for two crude oils the original crude oil spectrum, the asphaltene spectrum, and the composite spectrum resulting from adding the appropriate ratio of the asphaltene and maltene spectra. The broad attenuation of the crude oil spectrum superimposes closely with the composite spectrum for both crude oils. The small differences between the two curves in each figure result partially from the difficulty of accurately determining the asphaltene fraction for the crude oils. Solvent effects and differing asphaltene complex formation might also play a role in producing subtle spectra differences. The similarity of the broad attenuation in the composite and crude oil spectra strongly indicates that scattering does not contribute significantly to the attenuation cross section. The origin of the broad attenuation in the near-IR region is electronic absorption.

Figures 5 and 6 also indicate that both the maltenes and asphaltenes contribute significantly to the attenuation in the near-IR region. The resins that constitute some of the largest, most aromatic molecules of the maltenes are nevertheless characterized by much smaller molecules than the asphaltenes (10). Furthermore, with the *n*-heptane dilution of crude oils, the micelle structures are destroyed and the resins are pulled into solution. Given the small size of the resins and the lack of resin association in the *n*-heptane solutions, it is likely that the electronic absorption results in the broad attenuation observed in the maltene spectra.

**(D) Comparison of Theoretical and Experimental Results.** The experimental findings that absorption dominates scattering can be compared to the theoretical predictions. The scattering cross section for a single sphere with a 100-Å radius can be calculated; this radius is at the upper end for expectations of asphaltene particles in  $\text{CCl}_4$  and reasonable for micelles in crude oils. In eq 6,  $\epsilon$  represents the ratio of dielectric constants for the discrete and continuous phases. The HC ratio of asphaltenes is approximately 1.15 and this value can be used to estimate the index of refraction of asphaltenes to be 1.6 (12). We estimate the index of re-

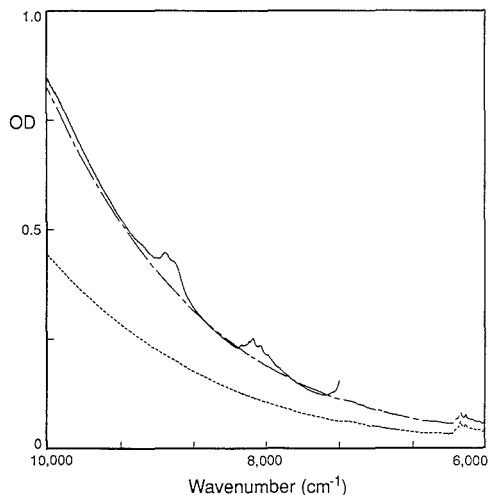


**Figure 6.** Comparison of a crude oil spectrum and the added spectra of the crude oil components. The solid line is the spectrum of the crude oil which is 2.5% asphaltene by weight. The dashed line is the spectrum of the asphaltene, scaled by its fraction in the crude oil, and the broken line is the sum of the asphaltene spectrum and broad attenuation portion of the maltene spectrum. The composite spectrum accounts for the broad attenuation in the crude oil.

fraction of crude oils to be 1.4, which is similar to that of saturated hydrocarbons. Thus, the ratio of the dielectric constants  $\epsilon = 1.31$ . For  $\lambda = 1.0 \mu\text{m}$ , eq 6 gives  $\sigma_{sc} \sim 1.1 \times 10^{-18} \text{ cm}^2$ . Of course, the cross section for a single sphere is quite small; its geometric cross section is  $1.3 \times 10^{-11} \text{ cm}^2$ .

The estimated scattering cross section can be used to determine the path length necessary to yield an optical density of one. Assuming single scattering, eq 9 applies. For an optical density of one and the above cross section,  $N = 2.1 \times 10^{18}$  particles/ $\text{cm}^2$ . For these 100-Å radius particles, a 3% asphaltene solution would require a path length of approximately 2 m to produce an OD of 1, smaller particles would require even longer path lengths. In fact, crude oils that are 3% asphaltene produce optical densities of one for 1 mm path length. That is, the estimated scattering cross section is 3 orders of magnitude below the measured cross section.

A factor of 10 increase in the assumed radius of the asphaltene particles (1000 increase in volume) would result in an estimated scattering cross section equal to the observed total cross section for the asphaltene solution. The experimental finding is that absorption dominates over scattering; thus the asphaltene particles must be significantly less than 1000 Å in size. The experimental observation is that scattering produced at most an attenuation of a few percent. Asphaltene particles of 500 Å would result in a scattering cross section of 10% of the observed cross section; thus, 500 Å is the upper limit for the asphaltene particle size. This finding is consistent with previous work (5-7).

As a check on the assumption that the asphaltenes are slightly lossy dielectrics, the complex part of the permittivity is estimated. Here, we assume that the observed cross section is entirely due to absorption and is described by eq 8. For slightly lossy media, the complex wave vector  $\mathbf{k}$  can be represented in terms of real  $\beta$  and imaginary  $\alpha$  components,  $k = \beta + i\alpha/2$ ; thus the attenuation coefficient for the plane wave  $e^{i\mathbf{k}\cdot\mathbf{r}}$  is  $\alpha$ . The attenuation coefficient for the asphaltenes can be estimated from the spectra. Figure 7 shows the spectrum of an asphaltene dissolved in  $\text{CCl}_4$  (62.2 mg of asphaltene/5

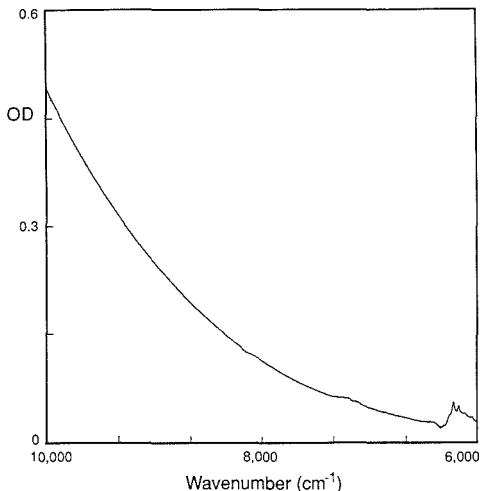


Figure 7. Spectrum of asphaltene. The asphaltene concentration is 62.2 mg/5 cm<sup>3</sup> and the sample path length is 2 mm.

cm<sup>3</sup>) for a path length of 2 mm. Normalizing the absorption of the dilute solution to the pure asphaltene, it is found that the asphaltene optical density is 18.6/mm at a wavelength of 1  $\mu$ m. This corresponds to a value of  $\alpha$ , the attenuation coefficient, of  $\sim 200$ /cm. For slightly lossy dielectrics, the imaginary part of the dielectric constant  $\epsilon''$  is related to the attenuation coefficient as (19)

$$\epsilon'' = \epsilon' \alpha / \beta \quad (11)$$

Thus, for  $\lambda = 1 \mu\text{m}$ ,  $\epsilon'' \sim 0.008$ ; this value is an upper limit based on the assumption that all attenuation is due to absorption. Indeed, the imaginary part of the dielectric constant is quite small for electronic transitions for which values of  $\epsilon''$  can be 1 or more. The small value of  $\epsilon''$  is due to the low energy of the photons, which corresponds to the red edge of electronic absorption of the asphaltenes.

The experimental findings that absorption dominates scattering in crude oils in the near-IR region are consistent with theoretical predictions and imply that parameter estimations for eq 6 and determination for eq 11 are reasonable.

### CONCLUSIONS

For the near-IR, the dominant light attenuation mechanism of the asphaltenes in crude oils is absorption, not scattering; thus, the near-IR range can be used with crude oils for

spectroscopic purposes. Scattering from the asphaltenes in the near-IR region is at most only a few percent of the absorption and in the present study was not distinguished from other small spectral effects related to differing solvents or asphaltene aggregation. The subtle spectral effects that accompany CCl<sub>4</sub> dilution of asphaltic crude oils sharply contrasts the large spectral changes which result upon similar dilutions of waxy crude oils. Comparison of spectra of crude oils with the added spectra of the crude oil components, asphaltenes and maltenes, again illustrates the dominance of absorption over scattering by asphaltic crude oils.

### ACKNOWLEDGMENT

The author is indebted to Steve Garoff, Reza Taherian, Jeff Tarvin, and Steve Cramer for many useful discussions.

### LITERATURE CITED

- (1) (a) Chilingarian, G. V.; Yen, T. F., Eds. *Bitumens, Asphalts and Tar Sands*; Elsevier Scientific Publishing Co.: New York, 1978. (b) Tissot, B. P.; Welte, D. H. *Petroleum Formation and Occurrence*, 2nd ed.; Springer-Verlag: New York, 1984.
- (2) Speight, J. G. *The Chemistry and Technology of Petroleum*; Marcel Dekker, Inc.: New York, 1980.
- (3) Bunger, J. W.; Li, N. C., Eds. *Chemistry of Asphaltens*; American Chemical Society: Washington, DC, 1981.
- (4) Yen, T. F.; Erdman, G.; Pollack, S. S. *Anal. Chem.* **1961**, *33*, 1587.
- (5) Pollack, S. S.; Yen, T. F. *Anal. Chem.* **1970**, *42*, 623.
- (6) Dwigjins, C. W. *J. Appl. Crystallogr.* **1978**, *11*, 615.
- (7) Dickie, J. P.; Haller, M. N.; Yen, T. F. *J. Colloid Interface Sci.* **1969**, *29*, 475.
- (8) (a) Hell, G.; Herron, S. P. *Chemistry of Asphaltens*; Bunge, J. W., Li, N. C., Eds.; American Chemical Society: Washington, DC, 1981; Chapter 8. (b) Skinner, F.; Strausz, O. P. *Chemistry of Asphaltens*; Bunge, J. W., Li, N. C., Eds.; American Chemical Society: Washington, DC, 1981; Chapter 6.
- (9) Speight, J. G.; Moschopedis, S. E. *Chemistry of Asphaltens*; Bunge, J. W., Li, N. C., Eds.; American Chemical Society: Washington, DC, 1981; Chapter 1.
- (10) Speight, J. G. *The Chemistry and Technology of Petroleum*; Marcel Dekker, Inc.: New York, 1980; Chapter 7.
- (11) Friedel, R. A.; Retcofsky, H. L.; Queiser, J. A. *Bull.—U.S., Bur. Mines* **1967**, No. 640, 1.
- (12) McCartney, J. T.; Ergun, S. *Bull.—U.S., Bur. Mines* **1967**, No. 641, 1.
- (13) Tschamler, H.; De Ruiter, E. *Chemistry of Coal Utilization*; Lowry, H. H., Ed.; Wiley: New York, 1963; suppl. vol.
- (14) Gettner, J. S. *J. Chem. Soc., Faraday Trans.* **1985**, *1*, 991.
- (15) Turro, N. J. *Modern Molecular Photochemistry*; Benjamin/Cummings Publishing Co.: London, 1978.
- (16) Yen, T. F. *Fuel* **1973**, *52*, 93.
- (17) Yen, T. F.; Young, D. K. *Carbon* **1973**, *11*, 33.
- (18) Ergun, S. *Chem. Phys. Carbon* **1968**, *3*, 45.
- (19) (a) Landau, L. D.; Lifshitz, E. M.; Pitaevskii, L. P. *Electrodynamics of Continuous Media*, 2nd ed.; Pergamon Press: New York, 1984. (b) Jackson, J. D. *Classical Electrodynamics*, 2nd ed.; John Wiley and Sons: New York, 1962.
- (20) Long, R. B. *Chemistry of Asphaltens*; Bunge, J. W., Li, N. C., Eds.; American Chemical Society: Washington, DC, 1981; Chapter 2.
- (21) Friedel, R. A.; Queiser, J. A. *Bull.—U.S., Bur. Mines* **1966**, No. 632, 1.

RECEIVED for review September 6, 1989. Accepted November 28, 1989.

# Elimination of z-Ejection in Fourier Transform Ion Cyclotron Resonance Mass Spectrometry by Radio Frequency Electric Field Shimming

Mingda Wang and Alan G. Marshall\*<sup>1</sup>

Department of Chemistry, The Ohio State University, 120 West 18th Avenue, Columbus, Ohio 43210

In Fourier transform ion cyclotron resonance (FT/ICR) mass spectrometry, coherent ion cyclotron orbital motion is produced by resonant radio frequency (rf) electric field excitation. However, because the excitation electrodes are of finite dimensions, the desired transverse (to the applied magnetic field) rf electric field is accompanied by an rf electric field component along the z- (magnetic field) direction, resulting in mass-dependent z-ejection and mass-dependent FT/ICR mass spectral peak relative magnitudes. Addition of several "guard wires" of voltage-divided rf amplitude allows the rf electric field to be "shimmed" to near-perfect uniformity. In this paper (see also the accompanying paper by Russell et al.), we introduce two types of rf-shimmed ion traps. In the first type, guard wires are placed only in front of the trapping electrodes. In the second type, guard wire rings are placed inside the detector and trapping electrodes. For either arrangement, SIMION simulations were used to adjust the rf voltages applied (by use of voltage dividers) to the guard wires or rings so as to produce an optimally uniform rf field within the trap. The virtual elimination of z-excitation is confirmed by plots of magnitude-mode relative peak height vs ICR orbital radius. Because the guard wires (or rings) tend to shield the ions from the trapping electrode potential, the shift in ICR frequency with trapping voltage is also reduced, but not as well as by a screened trap. In side-by-side tests of conventional and rf-shimmed traps mounted collinearly along the z-axis, the ICR signal strength was reduced to ~87% and ~25% of its unshimmed level by the addition of guard wires or guard rings, respectively.

## INTRODUCTION

Since its inception 15 years ago (1, 2), Fourier transform ion cyclotron resonance (FT/ICR) mass spectrometry has advanced both in the development of new instrumental techniques (3-8) and in the application of those techniques to fundamental and analytical ion-molecule chemistry (9-14), as summarized in the references cited above and other recent reviews (15, 16). FT/ICR mass spectrometry is now well established for providing ultrahigh mass resolution (17), analysis of low-volatility substrates, multistage MS<sup>n</sup>, laser desorption/ionization analysis, and qualitative versatility for determination of ion structures and ion-molecule reaction pathways. However, those experiments that depend upon quantitative accuracy in measurement of relative abundances of ions of different mass-to-charge ratio, *m/z*—namely, isotope ratio measurements, ion-molecule reaction rate constants, and equilibrium constants, etc.—remain limited by the large variation in FT/ICR mass spectral relative peak heights as a function of various experimental parameters (principally

radio frequency (rf) excitation energy). In this paper (see also the companion paper by Russell et al. in this issue), we address the principal remaining source of mass spectral peak height variation (namely inhomogeneous rf electric field) and propose two related solutions based on "shimming" of that rf electric field to near-uniformity.

In FT/ICR spectrometry, ions are stored inside an ion trap of, for example, cubic (18), orthorhombic (19, 20), cylindrical (21, 22), or hyperbolic (23, 24) geometry, by the combined effects of parallel static electric (trapping) and magnetic (cyclotron) fields. A coherent FT/ICR time-domain signal generated by resonant rf electric field excitation is detected from the image current induced on a second orthogonal pair of opposed transverse detector electrodes (25, 26).

**Origin of z-Excitation and z-Ejection.** Because the excitation electrodes are of finite dimensions, the electric excitation field is spatially nonuniform (27) and is necessarily accompanied by an rf field along the z- (i.e., magnetic field) direction. If the origin of a Cartesian coordinate system is located at the center of a conventional orthorhombic ion trap, then the (unwanted) z-component of the rf electric excitation field is given by (28)

$$E_z(x, y, z, t) = \frac{16V_{ex}(t)}{L\pi} \sum_{m=0}^{\infty} \sum_{n=0}^{\infty} (-1)^{m+n} \times \cos \left[ \frac{(2m+1)\pi y}{a} \right] \sin \left[ \frac{(2n+1)\pi z}{L} \right] \times \sinh \left[ \frac{K_{mn}\pi x}{a} \right] / \left\{ (2m+1) \sinh \left[ \frac{K_{mn}\pi}{2} \right] \right\} \quad (1a)$$

in which  $V(x, y, z, t) = V(\pm a/2, y, z, t) = \pm V_{ex}(t)$  is the rf detection voltage, *a* is the (transverse) separation between the detection electrodes (or the excitation electrodes, since the trap has square transverse cross-section), *L* is the (longitudinal) separation between the two "trap" electrodes, and

$$K_{mn} \equiv [(2m+1)^2 + (a^2/L^2)(2n+1)^2]^{1/2} \quad (1b)$$

As seen from eq 1, the relative amplitudes of the z- and xy-components of the rf electric field depend on ion position in the trap: the farther from the center of the trap, the stronger the z-excitation and the larger the amplitude of the ion "trapping" oscillation along the z-direction. Moreover, as for any harmonic oscillator, the z-oscillation initial amplitude in the absence of rf excitation depends on the initial position and z-velocity of the particle (in this case, an ion undergoing simple harmonic motion along the "trapping" z-direction). If z-oscillation amplitude increases sufficiently during excitation, ions will be lost ("ejected") along the magnetic field (z-) direction. The z-ejection effect is particularly objectionable because its efficiency varies with ionic mass-to-charge ratio, *m/z* (see below).

Analysis of z-excitation in orthorhombic traps (22, 28, 29) has shown that ion z-excitation and z-ejection vary directly

\* Author to whom correspondence should be addressed.

<sup>1</sup> Also a member of the Department of Biochemistry.

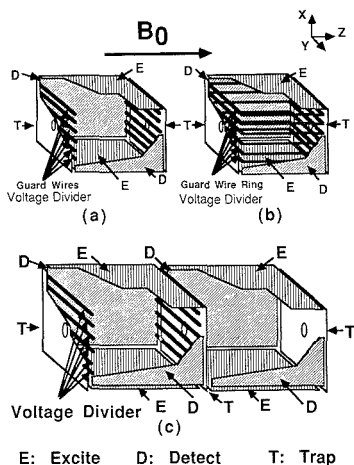


**Figure 1.** rf-shimmed ion traps for FT/ICR mass spectrometry. (a) In the  $z$ -shimmed trap, an array of guard wires whose voltages are divided from that applied to the excitation electrodes is placed interior to each of the two trapping electrodes. The resulting rf electric field in the trap is essentially independent of the  $z$ -coordinate. (b) In the  $y$ - and  $z$ -shimmed trap, an array of guard rings whose voltages are divided from that applied to the excitation electrodes is placed interior to both the detection and trapping electrodes. The rf electric field throughout the trap is nearly uniform in magnitude and direction. (c) In the two-section trap, conventional and rf-shimmed orthorhombic traps of the same dimensions are linked longitudinally along the magnetic field ( $z$ -) axis and share a common central trapping electrode, so that the behavior of ions in the two traps can be compared under the same experimental conditions. Interchange of the two traps then serves to disclose any systematic differences between the two halves of the arrangement.

with ion  $z$ -distance from the center of the trap, directly with excitation rf electric field amplitude, inversely with  $m/z$ , and inversely with applied trapping potential. Kofel et al. (22) have noted that  $z$ -excitation is most efficient when the rf excitation frequency is slightly higher than the ICR orbital frequency,  $\omega_0$ . (Conversely, if the rf excitation frequency is lower than  $\omega_0$ , then ion  $z$ -motion is damped.) Moreover, ion  $z$ -excitation and  $z$ -ejection may also result from transverse excitation at twice the trapping frequency,  $2\omega_T$  (30) and at the cyclotron frequency plus twice the trapping frequency,  $\omega_0 + 2\omega_T$  (31).

The detected FT/ICR signal is proportional to the number of ions and radius of ion cyclotron motion (25–27). Moreover, in conventional cubic or orthorhombic traps, the FT/ICR signal magnitude decreases with increasing ion preexcitation  $z$ -displacement away from the center of the ion trap (29, 32).

The net result of the above effects is that  $(m/z)$ -dependent  $z$ -excitation and  $z$ -ejection result in significant variation (up to an order of magnitude, as will be demonstrated in Figure 4 below) in FT/ICR mass spectral relative peak magnitude as a function of ICR orbital radius. Thus, the apparent relative abundances of ions of two different  $m/z$  values depend on the final ICR orbital radius of those ions after rf excitation, and quantitation of ion relative abundances from FT/ICR mass spectral relative peak heights or areas (33, 34) becomes problematic.

Methods for reducing undesirable  $z$ -excitation and/or  $z$ -ejection (28–31) have included the use of lower-amplitude, longer-duration rf excitation and/or elongation of the trap along the  $z$ -direction. For example, in a  $z$ -elongated ion trap, the coupling between  $xy$ - and  $z$ -excitation is reduced (at least near the center of the trap).

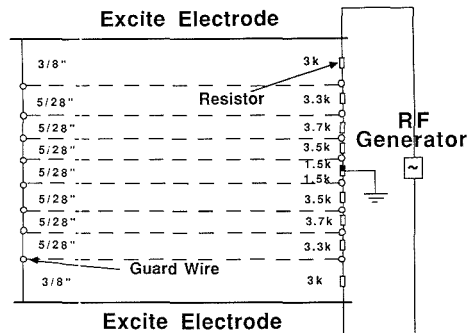


**Figure 2.** Simplified block diagram of the rf voltage divider, designed from the SIMON results shown in Figure 2 and used to “shim” the rf electric field in the ion trap. Each left- and right-hand pair of wires is connected by a third wire (dotted line) passing outside (exterior to) the detector electrodes (see text).

**The rf-Shimming Principle.** A method for “shimming” the rf electric field to near-uniformity was introduced almost 40 years ago in the “omegatron” detector (35), by the addition of “guard rings” (Figure 1b) to which different rf voltages were applied. In the original omegatron, excited ion cyclotron motion was detected by a separate collector fixed to the excitation electrode. In this paper and the companion paper by Russell et al. in this issue (36), various methods for adapting the guard rings principle to FT/ICR excitation/detection are presented.

Russell et al. (36) adapted the guard rings idea to an FT/ICR ion trap, by cutting the centermost guard ring in half and differentially detecting the oscillating charge induced on the two half-ring wires. We, on the other hand, employed conventional detector (plate) electrodes, but with the emplacement of either “guard wires” (Figure 1a) or guard rings (Figure 1b) interior to the usual detection and trapping electrodes. For both trap designs, SIMON simulations (Dahl, D. A.; Delmore, J. E. SIMON PC/PS2 Version 4.0; Idaho National Engineering Laboratory (EGG-CS-7233, Rev. 2, April, 1988)) were used to determine the electric potential contours resulting from application of various rf voltages to the guard wires or guard rings to produce an optimally uniform rf electric field directed normal to the  $z$ -axis.

Three effects of  $z$ -shimming were analyzed. First, the effect of  $z$ -shimming on  $z$ -excitation and  $z$ -ejection was tested by comparing FT/ICR magnitude-mode relative peak heights for conventional and shimmed traps of otherwise identical size and shape, mounted collinearly and interchangeably in a dual trap arrangement (see Experimental Section). Second, since the guard wires or guard rings are set to zero direct current (dc) potential, they are expected to shield the interior of the trap from the effect of the trapping potential applied to the trapping electrodes (37). We therefore measured the ICR orbital frequency shift as a function of trapping potential in conventional and rf-shimmed traps, to quantitate the shielding effect. Third, the same shielding effect is expected to reduce the ICR rf signal on the detector electrodes. We therefore compared relative ICR signal strength for conventional and rf-shimmed traps.

## EXPERIMENTAL SECTION

Each rf-shimmed orthorhombic ion trap,  $2.0 \times 2.0$  in. square cross section with 2.5-in. longitudinal ( $z$ -axis) separation between opposed parallel-wire planes, was constructed from flat solid oxygen-free hard copper electrodes separated by machinable ceramic (Macor) spacers. Each wire plane was placed  $\sim 1/8$  in. inside its adjoining trapping electrode. Figure 2 shows a schematic

diagram of the rf voltage divider, which was composed of ordinary coated carbon foil resistors (inductance-free). The guard wires (Figure 1a) were 0.015 in. diameter copper wires. Each pair of guard wires was connected by a third wire passing outside of one of the detector electrodes. The guard rings were made up of ceramic-coated 0.040 in. diameter aluminum wires located entirely within the region bounded by the detector and trapping electrodes (see Figure 1).

FT/ICR mass spectra were generated with a Nicolet FTMS-1000 (and, for cubic trap only, a 3-T Nicolet FTMS-2000) instrument operating at a magnetic field strength of 3.0587 T. Samples were introduced through a Varian No. 951-5100 leak valve.

To keep all parameters, especially sample pressure and electron beam current, as similar as possible for performance comparisons between conventional and rf-shimmed traps, all experiments were conducted in a home-built dual trap consisting of conventional and rf-shimmed traps mounted collinearly end-to-end along the *z*-axis (i.e., the magnetic field direction) and sharing a common middle trap electrode (see Figure 1c).

For determination of magnitude-mode FT/ICR relative mass spectral peak heights of perfluorotri-*n*-butylamine (PFTBA) fragment ions as a function of excitation magnitude, ions were produced by electron impact (70-eV electron beam of 10-ms duration at an emission current of 15 nA measured at a collector located outside the far end of the dual trap) of a gaseous sample at a pressure of  $2.3 \times 10^{-8}$  Torr. An ICR signal was excited by an rf broad-band frequency sweep from 0 to 2.667 MHz at a sweep rate of 150 Hz/ $\mu$ s (*z*-shimmed and nonshimmed) or 350 Hz/ $\mu$ s (*y*- and *z*-shimmed trap) and acquired by direct sampling at 5.247 MHz for 12.49 ms to yield 64K time-domain data points, to which another 64K zeros were added before discrete Fourier transformation. No apodization (windowing) was applied. Detection was switched back and forth manually between the rf-shimmed trap and the conventional trap. Trapping voltage was maintained at 1 V dc, and rf excitation magnitude was adjusted from 1.89 to 30 V (peak to peak) by variable attenuation. The spectrum produced in a 2 in.  $\times$  2 in.  $\times$  2 in. cubic trap was carried out with a Nicolet FTMS-2000 instrument (also operated at 3.0 T) at a sweep rate of 350 Hz/ $\mu$ s.

To determine the shift in ICR frequency of  $C_6H_6^+$  as a function of trapping voltage, we excited each time-domain signal by applying fixed-frequency rf excitation of 30-V (p-p) amplitude and detecting in heterodyne mode with a Nyquist bandwidth of 52.980 kHz (rf-shimmed, and unshimmed orthorhombic trap) or 62.992 kHz (screened trap (37)). Trapping dc potential was varied from 0.5 to 10 V.

To establish the reduction in detected ICR signal magnitude on introduction of guard rings or guard wires, we excited the ICR signal from  $C_6H_6^+$  by use of a broad-band (0–2.667 MHz) frequency-sweep excitation of 30-V (p-p) amplitude. Sweep rate was adjusted to produce the maximum signal magnitude (conventional trap: 550 Hz/ $\mu$ s; *z*-shimmed trap: 650 Hz/ $\mu$ s; *y*- and *z*-shimmed trap: 800 Hz/ $\mu$ s). FT/ICR signal relative magnitudes were determined from the average of 20 experimental measurements. Finally, to minimize any systematic differences between the two halves of the dual trap, the two halves were interchanged; the final reported relative FT/ICR signal magnitudes represent the average of measurements taken from initial and interchanged configurations.

## RESULTS AND DISCUSSION

### Effect of Guard Wires (Guard Rings) on rf-Shimming.

The isopotential contour lines in the two plots in Figure 3 represent the two-dimensional (*xz*) electrostatic potential of conventional and rf-shimmed ion traps of the same dimensions. Although our version of SIMION requires that the two *y*-electrodes must be taken as infinitely far apart in the computation, the results should nevertheless be qualitatively correct. Figure 3 clearly shows that rf-shimming significantly flattens the potential contours throughout the trap (and particularly for ions near the *x* = 0 central plane).

Many arrangements differing in number and spacing of shim wires, positioning and dimensions of excitation and trapping electrodes, and relative potentials on the various

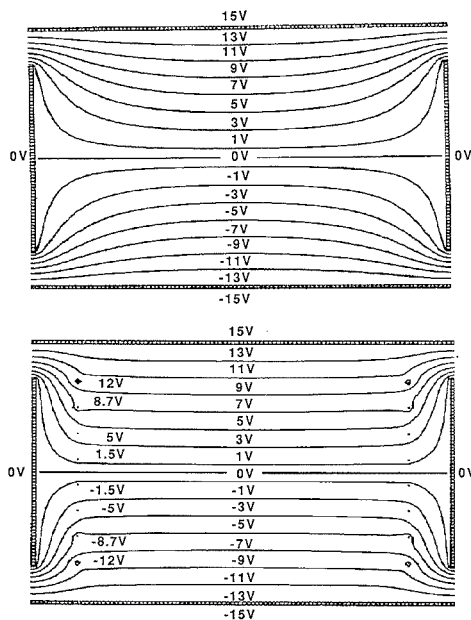


**Figure 3.** Two-dimensional SIMION contours of constant rf potential for conventional (top) and rf-shimmed (bottom) orthorhombic traps of the same dimensions. SIMION simulations, for which the separation between the two *y*-electrodes must be taken as infinite have been used to optimize the voltages on the guard wires so as to produce an optimally uniform rf field throughout the interior of the trap.

guard wires were SIMION-analyzed. The (somewhat unequally divided) voltages applied to the guard wires in Figure 3 represent an optimum, confirmed experimentally, for the illustrated length-to-width ratio ("aspect ratio") of the orthorhombic trap. The voltage divider shown in Figure 2 was designed from the SIMION results shown in Figure 3.

**FT/ICR Relative Magnitude-Mode Peak Heights vs ICR Orbital Radius.** Figure 4a shows the marked (factor of up to 20) variation with ICR orbital radius (produced in turn by variation in rf excitation amplitude) of FT/ICR magnitude-mode mass spectral relative peak heights, for a conventional cubic ion trap. The variation is reduced significantly by elongating the trap in the *z*-direction: Figure 4b shows the results for an orthorhombic 2 in.  $\times$  2 in.  $\times$  2.5 in. trap. Nevertheless, the relative peak heights still vary by a factor of up to  $\sim 2$  in the orthorhombic trap. rf-shimming produced by the addition of rf voltage-divided guard wires (*z*-shimming) or guard rings (*y*- and *z*-shimming) is analyzed in Figure 4c and Figure 4d, respectively. Because the rf excitation electric field is made significantly more homogeneous in magnitude and direction by the guard wires or guard rings, *z*-excitation and *z*-ejection during the excitation process are significantly reduced. As a result, the FT/ICR mass spectral relative peak heights no longer vary significantly with ICR orbital radius, once the ions have been excited to a sufficiently large radius that the Lorentz magnetic force dominates ion behavior (Figure 4c,d). The broad and flat segments of the plots in Figure 4c,d should make possible much more accurate and reproducible measurements of relative ion abundances by FT/ICR mass spectrometry, as for quantitation of gas-phase ion-molecule reaction kinetics and equilibria (9–12).

In other experiments (not shown), the ICR orbital radius was varied by changing the frequency-sweep rate at a constant rf voltage amplitude of 30 V (p-p). It was found that less

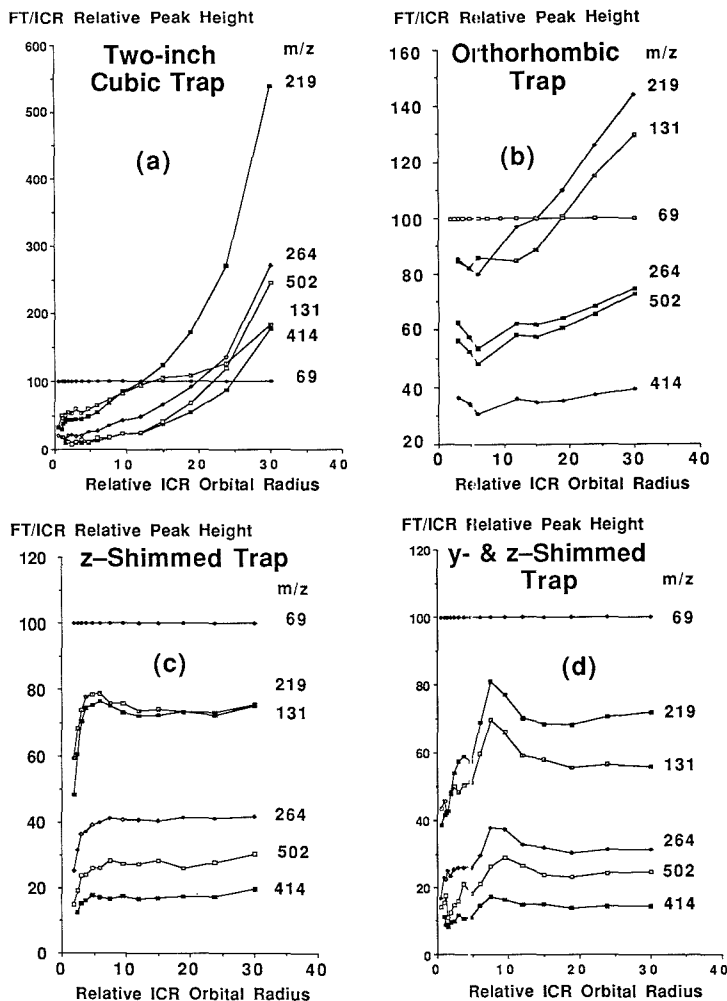


**Figure 4.** Comparison of  $z$ -ejection effects for four different ion trap designs. Each group is a plot of FT/ICR magnitude-mode relative peak height ( $=100$  for  $\text{CF}_3^+$  at  $m/z = 69$ ) versus relative ICR orbital radius (achieved by variation of frequency-sweep rf excitation voltage from 1.89 to 30 V (p-p), at fixed excitation period, swept frequency range, and sweep rate). The virtual elimination of  $z$ -ejection in the rf-shimmed traps is evident from the much reduced variation in relative peak height as a function of ICF orbital radius. Key: (a) cubic trap (2 in.  $\times$  2 in.  $\times$  2 in.); (b) orthorhombic trap (2 in.  $\times$  2 in.  $\times$  2.5 in.); (c)  $z$ -shimmed trap 2 in.  $\times$  2 in.  $\times$  2.5 in.; (d)  $y$ - and  $z$ -shimmed trap.

excitation energy was required to excite ions to a given ICR orbital radius in an rf-shimmed trap compared to that required in a conventional trap. In other words, by making the rf field more uniform, rf-shimming effectively makes the excitation process more efficient, since all the excitation voltage is applied in the  $x$ - $y$  plane rather than "wasting" part of it as  $z$ -excitation; the rf electric field lines which formerly terminated on the detection and trapping electrodes are now redirected to point from one excitation electrode to the other. An important corollary is that ion ejection should now be achieved to a greater extent from *transverse* excitation rather than (as with unshimmed traps) partly by (much less  $m/z$ -selective (30, 31))  $z$ -ejection. Thus, rf-shimming should improve the selectivity of ion ejection in the first stage of MS/MS experiments.

**Effect of rf-Shimming on Variation of ICR Orbital Frequency with Trapping Potential.** Because the

grounded guard wires (or rings) of the rf-shimmed traps of Figure 1c,b act to partially shield the ions from the (dc) trapping electrode potential, the effective trapping electric field "seen" by ions is reduced. A direct measure of the dc trapping field inside the trap is provided by the dependence of observed ICR frequency,  $\omega_0$ , on trapping potential,  $V_T$ . For the approximately quadrupolar electrostatic potential produced near the center of an orthorhombic trap, the dependence of  $\omega_0$  on trapping voltage is simply (37, 38)

$$\omega_0 = \omega_c - \frac{2\alpha V_T}{a^2 B_0} \quad (2)$$

in which  $\omega_c$  is the ion cyclotron orbital frequency (rad/s),  $B_0$  is the applied magnetic field strength (tesla), and  $\alpha$  is a relatively simple function of the cell dimensions.

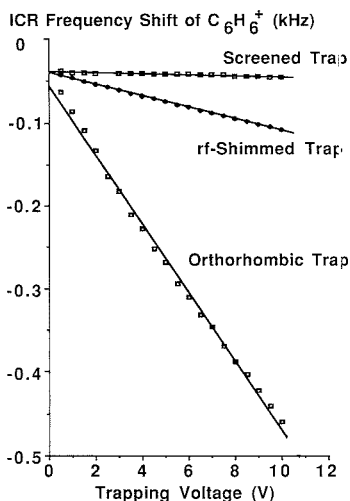


**Figure 5.** Experimental ICR orbital frequency shift of  $C_6H_6^+$  at 3 T as a function of trapping voltage in 2 in.  $\times$  2 in.  $\times$  2.5 in. rf-shimmed, screened (37), and unshielded orthorhombic ion traps. Because the guard wires (or guard rings) tend to shield the ions from the trapping electrode potential, the shift in ICR frequency with trapping voltage is also reduced, but not as completely as for a screened trap (37).

Figure 5 shows the experimental variation of observed ICR frequency as a function of trapping voltage for conventional, rf-shimmed, and screened (37) orthorhombic ion traps. From eq 2, we see that the slope of such a curve is a direct measure of the effective trapping potential,  $V_T$ , in the trap. Although the addition of guard wires does partially screen the ions from the effect of the dc trapping potential (compare the two lowermost curves in Figure 5), the reduction in effective  $V_T$  is not nearly as complete as with a two-dimensional grounded screen in front of each trap electrode (compare two uppermost curves in Figure 5).

#### Effect of rf-Shimming on ICR Detection Sensitivity.

The argument of the preceding section applied in reverse by the induced charge theorem (32) suggests that placement of an array of wires in front of each detector electrode should partially screen that detector electrode from the rf electric field associated with orbital ICR motion. Moreover, the addition of grounded wires changes the shape of the static electric field in the trap. Finally, one might expect to lose ions that contact or are deflected by the wires.

We therefore linked conventional and rf-shimmed traps collinearly (Figure 1c), in order to compare the ICR signal strength in the presence and absence of guard wires or guard rings. For the z-shimmed trap (i.e., guard wires in front of the trap electrodes only), the detected ICR signal drops to  $\sim 87\%$  of its value in the absence of the guard wires, probably due mainly to a slight drop in ion trapping efficiency. In contrast, the detected ICR signal magnitude in the y- and z-shimmed trap drops to  $\sim 25\%$  of its value in the absence of guard rings. In fact, one might have expected a much larger drop in signal, on the basis of SIMION simulations. However, one must keep in mind that SIMION computations of dc potential may not necessarily provide an accurate picture of ac potentials.

Although detection efficiency in the y- and z-shimmed trap (guard rings) is reduced compared to that in a conventional unshimmed trap, the highly uniform rf field gained from rf-shimming may be worth the loss in sensitivity, particularly for ions of low initial kinetic energy (and thus small ICR

orbital radius before excitation) (39, 40). Apart from the single-wire detector approach discussed in the following paper (36), other solutions to the sensitivity problem include (a) use of the same pair of electrodes for excitation and detection by switching back and forth between excite and detect circuits; or (b) floating the potential on the wires passing in front of the detector plates once the excitation is completed.

The relation between the present development and the previously published stored waveform inverse Fourier transform (SWIFT) rf excitation (5, 41) is worth noting. SWIFT was designed to produce uniform rf excitation magnitude at the transmitter plate(s) over a specified frequency (or  $m/z$ ) range. The development of rf-shimming ensures that that flat excitation power at the plates translates into uniform ion excitation radius for ions of different  $m/z$ . Thus, rf-shimming and SWIFT are complementary developments that, when combined, should significantly improve the uniformity of rf excitation (and thus measured relative ion abundances) in FT/ICR mass spectrometry.

We are continuing to experiment with ion trap designs that combine the desirable features of two-dimensional screens for reducing the dc trapping potential (37) and the present guard wires or guard rings for rf-shimming. Taken together, these two developments should go far to improve the mass resolution, mass accuracy, mass selectivity for MS/MS, reliability, upper mass limit, and quantitation of ion relative abundances from FT/ICR mass spectrometry.

#### ACKNOWLEDGMENT

The authors thank D. H. Russell and his collaborators for making known to us their independent progress in developing rf-shimmed ion traps for FT/ICR mass spectrometry (see accompanying paper). In particular, we acknowledge Russell's suggestion of a dual trap consisting of conventional and rf-shimmed traps linked end-to-end for a better-controlled comparison of the performance of the new trap designs.

#### LITERATURE CITED

- (1) Comisarow, M. B.; Marshall, A. G. *Chem. Phys. Lett.* **1974**, *25*, 282-283.
- (2) Comisarow, M. B.; Marshall, A. G. *Chem. Phys. Lett.* **1974**, *26*, 489-490.
- (3) Cody, R. B.; Bjarnason, A.; Weil, D. A. In *Lasers in Mass Spectrometry*; Lubman, D. M., Ed.; Oxford University Press: New York, in press.
- (4) Hanson, C. D.; Kerley, E. L.; Russell, D. H. In *Treatise on Analytical Chemistry*, 2nd ed.; Wiley: New York, 1988; Vol. 11, Chapter 2.
- (5) Marshall, A. G.; Wang, T.-C. L.; Chen, L.; Ricca, T. L. *ACS Symp. Ser.* **1987**, No. 359, 21-33.
- (6) Marshall, A. G. *Acc. Chem. Res.* **1985**, *18*, 316-322.
- (7) Gross, M. L.; Rempel, D. L. *Science* **1984**, *226*, 261-268.
- (8) Wanczek, K.-P. *Int. J. Mass Spectrom. Ion Processes* **1984**, *60*, 11-60.
- (9) Wilkins, C. L.; Chowdhury, A. K.; Nuwaysir, L. M.; Coates, M. L. *Mass Spectrom. Rev.* **1989**, *8*, 67-92.
- (10) Nibbering, N. M. M. *Adv. Mass Spectrom.* **1988**, *11*, 101-125.
- (11) Freiser, B. S. In *Techniques for the Study of Ion Molecule Reactions*; Farrar, J. M.; Saunders, W. H., Jr., Eds.; Wiley: New York, 1988; Vol. 20, Chapter 2, pp 61-118.
- (12) Nibbering, N. M. M. *Adv. Phys. Org. Chem.* **1988**, *24*, 1-55.
- (13) Asamoto, B. *Spectroscopy* **1988**, *3*, 38-46.
- (14) Russell, D. H. *Mass Spectrom. Rev.* **1986**, *5*, 167-189.
- (15) Marshall, A. G. *Adv. Mass Spectrom.* **1989**, *11A*, 651-669.
- (16) Buchanan, M. V.; Comisarow, M. B. In *Fourier Transform Mass Spectrometry: Evolution, Innovation, and Applications*; Buchanan, M. V., Ed.; ACS Symposium Series 359; American Chemical Society: Washington, DC, pp 1-20.
- (17) Amster, I. J.; McLafferty, F. W.; Castro, M. E.; Russell, D. H.; Cody, R. C.; Ghaderi, S. *Anal. Chem.* **1986**, *58*, 483-485.
- (18) Comisarow, M. B. *Int. J. Mass Spectrom. Ion Phys.* **1981**, *37*, 251-257.
- (19) Hunter, R. L.; Sherman, M. G.; McIver, R. T., Jr. *Int. J. Mass Spectrom. Ion Phys.* **1983**, *50*, 259-274.
- (20) Grosshans, P. B.; Wang, M.; Marshall, A. G. *Collected Abstracts: 36th American Society Mass Spectrometry Annual Conference on Mass Spectrometry & Allied Topics*, San Francisco, June, 1988; American Society for Mass Spectrometry: East Lansing, MI, 1988; pp 592-593.
- (21) Lee, S. H.; Wanczek, K.-P.; Hartmann, H. *Adv. Mass Spectrom.* **1980**, *88*, 1645.
- (22) Kofel, P.; Allemann, M.; Kellerhals, H.; Wanczek, K.-P. *Int. J. Mass Spectrom. Ion Processes* **1986**, *74*, 1-12.
- (23) Rempel, D. L.; Ledford, E. B., Jr.; Huang, S. K.; Gross, M. L. *Anal. Chem.* **1987**, *59*, 2527-2532.

- (24) Wang, M.; Ledford, E. B., Jr.; Marshall, A. G. FACSS XIV Annual Meeting, Detroit, MI October 1987; Abstract No. 43.
- (25) Cornisarow, M. B. *J. Chem. Phys.* **1978**, *69*, 4097-4104.
- (26) Cornisarow, M. B. In *Ion Cyclotron Resonance Spectrometry II*; Springer-Verlag: Berlin, 1982; pp 484-513.
- (27) Grosshans, P. B.; Marshall, A. G. *Collected Abstracts*; American Society for Mass Spectrometry 37th Annual Conference on Mass Spectrometry & Allied Topics, 1989; American Society for Mass Spectrometry: East Lansing, MI, 1989; pp 1232-1233.
- (28) Rempel, D. L.; Huang, S. K.; Gross, M. L. *Int. J. Mass Spectrom. Ion Processes* **1986**, *70*, 163-184.
- (29) Huang, S. K.; Rempel, D. L.; Gross, M. L. *Int. J. Mass Spectrom. Ion Processes* **1986**, *72*, 15-31.
- (30) Allemann, M.; Kofel, P.; Kellerhals, Hp.; Wanczek, K.-P. *Int. J. Mass Spectrom. Ion Processes* **1987**, *75*, 47-54.
- (31) Van der Hart, W. J.; Van De Guchte, W. J. *Int. J. Mass Spectrom. Ion Processes* **1988**, *82*, 17-31.
- (32) Dunbar, R. C. *Int. J. Mass Spectrom. Ion Processes* **1984**, *56*, 1-9.
- (33) Chen, L.; Cottrell, C. E.; Marshall, A. G. *Chemom. Intell. Lab. Syst.* **1986**, *7*, 51-58.
- (34) Liang, Z.; Marshall, A. G. *Anal. Chem.* **1990**, *62*, 70-75.
- (35) Sommer, H.; Thomas, H. A.; Hipple, J. A. *Phys. Rev.* **1951**, *82*, 697-732.
- (36) Hanson, C. D.; Castro, M. E.; Kerley, E. L.; Russell, D. H. *Anal. Chem.*, following paper in this issue.
- (37) Wang, M.; Marshall, A. G. *Anal. Chem.* **1989**, *61*, 1288-1293.
- (38) Beaucamp, J. L.; Armstrong, J. T. *Rev. Sci. Instrum.* **1969**, *40*, 123-128.
- (39) Kerley, E. L.; Russell, D. H. *Anal. Chem.* **1989**, *61*, 53-57.
- (40) Hanson, C. D.; Kerley, E. L.; Russell, D. H. *Anal. Chem.* **1989**, *61*, 83-85.
- (41) Marshall, A. G.; Wang, T.-C. L.; Ricca, T. L. *J. Am. Chem. Soc.* **1985**, *107*, 7893-7897.

RECEIVED for review August 7, 1989. Accepted November 6, 1989. This work was supported by grants (to A.G.M.) from the National Science Foundation (CHE-87-21498), the U.S. Public Health Service (NIH GM-31683), and The Ohio State University.

## Field-Corrected Ion Cell for Ion Cyclotron Resonance

Curtiss D. Hanson

Department of Chemistry, University of Northern Iowa, Cedar Falls, Iowa 50614

Mauro E. Castro, Eric L. Kerley, and David H. Russell\*

Department of Chemistry, Texas A&M University, College Station, Texas 77843

**The basis for mass analysis by Fourier transform ion cyclotron resonance (FT-ICR) is the motion of ions in a homogeneous magnetic field. Electric fields are used in FT-ICR to modify ion motion (i.e., trapping and excitation fields). Ion interaction with inhomogeneous radio frequency and direct current (dc) electric fields complicates the ion motion and leads to loss of both resolution and sensitivity. Modifying the geometry of the FT-ICR cell to produce uniform ion acceleration and homogeneous dc trapping fields results in simplified frequency measurements and studies of ion-molecule reactions.**

### INTRODUCTION

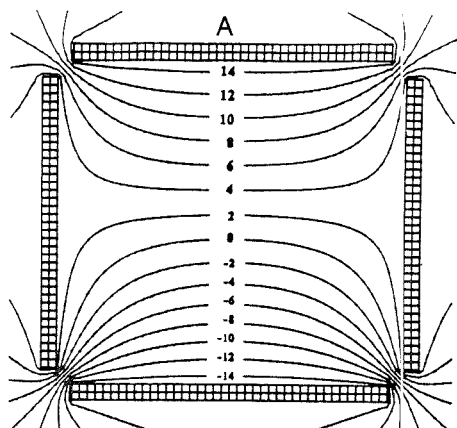
Mass analysis by Fourier transform ion cyclotron resonance (FT-ICR) is achieved by relating the frequency of an ion's periodic orbital motion (in a homogeneous magnetic field) to the mass-to-charge ( $m/z$ ) ratio (1-4). The fundamental consideration of mass analysis by FT-ICR is that an ion's orbital frequency is solely dependent upon its  $m/z$  ratio. The ICR ion cell is designed to trap ions in an electrostatic well, and acceleration of the ions is accomplished by applying a variable frequency radio frequency (rf) electric field. Consequently, the ions experience forces due to the electric fields and the materials used to construct the ICR cell have some degree of magnetic properties which result in regions of magnetic inhomogeneities. The additional forces acting on the ions (the applied electric fields or inhomogeneous magnetic fields) result in aberrations of the ion motion which must be accounted for by using correction factors or calibration tables (5, 6). Although early work showed that the effects of magnetic inhomogeneities can be ignored for single-cell experiments (7, 8), more recent work clearly demonstrates the importance of cell materials for experiments involving ion transportation through small orifices (i.e., two-section cell experiments and

injection from an external ion source) (9). Furthermore, ion motion resulting from an applied electrostatic trapping field has been shown to cause both frequency shifts and side bands (10, 11). On the basis of these considerations, both construction materials and cell geometries must be carefully selected to ensure predictable signal response. Corrections for the cyclotron frequency in a trapped ICR cell are difficult to derive because frequency perturbations caused by inhomogeneous  $\mathbf{E} \times \mathbf{B}$  fields are dependent upon the geometry of the ion cell (12). Although analytical treatment of the equations for ion motion have been derived for specific cell geometries, the resulting frequency corrections are difficult to use for ions either having large spatial distributions or existing in field boundaries where the  $\mathbf{E} \times \mathbf{B}$  fields are ill-defined.

In a pure homogeneous  $\mathbf{E} \times \mathbf{B}$  field, the dc electric trapping field only affects the motion of the ions along the  $Z$  axis. Conversely, in an inhomogeneous  $\mathbf{E} \times \mathbf{B}$  field, the electrostatic trapping field creates a net force perpendicular to the ion motion which alters the frequency of the ion's orbit. These effects are illustrated by evaluating the forces acting on an ion cyclotroning about the central axis of a symmetric trapping field where the radial force of the electric field is constant. Equation 1 shows the contributions of the radial magnetic and electric field forces acting on an ion of mass  $m$  and charge  $q$  in an  $\mathbf{E} \times \mathbf{B}$  field

$$mv_{\perp}^2/r + qE \sin \phi = qv_{\perp}B \quad (1)$$

where  $v_{\perp}$  is the scalar component of the ion velocity perpendicular to the magnetic field lines (in the  $X$ - $Y$  plane). Because the total outward radial force is the sum of the centrifugal and electric field forces, the radial force due to the applied dc electric field ( $E \sin \phi$ ) shifts the ion's cyclotron frequency to lower values. The frequency difference between an ion experiencing a radial electric field and the natural cyclotron frequency increases with the redirection of the



3 Volt Trapping Well in Cubic Cell

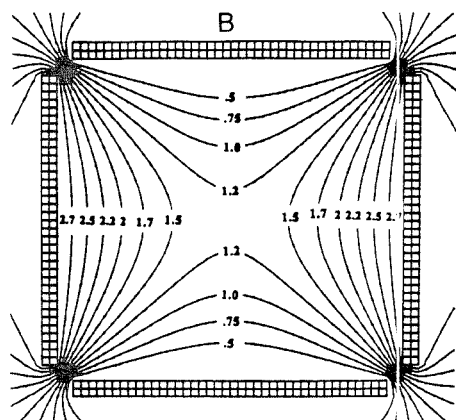


Figure 1. Computer simulation plots of the electric equipotential field lines generated by (A) an rf electric field and (B) a dc trapping field in a cubic FT-ICR cell.

electric field ( $E$ ) into the  $X$ - $Y$  plane (where  $\phi$  is the angle between the dc electric field vector and the magnetic field lines). Therefore, the angular velocity of an ion in an inhomogeneous  $E \times B$  field is not solely dependent upon the  $m/z$  ratio; it is also dependent upon the magnitude of the dc electric field (eq 2). In addition, the perpendicular component of the

$$\omega_{\text{ion}} = v_{\perp}/r = q/mv_{\perp}(v_{\perp}B - E \sin \phi) \quad (2)$$

applied trapping field causes a drift of the center of the orbital motion. The resulting magnetron motion causes sidebands flanking the main peak.

The trapped ion cell most commonly used for ICR consists of six electrically isolated plates arranged in cubical geometry (13, 14). Although this cell design was originally used to approximate a quadrupolar electric field, the six flat plates cause significant redirection of the electric fields used for trapping and excitation. Figure 1 contains plots of the field lines resulting from an rf excitation electric field (A) and the dc trapping field (B). The rf excitation field is contoured by the excite and receive plates and the dc trapping field contains lines of force which have components in the  $X$ - $Y$  and  $Z$  directions. Because the perpendicular component of the electric

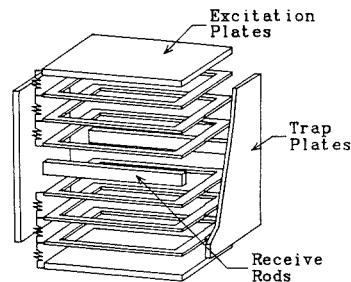
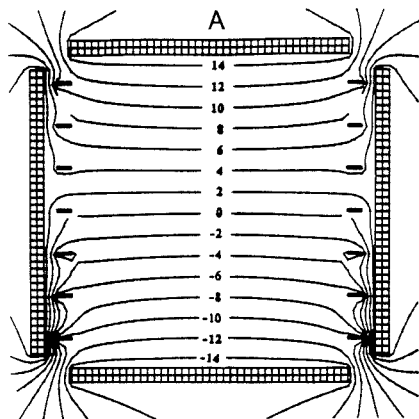


Figure 2. Field-corrected ion cell utilizes shimming rings similar to the omegatron to ensure a uniform rf excitation. The uniform excitation is achieved by linearly decreasing the magnitude of the voltages applied to the rings.

field is radially inhomogeneous, the frequency of an ion in a cubic ICR cell varies with cyclotron radius (i.e., ion position in the  $X$ - $Y$  plane) (15). Ion motion is also affected by the quadratic potential gradient along the  $Z$  axis; specifically, ions formed in the electrostatic well created by the trapping plates are accelerated along the  $Z$  axis (16). Ions that are trapped in the cell have a distribution of kinetic energies along the  $Z$  axis ranging between the translational energy of the neutral prior to ionization and the potential of the trapping well. Furthermore, the redirection of the excitation field causes an axial component of the excitation field resulting in  $Z$ -axis excitation (17-19).

To eliminate the problems associated with  $E \times B$  fields, cell designs have been introduced which reduce or eliminate the electric field within the detection region of the FT-ICR cell (17, 20-23). The ideal ion cell for FT-ICR would be constructed of plates having infinite dimensions. The infinite plates would eliminate the redirection of the electric field lines caused by multiple electrode interaction. Although it is impossible to construct such a cell, uniform field lines can be produced by incorporating shimming electrodes. The omegatron ion cell used for mass analysis by Sommer, Thomas, and Hipple (24-26) incorporated "guard rings" to shim the applied rf electric field. This design ensured uniform excitation fields at the boundaries of a finite ion cell. A uniform rf excitation field is achieved by linearly decreasing the magnitude of the voltages applied to the rings. However, the omegatron cell design is not compatible with an FT-ICR detection scheme. The field-corrected ICR cell (Figure 2) is a modified omegatron cell which is compatible with FT-ICR ion detection. Uniform electric fields (both dc and rf) are produced by placing guard rings between the excitation plates and in front of the trapping plates. Figure 3 contains plots of the rf and dc electric fields produced by the field-corrected ICR cell. Note that the rf excitation field is uniform throughout the full cell dimensions and that the trapping well is shielded eliminating frequency shifts during detection (23).

The obstacle to using the field-corrected cell for FT-ICR is the design of the electrode used to receive the signal. In order to ensure homogeneous rf electric fields, guard rings are used to shim the electric fields in both the  $X$ - $Z$  and the  $Y$ - $Z$  planes. Placement of guard rings in front of the signal receive electrodes shields the induced image current and causes signal loss. With receive electrodes inside the guard ring assembly, there is no shielding effect and signal loss. An ion cell utilizing single wire or small rod detection electrodes combined with guard rings ensures homogeneous electric fields and minimizes signal loss. The purpose of this paper is to evaluate the effects of (i) reducing the surface area of the receive electrodes (i.e., receive rods) and (ii) the use of guard rings on frequency measurements by FT-ICR.



3 Volt Trapping field in Field Corrected Cell

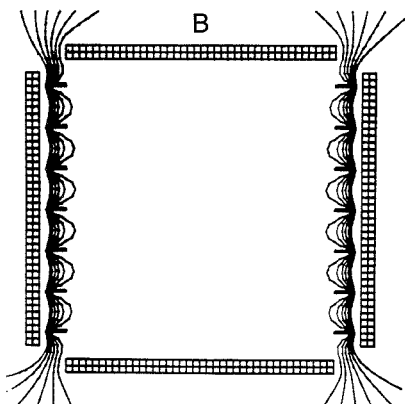


Figure 3. Computer simulation plots of the electric equipotential field lines generated by (A) an rf electric field and (B) a dc trapping field in a field-corrected cell.

### EXPERIMENTAL SECTION

All experiments were performed on a Texas A&M University (TAMU) two-section cell FT-ICR system. The system is equipped with an Oxford 3-T superconducting magnet and a Nicolet 1280 computer. In order to evaluate the effects of (i) reduction of the surface area of the receive electrodes and (ii) the use of guard rings, two different dual cell assemblies were constructed. Direct comparison of the different detectors (i.e., receive rods vis-a-vis receive plates) was accomplished by utilizing a two-section cell consisting of two cubic cells ( $3.81 \times 3.81 \times 3.81$  cm) with a common center trap plate. The detection plates of one cell were replaced with receive electrodes comprised of oxygen-free copper rods (3 mm diameter). Comparisons between the field-corrected cell that incorporates guard rings and an orthorhombic ICR cell were made in dual cell assembly consisting of both ion cell assemblies. The two cells were mounted collinearly along the central axis of the magnetic field. The two cells share a common center trap plate comprised of a stainless steel mesh to ensure pressure conditions were the same in both regions. Ions were formed in all experiments by electron impact (50-eV electrons, 200 nA) using a rhenium ribbon filament. The vacuum system was maintained by 220 L/s oil diffusion pumps. Background pressures for both sections of the vacuum system were  $1 \times 10^{-8}$  Torr or less. Gaseous reagents

were admitted to the detection regions by variable leak valves (Varian Series 951).

**Inductance-Free Resistors.** The voltage divider circuit between the shimming rings is produced by using noninductive resistors produced from Micronox resistive films. Use of noninductive resistors with rf circuits ensures linear resistance throughout the frequency range. The resistors used for the field-corrected cell (Caddock Electronics, Model No. MV261  $10 \Omega \pm 0.01\%$ ) were bench tested and proven linear in the frequency range of  $c \approx 5.0$  MHz with no propagation delay.

**Excitation Waveform Generator.** In the studies relating signal-to-noise ratio to cyclotron radius, ions of  $m/z$  78 were accelerated by single frequency excitation allowing facile calculation of the resulting cyclotron radius. The excitation waveforms were created with a LeCroy Model 9100 arbitrary waveform generator (AFG). The waveforms are created by an IBM-AT computer using LeCroy EasyWave software. The output ( $50 \Omega$ ) of the AFG is set at 1.5 V (peak to peak) and the signal is further amplified by a broad-band amplifier which outputs the rf waveform to the FT-ICR cell. Manipulation of all waveform parameters required for the excitation (i.e., sweep rate, mass window, etc.) are directly controlled by software commands from the IBM computer.

**Electrostatic Equipotential Plots.** Electrostatic contours were calculated and displayed by using the trajectory calculation program SIMION (version 4.0) on a math coprocessor equipped PC/AT type IBM compatible computer. SIMION PC/PS2 V4.0 was developed by D. C. McGilvery and modified by D. A. Dahl. The program is distributed by D. A. Dahl, Idaho National Engineering Laboratory. SIMION allows placement of electrodes in a user-defined array permitting user-defined equipotential electric field lines to be calculated for the array. The potential array used for all calculations was 100,50 points ( $x, y$  in SIMION;  $z, y$  in FT-ICR conventions). SIMION allows for potential boundary conditions in only two perpendicular directions, so the ICR cell was generated by circular rotation of the potential array about the  $X$  axis. The remainder of the parameters were set at the default settings.

### RESULTS AND DISCUSSION

The effect of reduced surface area must be evaluated in terms of the image current detected by the electrodes (i.e., signal sensitivity) and the production of harmonic signals in the frequency domain spectrum. The signal produced is proportional to the number of electric field lines produced by the ion packet which terminate on the surface of the receive plate. As illustrated in Figure 4A, the electric field lines generated by a charged ion packet terminate on the entire surface of the receive plate. The density of field lines terminating on the plate drops off as the square of the distance separating the ion packet from the plate. Reducing the area of the receive surface (Figure 4B) results in redirection of the field lines. Although some of the field lines generated by the cyclotronic packet will terminate on the steel vacuum chamber surrounding the ion cell, it is reasonable to assume that there will be negligible loss due to the distance between the cell and the vacuum chamber. Because the same number of field lines terminate on the rod (through the capacitance bridge), there is negligible loss of sensitivity compared to a larger surface area. Furthermore, the same number of field lines terminating on a smaller area increases the induced charge per unit area. The signal voltage (RMS) detected in this manner is described by eq 3 (27, 28), where  $V_s$  is the root mean square (RMS)

$$V_s(\text{RMS}) \propto (Nqr)/(dC) \quad (3)$$

voltage detected,  $N$  and  $q$  are the number and charge on the ions,  $r$  and  $d$  are the radius of the cyclotron orbit and distance between the receive plates, and  $C$  is the capacitance. Since the area of the detector plate is directly proportional to the capacitance, a reduction of the area by replacing the receive plates with rods should yield an increase in the signal voltage detected.

Figure 5 is a plot of the signal-to-noise ratio for ions of  $m/z$  78 (produced by electron impact ionization of benzene) de-

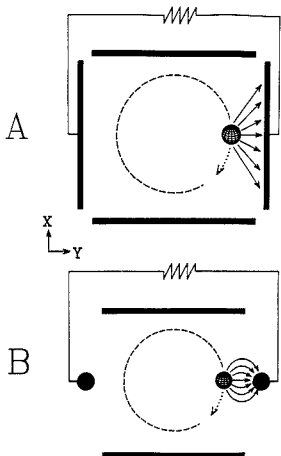


**Figure 4.** Electric field lines generated by a rotating ion packet. The same number of field lines terminate on both the plate (A) and rod (B) receive surfaces. Although some of the field lines generated by the cycloding packet will terminate on the steel vacuum chamber surrounding the ion cell, it is reasonable to assume that there will be negligible loss of signal because of the distance between the cell and the vacuum chamber.

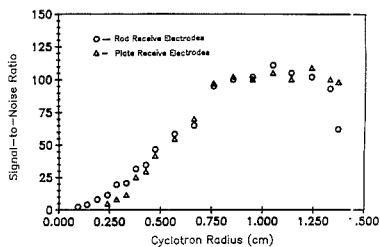


**Figure 5.** A plot of the signal-to-noise ratio for ions  $m/z$  78 as a function of radius. In this plot the relative sensitivity of receive rods vis-a-vis receive plates can be evaluated. The detected signal increases with radius resulting in an increase in the signal-to-noise ratio. It is important to note that at large cyclotron radii, the surface area of the receive plates had no effect on the signal-to-noise ratio.

ected by both plate surfaces and rod surfaces. The effect of reducing the receive surface area on detection can be investigated by comparing the signal-to-noise ratio as a function of cyclotron radius. Comparing signal-to-noise ratios as a function of cell geometry eliminates the effects of ion density differences between the two cells. Prior to excitation, the field lines produced by the random ion ensemble terminate equally on both receive surfaces resulting in common mode rejection and no detected signal. Upon excitation the ions are driven into coherence and a signal is detected. At small radii the signal detected is reduced by the produced field lines simultaneously interacting with both receive surfaces (resulting in common mode rejection) and the grounded excitation plates (resulting in loss of signal). The detected signal increases with radius resulting in an increase in the signal-to-noise ratio. It is important to note that at large cyclotron radii, the surface area of the receive plates had no effect on the signal-to-noise ratio. It can also be observed from Figure 5 that ion detection using receive rods was more sensitive to ions accelerated to small radii. This can be explained as a combination of both reduced surface area and an increased ability to drive ions into coherence. Both of these advantages result in increased performance in terms of initial ion detection.

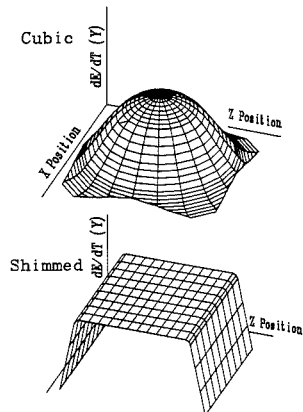


**Figure 6.** Plots of the rate at which energy is gained ( $\delta E_k/\delta t$ ) from an rf electric field applied in the Y direction) as a function of ion position in the trap. Because of the field perturbations created by the trapping and receive plates during excitation,  $\delta E_k/\delta t$  is strongly position dependent.

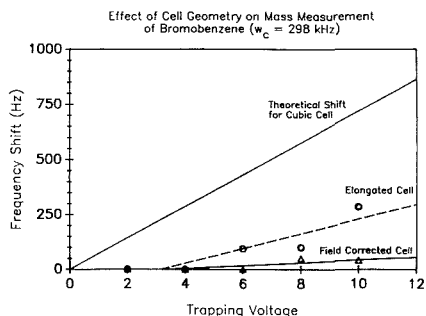


**Figure 7.** A plot of the shift in the observed frequency of bromobenzene ( $m/z$  156,  $\omega_c = 298$  kHz) as a function of cell geometry.

By regulation of the voltages applied to the rings, the field lines are redirected to produce a field that is homogeneous ( $\pm 1\%$ ) throughout ca. 95% of the dimensions of the ion cell. The increased homogeneity ( $X$ - $Y$  plane) of the rf electric field enhances the uniform acceleration of the sample ions. Figure 6 contains plots of the rate an ion gains energy ( $\delta E_k/\delta t$ ) from an rf electric field applied in the Y direction) as a function of ion position in the trap. Because of the field perturbations (cubic cell) created by the trapping and receive plates during excitation,  $\delta E_k/\delta t$  is strongly position dependent and ions which are spatially distributed along the Z axis receive different amounts of translational energy during excitation. The excitation profile for the field-corrected cell is uniform throughout the dimensions of the detection region, thus  $\delta E_k/\delta t$  is also uniform and all ions receive the same translational energy during excitation.

Figure 7 contains a plot of the shift in the observed cyclotron frequency of the bromobenzene molecular ions ( $m/z$  156,  $\omega_c = 298$  kHz) using both cell geometries. From the plot it is clear that at higher trapping potentials the perpendicular component of the electric field increases causing shifts in the observed frequency. Note that the field-corrected cell effectively shields ion detection even at high trapping potentials.

Figure 8 contains the narrow-band mass spectrum of the bromobenzene molecular ion. A trapping voltage of 10 V was used for both the cubic and field-corrected ion cells. At high trap voltage, the peak shapes produced in a cubic ICR cell

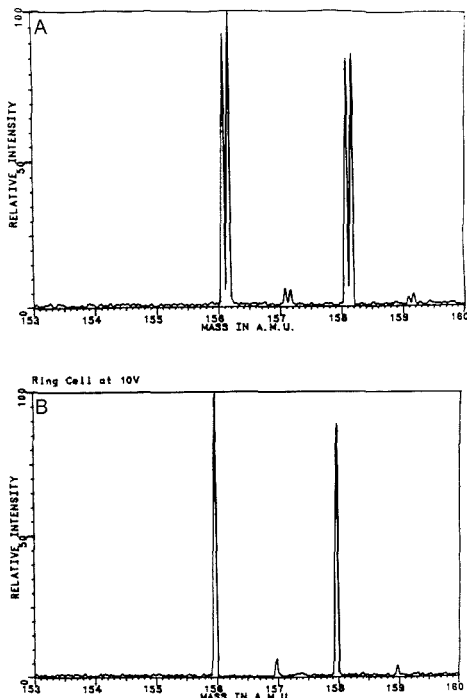


Figure 8. Narrow-band mass spectra of bromobenzene achieved at a trapping voltage of 10 V for (A) a cubic and (B) field-corrected ion cells.

are split into doublets. By reduction of the applied trapping field, a dramatic change in the peak shape is observed. Gross and Rempel have recently discussed the impact of high trapping field on peak shape and resolution (29, 30) and the signal-to-noise ratio was increased with corrected trapping fields (31).

Figure 9 contains a plot of the signal-to-noise ratio obtained for the cubic and field-corrected ICR cells. At low trapping potentials the signal-to-noise ratios are comparable (due to the limited  $E \times B$  field interaction), but at high trapping voltages the applied electric field causes a significant loss in ion signal.

#### ALTERNATIVE CELL DESIGNS

Cell designs used for ion-molecule studies do not need to incorporate shimming rings to produce a narrow kinetic energy distribution. Recently we showed that a cell constructed of receive rods and hemispherical trap plates closely mimics the field-corrected cell. The use of hemispherical trapping electrode was first suggested by Smalley and co-workers (32), but when coupled with receive rods, it is possible to produce both homogeneous excitation and trapping fields in the detection region of the ion cell. Figure 10 contains a plot of equipotential lines produced in an ion cell using hemispherical trapping electrodes. The concave geometry redirects the field lines such that a linear trapping field is approximated in the detection region. Ions that are produced outside the detection region (i.e., within the concave region of the hemispherical trap plates) are lost from the cell during excitation and do not interfere with subsequent reaction studies. The low potential gradient within the detection region results in an initial kinetic energy distribution allowing accurate low-temperature reaction

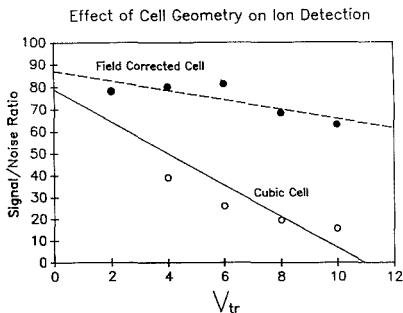


Figure 9. Plot of the signal-to-noise ratio obtained in the two ion cells. At low trapping potentials the signal-to-noise ratio is comparable due to the limited  $E \times B$  field interaction. Conversely, at high trapping voltages the effects of the applied electric field cause a significant loss in detected ion signal resulting in a reduction of the signal-to-noise ratio.

to be observed similar to the field-corrected cell. The excitation field lines are also redirected (Figure 11A) along the Z axis resulting in near-homogeneous excitation in the detection region. Shown in Figure 11B is a plot of the equipotential lines generated in the X-Y plane. Utilization of receive rods significantly reduces the radial inhomogeneities in the X-Y plane created by the interaction of the rf electric field with large receive plates.

#### PRACTICAL ASPECTS OF OPTIMUM CELL DESIGN

The performance characteristics predicted for FT-ICR have been demonstrated under conditions where the ions are trapped in the cell with thermal kinetic energies. Although the potential utility of FT-ICR for high mass detection is indicated by the recent success in the detection of laser-desorbed organic molecules (31), the loss of mass resolution of high mass ions produced in an external ion source has not yet been solved (33). At  $m/z$  values greater than 2500 amu, the duration of the time-domain is insufficient for high-resolution measurements. Ions that are injected into an ion cell from an external source require high trapping voltage to capture the translationally hot ions. Because the ions are trapped with initially high translational energy, high excitation fields or long rf excitation periods are required to produce detectable packets of ions. In a cubic FT-ICR cell the application of high electric fields produces strong potential gradients that complicate both ion trapping and detection. Therefore, a field-corrected cell is of importance when attempting to reach the theoretical potential of FT-ICR in terms of high mass biomolecules.

It is important to note that the development of a cell which eliminates  $E \times B$  field effects is equally suited for more conventional analytical application. The ability to produce and store a population of ions for extended periods of time makes FT-ICR an important technique for ion-molecule reaction studies. However, an important consideration of any energy-dependent reaction study is the initial kinetic energy distribution of the ion population. In a cubic FT-ICR cell, the initial kinetic energy distribution is determined by the trapping field. The translational energy acquired during the ionization event complicates kinetic studies. Furthermore, mass dependent Z-axis excitation and the effects of Z-axis motion in the presence of  $E \times B$  fields reduces the ability to accurately monitor ion-molecule reactions. Shimming both the excitation and trapping electric fields permits ion detection and ion storage to occur in an electric field free region. Ion production in the confines of a low potential gradient results in a narrow kinetic energy distribution. A narrow initial

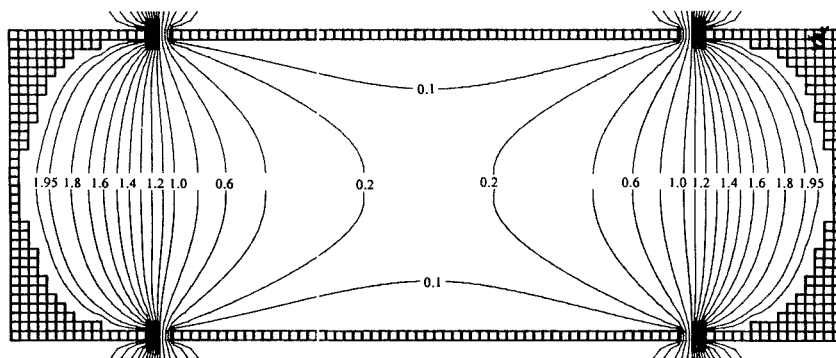


**Figure 10.** Plot of equipotential lines produced by using hemispherical trapping electrodes. The concave geometry redirects the field lines such that a linear trapping field is approximated by producing a high density of electric field lines which are perpendicular to the magnetic field. It is important to note the low potential gradient formed in the detection region of the cell relative to the potential gradient formed in a cubic ICR cell (Figure 1B).

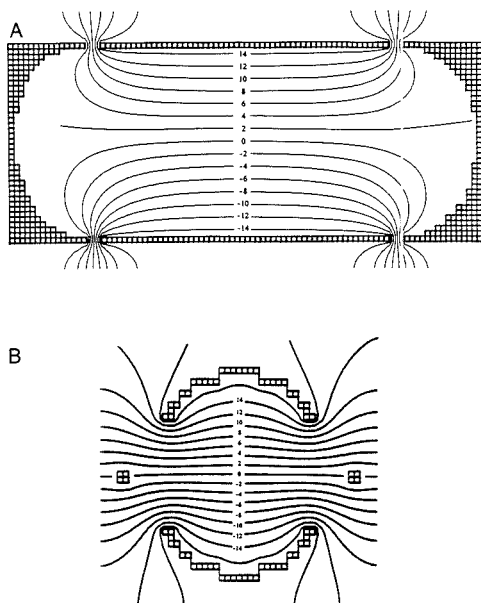


**Figure 11.** Plots of the equipotential lines generated in a cell constructed of hemispherical trapping plates in conjunction with receive rods and cylindrical excitation plates during excitation. A projection along the Z axis (A) shows that ions formed with low kinetic energies trapped in the center of the cell will experience uniform excitation. Ions that are formed at the extremes of the ion cell (and therefore acquire significant kinetic energies due to the high potential gradient) are discriminated against by the redirection of the field lines near the trap plates. A projection in the X-Y plane (B) shows that uniform excitation can be achieved regardless of ion position.

kinetic energy distribution coupled with uniform excitation greatly improves the accuracy of ion-molecule reaction measurements.

Recently, we demonstrated that phase synchronization occurs via a frequency shift induced by an applied rf excitation. Phase synchronization and production of the coherent ion packet requires a uniform excitation field. The rf excitation electric field lines produced in a cubic FT-ICR cell are distorted by the detection plates which are held at ground during excitation. The inhomogeneities result in electric field

vectors which are not uniformly applied in the Y direction. An rf electric field having a distribution of vector components in the X direction (i.e., radially inhomogeneous) causes misalignment of ions having initially different spatial locations and phase angles. Such differences in the alignments of the ions following excitation correspond to an inability to phase synchronize the ion population. In order to realize the potential of FT-ICR, modification of cell geometry to reduce the  $E \times B$  field effects is necessary.

#### ACKNOWLEDGMENT

The authors wish to thank R. E. Smalley for his helpful discussions pertaining to the effect of field line termination on ion detection. We also gratefully acknowledge the many discussions with A. G. Marshall pertaining to the process and studies of novel cell designs.

#### LITERATURE CITED

- (1) Comisarow, M. B.; Marshall, A. G. *J. Chem. Phys.* **1975**, *62*, 293.
- (2) Marshall, A. G.; Comisarow, M. B. *Anal. Chem.* **1975**, *47*, 491A.
- (3) White, R. L.; Ledford, E. B.; Ghaderi, S.; Wilkins, C. L.; Gross, M. L. *Anal. Chem.* **1980**, *52*, 1525.
- (4) Alleman, M.; Kellerhals, Hp.; Wanczek, K. P. *Int. J. Mass Spectrom. Ion Processes* **1983**, *46*, 139.
- (5) Ledford, E. B.; Ghaderi, S.; White, R. L.; Spencer, R. B.; Kulkarni, P. S.; Wilkins, C. L.; Gross, M. L. *Anal. Chem.* **1980**, *52*, 463.
- (6) Ledford, E. B.; Rempel, D. L.; Gross, M. L. *Anal. Chem.* **1984**, *56*, 2744.
- (7) Schuch, D.; Chung, K. M.; Hartmann, H. *Int. J. Mass Spectrom. Ion Processes* **1984**, *56*, 109.
- (8) Laukien, F. H. *Int. J. Mass Spectrom. Ion Processes* **1986**, *73*, 81.
- (9) Kerley, E. L.; Castro, M. E.; Hanson, C. D.; Russell, D. H., submitted for publication in *Anal. Chem.*
- (10) Sharp, T. E.; Eyster, J. R.; Li, E. *Int. J. Mass Spectrom. Ion Phys.* **1972**, *9*, 421.
- (11) Dunbar, R. C. *Int. J. Mass Spectrom. Ion Processes* **1984**, *91*, 2801.
- (12) Grese, R. P.; Rempel, D. L.; Gross, M. L. In *Fourier Transform Mass Spectrometry: Evolution, Innovation, and Applications*; Buchanan, M. V., Ed.; ACS Symposium Series 359; American Chemical Society: Washington, DC, pp 34-59.
- (13) McIver, R. T. *Rev. Sci. Instrum.* **1970**, *41*, 555.
- (14) Comisarow, M. B. *Int. J. Mass Spectrom. Ion Processes* **1981**, *37*, 251.
- (15) Grosshans, P. B.; Wang, M.; Ricca, T. L.; Ledford, E. B.; Marshall, A. G. *Proceedings of the 36th Annual Conference on Mass Spectrometry and Allied Topics, San Francisco*; American Society for Mass Spectrometry: 1988, p 592.
- (16) Hanson, C. D.; Castro, M. E.; Russell, D. F.; Shabanowitz, J. In *Fourier Transform Mass Spectrometry: Evolution, Innovation, and Applications*; Buchanan, M. V., Ed.; ACS Symposium Series 359; American Chemical Society: Washington, DC, pp 100-115.
- (17) Rempel, D. L.; Huang, S. K.; Gross, M. L. *Int. J. Mass Spectrom. Ion Processes* **1986**, *70*, 163.
- (18) Kofel, P.; Alleman, M.; Kellerhals, Hp.; Wanczek, K. P. *Int. J. Mass Spectrom. Ion Processes* **1986**, *74*, 1.
- (19) Huang, S. K.; Rempel, D. L.; Gross, M. L. *Int. J. Mass Spectrom. Ion Processes* **1986**, *72*, 15.
- (20) Grese, R. P.; Rempel, D. L.; Gross, M. L. In *Fourier Transform Mass Spectrometry: Evolution, Innovation, and Applications*; Buchanan,

- M. V., Ed.; ACS Symposium Series 359; American Chemical Society: Washington, DC, pp 34-59.
- (21) Wang, M.; Marshall, A. G. *Anal. Chem.* **1989**, *61*, 1288.
- (22) Wang, M.; Marshall, A. G. *Proceedings of the 36th Annual Conference on Mass Spectrometry and Allied Topics*, Miami, FL; American Society for Mass Spectrometry: 1989; RPA 9.
- (23) Hanson, C. D.; Castro, M. E.; Russell, D. H. *Proceedings of the 37th Annual Conference on Mass Spectrometry and Allied Topics*, Miami, FL; American Society for Mass Spectrometry: 1989; RPA 34.
- (24) Sommer, H.; Thomas, H. A.; Hipple, J. A. *Phys. Rev.* **1949**, *76*, 1877.
- (25) Sommer, H.; Thomas, H. A.; Hipple, J. A. *Phys. Rev.* **1950**, *80*, 487.
- (26) Sommer, H.; Thomas, H. A.; Hipple, J. A. *Phys. Rev.* **1951**, *82*, 697.
- (27) Shockley, W. J. *Appl. Phys.* **1938**, *9*, 635.
- (28) McIver, R. T.; Hunter, R. L.; Ledford, E. B.; Locke, M. J.; Francl, T. J. *Int. J. Mass Spectrom. Ion Processes* **1981**, *39*, 65.
- (29) Remple, D. L. *Proceedings of the 35th Annual Conference on Mass Spectrometry and Allied Topics*, Denver, CO; American Society for Mass Spectrometry: 1987, p 1124.
- (30) Remple, D. L.; Gross, M. L. *Proceedings of the 37th Annual Conference on Mass Spectrometry and Allied Topics*, Miami, FL; American Society for Mass Spectrometry: 1989; RPA 5.
- (31) Ijarres, C. F.; Wilkins, C. L. *J. Am. Chem. Soc.* **1988**, *110*, 2687.
- (32) Smalley, R. E., Department of Chemistry, Rice University, Houston, TX, private communication.
- (33) Hunt, D. F.; Shabanowitz, J.; Yates, J. R.; Zhu, N.-Z.; Russell, D. H.; Castro, M. E. *Proc. Natl. Acad. Sci.* **1987**, *84*, 620.

RECEIVED for review August 8, 1989. Accepted November 27, 1989. This work was supported by the National Science Foundation (CHE-8418457). We gratefully acknowledge the Texas A&M University Office of University Research Services and the College of Science for providing a portion of the funds for purchase of the Nicolet FTMS 1000 mass spectrometer.

## Combustion Tube Method for Measurement of Nitrogen Isotope Ratios Using Calcium Oxide for Total Removal of Carbon Dioxide and Water

Carol Kendall\* and Elizabeth Grim

U.S. Geological Survey, 431 National Center, Reston, Virginia 22092

The nitrogen isotope ratios of several organic and inorganic materials have been analyzed by a sealed-tube combustion method requiring on-line cryogenic purification and by a new sealed-tube combustion technique using CaO for the quantitative removal of CO<sub>2</sub> and water. Samples purified cryogenically are enriched in <sup>15</sup>N by an average of 0.11‰ relative to samples prepared with CaO. The enriched values of samples purified cryogenically probably result from the larger amounts of residual contaminants in samples prepared without CaO. Because samples prepared with the CaO technique require no additional purification, the technique is ideal for use with multisample mass spectrometer inlet systems.

### INTRODUCTION

In the years since Stump and Frazer (1) first proposed a dry combustion technique for the liberation of nitrogen, combustion techniques have become the preferred method for the analysis of organic and inorganic nitrogen samples for nitrogen isotopic composition. Most commonly, samples are combusted inside sealed tubes (2, 3), the tubes are cracked into a vacuum line, the contents are purified cryogenically to remove H<sub>2</sub>O and CO<sub>2</sub>, sometimes further purified by cycling through various furnaces (4), and then the nitrogen gas is concentrated before introduction into the mass spectrometer or into a sample vessel by using a Toepler pump (4), by freezing with He (5, 6), or by trapping onto a molecular sieve cooled by liquid nitrogen (7-9). The sample vessels may then be mounted on the mass spectrometer inlet system for isotope ratio measurement. Alternatively, samples may be combusted under vacuum in furnaces connected to the mass spectrometer and the purified gas frozen into a small inlet volume (10). All of these methods require considerable time and labor for the various purification and concentration steps. The recent availability of isotope ratio mass spectrometers equipped with multiple automated tube crackers makes sealed-tube tech-

niques that produce pure gas especially attractive. Such techniques have been developed for preparation of water for δD determination (11).

In their classic papers, Fiedler and Proksch (2, 12) describe their techniques and apparatus for the first multisample semiautomated inlet system for a nitrogen isotope ratio mass spectrometer. Their system enabled 80 samples to be processed per day. Samples were combusted in Pyrex tubes with copper and copper oxide, and CaO was added to absorb the resultant H<sub>2</sub>O, CO<sub>2</sub>, HCl, and other products. The low reaction temperature required by Pyrex produced incomplete yields (85-90%), which impaired precision and accuracy, making the technique unsuitable for natural abundance measurements. The authors rejected the use of quartz tubes because of cost, because of difficulty of handling, and because they found that quartz reacted with CaO at temperatures above 600 °C and cracked due to formation of calcium silicates. We have combined their use of CaO with our current 850 °C sealed-tube technique, which is modified after Macko (8), and have experienced no problem with reaction of CaO with Vycor tubes. The use of CaO results in complete removal of CO<sub>2</sub> and H<sub>2</sub>O and, hence, is ideal for use with a multiport tube-cracking inlet system.

This study compares our former and new sealed-tube combustion techniques for precision, accuracy, and ease of use. Samples prepared by either method are cracked directly into the inlet system of the mass spectrometer. However, samples prepared without CaO require cryogenic purification on-line prior to analysis, whereas samples prepared with CaO may be directly introduced into the mass spectrometer without further purification.

### EXPERIMENTAL SECTION

**Apparatus.** Samples are combusted in 9-mm Vycor tubes inside low nickel tubes in a muffle oven. The nickel tubes protect adjacent tubes from exploding if one tube explodes. After combustion, a custom-made temperature controller cools the samples for 17 h by automatically decreasing the temperature at

a rate of 50 °C per hour. A Finnigan Model 59670 12-port tube-cracker module designed for breaking 6-mm tubes inside glass cracker tubes by flexing of ball joints was modified to accept both 6-mm and 9-mm tubes.

To use the tube cracker, each tube is scored about 5 cm from the tip, a metal spring is dropped inside the cracker tube, and the sample tube is loaded into the cracker tube. The spring has two functions: to hold the Vycor tube above the base of the cracker tube so that the cracker is not strained during automatic tube cracking, and to allow tubes of various lengths to be used. The length of the spring is adjusted prior to insertion so that the score on the Vycor tube lines up with the base of the ball joint. The ball joint is liberally lubricated with Apiezon N grease, assembled, and held securely with a metal pinch clamp.

**Reagents.** Our normally used reagents and reagent-cleaning methods are as follows: Copper oxide wire (Baker Analyzed) is purified prior to use by heating in air to 600 °C for 3 h, then sieved through no. 45 mesh to remove dust. Copper metal accelerator granules (Alpha Resources, Inc., Stevensville, MI) are used without additional cleaning. CaO (Fisher Scientific) is "activated" by baking at 1000 °C for 1 h to remove absorbed water and stored in a sealed container. The Vycor tubes are baked for 4 h at 600 °C before use.

The normal cleaning method described above was compared with a higher temperature method modified after Minagawa et al. (13) where the tubes and copper oxide are heated to 850 °C for 2 h, and the copper is baked under vacuum to 750 °C for 2 h and then reduced with dry hydrogen. The Alpha copper and a finer-grained copper (Mallinckrodt, Inc., St. Louis MO) were tested for relative amounts of carbon contaminants by using the two cleaning methods.

**Procedure.** The following procedure is used in both combustion methods: 3 g of cupric oxide wire pieces is put into the 23 cm × 9 mm o.d. Vycor tube using a long-tipped funnel, followed by enough sample to produce 6–60 μM of N<sub>2</sub>, another 2 g of cupric oxide, and 5 g of copper granules. These amounts of copper and copper oxide could probably be reduced by 50%. For samples that might react with the Vycor, such as sodium nitrate, or samples on glass filters, the sample is placed inside a prebaked 6-mm o.d. Vycor tube which is then placed inside the 9-mm tube (13). If CaO is used, 10–500 mg is added after the sample and before the remaining reagents. The copper granules prevent sample and CaO powders from migrating into the vacuum system during evacuation. The tubes are evacuated and sealed to a length of about 18 cm. The tubes are shaken and vibrated with an engraving pen to mix the sample with the reagents and then combusted for 2 h at 850 °C, followed by slow cooling.

Samples prepared without CaO must be purified cryogenically. A 6-mm-o.d. stainless steel manually operated inlet system of the mass spectrometer was designed so that each sample can be purified on-line while the previously purified sample is being measured by the mass spectrometer. About two samples per hour can be purified and measured with this system. The tubes are loaded into a tube cracker (modified after Des Marais and Hayes (14), which is permanently mounted to the inlet system, and the system is evacuated. The tubes are frozen in liquid nitrogen for 15 min before loading, cracked open with the Dewar in place, and expanded into a 12-cm-long steel U-trap cooled in liquid nitrogen for an additional 15 min. These freezing times have proved necessary for total removal of H<sub>2</sub>O and CO<sub>2</sub> from 6C μM N<sub>2</sub> gas samples. At this point, the previous sample in the mass spectrometer is pumped away, the handvalve to the inlet system is opened, and the purified N<sub>2</sub> is expanded into the mass spectrometer for analysis.

Samples prepared with CaO require no further purification and are loaded in groups of up to 12 onto the multisample inlet system for computer-controlled analysis. After all the tube crackers are loaded and evacuated, the computer is started and the sample tubes are automatically cracked and analyzed under computer control. The CaO dust does not migrate out of the tubes; however, as a precaution, balls of copper wire turnings are stuffed into the inlet system between the tube cracker and pneumatic valves to protect the valve seats.

Isotope ratio measurements are performed on a Finnigan 251 EM triple-collecting mass spectrometer. After each analysis, a scan is made of the mass spectrum of the sample gas to determine

**Table I.** δ<sup>15</sup>N Values Relative to Air<sup>a</sup> of Samples Purified Cryogenically and with CaO

material	cryogenic purification	CaO purification	Δδ <sup>15</sup> N
potassium nitrate	+3.53 ± 0.10 (n = 15)	+3.49 ± 0.05 (n = 14)	0.04
ammonium sulfate	+0.57 ± 0.12 (n = 12)	+0.49 ± 0.07 (n = 15)	0.08
thiourea	-1.46 ± 0.10 (n = 9)	-1.53 ± 0.04 (n = 12)	0.07
peptone <sup>b</sup>	+6.72 ± 0.18 (n = 4)	+6.34 ± 0.17 (n = 6)	0.29
corn leaves	+3.44 ± 0.14 (n = 3)	+3.36 ± 0.16 (n = 5)	0.08
nitrogenous coal <sup>c</sup>	+7.83 ± 0.66 (n = 7)	+7.70 ± 0.05 (n = 3)	0.13
N-1 <sup>d</sup>	+0.58 ± 0.02 (n = 7)	+0.45 ± 0.05 (n = 10)	0.13
N-2 <sup>d</sup>	+20.39 ± 0.07 (n = 3)	+20.35 ± 0.02 (n = 3)	0.04

<sup>a</sup> Reported in per mil (‰) using values of -1.63 ± 0.03‰ for N-SVEC relative to NBS-14 and -2.81‰ for N-SVEC relative to Air. <sup>b</sup> Type 1 peptone. <sup>c</sup> Black band coal from Durham Basin, NC; obtained from M. D. Krohn, USGS. <sup>d</sup> International Atomic Energy Agency ammonium sulfate reference samples.

its purity. The peak heights at masses 18, 30, 32, 40, and 44 are automatically measured on the minor collector and recorded. One tube containing 120 μM of the NBS standard N-SVEC prepared by using a modification of Coplen and Kendall's (15) procedure is loaded each day to serve as a working standard and to determine the fractionation between capillaries. The precision of multiple measurements of the same gas is better than ±0.02%.

## RESULTS AND DISCUSSION

We have experienced no problems caused by weakening of either Vycor or quartz tubes by reaction of CaO with the walls of the tube. With our tube crackers, sample tubes are scored at the opposite end of the tube from the CaO so that if the tubes were weakened by reaction, they are not strained additionally. With the sample tubes being cracked *inside* the automated tube crackers, samples are not lost even if the tubes shatter upon cracking.

The nitrogen isotopic compositions of a variety of samples prepared with both the cryogenic and CaO purification techniques are given in Table I. Both techniques produce pure nitrogen with 44/29 and 18/29 mass ratios generally less than 0.03. The analytical precisions (1σ) range from ±0.02% for reagents to ±0.66% for cryogenic purification of a coal; the lower precision for natural samples is probably due to insufficient homogenization and trace contaminants. The average analytical precisions for samples prepared with and without CaO are 0.08 and 0.17%, respectively.

The mean values for cryogenically purified samples are consistently enriched in <sup>15</sup>N relative to samples prepared with CaO by 0.04 to 0.29%. The relative enrichment in <sup>15</sup>N for peptone samples prepared by the cryogenic purification method is twice the difference seen with any other type of sample. Peptone is often used as a standard because its organic complexity provides a more rigorous test of the performance of a technique than simpler materials (10). There is no correlation between the amount of isotopic fractionation and the δ<sup>15</sup>N values of these samples.

Fiedler and Proksch (2) suggested that the amount of CaO used should be twice the amount theoretically required for absorption, or about 5 mol of CaO per mole of CH<sub>2</sub>O. We used potassium nitrate, ammonium sulfate, and thiourea to determine the amount of CaO actually required to remove CO<sub>2</sub> and H<sub>2</sub>O quantitatively, and to check the effect of excess CaO on the δ<sup>15</sup>N value (Table II). These three nitrogen-bearing reagents were chosen because they contain, respectively, no carbon or hydrogen, only hydrogen, and both carbon and hydrogen. Sample sizes were chosen to produce 60 μM of N<sub>2</sub> (about 5–10 mg of sample).

The critical factor in determining the required amount of CaO to use is the amount of carbon rather than the amount of hydrogen (Table II). Use of 0.8 mol of CaO/mol of H<sub>2</sub>O

**Table II. Amount of CaO Required for Removal of CO<sub>2</sub> and H<sub>2</sub>O and Its Effect on  $\delta^{15}\text{N}$  Value<sup>a</sup>**

amt of CaO, mg	$\delta^{15}\text{N}_{\text{Air}}$		
	potassium nitrate	ammonium sulfate	thiourea
5	n.a. <sup>b</sup>	n.a.	-0.12 <sup>c</sup>
10	+3.53 ± 0.03 (n = 4)	+0.53 ± 0.04 (n = 3)	-0.25 <sup>c</sup>
50	+3.53 ± 0.01 (n = 2)	+0.48 ± 0.04 (n = 3)	-1.55 ± 0.05 (n = 3)
100	+3.47 ± 0.03 (n = 2)	+0.48 ± 0.06 (n = 3)	-1.54 ± 0.03 (n = 3)
250	+3.44 ± 0.01 (n = 2)	+0.48 ± 0.05 (n = 3)	-1.52 ± 0.04 (n = 3)
500	+3.48 ± 0.07 (n = 4)	+0.57 ± 0.08 (n = 3)	-1.52 ± 0.06 (n = 3)

<sup>a</sup> All samples produced 60  $\mu\text{M}$  of N<sub>2</sub> (5–10 mg of sample). Theoretically required amounts of CaO to absorb all the CO<sub>2</sub> and H<sub>2</sub>O produced by combustion of KNO<sub>3</sub>, (NH<sub>4</sub>)<sub>2</sub>SO<sub>4</sub>, and thiourea (as calculated from Fiedler and Proksch, 1972) are, respectively, 0, 67, and 34 mg of CaO. <sup>b</sup>Not analyzed. <sup>c</sup>No H<sub>2</sub>O (mass 18) present; however, the amount of CO<sub>2</sub> (mass 44) was more than 100 times normal background.

**Table III. Relationship between  $\delta^{15}\text{N}$  and Nitrogen Yield ( $\mu\text{M}$ ) for the CaO Technique**

total range in $\delta^{15}\text{N}$ , ‰	no. of samples	corr coeff	linear regression
0.15	n = 6	-0.540	$\delta^{15}\text{N} = -0.00017 \mu\text{M} + 0.49$
0.30	n = 6	-0.532	$\delta^{15}\text{N} = -0.00074 \mu\text{M} + 0.49$

appears sufficient to remove all H<sub>2</sub>O. On the basis of the results in Table II, we recommend using at least 15 mol of CaO/mol of carbon to ensure that all carbon is removed.

There is no correlation between the amount of excess CaO and the  $\delta^{15}\text{N}$  value for the samples tested (Table II). However, the differences in  $\delta^{15}\text{N}$  values between groups of samples prepared with different amounts of CaO are often greater than the analytical uncertainty within a group. Analytical scatter for samples prepared with 500 mg of CaO generally is slightly greater than that for samples prepared with less CaO.

Activation of the CaO improves its absorption efficiency. Fiedler and Proksch (2) suggested using CaO that was freshly activated at 1000 °C; however, we experienced no differences in absorption efficiency between freshly prepared CaO and CaO that had been stored in a bottle for 3 months. Samples containing 50 mg of unactivated CaO/5 mg of thiourea, measured on the mass spectrometer the day they were combusted, contained 50–200 times more water (mass 18), contained 2 times more CO<sub>2</sub> (mass 44), and had  $\delta^{15}\text{N}$  values enriched in

<sup>15</sup>N by up to 0.2‰ compared to samples prepared with activated CaO. However, when identical samples were left at room temperature for several weeks between combustion and analysis, all the water and CO<sub>2</sub> was absorbed by the CaO and the  $\delta^{15}\text{N}$  values were within 0.1‰ of the expected value. These limited data suggest that aging of combusted samples may increase absorption and permit use of less CaO. X-ray diffraction analysis of reacted CaO indicates the formation of Ca(OH)<sub>2</sub> and calcite; the relative amounts of CO<sub>2</sub> and water removed by chemical reaction versus absorption are unknown.

There is a slight inverse correlation between sample size and  $\delta^{15}\text{N}$  for ammonium sulfate samples prepared with the CaO purification technique (Table III). These two sets of samples, ranging from 6 to 60  $\mu\text{M}$  in size, were prepared by using the same size sample tube and quantity of reagents regardless of sample size. Because of the poor correlation and the small effect on sample  $\delta^{15}\text{N}$ , we have not corrected our results for this possible source of contamination.

Table V shows the results of an investigation of whether differences in the amounts of trace contaminants might be responsible for the enrichment of cryogenically purified samples relative to samples prepared by using CaO and for the slight enrichment of small samples relative to larger ones. For this experiment, the combustion tubes were identical in length and in weights of reagents, except for the presence of CaO. Two cleaning procedures and two varieties of granular copper were tested. Mass spectral data are all reported as ratios of peak heights, rather than as absolute intensities, to facilitate comparison with spectra produced by different mass spectrometers. Absolute amounts of N<sub>2</sub> or other gases in blanks were not calculated because of the difficulties associated with linear extrapolations of the relationships between ion intensities and amount and type of gas at low intensities.

The main contaminants that can affect the  $\delta^{15}\text{N}$  of a sample are as follows: nitrogen oxides, indicating incomplete reduction of the nitrogen with resultant isotope fractionation; carbon monoxide, with masses 28 and 29; and carbon dioxide, which produces daughter fragments with masses 28 and 29. Mass 30 (NO) is barely above background with both methods; hence, nitrogen oxide contamination is insignificant.

The critical factors in evaluating the merits of different procedures and reagents are (1) the absolute amount of the mass 28 background in the blanks and (2) amounts of masses 28 and 29 that are *not* due to N<sub>2</sub>. Because mass 14 is entirely produced from N<sub>2</sub> of mass 28, all peak heights in Table IV are reported relative to it. The best procedure is the one producing blanks (tubes with reagents but no sample) with the lowest absolute amount of mass 28 and the lowest ratios of other masses relative to mass 14.

Blanks prepared with CaO were substantially cleaner than blanks prepared without CaO and introduced into the mass

**Table IV. Amounts of Contaminants in Blanks Prepared with and without CaO, Using Different Types of Copper and Reagent-Cleaning Methods<sup>a</sup>**

CaO amt, mg	copper grain size <sup>b</sup>	reagent cleaning method <sup>c</sup>	magnitude of mass 28 peak, <sup>d</sup> %	ratios of peaks <sup>e</sup>			
				29/14	28/14	44/14	12/14
0	coarse	normal	1.7	0.41	34.1	266	12.3
0	coarse	higher T	1.1	0.33	25.8	376	7.5
0	coarse	normal/frozen	0.7	0.15	12.1	<0.1	0.1
50	fine	normal	0.7	0.16	12.1	<0.1	<0.05
50	fine	higher T	0.4	0.17	12.3	<0.1	<0.05
50	coarse	normal	0.5	0.21	11.8	<0.1	<0.05
50	coarse	higher T	0.4	0.17	11.7	<0.1	<0.05

<sup>a</sup>Blank combustion runs were prepared the same way as with samples (see text). <sup>b</sup>Two kinds of granular copper were used: fine granular copper (Mallinckrodt) and coarse-grained copper metal accelerator (Alpha). <sup>c</sup>The normal and higher temperature methods for reagent preparation are described in the text. The frozen blank was processed by using the cryogenic purification technique. <sup>d</sup>Magnitude of mass 28 peak of blanks compared to the mass 28 peak of a normal 60  $\mu\text{M}$  sample; intensities measured on the major electrometer. <sup>e</sup>Intensities measured on the minor electrometer.

spectrometer without additional purification (Table IV). Addition of CaO removes essentially all the carbon oxide species, as indicated by the low 28 peak and the low ratios of peaks produced by carbon oxides to the mass 14 peak. The cryogenically purified (frozen) blank contains slightly higher levels of contaminants than the blanks prepared with CaO. The fine-grained copper produces higher levels of contaminants than the coarser copper; the source of carbon in the finer copper cannot be removed by heating under vacuum followed by reduction with hydrogen gas. The normal cleaning procedure (no cleaning of the copper) is satisfactory if coarse Alpha copper is used with CaO.

The data in Table I demonstrate that the  $\delta^{15}\text{N}$  of samples prepared by using the cryogenic purification technique are 0.04–0.29‰ enriched in  $^{15}\text{N}$  compared to samples prepared by using CaO. The results in Table II suggest that the difference is not related to the amount of CaO, because extremely large excesses cause no additional changes in  $\delta^{15}\text{N}$  values. One explanation for the isotopic enrichment of cryogenically purified samples is the difference in the compositions of blank samples prepared with CaO and with the cryogenic purification method (Table IV). In particular, the lower amount of mass 28 and the approximately 3% lower ratio of mass 28 to mass 14 in blanks prepared with CaO and coarse copper, compared to the other blanks, are probably caused by more efficient oxidation of carbon monoxide to  $\text{CO}_2$ . Absorption of  $\text{CO}_2$  onto CaO lowers the  $\text{CO}_2$  fugacity during combustion and cooling, and necessarily causes the CO oxidation reaction to go further to completion. Because of the higher ratio of mass 29 to 28 in CO compared to  $\text{N}_2$ , significant additions of CO from contaminants in the reagents or from incomplete oxidation of refractory organics will cause enrichments in  $^{15}\text{N}$ . It is interesting to note that the sample on Table I with the greatest  $^{15}\text{N}$  enrichment of cryogenically purified samples relative to samples prepared with CaO is peptone, a sample known to be difficult to analyze with conventional techniques.

Part of the enrichment in  $^{15}\text{N}$  of cryogenically purified samples relative to the CaO-purified samples might be caused by fractionation of nitrogen gas in the inlet system at liquid nitrogen temperature. We have frequently noted that, if we expose our working standard nitrogen to an inlet system with a U-trap cooled with liquid nitrogen for long periods of time prior to expansion into the mass spectrometer, the  $\delta^{15}\text{N}$  of the gas is enriched by 0.05–0.3‰. The more thoroughly the inlet system was heated and evacuated prior to expansion and cooling the gas, the less the fractionation, suggesting that trace amounts of frozen water may be responsible for the fractionation.

Because the  $\delta^{15}\text{N}$  differences between the techniques are so small and because internationally recognized standard

values for N-1 and N-2 ammonium sulfate materials have not been established, it is difficult to demonstrate which method is more accurate. A compilation of data generated by using unspecified preparation methods in eight laboratories (16) gives mean values for N-1 and N-2 of  $+0.44 \pm 0.39\%$  and  $+20.19 \pm 0.70\%$ , respectively. Our values for samples prepared with CaO are closer to these values than the values for samples purified cryogenically.

We find that use of CaO in a sealed-tube combustion technique produces more precise and potentially more accurate  $\delta^{15}\text{N}$  values than those achieved with conventional cryogenic-purification methods. The CaO purification method is easier and faster to use because no further purification is required, and the method is ideal for use with an automated mass spectrometer inlet system. We recommend using 15 mol of activated CaO/mol of carbon; for samples of unknown carbon content, using 70 times as much CaO as sample should be sufficient.

#### ACKNOWLEDGMENT

We thank M. L. Fogel, D. J. Velinsky, E. C. Spiker, and C. J. Gwinn for valuable criticism of this manuscript.

**Registry No.** N, 7727-37-9; CaO, 1305-78-8;  $\text{CO}_2$ , 124-38-9;  $\text{H}_2\text{O}$ , 7732-18-5.

#### LITERATURE CITED

- (1) Stump, Ronald K.; Frazer, Jack W. *Nucl. Sci. Abstr.* **1973**, *28*, 746.
- (2) Fiedler, Rudolf; Proksch, Guenter *Anal. Chim. Acta* **1972**, *60*, 277–285.
- (3) Stumer, Daniel H.; Peters, Kenneth E.; Kaplan, Isaac R. *Geochim. Cosmochim. Acta* **1978**, *42*, 989–997.
- (4) Miyaki, Yasua; Wada, Eitaro *Rec. Oceanogr. Works Jpn.* **1967**, *9*, 37–53.
- (5) Freyer, H. D.; Kobel, K. *J. Phys. E.* **1975**, *8*, 712–713.
- (6) Becker, Richard H.; Clayton, Robert N. *Geochim. Cosmochim. Acta, Suppl.* **1977**, *no. 8*, 3685–3704.
- (7) Saino, T. Ph.D. Dissertation, University of Tokyo, 1977.
- (8) Macko, Stephen A. Ph.D. Dissertation, University of Texas, Austin, 1981.
- (9) Marriotti, Andre *Nature (London)* **1983**, *311*, 685–687.
- (10) Nevins, John L.; Altabet, Mark A.; McCarthey, James, J. *Anal. Chem.* **1985**, *57*, 2143–2145.
- (11) Kendall, Carol; Coplen, Tyler B. *Anal. Chem.* **1985**, *57*, 1437–1440.
- (12) Fiedler, Rudolf; Proksch, Guenter *Anal. Chim. Acta* **1975**, *78*, 1–62.
- (13) Minagawa, Masao; Winter, David A.; Kaplan, Isaac R. *Anal. Chem.* **1984**, *56*, 1859–1861.
- (14) Des Marais, David J.; Hayes, John M. *Anal. Chem.* **1976**, *48*, 1651–1652.
- (15) Coplen, Tyler B.; Kendall, Carol *Anal. Chem.* **1982**, *54*, 2611–2612.
- (16) Gonfiantini, Roberto. Advisory Group Meeting on Stable Isotope Reference Samples for Geochemical and Hydrological Investigations. Report to Director General, International Atomic Energy Agency, Vienna, 1984; 77 pp.

RECEIVED for review June 27, 1989. Accepted December 5, 1989. Use of trade names and trademarks in this publication is for descriptive purposes only and does not constitute endorsement by the U.S. Geological Survey.

# Suspended Trapping Procedure for Alleviation of Space Charge Effects in Gas Chromatography/Fourier Transform Mass Spectrometry

Jeremiah D. Hogan and David A. Laude, Jr.\*

Department of Chemistry, The University of Texas at Austin, Austin, Texas 78712

A suspended trapping pulse sequence is implemented in Fourier transform mass spectrometry detection of capillary gas chromatography effluent as a means to alleviate space charge effects in the trapped ion cell. The combination of intense ionization conditions and a suspended trapping delay extends the working range of gas chromatography/Fourier transform mass spectrometry (GC/FTMS) for which high-performance spectra are generated to 5 orders of magnitude, from detection limits of 10–100 pg to the limit of gas chromatography (GC) column capacity. This corresponds to a factor of  $10^3$  improvement compared to conventional trapping methods. Shifts in cyclotron frequency over the eluting GC peak profile are also reduced from as much as 210 Hz to less than 3 Hz over the same range of neutral analyte concentrations, which indicates accurate mass calibration can be achieved independent of initial ion population in the trapped ion cell. This capability is demonstrated as frequency assignments with low part-per-million error are obtained by GC/FTMS for mixture components of varying concentration from a single suspended trapping calibration table.

The application of Fourier transform mass spectrometry (FTMS) as a detector for capillary gas chromatography (GC) is recommended by the simultaneous ion detection, high mass resolution, and low part-per-million (ppm) error mass measurement capabilities of the spectrometer. The source/analyzer pressure conflict (1) that plagued early GC/FTMS work (2, 3) has been reconciled through the development of first the pulsed valve interface (4) and then differentially pumped external source (5, 6) and dual cell (7, 8) instrument configurations that now extend detection limits well below 1 ng without compromising the FTMS performance achieved at lower analyzer pressures. A continuing impediment to routine implementation of GC/FTMS, however, is the modest working range of the detector before space charge perturbs ion motion in the trapped ion cell (9, 10). The actual range of neutral analyte concentration for which acceptable spectra are generated for constant ionization parameters before Coulombic line broadening (11) and peak shape distortion arise, depends upon trapped ion cell capacity (12) but is only about 2 orders of magnitude in the 2 in. cubic cell. The working range for low ppm error mass measurement is even more restricted, typically less than an order of magnitude. Given that the minimum acceptable range for GC/MS performance should extend from the low picogram detection limits achieved with quadrupole and sector mass analyzers to the capacity of capillary GC columns which is typically tens of micrograms, it is necessary that present GC/FTMS performance be extended by 2 to 3 orders of magnitude to be competitive with other GC/MS instruments.

The restrictions to dynamic range imposed by Coulombic repulsive effects in the FTMS trapped ion cell are endemic to all ion trapping devices and similar problems were encountered with the ion trap detector (ITD) developed by Finnigan for GC/MS (13). The automatic gain control (AGC) solution arrived at for the GC/ITD utilizes a real-time interactive adjustment of electron ionization beam time to match ionization conditions with the expected neutral analyte population. The linear dynamic range for GC/ITD was found to improve 1000-fold with AGC as a  $10^6$  change in neutral concentration could be detected before the onset of space charge effects. An approach analogous to AGC for extending GC/FTMS performance is conceivable, but modifications to the trapped ion cell and detection circuitry to facilitate ion current monitoring and adjustment would be difficult and to date have not been implemented.

In a recent paper we described an alternative method for regulation of the ion population detected by FTMS that is based upon the suspension of trap plate potentials after the ionization event and prior to detection to permit the efflux of excess ions that contribute to space charge (14). The insertion of a suspended trapping delay of a few milliseconds was found to establish an ion population for detection that was independent of initial ionization conditions and neutral populations and yielded FTMS spectra with nearly identical relative mass intensities, mass resolution, and effective cyclotron frequencies. Application to detection of chromatographic effluent and to desorption experiments, each of which generate transient or fluctuating neutral analyte population, was suggested as a means to extend the working range for FTMS and to simplify mass calibration. In this paper the merits of suspended trapping for FTMS detection of GC effluent are evaluated.

## EXPERIMENTAL SECTION

The FTMS instrument used for all experiments is described elsewhere (14). Briefly, the system includes a 3-T superconducting magnet, a Nicolet analytical instruments dual cell assembly with 2 in. cubic cells, differential pumping with 700 L/s UHV diffusion pumps, and Nicolet FTMS-2000 data system and analog electronics. System base pressures are maintained in the mid  $10^{-9}$  Torr range as measured by Bayard-Alpert gauges mounted above the diffusion pumps outside the strong magnetic field. Electron ionization is accomplished with the standard Nicolet filament assembly mounted in the analyzer chamber. During the beam event an electron beam is gated to traverse the dual cell and strike a probe mounted collector placed 37 cm behind the source trap plate in the source chamber. Measured electron beam currents through the cell are 20% of software-requested values.

A Hewlett-Packard 5890 gas chromatograph was interfaced to the FTMS to perform the GC/FTMS measurements. A capillary split injector with 10:1 split ratio was used for sample injection onto a wide bore, short length capillary column with zero-grade helium as the carrier gas. This column was selected to increase sample capacity and to permit rapid repetitive separation of the simple mixtures used to evaluate suspended trapping performance. Methylene/hthalene separations from methylene chloride solvent

\* Author to whom correspondence should be addressed.

were performed isothermally at 50 °C. The three-component mixtures dissolved in methylene chloride were separated with a temperature program from 50 to 100 °C.

The interface to the mass spectrometer consisted of an open split measured at 100:1 at the column exit that is achieved by inserting a 100  $\mu\text{m}$  i.d.  $\times$  10 cm length of fused silica a distance of 3 cm into the GC column. The 100  $\mu\text{m}$  i.d. restrictor was connected with a zero-volume union to a 250  $\mu\text{m}$  i.d.  $\times$  2 m length of deactivated fused silica transfer line that terminated in the vacuum chamber a distance of 2 cm from the source side trapped ion cell. Source and analyzer pressures during GC experiments were  $1.1 \times 10^{-6}$  and  $1.1 \times 10^{-8}$  Torr, respectively. The transfer line to the FTMS was maintained at 100 °C with resistive heating and the FTMS vacuum system temperature was 165 °C.

FTMS data acquisition parameters were controlled with Nicolet FTMS-2000 software version 5.1R2. The suspended trapping pulse sequence used was identical with the conventional single resonance swept excitation pulse sequence (SGL) except for a variable delay event inserted after the beam event during which collector plate, source trap, conductance limit, and analyzer trap were set to 0.0 V. For all experiments a -21.5-V electron beam was used to minimize helium ion formation. Various combinations of electron beam currents, ranging from 5 to 40  $\mu\text{A}$  and beam times, ranging from 5 to 30 ms, generated desired initial ion populations. Ion equilibration between source and analyzer during the beam event with 1.3-V trap plate potentials and 0.0 V at the conductance limit yielded transfer efficiencies between 35% and 40% of the initial source population. Trap potentials for analyzer cell excitation and detection events were 1.3 V. Common to all experiments was 2.66-MHz broad-band excitation at a 3200 Hz/ $\mu\text{s}$  sweep rate. An 800-kHz bandwidth with 32K data points was used for GC/FTMS broad-band detection of the three-component mixture experiments. In experiments that examined frequency shifts in the molecular ion region of methylanthralene, narrow band detection of 16K data points over a 25.8-kHz window from masses 137 to 145 was used. Data processing of transients included base-line correction, addition of an equivalent number of zeroes, sine bell apodization, and a magnitude Fourier transform.

For the GC software subroutine employed, the minimum GC/FTMS scan time of 1.9 s was limited by the software overhead for background storage of transients to the storage module. It was found that a total of ten transients could be created and stored every 1.9 s for the broad-band experiments and four coadded transients could be stored in 1.9 s for mixer mode experiments. With typical peak widths of 10 to 20 s at the base line, the chromatographic profile was adequately defined. No threshold for data storage was used.

Chemical information extracted from spectra during post-run processing with Nicolet subroutines included relative peak height, signal to noise, peak centroid frequency, and mass resolution. In particular, the algorithm to calculate the peak centroid frequency extracts the peak maximum from the fit of an inverted parabola to the top of a sampled peak (15). Mass calibration tables were generated from spectra of perfluorotributylamine (PFTBA) that was leaked through a volatile inlet. Subsequent chromatography experiments were performed in the absence of calibrant. The software supplied calibration equation used to assign calibrant ion frequencies (16) accounts for the magnetic and trapping electric fields but does not include an ion density dependent electric field term.

## RESULTS AND DISCUSSION

**Selection of a Suspended Trapping Delay.** Application of suspended trapping to GC/FTMS measurements first requires the determination of an appropriate delay time during which excess ions exit the trapped ion cell. In previous work optimum delays of 1 to 2 ms were indicated by the suspended trapping ion flight profiles (14). However it was also noted that because the ion population remaining in the cell at extended delays was a function of cell cleanliness, the profile was not constant and occasional reevaluation of an optimum delay time would be necessary. In Figure 1a the flight of naphthalene molecular ions from the dual cell, obtained at the time of these GC/FTMS experiments, is presented. The large initial ion population at zero delay (which corresponds

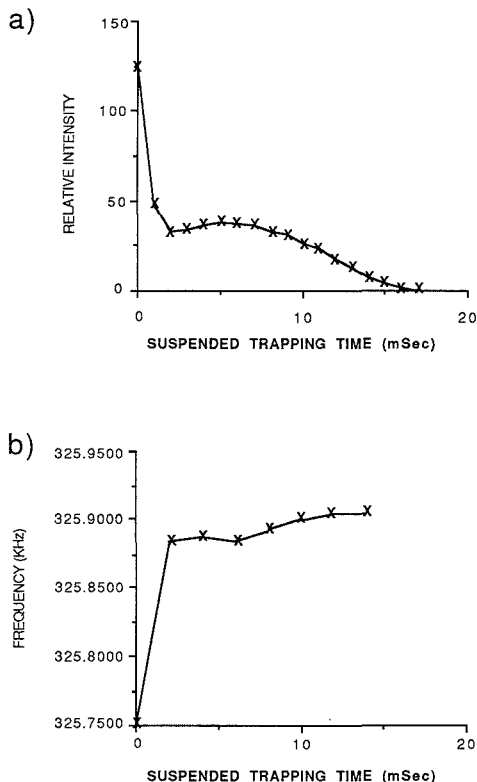


**Figure 1.** Profiles of suspended trapping ion intensity (a) and effective cyclotron frequency (b) at increasing suspended trapping delay times. Data are for the naphthalene molecular ion. Sample was leaked into the source at  $5 \times 10^{-8}$  Torr and ionized with a 10-ms, 10- $\mu\text{A}$  beam.

to the conventional ion trapping population) decays rapidly in the first several hundred microseconds due to strong local ion Coulombic forces. The sustained signal that follows is attributed both to the influx of ions during suspended trapping from the external well between the collector plate and source trap and to the low-energy ions retained in the cell due to surface charging on contaminated trap plates (17). Because the trapped ion cell had not been cleaned for several weeks, cell contamination was significant and the plateau in the ion profile extended for nearly 8 ms before the onset of a more pronounced decay.

Selection of an appropriate suspended trapping delay time is complicated in this work by the desire to generate spectra with high mass measurement accuracy. Sensitivity benefits achieved by reducing the selected delay time conflict with the expected reduction in mass measurement errors associated with smaller ion populations at longer trapping delays. As indicated in Figure 1b, the leveling of effective cyclotron frequency with increased suspended trapping delays is nearly complete at 12 ms. As a compromise between sensitivity and mass calibration requirements, a 10-ms suspended trapping time was selected for all subsequent GC/FTMS measurements. At the beginning of each work period the ion flight profile was reevaluated to ensure that suspended trapping conditions were not altered.

**Dynamic Range Enhancement.** The primary benefit of suspended trapping to GC/FTMS applications should be extension of the working range over which spectral quality

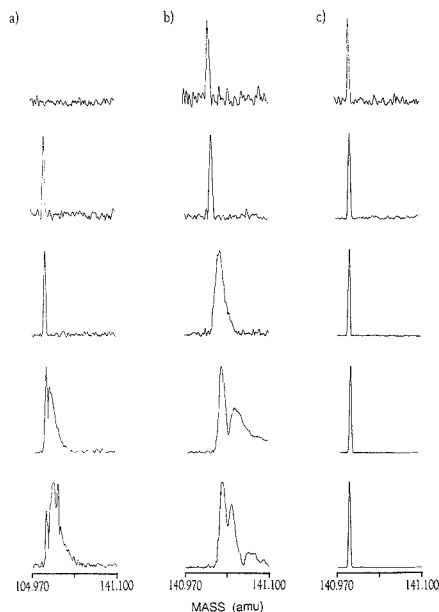


**Figure 2.** GC/FTMS spectra of methyl-naphthalene in the region around mass 141 for increasing concentrations of the analyte injected on the GC column. The estimated amounts of analyte introduced to the source are, in descending order in the figure, 10–100 pg, 100 pg–1 ng, 1–10 ng, 10–100 ng, and 50–500 ng. These absolute amounts are obtained from estimates of pre- and postcolumn split ratios, but relative ratios are correct. The maximum intensity spectrum from each GC profile is presented for three sets of ionization parameters: (a) 10- $\mu$ A electron current, 10-ms beam time with conventional trapping; (b) 40- $\mu$ A current, 30-ms beam with conventional trapping; (c) 40- $\mu$ A current, 30-ms beam with a 10-ms suspended trapping delay.

does not deteriorate due to space charge. Justification for suspended trapping detection when large neutral analyte populations elute from the GC column is apparent. However, the question arises whether this benefit is negated by a corresponding decrease in ion population for the case of small neutral populations. We argue that the signal detected for these smaller neutral populations with suspended trapping will not decrease but will actually improve, for two reasons. First, the rate of ion flight from the cell early in the suspended trapping period is reduced for smaller ion populations because ion Coulombic repulsive effects are smaller. Second, by use of stronger ionization conditions than space charge considerations would deem practical for conventional trapping experiments, the initial ion population generated would be larger.

Presented in Figure 2 are results from experiments designed to compare the working range of suspended trapping GC/FTMS with conventional trapping. The FTMS spectra presented are from GC separations in which increasing amounts of methyl-naphthalene were injected on column. For each injection the maximum intensity spectrum from the GC profile expanded in the region around mass 141 is shown. Injections were made at 11 increasing concentrations of methyl-naphthalene in solvent over a 6 order of magnitude range from below the FTMS detection limits up to the limit of GC column capacity. An examination of spectral peak shape was found to provide the best measure of the onset of space charge distortion. The data set in Figure 2a is for the ionization conditions typical of those commonly used in GC/FTMS, a 10-ms beam and a 10- $\mu$ A requested current with conventional

trapping. The first signal detected in a spectrum by spectrum search was for the GC injection that corresponded to between 100 pg and 1 ng being introduced to the source. Acceptable peak shapes were then observed for subsequent injections over a 2 order of magnitude range before obvious peak distortion in a maximum intensity file occurred. The spectra in Figure 2b are for a 30-ms beam and 40- $\mu$ A current with conventional trapping. As would be expected with more intense ionization conditions, detection limits were lowered, in this case by an order of magnitude. The ion capacity of the cell is constant, however, and again a 2 order of magnitude working range was observed before the onset of space charge. These spectra provide a clear indication of the limited accommodation of the FTMS trapped ion cell for any experiment in which the neutral population cannot be controlled.

Figure 2c presents suspended trapping spectra acquired for the identical experimental conditions that yielded the spectra in Figure 2b, with the single modification that a 10-ms suspended trapping delay time was inserted after the beam event. The most obvious feature of the suspended trapping data, in marked contrast with the data sets in parts a and b of Figure 2, is retention of peak shape quality and mass resolution over a nearly 5 orders of magnitude change in initial neutral population. The detection limit of 10–100 pg was similar to the limit found for conventional trapping. Surprisingly, spectral quality is superior for the suspended trapping case even though the number of analyte ions must be smaller. This reproducible effect may be due to a mass-dependent expulsion of lower mass background ions from air, water, and carrier gas during the suspended trapping event.

It is apparent from the data in Figure 2 that suspended trapping provides an effective approach to extending the range of FTMS detection of GC effluent. The magnitude of the improvement is similar to that observed with AGC for ion trap detectors. Suspended trapping has the advantage of being much simpler to implement because the detected ion population is self-regulating. The most important disadvantage of suspended trapping is the apparent loss of quantitative information usually available from integration of chromatographic peak areas. It can be argued however that given the already modest working range of conventional trapping FTMS measurements, this lost information is a minor inconvenience. In fact, reconstructed chromatograms from suspended trapping experiments are quite similar to those obtained by conventional trapping because if initial ion populations are within the space charge limit of the cell, then suspended trapping ion loss due to Coulombic repulsion is small. It is only for initial ion populations that exceed the space charge limit that the rate of ion loss due to Coulombic repulsive effects becomes large and quantitative information is lost. At these ion densities, however, conventional spectra also lose quantitative significance. There are, however, several approaches to regaining lost quantitative results including the use of auxiliary detectors like the flame ionization detector, implementing ion collection electrodes that monitor ion current exiting the cell during suspended trapping, or combining alternate suspended trapping and conventional pulse sequences during the GC experiment.

**Simplified Mass Calibration.** FTMS mass measurement accuracy at the low- and sub-ppm error level has been shown in numerous applications (15, 18–20), including GC/FTMS measurements in which low-ppm errors over a wide mass range in the absence of calibrant ions were demonstrated for simple synthetic mixtures (21–23). Routine low-ppm errors are possible, however, only when the analyte ion population is well controlled. Under these circumstances the important contributions to measured cyclotron frequency are a homogeneous magnetic field and the static electric trapping field. Several

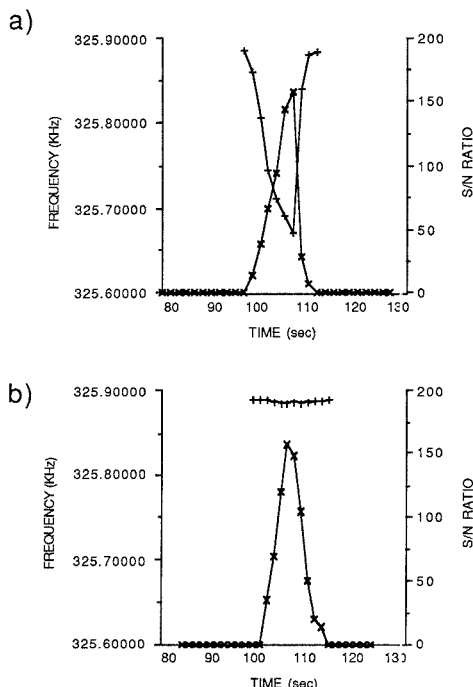


**Figure 3.** Chromatographic profile recreated for injection of 100 ng of methylnaphthalene into the GC with FTMS detection. Parameters extracted from individual FTMS spectra to yield the profiles are as follows: X, S/N of the ion at nominal mass 141; +, effective cyclotron frequency. Part a is for FTMS detection with 10- $\mu$ A beam and 10-ms beam time with conventional trapping, and part b is for 30-ms beam time and 40- $\mu$ A current with 10-ms suspended trapping time.

calibration equations that account for these two factors have been demonstrated (16). Unfortunately, as Gross and co-workers first showed, the local ion Coulombic electric field in the trapped ion cell also contributes with the trapping electric field to decrease the measured cyclotron frequency (15). Frequency shifts can be several hundred hertz for large ion populations, which renders calibration tables based solely on magnetic and trapping fields useless for other than nominal mass assignment. Calibration equations developed to account for the ion density dependent electric field (24) are effective only if the ion population is known or can be measured. This is rarely possible in routine analytical work and instead calibration equations are constructed either from ion populations similar to those expected for the analyte or at low ion densities so that the added ion Coulombic electric field term is negligible. Obviously for chromatography experiments in which neutral populations vary over several orders of magnitude, neither option is feasible. Successful accurate mass measurement studies reported in previous GC/FTMS work were obtained for mixtures with components of approximately equal concentration (21).

Suspended trapping is effective in simplifying mass calibration because the detected ion population is reduced to levels at which the ion Coulombic electric field term is negligible. It would be expected then that the measured frequency should be constant over the course of an eluting GC profile that yields spectra for a wide range of analytical concentrations. To demonstrate this, GC profiles that track the elution of a 100-ng injection of methylnaphthalene are presented in Figure 3. In Figure 3a, the signal to noise ratio (S/N) and

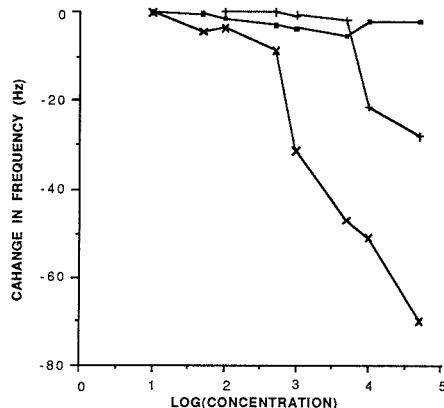


**Figure 4.** Comparison of effective cyclotron frequencies for the ion of methylnaphthalene at mass 141 for increasing concentrations injected on column. Frequencies are from spectra shown in Figure 2: X, 10 ms, 10  $\mu$ A with conventional trapping; +, 30-ms beam, 40- $\mu$ A current with conventional trapping; ■, 30-ms beam, 40- $\mu$ A current with 10-ms suspended trapping delay.

cyclotron frequency of the mass 141 ion are extracted and plotted as a function of time to obtain chromatograms for a 10- $\mu$ A, 10-ms beam experiment with conventional trapping; both parameters are observed to provide a useful measure of neutral analyte population. Unfortunately, the 210-Hz change in frequency corresponds at mass 141 for a 3-T magnet to a minimum fluctuation of about 650 ppm over the eluting GC peak if accurate mass measurement of the ion is attempted. The actual mass assignment error could be even greater if the calibration table generated for the calibrant ion population is outside the concentration range of the methylnaphthalene profile. In contrast with the results in Figure 3a, the S/N profile for suspended trapping also mimics the conventional trapping result but the frequency profile varies by less than 3 Hz, which suggests the possibility of low ppm error in mass measurement for fluctuating neutral populations.

To better assess the effective range of suspended trapping for improved mass calibration, frequency values from the spectra in Figure 2 were extracted and are plotted in Figure 4. As expected, large frequency shifts for conventional trapping spectra both precede and then accompany Coulombic broadening and peak distortion. The use of a 30-ms beam and 40- $\mu$ A current with conventional trapping apparently creates such a large trapped ion cell population (including both analyte and background ions) that mass calibration would be difficult over any concentration range. Better results would be expected with a 10-ms beam and 10- $\mu$ A current as the frequency shift of less than 10 ppm over a 10- to 100-fold concentration change suggests. Clearly, however, the coupling of suspended trapping with intense initial ionization affords the best performance as frequencies corresponding to less than a 10 ppm change are exhibited over the entire 5 order of magnitude range accessible to GC/FTMS.

Application of suspended trapping FTMS mass calibration to fluctuating GC populations is now demonstrated. The accurate mass data presented in Table I are from GC/FTMS analyses of two mixtures of *p*-xylene, methylnaphthalene and bromonaphthalene, one with components in equal concentration by weight and the other with concentrations varying by 2 orders of magnitude. Frequencies were assigned to the electron ionization fragments by interpolation of a PFTBA calibration table constructed just prior to the GC/FTMS experiments with the same ionization conditions and sus-

**Table I. Accurate Mass Data for Suspended Trapping GC/FTMS Measurements of a Three-Component Mixture**

	calculated mass, amu	measured mass, amu	error, ppm
<b>mixture 1<sup>a</sup></b>			
bromonaphthalene	207.970 516	207.972 122	-7.7
	205.972 562	205.973 117	-2.7
	127.054 226	127.055 73	-11.9
methylnaphthalene	142.077 701	142.078 650	-6.7
	141.069 876	141.070 110	-1.7
	115.054 226	115.055 040	-7.1
<i>p</i> -xylene	106.077 701	106.078 098	-3.7
	91.054 226	91.054 633	-4.8
	77.038 576	77.040 307	-22.5
<b>mixture 2<sup>b</sup></b>			
bromonaphthalene	207.970 516	207.967 230	+15.8
	205.972 562	205.972 790	-1.1
	127.054 226	127.055 172	-7.4
methylnaphthalene	142.077 701	142.078 440	-5.2
	141.069 876	141.069 900	-0.2
	115.054 226	115.054 850	-5.7
<i>p</i> -xylene	106.077 001	106.077 820	-1.1
	91.054 226	91.054 530	-2.9
	77.038 576	77.038 920	-4.5

<sup>a</sup> Equal amounts by weight of each compound were injected with approximately 10 ng of each entering the source. <sup>b</sup> Mixture components in the ratio of 100 ng of *p*-xylene, 10 ng of methylnaphthalene, and 1 ng of bromonaphthalene entering the source.

pended trapping time. Errors for the two mixtures averaged 7.6 and 7.3 ppm for nine fragment ions and are consistent with previous wide-band accurate mass GC/FTMS measurements for specific acquisition parameters used (21). The primary source of error for the data in Table I is associated not with the suspended trapping event but rather with the inadequate number of data points used to define the bandwidth. This is reflected by the increase in error for higher mass ions. Errors on the order of 2 to 3 ppm could be achieved out to mass 300, but this would require a reduction in bandwidth or increase in the number of data points acquired, which is not always feasible (21). The advantage of suspended trapping demonstrated here is not a reduction in absolute error of the measurement compared to static system measurements but rather the opportunity to obtain low ppm errors from mixture components differing by orders of magnitude in concentration from a single calibration table. With little concern given to either analyte or calibrant neutral populations, the leveling effect of suspended trapping should permit assignment of elemental composition for the relatively low mass ions encountered in GC/FTMS.

One possible limitation of suspended trapping that has not been addressed is the skewing of relative abundances compared to conventional spectra. The reason for this mass discrimination effect is that if all ions possess similar kinetic energies independent of mass, then during the suspended trapping event lower mass ions with higher velocities would preferentially exit the cell. Although this effect is observed, the skewing of relative peak intensities does not follow that expected from simple time-of-flight considerations. For example, the comparison electron ionization spectra in Figure 5 are from the suspended trapping GC/FTMS separation of the three-component mixture used to produce the data in Table I and from conventional trapping measurements of pure samples introduced through a volatile inlet. Two explanations are given for the nearly identical relative intensities. First, ions created in the external reservoir enter the trapped ion cell during suspended trapping thereby forming a more uniform distribution of the ion population to be detected. Second, the population of low-energy ions continuously retained in the cell by charging on the trap plates should be

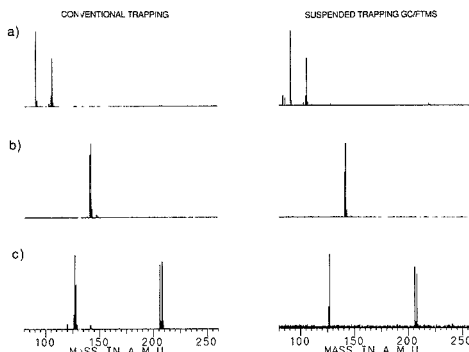


**Figure 5.** Suspended trapping GC/FTMS and conventional trapping FTMS spectra of *p*-xylene, methylnaphthalene, and bromonaphthalene in parts a, b, and c, respectively. Suspended trapping spectra are from the three-component mixture analyzed by GC/FTMS to yield accurate mass data in Table I. Ionization parameters included a -21.5-eV beam energy, 30-ms beam, 40- $\mu$ A beam current, and 10-ms suspended trapping delay. Conventional trapping spectra are for pure samples introduced through a variable leak valve and detected with -21.5-eV beam energy, 10-ms beam, and 10- $\mu$ A current.

representative of the ion population formed during the electron beam. If this population represents a significant fraction of the ions detected, then mass discrimination would be reduced proportionally.

**Summary.** A suspended trapping FTMS pulse sequence suggested as a means to eliminate space charge effects in spectra acquired from fluctuating neutral analyte populations is applied to GC/FTMS. By combination of intense ionization conditions with an appropriate suspended trapping delay, the working range extends from low picogram detection limits to the capacity of the GC column. GC/FTMS detection of complex mixtures should now be feasible. An additional benefit of the suspended trapping event is that the shift in cyclotron frequency associated with ion Coulombic repulsion is minimized so that a single mass calibration table is sufficient to generate data point limited low ppm error accurate mass measurement over the range of neutral concentrations.

#### LITERATURE CITED

- Lauce, D. A., Jr.; Juhlman, C. L.; Brown, R. S.; Weil, A.; Wilkins, C. L. *Mass Spectrom. Rev.* **1986**, *5*, 107-166.
- Ledford, E. B., Jr.; White, R. L.; Ghaderi, S.; Wilkins, C. L.; Gross, M. L. *Anal. Chem.* **1980**, *52*, 2450-2451.
- White, R. L.; Wilkins, C. L. *Anal. Chem.* **1982**, *54*, 2211-2215.
- Sack, R. M.; Gross, M. L. *Anal. Chem.* **1983**, *55*, 2419-2421.
- McIver, R. T., Jr.; Hunter, R. L.; Bowers, W. D. *Int. J. Mass Spectrom. Ion Processes* **1985**, *64*, 67-77.
- Kofel, P.; Allemann, M.; Kellerhaals, H.; Wanczek, K. P. *Int. J. Mass Spectrom. Ion Processes* **1985**, *67*, 97-103.
- Kofel, P.; Allemann, M.; Kellerhaals, H.; Wanczek, K. P. *Int. J. Mass Spectrom. Ion Processes* **1989**, *87*, 237-247.
- Giancaspro, C.; Vardun, F. R.; Muller, J. F. *Int. J. Mass Spectrom. Ion Processes* **1986**, *72*, 63-71.
- Wang, T. L.; Ricca, T. L.; Marshall, A. G. *Anal. Chem.* **1986**, *58*, 2931-2938.
- Jeffries, J. B.; Barlow, S. E.; Dunn, G. H. *Int. J. Mass Spectrom. Ion Processes* **1983**, *54*, 169-187.
- Wang, T.-C.; Marshall, A. G. *Int. J. Mass Spectrom. Ion Processes* **1986**, *68*, 287-301.
- Hunter, R. L.; Sherman, M. G.; McIver, Jr., R. T. *Int. J. Mass Spectrom. Ion Processes* **1983**, *50*, 259-274.
- Staford, G. C.; Taylor, D. M.; Bradshaw, S. C.; Syka, J. E. P. *Proceedings of the 35th ASMS Conference on Mass Spectrometry and Allied Topics, Denver, CO, May 24-29, 1987*; pp 775-776.
- Lauce, D. A., Jr.; Beu, S. C. *Anal. Chem.* **1989**, *61*, 2422-2427.
- Ledford, E. B., Jr.; Ghaderi, S.; White, R. L.; Spencer, R. B.; Kulkarni, P. S.; Wilkins, C. L.; Gross, M. L. *Anal. Chem.* **1980**, *52*, 463-466.
- Ledford, E. B., Jr.; Rempel, D. L.; Gross, M. L. *Anal. Chem.* **1984**, *56*, 274-274B.
- Rempel, D. L.; Huang, S. K.; Gross, M. L. *Int. J. Mass Spectrom. Ion Processes* **1986**, *70*, 163-184.
- White, R. L.; Onyifuka, E. C.; Wilkins, C. L. *Anal. Chem.* **1983**, *55*, 339-343.

- (19) Shomo, R. E., II; Marshall, A. G.; Weisenberger, C. R. *Anal. Chem.* **1985**, *57*, 2940-2944.
- (20) Rempel, C. L.; Ledford, E. B.; Sack, T. M.; Gross, M. L. *Anal. Chem.* **1989**, *61*, 749-754.
- (21) Juhlman, C. L.; Laude, D. A., Jr.; Wilkins, C. L. *Anal. Chem.* **1985**, *57*, 1040-1044.
- (22) Sack, R. M.; McCreery, D. A.; Gross, M. L. *Anal. Chem.* **1985**, *57*, 1290-1295.
- (23) Laude, D. A., Jr.; Juhlman, C. L.; Brown, R. S.; Ijames, G. F.; Wilkins, C. L. *Anal. Chim. Acta* **1985**, *19978*, 67-77.
- (24) Franci, I. J.; Sherman, M. G.; Hunter, R. L.; Locke, M. J.; Bowers, W. D.; McIver, R. T., Jr. *Int. J. Mass Spectrom. Ion Processes* **1984**, *54*, 189-199.

Received for review September 8, 1989. Accepted November 27, 1989. This work is supported by the Welch Foundation and by a grant from the Texas Advanced Technology and Research Program.

## Carbon-Isotopic Analysis of Dissolved Acetate

Jeffrey T. Gelwicks<sup>1</sup> and J. M. Hayes\*

*Biogeochemical Laboratories, Departments of Chemistry and of Geology, Indiana University, Bloomington, Indiana 47405*

Heating of dried, acetate-containing solids together with oxalic acid dihydrate conveniently releases acetic acid for purification by gas chromatography. For determination of the carbon-isotopic composition of total acetate, the acetate-containing zone of the chromatographic effluent can be routed directly to a combustion furnace coupled to a vacuum system allowing recovery, purification, and packaging of CO<sub>2</sub> for mass-spectrometric analysis. For analysis of methyl carbon, acetic acid can be cryogenically trapped from the chromatographic effluent, then transferred to a tube containing excess NaOH. The tube is evacuated, sealed, and heated to 500 °C to produce methane by pyrolysis of sodium acetate. Subsequent combustion of the methane allows determination of the <sup>13</sup>C content at the methyl position in the parent acetate. With typical blanks, the standard deviation of single analyses is less than 0.4‰ for acetate samples larger than 5 μmol. A full treatment of uncertainties is outlined.

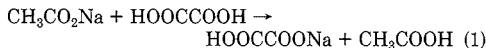
### INTRODUCTION

Acetate, a product of anaerobic microbial metabolism and an intermediate in the degradation of organic matter, is a substrate for both methanogenic and sulfate-reducing bacteria. Variations in the carbon-isotopic composition of sedimentary methane have been related to the distribution of acetate between these pathways of degradation (1, 2). Further study of this segment of the carbon cycle will be aided by techniques allowing determination of the isotopic composition of sedimentary acetate and of isotope effects associated with its production and degradation.

Although numerous techniques are available for measurement of concentrations of acetate in sediments and in aqueous media (3-9), reports of the carbon-isotopic composition of acetate in natural solutions are much less common (10-12). Because accurate measurement of low concentrations of acetate is difficult, vacuum distillation (13) and passive diffusion (14) have been employed to concentrate acetate in samples. However, the sample-size requirement for isotopic analyses generally limits the application of current isotope procedures to samples with acetate concentrations greater than 100 μM (10-12). Because concentrations of acetate are less than 50 μM in most marine and freshwater sediments (8, 15, 16), isotopic analyses of acetate in these environments have

not been achieved. We have developed techniques in which the carbon-isotopic composition of acetate and its methyl carbon can be measured in aqueous solutions at concentrations down to 20 μM. In this procedure, separation of acetate from other organic components, combustion of the acetate, and collection of the resultant CO<sub>2</sub> are combined.

Quantitative distillation of acetic acid from acidified aqueous solutions is impractical. Water and acetic acid codistill; quantitative removal of acetic acid requires quantitative removal of water from the sample and little is gained. Accordingly, we first evaporate water (after adjusting pH to prevent loss of acetic acid), then evaporate acetic acid from acidified residual solids. Acidification must be accomplished with an acid that (1) is strong enough to protonate acetate quantitatively to acetic acid, (2) will not superprotonate acetic acid, forming an involatile cation, and (3) is nonaqueous. Gaseous HCl will protonate solid acetate salts, but HCl is much more volatile than acetic acid. Evaporation of a mixture of NaCl and acetic acid yields HCl, not acetic acid. In contrast, oxalic acid dihydrate (pK<sub>a1</sub> = 1.23, pK<sub>a2</sub> = 4.29 at 25 °C) can protonate acetate and has other advantages. As a solid, it can be mixed with an acetate-containing powder with almost no reaction occurring until the oxalic acid is melted (mp = 101.5 °C). A mixture of acetate and oxalic acid dihydrate, when heated to melt the oxalic acid dihydrate and dissolve the acetate, will yield acetic acid by the reaction



The acetic acid can be volatilized and removed from the sample with the residual solids remaining in the reaction vessel. The purified acid can be handled as a gas in a vacuum line (13) and transferred to combustion tubes by cryogenic distillation (11).

### EXPERIMENTAL SECTION

**Apparatus.** The acetate-preparation system consists of a reaction vessel, a gas chromatograph, a combustion furnace, and a glass vacuum system (Figure 1). A disposable 6 cm × 9 mm o.d. Pyrex tube attached by an O-ring-sealed compression fitting (Cajon Ultratorr) to a U-trap at the inlet of a gas chromatographic column serves as a reaction vessel for liberation of acetate from samples. A Hewlett-Packard 5700A gas chromatograph was fitted with a 2.5 m × 4 mm i.d. Pyrex column packed with 80-100 mesh Porapak Q and was conditioned at 200 °C for 24 h prior to use. An external, dual-filament (gold sheathed tungsten), thermal conductivity detector (Gow-Mac, Model 10-301) is maintained at an operating temperature of 100 °C and a filament current of 150 mA. The flow rate of the carrier gas, helium, is 20-25 mL/min;

<sup>1</sup> Merck Chemical Manufacturing Division, Merck and Co., Inc., P. O. Box 2000, Rahway, NJ 07065-0904.

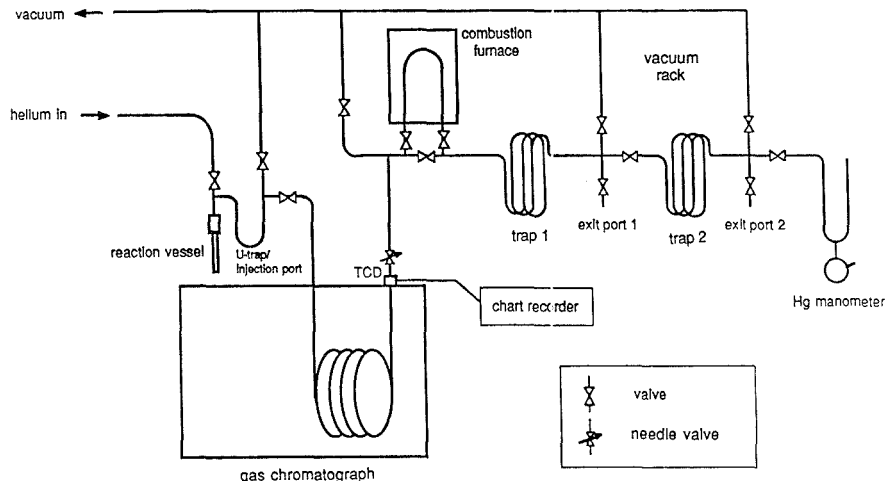


Figure 1. System for separation and combustion of acetic acid.

helium is drawn through the column at a rate set by the needle valve at the end of the column. The absolute helium pressure at the inlet of the gas chromatograph is 1000 Torr.

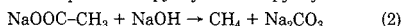
The vacuum system was constructed from 9-mm Pyrex tubing and consists of two three-loop traps and several 5-mm stopcocks (O-ring seals, Kel-F stems, Kontes). A 10 cm  $\times$  9 mm quartz tube packed with cupric oxide (wire form) is attached to the rack by O-ring-sealed compression fittings and is maintained at a temperature of 850 °C for the combustion of eluting compounds. Helium pressure downstream from the needle valve is less than 2 Torr. The water and CO<sub>2</sub> resulting from combustion are removed from the gas stream by traps cooled by pentane slush (-131 °C) and by liquid nitrogen.

**Reagents.** Two isotopically different samples of reagent-grade sodium acetate used as standards were dried at 100 °C for 24 h and stored in a desiccator until use. Standards were prepared for analysis of total carbon isotopic composition by sealed tube combustion (17, 18). Combustion of sodium acetate yields not only CO<sub>2</sub> and water but also sodium oxide, and in the conventional, sealed-quartz-tube technique, sodium oxide captures CO<sub>2</sub> as the combustion tube is cooled. Yields of CO<sub>2</sub> can be low, and isotopic analyses inaccurate. To neutralize sodium oxide, 50–250  $\mu$ L of 102.1% H<sub>3</sub>PO<sub>4</sub> was added to each combustion tube before evacuation. The abundance of <sup>13</sup>C in the methyl carbon of acetate standards was determined by analysis of methane produced by pyrolysis of acetate in the presence of excess NaOH (10, 19).

**Procedure.** Aliquots of standards were placed in a reaction vessel and mixed with excess oxalic acid dihydrate. The atmosphere in the reaction vessel was then replaced with ~500 Torr of helium from the carrier gas. Heating the reaction vessel until the oxalic acid melted resulted in the protonation of sodium acetate, yielding acetic acid. The acetic acid, along with other volatile compounds in the reaction vessel, was distilled under vacuum to the U-trap/injection port at the inlet of the gas chromatograph column. The volatile components were admitted to the chromatographic column by opening the valve between the trap and the column and beginning the flow of helium through the trap.

Temperature programming (100–150 °C) provided separation of the acetic acid from water and other volatiles. As acetic acid eluted from the column, the flow of gas was routed through the combustion furnace and traps 1 and 2; other compounds were removed by vacuum as they eluted. The resultant CO<sub>2</sub> was cryogenically distilled and collected for isotopic analysis.

To determine the isotopic composition of the methyl carbon of acetate, the gas chromatographically purified acetic acid was trapped on NaOH pellets and pyrolyzed. The pyrolysis reaction



selectively evolves methane from the methyl group of acetate (10, 19) at a reaction temperature of 500 °C. Pyrolysis of organic materials can yield traces of methane; therefore, the material to be pyrolyzed must contain only acetate. The methane produced was either (1) transferred by use of a Toepler pump to a quartz tube containing cupric oxide and combusted at 850 °C, or (2) trapped on Porapak Q at -196 °C and passed through a cupric oxide furnace (850 °C) for combustion. Products of combustion from either method were cryogenically purified and the CO<sub>2</sub> was collected for isotopic analysis.

Carbon isotope ratios were measured with Nuclide 6-60 (20) and Finnigan MAT Delta E isotope ratio mass spectrometers. Results are reported in terms of the delta notation

$$\delta^{13}\text{C}_{\text{PDB}} = [(R_{\text{sample}} - R_{\text{PDB}})/R_{\text{PDB}}] \times 1000 \quad (3)$$

where  $R = {}^{13}\text{C}/{}^{12}\text{C}$  and  $R_{\text{PDB}} = 0.0112372 \pm (9.0 \times 10^{-6})$ . Units for  $\delta$  are parts per thousand, termed "permil", and assigned the symbol ‰.

**Calculations.** For any sample, the measured  $\delta$  value is a weighted average of the  $\delta$  values of the sample itself and of the procedural blank

$$n_T \delta_T = n_s \delta_s + n_b \delta_b \quad (4)$$

where  $n$  terms represent molar quantities of carbon and subscripts refer to total CO<sub>2</sub> (T), sample (s), and blank (b). Since

$$n_T = n_s + n_b \quad (5)$$

eq 4 can be rearranged to yield

$$\delta_T = n_b(\delta_b - \delta_s)/n_T + \delta_s \quad (6)$$

an equation of the form  $y = mx + b$ . For multiple analyses of the same sample, regression of  $\delta_T$  on  $1/n_T$  will yield  $\delta_s$  as the intercept. (Both  $\delta_T$  and  $1/n_T$  are subject to error. Accordingly, derivation of the "major axis" is more appropriate than the simple regressor of  $y$  on  $x$ . If this is done, care must be taken that points at low values of  $1/n_T$ , which lie closest to  $\delta_s$ , are given high weighting factors. In practice, regression of  $\delta_T$  on  $1/n_T$  is far simpler and yields accurate results.) The slope of the line specified by eq 6 is

$$m = n_b(\delta_b - \delta_s) \quad (7)$$

Where analyses of two samples have yielded different slopes ( $m_1$ ,  $m_2$ ) and  $\delta_s$  values ( $\delta_1$ ,  $\delta_2$ ), two independent equations of this form can be written. Simultaneous solution allows determination of  $n_b$  and  $\delta_1$

$$n_b = (m_1 - m_2)/(\delta_2 - \delta_1) \quad (8)$$

$$\delta_b = (m_2 \delta_1 - m_1 \delta_2)/(m_2 - m_1) \quad (9)$$

Table I. Comparison of  $\delta^{13}\text{C}$ -total acetate and  $\delta^{13}\text{C}$ -methyl group from standard techniques and described method<sup>a</sup>

std	STC <sup>b</sup>	total acetate		methyl carbon	
		eq 10 <sup>c</sup>	regression	batch	this procedure
I	-29.52 ± 0.06 (3)	-29.33 ± 0.31 (5)	-29.27 ± 0.11 (5)	-28.27 ± 0.16 (4)	-28.36 ± 0.36 (4)
II	-17.47 ± 0.15 (2)	-17.43 ± 0.20 (5)	-17.32 ± 0.10 (4)	-20.76 ± 0.12 (3)	-20.78 ± 0.04 (4)

<sup>a</sup>Uncertainties are 95% confidence limits; numbers in parentheses indicate number of analyses. <sup>b</sup>Sealed-tube combustion. <sup>c</sup>Background corrected using  $n_b = 1.5 \pm 0.3$ ,  $\delta_b = -25 \pm 3\%$ .

When  $n_b$  and  $\delta_b$  are known, results of individual analyses can be corrected by use of eq 10

$$\delta_s = (n_T \delta_T - n_b \delta_b) / (n_T - n_b) \quad (10)$$

Where the  $\delta$  value for an acetate sample is determined by regression, extension of the regression calculations can yield an estimate of the standard deviation of the intercept and, thus, the uncertainty in  $\delta_s$ . If  $\delta_s$  is derived by correction for blank effects (eqs 8-10), the uncertainty assigned to  $\delta_s$  will depend on uncertainties in  $n_b$  and  $\delta_b$ . From

$$\sigma_{n_b}^2 = \left( \frac{\partial n_b}{\partial m_1} \right)^2 \sigma_{m_1}^2 + \left( \frac{\partial n_b}{\partial m_2} \right)^2 \sigma_{m_2}^2 + \left( \frac{\partial n_b}{\partial \delta_1} \right)^2 \sigma_{\delta_1}^2 + \left( \frac{\partial n_b}{\partial \delta_2} \right)^2 \sigma_{\delta_2}^2 \quad (11)$$

we obtain

$$\sigma_{n_b}^2 = (1/D^2)[\sigma_{m_1}^2 + \sigma_{m_2}^2 + (M^2/D^2)(\sigma_{\delta_1}^2 + \sigma_{\delta_2}^2)] \quad (12)$$

where, with the exception of  $\sigma_{n_b}$ , the calculated standard deviation of  $n_b$ , the  $\sigma$  terms are standard deviations derived from regression calculations,  $M = m_1 - m_2$ , and  $D = \delta_1 - \delta_2$ . By a similar propagation of uncertainties, we obtain

$$\sigma_{\delta_b}^2 = (1/M^2)[(D^2/M^2)(m_2^2 \sigma_{m_1}^2 + m_1^2 \sigma_{m_2}^2) + m_2^2 \sigma_{\delta_1}^2 + m_1^2 \sigma_{\delta_2}^2] \quad (13)$$

and, finally

$$\sigma_{\delta_s}^2 = (1/N^2)[(E^2/N^2)(n_b^2 \sigma_{n_T}^2 + n_T^2 \sigma_{n_b}^2) + n_T^2 \sigma_{\delta_T}^2 + n_b^2 \sigma_{\delta_b}^2] \quad (14)$$

where  $N = n_T - n_b$  and  $E = \delta_T - \delta_b$ .

## RESULTS AND DISCUSSION

Results of multiple analyses of two standards are graphically summarized in Figure 2. As shown in Table I, the value of  $\delta_s$  obtained by regression calculations is in good agreement with that obtained by sealed-tube combustion in the case of standard II but slightly discrepant (by at least 0.08‰) in the case of standard I. The reason for this disagreement is not known, though it is possible that standard I contains an impurity depleted in  $^{13}\text{C}$ . An impurity would affect the result of the sealed-tube combustion procedure but would be removed prior to combustion in the chromatographic procedure.

**Blanks.** For the present system, analyses of acetate-free samples yielded  $n_b = 1.1 \pm 0.6 \mu\text{mol C}$  and  $\delta_b = -13 \pm 5\%$  (means and standard deviations of populations,  $n = 5$ ). To evaluate these results, consider the graphs shown in Figure 2. In each case, as  $1/n \rightarrow \infty$ ,  $\delta_T \rightarrow \delta_b$ . Although  $\delta_b$  cannot be evaluated directly, the slopes of the lines indicate that  $\delta_b$  must be greater than -29.3‰ (the regression line for analyses of standard I slopes upward from that value) and less than -17.3‰ (the regression line for analyses of standard II slopes downward from that value). Accordingly, the  $\delta_b$  values obtained by analyses of acetate-free samples must be inaccurate.

Application of eqs 8 and 9 can yield improved estimates of  $n_b$  and  $\delta_b$ . Here, comparison of results of analyses of standards I and II yields  $n_b = 1.5 \pm 0.1 \mu\text{mol C}$  and  $\delta_b = -25.5 \pm 0.4\%$ . If these values are used to correct the results of individual analyses, accurate results are obtained (Table I, column headed "eq 10"), but precision, as assessed by eq 14, is not as good as that obtained by the regression technique.

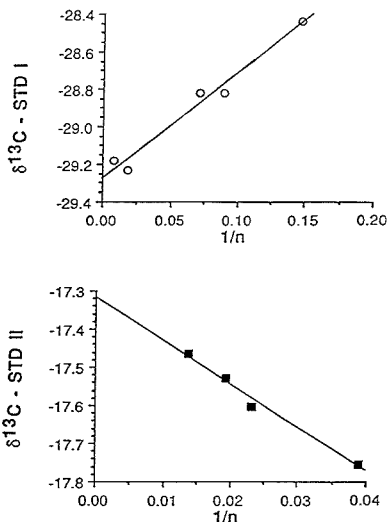


Figure 2. Data from analyses of standards plotted to demonstrate the straight-line relationship of eq 6. Values for standard I are  $\delta_s = -29.27 \pm 0.11\%$  and  $m = 5.60 \pm 0.52$  and for standard II are  $\delta_s = -17.32 \pm 0.10\%$  and  $m = -11.99 \pm 1.30$ .

There is, moreover, a question regarding the *realism* of such corrections. Contrary to underlying assumptions, the values of  $\delta_b$  and  $n_b$  may not be constant.

To examine fluctuations in the blank, results of repeated analyses of standard I were compiled (Table II). The dates of the analyses span more than 3 years. Because the same sample has been analyzed repeatedly, all observed variations must be due to variations in either or both  $n_b$  and  $\delta_b$ . In each case,  $n_T$  is known from measurement of the yield of gas. To estimate the magnitude of variations in  $\delta_b$ , it can be assumed that  $n_b$  was constant at  $1.5 \mu\text{mol C}$ . Then, if  $\delta = -29.27\%$  is accepted as the isotopic composition of standard I, application of eq 10 allows calculation of  $\delta_b$  for each analysis. Values obtained range from -22.05 to -33.15‰. Since apparent values of  $\delta_b$  vary by more than 11‰, an appropriate value for  $\sigma_{\delta_b}$  must be considerably greater than 0.4‰ (the result of application of eq 9 to data collected over a short time interval). With the goal of taking into account temporal variations in the blank as well as random errors in the determination of its characteristics, values might be assigned as follows:  $n_b = 1.5$ ,  $\sigma_{n_b} = 0.3$ ,  $\delta_b = 25\%$ , and  $\sigma_{\delta_b} = 3.0$ .

The merits of these estimated uncertainties can be objectively assessed. If they are used (eq 10) to correct the results of individual analyses, and if the uncertainties in the corrected values are assessed by use of eq 14, the results entered in the fourth column of Table II are obtained. The question then becomes, "Do the assigned confidence intervals include the correct result, or are they either too tight or too generous?" Comparison shows that significant differences between the

**Table II. Results of Repeated Analyses of Standards I and II**

date of analysis	$n_T$ ( $\mu\text{mol}$ of $\text{CO}_2$ )	$\delta^{13}\text{C}_{\text{obs}}$	$\delta^{13}\text{C}_{\text{corr}}^a$
10 Sept 1985	23.7	-28.88	-29.1 $\pm$ 0.4
12 Sept 1985	40.8	-29.14	-29.3 $\pm$ 0.2
	32.0	-28.96	-29.2 $\pm$ 0.3
	36.5	-29.15	-29.3 $\pm$ 0.3
17 Sept 1985	41.3	-29.44	-29.6 $\pm$ 0.2
	30.5	-29.41	-29.6 $\pm$ 0.3
27 Sept 1985	21.2	-29.39	-29.7 $\pm$ 0.5
3 Oct 1985	30.2	-29.27	-29.5 $\pm$ 0.3
	25.3	-29.20	-29.5 $\pm$ 0.4
	40.1	-29.22	-29.4 $\pm$ 0.3
28 May 1986	23.6	-29.05	-29.3 $\pm$ 0.4
29 May 1986	18.8	-29.12	-29.5 $\pm$ 0.5
	27.8	-28.88	-29.1 $\pm$ 0.4
	59.3	-29.63	-29.8 $\pm$ 0.2
9 July 1986	27.8	-28.87	-29.1 $\pm$ 0.3
10 July 1986	46.1	-29.04	-29.2 $\pm$ 0.2
30 July 1986	41.5	-29.03	-29.2 $\pm$ 0.2
	59.8	-29.24	-29.4 $\pm$ 0.2
	30.7	-29.26	-29.5 $\pm$ 0.3
16 Sept 1987	85.3	-29.56	-29.6 $\pm$ 0.1
5 May 1988	54.5	-29.23	-29.4 $\pm$ 0.2
	6.8	-28.43	-29.4 $\pm$ 1.8
	11.2	-28.82	-29.4 $\pm$ 1.0
	14.0	-28.82	-29.4 $\pm$ 0.8
	85.0	-28.96	-29.0 $\pm$ 0.2
	116.6	-29.18	-29.2 $\pm$ 0.1
5 Oct 1988 <sup>b</sup>	25.6	-17.75	-17.3 $\pm$ 0.4
	43.2	-17.60	-17.3 $\pm$ 0.3
	47.0	-17.91	-17.7 $\pm$ 0.2
	51.4	-17.53	-17.3 $\pm$ 0.2
	73.3	-17.47	-17.3 $\pm$ 0.2

<sup>a</sup>  $\delta_s \pm 2\sigma_s$ ; known isotopic composition, standard I,  $\delta^{13}\text{C}_{\text{PDB}} = -29.27 \pm 0.11\%$ ; corrected for influence of blank:  $n_b = 1.5 \pm 0.3$ ,  $\delta_b = -25 \pm 3\%$ . <sup>b</sup> Known isotopic composition, standard II,  $\delta^{13}\text{C}_{\text{PDB}} = -17.47 \pm 0.15\%$ .

corrected result and the accepted value appear in only 3 of 31 cases. For sample amounts larger than 5  $\mu\text{mol}$  of acetate, the procedure is evidently quite robust. Even when realistically variable characteristics are assigned to the blank (i.e., the wide standard deviations estimated above), the calculated 95% confidence intervals are commonly better than  $\pm 0.4\%$  and, more importantly, accurately reflective of the precision of the method in routine use.

**Methyl Group Analyses.** Results of isotopic analyses of methyl groups are also summarized in Table I. In one set of analyses (batch), standard samples of sodium acetate were pyrolyzed with sodium hydroxide according to the procedure described in the Experimental Section. In the other set (this procedure), acetic acid was liberated from the samples by treatment with oxalic acid and then chromatographically purified and trapped on sodium hydroxide for pyrolysis as described in the Experimental Section. Results indicate that isotopic fractionation of the methyl group of acetate does not occur with use of this technique.

**Efficiency of Recovery and Measurement of Quantities of Acetate.** Data from multiple analyses are summarized in a graph of the quantity of standard weighed before analysis vs the quantity of acetate measured after purification and combustion (Figure 3). Regression of the data yields a line with slope of 0.81, indicating an average yield of 81 ( $\pm 5$ )%. Recovery of the acetate with this technique is, therefore, not quantitative. However, as shown, values of  $\delta_s$  are accurate and, as illustrated in Figure 4, no relationship is observed between  $\delta_s$  and yield. Sample loss likely results from incomplete removal of the acetic acid from the reaction vessel.

**Resolution of Homologous Acids.** A 1:1:1 (weight ratio) mixture of sodium formate, sodium acetate (standard I), and sodium propionate was prepared to test the ability of this

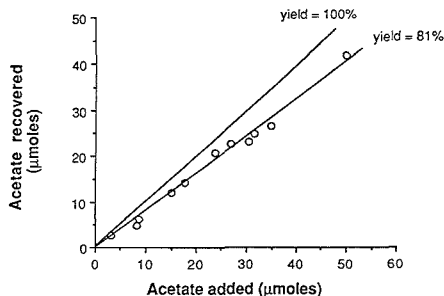


**Figure 3.** Data from multiple analyses of standards plotted to demonstrate 81% recovery of acetate.

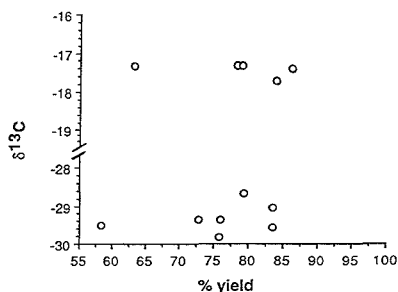


**Figure 4.** Data from multiple analyses of standards plotted to demonstrate that there is no relationship between  $\delta_s$  and yield.

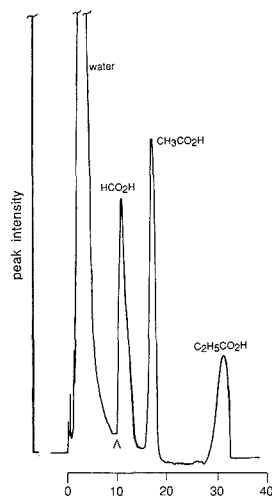


**Figure 5.** Sample chromatogram of formic, acetic, and propionic acids showing separation achieved in this technique. Arrow indicates time at which temperature was increased from 100 to 150  $^{\circ}\text{C}$ .

technique to separate these volatile fatty acids for isotopic analysis. As shown in Figure 5, separation of these compounds was achieved. Each acid was passed through the combustion furnace as it eluted from the chromatograph column. The procedure resulted in no isotopic fractionation (Table III).

## CONCLUSIONS

The technique described here provides an efficient method for isotopic analysis of acetate in mixtures of compounds.

**Table III. Accuracy of Isotopic Analyses of Chromatographically Separated Volatile Fatty Acids<sup>a</sup>**

	STC <sup>b</sup>	this technique
sodium formate	-32.0 ± 0.3 (2)	-32.3 ± 0.5 (3)
sodium acetate (std I)	-29.5 ± 0.1 (5)	-29.4 ± 0.1 (3)
sodium propionate	-32.2 ± 0.1 (2)	-32.3 ± 0.1 (3)

<sup>a</sup>Numbers in parentheses indicate number of measurements; uncertainties are 95% confidence limits. <sup>b</sup>Sealed-tube combustion.

Recovery of acetate as acetic acid is not quantitative, but there is no isotopic fractionation associated with incomplete yield. The primary advantage of this technique is its applicability to samples containing micromolar quantities of acetate. Large volumes of liquid containing low concentrations of acetate can be filtered and dried, with the acetate concentrated in the solid residue. This technique has been successfully applied to isotopic analysis of acetate in anaerobic, freshwater environments where concentrations of acetate are 20 μM.

#### ACKNOWLEDGMENT

We thank S. A. Studley for technical assistance.

#### LITERATURE CITED

- (1) Martens, C. S.; Blair, N. E.; Green, C. D.; DesMarais, D. J. *Science* **1986**, *233*, 1300-1303.

- (2) Whitcar, M. J.; Faber, E.; Schoell, M. *Geochim. Cosmochim. Acta* **1986**, *50*, 693-709.
- (3) Edwards, G. B.; McManus, W. R.; Bigham, M. L. *J. Chromatogr.* **1971**, *63*, 397-401.
- (4) Bethge, P. O.; Lindstrom, K. *Analyst* **1974**, *99*, 137-142.
- (5) Gardner, J. W.; Thompson, G. E. *Analyst* **1974**, *99*, 326-329.
- (6) Ansbaek, J.; Blackburn, T. H. *Microb. Ecol.* **1980**, *5*, 253-264.
- (7) Barcelona, M. J.; Liljestrand, H. M.; Morgan, J. J. *Anal. Chem.* **1980**, *52*, 321-325.
- (8) Christensen, D.; Blackburn, T. H. *Mar. Biol.* **1982**, *71*, 113-119.
- (9) Parkes, R. J.; Taylor, J. *Mar. Biol.* **1983**, *77*, 113-118.
- (10) Meinschein, W. G.; Rinaldi, G. G. L.; Hayes, J. M.; Schoeller, D. A. *Biomed. Mass Spectrom.* **1974**, *1*, 172-174.
- (11) Blair, N. E.; Leu, A.; Munoz, E.; Olsen, J.; Kwong, E.; DesMarais, D. E. *Appl. Environ. Microbiol.* **1985**, *50*, 996-1001.
- (12) Blair, N. E.; Martens, C. S.; DesMarais, D. J. *Science* **1987**, *236*, 66-68.
- (13) Tyler, J. E.; Dibdin, G. H. *J. Chromatogr.* **1975**, *105*, 71-77.
- (14) Molongoski, J. J.; Taylor, C. D. *Appl. Environ. Microbiol.* **1985**, *50*, 1112-1114.
- (15) Molongoski, J. J.; Klug, M. J. *Freshwater Biol.* **1980**, *10*, 507-518.
- (16) Jones, J. G.; Simon, B. M. *Appl. Environ. Microbiol.* **1985**, *49*, 947-948.
- (17) Kirsten, W. *Anal. Chem.* **1954**, *26*, 1097.
- (18) Buchanan, D. L.; Corcoran, B. J. *Anal. Chem.* **1959**, *31*, 1635-1638.
- (19) Oakwood, T. S.; Miller, M. R. *J. Am. Chem. Soc.* **1950**, *72*, 1849-1855.
- (20) Hayes, J. M.; DesMarais, D. M.; Peterson, D.; Schoeller, D.; and Taylor, S. P. *Adv. Mass Spectrom.* **1977**, *7*, 475-480.

RECEIVED for review July 28, 1989. Accepted December 12, 1989. This work has been supported by the National Aeronautics and Space Administration (NGR 15-003-118).

## CORRESPONDENCE

### Direct Resolution of Enantiomeric Diols by Capillary Gas Chromatography on a Chiral Polysiloxane Derived from (*R,R*)-Tartramide

*Sir:* Despite the great success in using a chiral stationary phase for affecting gas chromatographic enantiomer resolution, many problems still remain. Chiral diols, in particular, are important building blocks for the synthesis of natural products (1, 2), and thus, various gas chromatographic phases for determining enantio-excess in regard to asymmetric synthesis have been extensively studied (3-7). However, diols should be derivatized for application to gas chromatographic systems. For example, the enantiomer resolution of aliphatic diols as boronates and acetals has been carried out by complexation gas chromatography using optically active metal chelates by Schurig et al. (3). Aliphatic diol enantiomers have been resolved on XE-60-L-valine-(*R*)- $\alpha$ -phenylethylamide following conversion to cyclic carbonate using phosgen or by conversion to monoester with *N*-trifluoroacetyl-glycyl chloride on Chiral-Val (4, 5). König et al. conducted the enantiomer resolution of aliphatic diols as cyclic carbonates on a hexakis(3-*O*-acetyl-2,6-di-*O*-penty)- $\alpha$ -cyclodextrin chiral stationary phase and the enantiomer resolution of alicyclic 1,2- and 1,3-diols following trifluoroacetylation on heptakis(3-*O*-acetyl-2,6-di-*O*-penty)- $\beta$ -cyclodextrin (6, 7). These achiral derivatizations render the analytical procedure more complex.

In the present study, the direct enantiomer resolution of aliphatic and alicyclic diols without derivatization on a new chiral polysiloxane derived from (*R,R*)-tartramide was successfully conducted.

#### EXPERIMENTAL SECTION

**Apparatus.** The gas chromatograph was comprised of a Shimadzu GC-14A equipped with a split injector and flame ionization detector. Helium served as the carrier gas. The inlet pressure of the capillary column was adjusted to 0.9 kg/cm<sup>2</sup> and the split ratio was set at 1:60. The temperature of the injection port was maintained at 200 °C. Chromatographic signals were recorded and processed by a Shimadzu C-R4AX integrator.

**Reagents.** 3,3-Dimethyl-1,2-butanediol, 1,2-pentanediol, 2,4-pentanediol, 1,3-cyclopentanediol (mixture of *cis* and *trans*), and *trans*-1,2-cycloheptanediol were purchased from Aldrich. 1,2-Butanediol, 2,3-butanediol, 1,2-hexanediol, 2,5-hexanediol, 2-methyl-2,4-pentanediol, *trans*-1,2-cyclohexanediol, and 1,3-cyclohexanediol (mixture of *cis* and *trans*) were obtained from Tokyo Kasei and 1,2-propanediol and 1,3-butanediol, from Wako.

*trans*-1,2-Cyclopentanediol was synthesized according to the procedure of Owen et al. (8). *threo*- and *erythro*-2,3-Pentanediol were synthesized from *trans*- and *cis*-2-pentene, respectively, according to the literature (9).

**Synthesis of Chiral Polysiloxane.** Poly(hydromethylsiloxane) was synthesized according to the procedure of Bradshaw et al. (10). (*R,R*)-*N*-(10-Undecenyl)-*N'*-isopropylidene-tartramide was synthesized according to our own method (11).

Hydrosilylation was conducted in the presence of chloroplatinic acid. The resulting products were purified by using two Shodex GPC-A-80M columns in series with THF as the eluent. The pure acetyl polysiloxane thus obtained was hydrolyzed to give the gumlike product. IR (neat): 3600-3100, 2960, 2920, 1650, 1540,

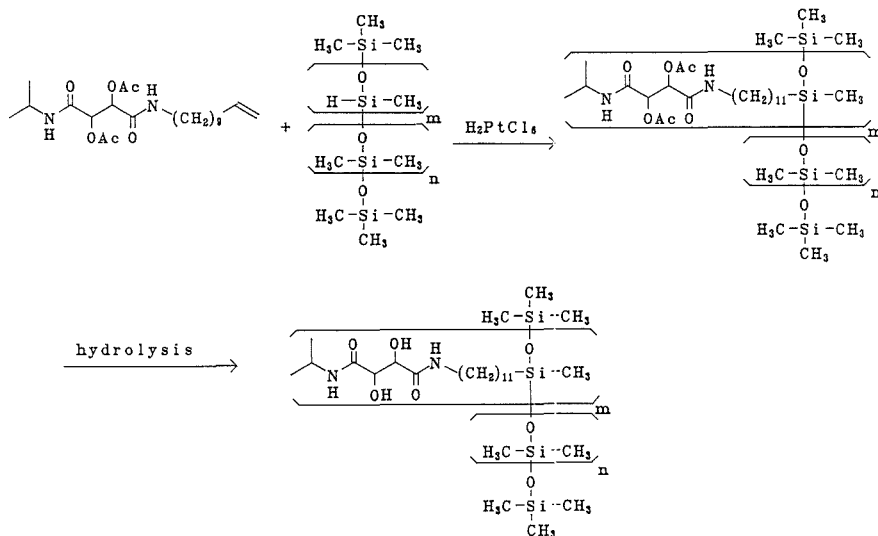
Scheme I. Synthetic Pathway of the Chiral Polysiloxane Derived from (*R,R*)-Tartramide

Table I. Gas Chromatographic Resolution of Enantiomeric Diols

compound	column temp, °C	$k_1'^a$	$k_2'^a$	$\alpha$	$R_s$
Aliphatic Diols					
1,2-propanediol	65	8.00	8.67	1.084	1.73
1,2-butanediol	65	17.31	18.21	1.052	1.89
1,2-pentanediol	65	37.08	38.19	1.030	0.92
1,2-hexanediol	75	41.38	42.02	1.015	0.71
1,3-butanediol	65	18.39	18.69	1.016	0.62
2,3-butanediol	65	7.32	7.71	1.053	1.25
2,4-pentanediol	65	20.90	21.85	1.045	1.87
2,5-hexanediol	65	54.52	55.49	1.018	0.86
2,3-pentanediol (threo)	65	13.40	13.72	1.024	0.78
(erythro)	65		15.88	1.000	
3,3-dimethyl-1,2-butanediol	65	33.32	35.44	1.064	2.34
2-methyl-2,4-pentanediol	65		17.05	1.000	
Alicyclic Diols					
<i>trans</i> -1,2-cyclopentanediol	90		18.37	1.000	
<i>trans</i> -1,2-cyclohexanediol	90	21.98	22.89	1.041	1.80
<i>trans</i> -1,2-cycloheptanediol	90	44.69	45.50	1.018	0.96
<i>trans</i> -1,3-cyclopentanediol	90	12.39	12.58	1.015	0.62
<i>trans</i> -1,3-cyclohexanediol	90	30.06	30.93	1.029	1.15

<sup>a</sup> Capacity factors were calculated according to (retention time of solute - retention time of methane gas)/retention time of methane gas.

1405, 1260, 1120-1000, 800  $\text{cm}^{-1}$ . Anal. Found: C, 38.86; N, 1.89; H, 8.36.

**Column Preparation and Efficiency.** A fused-silica capillary column (25 m  $\times$  0.25 mm i.d.) was washed with dichloromethane, dried through helium gas, and coated statically with a 0.30% solution of the chiral polysiloxane in dichloromethane. The column was subsequently conditioned with helium gas at a temperature range from 40 to 150 °C at 0.5 °C  $\text{min}^{-1}$ . The McReynolds constants were determined at 50 °C.  $\Delta I$  of each probe was obtained as 25 (benzene), 238 (1-butanol), 101 (2-pentanone), 121 (1-nitropropane), and 168 (pyridine), respectively. A TZ value of 35 (between *n*-nonane and *n*-decane) was obtained at the same temperature.

## RESULTS AND DISCUSSION

In our approach to the direct resolution of diol enantiomers by gas chromatography, the enantioselectivity of (*R,R*)-*N*,

*N'*-dialkyltartramide is applied. This derivative shows enantioselectivity toward a broad range of enantiomers through hydrogen bond association in solution (12). We have already developed a chiral stationary phase derived from (*R,R*)-tartramide for liquid chromatography and found it capable of directly resolving 1,2-diols (11). On the basis of the results of a NMR study and X-ray crystal analysis, the dual hydrogen bonds between amide carbonyls of tartramide and hydroxyls of 1,2-dioles were considered to be the association mode responsible for the observed enantioselection in solution (13).

Recently, novel chiral polysiloxanes derived from (*R,R*)-tartramide for gas chromatographic enantiomer resolution were prepared at our laboratory (14). Although its scope of application is relatively restricted, the resolution observed on these phases indicated the enantioselectivity of (*R,R*)-tartramide exerted in solution to also be applicable to the gas chromatographic systems.

To improve the performance of the chiral stationary phase derived from (*R,R*)-tartramide, the structure and preparation of the chiral polysiloxane were examined. In a newly designed chiral polysiloxane, the tartramide moiety was attached to the polysiloxane backbone through the long alkyl chain consisting of 11 methylene units. Increase in the distance between the polysiloxane backbone and tartramide moiety may enhance the accessibility of the solute enantiomers to tartramide moiety. The synthetic pathway presented in Scheme I involves the hydrosilylation of polyhydromethylsiloxane with alkenyl tartramide derivative. By this method of preparation, there can be no residual hydrogen bond sites such as amino and/or cyano functions which interact with solute enantiomers without enantioselectivity. The chiral polysiloxane obtained provided greater thermal stability than the previously developed chiral polysiloxane whose four methylene units served as a linkage of tartramide moiety to polysiloxane and underwent no loss of weight up to 240 °C, according to thermogravimetric analysis.

The new chiral polysiloxane was found to provide a greater scope of chiral recognition. As expected from the enantioselectivity of the (*R,R*)-tartramide in solution, the direct enantiomer resolution of diols by gas chromatography was possible without the need for derivatization on a new chiral polysiloxane derived from (*R,R*)-tartramide. The chromato-

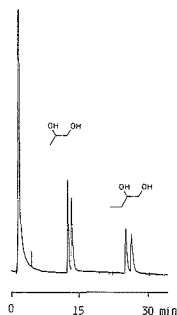


Figure 1. Enantiomer resolution of 1,2-propanediol and 1,2-butanediol: column temperature, 65 °C isothermal; carrier gas, 0.9 kg/cm<sup>2</sup> He.

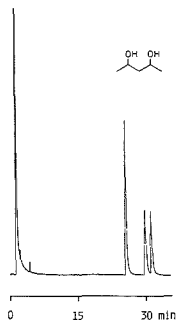


Figure 2. Separation of three isomers of 2,4-pentanediol: column temperature, 65 °C isothermal; carrier gas, 0.9 kg/cm<sup>2</sup> He.

graphic data are summarized in Table I.

In the case of aliphatic 1,2-diols, the highest separation factor  $\alpha$  of 1.084 was obtained from 1,2-propanediol, and the separation factors of aliphatic 1,2-diols decreased with the length of the main chain. The elution order was determined with (S)-(+)-1,2-propanediol (obtained from Aldrich). The S enantiomer was eluted prior to the R enantiomer. The absolute configuration is generally related to the elution order on chiral stationary phases. The S enantiomers of other aliphatic 1,2-diols may thus possibly be consistently eluted prior to R enantiomers. Figure 1 shows the enantiomer resolution of 1,2-propanediol and 1,2-butanediol.

Enantiomer resolution of aliphatic diols with C<sub>2</sub> symmetry was also successfully conducted. Figure 2 shows the enantiomer resolution of 2,4-pentanediol. The complete separation of three stereoisomers of 2,4-pentanediol was successfully carried out. As shown in Table I, the separation factors of aliphatic diols with C<sub>2</sub> symmetry varied according to the distance separating the two hydroxyls, and it is significant that the enantiomers of 2,5-hexanediol were separated when the separation factor was 1.018. Although a number of aliphatic diols was separated, this was not possible for the enantiomers of 2-methyl-2,4-pentanediol.

For 2,3-pentanediol containing threo and erythro isomers, the enantiomer resolution of *threo*-2,3-pentanediol was possible with a separation factor  $\alpha$  of 1.024 but that of the erythro isomer could not be done owing to anti conformation of the two hydroxyls (12).

Although the enantiomer resolution of *trans*-1,2-cyclohexanediol was previously achieved without derivatization on Chirasil-Val, it could not be done in the case of other alicyclic diols (5, 15). That of a series of alicyclic diols was achieved on a chiral polysiloxane derived from (*R,R*)-tartaric acid as shown in Table I. Figure 3 shows the direct enantiomer

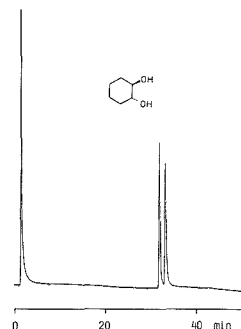


Figure 3. Enantiomer resolution of *trans*-1,2-cyclohexanediol: column temperature, 90 °C isothermal; carrier gas, 0.9 kg/cm<sup>2</sup> He.

resolution of *trans*-1,2-cyclohexanediol. Although *trans*-1,2-cyclopentanediol was not resolved, *trans*-1,3-cyclopentanediol was so with a separation factor  $\alpha$  of 1.015. The separation factor of *trans*-1,2-cyclohexanediol exceeded that of *trans*-1,3-cyclopentanediol.

The present new chiral polysiloxane was shown to function as a highly efficient stationary phase for the gas chromatographic resolution of diol enantiomers with small molecular weight. The enantioselectivity of (*R,R*)-tartramide based on hydrogen bond association is regenerated in the gas chromatographic system which permits highly sensitive detection and highly efficient resolution. In this paper, our discussion has been limited to the resolution of diol enantiomers. However, this chiral polysiloxane has a broad scope of application for enantiomer resolution. The extended application of polysiloxane derived from (*R,R*)-tartramide will be reported in the near future.

## LITERATURE CITED

- (1) Mori, K.; Sasaki, M.; Suguro, T.; Masuda, S. *Tetrahedron* **1979**, *35*, 1601-1605.
- (2) Asami, M.; Mukaiyama, T. *Chem. Lett.* **1983**, 93-96.
- (3) Schurig, V.; Wistuba, D. *Tetrahedron Lett.* **1984**, *25*, 5633-5636.
- (4) König, W. A.; Steinback, E.; Ernst, K. *Angew. Chem., Int. Ed. Engl.* **1984**, *23*, 527-528.
- (5) Koppenhoefer, B.; Walsler, M.; Bayer, E.; Abdalla, S. *J. Chromatogr.* **1986**, *358*, 159-168.
- (6) König, W. A.; Lutz, S.; Colberg, C.; Schmidt, N.; Wenz, G.; Bey, E.; Mosandl, A.; Günther, C.; Kustermann, A. *HRC CC, J. High Resolut. Chromatogr. Chromatogr. Commun.* **1988**, *11*, 621-625.
- (7) König, W. A.; Lutz, S.; Wenz, G.; Bey, E. *HRC CC, J. High Resolut. Chromatogr. Chromatogr. Commun.* **1988**, *11*, 506-509.
- (8) Owen, L. N.; Smith, P. N. *J. Chem. Soc.* **1952**, 4026-4035.
- (9) Milas, N. A.; Sussmann, S. *J. Am. Chem. Soc.* **1936**, *58*, 1302-1304.
- (10) Bradshaw, J.; Aggarwal, S. K.; Rouse, C. A.; Tarbet, B. J.; Markides, K. E.; Lee, M. L. *J. Chromatogr.* **1987**, *405*, 169-177.
- (11) Dobashi, Y.; Hara, S. *J. Org. Chem.* **1987**, *52*, 2490-2496.
- (12) Dobashi, Y.; Hara, S. *J. Am. Chem. Soc.* **1985**, *107*, 3406-3411.
- (13) Dobashi, Y.; Hara, S.; Iitaka, Y. *J. Org. Chem.* **1989**, *53*, 3894-3896.
- (14) Nakamura, K.; Hara, S.; Dobashi, Y. *Anal. Chem.* **1989**, *61*, 2121-2124.
- (15) Koppenhoefer, B.; Allmendinger, H.; Nicholson, G. *Angew. Chem., Int. Ed. Engl.* **1985**, *24*, 48-49.

Kouji Nakamura\*  
Takafumi Saeki  
Masaaki Matsuo

Analytical Chemistry Research Laboratory  
Tanabe Seiyaku  
3-16-89 Kashima, Yodogawa-ku, Osaka 532  
Japan

Shoji Hara  
Yasuo Dobashi

Tokyo College of Pharmacy  
1432-1 Horinouchi, Hachioji, Tokyo 192-03  
Japan

RECEIVED for review September 19, 1989. Accepted November 28, 1989.

## TECHNICAL NOTES

### Palladium Gate Metal-Oxide-Semiconductor Oxygen Sensors

Jonas Karlsson, Mårten Armgarth, Svante Ödman,<sup>1</sup> and Ingemar Lundström\*

Laboratory of Applied Physics, Linköping Institute of Technology, S-581 83 Linköping, Sweden

#### INTRODUCTION

Chemical sensors are electronic devices that are subjected to variations in the composition of their ambient. These variations may introduce not only the wanted electrical signal but also hysteresis and drift phenomena in the devices. We therefore found it of general interest to study the behavior of chemical sensors continuously operated close to steady state in terms of the response to the ambient. As an example we have studied the oxygen sensitivity of Pd metal-oxide-semiconductor (PdMOS) field effect hydrogen sensors. This has been done for two reasons: first, the indirect oxygen sensitivity of the PdMOS hydrogen sensors is well established (1, 2) and second, fast oxygen sensors with high-resolution capability should be very useful for measurements of small variations of oxygen concentration, e.g., in expired air.

The hydrogen sensitivity of the PdMOS field effect transistor is explained by the fact that hydrogen gas adsorbs and dissociates on the catalytic Pd surface (1). Hydrogen atoms formed diffuse rapidly through the thin gate and adsorb at the metal-insulator interface, which gives rise to a change of the electrical field in the gate insulator of the FET, hence decreasing the threshold voltage of the device. It was observed that the response to hydrogen of this very sensitive and selective sensor decreased in the presence of oxygen in the ambient. A catalytic combustion of hydrogen by oxygen to water on the Pd surface explains the reduction of the response to hydrogen. The response of the PdMOS devices to hydrogen in oxygen is reported to follow a Langmuir-like expression in steady state (1)

$$\Delta V = \Delta V_{\max} c (P_{\text{H}_2}/P_{\text{O}_2})^{1/2} / (1 + c(P_{\text{H}_2}/P_{\text{O}_2})^{1/2}) \quad (1)$$

where  $\Delta V$  is the change in threshold voltage of the PdMOS transistor.  $\Delta V_{\max}$  is about 0.5 V and  $c$  is a constant that depends on the rate constants governing the catalytic reactions between hydrogen and oxygen on the surface of the palladium gate.  $P_{\text{H}_2}$  and  $P_{\text{O}_2}$  denote the partial pressures of hydrogen and oxygen, respectively. With  $P_{\text{H}_2}$  in parts per million and  $P_{\text{O}_2}$  in percent, the constant  $c$  is typically about 0.1-0.5.

Only a few attempts have been made earlier to use the oxygen sensitivity of the hydrogen sensor to determine oxygen. The reason for this is the lack of a practical, reliable method to counteract some drift phenomena induced by hydrogen in the PdMOS devices (3). On the other hand, there have been observations of large changes in the response to hydrogen due to changes in the oxygen concentration at a given hydrogen to oxygen concentration ratio ( $P_{\text{H}_2}/P_{\text{O}_2} \approx 0.4$ ). This ratio is rationalized by the fact that the catalytic metal surface transforms from being oxygen to hydrogen covered at that number (4). The ratio may depend on the catalytic metal used (5). Also this effect turned out to be difficult to use due to, among other things, the hydrogen-induced drift mentioned above. The uncertainty of the response around the point of the steep change has been estimated to be at least 10%, which does not give the necessary resolution in oxygen concentration.

<sup>1</sup>Center for Microtechnology, Linköping Institute of Technology, S-581 83 Linköping, Sweden.

We show here that small perturbations from a steady-state response can be used to detect oxygen with a high sensitivity. In such experiments, the sensor is exposed to a mixture of a given hydrogen gas concentration and an oxygen reference gas concentration within the actual measurement range. When the sensor signal has reached steady state, the gas to be tested and the oxygen reference gas are pulsed consecutively into the hydrogen gas stream, flowing continuously over the sensor (see the insert of Figure 1). The changes in threshold voltage are then in the order of  $\pm 10$  mV, which is much lower than the 100 mV changes obtainable at the critical  $P_{\text{H}_2}/P_{\text{O}_2}$  ratio (4). Still, these changes are well above the noise level of the threshold voltage. The threshold voltage change can be negative or positive depending on whether the oxygen concentration is highest in the test or reference gas as illustrated in Figure 1. The change in the threshold voltage is given by

$$\delta V = \Delta V(t_p P_{\text{O}_2} P_{\text{H}_2}) - \Delta V(t'_p P_{\text{O}_2}^{\text{ref}} P_{\text{H}_2}) \quad (2)$$

where  $t_p$  and  $t'_p$  are the durations of the test gas and the reference gas pulses, respectively. Since  $\Delta V$  in eq 2 is limited by the steady-state responses given by eq 1, then

$$\delta V < \Delta V_{\max} [c(P_{\text{H}_2}/P_{\text{O}_2})^{1/2} / (1 + c(P_{\text{H}_2}/P_{\text{O}_2})^{1/2}) - c(P_{\text{H}_2}/P_{\text{O}_2}^{\text{ref}})^{1/2} / (1 + c(P_{\text{H}_2}/P_{\text{O}_2}^{\text{ref}})^{1/2})] \quad (3)$$

It can readily be seen that the maximum response  $\delta V_{\max}$  for a given difference in oxygen concentration of the test gas and the reference gas, is obtained by choosing the hydrogen concentration to

$$P_{\text{H}_2} = (P_{\text{O}_2} P_{\text{O}_2}^{\text{ref}} / c^2)^{1/2} \quad (4)$$

giving

$$\delta V_{\max} < \Delta V_{\max} (1 - (P_{\text{O}_2} / P_{\text{O}_2}^{\text{ref}})^{1/4}) / (1 + (P_{\text{O}_2} / P_{\text{O}_2}^{\text{ref}})^{1/4}) \approx 0.125 \Delta V_{\max} (1 - P_{\text{O}_2} / P_{\text{O}_2}^{\text{ref}}) \quad (5)$$

The maximum sensitivity is estimated to be 3 mV/%  $\text{O}_2$  change with an assumed  $P_{\text{O}_2}^{\text{ref}} = 20\%$  and  $\Delta V_{\max} = 0.5$  V. The linear approximation in eq 5 introduces a relative error < 10% in the range of 16% to 24%  $\text{O}_2$ .

It should be pointed out that also other catalytic metals, like Pt and Ir, show hydrogen sensitivity in the presence of oxygen. A comparison between different metals (6) and especially between Pd and Pt (5) indicates that Pd is the metal of choice for the present application.

#### EXPERIMENTAL DETAILS

The hydrogen sensor used in the experiments was a PdMOS field effect transistor integrated with a temperature control circuit. The sensor was operated at 150 °C. The sensor was connected to a hydrogen leak detector (Sensistor Model 12N). It gives a voltage output which is a measure of the threshold voltage of the PdMOS hydrogen sensor. The gas manifold used was a computerized, general purpose system, designed for mixing different gases (from bottles) under well-controlled conditions. The different gas flows were regulated by mass flow controllers. The gas manifold was controlled by a PC (Ericsson), enabling automatic setting of the desired parameters building up a test sequence. The

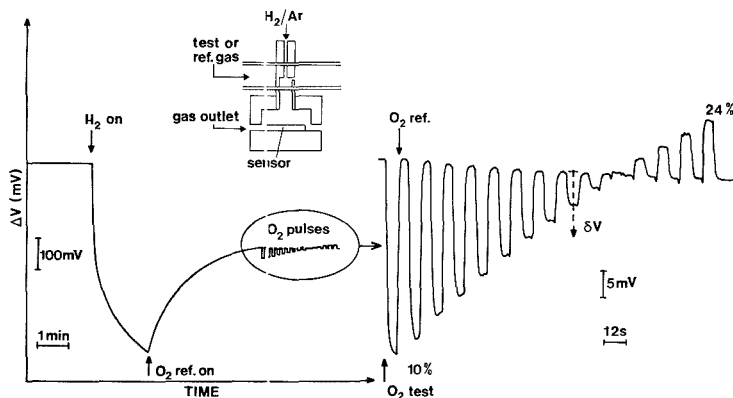


**Figure 1.** Example of the sensor response. The sensor, operating at 150 °C, is exposed to 850 ppm H<sub>2</sub> in argon (H<sub>2</sub> on). After a few minutes, the O<sub>2</sub> reference gas is mixed into the hydrogen/argon stream through the ejector. When a steady state is achieved, the sensor is exposed to alternating test and reference gas pulses. Response to 6 s long alternating exposures to test and reference gases, respectively. The O<sub>2</sub> concentration in the test gas varied from 10 to 24%. The reference gas contained nominally 20% O<sub>2</sub>.  $\delta V$  defined by eq 2 is indicated in the drawing. According to this definition  $\delta V > 0$  when the test gas contains less oxygen than the reference gas. Insert: Ejector used to mix the hydrogen containing carrier gas with the oxygen containing gas (see the text for further description).

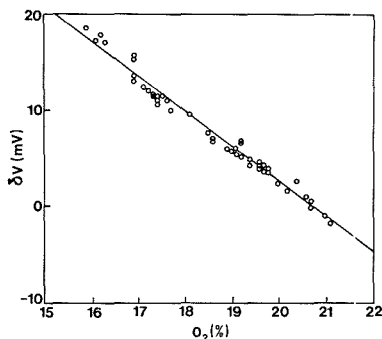


**Figure 2.** Sensor response  $\delta V$  (defined by eq 2 and in Figure 1) for 6 s long O<sub>2</sub> pulses with randomized O<sub>2</sub> concentration in the test gas pulses. The O<sub>2</sub> concentration in the reference gas is determined to 20.7% from the drawing (at  $\delta V = 0$ ).

gas flows containing the oxygen/argon mixtures were stabilized, while fed to a gas drain, before they were switched over to the sensor. However, for pulse times shorter than about 1 s, a complete stability of the gas concentrations was not obtained.

The hydrogen- and oxygen-containing gases were mixed in an ejector before reaching the sensor. A schematic of the ejector is shown as an insert of Figure 1. It was made out of two steel tubes (actually surgical cannulas) where the inner one ended close to a hole in the outer tube. Hydrogen in argon with a flow rate of 60 mL/min passed through the inner tube. Measurements showed that flow rates above 40 mL/min were enough to cause a vacuum, which sucked gas through the hole in the wall. The gas stream outside the ejector consisting either of the test or the reference gas flowed through a wider tube with low resistance to flow. The flow rate through this tube was 260 mL/min.

The amount of gas sucked through the hole in the ejector was not known. The gas composition at the sensor was therefore unknown. It is, however, not necessary to know that composition in the present mode of operation.

The measurement setup was tested for a number of different parameters, such as the duration of the test and reference gas pulses and hydrogen and oxygen flow rates. Each measurement series was initiated by exposing the sensor to a mixture of the oxygen reference gas and the hydrogen gas for a few minutes. With this procedure, the sensor response was allowed to reach almost steady state before the actual measurements started (see Figure 1).

The influence of pulse duration was, as expected, that the response increased with increased pulse duration. In the case of a 1-s pulse, the gas manifold system was too slow. However, since the responses for 6- and 11-s pulses were about the same, the response must saturate rather fast with time. In fact, the response curves have a nearly rectangular waveform (see Figure 1). This implies that greater pulse durations do not need to be well controlled, still having a high overall measurement accuracy. Secondly, the response of the hydrogen sensors is rather fast, upon a small change in the gas composition, compared with the response with rather long response times when the oxygen gas is introduced (see Figure 1). This difference can be explained by the fact that when a steady state has been obtained, both the hydrogen adsorption sites giving the Langmuir-like response and the sites responsible for the drift are in equilibrium with hydrogen in the palladium. The hydrogen-induced drift is attributed to hydrogen adsorption sites on the oxide side of the Pd-SiO<sub>2</sub> interface. They appear to be determined by (sodium) impurities in the oxide (3). The time constants for hydrogen adsorption and desorption in these sites are, however, much longer than the duration of the oxygen pulses. The occupancy of the slow sites does not change significantly during a single oxygen pulse. The pulse response is therefore rapid and reproducible even if there may be a slow base-line drift (as observed in Figure 1).

A too low, or too high, hydrogen concentration will decrease the sensitivity. However, a large interval of useful hydrogen concentrations was found. As a consequence the hydrogen concentration does not have to be carefully controlled to maintain the maximum sensitivity. From eqs 3-5, it is found that the hydrogen concentration can be increased by a factor of 4, or decreased to one-fourth, of the optimum value, keeping the sensitivity within 90% of the maximum value.

In the present mode of operation, the interference from other molecules is expected to be small. Hydrogen sulfide gives hydrogen-like responses. Molecules like ethanol and ethylene give only small response at an operation temperature of 150 °C. Since there is hydrogen in the ambient of the sensor all the time and since the hydrogen concentration is not critical, their influence will, however, be small. Oxidizing molecules like chlorine and hydrogen peroxide in the test gas may interfere with the oxygen-induced pulse response. It is not likely, however, that they will be present in large enough concentrations in the applications envisaged. Water vapor does not interfere with the Pd-gate device operated at 100-150 °C. At operation temperatures below 100 °C, water vapor may interfere with the oxygen signal.

## RESULTS

The results in the right-hand part of Figure 1 were obtained with the oxygen concentration in the test gas changed in steps

of 1%. No hysteresis was observed going up and down in the oxygen concentration.

In Figure 2, the sensor was exposed to a number of test gas pulses with randomized oxygen concentrations keeping the oxygen concentration in the reference gas pulse constant. It was observed that the spread in the data occurred upon large successive changes in the oxygen concentration. The spread is assumed to be caused mainly by the gas manifold, due to hysteresis and delays in the valves.

The sensitivity to oxygen can be estimated, from the slope of the curve in Figure 2, to 3.6 mV/% O<sub>2</sub> change, which should be compared to the estimated value of 3 mV/% O<sub>2</sub> from eq 5 assuming  $\Delta V_{\max} = 0.5$  V.

In conclusion we have shown that it is possible to use a PdMOS sensor for oxygen. This is achieved by the use of short alternating exposures of the sensor to a reference gas and the gas to be tested. Hence a high sensitivity and a fast detection of small changes in the oxygen concentration around 20% O<sub>2</sub> were demonstrated. The concept may be described as keeping the sensor in a mode of operation that is always as close as possible to steady state. The hydrogen reference gas concentration and the length of the oxygen pulses do not have to be critically controlled. The range may be extended outside the 15–24% O<sub>2</sub> studied here with a loss of linearity at large deviations from the reference gas concentration. The most

appropriate way to extend the dynamic range is, however, to change the oxygen concentration in the reference gas and the background hydrogen concentration. Further work will include improvements in the gas manifold, minimizing dead spaces in valves to optimize the time response. Furthermore, field tests are imperative to evaluate the possibilities of the described method for the monitoring of oxygen, e.g., in expired air.

#### LITERATURE CITED

- (1) Lundström, I.; Svensson, C. In *Solid State Chemical Sensors*; Janata, J., Hlber, R. J., Eds.; Academic Press: New York, 1985; pp 1–63.
- (2) Lundström, I.; Söderberg, D. In *Monitoring of Vital Parameters during Extracorporeal Circulation*, Kimmich, H. P., Ed.; Karger: Basel, 1981; pp 281–296.
- (3) Nylander, C.; Armgarth, M.; Svensson, C. *J. Appl. Phys.* **1984**, *56*, 1177–1188.
- (4) Söderberg, D.; Lundström, I. *Solid State Commun.* **1983**, *45*, 431–434.
- (5) Armgarth, M.; Söderberg, D.; Lundström, I. *Appl. Phys. Lett.* **1982**, *41*, 654–655.
- (6) Yamamoto, N.; Tonomura, S.; Matsuo, T.; Tsubomura, H. *Surf. Sci.* **1980**, *92*, 400–406.

RECEIVED for review May 19, 1989. Revised manuscript received October 18, 1989. Accepted November 27, 1989. Our work on chemical sensors is supported by a grant from the National Swedish Board for Technical Development.



# JANAF THERMOCHEMICAL TABLES

## Third Edition

A Major Supplement from JOURNAL OF PHYSICAL AND CHEMICAL REFERENCE DATA

Presenting Reliable Data Utilized by Chemists, Chemical Engineers, and Materials Scientists from Around the World for Over 25 Years

JOURNAL OF PHYSICAL AND CHEMICAL REFERENCE DATA is very pleased to publish the Third Edition of the JANAF THERMOCHEMICAL TABLES.

Since the first version appeared 25 years ago, the JANAF THERMOCHEMICAL TABLES have been among the most widely used data tables in science and engineering.

You'll find:

- Reliable tables of thermodynamic properties of substances of wide interest
- A highly professional approach with critical evaluations of the world's thermochemical and spectroscopic literature
- A concise and easy-to-use format

This Third Edition presents an extensive set of tables including thermodynamic properties of more than 1800 substances, expressed in SI units. The notation has been made consistent with current international recommendations.

There is no other reference source of thermodynamic data that satisfies the needs of such a broad base of users.

Order your 2-volume set of the JANAF THERMOCHEMICAL TABLES today! You'll get over 1890 pages of valuable information that is crucial to your research—in two hardback volumes.

### SUBSCRIPTION INFORMATION

The JANAF THERMOCHEMICAL TABLES, THIRD EDITION is a two-volume supplement of *Journal of Physical and Chemical Reference Data*.

1896 pages, 2 volumes, hardcover  
ISBN 0-88318-473-7  
Supplement Number 1 to Volume 14, 1985

U.S. & Canada	\$130.00
All Other Countries	\$156.00

(Postage included.)

All orders for supplements must be prepaid.

Foreign payment must be made in U.S. currency by international money order, UNESCO coupons, U.S. bank draft, or order through your subscription agency. For rates in Japan, contact Maruzen Co., Ltd. Please allow four to six weeks for your copy to be mailed.

For more information, write American Chemical Society, Marketing Communications Department, 1155 Sixteenth Street, NW, Washington, DC 20036.

In a hurry? Call TOLL FREE **800-227-5558** and charge your order!

#### Editors:

**M.W. Chase, Jr.**  
National Institute of  
Standards and Technology

**C.A. Davies**  
Dow Chemical U.S.A.

**J.R. Downey, Jr.**  
Dow Chemical U.S.A.

**D.J. Frurip**  
Dow Chemical U.S.A.

**R.A. McDonald**  
Dow Chemical U.S.A.

**A.N. Syverud**  
Dow Chemical U.S.A.



Published by the American Chemical Society and the American Institute of Physics for the National Institute of Standards and Technology

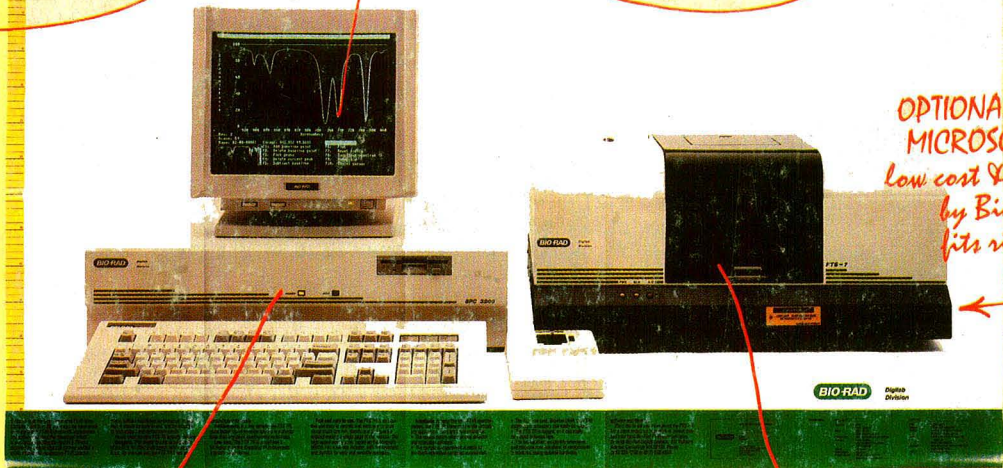
# A low cost FT-IR spectrometer that fits virtually all routine applications.

*BRAND NEW Spectrometer from Bio-Rad, the leader in high performance FT-IR.*

*INTUITIVE OPERATION. Novices & experts alike can use it without reading the manual.*

*LOW COST... just a little more than dispersive IR. Fits nicely into the budget.*

## FTS 7R: A Compact FT-IR With A Compact Price.



*OPTIONAL MICROSCOPE. Low cost & made by Bio-Rad fits right here*

*POWERFUL DATA SYSTEM ...can do search & quantitative analysis (with options).*

*SMALL FOOTPRINT. Occupies little bench space. Needs NO H<sub>2</sub>O or N<sub>2</sub>.*

*RUNS ALL SAMPLES. Accepts Bio-Rad's high performance sampling accessories.*

### Try the FTS 7R on for size. Send for our life size presentation (above).

Bio-Rad, the FT-IR technology leader, is proud to introduce the FTS 7R™, a new FT-IR spectrometer with a small footprint and a small price tag, but with so many options and accessories that it can be configured to fit virtually any analytical application.

"Fit" is a key word here. That's why we produced a life sized poster. We want you to "size up" our new FTS 7R against the needs of your laboratory.

As you spread out the poster, you will see how Bio-Rad has engineered a high sensitivity FT-IR spectrometer into a compact package.

To ask for your poster, call (617) 868-4330. Or fill out this coupon and return it to: Bio-Rad Digilab Division, 237 Putnam Ave. Cambridge, MA 02139.

Name: \_\_\_\_\_

Title: \_\_\_\_\_

Company: \_\_\_\_\_

Street & No.: \_\_\_\_\_

City & State: \_\_\_\_\_ Zip: \_\_\_\_\_

Telephone: \_\_\_\_\_

**BIO-RAD**

**Digilab  
Division**